ICSET2023

ISBN: 978-604-920-208-7

THE 2023 INTERNATIONAL CONFERENCE ON SUSTAINABLE ENERGY TECHNOLOGIES

The 2023 International Conference on Sustainable Energy Technologies

PROCEEDING – ICSET2023

November 9-11, 2023

Organized by
Industrial University of Ho Chi Minh City (IUH)
Vietnamese-German University (VGU)
Ho Chi Minh City University of Technology (HUTECH)
Department of Science and Technology of Ho Chi Minh City

International Conference on Sustainable Energy Technologies (ICSET2023)

INDUSTRIAL UNIVERSITY OF HO CHI MINH CITY
PUBLISHING HOUSE

The International Conference on Sustainable Energy Technologies - 2023

PROCEEDING Sustainable Energy Technologies

ICSET2023

November 9-11, 2023

Organized by

Industrial University of Ho Chi Minh City (IUH), Vietnam

Vietnamese-German University (VGU), Vietnam

Ho Chi Minh City University of Technology (HUTECH), Vietnam

Department of Science and Technology (DOST), Ho Chi Minh City, Vietnam

INDUSTRIAL UNIVERSITY OF HO CHI MINH CITY PUBLISHING HOUSE

The 2023 International Conference on Sustainable Energy Technologies –(ICSET 2023)

Editors

Sivanappan Kumar, Faculty of Engineering, Naresuan University, Phitsanulok Province, Thailand.

Seung-Bok Choi, Department of Mechanical Engineering, State University of New York, Korea (SUNY Korea) Incheon, Korea.

Hung Quoc Nguyen, Faculty of Engineering and Director of Industrial Relation and Technology Transfer Center (IRTTC), Vietnamese German University (VGU) 4th Ring Road, Thoi Hoa Commune, Ben Cat District, Binh Duong Province, Vietnam.

Djourkov Todor Georgiev, Department of Technology of Tobacco, Sugar, Vegetable And Essential Oils, University of Food Technologies, Bulgaria, Plovdiv, Bulgaria.

Hung Xuan Nguyen, CIRTech Institute, Ho Chi Minh City University of Technology (HUTECH), Binh Thanh District, Ho Chi Minh City, Vietnam.

Thanh Trung Bui, Faculty of Heat and Refrigeration Engineering, Industrial University of Ho Chi Minh City, Go Vap District, Ho Chi Minh City, Vietnam.

Preface

On behalf of the Organizing Committee, we are delighted to issue the proceeding of Sustainable Energy Technologies (ICSET 2023), held from 9-11 November 2023 at the Industrial University of Ho Chi Minh City, Ho Chi Minh City, Vietnam.

This year 2023, the ICSET 2023 at the Industrial University of Ho Chi Minh City would like to evolve into one of the leading academic conferences in the field of sustainable energy technologies through insightful lectures and presentations for even more attendees.

During the conference, we were particularly pleased with the extended exchanges between the existing participants and Vietnamese researchers. The Industrial University of Ho Chi Minh City (IUH) hosted joint workshops in collaboration with the Vietnamese-German University (VGU), the Ho Chi Minh City University of Technology (HUTECH), and the Department of Science and Technology of Ho Chi Minh City.

The purpose of this ICSET2023 is to explore and ensure an understanding of critical aspects contributing to sustainable energy development, especially new technologies of energy and energy use, materials, machines, and methods. From such understanding, the conference aims to provide an overall approach to assist policymakers, industries, and researchers at various levels in positioning local technological development towards sustainable energy development in the global context. The goal is to aid decision-making for a greener approach, particularly concerning materials, machines, and methods.

We would like to express our gratitude to the members of the International Organizing and Academic Committees of the conference, for their hard work and advice which was helpful in maintaining the high level of the conference. We thank to Vingroup Innovation Foundation (VINIF – VINBIGDATA) for the sponsorship of the International Conference "Sustainable Energy Technologies - ICSET 2023". We also thank the Industrial University of Ho Chi Minh City publishing house for publishing the selected papers. We hope that all the papers will serve as a valuable source of information for academics, researchers, engineers, and students in their scientific work.

Best regards!

Sivanappan Kumar
Djourkov, Todor Georgiev.
Seung-Bok Choi
Hung Xuan Nguyen
Hung Quoc Nguyen
Thanh Trung Bui

Committees

1. Organizing Committee

- Assoc. Prof. Bui Trung Thanh, Faculty of Heat & Refrigeration Engineering, Industrial University of Ho Chi Minh City, Vietnam
- Assoc. Prof. Trinh Ngoc Nam. Director of Office for Science management & International affair of Industrial University of Ho Chi Minh City (IUH)
- Dr. Trung Vinh La Acting Head of Research Management Vietnamese German University (VGU)
- Assoc. Prof. Viet Pham Van, Ho Chi Minh City University of Technology (HUTECH)

2. International Organizing Committee

Prof. Djourkov Todor Georgiev	Department of Technology of Tobacco, Sugar, Vegetable And Essential Oils, University of Food Technologies, Bulgaria, Plovdiv, Bulgaria
Prof. Sivanappan Kumar	Faculty of Engineering, Naresuan University, Thailand
Prof. Seung-Bok Choi	Department of Mechanical Engineering, State University of New York, Korea (SUNY Korea) Incheon, Korea
Prof. Trygve Magne Eikevik	Department of Energy and Process Engineering, Faculty of Engineering, Norwegian University of Science and Technology, Kingdom of Norway
Prof. Dung-An Wang	Distinguished Professor, Graduate Institute of Precision Engineering, National Chung Hsing University, Taiwan.
Prof. Bong-Kee Lee	Multiscale Molding & Manufacturing (M3) Lab. @ CNU, School of Mechanical Engineering, Chonnam National University, Korea
Prof. Ruey-Lung Hwang,	Heat Engineering, National Kaohsiung Normal University
Prof.Tanongkiat Kiatsiriroat,	Faculty of Engineering, Chiang Mai University, Thailand.
Prof. Professor Herri Susanto,	Faculty of Chemical Engineering, Bandung Institute of Technology, Indonesia

3. International & Scientific Advisory Committee

Prof. Nguyen Xuan Hung	Director of Computational Mechanics, CIR Tech Institute, Ho Chi Minh City University of Technology (HUTECH), Vietnam
Prof. Nguyen Quoc Hung	Dean of Faculty of Engineering, Vietnamese-German University (VGU), Vietnam
Prof. Le Chi Hiep	Faculty of Mechanical Engineering Ho Chi Minh City University of Technology, Vietnam
Prof. Nguyen Hay	Faculty of Engineering & Technology, Nong Lam University, Vietnam
Prof. Nguyen Thanh Nam	Faculty of Mechanical Engineering, Industrial University of Ho Chi Minh City, Vietnam
Prof. Ho Pham Huy Anh	Faculty of Electrical – Electronics, Ho Chi Minh City University of Technology, Vietnam
Assoc. Prof. Pham Hoang Luong	Hanoi University of Science and Technology, Vietnam
Assoc. Prof. Nguyen Duc Nam	Faculty of Mechanical Engineering, Industrial University of Ho Chi Minh City, Vietnam

Assoc. Prof. Nguyen Huy Bich	Faculty of Engineering & Technology, Nong Lam University, Vietnam
Assoc. Prof. Dang Thanh Trung	Ho Chi Minh City University of Technology and Education, Vietnam
Assoc. Prof. Le Anh Duc	Faculty of Engineering & Technology, Nong Lam University, Vietnam
Assoc. Prof. Nguyen Viet DZung	School of Mechanical Engineering, Hanoi University of Science and Technology, Vietnam
Assoc. Prof. Tran Thanh Son	Faculty of Heat and Refrigeration Technology, Da Nang University, Vietnam
Assoc. Prof. Bui Trung Thanh	Faculty of Heat & Refrigeration Engineering, Industrial University of Ho Chi Minh City, Vietnam
Assoc. Prof. Nguyen Minh Phu	Faculty of Heat & Refrigeration Engineering, Industrial University of Ho Chi Minh City, Vietnam.
Assoc. Prof. Chau Minh Thuyen	Faculty of Electrical Engineering Technology, Industrial University of Ho Chi Minh City, Vietnam
Assoc. Prof. Nguyen Van Nho	Faculty of Electrical Engineering, Ho Chi Minh City University of Technology, Vietnam
Prof. Duong Ngoc Huyen	Faculty of Electrical Engineering, Ho Chi Minh City University of Technology, Vietnam
Assoc. Prof. Vo Ngoc Dieu	Faculty of Electrical Engineering, Ho Chi Minh City University of Technology, Vietnam
Assoc. Prof. Hoang An Quoc	Ho Chi Minh City University of Technology and Education, Vietnam
Assoc. Prof. Pham Van Sang	School of Mechanical Engineering, Hanoi University of Science and Technology, Vietnam
Assoc. Prof. Nguyen Hung	HUTECH Institute of Engineering, Ho Chi Minh City University of Technology (HUTECH), Vietnam
Assoc. Prof. Dr. Thai Van Nam	HUTECH Institute of Applied Sciences, Ho Chi Minh City University of Technology (HUTECH), Vietnam
Assoc. Prof. Vo Dinh Bay	Ho Chi Minh City University of Technology (HUTECH), Vietnam
Prof. Nguyen Trung Kien	Ho Chi Minh City University of Technology (HUTECH), Vietnam
Dr. Ha Anh Tung	Department of Heat and Refrigeration Engineering, Ho Chi Minh City University of Technology, Vietnam
Dr. Nguyen Duc Khuyen	Faculty of Engineering & Technology, Nong Lam University, Vietnam
Dr. Le Minh Nhut	Department of Heat and Refrigeration Engineering, Ho Chi Minh City University of Technology and Education, Vietnam
Assoc Prof. Nguyen The Bao	Department of Heat and Refrigeration Engineering, Ho Chi Minh City University of Technology, Vietnam
Assoc. Prof. Nguyen Van Tuong	Faculty of Mechanical Engineering, Nha Trang University, Vietnam

4. Scientific Committeee

4.1. Scientific Committeee of Heat and Refrigeration Engineering

Dr. Tran Dinh Anh Tuan	Faculty of Heat and Refrigeration Engineering, Industrial University of Ho Chi Minh City (IUH), Ho Chi Minh City, Vietnam
Dr. Nguyen Hoang Khoi	Faculty of Heat and Refrigeration Engineering, Industrial University of Ho Chi Minh City (IUH), Ho Chi Minh City, Vietnam.
Dr. Nguyen Hieu Nghia	Faculty of Heat and Refrigeration Engineering, Industrial University of Ho Chi Minh City (IUH), Ho Chi Minh City, Vietnam.
Dr. Nguyen Trung Kien	Faculty of Heat and Refrigeration Engineering, Industrial University of Ho Chi Minh City (IUH), Ho Chi Minh City, Vietnam
Assoc. Prof. Le Anh Duc	Faculty of Engineering Technology, Nong Lam University - Thu Duc City - Ho Chi Minh City, Vietnam
Assoc. Prof. Nguyen Minh Phu	Faculty of Heat and Refrigeration Engineering, Industrial University of Ho Chi Minh City (IUH), Ho Chi Minh City, Vietnam.
Dr. Nguyen Van Hap	Department of Thermal Technology, Ho Chi Minh City University of Technology (HCMUT), Ho Chi Minh City, Vietnam
Dr. Vo Kien Quoc	Department of Thermal Technology, Ho Chi Minh City University of Technology (HCMUT), Ho Chi Minh City, Vietnam.
Dr. Phan Thanh Nhan	Department of Thermal Technology, Ho Chi Minh City University of Technology (HCMUT), Ho Chi Minh City Vietnam
Dr. Huynh Phuoc Hien	Department of Thermal Technology, Ho Chi Minh City University of Technology (HCMUT), Ho Chi Minh City, Vietnam
Dr. Dang Hung Son	Department of Thermal-Electrical Technology, Ho Chi Minh City University of Technology and Education, Vietnam
Dr. Doan Minh Hung	Department of Thermal-Electrical Technology, Ho Chi Minh City University of Technology and Education, Vietnam.
Dr. Tran Thanh Tinh	Department of Thermal-Electrical Technology, Ho Chi Minh City University of Technology and Education, Vietnam
Dr. Nguyen Tran Phu	Department of Renewable Energy, Ho Chi Minh City University of Technology and Education, Vietnam
Assoc. Prof. Dang Thanh Trung	Department of Thermal-Electrical Technology, Ho Chi Minh City University of Technology and Education, Vietnam
Dr. Pham Thanh Tuan	Department of Renewable Energy, Ho Chi Minh City University of Technology and Education, Vietnam

Dr. Huynh Ngoc Hung	Faculty of Thermal-Electrical Technology University of Science and Technology - The University of Da Nang, Vietnam
Assoc. Prof. Vo Chi Chinh	Faculty of Thermal-Electrical Technology University of Science and Technology - The University of Da Nang, Vietnam
Dr. Nguyen Van Trung	Department of Thermal-Electrical Technology, Ho Chi Minh City University of Technology and Education, Vietnam
Dr. Nguyen Duc Khuyen	Faculty of Engineering Technology, Nong Lam University - Thu Duc City - Ho Chi Minh City, Vietnam
Dr. Nguyen Trong Hieu	Department of Thermal-Electrical Technology, Ho Chi Minh City University of Technology and Education, Vietnam
Dr. Nguyen Van Vu	Department of Thermal-Electrical Technology, Ho Chi Minh City University of Technology and Education, Vietnam
Dr. Huynh Minh Thu	Department of Renewable Energy, Ho Chi Minh City University of Technology and Education, Vietnam
Dr. Le Kieu Hiep	Faculty of Thermal Energy, School of Mechanical Engineering, Hanoi University of Science and Technology, Vietnam
Dr. Nguyen Ba Chien	Faculty of Thermal Energy, School of Mechanical Engineering, Hanoi University of Science and Technology, Vietnam
Dr. Tran Thi Thu Hang	Faculty of Thermal Energy, School of Mechanical Engineering, Hanoi University of Science and Technology, Vietnam
Dr. Bui Trung Hieu	VK-Tech Center, Hi-Tech Institute, Nguyen Tat Thanh University, Ho Chi Minh City, Vietnam
Dr. Dang Tran Tho	Faculty of Thermal Energy, School of Mechanical Engineering, Hanoi University of Science and Technology, Vietnam
Assoc.Prof. Bui Trung Thanh	Faculty of Heat and Refrigeration Engineering Industrial University of Ho Chi Minh City (IUH), Ho Chi Minh City, Vietnam

4.2. Scientific Committee of Mechanical Engineering

Assoc. Prof. Nguyen Duc Nam	Faculty of Mechanical Engineering, Industrial University of Ho Chi Minh City, Vietnam
Assoc. Prof. Le Thanh Danh	Faculty of Mechanical Engineering, Industrial University of Ho Chi Minh City, Vietnam
Dr. Duong Cong Truyen	Faculty of Mechanical Engineering, Industrial University of Ho Chi Minh City, Vietnam
Dr. Nguyen Khoa Trieu	Faculty of Mechanical Engineering, Industrial University of Ho Chi Minh City, Vietnam
Dr. Nguyen Vien Quoc	Faculty of Mechanical Engineering, Industrial University of Ho Chi Minh City, Vietnam

Dr. Tran Ngọc Dang Khoa	Faculty of Mechanical Engineering, Industrial University of Ho Chi Minh City, Vietnam
Dr. Huynh Xuan Khoa	Faculty of Mechanical Engineering, Industrial University of Ho Chi Minh City, Vietnam
Dr. Dang Hoang Minh	Faculty of Mechanical Engineering, Industrial University of Ho Chi Minh City, Vietnam
Dr. Le Ngoc Tran	Faculty of Mechanical Engineering, Industrial University of Ho Chi Minh City, Vietnam
Dr. Diep Bao Tri	Faculty of Mechanical Engineering, Industrial University of Ho Chi Minh City, Vietnam
Dr. Bui Quoc Duy	Faculty of Mechanical Engineering, Industrial University of Ho Chi Minh City, Vietnam
Dr. Ao Hung Linh	Faculty of Mechanical Engineering, Industrial University of Ho Chi Minh City, Vietnam
Dr. Ngo Tien Hoang	Faculty of Mechanical Engineering, Industrial University of Ho Chi Minh City, Vietnam
Dr. Nguyen Van Nam	Faculty of Mechanical Engineering, Industrial University of Ho Chi Minh City, Vietnam
Dr. Nguyen Phuong Bac	Faculty of Mechanical Engineering, Industrial University of Ho Chi Minh City, Vietnam
Dr. Pham Huu Loc	Faculty of Mechanical Engineering, Industrial University of Ho Chi Minh City, Vietnam
Dr. Lang Van Thang	Faculty of Mechanical Engineering, Industrial University of Ho Chi Minh City, Vietnam
Dr. Mai Tien Hau	Faculty of Mechanical Engineering, Industrial University of Ho Chi Minh City, Vietnam
Dr. Tran Trong Nhan	Faculty of Mechanical Engineering, Industrial University of Ho Chi Minh City, Vietnam
Dr. Tran Minh Hien	Faculty of Mechanical Engineering, Industrial University of Ho Chi Minh City, Vietnam
Dr. Vo Ngoc Yen Phuong	Faculty of Mechanical Engineering, Industrial University of Ho Chi Minh City, Vietnam
Dr. Chau Ngoc Le	Faculty of Mechanical Engineering, Industrial University of Ho Chi Minh City, Vietnam
Assoc. Prof. Pham Son Minh	Faculty of Mechanical Engineering, Ho Chi Minh City University of Technology and Education, Vietnam
Dr. Tran Van Tron	Faculty of Mechanical Engineering Ho Chi Minh City University of Technology and Education, Vietnam
Dr. Luu Tuan Anh	Faculty of Mechanical Engineering, Tran Dai Nghia University, Vietnam
Dr. Tran Trong Tai	Faculty of Mechanical Engineering, Tran Dai Nghia University, Vietnam

Dr. Pham Anh Duc	Faculty of Mechanical Engineering, Da Nang University, Vietnam
Dr. Nguyen Van Son	Faculty of Mechanical Engineering, Le Quy Don Technical University, Vietnam
Dr. Le Van Thao	Faculty of Mechanical Engineering, Le Quy Don Technical University, Vietnam
Dr. Tran Hong Van	Faculty of Mechanical Engineering Duc College of Technology
Assoc. Prof. Do Xuan Phu	Faculty of Vietnamese-German University (VGU), Viet Nam
Dr. Chau Minh Quang	Faculty of Mechanical Engineering, Industrial University of Ho Chi Minh City (IUH), Viet Nam
Dr. Truong Van Men	Faculty of Mechanical Engineering, Tra Vinh University, Vietnam
Dr. Nguyen Trong Son Ha	Faculty of Mechanical Engineering, Industrial University of Ho Chi Minh City, Vietnam
Dr. Nguyen Huu Tho	Faculty of Mechanical Engineering, Nguyen Tat Thanh University, Vietnam
Dr. Huynh Ngoc Thai	Faculty of Mechanical Engineering, Ho Chi Minh City University of Industry and Trade, Vietnam
Prof. Dung-An Wang	Graduate Institute of Precision Engineering, National Chung Hsing University, Taiwan
Prof. Lee Bong-Kee	Chonnam National University, Korea

4.3. Scientific Committee of Automotive Engineering Technology

Assoc. Prof. Tran Van Nhu	University of Transport and Communications, Ha Noi, Vietnam
Assoc. Prof. Huynh Thanh Cong	Department of Science and Technology, Vietnam National University-Ho Chi Minh, Vietnam
Assoc. Prof. Vu Van Tan	University of Transport and Communications, Ha Noi, Vietnam
Assoc. Prof. Ly Hùng Anh	Ho Chi Minh City University of Technology (HCMUT), Viet Nam National University-Ho Chi Minh City, Vietnam
Assoc. Prof. Ly Vinh Đat	Ho Chi Minh City University of Technology and Education (HCMUTE), Vietnam
Dr. Tran Dang Long	Ho Chi Minh City University of Technology (HCMUT), Viet Nam National University-Ho Chi Minh City, Vietnam
Dr. Nguyen Van Trang	Ho Chi Minh City University of Technology and Education (HCMUTE), Vietnam
Dr. Duong Hoang Long	Faculty of Mechanical Engineering, Nguyen Tat Thanh University, Vietnam
Dr. Dang Tien Phuc	Faculty of Automotive Engineering Technology, Industrial University of Ho Chi Minh City (IUH), Ho Chi Minh City, Vietnam.

Dr. Nguyen Van Sy	Faculty of Automotive Engineering Technology, Industrial University of Ho Chi Minh City, Ho Chi Minh City, Vietnam.
Dr. Vo Tan Chau	Faculty of Automotive Engineering Technology Industrial University of Ho Chi Minh City, Ho Chi Minh City, Vietnam.
Dr. Ho Thanh Tho	Faculty of Automotive Engineering Technology, Industrial University of Ho Chi Minh City, Ho Chi Minh City, Vietnam.
Dr. Pham Tuan Anh	Thu Dau Mot University (TDMU), Vietnam
Dr. Nguyen Van Luc	Vietnam Aviation Academy
Dr. Le Thanh Long	Ho Chi Minh City University of Technology (HCMUT), Viet Nam National University-Ho Chi Minh City, Vietnam
Dr. Luong Hung Truyen	Nguyen Tat Thanh University
Dr. Le Thanh Phuc	Ho Chi Minh City University of Technology and Education (HCMUTE), Vietnam
Dr. Do Quoc Am	Ho Chi Minh City University of Technology and Education (HCMUTE), Vietnam
Dr. Tran Huu Nhan	Ho Chi Minh City University of Technology (HCMUT), Viet Nam National University - Ho Chi Minh City, Vietnam
Assoc. Prof. Le Tuan Phuong Nam	Vietnam Aviation Academy
Dr. Nguyen Thanh Tam	Qui Nhon University, Vietnam
Dr. Nguyen Phi Truong	Hanoi University of Industry, Vietnam
Dr. Nguyen Phu Thuong Luu	Van Lang University, Vietnam
Dr. Pham Cong Duy	Industrial University of Ho Chi Minh City, Ho Chi Minh City, Vietnam.
Dr. Bui Trong Kien	The Institute of Mathematics, Vietnam Academy of Science and Technology
Assoc. Prof. Do Duc Thuan	Hanoi University of Science and Technology, Vietnam

4.4. Scientific Committee of Electronics Technology

Prof. Thuong Le	Ho Chi Minh City University of Technology (HCMUT) –Vietnam National University-Ho Chi Minh City (VNU-HCMC)
Prof. Ho Pham Huy Anh	Ho Chi Minh City University of Technology (HCMUT) –Vietnam National University-Ho Chi Minh City (VNU-HCMC)
Dr. Mai Thang Long	Faculty of Electronics Technology, Industrial University of Ho Chi Minh City, Vietnam

Assoc. Prof. Nguyen Ngoc Son	Faculty of Electronics Technology, Industrial University of Ho Chi Minh City, Vietnam
Assoc. Prof. Le My Ha	Ho Chi Minh City University of Technology and Education Ho Chi Minh City, Vietnam
Assoc. Prof. Truong Ngoc Son	Ho Chi Minh City University of Technology and Education Ho Chi Minh City, Vietnam
Dr. Pham Ngoc Son	Ho Chi Minh City University of Technology and Education Ho Chi Minh City, Vietnam
Dr. Tran Duc Thien	Ho Chi Minh City University of Technology and Education Ho Chi Minh City, Vietnam
Assoc. Prof. Tran Trung Duy	Posts and Telecommunications Institute of Technology, Ho Chi Minh City, Vietnam
Dr. Nguyen Quang Sang	Ho Chi Minh City University of Transport
Dr. Ta Quang Hien	International University, Vietnam National University-Ho Chi Minh City, Vietnam
Assoc. Prof. Nguyen Chanh Nghiem	Can Tho University, Vietnam
Dr. Ong Mau Dung	Faculty of Electronics Technology, Industrial University of Ho Chi Minh City, Vietnam
Dr. Tran Huu Toan	Faculty of Electronics Technology, Industrial University of Ho Chi Minh City, Vietnam
Dr. Nguyen Van Lanh	Faculty of Electronics Technology, Industrial University of Ho Chi Minh City, Vietnam
Dr. Nguyen The Ky Suong	Faculty of Electronics Technology, Industrial University of Ho Chi Minh City, Vietnam
Dr. Nguyen Tien Tung	Faculty of Electronics Technology, Industrial University of Ho Chi Minh City, Vietnam
Dr. Pham Minh Nam	Faculty of Electronics Technology, Industrial University of Ho Chi Minh City, Vietnam
Dr. Tran Minh Chinh	Faculty of Electronics Technology, Industrial University of Ho Chi Minh City, Vietnam
Dr. Nguyen Tan Loc	Faculty of Electronics Technology, Industrial University of Ho Chi Minh City, Vietnam
Dr. Nguyen Anh Vinh	Faculty of Electronics Technology, Industrial University of Ho Chi Minh City, Vietnam
Dr. Cao Van Kien	Faculty of Electronics Technology, Industrial University of Ho Chi Minh City, Vietnam

4.5. Scientific Committee of Electrical Engineering Technology

Dr. Nguyen Hoai Thuong	Faculty of Electrical Engineering Technology, Industrial University of Ho Chi Minh City, Vietnam
Dr. Bach Thanh Quy	Faculty of Electrical Engineering Technology, Industrial University of Ho Chi Minh City, Vietnam
Dr. Le Van Đai	Faculty of Electrical Engineering Technology, Industrial University of Ho Chi Minh City, Vietnam
Dr. Nguyen Ngoc Au	Faculty of Electrical Engineering Technology, Ho Chi Minh City University of Technology and Education, Vietnam
Dr. Nguyen Trung Thang	Faculty of Electrical Engineering Technology, Ton Duc Thang University, Vietnam
Dr. Nguyen Tung Linh	Electric Power University, Vietnam
Dr. Duong Thanh Long	Faculty of Electrical Engineering Technology, Industrial University of Ho Chi Minh City, Vietnam
Dr. Pham Cong Duy	Faculty of Electrical Engineering Technology, Industrial University of Ho Chi Minh City, Vietnam
Dr. Tran Quang Tho	Ho Chi Minh City University of Technology and Education
Dr. Tran Tan Tai	Faculty of Electrical Engineering Technology, Industrial University of Ho Chi Minh City, Vietnam
Assoc. Prof. Chau Minh Thuyen	Faculty of Electrical Engineering Technology, Industrial University of Ho Chi Minh City
Dr. Pham Quoc Khanh	Faculty of Electrical Engineering Technology, Industrial University of Ho Chi Minh City, Vietnam
Dr. Nguyen Trung Nhan	Faculty of Electrical Engineering Technology, Industrial University of Ho Chi Minh City
Dr. Ngo Thanh Quyen	Faculty of Electrical Engineering Technology, Industrial University of Ho Chi Minh City, Vietnam
Assoc. Prof. Truong Viet Anh	Faculty of Electrical Engineering Technology, Ho Chi Minh City University of Technology and Education
Dr. Tran Thanh Ngoc	Faculty of Electrical Engineering Technology, Industrial University of Ho Chi Minh City, Vietnam

5. Contact

Email: icset2023@iuh.edu.vn

Website: https://icset2023.iuh.edu.vn/

Contact Person

1. Assoc. Prof. Bui Trung Thanh,

Email: buitrungthanh@iuh.edu.vn Phone: (+84) 91 392 1407

2. Dr. Tran Dinh Anh Tuan

Email: trandinhanhtuan@iuh.edu.vn Phone: (+84) 98 299 7973

3. Dr. Nguyen Hoang Khoi

Email: nguyenhoangkhoi@iuh.edu.vn Phone: (+84) 93 706 7115

4. Dr. Nguyen Trung Kien

Email: nguyentrungkien.08@iuh.edu.vn Phone: (+84) 93 383 2338

CONTENTS

BIOMASS POWER GENERATION SOLUTIONS FOR CARBON NET ZERO TARGET

ANH T. HOANG [1*], BAO T. NGUYEN [2]

[1] *Khoa Nguyen Installation Construction Company Limited*
[2] *Division of Heat & Refrigeration Engineering, Faculty of Mechanical Engineering, Ho Chi Minh City University of Technology, VNU-HCM*
[*] *ceo@knic.co*

Abstract. To achieve the goal of Vietnam's commitment to be carbon neutral by 2050 at the 26 COPs, avoid long-distance power loss, local electricity shortages and reduce high pressure from source-grid investment costs, Vietnam needs to decentralize the large power stations to district-scaled plants. Furthermore, based on the potential of Vietnam's biomass from the main export items being rice and wood, a study to evaluate and optimize the heat balance diagram of the power plant using Thermal flow's steam-pro software is carried out, including checking the power flow of the unit used the Siemens's PSS/ E software. The article also evaluates and compares heat balance diagram types in terms of total investment, fuel consumption costs and feet-in-tariff electric incentive prices, thereby making suitable proposals for choosing a standard design of a new biomass power plant in Vietnam in the near future. In addition, the study also evaluates and makes relevant recommendations in converting the existing bagasse-burning cogeneration plant into an independent power generation plant combining by optimizing the modeling combustion replacement biomass fuel using Ansys software and by an experimental evaluation for performance guarantees using the on-line measure-directed method. Moreover, the carbon net zero curves between mixed rates and outlet flue gas temperature at all stable loads was build up and vertified by the simulations of combustion modeling of biomass co-firing in domestic anthracite coal-fired sub-critical and imported sub-bitumen coal-fired supercritical larger-scale (+600 MW) power units at mix rate 16.67% and 33.33% of new added burners for rice husks in W-flame furnace and existing pulverized system for wood pellets in L-flame combustion chamber, respectively. From the results of this study, it is found that wood pellets is not available at 8.47 US Cents per kWh of FIT price and gram of capacity is 10 MW for new biomass power unit for a district scale is suitable in Vietnam conditions. Additionally, the loss of fuel consumption rate at 87 g/kWh of forest residuals is found when switching from a bagasse combine heat and power unit to a forest residuals independent power plant. The difference temperature among 100%RO and 75%RO of W-flame furnace are better than subcritical units by about 4 deg.C. As a result, a road map for biomass co-firing in pulverized coal larger-scale plants should be immediately performed. It is also suggested that the PG_cal program should be used for the performance guarantees and tests at all stable loads not only in new biomass plants, but also in biomass co-firing coal power plants in order to achieve the decarbonization practical imperative for Vietnam's "net zero" goal of 2050 in the field of power generation in general as well as to establish policies on environmental protection for industries.

Keywords. Biomass, power plant, energy efficiency, power flow, performance guarantees, carbon neutral, CFD, co-firing, Flue gas temperature.

1 INTRODUCTION

Recently, Vietnam has significantly increased its solar and wind power installed capacity with Feed-in-tariff incentive electricity price policies [1]. However, these energy sources are high fluctuated from actual operation. Typically, on March 19, 2022, the total generating capacity of Vietnam's wind power dropped to only 15 MW from the total installed capacity of 3,980 MW, as shown in [2], while the load demand of the whole system remained stably. This shows that solar and wind power are not reliable until the large-scale power storages such as batteries, pump storage hydro-powers, hydrogen technology and so on, are available. Therefore, the short-term solutions to reduce emissions carbon should be considered in Vietnam is biomass energy.

In another aspect, although new coal-fired larger-scale power plant has been stopped, the remaining delayed larger-scale coal fired units in Vietnam are still under construction and have not been COD yet such as Van

Phong 1, Quang Trach 1, Thai Binh 2, etc. Moreover, according to the draft of the Power Development Plan 8 [1], by 2045, the proportion of coal-fired power plants still contribute from 9.7% to 13.2% in total generation capacity in Vietnam.

Based on the above analyses, the problems of biomass potential, ability of power grid to release capacity, selection of optimal heat balance diagram, simulation of combustion modeling, guaranteed performances, economic and financial analysis based on intensive electricity prices should be reviewed, evaluated and proposed roadmap. This is not only necessary for the construction of new biomass power plants, but also important in the conversion of biomass combined heat and power to independent power plants, and especially the biomass co-firing in the existing coal-fired plant to meet the target of carbon neutrality by 2050 in Vietnam.

2 LITERATURE REVIEW

Co-firing technologies have been verified in coal-fired power plants, including (i) direct co-firing in Gelderland Power Station, Nijmegen, The Netherlands and Wallerawang Power Station, NSW, Australia; (ii) indirect co-firing in Zeltweg Power Plant, Austria and Amer Power Plant, The Netherlands, and (iii) parallel co-firing in Avedøre Power Plant, Denmark [3-4]. Biomass firing in coal plants can result in increasing tube corrosion/fouling and slagging caused by chlorine and alkali metals [5-16]. In negative side of co-firing applications, the reduction in boiler efficiency 0.2- 4% with biomass percentage 5-30% respectively, was shown in [15]. A process model to optimize the soot-blowing for ash deposits to reduce CO2 has been carried out in [17]. A review for carbon-negative fuels as syngas productions from biomass has shown in [18]. However, in the positive side, co-firing has helped to reduce CO2 emissions in coal-fired power plants with minimal modifications and moderate investment [19-20]. The change in CO2 emissions from 800 to 400 kg CO2/MWhe was linear with the amount of coal offset by biomass from 0 to 50%, as presented in [21]. A life cycle assessment of co-firing wood pellets at 10% mixing rate was reported to reduce GHG emissions by 9% in the United States [22]. In Vietnam, an integrated model simulating the economics, environmental and social implications of blending 5% of rice straw in two existing coal power plants indicated the saving coal of 6,808 mil. USD per year for Mong Duong 1 Plant and 1,742 mil. USD per year for Ninh Binh Plant, reflectively [23]. For country-scale, Tere Vad´en et al. [24] suggested that Finland needed over 140 Mm3 of forest biomass for their goal of carbon neutrality by 2035. For the numerical aspect, F. O. Centeno-González et al. [25] carried out a CFD model on an boiler burning sugarcane bagasse by using Ansys fluent software to define devolatilization phenomenon through the particle trajectory to predicting the thermal fields. In term of biomass ration in co-firing, most of the biomass fuel mix ratio in pulverized coal plants is less than 10%, circulating fluidized bed (CFB) can be up to 15%, and grate combustion or bubbling fluidized bed (BFB) can be completely [26].

Based on the above literature review, the study on the problems when switching from a biomass combine heat and power unit to an independent power plant has not been found. Furthermore, the characteristic curves between mixed rates and outlet flue gas temperature and the performance guarantees and tests of thermal power plant at all stable loads in biomass plants as well as biomass co-firing coal power plants have not been studied. Therefore, this study will focus on these issues.

The contents of this paper include (i) the evaluation of woody and rice husks reserves, transport capacity, checking power flow for a district scale in Vietnam in order to choose the standard capacity of power unit, (ii) the selection of optimized heat balance diagram, increasing and decreasing steam parameters, number of heat exchangers, biomass fuel ratios including wood pellets, forest residuals and rice husks in order to evaluate efficiency, fuel consumption, and CO_2 emissions, (iii) the economic and financial analysis based on changes in total investment, fuel consumption and preferential electricity prices, (iv) the consideration of an existing combined heat and power unit switching to an independent power generation unit under modeling combustion of biomass-fired using Ansys software and experimental evaluation for performance guarantee using the on-line measure-directed method and (v) draws the carbon net zero curve between mixing rate and flue gas temperature at exit furnace and verify by the simulation of combustion modeling of co-firing in domestic coal-fired sub-critical and imported coal-fired supercritical larger-scale (+600 MW) power units.

3 METHOD AND DATA

Research methods are based on specific evidence, explicitly cites and used primary source data with high reliability. The conclusions was drawed complying with objective and rigorous evidence by high-precision calculation tools as Ansys, Siemens's PSS/ E software and Thermal flow's steam-pro.

The sumary of combustion calculated is denote in Table 1, [27].

Table 1: Sumary of Furnace exit temperature.

Name	Formular
The theoretical air volume required to burned 1 kg of fuel completely	$V^0 = 0.0889(C^p + 0.375S^p_{op+k}) + 0.265H^p - 0.0333O_p$
The resultant volume of the sum CO_2 and SO_2 produced from 1 kg of fuel burnt	$V_{RO2} = 1.866\dfrac{C^p + 0.375S^p_{op+k}}{100}$
The theoretical nitrogen volume	$V^0_{N_2} = 0.79V^0_B + 0.008N^p$
The total volume of water from 1 kg fuel	$V^0_{H_2O} = 0.111H^p + 0.0124W^p + 0.0161V^0$
The total water vapor volume in flue gas volume:	$V_{H_2O} = V^0_{H_2O} + 0.0161(\alpha - 1)V^0$
Volume fraction of CO_2 and SO_2	$r_{RO_2} = V_{RO_2}/V_r$
Volume fraction of water vapor	$r_{H_2O} = V_{H_2O}/V_r$
The concentration of fly ash:	$\mu = 10A^p a_{yH}/V_p$
The excess air coefficient	$\alpha = \dfrac{V}{V^0}$
The enthalpy of total air required for combustion of 1 kg fuel	$I_B = V^0(ct)_B$
The enthalpy for theoretical amount of flue gas	$I^0_\Gamma = V_{RO_2}(c\vartheta)_{RO_2} + V^0_{N_2}(c\vartheta)_{N_2} + V^0_{H_2O}(c\vartheta)_{H_2O}$
The enthalpy of the flue gas at a temperature	$I_\Gamma = I^0_\Gamma + (\alpha - 1)I^0_B$
Fuel consumption of boiler	$B = \dfrac{D(i_\pi - i_{\pi.B}) + D_{\pi p}(i_{KH\pi} - i_{\pi.B})}{Q^p_p \eta_{\pi\Gamma}}$
Waste gas lose	$q_2 = \dfrac{(I_{yx} - \alpha_{yx}I^0_{X.B})(100 - q_4)}{Q^p_p}$
Heat release rate per unit volume	$q_V = BQ^p_H/V_\tau$
Heat release rate per unit cross sectional area	$q_R = BQ^p_H/R$
The coefficient of radiant absorption due to tri-atomic gases	$k_\Gamma = \left(\dfrac{7.8 + 16r_{H_2O}}{3.16\sqrt{p_n s}} - 1\right).\left(1 - 0.37\dfrac{\vartheta"_T + 273}{1000}\right)$
Furnace exit temperature	$\vartheta"_T = \dfrac{T_a}{M\left(\dfrac{5.67\psi_{cp}F_{CT}a_T T_a^3}{10^{11}\varphi B_p V c_{cp}}\right)^{0.6} + 1} - 273$

Fuel characteristics and furnace chamber dimensions and simulation were created as shown in Table 2&3.

Table 2: Fuel characteristics.

	Unit	Rice Husk	Wood pellets	Forest Residuals	Anthracite	Sub-bitumen
Proximate Analysis (weight %)						
Moisture	%	10.94	8.7	48.91	7.4	27.33
Ash	%	18.05	0.5	2.03	34.86	5.62
Volatile Matter	%	56.57	74.4	42.1	6.5	33.7
Fixed Carbon	%	14.44	16.4	6.96	51.24	33.35
Total	%	100	100	100	100	100
Heating Values HHV	kJ/kg	14,106.3	18,197.0	10,301	19,577	19,744
Bulk density (dry)	Kg/m3	85.60	585.00	130.9	1400	850

Table 3: Furnace chamber dimensions and simulation.

Name	Unit	688MW	622.5MW	25MW
Lengh	M	20.6	34.4	8.48
Width	M	15.5	15.6	8
Number of Burner		30	36	6
Diameter of burner	Mm	1168	770	300
Mesh Sized	M	0.8	0.8	0.1
Viscous model		k-epsilon	k-epsilon	k-epsilon

4 RESULTS AND DISCUSSION

4.1 New biomass power plant

Rice husk reserves and 40-tons barges transport capacity with the interlaced canal system of the Mekong River Delta are considered convenient for biomass power plants. With an annual output of 24 million tons of paddy, as shown in [28], the rice husks quantity is about 4.8 million tons per year that is enough to meet the power capacity of 70 MW for 13 provinces in the Mekong River Delta.

Wood material in Vietnam is mainly transported by trucks with a payload of 20-40 tons, the total amount of timber within a district is assessed based on the Forestry data sharing system, for example as shown [29], with 9.5 million cubic meters in Minh Hoa District, Quang Binh Province with the average time of planting from about 6 years, this volume is enough capacity to meet the power unit for 10 MW.

In order to examine the scenarios of decentralize the power stations to district-scales, the PSS/E software from Siemens was used to calculate the performances of power flows and short circuits for different districts in Vietnam. Fig. 1 and 2 show the power flows for 10 MW unit in the scenarios of 2025 and 2030 respectively in Long My district, Hau Giang province as an example. As shown in these figures, in the normal operating mode as well as in the fault mode N-1, the lines synchronizing with the power plant are normally loaded and none of the lines are overloaded.

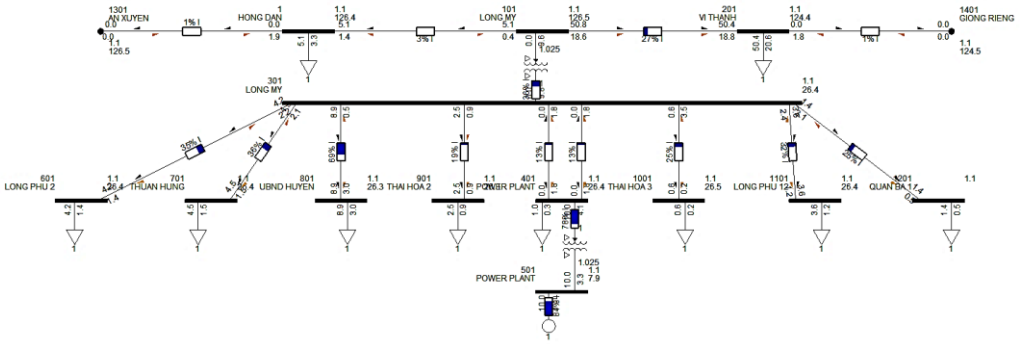

Figure 1: Power flow for 10 MW unit in scenario 2025.

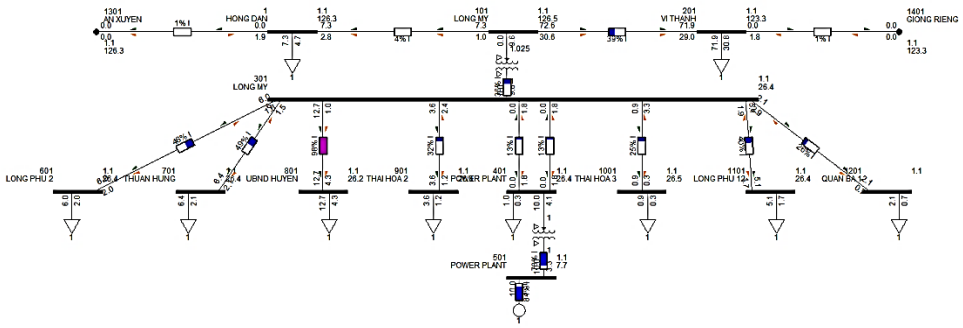

Figure 2: Power flow for 10 MW unit in scenario 2030.

Then, the Thermal flow's steam-pro software was used to design the different types of heat balance diagrams

including (i) 63.3 bar, 480 deg.C (ii) 100 bar, 520 deg.C and one low pressure heater, change fuel burned in furnace such as (i) wood pellets, (ii) rice husks and (iii) forest residuals providing that the changes in plant efficiency, fuel consumptions and CO2 emissions as illustrated in Figs. 3-4 and Table 1. The input data are the ambient conditions such as 1.013 bar, 27 deg.C, 84% relative humidity and 24.84 deg.C temperature wet bulb.

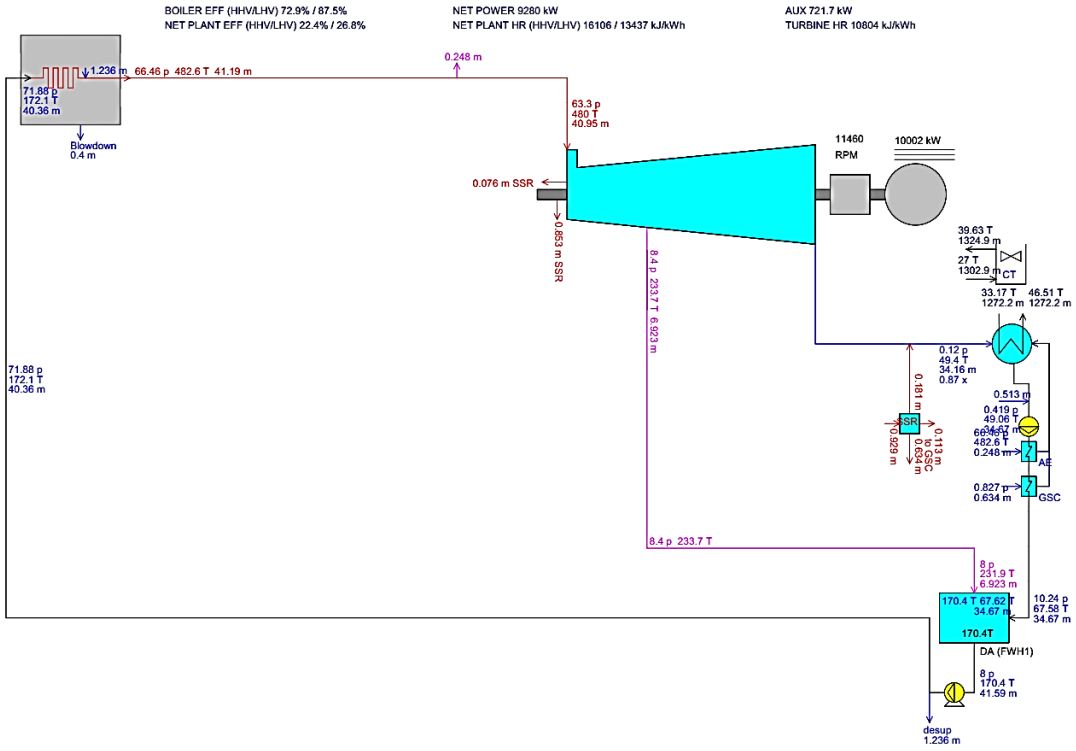

Figure 3: Heat balance diagram of Forest Residuals unit at 63.3 bar, 480 deg.C.

Plant gross power	10002	kW
Plant net power	9280	kW
Number of units	1	
Plant net HR (HHV)	16106	kJ/kWh
Plant net HR (LHV)	13437	kJ/kWh
Plant net eff (HHV)	22.35	%
Plant net eff (LHV)	26.79	%
Aux. & losses	721.7	kW
Fuel heat input (HHV)	149.5	GJ/h
Fuel heat input (LHV)	124.7	GJ/h
Fuel flow	348	t/day

Ambient
1.013 p
27 T
84% RH
24.84 T wet bulb

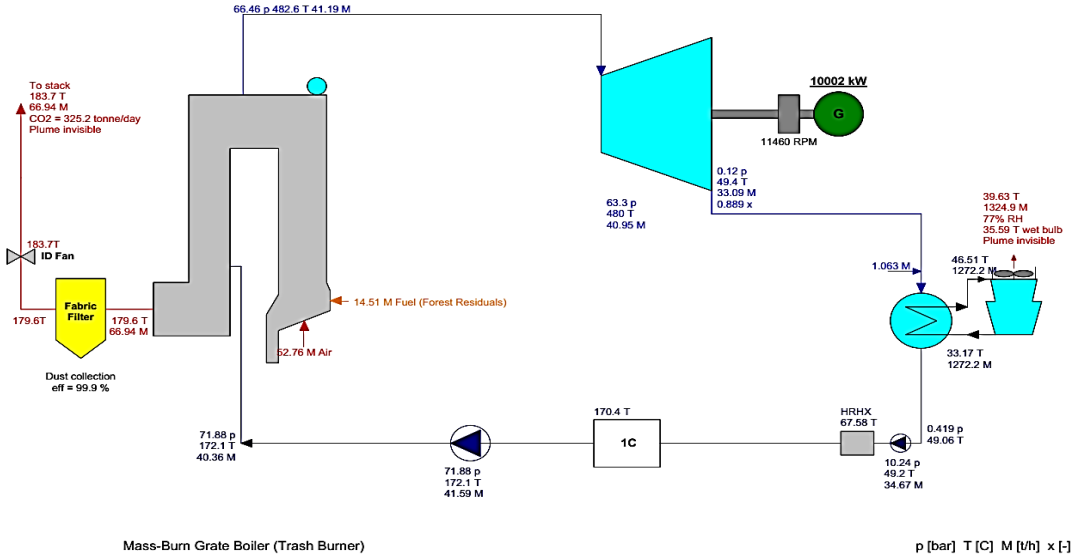

Figure 4: Forest Residuals consumption and CO2 rates at 63.3 bar, 480 deg.C.

The calculated results as indicated on Table 4 including carbonic emission rates, but a biomass plant are usually negative carbon dioxide emission in comparison with amount of absorbed by plants. In constract, with reference from carbon emission factor 0.8041 tCO2/MWh [30] of Vietnam power grid system, the volume of CO2 reduction in comparison with fosis unit with number of operation 6,500 hours per year is 48,1~48,9 thousand tCO2/year.

Table 4: The output of calculation for biomass power units.

Name	**Unit**	**63.3 bar, 480 deg.C**			**100 bar, 520 deg.C**		
		Wood pellets	**Forest residuals**	**Rice husks**	**Wood pellets**	**Forest residuals**	**Rice husk**
Plant gross power	kW	10002	10002	10002	10002	10002	10002
Plant net power	kW	9363	9280	9260	9317	9238	9212
Plant net HR (HHV/LHV)	kJ/kWh	14117/ 13021	16106 13437	14562/ 13334	13431/ 12388	15305/ 12768	13867/ 12697
Plant net eff (HHV/LHV)	%	25.5/27.65	22.35/ 26.79	24.72/ 27	26.8/ 29.06	23.52/ 28.2	25.96/ 28.35
Aux. & losses flow	kW	638.1	721.7	741.5	684.7	763.8	789.7
Fuel heat input (HHV/LHV)	GJ/h	132.2/ 121.9	149.5/ 124.7	134.9/ 123.5	125.1/ 115.4	141.4 118	127.7/ 117
Fuel flow	ton/day	174	348	229	165	329	217
BOILER EFF (HHV/LHV)	%	82.5/ 89.5	72.9/ 87.5	80.8 / 88.4	82.7/ 89.7	73.2 / 87.8	81/ 88.5
TURBINE HR	kJ/kWh	10804	10804	10804	10223	10223	10223
CO_2	ton/day	290.2	325.2	288.4	274.8	307.6	273.2

From the assessment of fuel reserves, transportation ability within a radius of 60 kilometers, average load demand per district, reduction in construction costs of 110 kV switchyard substations, power loss from transmission lines, the gram of capacity 10 MW power unit for a district scale is suitable in Vietnam conditions. In term of the economic and financial analysis, the total investment cost was reference with the quotation of main equipment from suppliers such as Siemens, Shinko, Howden, Babcock & Wilcock, Valmet, Vyncke, Nantong Wanda Boiler, ABB, Schneider, etc. to KNIC. The different investment costs between US $13,373,839.85 of 63.3 bar, 480 deg.C and US $15,191,335.33 of 100 bar, 520 deg.C unit caused of increasing the alloy metal costs. The total investment cost was considered in condition of existing environmental standards in Vietnam as fabric filter at downstream of flue gas.

Table 5: Financial analysis for Steam parameters.

Name	**Unit**	63.3 bar, 480 deg.C unit			100 bar, 520 deg.C unit		
		Rice husks	**Forest residuals**	**Wood pellets**	**Rice husks**	**Forest residuals**	**Wood pellets**
Plant net efficiency HHV	%	24.72	22.35	25.5	25.96	23.52	26.8
Fuel consumption	t/h	9.559	14.51	7.264	9.056	13.73	6.877
Fuel cost	USD/tons	max. 32.37	max. 21.58	max. 44.02	Max. 28.05	Max. 18.56	Max. 37.98
WACC	%	8.28	8.28	8.28	8.28	8.28	8.28
FIRRe	%	12.16	11.96	11.93	11.89	12.00	11.97
NPVp	USD	90,694.61	18,939.89	9,804.15	307.44	41,589.27	31,440.17
B/Cp		1.006	1.004	1.004	1.003	1.004	1.004

Fuel costs of new plant are maximum at 32.37 and 21.58 USD per ton of rice husks and forest residual, respectively, in 63.3 bar, 480 deg.C and 28.05 and 18.56 USD per tons in 100 bar, 520 deg.C for rice husks and forest residual, respectively in order to make this plant financially feasible as indicated in Table 5.
With the price of wood pellets at 130 USD per ton at International Seaport in Nghi Son, Quang Ninh, Phu

My and [31], a new biomass power plant with feed-in-tariffs of 8.47 cents per kWh is financially infeasible. In the recent energy crisis in the World, the price of coal is nearly equivalent to that of wood pellets [32], making the biomass co-firing in the exiting coal-fired plants more financially feasible. On the other hand, to achieve the goal of Vietnam's commitment to be carbon neutral by 2050 at the 26 COPs, Vietnamese government should have policies to attract more investors in biomass power plants and biomass co-firing in the exiting coal-fired plants such as carbon credit market, CO_2 tax and preferable loans.

4.2 Cogeneration switched to independent power plant

Experimental evaluation for performance guarantees and combustion modeling of 25 MW biomass-fired combined heat and power unit switched to independent power generation units in Viet Nam was implemented. The cogeneration plant in Tuyen Quang, Viet Nam, a sugar plant with extraction steam and condenser, but due to the difficulty of bagasse materials, the plant is only operated two months per year. Therefore, with an incentive price of electricity, the switch to an independent power plant with forest residuals has been carried out in order to increase the number of operation hours per year.

The combustion modeling of boiler fired forest residual replace to bagasse is performed, the field distribution of temperature and oxidation in the furnace verified stable as illustrated in Figs. 5.

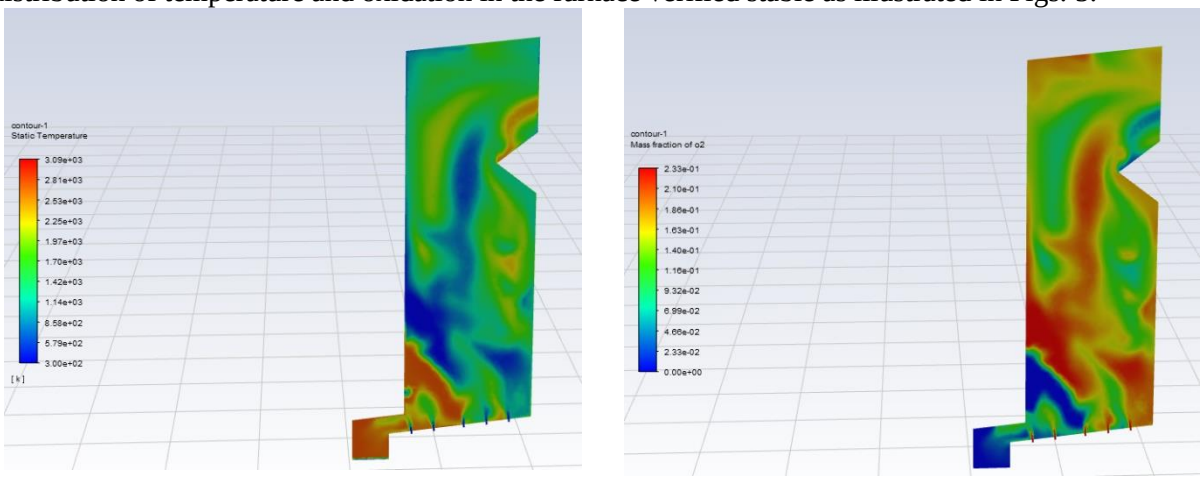

Figure 5: field distribution of temperature and oxidation diffusion of cogeneration plant switched to independent power plant.

The on-line measure-directed method using the meters of fuel feeders and tariff metering to focus on the coal consumption rates as shown on operation parameters, combine heat and power is 1.321 kg/kWh in comparison with independent power plant is 1.234 kg/kWh net at the same parameter of steam and combustion. The variated of 87 g/kWh is not large in considering of the condition that the unit has paid off with a incentive feed-in-tariffs.

4.3 Biomass co-firing in existing coal-fired power plant

The able 6 was denoted that the calculated results of flue gas temperature at the exit of the furnace W-flame which extracted from calculation program using Microsoft excel tool.

Table 6: The calculated results of flue gas temperature at the exit of the furnace W-flame.

Name		Unit	100% Anthracite	100%Rice Husk	50%Rice Husks	33.33%Rice Husks	16.67%Rice Husks
Heat release per unit volume in the furnace	q_V	kW/m3	73.89	72.31	73.22	73.47	73.69
Heat release per unit cross area of the furnace	q_R	kW/m2	2219.85	2172.38	2199.79	2207.14	2213.79
Effective radiant layer thickness of the furnace	s	m	15.07	15.07	15.07	15.07	15.07

Name		Unit	100% Anthracite	100%Rice Husk	50%Rice Husks	33.33%Rice Husks	16.67%Rice Husks
Coefficient	M		0.44	0.44	0.44	0.44	0.44
excess air coefficient	α		1.70	1.70	1.70	1.70	1.70
Temperature of the cold air	t_{kk}		30.00	30.00	30.00	30.00	30.00
Theoretical enthalpy of the coal air	I_{0kk}	kJ/kg	204.98	122.52	163.75	177.49	191.23
Heat carried into the furnace by the air	Q_{kk}	kJ/kg	348.46	208.28	278.37	301.74	325.09
Heat carried into the furnace by per unit kg fuel	Qb®	kJ/kg	20051.96	14314.28	17183.12	18139.59	19095.49
Average specific heat of the combustions products	V_{ctb}	kJ/kg.K	15.62	10.40	13.03	13.89	14.82
Volume faction of the water vapor	r_{H2O}		0.05	0.11	0.07	0.06	0.05
Volume faction of the tri-atomic gas	r_{RO2}		0.11	0.11	0.11	0.11	0.11
Furnace pressure	p	MPa	0.10	0.10	0.10	0.10	0.10
Radiant absorption coefficient of the tri-atomic gas	k_Γ		1.39	1.85	1.57	1.50	1.44
Flame emissivity	a_fl		0.93	0.97	0.95	0.95	0.95
Fuel consumption	B	Kg/s	60.59	82.83	69.99	66.55	63.43
Flue gas temperature at the exit of the furnace	ϑ''_T	°C	973.00	989.00	979.00	977.00	975.00

The Carbon Net Zero Curves between Mixed Rates and Outlet Flue gas Temp. of Furnace W and L-flame at all stable loads was indicated in Fig. 6 & 7.

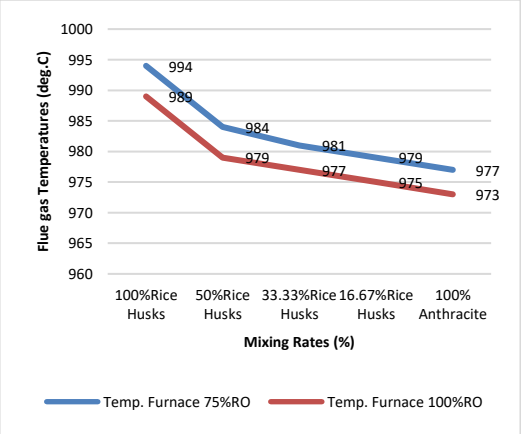

Figure 6: The Carbon Net Zero Curves between Mixed Rates and Outlet Flue gas Temp. of 622.5 MW Furnace W-flame at all stable loads.

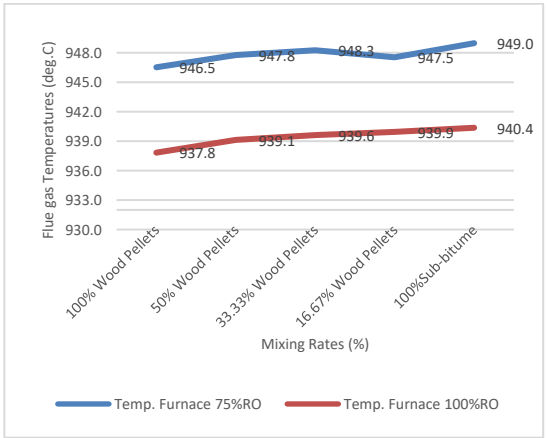

Figure 7: The Carbon Net Zero Curves between Mixed Rates and Outlet Flue gas Temp. of 688 MW Furnace L-flame at all stable loads.

The difference temperature W-flame furnace is better than subcritical units by about 4 deg.C at 100%RO or 75%RO, as illustrated in Figures 6–7. This is due to the fact that wood pellets with minimal modifications and moderate investment in comparison with rice husks subcritical technology.

To verify the calculation results, the simulating of combustion modeling of co-firing in domestic anthracite coal-fired sub-critical (622.5 MW) and imported sub-bitumen coal-fired supercritical larger-scale (688 MW) power units was built by Ansys software.

The imported sub-bitumen supercritical combustion chamber inserts wood pellets of 16.67% and 33.33% using existing burners. The domestic anthracite sub-critical furnace injects rice husk in the same mixed rate using new burners put on top of exiting burners.

The combustion modeling of boiler fired is performed, the field distribution of temperature and oxidation in the furnace verified stable as illustrated in Figs. 8-9. The temperatures between calculated and modeling are equivalent and the deviation is negligible.

(i) 16.67% wood pellets (ii) 33.33% wood pellets

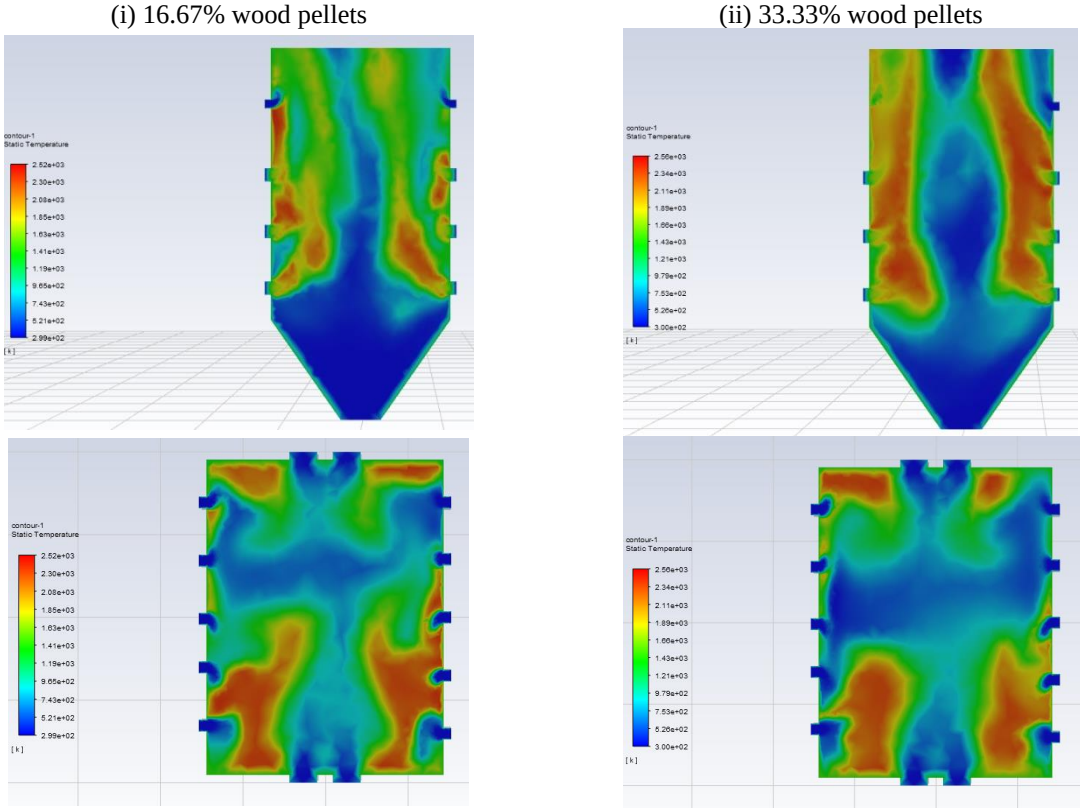

Figure 8: Static temperature and mass faction of oxidation in super-critical import sub-bitume coal 688MW furnace with mixed rates of (i) 16.67% and (ii) 33.33% wood pellets, replectively.

(a) 16.67% Rice Husks. (b) 33.33% Rice Husks.

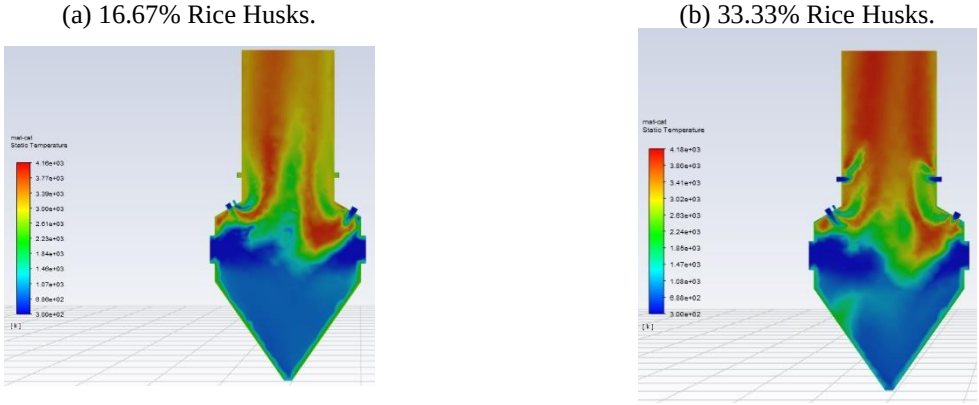

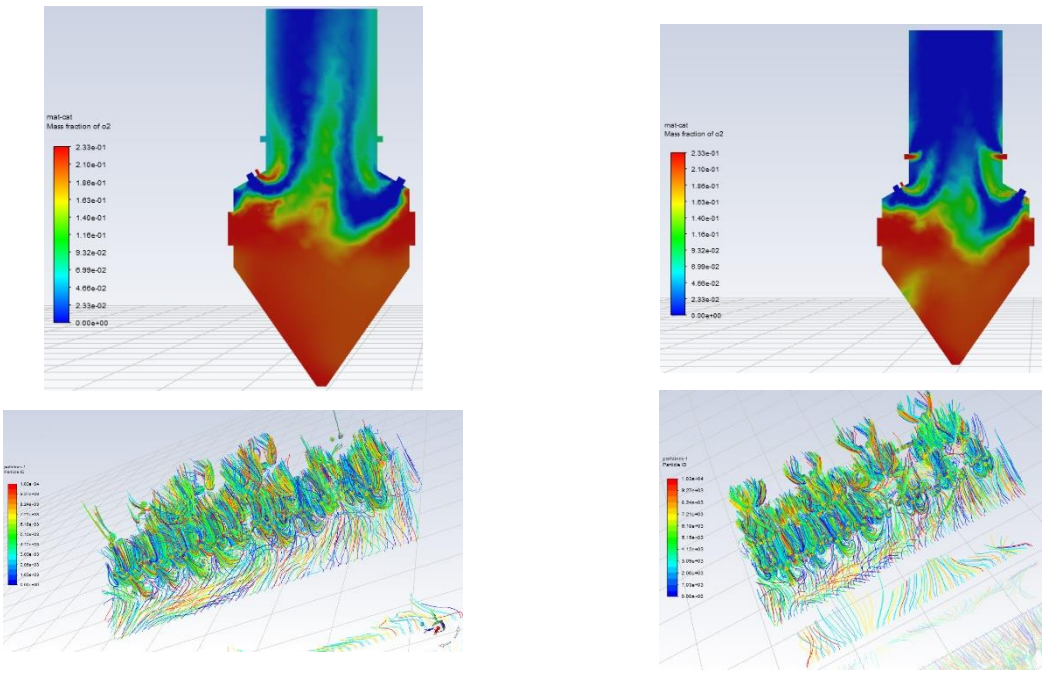

Figure 9: Static temperature, mass faction of oxidation and particle in sub-critical domestic anthracite coal 622.5MW furnace with mixed rates of (a) 16.67%, and (b) 22.22% rice husks, replectively.

For the specific case in Vietnam, the authors suggest using three options as analyzed above to reduce carbon emissions. The continuous works should be carryout performance guarantes test and calculate using PG_Cal created by the authors as meansion in [1] for all stable loads of power generation units to meet the Vietnam's "net zero" goal in 2050.

5 CONCLUSION

From the above analysis of technical and economic in incentives electrical price, taking into account the limiting factor of environmental emissions to propose the choice of capacity for new biomass power unit as appropriate in Vietnam, 10 MW biomass power units for district-scales are proposed. The authors found that wood pellets is not available at 8.47 US Cents per kWh of FIT price for new biomass plant, 87 g/kWh loss in cogeneration switched to independent power plant under paid back conditions is acceptable, the difference of outlet temperature between 100%RO and 75%RO of W-flame furnace are about 5 deg.C and L-flame is about 9 deg.C in the mixed rated of 16.67%, 33.33%, 50% and 100% , respectively. and biomass co-firing was suitable for pulverized coal larger-scale plants regarding to field distribution of temperature and oxidation diffusion and its road map should be immediatly performed even on the covid period. The results of the article are not only meaningful in building a new biomass plant, but also in co-firing biomass in coal-fired plant to reduce carbon with the goal of "net zero" 2050 in the field of electricity generation in general as well as in setting policies on environmental protection in industries.

REFERENCES

[1] Hoang, A.T.; Nguyen, T.V.; Nguyen, B.T. The Experimental Evaluation of Energy Efficiency and Carbonic Emission Rates for All Stable Loads of Larger-Scale (+600MW) Coal-Fired Power Generation Units in Vietnam. *Energies* 2022, 15 (6), 2185. https://doi.org/10.3390/en15062185

[2] *https://www.nldc.evn.vn/*

[3] W. YANG, "Biomass Co-firing Studies for Commercial-Scale Applications in Korea," presented at the *European Biomass Conference and Exhibition (EUBCE)*, Stockholm, Sweden, 2017.

[4] *The Handbook of Biomass Combustion and Co-firing*. London • Sterling, VA: Earthscan.

[5] P. Basu, J. Butler, and M. A. Leon, "Biomass co-firing options on the emission reduction and electricity generation costs in coal-fired power plants," *Renewable Energy*, vol. 36, no. 1, pp. 282-288, 2011. https://doi.org/10.1016/j.renene.2010.06.039

[6] K. Z. Y. Wang, L. Jiang et al., "Research on the cocorrosion characteristics of sulfur chloride in the combustion process of biomass mixed coal," *Journal of University Chemical Engineering & Technology*, vol. 6, pp. 1422-1429, 2015.

[7] H. J. Grabke, E. Reese, and M. Spiegel, "The effects of chlorides, hydrogen chloride, and sulfur dioxide in the oxidation of steels below deposits," *Corrosion Science*, vol. 37, no. 7, pp. 1023-1043, 1995. https://doi.org/10.1016/0010-938X(95)00011-8
[8] P. A. Jensen, F. J. Frandsen, K. Dam-Johansen, and B. Sander, "Experimental Investigation of the Transformation and Release to Gas Phase of Potassium and Chlorine during Straw Pyrolysis," *Energy & Fuels*, vol. 14, no. 6, pp. 1280-1285, 2000.
[9] K. Z. Y. Wang, L. Jiang et al., "“Study on sulfur-chlorine synergistic corrosion in biomass and coal co-firing,”" *Journal of Chemical Engineering of Chinese Universities*, vol. 29, pp. 1422-1429, 2015.
[10] A. Miltner, G. Beckmann, and A. Friedl, "Preventing the chlorine-induced high temperature corrosion in power boilers without loss of electrical efficiency in steam cycles," *Applied Thermal Engineering*, vol. 26, no. 16, pp. 2005-2011, 2006. https://doi.org/10.1016/j.applthermaleng.2006.01.006
[11] S. G. G. Li, X. Zhao, "High temperature chloridization corrosion on the bio-fuel boiler," *Total Corrosion Control*, vol. 23, pp. 44-45, 2009.
[12] W. Y. S. Li, and L. Fang, "The mechanism of the high temperature chloridization corrosion on the heat transfer surface of utility boiler," *Boiler Manufacturing*, vol. 1999, pp. 19-23, 1999.
[13] Y. Wang, Y. Sun, L. Jiang, L. Liu, and Y. J. J. o. C. Li, "Characteristics of Corrosion Related to Ash Deposition on Boiler Heating Surface during Cofiring of Coal and Biomass," *Hindawi Journal of Chemistry*, vol. 2020, 2020. https://doi.org/10.1155/2020/1692598
[14] J. Koppejan and L. L. Baxter, "Global operational status on cofiring biomass and waste with coal Experience with different cofiring concepts and fuels," *IEA Bioenergy-Task*, 2006.
[15] S. De, M. J. B. Assadi, and Bioenergy, "Impact of cofiring biomass with coal in power plants–A techno-economic assessment," *Biomass and Bioenergy*, vol. 33, no. 2, pp. 283-293, 2009. https://doi.org/10.1016/j.biombioe.2008.07.005
[16] F. Al-Mansour and J. Zuwala, "An evaluation of biomass co-firing in Europe," *Biomass and Bioenergy*, vol. 34, no. 5, pp. 620-629, 2010. https://doi.org/10.1016/j.biombioe.2010.01.004
[17] Jonghun Lim, Junghwan Kim. Optimizing ash deposit removal system to maximize biomass recycling as renewable energy for CO2 reduction. *Renewable Energy* 190 (2022) 1006-1017. https://doi.org/10.1016/j.renene.2022.03.095
[18] José Juan Bolívar Caballero, Ilman Nuran Zaini, Weihong Yang. Reforming processes for syngas production: A mini-review on the current status, challenges, and prospects for biomass conversion to fuels. *Applications in Energy and Combustion Science* 10 (2022) 100064. https://doi.org/10.1016/j.jaecs.2022.100064
[19] M. S. Roni, S. Chowdhury, S. Mamun, M. Marufuzzaman, W. Lein, and S. Johnson, "Biomass co-firing technology with policies, challenges, and opportunities: A global review," *Renewable and Sustainable Energy Reviews*, vol. 78, pp. 1089-1101, 2017. https://doi.org/10.1016/j.rser.2017.05.023
[20] P. J. I.-E. Lempp and IRENA, "Biomass co-firing: Technology brief," 2013.
[21] "Biomass Co-firing Technology Brief," IEA-ETSAP and IRENA© Technology Brief E21 – January 2013.
[22] B. Morrison and J. S. Golden, "Life cycle assessment of co-firing coal and wood pellets in the Southeastern United States," *Journal of Cleaner Production*, vol. 150, pp. 188-196, 2017. https://doi.org/10.1016/j.jclepro.2017.03.026
[23] A. H. Truong, M. Ha-Duong, and H. A. Tran, "Economics of co-firing rice straw in coal power plants in Vietnam," *Renewable and Sustainable Energy Reviews*, vol. 154, p. 111742, 2022. https://doi.org/10.1016/j.rser.2021.111742
[24] Tere Vad´en et al. Sectoral low-carbon roadmaps and the role of forest biomass in Finland’s carbon neutrality 2035 target. *Energy Strategy Reviews* 41 (2022) 100836. https://doi.org/10.1016/j.esr.2022.100836
[25] Felipe Orlando Centeno-González et al. CFD modeling of combustion of sugarcane bagasse in an industrial boiler. *Fuel* 193 (2017) 31–38. http://dx.doi.org/10.1016/j.fuel.2016.11.105
[26] "IEA Bioenergy Task 32: Biomass Combustion and Co-firing, Database of Biomass Co-firing.," Available: http://www.ieabcc.nl/.
[27] Basu P., Kefa C. and Jestin L (2000) *Boilers and Burners - Theory and Design*. Springer -Verlag, Newyork, Inc. USA.
[28] *The Statistical Yearbook of 13 Provinces in Mekong Delta*, 2019.
[29] MONRE, 2020. *Letter No. 1316/BDKH-TTBVTOD dated 31st December 2020 Concerning about Carbon emission factor for Vietnam power grid system, Department of Climate Change of Ministry of Natural Resources and Environment of the Government of the Socialist Republic of Viet Nam.*
[30] *http://maps.vnforest.gov.vn/*
[31] *https://www.propellets.at/en/international-prices-wood-pellets*
[32] *https://www.eia.gov/coal/markets/*

A STUDY ON THE PRE-PROCESSING AND PRESERVATION OF JULIENNE-CUT WHITE RADISH *(Raphanus raphanistrum)*

DUY H. TRUONG [1], THI MAI HUONG NGUYEN [1*]

[1] *Institute of Biotechnology and Food technology, Industrial University of Ho Chi Minh city, Vietnam*
[*] *nguyenthimaihuong@iuh.edu.vn*

Abstract. Julienne-cut white radish *(Raphanus raphanistrum)* was utilized as the raw material for the production process of pickled white radish. Canned pickled white radish was a product that can mitigate post-harvest losses and enhance the value of local agricultural produce. However, the production process of canned pickled white radish often encounters issues such as discoloration and reduced crispness of the julienne-cut white radish within a short period of time. The objective of this study is to investigate the technologies for the pre-processing stage of julienne-cut white radish and its storage conditions prior to its use in the production of canned pickled white radish. During the pre-processing stage, the julienne-cut white radish was soaked in water, NaCl, $NaHSO_3$, and citric acid before being dried, and the color change was measured after 1, 15, 30, and 45 days of storage. Correspondingly, $NaHSO_3$ concentrations ranging from 0.01% to 0.03% were also implemented. The drying temperature for the julienne-cut white radish ranged from 50°C to 80°C. When storing the julienne-cut white radish, ambient preservation methods and refrigeration (5-10°C) were applied, and color parameters were measured. The results demonstrated that using a 0.02% concentration of $NaHSO_3$ for pre-soaking, combined with refrigeration storage at 5-10°C, yielded favorable results after a 45-day investigation period. The adjustment and control of these stages are necessary to improve product quality and address the issue of product discoloration.

Keywords. julienne-cut white radish, pickled white radish, storage, pre-processing stage, ambient preservation, refrigeration method

1 INTRODUCTION

Raphanus raphanistrum commonly known as radish, belongs to the genus Raphanus, within the Brassicaceae family. It stands as one of the prevalent cultivated plant species worldwide, with significant cultivation hubs in regions such as China, Japan, South Korea, and Southeast Asian countries [1, 2]. In Vietnam, radishes are extensively cultivated in Mekong Delta, where they exhibit high yields [2]. Within the composition of radish, water constitutes the majority (95%), while dry matter constitutes a minor portion (5%). Among the dry matter, carbohydrates (2.63%) are the most abundant, comprising sugars (1.23%) and dietary fiber (1.4%). Protein content (1.1%) and lipids (0.1%) contribute relatively modest proportions. The predominant fatty acids found in the lipids are linolenic acid, erucic acid, and palmitic acid [3–5].

According to Manivannan et al. (2019), the medical nutritional value of radishes has been empirically substantiated [6]. The potential of these radishes was attributed to the presence of certain beneficial secondary metabolites, such as glucosinolates, polyphenols, and isothiocyanates. Glucosinolates represent a distinct class of metabolites exclusively identified in vegetables of the cruciferous family. Additionally, according to research findings by Maina et al. (2020), glucosinolates and their hydrolyzed products manifest bioactivity at the molecular level [7].

White radishes, which contain approximately 95% water, are prone to spoilage within a few days. Consequently, various preparations are employed to facilitate preservation. As stated by Gamba et al. (2021), white radishes can be cooked until tender, pickled with other vegetables, or processed into pickles or canned products [8]. Moreover, according to Wills et al. (2003), Asian white radishes have been extensively processed and are widely utilized in Japan and South Korea, consumed in various forms such as fresh, dried, salted, and pickled [9]

As per Jones et al. (1943), regarding salt-soaked and picked radish products, each product involves distinct

soaking and salting techniques. Based on research findings, salt-soaked radish preservation stands as the oldest traditional food preservation method, encompassing four salt-soaking techniques—two employing dry salt and two utilizing brine soaking. The nutritional value of salt-soaked radish is significantly retained, and the presence of microorganisms in salt-soaked radish is nearly negligible. In the case of pickled white radish, fresh radishes, after undergoing drying, are subjected to water immersion [10].

The use of dehydrated radishes must ensure a moisture content below 10% as a primary consideration. The distinctive characteristics of pickled white radish include their typical white color, odorless and non-pungent brine, and absence of foreign matter. The texture of the radishes is crisp, devoid of softness or limpness. As indicated by Bae et al. (2012), alterations in nutritional content occur due to thermal treatment compared to untreated conditions [11]. In the case of pickled white radish products, the processing approach directly influences color development, demanding the guarantee of minimal susceptibility to discoloration in radishes. Apart from product color, maintaining structural integrity is of equal significance. When delivered to consumers, radishes should exhibit a crisp texture rather than softness. Thus, process standardization is essential to fulfill these criteria.

The conversion of pickled white radish products from a traditional to an industrial scale poses several significant challenges, with the most prominent being the susceptibility to radish darkening and structural alterations due to soaking and washing activities over time. The technology employed for manufacturing canned pickled products in such cases often utilizes dried radishes to ensure both crispness and elasticity, simultaneously enhancing the product's soaking fluid permeability [12]. The dehydration process of radishes also results in the accumulation of amino acids, including alanine, proline, and GABA, during processing, contributing to flavor and health benefits. However, due to the effects of enzymes and oxidative colorants inherent in radishes, gradual darkening occurs during drying and storage. This is precisely why, before immersing radishes in vinegar, the washing and soaking steps are essential. This pretreatment process significantly impacts both the color and the structure of the product over time.

The aim of this research is to investigate the technologies for the pre-processing stage of julienne-cut white radish and its storage conditions prior to its use in the production of canned pickled white radish.

2 MATERIALS AND METHODS

2.1 Materials

The white radish utilized was of the Hong Kong cultivar and must possess the following attributes: freshness, bright white skin, and minimal blemishes. Radishes aged 40 - 45 days are employed, with an average root weight of 250 - 300g. The outer skin should exhibit a bright white hue, while undersized, withered, soft, or discolored radishes are excluded. Quality standards entail a brix level within the range of 5-6, a fruit solution pH of 4 - 4.5, and radishes meeting VIETGAP certification. No plant protection agents are permitted to be applied within 15 days prior to harvest.

2.2 Prepare the julienne-cut white radish

The process begins with washing and peeling the radish, followed by cutting it into 1cm-thick slices called julienne-cut white radish. Subsequently, the slices are subjected to a whitening treatment involving immersion (for 30 minutes) with predetermined concentrations of whitening immersion solution. After the whitening treatment, the julienne-cut white radish undergoes a single rinsing step. Next, they are subjected to a drying process, the temperature of which is meticulously monitored.

The whitening immersion solution comprises of NaCl, citric acid, and $NaHSO_3$.

2.3 Experiment design

2.3.1 Study 1. The effect of the whitening immersion solution on the color of dried julienne-cut white radish

The whitening immersion solution to soak julienne-cut white radish before drying are described in **Table 1**

Table 1: The whitening immersion solution to soak julienne-cut white radish.

Sample names	M1	M2	M3	M4
The whitening immersion solution	Untreated	NaCl 1%	Acid citric 0.1%	$NaHSO_3$ 0.02%

Soaking time: 30 minutes
Drying temperature: 60 ºC
Drying time: 10 - 12 hours
Storage time: 1 – 45 days
Moisture content after drying: < 10%

2.3.2 Study 2. The effect of the concentration of whitening immersion solution on the color of dried julienne-cut white radish

The concentration of whitening immersion solution to soak julienne-cut white radish before drying are described in **Table 2**

Table 2: The concentration of whitening immersion solution to soak julienne-cut white radish.

Sample names	MH1	MH2	MH3	MH4	MH5
The concentration of whitening immersion solution	0.01%	0.015%	0.02%	0.025%	0.03%

The whitening immersion solution: selected from study 1
Soaking time: 30 minutes
Drying temperature 60 ºC
Drying time: 10 - 12 hours
Storage time: 1 – 45 days
Moisture content after drying: < 10%

2.3.3 Study 3. The effect of drying temperature on the color of dried julienne-cut white radish

Table 3 describes sample names and parameters of drying temperature changed in the experiment

Table 3: The parameters of drying temperature.

Sample names	MA1	MA2	MA3	MA4
Drying temperature	50 ºC	60 ºC	70 ºC	80 ºC

The whitening immersion solution: selected from study 1
The concentration of whitening immersion solution: selected from study 2
Soaking time: 30 minutes
Drying time: 10 - 12 hours
Storage time: 1 – 45 days
Moisture content after drying: < 10%

2.3.4 Study 4. The effect of storage conditions on the color of dried julienne-cut white radish

Table 4: Storage conditions.

Sample names	MP1	MP2
Storage conditions	25 - 29 ºC	5 - 10 ºC

The whitening immersion solution: selected from study 1
The concentration of whitening immersion solution: selected from study 2
Soaking time: 30 minutes
Drying temperature: selected from study 3
Drying time: 10 - 12 hours
Storage time: 1 – 45 days
Moisture content after drying: < 10%

2.4 Color measurement method

The color of the julienne-cut white radish was determined using a Minolta CR400 colorimeter (Konica Co., Japan). Measurements are conducted on each surface of the sample. Color was recorded utilizing the standardized CIE-Lab* color space.
Where:
L*: Represents lightness (brightness or darkness)
a*: Represents color on the green (-) to red (+) axis
b*: Represents color on the blue (-) to yellow (+) axis
The numerical values of L, a, and b are employed for estimating the overall color difference (ΔE).
The outcome was the average value obtained from three readings for each batch of samples. The parameter ΔE* signifies the color deviation concerning the standard sample (white background of the colorimeter).

2.5 Data analysis

A one-way analysis of variance (ANOVA) method was applied to the data in order to compare significant differences with a significance level of $p < 0.05$, utilizing the Stargraphics Centurion XV.I software. The visualization of the average outcomes was created using Microsoft Excel 2019 software.

3 RESULTS AND DISCUSTIONS

3.1 Study 1. The effect of the whitening immersion solution on the color of dried julienne-cut white radish

Table 5: The change in color of dried julienne-cut white radish treated with different whitening immersion solution after storage time.

Samples		Storage time (day)			
		1	15	30	45
L*	M1	59.9±1.7^{a}	58.2±1.6^{a}	42.0±0.3^{a}	38.2±2.0^{a}
	M2	60.4±0.5^{a}	60.0 ±0.8^{a}	49.3±0.6^{b}	40.8±0.4a^{b}
	M3	66.6±2.4^{b}	65.9±0.6^{b}	49.4±2.9^{b}	43.1±0.7^{b}
	M4	72.5±1.2^{c}	72.0±0.4^{c}	70.6±1.2^{c}	64.2±2.1^{a}
a*	M1	4.25±0.16^{bc}	9.18±0.38^{d}	10.31±0.71^{c}	14.12±0.21^{c}
	M2	5.32±0.43^{c}	6.35 ±0.25^{c}	7.73±0.71^{b}	11.33±1.53^{b}
	M3	2.45±1.21^{a}	7.62±0.27^{b}	9.92±1.20^{c}	11.36±1.41^{b}
	M4	3.01±0.7a^{b}	4.89±0.4^{a}	6.07±0.2^{a}	5.91±0.14^{a}
b*	M1	34.0±1.5^{b}	41.4±2.7^{c}	34.3±3.1^{b}	29.8±1.0^{b}
	M2	32.0±6.1^{b}	34.3±3.3^{b}	37.7±0.7^{c}	38.2±0.7^{d}
	M3	24.5 ±0.7^{a}	30.8±2.1^{b}	33.9±1.2^{b}	35.5±0.2^{c}
	M4	21.7±1.8^{a}	24.9±0.2^{a}	26.3±0.9^{a}	27.0±0.8^{a}
ΔE*	M1	46.5±2.1^{c}	53.5±1.5^{d}	62.1±1.3^{c}	64.0±1.6b^{c}
	M2	45.2±3.7^{c}	46.9±1.7^{c}	57.4±0.7^{b}	65.2±0.4^{c}
	M3	35.2±1.6^{b}	40.5±1.2^{b}	55.6 ±1.9^{b}	61.9±0.6^{b}
	M4	28.9±2.1^{a}	31.6±0.4^{a}	33.8±0.3^{a}	39.0 ±1.5^{a}

Different letters in same column indicate statistically significant differences (α = 5 %)

The color measurement outcomes of the julienne-cut white radish subjected to diverse chemical treatments are illustrated in **Table 5**. The results exhibit significance in the distinctions among the samples' color indices. The L* values of all samples exhibit a consistent declining trend over the storage duration. Chemically treated samples (M2, M3, M4) manifest higher L* brightness values and less pronounced levels of discoloration compared to the untreated sample (M1). Notably, sample M4 showcases the highest luminosity and the most resilient maintenance of brightness, as manifested by the lowest ΔE* value. The a* values of all samples cluster around 0, signifying the midpoint between the red and green color spectrums. As the storage duration advances, all samples exhibit a progressive shift towards the red spectrum, indicative of a darkening inclination. Positive b* values denote a progressive trend towards yellow hues, intensifying into deeper shades of yellow with prolonged storage. These findings harmonize with the research conducted by Impaprasert et al. (2020) on Konjac [13].

Different chemical treatments exhibit distinct mechanisms for mitigating color changes. The primary cause of color alteration over time is attributed to the action of the polyphenol oxidase (PPO) enzyme, which catalyzes the o-hydroxylation of monophenols into o-diphenols and subsequently oxidizing o-diphenols into o-quinones in the presence of molecular oxygen. The ensuing quinone polymerization leads to the formation of brown or black pigments. The highly effective outcome of using $NaHSO_3$ might be attributed to its dual capacity as an oxidative agent, capable of oxidizing chromogens, and an inhibitor of the inherent PPO enzyme within the radishes, thereby restraining microbial activity over time. The color-preserving effect of NaHSO3 has also been noted in the study by Ling Li et al. (2018) on fresh-cut potato [14].

Sodium chloride (NaCl) acts as a strong electrolyte that inhibits microbial activity and the functioning of the PPO enzyme. It also restricts the penetration of oxygen into cellular structures during drying, in brighter color compared to untreated samples. However, the color changes significantly during storage. This conclusion aligns with the findings of Win Yee et al. (2019) on sweet potatoes [15].

Citric acid, as a reducing agent, can convert quinols to phenols and lower pH, slowing down color transformation reactions. Additionally, it acts as a metal chelator, promoting oxidative color reactions. Hence, citric acid imparts a brighter color compared to samples without chemicals or salt, albeit less effectively than $NaHSO_3$ [16]. Nevertheless, beyond 30 days, all samples experience rapid and noticeable color degradation, as evidenced by the L* values. This could be attributed to the reactivation of residual polyphenol oxidase, leading to further enzymatic browning reactions [17]. Consequently, it can be asserted that pre-drying chemical treatments significantly impact color changes over time. The results confirm that the use of $NaHSO_3$ yields the most beneficial effect in enhancing julienne-cut white radish color during both drying and storage.

3.2 Study 2. The effect of the concentration of whitening immersion solution on the color of dried julienne-cut white radish

The outcomes indicate significant variations in color parameters among different samples **(Table 6)**. Over the storage duration, there is a consistent decrease in the L* values. Samples treated with higher concentrations (MH3, MH4, MH5) exhibit higher L* values, indicating brighter color and slower color degradation compared to samples treated with lower concentrations (MH1, MH2). After one day of drying, there is no discernible difference in brightness among the four samples MH2, MH3, MH4, and MH5. This demonstrates the effectiveness of using $NaHSO_3$ for treatment compared to untreated samples, as well as the beneficial effect of higher chemical concentrations in Sample M1. This outcome could be attributed to the sufficient concentration of chemicals in sample M2, which effectively mitigated surface discoloration immediately after drying. However, there is no significant difference between samples M1 and M2 after 15 and 45 days of storage. This color degradation might be due to accelerated oxidation of the porous fiber structure upon drying or inadequate chemical concentration to fully oxidize internal pigments, leading to quicker discoloration in samples with higher concentrations. In a study on *Nevadar* radish, Rosario Goyeneche et al. (2003) explained that changes in color (L*) are related to variations in soluble and insoluble pectic substances, total glucosinolates, and other color-producing compounds [18]. This suggests that the enhanced effectiveness of higher concentrations in samples MH3, MH4, MH5 in maintaining brightness might stem from their sufficient concentration to oxidize these color-producing compounds. Samples MH3, MH4, MH5 exhibit similar color maintenance capabilities over the storage duration.

Furthermore, as storage duration increases, the color of dried julienne-cut white radish intensifies, as evidenced by the significant increase in a* and b* values. This phenomenon could result from the transformation of 1-(2-thioxopyrrolidin-3-yl)-1,2,3,4-tetrahydro-β-carboline-3-carboxylic acid into the yellow pigment 2-[3-(2-thioxopyrrolidin-3-ylidene)methyl]-tryptophan [19]. Based on these results, selecting sample MH3, which utilizes 0.02% $NaHSO_3$, provides a high level of brightness, maintains stable brightness, and requires a moderate amount of chemicals for treatment.

Table 6: The change in color of dried julienne-cut white radish treated with various concentration of whitening immersion solution after storage time ($NaHSO_3$).

Samples		Storage time (day)			
		1	15	30	45
L*	MH1	70.4±0.4^{a}	70.5 ±2.2^{a}	62.9± 1.4^{a}	59.9±2.1^{a}
	MH2	72.8±1.1^{b}	69.9±2.9^{a}	65.1±1.0^{b}	59.8±0.8^{a}
	MH3	72.4 ±0.6^{b}	72.5±1.3^{a}	70.6 ±1.2^{d}	64.2±2.1^{b}
	MH4	72.2±0.8^{b}	73.1±0.8^{ab}	68.2±1.1^{c}	62.8±0.6^{b}
	MH5	72.5±0.7^{b}	75.8 ±0.3^{b}	68.1±1.2^{c}	62.8±0.2^{b}
a*	MH1	3.79±0.17^{c}	4.50±0.21^{c}	7.54±0.33^{b}	8.80±0.30^{c}
	MH2	3.58±0.04^{bc}	3.09±0.2^{b}	7.29±0.54^{b}	7.56±0.36^{b}
	MH3	3.45±0.23^{b}	3.16±0.22^{b}	6.27±0.23^{a}	6.23±0.10^{a}
	MH4	3.44±0.07^{b}	2.89±0.19^{b}	6.23±0.12^{a}	6.42±0.10^{a}
	MH5	3.18±0.07^{a}	1.54±0.18^{a}	6.35±0.3^{a}	6.57±0.29^{a}
b*	MH1	28.4±0.4^{bc}	33.1±0.3^{b}	33.3±0.3^{b}	36.8±2.3^{b}
	MH2	25.2±2.7^{a}	30.3±2.0^{b}	35.1±2.7^{b}	36.3±1.5^{b}
	MH3	26.6±0.7^{ab}	25.9 ±1.2^{a}	26.3±0.9^{b}	27.0 ±0.8^{a}
	MH4	31.7±1.3^{d}	32.0 ±2.5^{b}	34.3±1.2^{b}	35.7±05^{b}
	MH5	31.0±0.9^{cd}	33.1±0.7^{b}	34.6±0.5^{b}	35.3±2.7^{b}
ΔE*	MH1	35.0±0.4^{b}	38.5±1.7^{c}	44.2±0.9^{c}	49.1±0.6^{c}
	MH2	31.1±1.3^{a}	36.6±3.0^{bc}	43.9±1.4^{c}	48.5±1.0^{c}
	MH3	32.3±0.5^{a}	31.7±1.7^{a}	33.8±0.3^{a}	39.1±1.5^{a}
	MH4	36.2±1.5^{b}	35.9±1.6^{bc}	41.2±0.9^{b}	45.8±0.7^{b}
	MH5	35.5±1.5^{b}	35.1±0.5^{b}	41.5±0.7^{b}	45.5±1.9^{b}

Different letters in same column indicate statistically significant differences (α = 5 %)

3.3 Study 3. The effect of drying temperature on the color of dried julienne-cut white radish

The color measurement results of the samples when subjected to drying at different temperatures are depicted in **Table 7**. The findings indicate significant color variations among samples dried at different temperatures. The L* values decrease with increasing temperature, and Sample MA1 possesses higher brightness than the other three samples (MA2, MA3, MA4). Sample MA1 exhibits the highest luminosity, evident by the smallest ΔE* value. The a* values of all samples are positive, indicating a shift towards red hues, with higher drying temperatures resulting in increased a* values. Positive b* values suggest a tendency towards yellow hues. These results also align with the study conducted by Vega-Gálvez et al. (2012) on apples [20]. These outcomes demonstrate the influence of temperature on color changes attributed to non-enzymatic browning phenomena. The radish composition includes amino acids and sugars, which may engage in Maillard reactions leading to discoloration. These reactions are more pronounced when water loss is substantial, increasing the concentration of dry matter. Greater water loss occurs at higher temperatures, accelerating the reaction rate. Surface characteristics of the fiber alter due to rapid dehydration, reducing water evaporation rate from the outer surface, as governed by the drying process. This leads to enhanced internal oxidation and color alteration in samples dried at higher temperatures, such as MA2, MA3, and MA4. Surface color changes may be due to high temperature or prolonged drying time, combined with the presence of convective air oxygenation, enhancing the color development of julienne-

cut white radish color compounds like anthocyanins. Extended drying at higher temperatures triggers browning reactions, which reduce L* values. The changes in L*, a*, and b* values might arise from the degradation of color pigments or Maillard browning reactions [21]. To ensure bright color in dried julienne-cut white radish, a temperature of 50°C is optimal. However, to achieve moisture content < 10%, it requires more than 18 hours, whereas drying at 60 °C only necessitates 10-12 hours while maintaining the required brightness. Drying at 60 °C not only saves energy but also offers higher economic efficiency. Hence, a temperature of 60 °C is the best choice for fiber drying.

Table 7: The change in color of dried julienne-cut white radish treated with different drying temperatures.

Samples	MA1	MA2	MA3	MA4
L*	71.8 ± 0.6^{c}	59.9 ± 1.7^{b}	55.4 ± 0.7^{a}	54.7 ± 1.3^{a}
a*	2.40 ± 0.36^{a}	4.25 ± 0.16^{b}	4.76 ± 0.14^{c}	5.33 ± 0.23^{d}
b*	21.7 ± 2.0^{a}	34.0 ± 1.5^{b}	38.8 ± 0.6^{c}	34.6 ± 0.3^{b}
ΔE*	29.4 ± 0.8^{a}	46.5 ± 2.0^{b}	53.0 ± 0.3^{c}	50.9 ± 1.3^{c}

Different letters in same row indicate statistically significant differences (α = 5 %)

3.4 The effect of storage conditions on the color of dried julienne-cut white radish

Table 8: The change in color of dried julienne-cut white radish treated with different storage conditions after storage time.

Samples		Storage time (day)			
		1	15	30	45
L*	MP1	59.9 ± 1.7^{c}	58.2 ± 1.6^{c}	42.0 ± 0.3^{b}	38.2 ± 2.0^{a}
	MP2	59.9 ± 1.7^{c}	58.2 ± 0.8^{c}	48.8 ± 0.3^{b}	42.1 ± 1.3^{a}
a*	MP1	4.25 ± 0.16^{a}	9.18 ± 0.38^{b}	10.31 ± 0.71^{c}	14.12 ± 0.21^{d}
	MP2	4.25 ± 0.16^{a}	5.34 ± 0.44^{b}	9.45 ± 0.76^{c}	10.50 ± 0.64^{d}
b*	MP1	34.0 ± 1.5^{ab}	41.4 ± 2.7^{c}	34.3 ± 3.1^{b}	29.8 ± 1.0^{a}
	MP2	34.0 ± 1.5^{a}	37.9 ± 0.3^{b}	34.1 ± 1.4^{a}	32.2 ± 0.8^{a}
ΔE*	MP1	46.5 ± 2.1^{a}	53.5 ± 1.5^{b}	62.1 ± 1.3^{c}	64.0 ± 1.6^{c}
	MP2	46.5 ± 2.1^{a}	50.4 ± 0.4^{b}	56.1 ± 0.8^{c}	60.9 ± 1.0^{d}

Different letters in same row indicate statistically significant differences (α = 5 %)

The color measurement results of the sample after different storage conditions are presented in **Table 8**. The findings indicate significant color variations among samples stored under different conditions. The L* values of both samples tend to decrease over time. Samples stored under refrigeration exhibit brighter and slower color deterioration compared to those stored at room temperature. Refrigerated samples with brighter appearance also demonstrate better color retention, as evidenced by lower ΔE* values. The a* values of both samples gradually increase, shifting towards red hues. Positive b* values suggest a tendency towards yellow hues. These results are in line with the findings of Liuquing et al. (2018), they investigated the influence of different storage conditions on the sensory attributes of freeze-dried *Agaricus bisporus* slices [22]. These outcomes may arise from the influence of enzyme activity affected by storage temperature. Low temperatures inhibit enzyme activity, resulting in slower color changes in dried julienne-cut white radish. Storage temperature significantly impacts the rate of browning. According to Rosselló et al. (1994), the minimum temperature for non-enzymatic browning is 4 °C, and the browning rate starts to increase above 20 °C [23].

4 CONCLUSIONS

The results of this study have highlighted that immersion in a 0.02% $NaHSO_3$ solution followed by drying at 60°C is capable of enhancing the color of julienne-cut white radish after drying over storage duration. The rapid discoloration resulting from the occurrence of browning during storage can be mitigated by employing this solution, coupled with refrigerated storage, to achieve prolonged preservation effectiveness. However, numerous studies have indicated that $NaHSO_3$ negatively affects the condition of individuals

with asthma, hence over time, it could be replaced with natural browning inhibitors such as citric acid, and their concentrations should be re-evaluated to achieve optimal efficacy. Immersing julienne-cut white radish is a pre-processing step prior to optimal canning to avoid affecting the color and structure of the product. Nonetheless, after a storage period of 5 months, the product's structure also noticeably diminishes, falling short of sensory quality requirements. Consequently, there is a need to adopt an alternative method to improve the product's structure. As suggested by Xiang Li et al. (2018), pre-treatment with ferulic acid could potentially mitigate the softening of julienne-cut white radish during heat processing [24].

ACKNOWLEDGMENT

The work was supported by Institute of Biotechnology and Food Technology, Industrial University of Ho Chi Minh city.

REFERENCES

[1] Z. LU *et al.*, "Analysis and Evaluation of Nutritional Quality in Chinese Radish (Raphanus sativus L.)," *Agric. Sci. China*, vol. 7, no. 7, pp. 823–830, 2008, doi: https://doi.org/10.1016/S1671-2927(08)60119-4.

[2] G. Nayik and A. Gull, *Antioxidants in Vegetables and Nuts - Properties and Health Benefits*. Springer Nature Singapore Pte Ltd, 2020.

[3] R. M. P. Gutiérrez and R. L. Perez, "Raphanus sativus (Radish): their chemistry and biology.," *ScientificWorldJournal.*, vol. 4, pp. 811–837, Sep. 2004, doi: 10.1100/tsw.2004.131.

[4] S. Manchali, K. N. Chidambara Murthy, and B. S. Patil, "Crucial facts about health benefits of popular cruciferous vegetables," *J. Funct. Foods*, vol. 4, no. 1, pp. 94–106, 2012, doi: https://doi.org/10.1016/j.jff.2011.08.004.

[5] T. Shin, M. Ahn, G. O. Kim, and S. U. Park, "Biological activity of various radish species," *Orient. Pharm. Exp. Med.*, vol. 15, no. 2, pp. 105–111, 2015, doi: 10.1007/s13596-015-0183-9.

[6] A. Manivannan, J.-H. Kim, D.-S. Kim, E.-S. Lee, and H.-E. Lee, "Deciphering the Nutraceutical Potential of Raphanus sativus-A Comprehensive Overview.," *Nutrients*, vol. 11, no. 2, Feb. 2019, doi: 10.3390/nu11020402.

[7] S. Maina, G. Misinzo, G. Bakari, and H.-Y. Kim, "Human, Animal and Plant Health Benefits of Glucosinolates and Strategies for Enhanced Bioactivity: A Systematic Review.," *Molecules*, vol. 25, no. 16, Aug. 2020, doi: 10.3390/molecules25163682.

[8] M. Gamba *et al.*, "Nutritional and phytochemical characterization of radish (Raphanus sativus): A systematic review," *Trends Food Sci. Technol.*, vol. 113, pp. 205–218, 2021, doi: https://doi.org/10.1016/j.tifs.2021.04.045.

[9] R. B. H. Wills and R. C. Coogan, "Cultural differences in degree of liking of asian white radish (*Raphanus sativus L.*)," *J. Sens. Stud.*, vol. 18, no. 1, pp. 83–87, Mar. 2003, doi: https://doi.org/10.1111/j.1745-459X.2003.tb00375.x.

[10] W. Jones, "Preservation of Vegetables by Salting and Pickling," *Bull. Agric. Ext. Serv.*, vol. 131, 1943.

[11] R.-N. Bae, Y.-K. Lee, and S.-K. Lee, "Changes in Nutrient Levels of Aqueous Extracts from Radish (Raphanus sativus L.) Root during Liquefaction by Heat and Non-heat Processing," *Korean J. Hortic. Sci. Technol.*, vol. 30, pp. 409–416, Aug. 2012, doi: 10.7235/hort.2012.11141.

[12] H. Kaymak, F. Kalkan, and I. Ozturk, "Some physico-mechanical properties of radish (Raphanus sativus L.) cultivars," vol. 69, pp. 945–952, Jan. 2016.

[13] R. Impaprasert, Z. Jianrong, G. Srzednicki, Y. Lei, and T. Ruixuan, "Postharvest Technology of Konjac," 2020, pp. 161–171.

[14] L. Li, M. Wu, M. Zhao, M. Guo, and H. Liu, "Enzymatic properties on browning of fresh-cut potato," *IOP Conf. Ser. Mater. Sci. Eng.*, vol. 397, p. 12116, Aug. 2018, doi: 10.1088/1757-899X/397/1/012116.

[15] L. Win Yee, C. Cheun, and C. W. Wong, "Inhibition of enzymatic browning in sweet potato (Ipomoea batatas (L.)) with chemical and natural anti-browning agents," *J. Food Process. Preserv.*, vol. 43, Oct. 2019, doi: 10.1111/jfpp.14195.

[16] G. Srzednicki and C. Borompichaichartkul, *Konjac Glucomannan: Production, Processing, and Functional Applications*. CRC Press, 2020.

[17] L. Sun, Q. Liu, C. Bao, and J. Fan, "Comparison of Free Total Amino Acid Compositions and Their Functional Classifications in 13 Wild Edible Mushrooms.," *Molecules*, vol. 22, no. 3, Feb. 2017, doi: 10.3390/molecules22030350.

[18] M. Schreiner, S. Huyskens-Keil, A. Krumbein, H. Prono-Widayat, and P. Lüdders, "Effect of film packaging and surface coating on primary and secondary plant compounds in fruit and vegetable products," *J. Food Eng.*, vol. 56, no. 2, pp. 237–240, 2003, doi: https://doi.org/10.1016/S0260-8774(02)00259-5.

[19] H. Matsuoka, A. Takahashi, Y. Ozawa, Y. Yamada, Y. Uda, and S. Kawakishi, "2-[3-(2-Thioxopyrrolidin-3-ylidene)methyll-tryptophan, a novel yellow pigment in salted radish roots.," *Biosci. Biotechnol. Biochem.*, vol. 66, no. 7, pp. 1450–1454, Jul. 2002, doi: 10.1271/bbb.66.1450.

[20] A. Vega-Gálvez *et al.*, "Effect of temperature and air velocity on drying kinetics, antioxidant capacity, total phenolic content, colour, texture and microstructure of apple (var. Granny Smith) slices," *Food Chem.*, vol. 132, no. 1, pp. 51–59, 2012, doi: https://doi.org/10.1016/j.foodchem.2011.10.029.

[21] S. Aral and A. V. Beşe, "Convective drying of hawthorn fruit (Crataegus spp.): Effect of experimental parameters on drying kinetics, color, shrinkage, and rehydration capacity," *Food Chem.*, vol. 210, pp. 577–584, 2016, doi: https://doi.org/10.1016/j.foodchem.2016.04.128.

[22] W. Liuqing, H. Qiuhui, P. Fei, M. Alfred Mugambi, and Y. Wenjian, "Influence of different storage conditions on physical and sensory properties of freeze-dried Agaricus bisporus slices," *LWT*, vol. 97, pp. 164–171, 2018, doi: https://doi.org/10.1016/j.lwt.2018.06.052.

[23] C. Rosselló, A. Mulet, S. Simal, A. Torres, and J. Cañellas, "Quality of dried apricots: Effect of storage temperature, light and SO2 content," *J. Sci. Food Agric.*, vol. 65, no. 1, pp. 121–124, May 1994, doi: https://doi.org/10.1002/jsfa.2740650118.

[24] X. Li, G. Liu, Y. Tu, J. Li, and S. Yan, "Ferulic acid pretreatment alleviates the decrease in hardness of cooked Chinese radish (Raphanus sativus L. var. longipinnatus Bailey)," *Food Chem.*, vol. 278, pp. 502–508, 2019, doi: https://doi.org/10.1016/j.foodchem.2018.10.086.

DESIGN OF AN EJECTOR REFRIGERATION SYSTEM USING A PAIR OF R134A/R410A

NGUYEN VAN TUAN[1], TRAN DINH ANH TUAN [*], HO THI KHANH PHUONG [1], NGUYEN VAN CUNG [2]

[1] *Faculty of Heat and Refrigeration Engineering, Industrial University of Ho Chi Minh City*

[2] *Faculty of Automotive Engineering Technology, Industrial University of Ho Chi Minh City*

nguyenvantuan@iuh.edu.vn, trandinhanhtuan@iuh.edu.vn*, hothikhanhphuong@iuh.edu.vn, nguyenvancung@iuh.edu.vn*

Abstract. Ejector refrigeration system has widely used in the purpose of saving energy. The ejector refrigeration system is proposed in this study. The refrigerant R134A and R410A were chosen as a pair of working fluid. The R410A was used for the vapor compression cycle, and R134A was used for the ejection cycle. The size of the ejector was determined by using mathematical models. The experiment was conducted to evaluate the performance of the ejector refrigeration system. The freezer cabinet with the volume of 90 liters was employed. The experimental result showed that the proposed system obtained at -25.4 ^{o}C for the case of empty freezer cabinet, at -21.8 ^{o}C for the case of 1kg basa fish in the freezer cabinet.

Keywords. ejector, saving energy, R134A, R410A, working fluid.

Nomenclature

A_3	Cross sectional area of the constant area chamber in the ejector (m^2)
A_{ey}	Cross sectional area, required for the secondary flow at the constant area chamber the ejector (m^2)
A_{g1}	Cross sectional area at the exit of the primary nozzle (m^2)
A_{gy}	Cross sectional area, required for the primary flow at the constant area chamber in the ejector (m^2)
Ma_{ey}	Mach number of the secondary flow in the constant area chamber in the ejector
Ma_g	Mach number of the primary flow from the generator
Ma_{g1}	Mach number of the fluid from the generator, which expands through the nozzle
Ma_{gy}	Mach number of the primary flow in the constant area chamber in the ejector
P_e	Evaporator pressure (Pa)
P_{ey}	Pressure of the secondary flow at the entrance of the constant area chamber in the ejector (Pa)
P_g	Generator pressure (Pa)
P_{g1}	Pressure at the exit of the primary nozzle (Pa)
P_{gy}	Pressure of the primary flow at the entrance of the constant area chamber in the ejector (Pa)
P_m	Pressure of the mixed flow in the constant area chamber (Pa)
P_t	Pressure at the throat of the nozzle (Pa)
P_y	Pressure at the entrance of the constant area chamber (Pa)
T_e	Evaporator temperature (°C)
T_{ey}	Temperature of the secondary flow in the constant area chamber (K)
T_g	Generator temperature (K)
t_g	Generator temperature (°C)
T_{gy}	Temperature of the primary flow in the constant area chamber (K)
φ_g	Arbitrary coefficient for the primary flow

1 INTRODUCTION

In low temperature freezers techique, the common refrigeration system often employs multi-compressor. It means that this leads to the need to consume a lot of energy for compressors in the common refrigeration

system. Therefore, a cascade refrigeration system with ejector could achieve a considerable saving energy. Ejector equipment which is one of components in the auto-cascade refrigeration system, has developed in decades. The feature ejector has a simple structure, low manufacturing cost and good expansion work recovery effect. Thus, it has attracted much attention by scholars to improve the vapor compression refrigeration in the past few years. Yu et al. [1] was conducted an auto-cascade refrigeration system using the refrigerant mixture of R23/R134a with two different ejectors and the results showed the improvement in COP could gained 19.1%. Similarly, an experimental evaluation of an auto-cascade refrigeration system with ejector in the steady state operation indicated that this system increased by 25.1% of the system exergy efficiency in comparision to the conventional cycle [2]. The advantages of the ejector-assisted refrigeration system have also been demonstrated in a series of publications [3–5].

The starting point of the research on applying ejectors to refrigeration systems was using water as the refrigerant. However, the disadvantage of this system was that it had a low COP and reached temperatures around 0 °C [6]. Therefore, halocarbon refrigerant has been proposed for use in ejector-supported refrigeration systems to overcome this shortcoming. Various common halocarbon compound refrigerants were proposed and tested, including R123 [7], R134a [7–9], mix R290/R600a [3]. However, the choice of working fluids in an ejector refrigeration system that is environmentally friendly, especially using zero ozone depletion HFC refrigerants, is getting more and more attention. Nowaday, as an alternative to the widely used R12, the pure refrigerant R134a, a kind of HFC, has been selected as the most preferred choice as the working fluid in a refrigeration system. In detail, it can be found that R134a was proposed by Zhao et al. [5], Kim and Kim [4], as the working fluid in an ejector refrigeration system. Besides the R134a refrigerant, the R410A refrigerant is widely used in numerous refrigeration systems. For instance, Heredia-Aricapa Y et al. [10] presented a study that proved that refrigerants R134a and R410A still prevail in different commercial refrigeration systems. Gustavo Potker et al. [11] also conducted the experimental performance data of a ejector-based refrigeration system using R410a. The result showed that R410A has greater work recovery potential than most of conventional refrigerants due to its relatively high throttling losses.

Considering these findings, as a result, with a system cooling capacity of 0.5 kW, a set of feasible design conditions will be obtained using a parametric study altering the generator, condenser, and evaporator temperatures and employing a validated multi-geometry ejector mathematical model. The operating fluids are 410A and 134a refrigerant mixes.

2 OPERATING PRINCIPLE OF EJECTOR SYSTEM

Figure 1 illustrates the schematic diagram of the proposed cascade ejector system setup. There are two cycles including the vapor compression cycle and the ejection cycle. The apparatuses of proposed system setup consist of a compressor, an air-cooled condenser, a separator, an ejector, an evaporation condenser and a freezer cabinet. The working fluid is the common refrigerant couple R134a/R410a. The working theory of this system is described as follows: The superheated vapor mixture (state point 1) after the evaporator-condenser (e) is drawn by the compressor (a) and becomes high-temperature and pressure vapor (state point 2). Then, it is separated from the oil at the oil separator (b). After the oil separator, the refrigerant mixture partially condenses when it goes through the condenser (c) (state point 3). Therefore, the refrigerant mixture becomes a two-phase fluid in the separator (d). At the separator, most of the R134a condensed into a high-temperature and pressure refrigerant liquid (state point 4) due to its higher boiling point of this medium (-26.1^{o}C), while most of the refrigerant R410A enters the separator as a refrigerant vapor (state point 5) due to its low boiling temperature point (-82^{o}C). This two-phase fluid is separated in the separator. As a result, two different refrigerant streams can be obtained by shifting the composition of the refrigerant mixture. After being separated, the plurality vapor R410A continues to enter the evaporator-condenser to release isostatic heat for the condensate R134a to convert phase to liquid (state point 6), then through the expansion valve (f). As a result of the expansion process, the subcooling fluid R410a vaporizes partially, and its temperature decreases (state point 7). The cooled refrigerant then passes through an evaporator (state point 8), where it absorbs heat in the cabinet.

Meanwhile, the R134a refrigerant liquid (state point 4) in the separator enters the ejector nozzle and

expands as an ultrasonic two-phase liquid at the ejector inlet (state point 4'). The low-pressure R410A coming from evaporator (state point 8) is drawn into the nozzle due to the pressure difference. The mixing and diffusion processes in the ejector device are performed. Then the pressure of two-phase fluid is increased (state point 10) and leave the ejector vaporizes as superheated steam in the evaporator-condenser and return to the compressor.

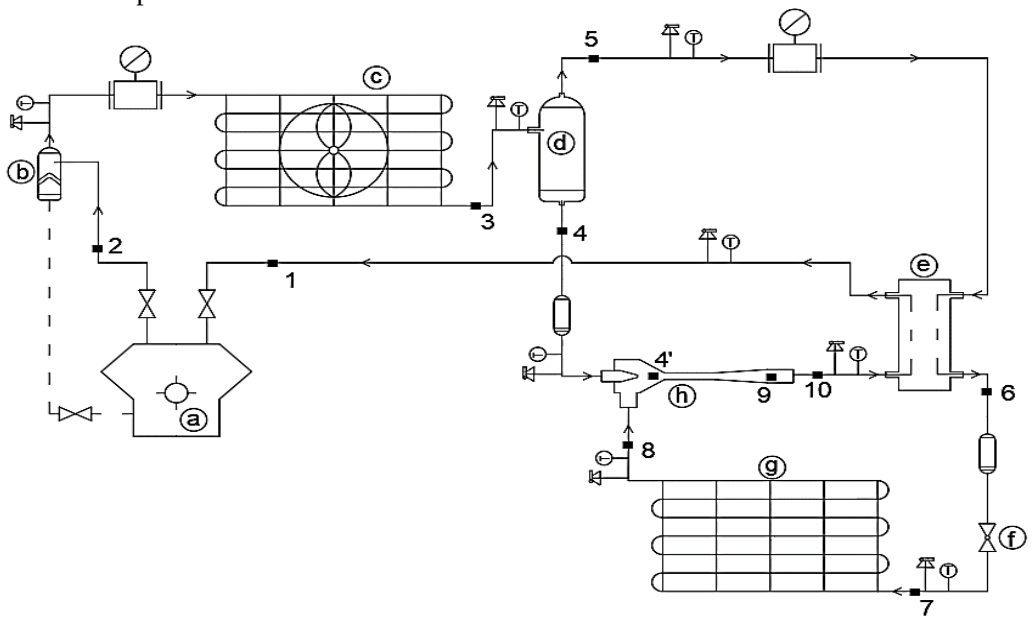

a. compressor; b. oil separator; c. Condenser; d. separator; e. Evaporation/Condenser; f. expansion valve; g. evaporator; h. ejector

Figure 1: Schematic diagram of the ejector refrigeration system.

3 MATHEMATICAL DESIGN OF EJECTOR

3.1 The expansion process of the primary flow through the nozzle.

Vapour from the generator expands irreversibly in the primary nozzle creating a partial vacuum at the nozzle exit. Applying the first law of thermodynamics by using the energy balance equation:

$$q = \varepsilon_t + h_e - h_y + \frac{c_{ey}^2 - c_{my}^2}{2} + g.\left(z_{ey} - z_{my}\right) \tag{1}$$

With the assumption of adiabatic condition (q = 0), no work (ε_t =0), and no influence of elevation change ($z_{gy} = z_{my}$), the velocity of the stream at the nozzle exit (c_{ey}) can be expressed as

$$c_{ey} = \sqrt{2.\left(h_e - h_y\right)} = \sqrt{2.\eta_N.\left(h_e - h_{ey,is}\right)} \tag{2}$$

The mass flow from the generator through the nozzle at choking condition can be expressed as,

$$m_g = P_g.A_t.\sqrt{\frac{\eta_N.\gamma}{T_g.R}\left(\frac{2}{\gamma+1}\right)^{\frac{k+1}{k-1}}} \tag{3}$$

The mach number of the fluid from the generator (Mag,1), which expands through the nozzle can be depicted as,

$$Ma_{g1} = \sqrt{\frac{2\eta_N}{\gamma-1}\left[1-\left(\frac{p_1}{p_g}\right)\right]^{\frac{k-1}{k}}} \tag{4}$$

The relation between the Mach number and the cross sectional area can be depicted as,

$$\frac{p_g}{p_{g1}} \approx \left[\left(1+\frac{\gamma-1}{2}.Ma_{g1}^2\right)\right]^{\frac{k}{k-1}} \rightarrow p_{g1} \tag{5}$$

$$\left(\frac{A_{g1}}{A_t}\right)^2 \approx \frac{1}{Ma_{g1}^2}\left[\frac{2}{\gamma+1}\left(1+\frac{\gamma-1}{2}.Ma_{g1}^2\right)\right]^{\frac{k+1}{k-1}} \tag{6}$$

The Mach number of the primary flow at cross section y-y can be calculated from

$$\frac{p_{gy}}{p_{g1}} \approx \left[\frac{1+\left(\frac{k-1}{2}\right).Ma_{g1}^2}{1+\left(\frac{k-1}{2}\right).Ma_{gy}^2}\right]^{\frac{k}{k-1}} \rightarrow Ma_{gy} \tag{7}$$

3.2 The secondary flow

The secondary flow rate at choking condition (section y-y) is illustrated as,

$$m_e = \frac{P_e.A_{ey}}{\sqrt{T_e}}\sqrt{\frac{\gamma}{R}\left(\frac{2}{\gamma+1}\right)^{\lambda+1/k-1}}.\sqrt{\eta_{Ne}} \tag{8}$$

Assuming that the entrained flow reaches choking conditions, the Mach number of the secondary flow at section y-y is approximately one,

$$Ma_{ey} = \sqrt{\frac{2}{\gamma-1}\left[1-\left(\frac{P_e}{P_{ey}}\right)^{\frac{k-1}{k}}\right]} \tag{9}$$

3.3 Cross-sectional area at section y-y (A_3)

A cross-sectional area at y-y is the summation of the area for primary flow (A_{gy}) and entrained flow (A_{ey}),

$$A_3 = A_{gy} + A_{ey} \tag{10}$$

3.4 Mixing section

Energy balance at the mixing point can be expressed as

$$\emptyset_m\left(m_g.h_{g,exp} + m_e.h_e\right) = \left(m_g + m_e\right).c_m$$

where

h_m: enthalpy of the mixing fluid at the mixing point

h_e: enthalpy of the entrained refrigerant (secondary fluid) from the evaporator

$h_{g,exp}$: enthalpy of the driving fluid from the generator after expansion through the nozzle

m_e: the secondary flow rate

m_g: the mass flow from the generator through the nozzle

The direction of the mixing portion will be determined by the relationship to the nozzle adhesive line:

$$L_{mix} = 4.D_3$$

The angle of the mixing section is also important. The spray efficiency will decrease if the angle is too large, conversely, if the angle is too small, the sprayer will not be able to compress the steam flow to design the condenser pressure. The angles of the mixing section cone are about 7-10 degrees for the first part and

3 to 4 degrees for the second part[12].

$$\frac{T_g}{T_{gy}} = 1 + \frac{k_{R134} - 1}{2}.Ma_{gy}^2 \rightarrow T_{gy} = T_g.\left[1 + \frac{k_{R134} - 1}{2}.Ma_{gy}^2\right]$$

$$c_{gy} = Ma_{gy}.\sqrt{\gamma_{R134}.R.T_{gy}}$$

An arbitrary coefficient accounting for friction loss ϕ_m, varies with the ejector area ratio (A_3/A_t). Huang and Chang [12], reported that

$$\phi_m = 0,80 \text{ for} \frac{A_3}{A_t} > 8,3 \quad (11)$$

$$\phi_m = 0,82 \text{ for} 6,9 \leq \frac{A_3}{A_t} \leq 8,3 \quad (12)$$

$$\phi_m = 0,84 \text{ for} \frac{A_3}{A_t} < 6,9 \quad (13)$$

The performance of an ejector is generally defined in terms of the mass flow rate ratio ω between the streams from the evaporator and generator.

$$\omega = \frac{m_e}{m_g} \quad (14)$$

4 RESULTS

4.1 Determination of parameters in ejector refrigeration cycle

The input parameters for calculation were as follow: the cooling load was Q_o = 0,5kW, the evaporating temperature was T_e = -25°C, the condensing temperature was T_c = 40 °C. The other operating parameters at each point was determined in Table 1.

Table 1: Results of determination for parameters at points.

Point	Temperatue T [°C]	Pressure p [bar]	specific volume, v[m³/kg]	Enthalpy h [kJ/kg]	Entropy S [kJ/K]	Refrigerant	State of Refrigerant
1	13.602	12	0.022067	429.520	1.8013	R410a	gas
1’	46.322	12	0.016632	420.959	1.7052	R134a	gas
2	37.708	18.6	0.014478	441.234	1.8013	R410a	gas
2’	65.923	18.6	0.010306	429.556	1.7052	R134a	gas
3	36.107	18.6	0.01432	439.63	1.796	R410a	gas
3’	64.322	18.6	-	294.563	-	R134a	liquid
4=3’	64.322	18.6	-	294.563	-	R134a	liquid
5=3	36.107	18.6	0.01432	439.63	1.796	R410a	gas
6	29.613	18.6	-	250	1.170	R410a	liquid
7	-25	3.347	-	249.973	-	R410a	liquid
8	-25	3.347	0.078628	412.681	1.8658	R410a	gas
10’	46.322	12	-	294.563	-	R134a	liquid

Based on the equations (1-14) and the results in Table 1, the dimensions of the ejector were shown in the Table 2.

Table 2: Ejector dimensions.

Specifications		Result
Primary part	Mass flow m_g (kg/s)	$4,035.10^{-3}$
	Nozzle neck diameter d_t (mm)	5,22
	Inlet diameter d_{g1} (mm	23,028
	Outlet diameter ra d_{gy} (mm)	27,25
Secondary part	Mass flow m_e (kg/s)	$3,073.10^{-3}$
	Diameter d_{ey} (mm)	19,5

Mixing section	Length L_{mix} (mm)	134
Constant Area Section	Diameter d_3 (mm)	33,5
	Length L_3 (mm)	167,5
Diffuser	Inlet diameter d_3 (mm)	33,5
	Outlet diameter d_4 (mm)	60,5
	Length L_D	210

The designed ejector is illustrated in the Figure 2 as bellows.

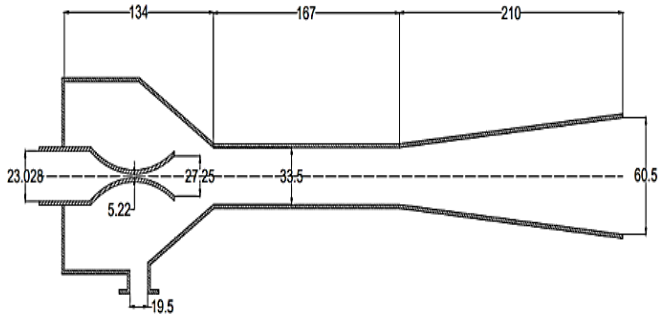

Figure 2: The designed ejector.

4.2 Experimental for validation

The experiment was conducted to validate the operation of the system with the designed ejector in this study. The experimental procedures are as follows:

i) Dry nitrogen was employed for testing leakage detection in the system

ii) The mixture of refrigerant was charged by following the higher boiling temperature R134a first and the lower boiling temperature R410a with the assistance of the compressor. The amount of mixture of refrigerant was referred to as the ratio mass flow rate ratio ω. The ω was about 0.76 in this study by calculation

iii) The system was conducted in the laboratory room with a temperature of ambient about 25 ^{o}C

The experiment was tested in two conditions without and with load (about 1kg of catfish). The data was recorded in an interval of 5 minutes. The average of three times data was given in Table 3

Table 3: The results of the validated experiment.

No.	Time	Temperature in chamber with load	Temperature in chamber without load
1	10h00	30	29.7
2	10h05	27.3	27
3	10h10	24	23.3
4	10h15	21.2	18.7
5	10h20	16.4	14.3
6	10h25	11.5	11.7
7	10h30	6.3	7.7
8	10h35	4.2	4.1
9	10h40	1.8	1.4
10	10h45	0.8	-2.7
11	10h50	-3.1	-6.1
12	10h55	-6.7	-12.1
13	11h00	-9.6	-16.6
14	11h05	-12.3	-19.7
15	11h10	-15.7	-21.6
16	11h15	-17.2	-23.1
17	11h20	-19	-23.4
18	11h25	-20.3	-24.3
19	11h30	-21.6	-25.1
20	11h35	-21.8	-25.4
21	11h40	-21.8	-25.4

The results of experiments are indicated in Figure 3

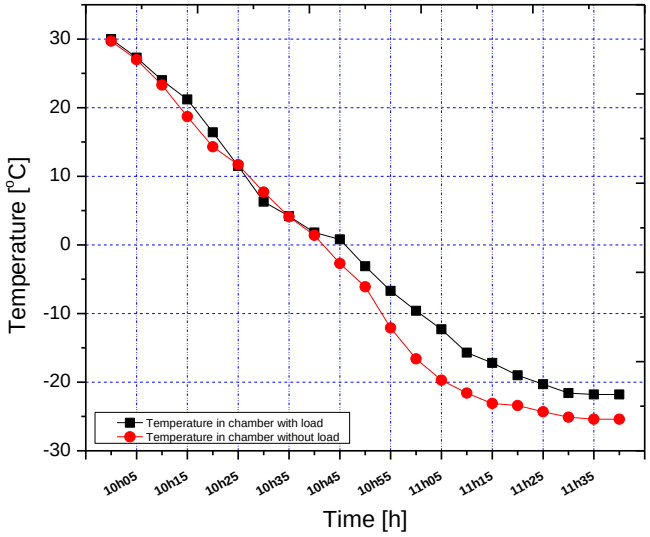

Figure 3: Temperature changes throughout the experiment.

The results in Figure 3 showed that the lowest temperature achieved by the ejector refrigeration system during 1 hour and 40 minutes was -21.8 °C for the case with a cooling load and -25.4 °C for the case without a cooling load. During the first period, i.e., from 10:00 h to 10:40 h, the temperature decrease in both cases was not much different. However, in the later stage, in the experimental case without a cooling load, the temperature decrease in the cold chamber was faster than in the experimental case with a cooling load. This can be explained because, in the early stages, the heat entering is much greater than that generated from 1kg of fish. Once this heat has been rejected, the remaining heat inside the freezer chamber is mainly that of 1kg of fish.

5 CONCLUSIONS

The current study develops a rejector design that works with R134a/R410a. The vapor compression cycle used R410A, whereas the ejection cycle used R134A. Mathematical models were used to establish the size of the ejector. The experiment was carried out in order to validate the performance of the refrigeration system with the designed ejector. In the experiment, a freezer cabinet with a volume of 90 liters was used. Moreover, the experiment was carried out in two cases with and without a cooling load in the freezer cabinet. The experimental results revealed that the suggested system obtained at -25.4 °C for an empty freezer cabinet and at -21.8 °C for a freezer cabinet containing 1kg basa fish.

REFERENCES

[1] Yu J, Zhao H, Li Y. Application of an ejector in autocascade refrigeration cycle for the performance improvement. International Journal of Refrigeration 2008; 31:279–86. https://doi.org/https://doi.org/10.1016/j.ijrefrig.2007.05.008.

[2] Bai T, Yan G, Yu J. Experimental investigation of an ejector-enhanced auto-cascade refrigeration system. Appl Therm Eng 2018;129:792–801. https://doi.org/https://doi.org/10.1016/j.applthermaleng.2017.10.053.

[3] Fan C, Yan G, Yu J. Thermodynamic analysis of a modified solar assisted ejector-compression heat pump cycle with zeotropic mixture R290/R600a. Appl Therm Eng 2019;150:42–9. https://doi.org/https://doi.org/10.1016/j.applthermaleng.2019.01.011.

[4] Kim SG, Kim MS. Experiment and simulation on the performance of an autocascade refrigeration system using carbon dioxide as a refrigerant. International Journal of Refrigeration 2002;25:1093–101. https://doi.org/https://doi.org/10.1016/S0140-7007(01)00110-4.

[5] Zhao L, Zheng N, Deng S. A thermodynamic analysis of an auto-cascade heat pump cycle for heating application in cold regions. Energy Build 2014;82:621–31. https://doi.org/https://doi.org/10.1016/j.enbuild.2014.07.083.

[6] Da-Wen Sun, Ian W. Eames. Recent developments in the design theories and applications of ejectors. Journal of the Institute of Energy 1995;68:65–79.

[7] Cizungu K, Mani A, Groll M. Performance comparison of vapour jet refrigeration system with environment friendly working fluids. Appl Therm Eng 2001;21:585–98. https://doi.org/https://doi.org/10.1016/S1359-4311(00)00070-3.

[8] Alexis GK, Karayiannis EK. A solar ejector cooling system using refrigerant R134a in the Athens area. Renew Energy 2005;30:1457–69. https://doi.org/https://doi.org/10.1016/j.renene.2004.11.004.

[9] Selvaraju A, Mani A. Experimental investigation on R134a vapour ejector refrigeration system. International Journal of Refrigeration 2006;29:1160–6. https://doi.org/https://doi.org/10.1016/j.ijrefrig.2006.01.004.

[10] Heredia-Aricapa Y, Belman-Flores JM, Mota-Babiloni A, Serrano-Arellano J, García-Pabón JJ. Overview of low GWP mixtures for the replacement of HFC refrigerants: R134a, R404A and R410A. International Journal of Refrigeration 2020;111:113–23. https://doi.org/https://doi.org/10.1016/j.ijrefrig.2019.11.012.

[11] Gustavo Pottker, Bei Guo, Predrag S. Hrnjak. Experimental Investigation of an R410A Vapor Compression System Working With an Ejector. International Refrigeration and Air Conditioning Conference 2010:1135.

[12] Huang BJ, Chang JM. Empirical correlation for ejector design. International Journal of Refrigeration 1999;22:379–88. https://doi.org/https://doi.org/10.1016/S0140-7007(99)00002-X.

SOLUTIONS FOR CONTROL OF CONDENSATION TEMPERATURE TO SAVE ENERGY IN THE INDUSTRIAL REFRIGERATION SYSTEM

VU DUC PHUONG*, LE TRAN CANH

Faculty of Heat and Refrigeration Engineering, Industrial University of Ho Chi Minh city, Vietnam, vuducphuong@iuh.edu.vn, letrancanh@iuh.edu.vn

Abstract. The efficient energy using depends a lot on the design and installation of the refrigeration system, especially the system operation. The refrigeration system with efficient operating helps reduce energy costs for production thereby reducing product costs and increasing the competitiveness of enterprises is necessary problem of any enterprise. In addition, the efficient energy using also contributes to reducing CO_2 emissions - the main factor causing the greenhouse effect and climate change globally. In this paper, solutions for control of condensation temperature have been applied at Minh Dang company such as installing inverters for fans and pumps, installing anti-fouling equipment, calculating pressure loss, separating non-condensing air and oil restriction at the condenser have reduced the condensation temperature by 5°C corresponding to a potential energy saving of 15% of the entire refrigeration system.

Keywords. Industrial refrigeration system, control of condensation temperature, efficient energy using, energy saving, Minh Dang company.

1 INTRODUCTION

The refrigeration system plays a important role in the operation of food processing factories in general and seafood processing factories in particular. The refrigeration system used in the factories is a continuous refrigeration system and uses electricity. used for the refrigeration system accounts for 80-85% of the total energy consumption of the factory

In a food processing plant, to increase the shelf life of products, it is necessary to bring the product temperature below the activation temperature of most enzymes and microorganisms. cold system. Depending on the requirements of the product, the refrigeration system will create a different temperature environment.

The power consumption of the cooling system of the condenser accounts for about 20-25% of the total power consumption of the refrigeration system. Power consumption accounts for a relative percentage of power consumption, but it determines the performance of the refrigeration system Normally, when designing a refrigeration system, the condensing temperature t_c = 40 – 43 °C is chosen, but the average annual temperature of the southern provinces usually ranges from 25 – 28 °C, moreover, about half of the year the ambient temperature is below 26 °C. Reducing the condensation temperature of the medium, controlling the power of the fan and pump of the condenser according to the ambient temperature helps the refrigeration system operate more efficiently. To measure efficiency, the energy efficiency coefficient COP (Coeficient of Performance) is used.

2 METHODOLOGY

2.1 Theoretical basis

Calculating the heat of condensers is based on two basic equations [1]:

Heat balance equation:

$$G_1 C_{p1}\left(t'_1 - t''_1\right) = G_2 C_{p2}\left(t''_2 - t'_2\right) = Q \quad (1)$$

Heat transfer equation:

$$dQ = k(t_1 - t_2)dF = k\Delta t.dF \quad (2)$$

Where:

K: heat transfer coefficient, [W/(m^2 .K)]

t_1 - t_2 = Δt Logarithmic mean temperature difference (K)

Integrating equation (2) over the entire surface of the condenser, we get the heat exchanged at the condenser:

$$Q = \int_F kF\Delta t \quad (3)$$

In most cases, the change in coefficient k is not significant (k=const), so equation (3) is rewritten:

$$Q = k\overline{\Delta t}\, dF \quad (4)$$

Continuous refrigeration systems in seafood processing factories use evaporative condensers, so the cooling medium is water and air, from here we determine the water and air flow needed to cool the machine. The condenser is:

The water flow rate G_w (kg/s) is determined by the formula:

$$G_w = \frac{Q_a}{C_w \rho_w \Delta t_w} \quad (5)$$

Where:

C_w – Specific heat capacity of water, kJ/(kg.K).

ρ_w – Density of water, kg/m^3.

Δt_w - Logarithmic mean temperature difference, K

The air flow rate G_a (kg/s) is determined by the formula:

$$G_a = \frac{Q_a}{C_a \rho_a \Delta t_a} \text{kg/s} \quad (6)$$

Where:

C_a – Specific heat capacity of air, kJ/(kg.K).

ρ_a – Density of air, kg/m ^{3}.

Δt_a - Logarithmic mean temperature difference, K.

COP is the energy efficiency coefficient (Coefficient Of Performance) equivalent to the cooling coefficient and is calculated according to the following formula:

$$\text{COP}_{\text{cooling}} = \frac{Q_0}{N_e} \quad (7)$$

Where:

Q_0 : Useful cooling capacity obtained at the evaporator , kW

N_e : Useful compressive work, kW

Normally, the COP coefficient is calculated only for the compressor, but in reality, the refrigeration system has many power-consuming devices such as fans, pumps, resistors...etc. Therefore, to determine the efficiency of the system, the power consumed from the auxiliary equipment must be added, for seafood processing plants, it is calculated by the coefficient of kWh/1 ton of product.

2.2 Research subjects

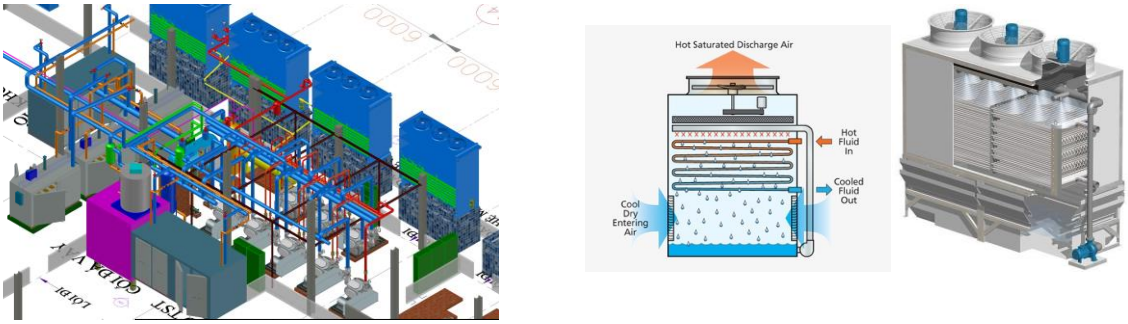

Figure 1: Continuous refrigeration system and evaporative condenser at Minh Dang Company

The continuous refrigeration system of Minh Dang Co., Ltd. in My Xuyen District - Soc Trang Province is the object of research, the continuous system using NH_3 refrigerant includes : 01 N4A – 30 kW compressor; 04 compressors N62B – 90 kW; 05 compressors N42B – 55 kW; 01 compressor SRM 1612SL – 110 kW; 01 compressor SRM 2016SL – 200 kW; 01 compressor N62WB – 90 kW; 02 compressors N62M – 90 kW, condenser system for continuous refrigeration system including: 01 condenser with capacity of 584 kW, 02

condensers with capacity of 500 kW, 03 condensers with capacity of 300 kW. The potential for energy savings for this system is great if the condensing temperature of the refrigerant in the system is well controlled.

2.3 Condenser control solutions

When calculating the design of a refrigeration system, it is common to choose the ambient temperature parameters of the hottest day of the year, in addition, consider the system operating at its maximum capacity. In fact, seafood processing factories have appropriate technology requirements depending on the season and orders. Therefore, the refrigerating system operates with a variable coefficient of concurrency.

The climate in the Southwest region in general and Soc Trang in particular is often sunny during the day but at night the ambient temperature is lower. In addition, during the rainy season, the temperature will generally be lower than the average temperature. of year. If we can control the condensation temperature according to the ambient temperature, this is also the potential to save energy for the continuous refrigeration system [2].

2.3.1 Installation of inverter for fan and pump in condenser

Normally the condenser fan and pump parameters are fixed according to the manufacturer, the air and water flow cannot be adjusted.

In cases where due to production requirements, only one IQF system or contact freezer, air freezer, etc., is operated, it is not necessary that all compressors in the system operate but operate according to actual cooling load requirements. There are cases where even though the compressor load has been reduced, there is still excess cooling capacity due to the air and water flow supplied to the condenser remaining unchanged. In case the ambient temperature is low, such as in the morning or when it rains, the fan and pump power cannot be adjusted to maintain the condensation temperature, causing ineffective energy use.

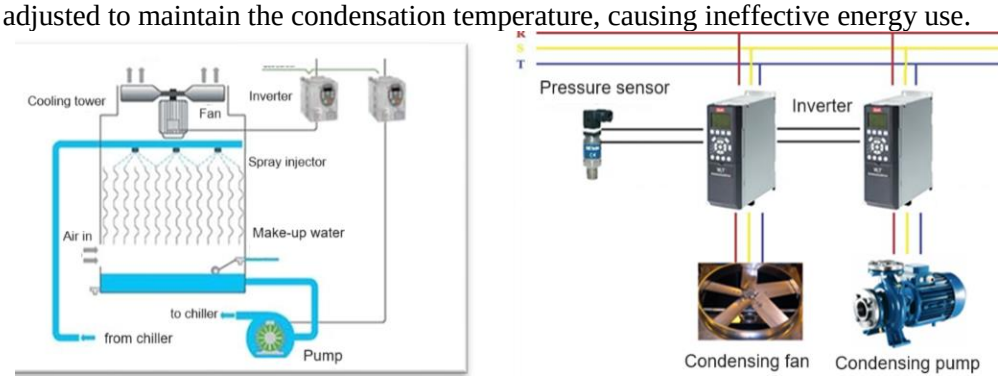

Figure 2: Installation of inverter for fan and pump [3]

Therefore, installing an inverter for the fan and pump of the condenser will make the flow control of the fan and pump more flexible. The input signal to control the fan and pump is the condensing temperature of the refrigerating system. When the condenser temperature increases, the inverter will increase the frequency to increase the flow of the air and the fan. If the temperature still exceeds the set value, it will give a signal to the next condenser in the system to operate and vice versa.

2.3.2 Installation of anti-scale device for condenser

After the operation time of the refrigeration system, there is the formation of scale deposits on the pipes of the condenser, when scale is formed, reducing the ability to exchange heat between the refrigerant and the cooling environment.

As the condensing temperature increases, the condensing area must increase to ensure heat exchange, but the heat exchange area (F) cannot be changed, so the only option is to maintain the heat exchange coefficient. This means that the condenser temperature must be at the design temperature.

In the problems that increase the condenser temperature, the fouling of scale has a great influence on the condenser. Therefore, to ensure the designed heat exchange area, scale removal is necessary for the system to operate stably [4].

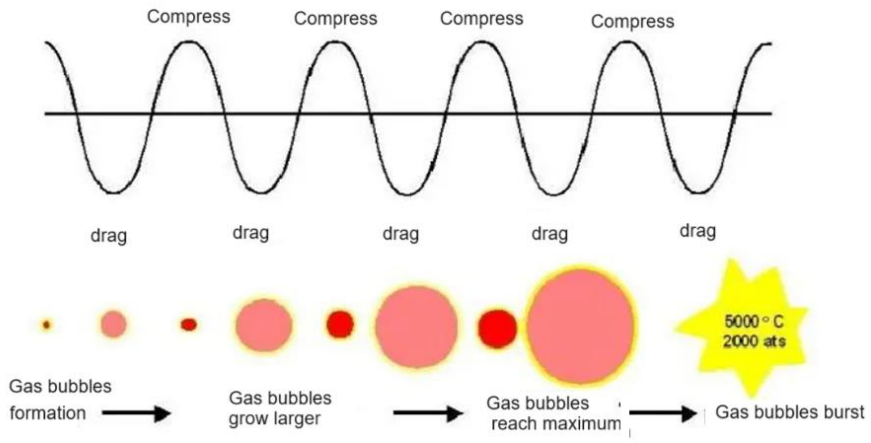

Figure 3: The process of formation, development and rupture of air bubbles [5].

Installing an anti-scaling system in an ultrasonic condenser is a solution that many installation projects bring great efficiency, minimizing the possibility of scale build-up and reducing maintenance labor costs. system maintenance, in addition to be more effective, we can apply other solutions such as running chemicals periodically.

2.3.3 Calculation of pressure loss at condenser

After condensing, the refrigerant must be brought back to the high-pressure container to release the volume occupied by the liquid, so that the heat exchange area of the condenser is always the largest.

In fact, when designing - constructing contractors, they depend a lot on the installation space of the factory, further reducing costs by saving materials, so they usually don't care much about pressure loss when installing the system. condensation. It is the low pressure loss on the pipeline that reduces the ability of the liquid after condensing to return to the high-pressure container.

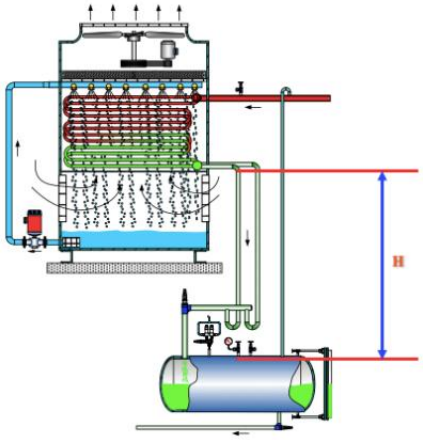

Figure 4 : Calculation of pressure loss and condenser height [6]

Based on Bernoulli's equation, it is found that if the pressure loss at the condenser is 0.1bar, it is necessary to raise the height of the condenser by 1700 mm to compensate for this pressure loss, ensuring the refrigerant liquid returns to the high-pressure reservoir completely.

2.3.4 Separation of non-condensing air

In the industrial refrigeration system, there is always an amount of non-condensable gas in the system, non-condensable gas enters the system when maintaining and repairing the system, decomposing the refrigerant, and lubricating oil. When the system exists non-condensable gas, it causes the condensate pressure to increase, reducing the efficiency of the system, and reducing the reliability of the system.

Normally, refrigeration systems have installed a non-condensing air separator, but like other equipment, contractors design and manufacture it themselves, so the efficiency is not high, in addition, how to operate

the air separator. This is also not taken care of, leading to the existence of a large amount of non-condensable gas in the system, leading to reduced efficiency of the condenser, leading to a decrease in system efficiency [8].

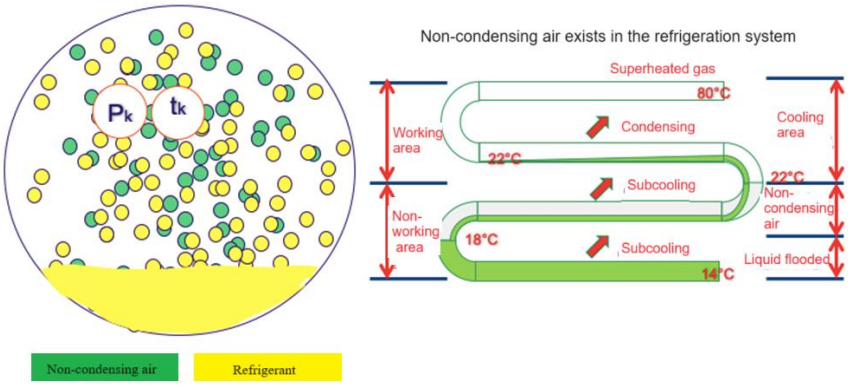

Figure 5: Location of non-condensable gas at the condenser [7].

2.3.5 Limitation of oil in condenser

During the process of compressing the refrigerant at the compressor, there is always a certain amount of lubricating oil accompanying the refrigerant. Even though every refrigeration system has an oil separator, the ability to separate the oil is not thorough, especially in reality in Vietnam. Oil separators are often self-made and not scientifically designed, so the amount of oil separated is not thorough [9].

When the oil follows the medium to the condenser, it will create a thermal resistance layer that prevents heat exchange between the medium and the cooling medium, leading to reduced performance of the condenser.

NH_3 and lubricating oil do not dissolve, so when the amount of oil on the condenser is high, it will be deposited in the condenser, the space occupied by the oil will reduce the actual heat exchange area of the device. condensation.

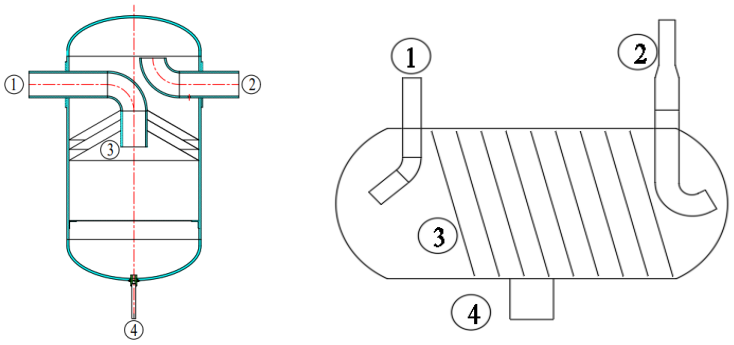

Figure 6: Oil separator in industrial refrigeration system.

The continuous refrigeration system at Minh Dang company uses a horizontal oil separator designed and manufactured by the contractor, currently using a traditional vertical oil separator, the pipe diameter does not change from the ceramic pipe to the bottom. oil separator. Newly designed horizontal oil separator with multiple flow barriers, the pipe diameter from the sump and the oil separator has been increased to increase the oil separation efficiency of the device.

In addition, periodically draining the oil from the oil concentration location at the condenser also contributes to reducing the amount of oil deposited in the condenser.

3 RESULTS AND DISCUSSION

The control of condensing temperature in general and of the continuous refrigeration system at Minh Dang company in particular must apply many solutions in a synchronous manner to bring about the best energy

efficiency, these solutions have a close relationship with each other, complement each other to maintain the condensing temperature of the system.

3.1 Evaluation of condenser temperature control solutions

The continuous refrigeration system at Minh Dang company is being designed with a condensing temperature of 40°C, after applying the solutions mentioned above, it will maintain the condensing temperature of the system at 35°C.

With the option of installing an inverter, it is possible to flexibly control the air flow and water flow according to the condensation temperature signal at times when the ambient temperature is low such as: night, rain... or flexibly. Operating when the cooling capacity according to production requirements changes can save 20% on the total energy of the fan pump and condenser pump.

Table 1: Energy saving potential at condensers.

No	Condenser	Power (kW)	Fan power (kW)	Pump capacity (kW)	Savings potential (%)
1	Condenser 1	500	20	3	20
2	Condenser 2	500	20	3	20
3	Condenser 3	300	12	3	20
4	Condenser 4	300	12	3	20
5	Condenser 5	300	12	3	20
6	Condenser 6	584	20	3	20

With the average operating coefficient of the system, the condenser is 60 – 70% of the load in the year, the amount of power needed for the pump and the condenser fan is: 669,000 kWh, when saving 20% corresponds to the energy consumed. consumption reduced by 139,800 kWh.

The solution of installing anti-scale ultrasonic equipment will reduce the cost of labor and maintenance of the system but also ensure the heat exchange efficiency of the refrigeration system.

Non-condensing air separation solution is to replace low efficiency non-condensing air separators with higher efficiency non-condensing air separators that have been calculated and designed to suit the capacity of the refrigeration system at Minh Dang.

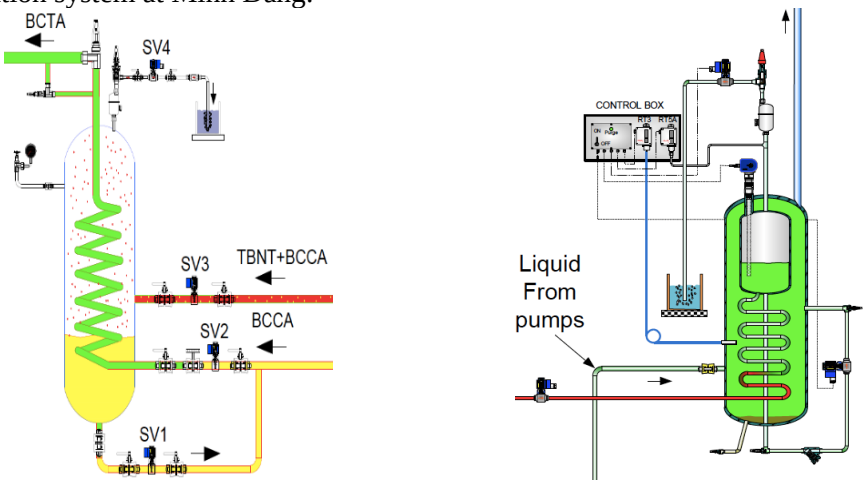

Figure 7: Non-condensing air separator.

Similarly, replace the oil separator that is not calculated and designed properly according to the capacity of the system with a calculated and designed oil separator, to ensure the maximum reduction of oil according to the medium to the condenser.

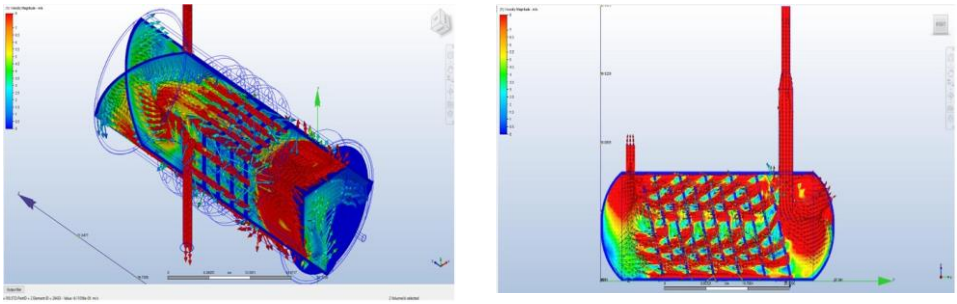

Figure 8: Efficiency analysis of old and new air separators.

In addition, the solutions are complementary to each other to reduce the condensing temperature of the system from t_k = 40°C, down to the condensing temperature t_k = 35°C.

3.2 Evaluation of energy saving potential

According to previous studies [7], when we increase the condensing temperature by 1°C, respectively, the cooling capacity decreases by 1% and the power consumption increases by 3%. Therefore, when applying solutions to control the condensing temperature of the system at the temperature t_c = 35°C, it is reduced by 5°C compared to the original.

With the condensing temperature reduced by 5°C corresponding to the energy saving potential of the entire system of 15%, the average total power of Minh Dang company is 3,564,064 kWh/ year, the potential for energy saving The amount for this refrigeration system is very large.

In order to effectively control the condenser temperature, it is necessary to implement solutions in a synchronous manner and strictly follow the operation and maintenance procedures of the system to ensure stable and long-term effectiveness.

4 CONCLUSIONS

The problem of global warming is an urgent issue today, all countries must join hands to reduce CO_2 emissions, the main cause of this phenomenon. In order to contribute to reducing CO_2 shortage, efficient use of energy is essential.

The potential for energy savings for the current refrigeration system is very large, the refrigeration systems in food processing plants are usually continuous refrigeration systems with large capacity, the equipment in the system is a complete system. most closely related to each other. Therefore, the research to come up with solutions must be synchronized for all devices in the system.

Due to the close and consistent relationship between the devices in the system, it is impossible to separate each device for research in addition to production factors, so the simultaneous operation of the devices is not uniform, so the 15% energy saving potential is a relative estimate when analyzing relevant factors that lead to changes in system operating parameters.

REFERENCES

[1] Hoang Dinh Tin. *Heat transfer and heat exchanger calculation*, Science and Technology Publishing House, 2001.

[2] Do Huu Hoang. *Energy saving solutions in industrial refrigeration systems*. 2016.

[3] Tran Van Thinh. *Automation and control of electrical equipment*. Vietnam Education Publishing House, 2016.

[4] Mai Xuan Sy. *Report on the design and manufacture of ultrasonic washing machines in Vietnam*. Institute of Technology Application, Ministerial Project, 2008.

[5] *Report on the design and manufacture of ultrasonic washing machines in Vietnam*. Science and Technology Institute of Applied Technology, Hanoi, 2008.

[6] Danfoss documents. *Eka Kool*, 2010.

[7] Per Skaerbaek Nielsen, Mech. Engineer Danfoss A/S, Denmark. Effects of Water Contamination in Ammonia. *Refrigeration Systems*, 2000.

[8] Nguyen Duc Loi. *Refrigerant*. Educational Publishing House, 2009.

[9] Nguyen Duc Loi. *Refrigeration system design guidelines*. Science and Technology Publishing House, 2005

[10] Nguyen Duc Loi. *Generations of refrigerants and the battle to protect the living environment*. Vietnam Association of Refrigeration and Air Conditioning Science and Technology, 2015.

ENERGY ANALYSIS OF A NOVEL COUPLED EJECTOR REFRIGERATOR AND ORGANIC RANKINE CYCLE

NGUYEN MINH PHU [1]*, DOAN THI HONG HAI [1], PHAN HA NHU NGOC [2]

[1] *Faculty of Heat and Refrigeration Engineering, Industrial University of Ho Chi Minh City (IUH), Ho Chi Minh City, Vietnam,*

[2] *Faculty of Garment Technology - Fashion, Industrial University of Ho Chi Minh City (IUH), Ho Chi Minh City, Vietnam;*

** Corresponding author: nguyenminhphu@iuh.edu.vn*

Abstract. A combination of the Rankine cycle and the cold ejector cycle is analyzed in this study. Steam from the high-pressure turbine is partially extracted for the motive flow of the ejector. The study was carried out with 7 different working substances. The fraction of steam extracted (MF) varies between 0.2 and 0.8. Boiler temperature (T_b), generation temperature (T_g), condenser temperature (T_c), and evaporator temperature (T_e) are varied in the range of 100 to 130°C, 55 to 90°C, 30 to 40°C, and -10 to 0°C, respectively. The mathematical model was written in EES software to investigate the effect of the key parameters on the useful output energy and the coupled cycle efficiency. The results indicate that the working fluid of ethanol achieves the greatest energy efficiency. At high evaporator temperatures, the extracted vapor for the ejector cycle should increase. The useful output is greatest at the optimum generator temperature of 72.5°C and MF of 0.2. When the condenser temperature is high, the amount of refrigerant extracted for the ejector system should be reduced. The efficiency increases by about 5% as boiler temperature increases in the examined range.

Keywords. Combined cycle, Thermodynamic analysis, Fluid selection, Integrated power and cooling system.

1 INTRODUCTION

A combined power and cooling cycle, also known as a cogeneration system, is a highly efficient energy system that simultaneously generates both electricity and useful thermal energy for cooling purposes [1]. It integrates the processes of power generation and thermal energy utilization to maximize overall energy efficiency. The basic principle behind a combined power and cooling cycle is to capture and utilize the waste heat produced during power generation. In traditional power plants, a significant amount of heat is generated as a byproduct and released into the atmosphere, resulting in a considerable energy loss. In a combined cycle system, this waste heat is harnessed and used for various heating or cooling applications, thus increasing the overall efficiency of the system [2]. The combined cycle of refrigeration and power, also known as a combined cooling, heating, and power (CCHP) system, is a highly efficient and environmentally friendly approach to meeting multiple energy needs simultaneously. It combines the generation of electricity, heating, and cooling within a single system. The combined cycle of refrigeration and power, or combined cooling, heating, and power systems, provides a holistic and efficient approach to meeting multiple energy needs, offering economic, environmental, and operational advantages across various applications.

Researchers often use waste heat from a power cycle to drive an absorption cooling cycle [3, 4]. However, the combined cycle of organic Rankine and ejector cooling lacks attention [5]. The cycle is composed of a standalone ejector refrigerator and a standalone organic Rankine cycle. The ejector refrigerator, also known as an ejector-driven refrigeration system or ejector cycle, offers several advantages compared to conventional refrigeration systems. Ejector refrigerators have a simple design with fewer moving parts compared to traditional refrigeration systems, such as vapor compression refrigeration. Ejector refrigerators typically use environmentally friendly refrigerants, such as water, ammonia, or carbon dioxide (CO_2).

Ejector refrigerators can achieve higher energy efficiency compared to conventional refrigeration systems. Ejector refrigerators can use various heat sources, including waste heat, solar thermal energy, or low-grade heat, to drive the refrigeration cycle [6]. Ejector refrigeration systems can be easily scaled up or down to meet different cooling demands. Due to their improved energy efficiency and the ability to use waste heat as a heat source, ejector refrigerators can result in lower operating costs compared to traditional refrigeration systems. Ejector refrigerators tend to operate at lower noise levels compared to conventional refrigeration systems. The absence of mechanical compressors and reduced vibration contribute to a quieter operation, which can be particularly advantageous in noise-sensitive environments, such as residential or office spaces. It's important to note that while ejector refrigerators offer several advantages, they also have some limitations, such as relatively lower coefficient of performance (COP) compared to vapor compression refrigeration systems and higher initial costs for certain applications. Therefore, a thorough evaluation of specific requirements and considerations should be conducted when considering the implementation of an ejector refrigerator.

The Organic Rankine Cycle (ORC) is a thermodynamic cycle that uses organic fluids, such as hydrocarbons or refrigerants, as the working fluid instead of water, allowing for the conversion of low-temperature heat sources into useful power. The ORC has several advantages over traditional steam Rankine cycles when it comes to certain applications. Overall, the Organic Rankine Cycle offers unique advantages in terms of low-temperature heat utilization, compatibility with diverse heat sources, environmental benefits, scalability, flexibility in fluid selection, and higher efficiency in certain applications. These advantages make it an attractive choice for various sectors, including renewable energy generation, waste heat recovery, and distributed power generation.

In this paper, the Rankine cycle is intermediately superheated and partial vapor leaving the high-pressure turbine is used as a motive vapor of an ejector refrigerator. Energy analysis of each component of the combined cycle is performed and the combined cycle efficiency is evaluated. In addition, seven working fluids are considered to determine the optimal fluid for maximum efficiency.

2 MODEL DESCRIPTION

Figures 1 and 2 show the schematic diagram of the combined cycle of the organic Rankine cycle and the ejector refrigeration cycle. The superheated vapor (state 9) enters the high-pressure turbine of the Rankine cycle. The saturated vapor leaving the turbine (corresponding to generator temperature T_g of an ejector refrigerator) is divided into two streams. A stream passes through the reheater and the other enters the ejector of the ejector refrigeration cycle. The former stream expands in the low-pressure turbine and condenses in condenser 1. The latter stream travels the nozzle of the ejector to the state "a" to suck the vapor out of the evaporator (state 2) and mix into state "b". The stream of the state "b" is pressurized in the diffuser of the ejector to condenser pressure. The saturated liquid coming out of the two condensers is mixed to state 7 and pumped into the boiler. The vapor temperatures entering the turbines are assumed to be the same in this study, i.e., $T_9=T_{10}$.

The energy analysis model of the combined cycle is presented below with the following assumptions:

- The flow is steady, and changes in kinetic energy and potential energy are ignored.
- The heat loss from equipment to the environment is negligible.

The thermodynamic analysis model of the combined cycle is written as follows [7, 8]:

Enthalpy of the state "b" is estimated from energy balance as [9]:

$$h_b = h_3 - \frac{h_1 - h_a}{(1+w)^2} \tag{1}$$

Nozzle efficiency:

$$\eta_{nozzle} = \frac{h_1 - h_a}{h_1 - h_{1s}} \tag{2}$$

Diffuser efficiency:

$$\eta_{diffuser} = \left(h_b - h_{3s}\right) / \left(h_b - h_3\right) \tag{3}$$

Mass conservation in ejector cycle:

$$\dot{m}_g + \dot{m}_e = \dot{m}_c \tag{4}$$

Mass conservation in Rankine cycle:

$$\dot{m} = \dot{m}_g + \dot{m}_{LT} \tag{5}$$

Flow entrainment ratio of ejector:

$$w = \dot{m}_e / \dot{m}_g \tag{6}$$

Extracted stream to ejector cycle is determined by mass fraction (MF) as:

$$\dot{m}_g = MF \cdot \dot{m} \tag{7}$$

Heat transfer rate of the boiler:

$$Q_b = \dot{m} \cdot \left(h_9 - h_8\right) \tag{8}$$

Power of the high-pressure turbine:

$$W_{HT} = \dot{m} \cdot \left(h_9 - h_1\right) \tag{9}$$

Heat transfer rate of the reheater:

$$Q_{RH} = \dot{m}_{LT} \cdot \left(h_{10} - h_1\right) \tag{10}$$

Power of the low-pressure turbine:

$$W_{LT} = \dot{m}_{LT} \cdot \left(h_{10} - h_{11}\right) \tag{11}$$

Heat transfer rate of the condenser 1:

$$Q_{c1} = \dot{m}_{LT} \cdot \left(h_{11} - h_6\right) \tag{12}$$

Heat transfer rate of the condenser 2:

$$Q_{c2} = \dot{m}_c \left(h_3 - h_4\right) \tag{13}$$

Heat transfer rate of the evaporator:

$$Q_e = \dot{m}_e \cdot \left(h_2 - h_5\right) \tag{14}$$

Power of the pump:

$$W_p = \dot{m} \cdot \left(h_8 - h_7\right) \tag{15}$$

Net power and cooling capacity of the combined cycle:

$$Output = W_{HT} + W_{LT} + Q_e - W_p \tag{16}$$

Thermal efficiency of the coupled cycle:

$$\eta_{couple} = \frac{W_{HT} + W_{LT} + Q_e - W_p}{Q_b + Q_{RH}} \tag{17}$$

Table 1 presents the values of the fixed parameters and the independent parameters to investigate their effects on the output and the coupled cycle efficiency. The calculation program is written in EES software.

Table 1: Input parameters.

Parameter	Value/Range
Nozzle efficiency, η_{nozzle}	0.9
Diffuser efficiency, $\eta_{diffuser}$	0.85

Boiler mass flow rate, $\dot{m}$	1 kg/s
Mass fraction, MF	0.2 – 0.8
Generator temperature, T_g	55 - 90°C
Boiler temperature, T_b	100 - 130°C
Condenser temperature, T_c	30 - 40°C
Evaporator temperature, T_e	-10 - 0°C

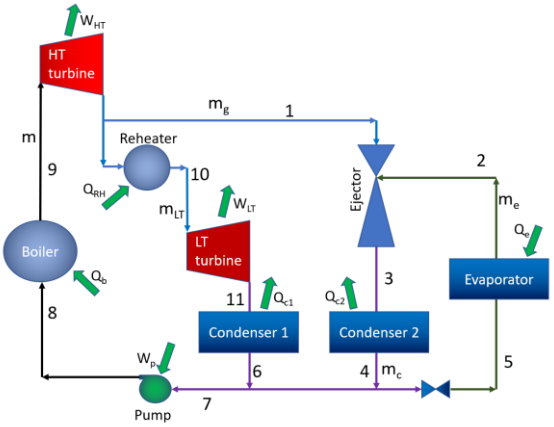

Figure 1: Process flow diagram of the combined power and cooling cycle.

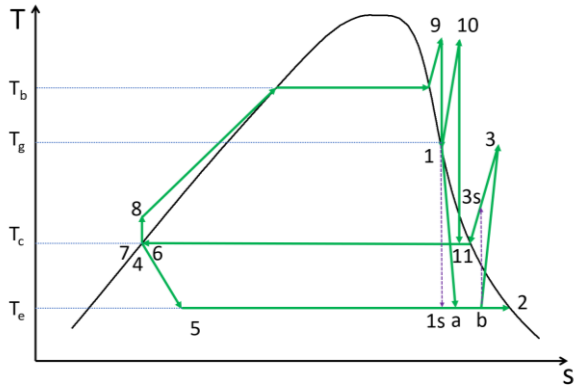

Figure 2: T-s diagram of the combined power and cooling cycle.

3 MODEL VALIDATION

Figure 3 presents a comparison of the effect of evaporator temperature on the flow entrainment ratio of ejector cycle. Table 2 compares the energies of the components in the reheated Rankine cycle. The results showed very good agreement between the present study and others.

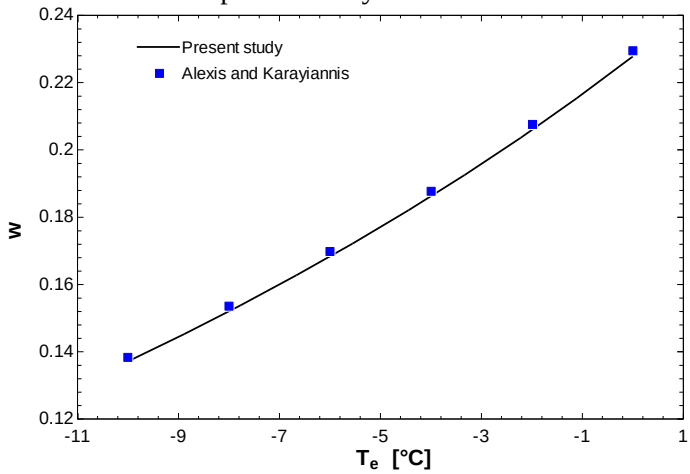

Figure 3: The comparison of flow entrainment ratio between the present study and published data [9].

Table 2: The comparison of results from Hysys simulator and developed EES code for the Rankine cycle.

Component	HYSYS	EES	error (%)
Q_B (kW)	185.7	180.9	2.6
W_{HT} (kW)	2.929	2.938	0.3
Q_{RH} (kW)	25.06	27.19	8.5
W_{LT} (kW)	28.72	28.74	0.1
Q_{c1} (kW)	181.8	179	1.5

Wp (kW)	2.692	2.663	1.1

4 RESULTS AND DISCUSSION

Figure 4 shows the effect of the working fluids on the combined cycle efficiency. R236fa had the smallest yield and ethanol achieved the greatest yield. The use of ethanol as a refrigerant offers several advantages compared to conventional refrigerants. Ethanol is a natural and renewable refrigerant derived from biomass sources, such as sugarcane or corn. Ethanol has favorable thermodynamic properties, including a high latent heat of vaporization, which contributes to efficient heat transfer and energy efficiency. Ethanol is considered a safer refrigerant option compared to certain synthetic refrigerants. Ethanol is compatible with common materials used in refrigeration systems, such as copper, steel, and aluminum. Ethanol is widely available and produced on a large scale as a biofuel. Ethanol can be produced from biomass or agricultural waste, creating a link between energy production and waste utilization. Retrofitting existing refrigeration systems to use ethanol as a refrigerant can be relatively straightforward in some cases. Therefore, ethanol is selected for further investigation.

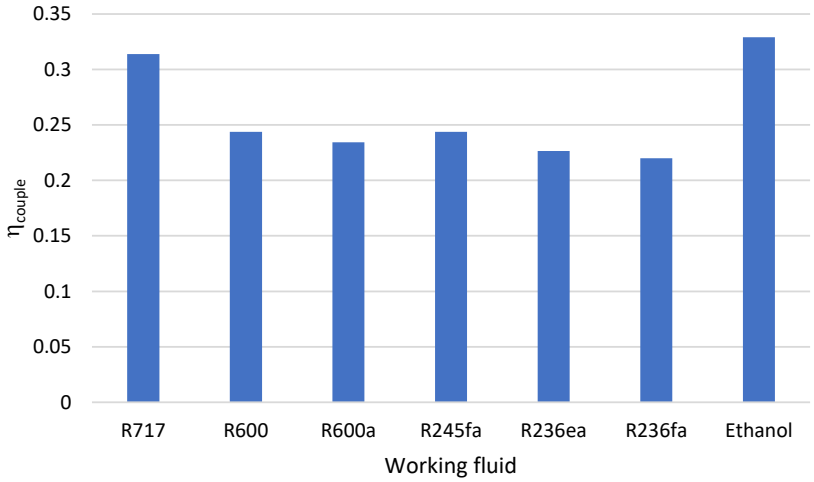

Figure 4: Effect of working fluids on the coupled cycle efficiency.

Figure 5 shows the effect of generator temperature on powers and thermal duties at mass flow ratio MF = 0.2. When the temperature is increased, the capacity of the evaporator increases because the energy of the motive vapor increases, increasing the flow of refrigerant through the evaporator. Cooling capacity Q_e increases from 2.6 W to 33.7 W (13 times) when increasing T_g from 55 to 90°C. Enthalpy of the vapor leaving the low-pressure turbine (h_{11}) decreases dramatically with the temperature so that W_{LT} doubles when T_g increased from 55 to 90°C. The increase of T_g reduces the high-pressure turbine power (W_{HT}). In addition, the increase also reduces the temperature T_{10} thereby reducing the reheater capacity. The trade-off between the increase and the decrease results in maximum output at the optimum temperature T_g of 72.5°C at MF=0.2 as shown in Fig. 6. At larger mass ratios, the increase of Q_e and W_{LT} is larger than the decrease of W_{HT} so the output increases with the generator temperature T_g.

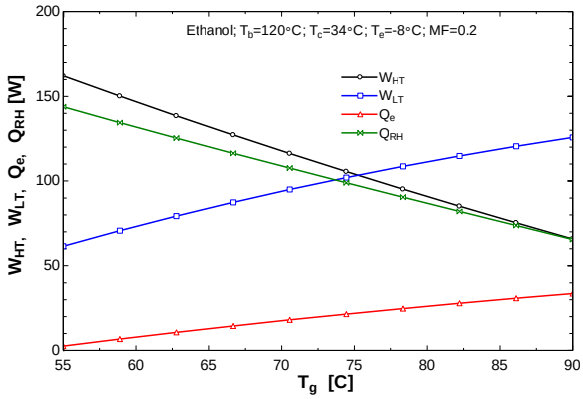

Figure 5: Effect of generator temperature on the powers and heat transfer rates.

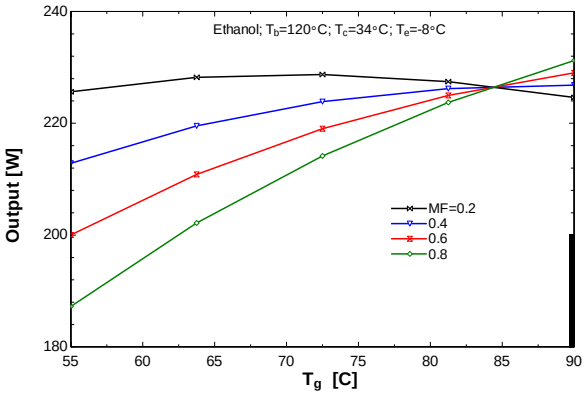

Figure 6: Effect of generator temperature on the output.

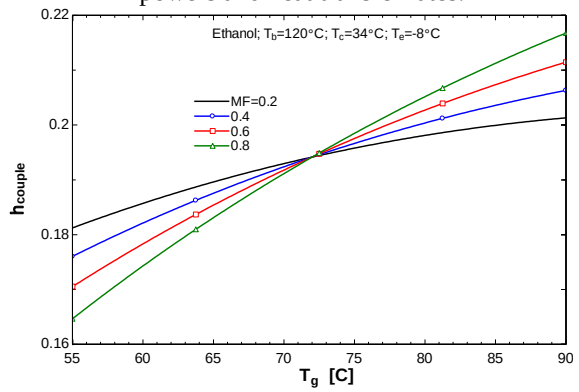

Figure 7: Effect of generator temperature on the coupled cycle efficiency.

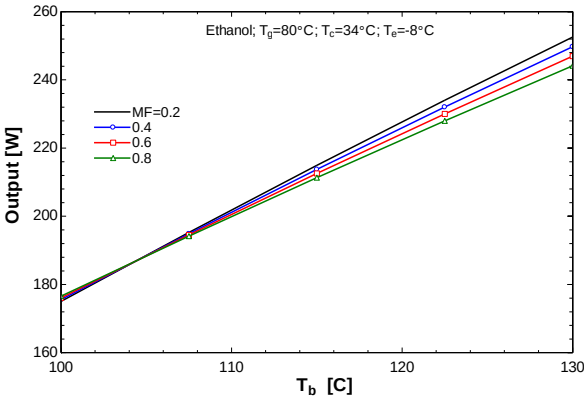

Figure 8: Effect of boiler temperature on the output.

The coupled cycle efficiency varies with MF and T_g, as shown in Figure 7. As a result of the increase in the useful output, the efficiency increases with T_g. As MF increases, the slope of the curves increases. This is because Q_e increases sharply with MF. As the boiler temperature (T_b) increases the output increases as shown in Figure 8. Because as T_b increases, W_{HT} increases, and W_{LT} also increases. This leads to an increase in efficiency with T_b as shown in Figure 9. In addition, as MF increases, Q_e increases significantly so efficiency increases with T_b and MF. Efficiency increases by about 5% as boiler temperature increases from 100 to 130°C. This increase is considerable because the combined cycle uses a low-temperature heat source thus the efficiency of the cycle is low.

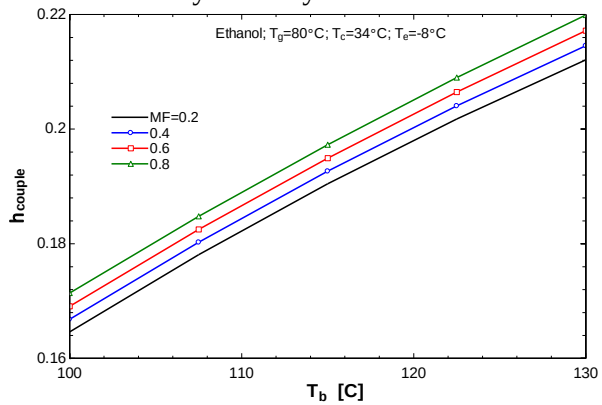

Figure 9: Effect of boiler temperature on the coupled cycle efficiency.

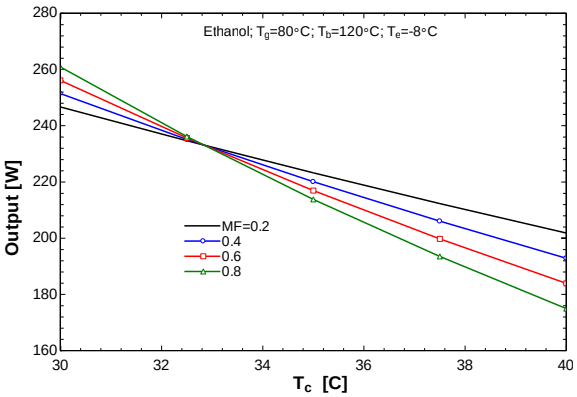

Figure 10: Effect of condenser temperature on the output.

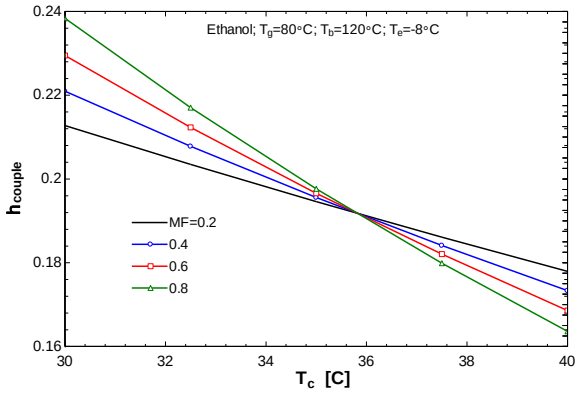

Figure 11: Effect of condenser temperature on the coupled cycle efficiency.

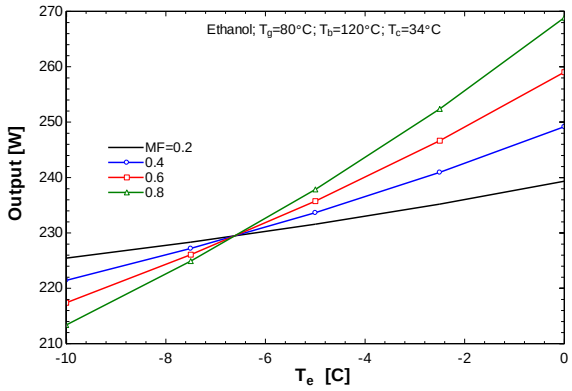

Figure 12: Effect of evaporator temperature on the output.

As the condenser temperature (T_c) increases, the output and the efficiency decrease as shown in Figures 10 and 11. This is obvious because the efficiencies of both the power cycle and the cold cycle are inversely proportional to the condenser temperature. At low condenser temperature, a high mass ratio (MF) should be selected and vice versa.

The effect of evaporating temperature (T_e) as shown in Figures 12 and 13 is opposite to that of condensing temperature. This means that when increasing the evaporator temperature, the output and efficiency increase. Especially, when the evaporator temperature is high, large MF should be selected. At T_e = 0°C, the efficiency increased from 21% to 25% as the MF increased from 0.2 to 0.8.

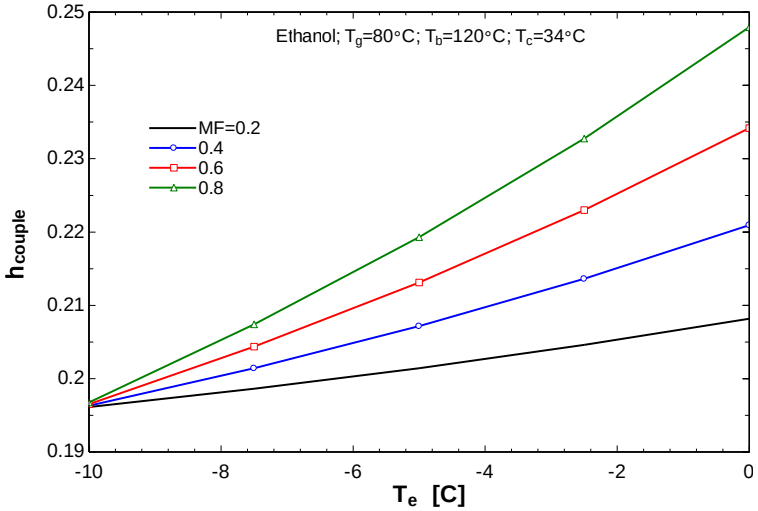

Figure 13: Effect of evaporator temperature on the coupled cycle efficiency.

5 CONCLUSIONS

The thermodynamic analysis of an integrated cycle of organic Rankine and ejector chiller was performed in this study. The vapor after the high-pressure turbine is fed directly into the ejector without using an intermediate device to heat the generator of the ejector cooling system. The main results are drawn as follows:

- Among the 7 refrigerants investigated, ethanol achieved the greatest efficiency.
- At high evaporator temperatures, the extracted flow for the ejector cycle should increase.
- The maximum useful output obtained at the optimum generation temperature of 72.5°C and the mass ratio of 0.2.
- When the condenser temperature is high, the amount of refrigerant extracted for the ejector system should be reduced.
- Efficiency increases by 5% when boiler temperature increases from 100 to 130°C.

REFERENCES

[1] N. M. Huy, D. Van Hai, and N. M. Phu, Energy, Exergy and Economic (3E) Analysis and Optimization of a Combined Heat and Power (CHP) Plant, in *2021 24th International Conference on Mechatronics Technology (ICMT)*, 2021, pp. 1-7: IEEE.

[2] A. Alabdulkarem, Y. Hwang, and R. Radermacher, Energy consumption reduction in CO2 capturing and sequestration of an LNG plant through process integration and waste heat utilization, *International journal of greenhouse gas control,* vol. 10, pp. 215-228, 2012.

[3] P. M. Nguyen, Energy and exergy estimation for a combined cycle of solid CO2 production and NH3-H2O single effect absorption chiller, *Science and Technology Development Journal,* vol. 19, no. 1, pp. 61-69, 2016.

[4] S. Vijayaraghavan and D. Y. Goswami, On evaluating efficiency of a combined power and cooling cycle, *J. Energy Resour. Technol.,* vol. 125, no. 3, pp. 221-227, 2003.

[5] X. Chen, Y. Su, S. Omer, and S. Riffat, Theoretical investigations on combined power and ejector cooling system powered by low-grade energy source, *International Journal of Low-Carbon Technologies,* vol. 11, no. 4, pp. 466-475, 2016.

[6] T. H. H. Doan, V. H. Nguyen, and M. P. Nguyen, Phân Tích Nhiệt Động Chu Trình Kalina Sử Dụng Nguồn Nhiệt Nhiệt Độ Thấp, *Journal of Technical Education Science,* no. 72B, pp. 12-20, 2022.

[7] B. Zheng and Y. Weng, A combined power and ejector refrigeration cycle for low temperature heat sources, *Solar Energy,* vol. 84, no. 5, pp. 784-791, 2010.

[8] N. V. Hap and N. M. Phu, Energy and exergy analyses of the Kalina system integrated with a two-phase turbine, *Journal of Mechanical Science and Technology,* vol. 37, no. 1, pp. 435-443, 2023.

[9] G. Alexis and E. Karayiannis, A solar ejector cooling system using refrigerant R134a in the Athens area, *Renewable Energy,* vol. 30, no. 9, pp. 1457-1469, 2005.

ASSESSING THE SUITABILITY OF THE OFF-GRID OR ON-GRID HOUSEHOLD PV SYSTEM FOR A RURAL AREA AND URBAN AREA IN SOUTHERN VIETNAM

NGHIA-HIEU NGUYEN[1,a,*], KIEN-TRUNG NGUYEN [1,b], TRON–THANH GIANG [2,c], LE-NGOC NGUYEN [2,d]

[1] *Faculty of Heat & Refrigeration Engineering, Industrial University of Ho Chi Minh City, Ho Chi Minh, Vietnam,*
[2] *Faculty of Information Technology, Industrial University of Ho Chi Minh City, Ho Chi Minh, Vietnam;*

[a]*nguyenhieunghia@iuh.edu.vn,* [b]*nguyentrungkien.08@iuh.edu.vn,* [c]*trontg@iuh.edu.vn,*
[d]*nguyenngocle@iuh.edu.vn*

Abstract. Electricity development on the principle with overall optimization of the power source factors, electricity transmission, electricity distribution, economical and efficient use of electricity, Vietnam strives to have 50% of office buildings and 50% of households use rooftop solar system for self-produced and self-consumed by 2030. To solve this urgent problem, the evaluation of household PV systems to find the most suitable solar model was presented in this article. This household PV system to be applied must provide efficient energy supply, reduce transmission to the national power grid, save land, and satisfy daily energy load demand of Vietnamese households in rural and urban areas. That would be analyzed the benefits and conformity assessment based on the specific simulation results, helping the investor to select and contractor to construct have a common voice with high consensus.
Keywords. Homer, solar home system, off-grid PV; on-grid PV.

1 INTRODUCTION

Please In front of fighting climate change and protecting the environment are two big issues of world concern from social organizations to national governments. On the basis of the National Determined Contributions - NDC on Climate Change in Paris (Paris Agreement - COP21) in 2015, all of the countries have a step-by-step roadmap for limiting, eliminating fossil fuel sources, and setting targets for developing renewable energy [1]. Vietnam is strongly innovating to integrate with the world's development trends, taking responsibility for future generations in protecting the living environment. Especially, green power innovation is one of the most concern fields.

Vietnam prioritizes strongly developing renewable energy sources for electricity production, reaching a rate of 30.9-39.2% by 2030 and 67.5-71.5% by 2050 promulgated in Power Plan VIII [2]. The highlights of Solar home system (SHS) are promoting a shift in energy consumption and associating practices [3]. SHSs also play an important role which are reconfigured to match the temporal practices; so, it is easy to blend Off-grid PV with other resource or storage.Vietnam strives that 50% of office buildings and 50% of residential homes will use self-produced/self-consumed rooftop PV system (for on-site consumption, not selling electricity to the national grid) with policies and programmes by 2030. These mandatory requirements make the researches on renewable energy exploitation and the incentive programs of rooftop PV system have been strongly deploying.

The three big trends for the renewable energy sector are cost declines, local manufacturing and distributed energy. From two new options of energy access, grid extention and diesel generators are replaced by minigrids or SHSs. Hybrid minigrids are clearly preferable, but they require high capital cost. SHS can supply small isolated areas because of economics [4]. For a long time, diesel generators still idea for backup power. But PV + batteries now less expensive and low operating cost, utilised as a backup power that enables an emergency response to any disturbance. This is suitable for households. Diesel backup used infrequently provides reliability in big load size to reduce size of solar + batteries.

Most of researchers use Homer, some of them use analytical method; there are other popular industrial-standard for PV system simulation software: PVsyst, HelioScope…. In this study, in spite of our reliance on Homer for designing SHS and the undertaking pre/post-Homer analyses, our contribution arises from three novel features: 1) most of the studies in the past have considered the blended renewable systems whereas we have considered three streamlining design diagrams of Off-grid PV, On-grid PV, and Off/on-grid PV systems; 2) the load respond analysis of the Off-grid PV system, the On-grid solar system for both low-income rural household and high-income urban household; 3) the aid of a diesel generator used for CO_2 credit mitigation evaluation and finding the optimal blended SHS/generator. These novel features help to select and construct strong quickly when the investment product is clearly evaluated from suited cases analysis. Pre-determined eligibility criteria based on some main principles related to the SHS configuration [5-10]. Model of optimal sizing methodology for solar home system which are classified and arranged according to typical standards for the streamlining of the system design diagrams.

2 METHODOLOGY

2.1 Household Loads Assessment

In 2023, Vietnam's population is expected to increase 745,096 people and reach 100,059,299 people in early 2024. 38.77% of the population lives in urban areas (38,361,911 people in 2019) [11]. Based on their economic income, rural households are low appliances and urban households are high appliances. Household's energy consumption is closely related to routinised usages [12-14]. The proposed loads are compared with the load types, used for typical rural and urban household in Vietnam nowadays. The electricity for rural households is lower than urban households which are estimated average daily working hours of the appliances are listed in Table 1 and Table 2.

Table 1: Typical loads of low-income households in rural areas.

Appliance	**Power (W)**	**Quantity**	**ACLoad (W)**	**Use (h/d)**	**AC Daily load (Wh)**
Lighting	10	3	30	6	180
pump	370	1	370	0.5	185
radio	14	1	14	3	42
TV set	60	1	60	3	180
Fan	15	2	30	11	330
Mobile charger	4	2	8	2.5	20
Refrigerator	80	1	80	24	1920
stove	1000	1	1000	2	2000
Laptop	130	1	130	4	520
		AC total load: 1722 W		AC daily load: 5377 Wh	

Table 2: Typical loads of high-income households in urban areas.

Appliance	**Power (W)**	**Quantity**	**AC Load (W)**	**Use (h/d)**	**AC Daily load (Wh)**
Lighting	10	5	50	5	250
pump	370	1	370	0.5	185
radio	14	1	14	3	42
TV set	60	1	60	4	240
Fan	15	2	30	10	300
Mobile charger	4	2	8	4.5	36
Refrigerator	132	1	132	24	3168
stove	1500	1	1500	2	3000
Air-con	1100	1	1100	4	4400
Laptop	130	2	260	4	1040
		AC total load: 3524 W		AC daily load: 12661 Wh	

Figure 1, Figure 2 illustrate the hourly load profiles of rural low-income households and urban high-income households. In both cases, the refrigerator working all day and night. Load consumption is relatively uniform during the day from 6 AM to 10 PM with three peak loads in the morning, afternoon and evening because of family reunion and dinner preparation at this time. However, three peak loads in rural areas are 1 hour earlier than those in urban areas. The average daily load demand and the peak load of rural low-income households and urban high-income households are 5377 Wh/day, 1722 W and 12661 W, 3524 W, respectively.

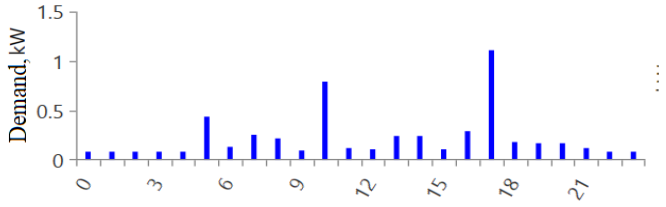

a. Hourly load of the low income in rural areas

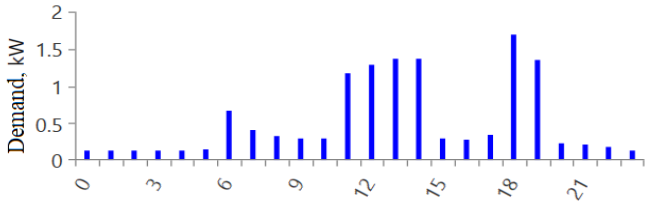

b. Hourly loads of the high income in urban areas

Figure 1: Hourly load profiles of the households.

2.2 Energy resources assessment

The total land area in the south is 77,700 km^2, has a population of about 36 million people (37% of the country's population). Intensity of solar radiation in the end South Central and Southern regions are 4.3 – 4.9 (kWh/m^2/day), number of sunny hours in a year are 2.200 – 2.500 hours. The location is selected in Go Vap district, Ho Chi Minh City, Vietnam (at 10 ^{o}N, 106 ^{o}E) is given in Figure 3. The amount of solar radiation, the ambient temperature and the wind speed downloaded from Nasa prediction of Worldwide Energy Resource database on August 29, 2023. Consequently, the monthly average values of those are used as input parameters [6].

Figure 2: Data resources extraction in Go Vap, Vietnam.

The global horizontal solar radiation ranges and the clearness index ranges 4.57 ÷ 6.01 kWh/m^2/day and 0.443-0.599, respectively with a scaled annual average of 5.09 kWh/m^2/day. Compared with other places in Vietnam, solar radiation levels observed in the studied area are higher, offering attractive potency for the utilization of PV technology. The monthly average ambient temperature for southern Vietnam ranges 25.75 ÷ 30.13 ^{o}C. The annual average ambient temperature is 27.43 ^{o}C. The last role is wind speed. The monthly average wind speed ranges 4.05-5.84 m/s, and the annual average is 4 m/s.

2.3 Household components assessment

The SHS Suitability analysis was performed using the HOMER software. Figure 3 shows the schematic diagram considered in the optimization. The components considered are PV, converter, battery bank and loading system.

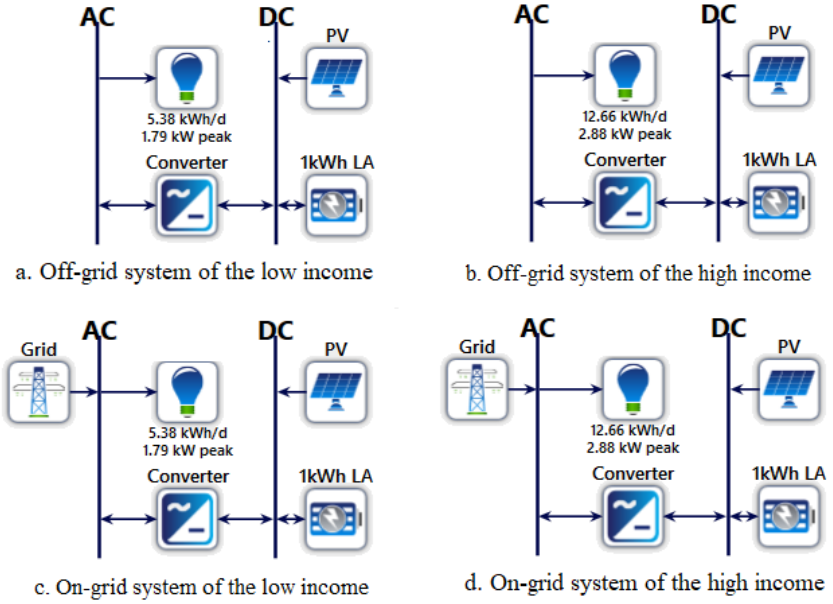

Figure 3: The schematic diagram considered in the optimization.

The parameters of PV arrays, batteries, converter, and diesel generator review in similar work [4, 7, 15-18]. The simulation parameters are shown in Table 3. Homer takes into account the number of units, capital costs, replacement and O&M costs, and operating hours to simulate the system. PV array takes into account the Generic flat plate PV module. Battery bank use kinetic battery model 12V. Converter is a generic system converter, combines the tasks of battery charger, inverter, and controller.

Table 3: Economic analysis results

Parameter	PV	Batt.	Conv.	Gen.
Rate power	1 kW	1 kWh	1 kW	1 kW
Capital cost	4000 $/kW	200 $/kWh	470 $/kW	220 $/kW
Rep. cost	4000 $/kW	200 $/kW	470 $/kW	200 $/kW
O&M cost	10 $/yr	8 $/yr	10 $/yr	0.03 $/kW/hour
Lifetime	25 yr	10 yr	15 yr	15,000 h

3 RESULTS AND DISCUSSION

3.1 Optimal SHS

Discount rate and inflation rate are economic input parameters, are presumed to be 8% and 2%, respectively. The project lifetime is assumed to be 25 years [21]. Because reported SHS adopters were unable to provide 100% the energy required to energy needs such as India 43.4% [19]. SHS provided predominantly TV, stereo, phones and light [20]; next priority is as rice cookers, electric kettles, and electric stoves [21]. The results are demonstrated range from 100% solar fraction to 40% solar fraction in an overall form based on their categorized optimization, in which the possible low cost is regarded for each optimal system of household satisfaction percent. Table 4 and Table 5 show thoes multiple optimal cases of Off-grid and On-grid PV systems with their total net present cost (NPC) and their cost of energy (COE).

Table 4: Categorized optimization results of rural low-income households.

SHS	PV (kW)	1 kWh LA	Conv. (kW)	NPC ($)	COE ($)	O&M cost ($/yr)	Initial capital ($)	Grid Frac. (%)	PV capital cost ($)	PV production (kWh/yr)
Off-grid	2.85	23	2.02	23,813	0.616	529,68	16,965	0	11,418	4,323
On-grid	1.92	26	1.73	21,108	0.925	573.43	13,695	10	7,680	2,908
	2.09	20	1.54	18,944	0.934	451.9	13,102	20	8,378	3,172
	1.63	19	1.76	16,758	0.945	432.57	11,166	30	6,536	2,475
	1.31	17	1.62	14.410	0.946	386.48	9,414	40	5,252	1,988
	1.11	14	1.00	11,740	0.926	311.09	7,718	50	4,447	1,684
	1.04	10	0.874	9,538	0.941	228.28	6,587	60	4,176	1,581

Table 5. Categorized optimization results of urban high-income households.

SHS	PV (kW)	1 kWh LA	Conv. (kW)	NPC ($)	COE ($)	O&M cost ($/yr)	Initial capital ($)	Grid Frac. (%)	PV capital cost ($)	PV production (kWh/yr)
Off-grid	5.04	63	3.97	52,580	0.881	1,388	34,633	0	20,165	7,635
On-grid	4.38	58	2.85	46,717	0.87	1,257	30,464	10	17,525	6,635
	4.74	45	2.98	42,359	0.887	1,006	29,352	20	18,951	7,175
	4.45	37	2.64	37,260	0.892	837.18	26,437	30	17,794	6,737
	3.51	34	2.33	31,780	0.887	761.26	21,938	40	14,043	5,317
	2,71	30	1.54	26,064	0.873	656.28	17,580	50	10,855	4,110
	1.85	27	1.26	20,896	0.869	581.79	13,375	60	7,383	2,795

3.2 Economic and emission comparison

The diesel generator has capital, replacement, and O&M cost of $220/kW, $200/kW, and $0.03/kW/hours, respectively with a lifetime of 15,000 h [3]. The current diesel price in Vietnam is around $0.8/L. The total cost of the Off-grid PV system of low and high income household projects are 25.1% ($23.81 vs $31.78) and 0.1% ($52.58 vs $52.62) lower than the diesel generator case, respectively as shown in Table 6.

Table 6: Off-grid system and generator costs comparison.

Cost ($)	Rural low-income		Urban high-income	
	Off-grid system	Generator	Off-grid system	Generator
Power (kW)	2.85	2	5.04	3.2
Capital ($)	16,965	440	34,633	704
Replacement ($)	4,466	2,902	11,924	4,642
O&M ($)	3,008	6,842	7,681	10,951
Fuel ($)	0	21,634	0	36,380
Salvage ($)	-627	-38.33	-1,658	-61.33
Total ($)	23,813	31,780	52,580	52,616

The aid of a diesel generator used for CO_2 credit mitigation evaluation. These credits can be traded in international market as per the current price \$0.67/*ton*CO_2 [5] . The high diesel fuel consumptions lead to an increase in the CO_2 emissions [6]. Since a private generator is usually installed beside the house, these emissions have a severe negative impact on the health of residents, not to mention their impacts on the local environment. Table 7 shows the CO_2 mitigation and CO_2 Credits of rural low-income households and urban high-income households compared to a generator.

Table 7. Carbon credit of SHS.

SHS	CO_2 mitigation (ton/yr)	Price ($/ton)	Credit ($/yr)	Project life (yr)	Credit of Project ($)
Rural low-income	5.476	0.67	3.66892	25	91.723
Urban high-income	9.208	0.67	6.16936	25	154.234

3.3 Inserting a diesel generator in proposed SHS

A diesel generator of 2 kW is integrated into the Off-grid PV system for the low-income in rural areas to decrease the initial capital and also provides reliability which the PV and battery outputs are not enough to satisfy the load. The optimum blended SHS/generator system configuration consists: 0.885 kW PV arrays, and 5 x 1 kWh LA unit batteries each of which contained 1 kWh of sized power, 0.451 kW converter, 2 kW generator. This system has IRR = 39%, ROI 34%, Simple payback 2.5 yr as shown in Figure 4.
In blended SHS/generator system of rural low-income household, the generator is found to have high operating hours, calculated 1,440 h/yr with high fuel consumption of 386 L/yr, decrease the solar fraction from 100% to 51.4%.

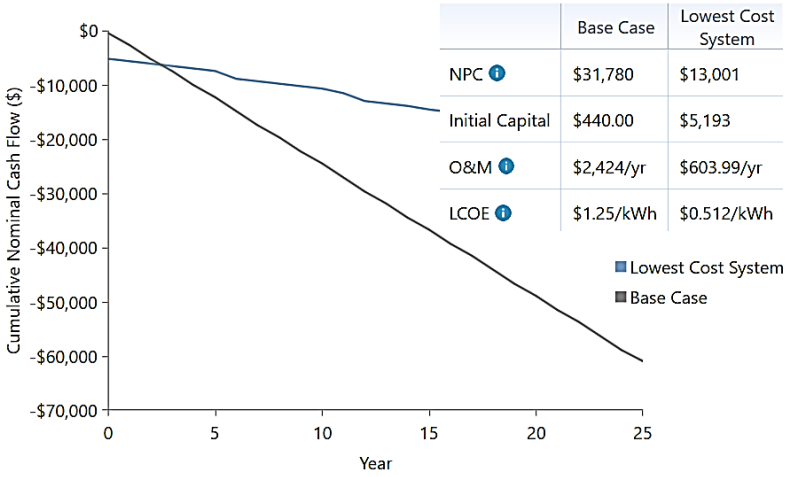

Figure 4: Money saving of the blended SHS/generator for rural low-income.

A diesel generator of 3.2 kW is integrated into the Off-grid PV system for the high-income in urban areas to decrease the initial capital and also provides reliability which the PV and battery outputs are not enough to satisfy the load. The optimum blended SHS/generator system configuration consists: 1.77 kW PV arrays, and 9 x 1 kWh LA unit batteries each of which contained 1 kWh of sized power, 1.71 kW converter, 3.2 kW generator. This system has IRR = 29%, ROI 24%, Simple payback 3.2 yr as shown in Figure 5.
In blended SHS/generator system of urban high-income household, the generator is found to have high operating hours, calculated 1,210 h/yr with high fuel consumption of 827 L/yr, decrease the solar fraction from 100% to 40%.

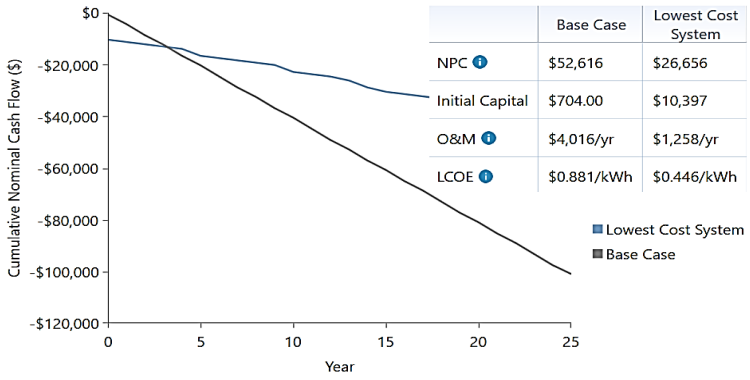

Figure 5: Money saving of the blended SHS/generator for urban high-income.

4 CONCLUSIONS

Responding to Vietnam's self-produced/self-consumed electricity planning policy of rooftop PV system, we found: 1) The optimal SHS consists of 2.85 kW PV arrays, 23 x 1 kWh Lead Acid batteries, a 2.02 kW converter, without the power of the national grid which has an initial capital $16,965 and a PV production 4,323 kWh/yr satisfy 100% typical load demand for rural low-income household. 2) The optimal SHS consists of 5.04 kW PV arrays, 63 x 1 kWh Lead Acid batteries, a 3.97 kW converter, without the power of the national grid which has an initial capital $34,633 and a PV production 7,635 kWh/yr satisfy 100% typical load demand for urban high-income household. Depend on the satisfaction requirement of the household, the SHS capacity can be reduced by 10%, 20%, 30%…. are also analyzed.

In addition of the national grid has provided electricity to 100% of communes and over 99% of rural households, Off/on-grid PV system is the most reasonable SHS solution can both use electricity from the grid to meet peak load and also be self-produced/self-consumed to reduce transmission to the national grid, save land. This Off/on-grid PV system applies the new converter technologies to ensure uninterruptible supply with the competitive price.

About economics and emissions, the total cost of the Off-grid PV system of low and high income household projects are 25.1% ($23.81 vs $31.78) and 0.1% ($52.58 vs $52.62) lower than the diesel generator case; and Carbon credits of CO2 mitigation projects equal $91.72 (3.66 $/yr) and $154.23 (6.17 $/yr), respectively.

If the householders want to invest the blended SHS/generator to decrease the initial capital because the aid of a diesel generator can be done later. The optimal combination for rural low-income household consists of 0.885 kW PV arrays, 5 x 1 kWh Lead Acid batteries, a 0.451 kW converter and 2 kW diesel generator, without the power of the national grid. This case has a NPC of $13,001 and an initial capital $5,193 which is about 59.1% lower and 91.6% higher than those of generator case, respectively. The optimal combination for urban high-income household consists of 1.17 kW PV arrays, 9 x 1 kWh Lead Acid batteries, a 1.71 kW converter and a 3.2 kW diesel generator, without the power of the national grid. This case has a NPC of $26,656 and an initial capital $10,397 which is about 49.3% lower and 93.2% higher than those of generator case, respectively.

REFERENCES

[1] Nguyen, N.-H.; Le, B.-C.; Nguyen, L.-N.; Bui, T.-T. *Technical Analysis of the Large Capacity Grid-Connected Floating Photovoltaic System on the Hydropower Reservoir*. Energies 2023, 16, 3780. https://doi.org/10.3390/en16093780.

[2] Decision No. 500/QD-TTg; Decision was signed on May 15, 2023.

[3] Ojong, N. *Solar Home Systems in South Asia: Examining Adoption, Energy Consumption, and Social Practices*. Sustainability 2021, 13, 7754. https://doi.org/10.3390/ su13147754.

[4] Haratian, Mojtaba & Tabibi, Pouya & Sadeghi, Meisam & Vaseghi, Babak & Poustdouz, Amin. *A Renewable Energy Solution for Stand-alone Power Generation: A Case Study of KhshU Site-Iran. Renewable Energy*, 2018. 125. 10.1016/j.renene.2018.02.078.

[5] Sharma, Santosh & Palwalia, Dheeraj & Shrivastava, Vivek. (2019). *Performance Analysis of Grid-Connected 10.6 kW (Commercial) Solar PV Power Generation System*. Applied Solar Energy. 55. 269-281.

[6] Aziz, Ali & Tajuddin, Mohammad Faridun Naim & Adzman, Mohd Rafi & Mohammed, Mohd & Anwari, Makbul. (2019). *Feasibility analysis of grid-connected and islanded operation of a solar PV microgrid system: A case study of Iraq.* Energy. 116591. 10.1016/j.energy.2019.116591.

[7] Al-Karaghouli, Ali & Kazmerski, L.. (2010). *Optimization and life-cycle cost of health clinic PV system for a rural area in southern Iraq using HOMER software*. Solar Energy - SOLAR ENERG. 84. 10.1016/J.SOLENER.2010.01.024.

[8] Algaddafi, Ali & Alshahrani, Jubran & Hussain, Sabir & Elnaddab, Khalifa & Diryak, Eljaroshi & Daho, Ibrahim. (2016). *Comparing the impact of the off-grid system and on-grid system on a realistic load*. 10.4229/EUPVSEC20162016-5BV.3.13.

[9] Heydari A, Askarzadeh A. *Optimization of a biomass-based photovoltaic power plant for an off-grid application subject to loss of power supply probability concept*. Appl Energy 2016; 165: 601-11

[10] Nacer T, Hamidat A, Nadjemi O, Bey M. *Feasibility study of grid connected photovoltaic system in family farms for electricity generation in rural areas*. Renew Energy 2016; 96: 305-18.

[11] https://danso.org/viet-nam/ [Accessed: 27/09/2022]

[12] Bisaga, I.; Parikh, P. *To climb or not to climb? Investigating energy use behaviour among Solar Home System adopters through energy ladder and social practice lens*. Energy Res. Soc. Sci. 2018, 44, 293–303.

[13] Shove, E.; Walker, G. *What is energy for? Social practice and energy demand*. Theory Cult. Soc. 2014, 31, 41–58.

[14] Khalid, R.; Sunikka-Blank, M. *Homely social practices, uncanny electricity demands: Class, culture and material dynamics in Pakistan*. Energy Res. Soc. Sci. 2017, 34, 122–131.

[15] Nag AK, Sarkar S. *Modeling of hybrid energy system for futuristic energy demand of an Indian rural area and their optimal and sensitivity analysis*. Renew Energy 2018; 118: 477-88.

[16] Halabi LM, Mekhilef S, Olatomiwa L, Hazelton J. *Performance analysis of hybrid PV/diesel/battery system using HOMER: a case study Sabah, Malaysia*. Energy Convers Manag 2017; 144: 322-39.

[17] Al Garni HZ, Awasthi A, Ramli MA. *Optimal design and analysis of gridconnected photovoltaic under different tracking systems using HOMER*. Energy Convers Manag 2018; 155: 42-57.

[18] Sen, R., Bhattacharyya, SC., 2014. *Off-grid electricity generation with renewable energy technologies in India: An application of HOMER*. Renewable Energy, 62, 388-398

[19] Barman, M.; Mahapatra, S.; Palit, D.; Chaudhury, M. *Performance and impact evaluation of solar home lighting systems on the rural livelihood in Assam, India*. Energy Sustain. Dev. 2017, 38, 10–20.

[20] Turner, B. *Diffusion on the ground: Rethinking the logic of scale and access in off-grid solar in Sri Lanka*. Energy Res. Soc. Sci. 2019, 50, 1–6.

[21] Sovacool, B.; Drupady, I. *Summoning earth and fire: The energy development implications of Grameen Shakti (GS) in Bangladesh*. Energy 2011, 36, 4445–4459.

EXPERIMENTAL INVESTIGATION OF HEAT TRANSFER IN MULTIPORT MINI CHANNEL FOR VARIABLE REFRIGERANTS

PHAM QUANG VU [1], NGUYEN QUOC UY [1]

[1]*Faculty of Energy Technology, Electric Power University*
vupq@epu.edu.vn, uynq@epu.edu.vn,

Abstract. This paper presents an experimental investigation of the heat transfer coefficient of refrigerants R410A, R32, R22, and propane inside a mini-channel multiport tube. The experiments were conducted at an average saturation temperature of 48°C and a mass flux range of 50-300 kg/m2s. The results show that the heat transfer coefficient increases with the increase in mass flux for all refrigerants. propane has the highest heat transfer coefficient among the four refrigerants, followed by R410A, R22, and R32. The experimental data were used to develop a new heat transfer coefficient correlation for each refrigerant. The developed correlations were compared with existing correlations available in the literature. The results show that the new correlations provide better heat transfer coefficient predictions than existing ones. The maximum deviation between the predicted and experimental heat transfer coefficient values for the developed correlations is less than 15%. The results of this study provide helpful information for designing and optimizing mini-channel multiport heat exchangers using refrigerants R410A, R32, R22, and propane.
Keywords. Heat transfer, correlation, multiport

1 INTRODUCTION

The heat transfer coefficient of refrigerants is affected by several factors, including the refrigerant properties, the flow conditions, and the heat exchanger geometry. The multiport mini-channel tube is used as a heat exchanger that can improve the heat transfer coefficient of refrigerant. This design provides a large surface area for heat transfer and increases high turbulence in the flow of fluids. There have been a number of studies that have investigated the heat transfer coefficient of refrigerants in mini-channel multiport tubes [1–8]. These studies have generally found that the heat transfer coefficient of refrigerants in mini-channel multiport tubes is higher than in conventional heat exchangers [9].

Zhang et al. investigated the heat transfer coefficient of R134a in mini-channel multiport tubes with different channel sizes and port configurations. They found that the heat transfer coefficient was higher in tubes with smaller channels and more ports. This is because the smaller channels and more ports create a larger surface area for heat transfer. The heat transfer coefficient in microchannels is often calculated using correlations that assume a thin liquid film on the wall. This assumption is valid because the influence of gravity can be neglected in microchannels, and the surface tension predominates. This leads to an accumulation of liquid at the corners of rectangular or triangular channels. A promising theoretical model for heat transfer in microchannels has been proposed by Jige et al. [10]. This model assumes a thin liquid film with a constant thickness throughout the circumference of the channel. They introduced terms for the vapor shear stress effect and the surface tension effect on the Nusselt number. These terms capture the relevant influences of mass flux and vapor quality on heat transfer. In study of Sakamatapan et al. [11] investigates the condensation heat transfer characteristics of R-134a flowing inside multiport minichannels. The authors experimented with different channel sizes, port configurations, and mass fluxes. They found that the condensation heat transfer coefficient increased with decreasing channel size, port density, and mass flux.

Although hydrochlorofluorocarbons (HCFCs) exhibit significantly lower ozone depletion potential (OPD) compared to chlorofluorocarbons (CFCs), the global warming potential (GWP) of these substances has emerged as a growing apprehension. Consequently, a concerted endeavor has been made to identify drop-in replacements that leverage existing equipment and infrastructure. Some hydrofluorocarbons (HFCs), such as R410a, have achieved this objective. Nevertheless, there has been a drive to regulate and ultimately

eliminate HFCs due to their elevated GWP. Consequently, natural refrigerants are being reconsidered as viable alternatives. R290 stands out as one of the most extensively examined hydrocarbon refrigerants. While R290 closely resembles R22 regarding thermodynamic properties, its major drawback lies in its flammability. By adopting a mixed principle that capitalizes on complementary advantages, near-azeotropic mixtures of R32 and R290 in mass fraction ratios ranging from 70/30 to 60/40 have been proposed by Yu et al. [12] and Higashi. [13] R32, a constituent of R407C and R410A, possesses a relatively lower GWP value and offers a higher cooling capacity per unit volume, making it a promising alternative that has garnered considerable attention, as highlighted by Ro et al.[14] . However, it is essential to note that R32 exhibits weak flammability and operates at higher working pressures, particularly with a discharge temperature approximately 20K higher than R410A, posing potential risks to compressor safety during operation.

This paper conducts an experimental investigation on condensation heat transfer of R410A, R22, R32, and R290 inside a horizontal multiport minichannel tube. The authors also developed a theoretical model to predict the condensation heat transfer coefficient. The model considers the effects of channel size, port density, mass flux, and vapor quality. The model was in good agreement with the experimental data.

2 EXPERIMENTAL APPARATUS

A schematic diagram represents the experimental apparatus depicted in Fig. 1. The system comprises four main parts: a refrigerant cycle system, a cooling water system, a circulatory system for ethylene glycol, and data acquisition systems. This facility allows for the control, measurement, and variation of all variables of interest, including the saturation temperature or refrigerants, vapor quality at the refrigerant inlet, mass flux, and heat flux.

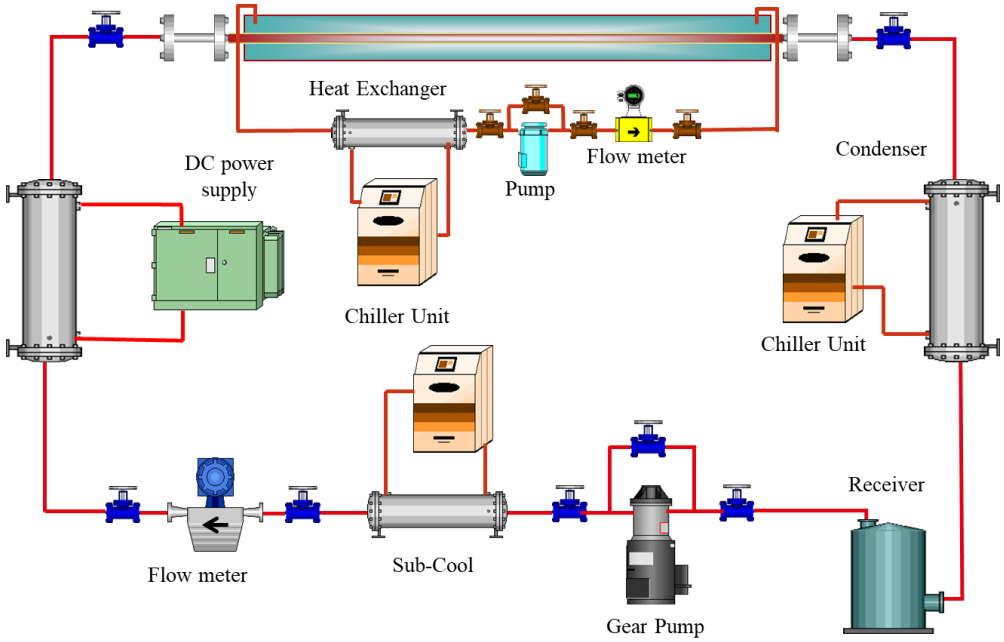

Figure 1: Experimental apparatus.

The condensation heat transfer coefficients of R22, R410A, R32, and R290 were determined using multiport minichannel tubes of 18 rectangular channels. The test section lengths were 200mm and 500mm. For the 200mm test section, the mass flux values were set at 50, 100, and 200 kg/m^{2}s, while for the 500mm test section, the mass flux was set at 300 kg/m^{2}s. To measure the outside wall tube temperature, 20 T-type thermocouples with a diameter of 0.13mm were attached at 5 points along the test section tube on both the top and bottom sides. Four resistance temperature detectors (RTDs) of class-A sensors were placed at the inlet and outlet of both the refrigerant and cooling water to measure their respective temperatures. The energy balance reliability was verified by conducting initial tests on single-phase flow heat transfer of

water-water in the test section. The heat balance error between the cooling water side and the inside hot fluid was consistently within ±3%. The specific details of the test section can be observed in Fig. 2.
In addition, Figure 3 compares fluid and thermal properties between R22, R410A, R32, and R290 at a saturation temperature 48°C. Propane demonstrates a higher latent heat and lower density than conventional refrigerants while maintaining a comparable saturation pressure and thermal conductivity.

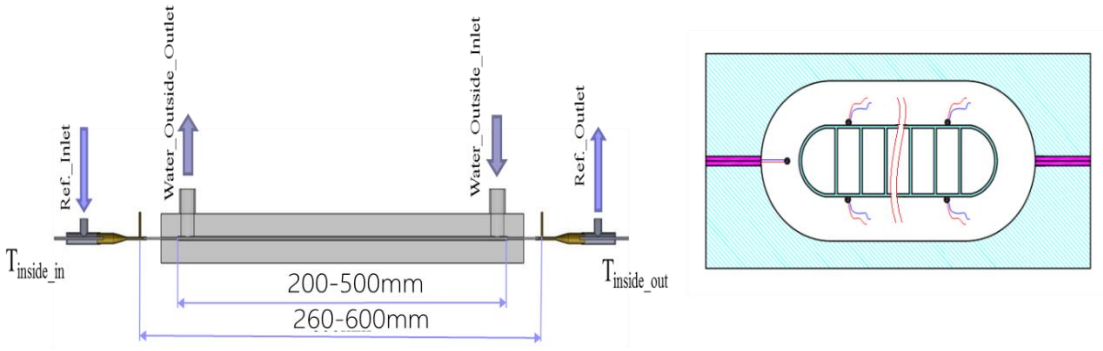

Figure 2: Detail of the test section.

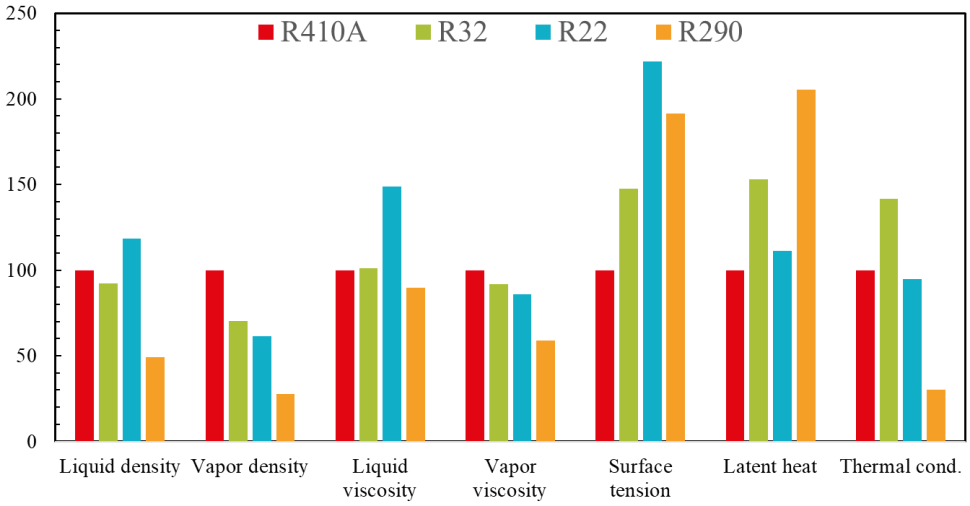

Figure 3: Thermal properties comparison.

The heat flow rate transferred in the test section is derived from a thermal balance on the cooling water side along with measured data of the refrigerant flow rate, the wall heat flux, and the pressure, the quality change in the test section is calculated as follows:

$$x_{inlet} = \frac{1}{h_{fg}}\left[\frac{Q_{pre}}{m_{ref}} - C_p\left(T_{sat} - T_{p,inlet}\right)\right] \quad (1)$$

And the average condensation heat transfer coefficient is obtained as:

$$h = \frac{A_{external}}{A_{internal}}\frac{q}{(T_{sat} - T_{w,i})} \quad (2)$$

Where Q_{pre} is the heat supplied to the pre-heater and $T_{p,inlet}$ is the refrigerant temperature into the pre-heater. $A_{external}, A_{internal}$ are the outer and the inner area surface of test tube, q is the wall heat flux based on the outer surface area of the test tube, and $T_{w,i}$ is the internal wall temperature. The physical properties in data reduction of each experiment are calculated using the REFPROP Version 8.0.

3 RESULTS AND DISCUSSION

An experiment was conducted to investigate the influence of various parameters on the condensation heat transfer coefficient (HTC) of refrigerants. The parameters investigated included the vapor quality at the inlet of the test section (ranging from 0 to 0.9), mass flow rate (ranging from 50 to 500 kg/m^{2}s), and heat flux (ranging from 3 to 12 kW/m^2) at a saturation temperature of 48°C. The relationship between HTC, vapor quality, and mass flux for R22, R410A, R32, and propane is presented in Fig. 4. The results show that the HTC increases as the mass flux increases for all four refrigerants. This can be attributed to the higher mass flux, which leads to increased velocities of the vapor and liquid phases, thereby enhancing turbulence at the interface between the liquid film and the vapor phase. The turbulence promotes more effective heat transfer between the two phases. The HTC of refrigerants is influenced by both surface tension and shear stress. Surface tension causes the liquid film to become thinner and more uniform, thereby improving heat transfer. On the other hand, shear stress is generated by the movement of the vapor and liquid phases and contributes to increased turbulence, further enhancing heat transfer.

At low vapor qualities and low mass fluxes, the HTC shows minimal dependence on the mass flux. This behavior can be attributed to the dominance of surface tension in heat transfer under these conditions. The surface tension of the liquid film results in a thinner and more uniform film at the edges of the rectangular mini channels, which enhances heat transfer. However, at high mass fluxes, the contributions of forced convective condensation HTC and shear stress effects become dominant. Conversely, under low mass flux conditions, surface tension plays a more significant role, and shear stress effects may be diminished. The findings of this research can be utilized to improve the design and operation of refrigeration systems. By optimizing parameters such as mass flow rate and vapor quality, it is possible to enhance the HTC of refrigerants, thus improving the overall efficiency of the system.

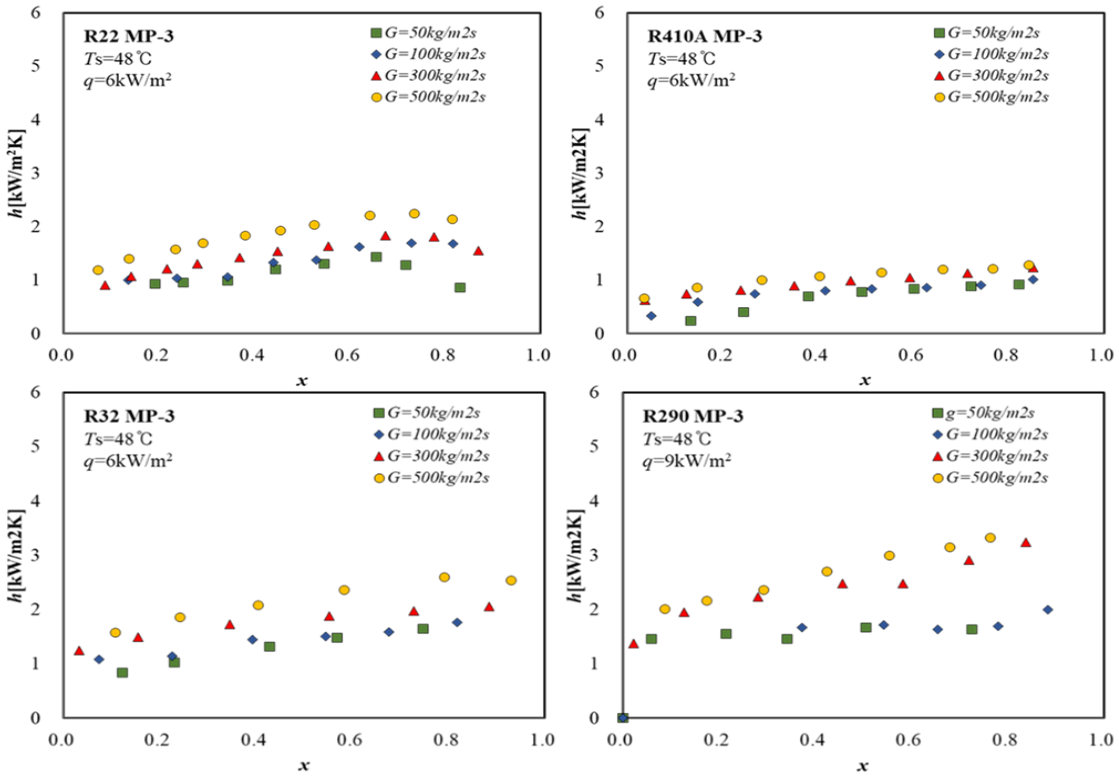

Figure 4: The effect of mass flux on the heat transfer coefficients.

The relationship between the average heat flux and the condensation heat transfer coefficient can be observed in Fig. 5. As the heat flux increases, there is a corresponding rise in the heat transfer coefficient. This behavior can be attributed to the phenomenon of subcooling. Subcooling refers to the temperature difference between the condensing surface and the saturated vapor temperature. With increased heat flux,

the condensate experiences greater subcooling, which enhances its thermal conductivity. This improved thermal conductivity leads to a significant increase in the heat transfer coefficient. These findings align with the research conducted by Zhang et al. [15], who also reported that the heat transfer coefficient increases with higher heat flux due to the combined effects of mass flux and heat flux on the interface temperature between the liquid film and bulk vapor.

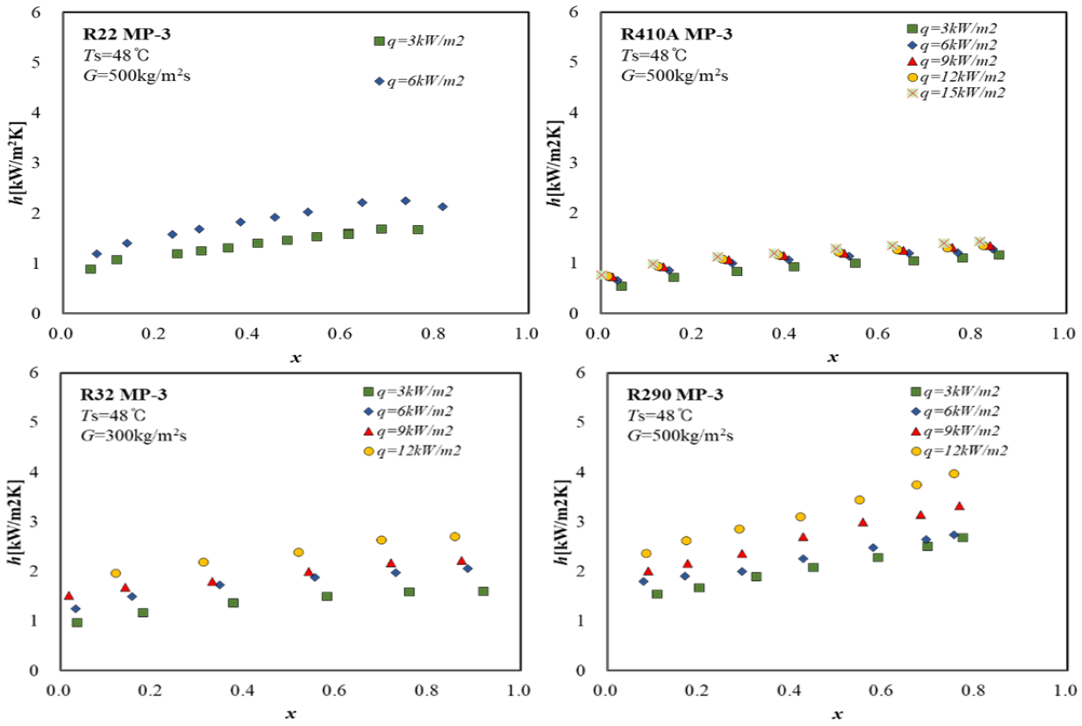

Figure 5: The effect of heat flux on the heat transfer coefficients.

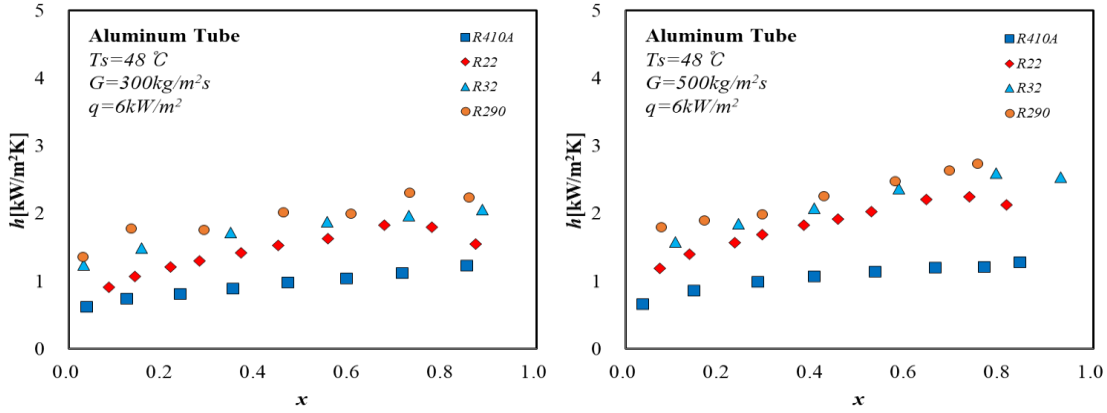

Figure 6: Heat transfer coefficient comparison between four refrigerants.

Comparing the heat transfer coefficients of R22, R410A, R32, and propane in Fig. 6, we can observe differences resulting from their distinct thermophysical properties. Propane exhibits lower liquid density, vapor density, liquid and vapor viscosities, surface tension, and higher latent heat compared to the other refrigerants. These variations in properties contribute to differences in heat transfer coefficients among the refrigerants. For example, the condensation heat transfer coefficient of R410A is 3-11% smaller than that of R22 and 17.8-52.2% lower than that of R32, primarily due to these physical property differences.

In the case of a multiport tube, the condensation heat transfer coefficient is strongly influenced by surface tension and liquid density. At a temperature of 48°C, R22 exhibits a liquid density that is 13% greater than that of R410A. This higher liquid density causes the condensed liquid film at the top wall to fall more

easily, resulting in a higher heat transfer coefficient. Additionally, R22's higher surface tension generates a thinner liquid film compared to R410A, which reduces thermal resistance and further enhances heat transfer.

The primary objective of this study is to evaluate, analyze, and improve the design of heat exchangers used in refrigeration, heat pumps, and air-conditioning systems. However, due to the complexity of the experimental conditions and the channel geometry, existing models may fail to accurately predict the findings of this study. Consequently, a new correlation for the condensation heat transfer coefficient has been proposed, taking into consideration data obtained from experiments conducted on four different types of tubes under varying testing conditions. The proposed correlation builds upon the heat transfer correlation previously introduced by Pham et al. [16] for a multiport rectangular channel. This correlation serves as the foundation for the newly suggested approach. Additionally, Shah and London [17] have proposed a correlation that accounts for the influence of channel geometry on heat transfer. This correlation considers the effect of channel geometry on the heat transfer coefficient and provides valuable insights for the current study.

$$h = 2.67Bo^{0.128}\mathrm{Re}_{eq}^{0.507}\left(\frac{1-x}{\mathrm{Pr}_l}\right)^{-0.154}\left((1-x)^{0.8}+\frac{x}{p_r}\right)^{0.092}\left(\frac{q}{Gh_{lv}}.\frac{A_{external}}{A_{\mathrm{internal}}}\right)^{0.293}\left(\frac{\phi_v}{X_{tt}}\right)^{-0.034}\frac{k_l}{d} \quad (3)$$

This correlation allows for a more comprehensive understanding of the interaction between channel geometry and heat transfer. The development of the new correlation involved regression analysis techniques, which enabled the formulation of equations that accurately represent the relationship between the various parameters involved.

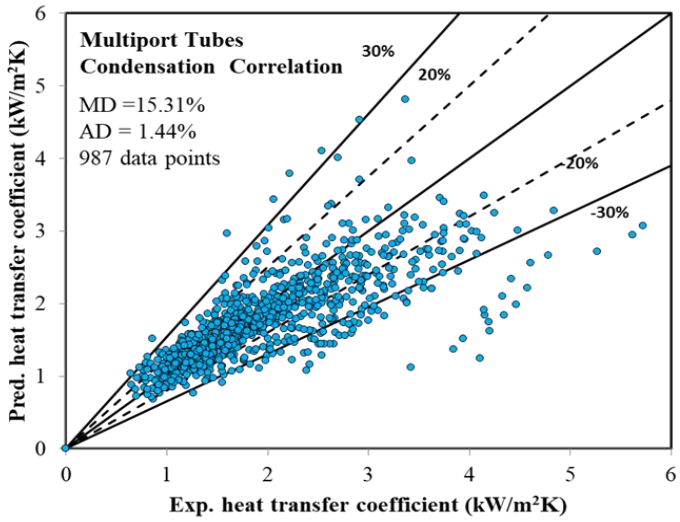

Figure 7: Comparison between the measured data and developed correlation

In Figure 7, a comparison is presented between the experimental data and the prediction value of the condensation heat transfer coefficient based on the new correlation. The results indicate that the proposed heat transfer correlation aligns well with established correlations and exhibits a mean deviation of just 15.31%.

These newly developed equations and correlations provide a more refined and accurate approach to predicting the condensation heat transfer coefficient, considering the complexities of the experimental setup and channel geometry. By incorporating these advancements, researchers and engineers can enhance the design and performance of heat exchangers in refrigeration, heat pump, and air-conditioning systems, ultimately leading to improved system efficiency and effectiveness.

4 CONCLUSION

This study investigated the influence of various parameters on the condensation heat transfer coefficient of refrigerants inside a multiport mini-channel tube. The results showed that the heat transfer coefficient increases with higher mass flux, primarily due to increased velocities and turbulence at the liquid-vapor interface.

Furthermore, the study demonstrated the relationship between average heat flux and the condensation heat transfer coefficient. As the heat flux increases, the subcooling effect enhances the thermal conductivity of the condensate, leading to an increase in the heat transfer coefficient.

The comparison of heat transfer coefficients among different refrigerants highlighted the impact of thermophysical properties. Variations in properties such as liquid density, vapor density, viscosities, surface tension, and latent heat influenced the heat transfer coefficients.

The study also addressed the influence of channel geometry on the heat transfer coefficient, proposing a new correlation that considers the effects of channel geometry, surface tension, and shear stress. The new correlation, derived through regression analysis, provides an improved understanding of the relationship between parameters and accurately predicts the condensation heat transfer coefficient.

Overall, the findings of this study contribute to the optimization of heat exchanger design and operation in refrigeration, heat pump, and air-conditioning systems. By considering parameters such as mass flow rate, vapor quality, and heat flux, engineers can enhance the heat transfer coefficient and ultimately improve the efficiency of these systems. The proposed correlation incorporating channel geometry provides a more accurate prediction method, aiding in the design and performance optimization of heat exchangers.

REFERENCES

[1] D. Jige, M. Nobunaga, T. Nogami, and N. Inoue, “Boiling heat transfer of binary and ternary mixtures in multiple rectangular microchannels,” *Appl Therm Eng*, vol. 229, p. 120613

[2] D. Jige, M. Nobunaga, T. Nogami, and N. Inoue, “Condensation heat transfer of binary and ternary mixtures inside multiport tubes,” *Int J Heat Mass Transf*, vol. 207, p. 123981

[3] A. López-Belchí, F. Illán-Gómez, J. R. García Cascales, and F. Vera García, “R32 and R410A condensation heat transfer coefficient and pressure drop within minichannel multiport tube. Experimental technique and measurements,” *Appl Therm Eng*, vol. 105, pp. 118–131

[4] N. B. Chien, P. Q. Vu, C. Il, J. Oh, and H. Cho, “Saturated flow boiling of R410a in various multiport- tubes with rectangular microchannels,” pp. 1–10, 2018.

[5] P. Knipper, J. Arnsberg, D. Bertsche, R. Gneiting, and T. Wetzel, “Modelling of condensation pressure drop for R134a and R134a-lubricant-mixtures in multiport flat tubes,” *International Journal of Refrigeration*, vol. 113, pp. 239–248, May 2020

[6] P. Knipper, D. Bertsche, R. Gneiting, and T. Wetzel, “Experimental investigation of heat transfer and pressure drop during condensation of R134a in multiport flat tubes,” *International Journal of Refrigeration*, vol. 98, pp. 211–221, 2019

[7] Q. V. Pham, K.-I. Choi, and J.-T. Oh, “Condensation Heat Transfer Characteristics and Pressure Drops of R410A, R22, R32, and R290 in Multiport Rectangular Channel,” *Sci Technol Built Environ*, vol. 212, no. Ii, pp. 1–20, Sep. 2019

[8] C. H. Kim, Y. Shah, and N. H. Kim, “Condensation heat transfer and pressure drop of low GWP R-404A alternative refrigerants in a multiport tube,” *Int J Heat Mass Transf*, vol. 179, Nov. 2021

[9] L. Wang, P. Jiao, C. Dang, E. Hihara, and B. Dai, "Condensation heat and mass transfer characteristics of low GWP zeotropic refrigerant mixture R1234yf/R32 inside a horizontal smooth tube: An experimental study and non-equilibrium film model development," *International Journal of Thermal Sciences*, vol. 170, p. 107090, Dec. 2021

[10] D. Jige, N. Inoue, and S. Koyama, "Condensation of refrigerants in a multiport tube with rectangular minichannels," *International Journal of Refrigeration*, vol. 67, pp. 202–213, Jul. 2016

[11] K. Sakamatapan, J. Kaew-On, A. S. Dalkilic, O. Mahian, and S. Wongwises, "Condensation heat transfer characteristics of R-134a flowing inside the multiport minichannels," *Int J Heat Mass Transf*, vol. 64, pp. 976–985, 2013

[12] J. Yu, Z. Xu, and G. Tian, "A thermodynamic analysis of a transcritical cycle with refrigerant mixture R32/R290 for a small heat pump water heater," *Energy Build*, vol. 42, no. 12, pp. 2431–2436, Dec. 2010,

[13] Y. Higashi, "Experimental determination of the critical locus for the difluoromethane (R32) and propane (R290) system," *Fluid Phase Equilib*, vol. 219, no. 1, pp. 99–103, May 2004

[14] S. T. Ro, J. Y. Kim, and D. S. Kim, "Thermal conductivity of R32 and its mixture with R134a," *Int J Thermophys*, vol. 16, no. 5, pp. 1193–1201, Sep. 1995

[15] H. Y. Zhang, J. M. Li, N. Liu, and B. X. Wang, "Experimental investigation of condensation heat transfer and pressure drop of R22, R410A and R407C in mini-tubes," *Int J Heat Mass Transf*, vol. 55, no. 13–14, pp. 3522–3532, 2012

[16] Q.-V. V. Pham, K.-I. K.-I. K.-I. Choi, J.-T. J.-T. Oh, and H. Cho, "An Experimental Investigation of Condensation Heat Transfer Coefficients and Pressure Drops of Refrigerants Inside Multiport Mini-channel Tubes," *International Journal of Air-Conditioning and Refrigeration*, vol. 25, no. 02, p. 1750013, Mar. 2017

[17] R. K. Shah and A. L. London, "Rectangular Ducts," in *Laminar Flow Forced Convection in Ducts*, Elsevier, 1978, pp. 196–222.

ENHANCING MELALEUCA OIL DISTILLATION WITH STEAM EXPLOSION TECHNOLOGY

TRAN THANH SON[1], NGO PHI MANH[1]

[1] *Danang University of Science and Technology, The university of Danang*
ttson@dut.udn.vn

Abstract. Melaleuca oil serves as a potent immune system booster, swiftly combating various viral, bacterial, and fungal infections. Despite its potential, Melaleuca oil production in Vietnam remains limited due to outdated techniques. This research focused on enhancing production by employing the steam explosion method prior to steam distillation for two Melaleuca species: *alternifolia* and *quinquenervia*. Steam explosion, which plays as a preliminary treatment, subjects Melaleuca material to rapid pressure changes, causing a mechanical 'explosion.' This process fractures the material's structure, facilitating essential oil migration from the interior to the surface, and significantly shortening distillation time. Experiments varying steam explosion duration (1, 3, and 5 minutes) were conducted at the steam pressure of 5 bar_g. With a 5-minute steam explosion, approximately 9.6 mL of essential oil was extracted from 3 kg of raw Melaleuca *quinquenervia* – nearly doubling traditional non-explosive methods. Moreover, distillation time was reduced by 60%. The needle-like leaves of *alternifolia* contributed to steam explosion's efficacy, yielding more oil. These findings underscore the importance of pretreatment in enhancing oil extraction efficiency, including yield and energy consumption.
Keywords. Melaleuca oil, pretreatment, oil yield, steam explosion

1 INTRODUCTION

Essential oil has emerged as a pivotal component within the realm of medicinal herbs, commanding substantial trust and a significant market share in present-day consumption. Notably, Vietnam has made remarkable strides in exporting essential oils to approximately 30 out of 167 countries that display a demand for such imports. This achievement accounts for 1.16% in volume and 0.6% of the global essential oil market [1], underscoring the transformative positive evolution of the country's oil production and extraction sector, which now stands as a promising industry. There are two types of Melaleuca oil extracted from two species, *alternifolia* and *quinquenervia*. The latter type is commonly used in Vietnam. However, the raw *quinquenervia* material source is scattered, difficult to cultivate, and has low leaf yield. Meanwhile, the *alternifolia* type is relatively easy to cultivate and offers a higher leaf yield. This type of essential oil owns highly antimicrobial activity [2] and widely popular in Australia and European countries. Currently, Vietnam is focusing on cultivating and exploiting this promising *alternifolia* species for distilling the essential oil from its leaves.

In Vietnam, the existing models for Melaleuca oil distillation remain constrained by small-scale, manually-driven processes that rely heavily on outdated technology and experiential knowledge. Advanced methodologies have yet to be explored or implemented to enhance the efficiency of oil extraction. In particular, an on-site study of the actual production procedures at Bao Ngoc Melaleuca Essential Oil Co., Ltd. in Hai Lang town, Quang Tri province, reveals a steam distillation approach necessitating an average distillation time of 360-480 minutes per batch of 200 kg of raw material. A significant drawback of this method is its prolonged duration, which leads to heightened energy and water consumption, consequently driving up production costs and dampening competitiveness within the market.

Moreover, the manual distillation process lacks stringent testing protocols, resulting in inconsistent and subpar product quality. This inconsistency further contributes to the wastage of substantial quantities of raw materials and energy resources. Consequently, these challenges have culminated in the selection of this topic, aiming to address and overcome the issues posed by the existing practices.

This study employs the steam explosion technique [3-6] to disrupt the composition of Melaleuca prior to its introduction into the distillation process, departing from the conventional method. The primary objective centers on expediting distillation duration, consequentially curtailing energy consumption, while concurrently augmenting essential oil yield—effectively enhancing product competitiveness.

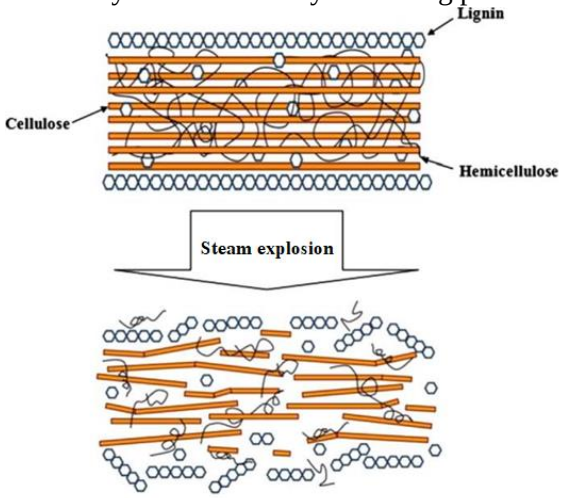

Figure 1: Disrupted structure of biomass fibers post steam explosion.

The steam explosion method's pretreatment stage stands as a pivotal facet in the overall biomass conversion sequence, facilitating the breakdown of the plant's external protective layer. During steam explosion, high-pressure saturated steam rapidly engulfs the melaleuca material for a brief interval before swiftly plummeting to atmospheric pressure. This abrupt pressure reduction prompts a swift expansion of water vapor within the material, akin to a mechanical "explosion." Consequently, the material's structure (encompassing lignin, hemicellulose, and cellulose) is fractured, as illustrated in Fig. 1. Consequently, the resistance for essential oil immigrating from the inner to surface of materials is reduced, then distillation duration experiences significant reduction. Furthermore, this mechanical expansion procedure preconditions the input material, resulting in diminished water requirements for subsequent distillation, when contrasted with the conventional manual method that relies purely on water's thermal energy for material structure disruption and steam for essential oil extraction.

2 EXPERIMENTAL

2.1 Production process diagram

Figure 2 illustrates a typical essential oil production process. The raw materials, consisting of Melaleuca branches and leaves, progress through a sequence of stages: collection, processing, and cleansing. Following this, they are introduced into the distillation pot, which functions as the essential oil extraction tank. The specific technology chosen dictates the approach: either the materials are immersed in water (hydro-distillation) or the distillation pot's lower portion is filled with water, enabling only steam to pass through the materials (steam distillation).

In this study, steam distillation is employed to extract oil from Melaleuca. Specifically, water at the base of the pot is heated until it reaches its boiling point, generating steam. This steam then traverses through the material's cavity, warming the material in the process. The oil present in the material vaporizes and mingles with the steam, subsequently advancing to the condenser. Within the condenser, the mixed vapor undergoes condensation, transforming into a liquid state.

The resultant liquid is subsequently directed to a dissociation apparatus, from which the uppermost layer of condensed essential oil is separated (referred to as crude oil). This separation is feasible due to the lower density of essential oil in comparison to water. The water settled at the base of the dissociation apparatus is recycled back into the distillation vessel to sustain the ongoing distillation process, as it retains a certain quantity of essential oil. Upon the completion of the extraction of all essential oils from the raw materials,

the distillation procedure concludes. The remaining residue can serve as a potential source of fuel or as organic fertilizer.

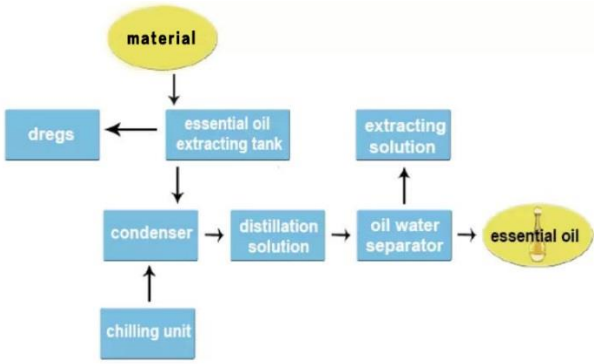

Figure 2: Flowchart of essential oil production process.

2.2 Principle diagram of a steam explosion device

Prior to introducing materials into the essential oil distillation apparatus, as shown in Fig.2, they undergo a pretreatment known as steam explosion. The process for steam exploding Melaleuca leaves and branches is depicted in Fig. 3. Freshly harvested Melaleuca (comprising leaves and terminal branches) are first cut into sizes ranging from 1 to 3 cm. It's important to ensure that the materials are shielded from high temperatures and humid conditions, as excessive humidity can hinder the extraction of the maximum amount of oil.

Before placing the Melaleuca material into the explosion reactor, careful attention is required to eliminate impurities such as grass and debris that may have become mixed in during the collection process. Subsequently, the prepared Melaleuca leaves are loaded into the reactor. For each experimental run, the parameters of saturated steam (gauge) pressure are adjusted accordingly. Valves connecting the reactor and the receiver are securely fastened. Once the pressure reaches the desired parameters, the time relay for the steam explosion is set.

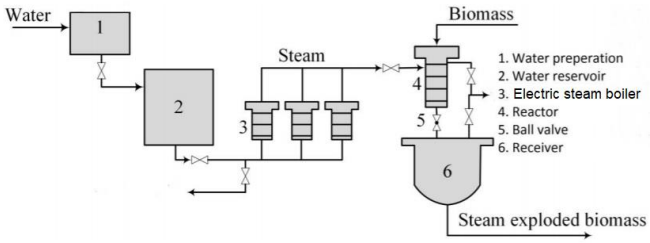

Figure 3: Diagram of steam explosion device.

At this point, the steam supply valve to the reactor is opened, allowing the reactor to be filled with steam while maintaining a consistent pressure throughout each test. This practice ensures that the steam temperature remains constant for the duration of the experiment.

Once the material temperature reaches the designated test value, the time relay initiates its countdown. Upon the completion of the predetermined holding time, an audible alert from a buzzer indicates the end of this phase. Swiftly, the connecting valve linking the reactor and the receiver is opened to execute the steam explosion procedure. The abrupt drop in pressure triggers the fragmentation and splitting of the Melaleuca into smaller fragments. In the context of the current paper, the specified holding times are set at intervals of 1, 3, and 5 minutes. Furthermore, the steam distillation was carried out on *Quinquenervia* materials without the aid of steam explosion for clarifying the advantage of the steam explosion pretreatment.

2.3 Essential oil distillation

Upon completing the pretreatment through the steam explosion method, the outlet located under the receiver (6), as shown in Fig. 3, is opened to gather the treated materials. These materials are then directly loaded

into the distillation apparatus. Care should be taken not to overly compress the material during loading, as excessive compression can hinder the uniform distribution of steam throughout the material block. Conversely, the material shouldn't be loaded too loosely and porous, as this would cause steam to escape through voids without adequately interacting with the entire block of raw materials.

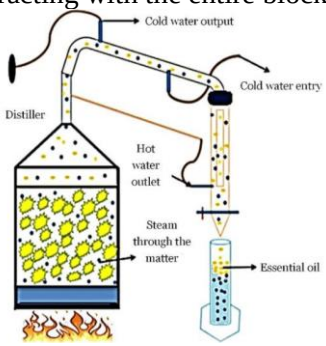

Figure 4: Schematic image of an essential oil distillation device.

Once the materials are loaded, secure the lid of the distillation apparatus and initiate the distillation process using an electric stove. The distillation procedure is considered stable when the temperature reaches a constant level and the mixture of condensed liquid (oil and water) flows evenly and continuously from the water-cooled condenser. This composite solution of oil and water then proceeds into the dissociation device. Melaleuca essential oil, due to its lower density, floats atop the water layer, enabling its separation from the water and allowing for the extraction of the essential oil.

During the distillation process, the quantity of extracted oil is monitored at regular intervals, usually every 30 minutes, for all three experimental cases. Additionally, a simple method to ascertain the completion of distillation involves using a glass container to collect a small portion of the condensate. If oil is discernible on the glass, it signifies that the distillation process has not concluded.

Furthermore, the author conducted an additional experiment involving the extraction of Melaleuca essential oil using steam distillation without incorporating the step of steam explosion. This experiment serves as a representation of the conventional method and will serve as a benchmark for comparison with the experiments involving steam explosion.

3 RESULTS AND DISCUSSION

In all experiments, Melaleuca leaves and terminal branches were cut into pieces ranging in size from 1 to 3 cm, as depicted in Figure 5a. Each experiment utilized 3 kg of materials (before steam explosion). Figure 5b displays images of the materials post-steam explosion, highlighting three different holding durations at a pressure of 5 bar_g.

(a) (b)

Figure 5: Quinquenervia materials after steam explosion at 3 different holding durations.

The current steam pressure was determined based on our prior research [3]. It is evident that a higher explosion pressure leads to more efficient interior destruction of biomass materials. However, it's crucial to consider that in essential oil extraction, steam temperature plays a significant role in oil yield, as high temperatures can lead to oil decomposition. In line with our earlier work [3], it was observed that the highest

oil yield was achieved at an explosion pressure of 5 bar_g, surpassing the results obtained at pressures of 3 and 7 bar_g

Materials following the steam explosion demonstrated a volume increase of 20-25% compared to the weight of the original feed material due to heightened moisture content. Figure 6 illustrates the essential oil yield over time for both the steam explosion method and the traditional method (without steam explosion). The graph in Figure 6 reveals several key points of significance:

(1) The oil extraction rate is faster if there is a steam explosion pretreatment and the oil extraction time is reduced to 90 minutes compared to 150 minutes without steam explosion (traditional method). Certainly, incorporating the steam explosion step to assist in the distillation process contributes to a reduction in the required distillation time. Specifically, the distillation time is shortened to just 90 minutes, equivalent to 60% of the time needed for traditional distillation without steam explosion. Consequently, this reduction in time leads to lowered energy consumption and labor costs.

(2) The essential oil yield in the scenario where steam explosion was employed as a pretreatment at a pressure of 5 bar_g and for a duration of 5 minutes amounted to 9.6 mL, nearly twice the amount obtained through the traditional method (5.3 mL).

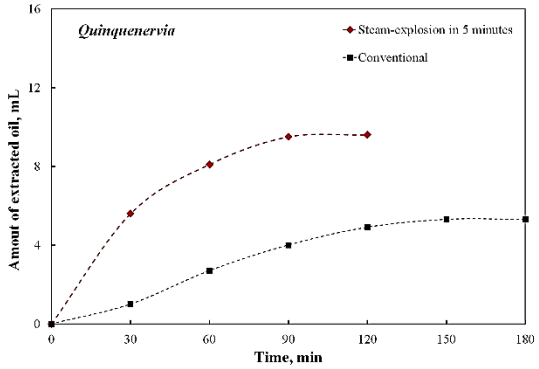

Figure 6: Comparison between extracted oils without steam explosion (Conventional) and with 5-minute steam explosion at 5 bar_g.

In addition, when considering the sensory attributes of the essential oil, observations have shown that the oil obtained through the steam explosion pretreatment method showcases a marginally darker and more concentrated color. Moreover, it carries a more pronounced aroma compared to the essential oil derived from the traditional distillation process. On the contrary, the oil obtained through the conventional method is characterized by a lighter color and a more diluted consistency, accompanied by a subtler fragrance. However, in order to thoroughly assess the quality of the essential oil in both methods, more detailed compositional analyses are required in subsequent studies.

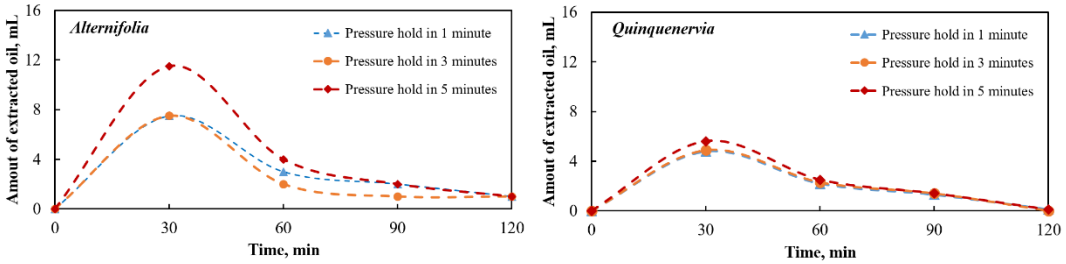

Figure 7: Amount of oil from two types of Melaleuca with steam explosion collected every 30 minutes during distillation.

Figure 7 shows the amount of oil obtained after every 30 minutes of distillation from two types of Melaleuca with steam explosion. From this graph, it can be seen that the highest oil yield after the first 30 minutes in both types. The amount of oil extracted from *Alternifolia* material is significantly higher than that from *Quinquenervia* material, especially within the first 30 minutes. The highest oil yield is achieved when the steam explosion process is extended to 5 minutes. This result indicates that as the steam explosion duration

increases, the internal structure of the material undergoes more significant disruption, leading to a greater release of oil.

During the time interval from 90 to 120 minutes, the oil yield is very low for all steam explosion durations and both material types. From this, a preliminary conclusion can be drawn that the combined steam explosion and distillation time should not exceed 90 minutes.

Figure 8 illustrates the total amount of extracted oil from the distillation process employing steam explosion for two types of raw materials. It is evident that the amount of oil obtained from *Alternifolia* type is consistently greater than the combined oil yield from *Quinquenervia* type. The most pronounced difference is observed when a 5-minute steam explosion is applied, where the oil yield from *Alternifolia* type (18.5 mL) is nearly twice that of *Quinquenervia* type (9.6 mL). Since the oil content in the two Melaleuca species is nearly the same, ≤ 2% (or approximately 67 mL per 3 kg of material) [2, 7, 8], the main difference in the total oil yield might primarily arise from the distinct biological characteristics of these two types. Specifically, the leaves of the *Alternifolia* type are needle-shaped and measure from 1 to 3 cm in length. Therefore, under the impact of the steam explosion within 5 minutes, the internal structure of *Alternifolia* type is more susceptible to disruption compared to the *Quinquenervia* type, which has broader and oval-shaped leaves. In other words, the Quinquenervia species requires a longer steam distillation time to extract a higher quantity of oil.

Additionally, in the steam distillation method, whether or not the steam explosion method (as a pretreatment step) is employed, the extraction efficiency remains low. Specifically, when using steam explosion, the oil yield only reaches 27.6% (18.5/67 mL/mL) for *Alternifolia* and 14.3% (9.6/67 mL/mL) for *Quinquenervia*, compared to the theoretically extractable oil content. In cases where steam explosion is not utilized, the oil yield is considerably lower, at only 7.9% or 5.3/67 mL/mL of the theoretical oil content in the raw material. However, the steam distillation method is characterized by its simplicity, ease of implementation, and suitability for large-scale production. Therefore, in large-scale production, if the steam explosion method is integrated as a pretreatment step, the efficiency of the water-driven steam distillation process can be enhanced.

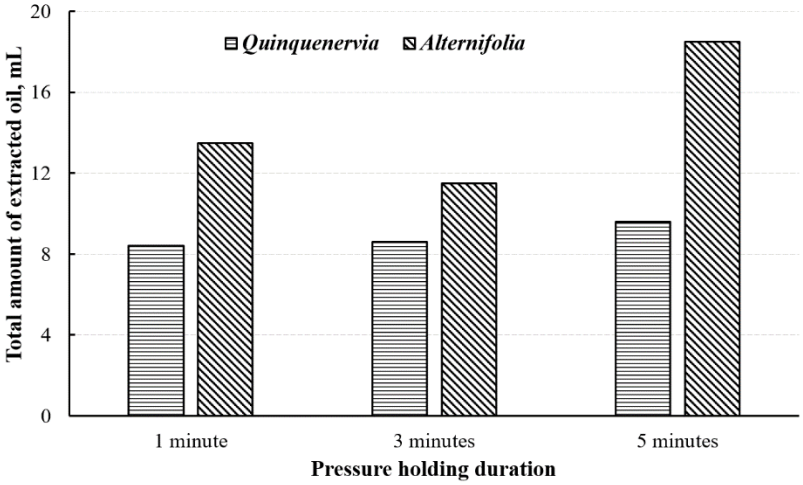

Figure 8: Total amount of oil extracted from two species of Melaleuca with steam explosion at three different pressure holding durations.

4 CONCLUSION

The process of distillation and essential oil collection, both in general and with specific focus on Melaleuca essential oil, has been innovatively enhanced through the incorporation of the steam explosion pretreatment method. This novel approach presents a multitude of advantages when compared to traditional methodologies. Findings from this study, conducted with Melaleuca trees in Thua Thien Hue province, showcase a noteworthy reduction in distillation time for essential oil extraction, amounting to 60% less time than conventional methods. This abbreviated time frame leads to a substantial reduction in energy consumption, facilitated by the preliminary treatment of materials using the steam explosion technique.

The experimental investigations yield several key conclusions:

Employing the steam explosion pretreatment at the specified conditions (5 bar_g pressure, 5 minutes of steam explosion) results in an essential oil yield of 9.6 mL per 3 kg of input material, nearly twice the yield of traditional oil production methods. Although the oil yields supported by steam explosion are lower than the maximum theoretically value (approximately 67 mL per 3 kg of material), the effectiveness of steam explosion is evident when compared to the conventional method (without steam explosion).

With the same initial oil content, the type of *Alternifolia*, when combined with the steam explosion method, yields a higher amount of oil compared to *Quinquenervia*.

Moreover, the essential oil obtained through steam explosion pretreatment exhibits distinct sensory characteristics, including a deeper hue, denser consistency, and a more pronounced and characteristic aroma when compared to oil obtained through traditional means.

While these preliminary research outcomes represent significant advancements in enhancing essential oil extraction efficiency and reducing energy consumption, there remains room for further refinements in the essential oil production system incorporating steam explosion pretreatment. This approach can be readily extended to the production of other essential oils, such as basil, lemongrass, and orange peel, heralding promising prospects for the broader essential oil industry.

REFERENCES

[1] "Sử Dụng và Khai Thác Nguồn Tài Nguyên Thực Vật Có Tinh - GFS Group - Tập Đoàn GFS." Gfs.com.vn, gfs.com.vn/su-dung-va-khai-thac-nguon-tai-nguyen-thuc-vat-co-tinh-dau-viet-nam-d3412. Accessed 21 Aug. 2023.

[2] Carson, C. F., et al. "Melaleuca Alternifolia (Tea Tree) Oil: A Review of Antimicrobial and Other Medicinal Properties." *Clinical Microbiology Reviews*, vol. 19, no. 1, 1 Jan. 2006, pp. 50–62

[3] Nguyễn Thành Phương, Trần Thanh Sơn, "Nghiên cứu thiết bị sản xuất tinh dầu sả bằng phương pháp nổ hơi", *Journal of Science and Technology* (JST-UD), Vol. 18, No. 3, 2020; pp 37-4.

[4] Wenjie Sui, Hongzhang Chen, "Water Transfer in Steam Explosion Process of Corn Stalk", *Industrial Crops and Product*, Elsevier Publisher, 2015.

[5] Kunwang, Jinghuan Chen, Shao Ni Sun, Run Cang Sun, "Steam Explosion", *Elsevier Publisher*, 2015

[6] B. Focher. A. Marzetti. and V. Crescenzi, "*Steam Explosion Techniques: Fundamentals and Industrial Applications*", Milan, Italy, Gordon & Breach Science Publishers, 1988.

[7] Cicció, José F., and Carlos Chaverri. "Chemical Composition of Essential Oils of the Tree Melaleuca Quinquenervia (Myrtaceae) Cultivated in Costa Rica." *UNED Research Journal*, vol. 13, no. 1, 21 Apr. 2021, p. 10.

[8] Carson, C. F., et al. "Melaleuca Alternifolia (Tea Tree) Oil: A Review of Antimicrobial and Other Medicinal Properties." Clinical Microbiology Reviews, vol. 19, no. 1, 1 Jan. 2006, pp. 50–62.

A COMPARISON OF METHODS ON ENERGY EFFICIENCY MODELING FOR RESIDENTIAL AIR CONDITIONERS IN VIETNAM

CUNG DUC HUY [1], TRINH QUOC DUNG [1*], NGUYEN VIET DZUNG [1], TRUONG MINH THANG [2]

[1] *Department of Thermal Energy Engineering, School of Mechanical Engineering, Hanoi University of Science and Technology, No.1, Dai Co Viet Road, Hanoi, Vietnam*
[2] *Department of Heat Engineering, Faculty of Mechanical Engineering, University of Transport and Communications, No.3, Cau Giay Road, Hanoi, Vietnam*

dung.trinhquoc@hust.edu.vn

Abstract. This paper shows a comparison of energy efficiency assessment methods for residential inverter air conditioners. The study indicates similarities between the two methods come from the principle of the bin method. Still, the differences are caused by distinctive approaches to their core method to be compatible with different climatic zones. Additionally, the study assesses the influence of these methods on consumers, manufacturers and governments from economic and technical perspectives. The data of some air-cooled air conditioners that have nominal cooling up to 24000 BTU/h were used in this study. Additionally, seasonal energy efficiency ratio (SEER) of those air conditioners in conditions of ISO 16358 was calculated. Furthermore, energy efficiency decreased, and power consumption rose considerably when changing the operating condition from EN 14825:2012 to ISO 16358-1:2013 because of the transition in equivalent active hour and bin temperature.

Keywords. Air conditioner, bin temperature method, energy efficiency, power consumption, SEER

1 INTRODUCTION

According to International Energy Agency (IEA), the number of operating air conditioners has passed the two billion units mark and is forecasted to rise to 40% in the following years when the world goes to the year 2030 [1]. Air conditioners have become essential equipment in hot climates, especially when outdoor temperatures go above 30ºC. However, only twelve per cent of people who live in tropical climates own at least one air conditioner [1]. The chance to expand the air conditioning market is still available, especially in developing countries such as Vietnam, which is evaluated up to 2.4 billion USD with more than 50 per cent of households not having this equipment [2]. In addition, 44 per cent global population lives in tropical climates, but only twelve per cent of people own at least one air conditioner [1]. The chance for expanding the air conditioning market is still many, especially in developing countries such as Vietnam, which is evaluated up to 2.4 billion USD with more than 50 per cent of households don't have this equipment [2]. In Vietnam, split air conditioner holds a major part of the market with more than 9 of 10, and most of them are household air conditioners [3].

In recent years, electricity peak demand in Vietnam has gone up with the following years higher than in previous years, especially in the summer when Vietnamese people need air conditioners for cooling. Energy efficiency policies in Vietnam have been mandatory since 2011, and the government recommends people choose high energy efficiency with less power consumption equipment, including air conditioners, to limit the substantial rise of peak demand. With the introduction of cooling seasonal performance factor (CSPF) by ISO (International Organization for Standardization), Vietnam quickly adopted and published the National standard TCVN 10273-1:2013 (equivalent to ISO 16358-1:2013) that covered the assessment method based on it. In 2015, National standard TCVN 7830:2015 was the first Minimum Energy Performance Standard (MEPS) compulsory to use only this method for all household air conditioners with the cooling capacity smaller than 41,000 BTU/h. However, TCVN 10273-1:2013 has the reference outdoor temperature bin that is more suitable for moderate climates, for instance, Europe or the USA. Additionally, CSPF only evaluates the operation state of the air conditioner without considering other modes, including

thermostat-off and standby, so CSPF in Vietnam may not reflect precisely the energy efficiency and total power consumption for air conditioners. On the other hand, there is a method that is also based on the bin method: it uses the seasonal energy efficiency ratio (SEER) in Europe (EU), in European standard EN 14825. This methodology evaluates all mode power consumption which is an advantage over using CSPF. This paper will examine thoroughly and compare these assessment methods based on various aspects, such as experimental conditions. It also evaluates the suitable level of methods to apply in Vietnam. In addition, the SEER of air conditioners in conditions of ISO 16358 and original EN 14825 will be calculated to investigate the shift in energy efficiency and power consumption for some household Inverter air conditioners that have nominal cooling capacity from 9000 BTU/h (2.5 kW) to 24000 BTU/h (7.1 kW) and operate in Europe.

2 INPUT PARAMETERS

2.1 Reference outdoor temperature bins and reference hours for modes of air conditioners

Table 1 describes the reference temperature distributions for SEER and CSPF. Although SEER applies for temperate climates in Europe, the highest temp is 39°C. CSPF also represents for moderate climate, but the highest temperature is only 35°C. Each bin has a distinctive temperature range: for SEER, it gathers around 17 to 23°C with a total of 2602 hours while the other is from 24 to 28°C.

Table 1: Sample outdoor temperature used for calculation CSPF and SEER [4], [5].

t_j, °C		17	18	19	20	21	22	23	24	25	26	27	28	29
Hour	CSPF	-	-	-	-	100	139	165	196	210	215	210	181	150
	SEER	205	227	225	225	216	215	218	197	178	158	137	109	88

Table 1. (continue)

t_j, °C		30	31	32	33	34	35	36	37	38	39	Total
Hour	CSPF	120	75	35	11	6	4	-	-	-	-	1817
	SEER	63	39	31	24	17	13	9	4	3	1	2602

As mentioned earlier, the calculation of SEER includes the power consumption from all modes of the air conditioner. These reference hours are shown in Table 2 and depict how an air conditioner operates in a year.

Table 2: Reference hours used for SEER calculation [4].

	Modes	Number of hours	
		Cooling only	Reversible
A	Total hours per year	8760	8760
B	Off mode (H_{OFF})	5088	0
C	Hours for the reference cooling season (= A – B)	3672	3672
D	Thermostat off (H_{TO})	221	221
E	Standby (H_{SB})	2142	2142
F	Active mode hours without setback correction (= C – D – E)	1309	1309
G	Setback correction	355	355
H	Active mode hours corrected for setback impact (= F – G or F · 0,73)	954	954
I	Equivalent active hours (H_{CE})	350	350
K	Crankcase heater mode (H_{CK})	7760	2672

2.2 Equations and technical data of air conditioners

The British Standard Institution [4] and Vietnam National Standard [5] have described the calculations of SEER and CSPF, respectively. The CSPF is derived from:

$$\mathrm{CSPF} = \frac{\mathrm{L_{CST}}}{\mathrm{C_{CSE}}} \tag{1}$$

where: $\mathrm{L_{CST}}$ – Cooling seasonal total load, W·h or kW·h, is calculated by:

$$\mathrm{L_{CST}} = \sum_{j=1}^{m} \mathrm{L_c}(t_j) \cdot n_j + \sum_{j=m+1}^{n} \phi_{ful}(t_j) \cdot n_j \tag{2}$$

with $\mathrm{L_c}(t_j)$ – Cooling load at outdoor temperature t_j, W or kW; $\phi_{ful}(t_j)$ – Cooling full capacity at outdoor temperature t_j, W or kW;

and $\mathrm{C_{CSE}}$ – Cooling seasonal energy consumption, W·h or kW·h, is calculated by:

$$\mathrm{C_{CSE}} = \sum_{j=1}^{p} \frac{X(t_j) \cdot P_{haf}(t_j) \cdot n_j}{F_{PL}(t_j)} + \sum_{j=p+1}^{m} P_{hf}(t_j) \cdot n_j + \sum_{j=m+1}^{n} P_{ful}(t_j) \cdot n_j \tag{3}$$

where $X(t_j)$ – Ratio of cooling load and cooling capacity in half load operation; $P_{haf}(t_j)$ – Power input in half load operation at outdoor temperature t_j, W; $F_{PL}(t_j) = 1 - C_D[1 - X(t_j)]$ – Part load factor at outdoor temperature t_j; C_D – Degradation coefficient with a default value is 0.25; $P_{hf}(t_j)$ – Power input between half and full load operation, W or kW; $P_{ful}(t_j)$ – Power input in full load operation at outdoor temperature t_j, W or kW.

If the examination acquires minimum specifications:

$$\mathrm{C_{CSE}} = \sum_{j=1}^{k} \frac{X(t_j) \cdot P_{min}(t_j) \cdot n_j}{F_{PL}(t_j)} + \sum_{j=k+1}^{p} P_{mh}(t_j) \cdot n_j + \sum_{j=p+1}^{m} P_{hf}(t_j) \cdot n_j + \sum_{j=m+1}^{n} P_{ful}(t_j) \cdot n_j \tag{4}$$

with $X(t_j)$ – Ratio of cooling load and cooling capacity in minimum load operation; $P_{mh}(t_j)$ – Power input between minimum and half load operation, W or kW.

About SEER, it works out in Eq. (5) and Eq. (6):

$$\mathrm{SEER} = \frac{Q_C}{\frac{Q_C}{\mathrm{SEER_{on}}} + H_{TO} \cdot P_{TO} + H_{SB} \cdot P_{SB} + H_{CK} \cdot P_{CK} + H_{OFF} \cdot P_{OFF}} \tag{5}$$

$$\mathrm{SEER_{on}} = \frac{\sum_{j=1}^{n} h_j \cdot P_c(T_j)}{\sum_{j=1}^{n} h_j \cdot \left[\frac{P_c(T_j)}{\mathrm{EER_{PL}}(T_j)}\right]} \tag{6}$$

where $Q_C = P_{designc} \cdot H_{CE}$ – Reference annual cooling demand, kW·h; $P_{designc}$ – Cooling capacity at design temp 35°C; H_{CE} – Equivalent active hour; $\mathrm{SEER_{on}}$ – Seasonal energy efficiency ratio of active mode; P_{TO}, P_{SB}, P_{CK}, P_{OFF}: The power input during respectively thermostat-off mode, standby mode, crankcase heater mode and off mode correspond with the number of hours H_{TO}, H_{SB}, H_{CK}, H_{OFF}.

Most specifications of air conditioners come from the Eurovent Certification website with a total of 32 models. Table 3 shows performance data of air conditioners which have up to 12000 BTU/h (3.5 kW) cooling capacity. Cung [6] mentioned other data up to 24000 BTU/h (7.1 kW) cooling capacity air conditioners.

Table 3: Technical data of Inverter air conditioners for SEER.

Brand	No. 1S		No. 2S	No. 3S	No. 4S	No. 5S	No. 6S
Model	SB-13SJ	SB-13SK	SC-35TF	SD-14QS	SE-35ZX	SG-35XA	SG-35AX
$P_{designc,}$ kW	3.50	3.50	3.50	4.10	3.50	3.40	3.44

Technical data	Q_{30}, kW	2.58	2.58	2.60	2.77	2.58	2.51	2.34
	Q_{25}, kW	1.66	1.66	1.90	1.87	1.66	1.61	1.54
	Q_{20}, kW	1.00	0.90	1.80	1.41	1.28	1.33	1.36
	EER_{35}	3.89	4.38	4.61	3.23	4.49	4.37	3.30
	EER_{30}	7.85	7.27	7.50	5.20	7.20	6.28	5.14
	EER_{25}	10.60	11.22	11.70	8.74	12.40	10.58	8.57
	EER_{20}	12.65	12.00	16.30	15.95	16.60	16.21	12.70
	P_{off}, kW	0.001	0.001	0.001	0.009	0.004	0.001	0.002
	P_{sb}, kW	0.001	0.001	0.001	0.009	0.004	0.001	0.002
	P_{to}, kW	0.024	0.029	0.012	0.010	0.011	0.007	0.024
	SEER	**8.60**	**8.70**	**9.00**	**6.80**	**9.20**	**8.73**	**6.78**

Table 4. (continue)

Brand		No. 1S		No. 4S	No. 5S		No. 6S	
Model		SB-10SJ	SB-10SK	SE-25ZX	SF-20ZK	SF-25ZK	SG-25XA	SG-25AX
Technical data	$P_{designc,}$ kW	2.50	2.50	2.50	2.10	2.50	2.50	2.57
	Q_{30}, kW	1.84	1.84	1.84	1.60	1.86	1.84	1.78
	Q_{25}, kW	1.18	1.18	1.18	1.33	1.30	1.18	1.29
	Q_{20}, kW	0.90	1.24	1.25	1.33	1.38	1.29	1.35
	EER_{35}	4.63	4.63	5.68	4.56	4.90	4.46	3.30
	EER_{30}	7.85	8.03	8.65	7.25	7.59	6.79	5.47
	EER_{25}	10.85	11.00	12.50	10.38	12.05	10.35	8.96
	EER_{20}	12.70	13.30	17.30	13.85	17.01	16.30	11.70
	P_{off}, kW	0.001	0.001	0.004	0.001	0.001	0.001	0.002
	P_{sb}, kW	0.001	0.001	0.004	0.001	0.001	0.001	0.002
	P_{to}, kW	0.024	0.029	0.017	0.017	0.020	0.007	0.021
	SEER	**8.60**	**8.60**	**9.40**	**8.10**	**9.40**	**8.74**	**6.74**

2.3 Conversion between SEER and CSPF reference equivalent active hours

In SEER equations, the equivalent active hour (H_{CE}) is a crucial factor to determine power consumption and annual cooling demand. It is also a way to evaluate and compare the average cooling load of bin temperature. However, this parameter is established most by using simulations because there is no data in reality, and it depends on the type of building and climatic zones. European Commission has a review of Regulation 206/2012 which is the same as EN 14825:2012, and it is including an equivalent active hour's study for EN 14825 and other standards in [7]. Table 5 describes H_{CE} for some standards.

Table 5: Equivalent active hour of some energy efficiency standard [7].

Parameters	Standards		
	EN 14825:2012	AHRI 210/240	ISO 16358:2013
Average temp, °C	25.6	27.8	27.5
Average load, %	51	57	50
H_{CE}, hour	350	730	800

In section 3.2, the authors will discuss more the energy efficiency of some air conditioners that use SEER rating and how they would perform in ISO bin temperature based on H_{CE} for ISO 16358:2013. Because of the lack of detail time in other modes of ISO 16358-1:2013, the power consumption of those air

conditioners, by using equations from SEER, will apply temporarily the reference hours for other modes in Table 2.

3 RESULTS AND DISCUSSIONS

3.1 SEER and CSPF – Same core method but the difference in approaching directions

When the air conditioner was invented, the only tool to calculate energy efficiency was Energy Efficiency Ratio (EER). It is simple, but it also has a limitation: it calculates in a constant condition only, generally, it's at 35 °C outdoor temperature and 27 °C indoor temperature. Furthermore, when the inverter technology is adapted to control the compressor, EER is no longer suitable to illustrate energy efficiency because this technology can change power input to match the cooling capacity and the heat load of room (zone). On account of that, a new method needs to be applicable for all air conditioners and all operating situations, so SEER and CSPF exist to remove the limitation of EER.

SEER and CSPF have the same core methodology – the bin method, so they share some factors. The bin method calculates at cooling load at many temperatures and hypothesises the heat load of a comfortable zone that depends only on outdoor temperature while the indoor heat load is consistent. Moreover, there always exists a balance temperature point which has a net heat transfer equal to zero: in SEER of Europe, it is 16°C, and in CSPF of ISO, it is 20 °C. Another similar factor is the calculation power input which equals cooling loads divided by interpolation EER at matching temperatures. Finally, although the equations have different parameters, they still have the same energy efficiency calculation that divides the total cooling load by total power consumption in a year, nearly the same meaning as EER.

On the other hand, the distinctive approaches of these methods make their calculations different in complexity. SEER mandates testing air conditioners at four different outdoor temperatures: 20, 25, 30 and 35 °C for all types of air conditioners while the indoor temperature is constant at 27 °C as described in [4]. SEER closely links with the bin method to examine air conditioners operating at different temperatures, especially inverter air conditioners depending on control algorithms of control circuits. Therefore, it increases the accuracy of inspection energy efficiency and gives the policymakers and researchers specifically technical insights, it also provides data analysis reports that help manufacturers to enhance the product more efficiently. However, two set point outdoor temperatures, 20 and 25°C, are difficult to conduct in warm and hot climate countries such as Vietnam. Because testing facilities simulate environment (outdoor) temperature by using high-precision air conditioners, they consume large electricity to attain that required temp. Thus, it increases the cost of examination and leads to a price rise for a single air conditioner, which means air conditioners are harder to approach customers. Furthermore, at these outdoor temperatures, consumers usually choose other cooling solutions such as electric fans combined with opening the window to have natural ventilation which are simpler and save more energy than air conditioners, so those test points may not have much practical value in daily life.

Another difficulty of using SEER to evaluate the energy efficiency of air conditioners are identifying the reference hours and equivalent active hour (H_{CE}), especially H_{CE}. Before the EN 14825:2012 was approved and published in 2012, research had been conducted to specify the characteristics of building, climate and consumer behaviour in Europe from 2005 to 2009, described in P. Riviere et al. [8] and explained in ARMINES and V. Maagøe [7]. Then, from the data, they determined the reference hours and equivalent active hours for most European countries. H_{CE} is unique because only EN 14825 in Europe is using it, and the bin method does not mention this specification. In Vietnam, there is no related research which had been conducted or available data to establish these parameters. Because of that, it is not practical to use SEER in Vietnam to convert directly European bin temperature to more appropriate Vietnamese bin temperature.
Because of the above limitations in hot climates, ISO reduces the compulsory testing point to 35 °C only which is equivalent to full capacity for most air conditioners. Nonetheless, variable-speed air conditioners need more than one examination point to calculate exact energy efficiency, so ISO requires a half-capacity test at an outdoor temperature of 35 °C and leaves an option to check in minimum capacity. To have data at lower temps, these parameters interpolate with the standard value at the outdoor temperature of 29 °C as

it is shown in [5]. Because the number of tests reduced in half, this may help the performance audit in hot climates to be conducted more easily than the requirements in EN 14825, so the government and manufacturers would cost less for the inspections than EN 14825, and consumers are going to have a more affordable price for air conditioners. However, it leads to other problems: one, intermediate parameters exist between air conditioner modes and two, it could decrease the test accuracy. In Eq. (3), $P_{hf}(t_j)$ is an intermediate parameter, but in [5], the control level of the air conditioner is more complicated, more parameters participate in the calculation process and appear in final equations, especially in variable-speed air conditioners that have minimum specifications as in Eq. (4). Therefore, they make the calculation more difficult than SEER noticeably.

3.2 SEER of air conditioners in ISO bin temperature

With distinctive test procedures, calculations and reference temperature bins as discussed above, if an air conditioner which evaluated through EN 14825:2012 is reassessed based on ISO 16358-1:2013, the CSPF value is not the same as SEER. Because of that, policymakers usually conduct inspections to import air conditioners and make sure they meet requirements of regional MEPS, it also means the governments and manufacturers would cost a significant budget for the re-examination of energy efficiency leading to an increase in the price of those air conditioners. Park et al. [9] have established convert equations between some energy efficiency metrics based on large air conditioner technical databases from various regions, including EU SEER and ISO CSPF. With much sample data, the accuracy of those equations is high and trusted enough to be an extremely useful tool for researchers and policymakers to switch between energy efficiency metrics, and it could reduce the number of tests for import air conditioners and save a considerable amount of money for the governments and manufacturers.

However, there is another way to compare EU SEER and ISO CSPF: Using ISO bin temperature to calculate SEER. As mentioned in 2.3**Error! Reference source not found.**, ARMINES and V. Maagøe [7] analysed H_{CE} for some energy standards, including ISO 16358-1:2013 and EN 14825:2012. H_{CE} is a critical factor in calculating SEER, so SEER based on ISO bin temperature can be established. The only limitation of this computation is the reference hours of non-active mode for ISO such as Thermostat-off, Standby and Off mode. Although ISO 16358-1:2013 described these reference hours in Total Cooling Seasonal Performance Factor (TCSPF) or Appendix B [5] which is rarely used on air conditioners, these reference hours are not calculated in detail as EN 14825:2012. Because of that, the reference hours from EU SEER in Table 2 are temporarily used for the calculation of SEER with ISO bin temperature. SEERs of up to 12000 BTU/h (3.5 kW) cooling capacity air conditioners by two different bins are depicted in Figure 3.

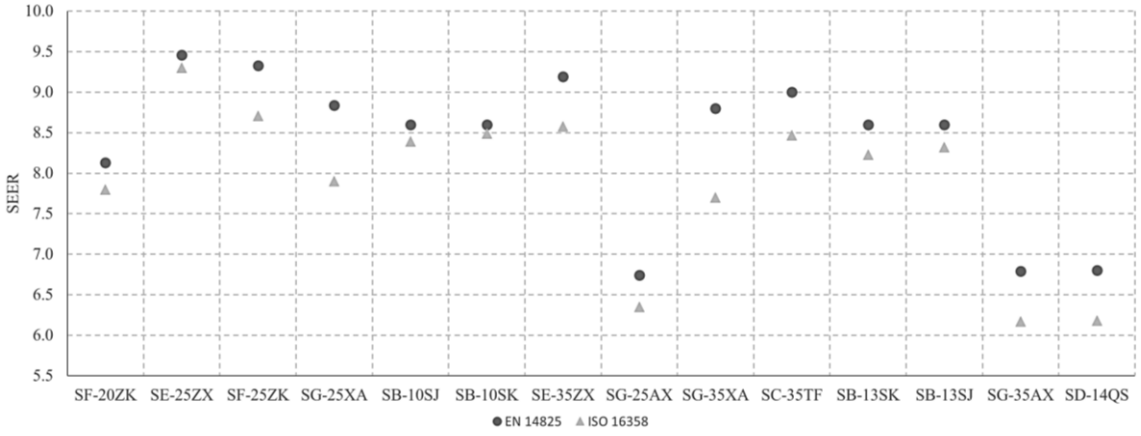

Figure 3: SEERs of up to 3.5 kW cooling capacity air conditioners by different bins.

The energy efficiency of these models in ISO 16358 dropped off markedly in the range from 1.28% to 12.50%, with the highest belonging to SG-35XA and the smallest being SB-10SK. Additionally, the average decrease of SEER is 5.95% which is a noticeable decline for air conditioners. Next, the power consumption of 3.5 kW air conditioners in ISO bin temp rocketed up more than double the power consumption in Europe. Figure 4 illustrates these results in detail.

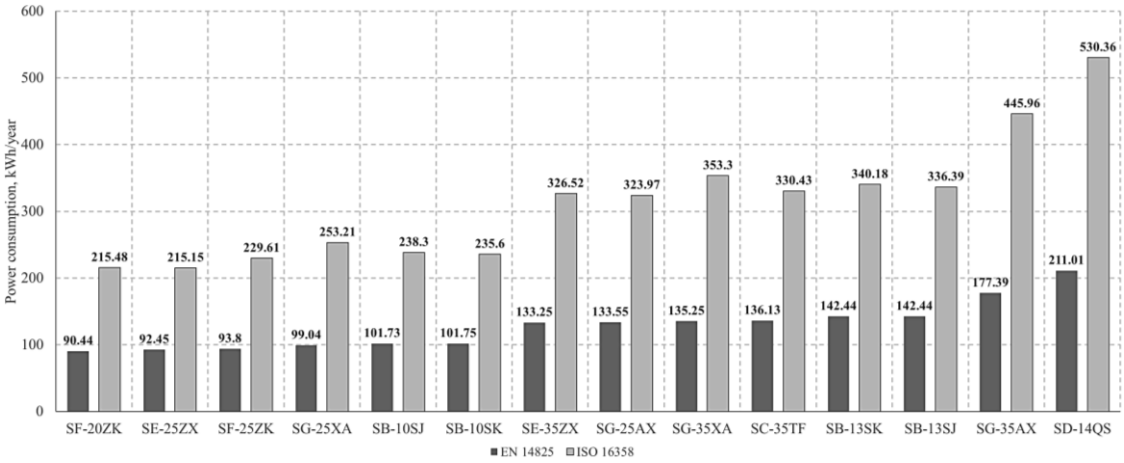

Figure 4: Power consumption of up to 3.5 kW cooling capacity air conditioners by different bins.

One of the reasons is ISO bin temp has more hours at higher temperatures than EN 14825, thus, it raises power consumption and decreases $SEER_{on}$. Another reason is the active hour of EN 14825 lower than ISO 16358. In Table 2, the numbers of active hours without and with setback correction are 1309 and 954, respectively. These numbers are not the same as the total hour of bin temperature in EN 14825 while the active hour in ISO 16358 equals the total hour in its bin. Therefore, the equivalent active hour in EN 14825 only has 350 hours while ISO 16358 has 800 hours. In Eq. (5), Q_C depends on H_{CE} and affects the calculation of power consumption, hence, power consumption with conditions of ISO 16358 increase at least 2.28 times compare to EN 14825. However, these results for ISO are not accurate 100% and may change because the calculation temporarily uses reference hours in Table 2. Detail reference hours at other modes for ISO 16358 need more time to study to have more precise results.

4 CONCLUSIONS

The paper has conducted the analysis and comparison of energy efficiency assessment methods for inverter air conditioners based on the bin method. This work also studied the change in energy efficiency and power consumption of air conditioners when they operate in conditions of ISO 16358:2013. The similarities of both methods are from the bin method, but the differences in approaching this method affect substantially experiment conditions and equations. In conditions of ISO 16358, air conditioners declined in SEER and rose power consumption considerably compare to the original calculation EN 14825 because of the change of bin temperature and equivalent active hour. Although reference hours at other modes were used temporarily from EN 14825, the results still give the overview about the distinction between these methods to evaluate energy efficiency and power consumption of variable-speed air conditioners from European Standard and ISO.

REFERENCES

[1] C. Delmastro, T. Abergel, K. Lane and Y. Monschauer, "Cooling - Analysis - IEA," November 2021. [Online]. Available: https://www.iea.org/reports/cooling.

[2] T. T. newspaper, "Vietnam's air conditioner market, which is valued at about 2.4 billion, has a new domestic competitor," 2022. [Online]. Available: https://tuoitre.vn/thi-truong-dieu-hoa-viet-2-4-ti-usd-co-them-tan-binh-noi-dia-20220107174412427.htm.

[3] CLASP and E. a. E. I. , "Vietnam Room Air Conditioner Market Assessment and Policy Options Analysis," 2019.

[4] T. B. S. Institution, British Standard, Air conditioners, liquid chilling packages and heat pumps, with electrically driver compressors, for space heating and cooling - Testing and rating at part load conditions and calculation of seasonal performance, BS EN 14825:2012, 2012.

[5] "National Standard TCVN 10273-1:2013 (ISO 16358-1:2013), Air-cooled air conditioners and air-to-air heat pumps - Testing and calculating method for seasonal performance factor - Part 1: Cooling seasonal performance factor," Hanoi, 2013.

[6] D. H. Cung, Analysis and comparison of energy efficiency assessment methods for household inverter air conditioners in Vietnam based on bin method, Master Thesis, Hanoi, 2023.

[7] A. and V. Maagøe, "Review of Regulation 206/2012 and 626/2011 Air conditioners and comfort fans - Task 3 Users," 2018. [Online]. Available: https://www.eceee.org/ecodesign/products/airco-ventilation/.

[8] P. Riviere et al, "Preparatory study on the environmental performance of residential room conditioning appliances (airco and ventilation) - Final report of Task 4, TECHNICAL ANALYSIS OF EXISTING PRODUCTS," 2009. [Online]. Available: https://www.eup-network.de/product-groups/preparatory-studies/completed/ & https://www.eceee.org/ecodesign/products/airco-ventilation/.

[9] W. Y. Park, N. Shah, J. Y. Choi, H. J. Kang, D. H. Kim and A. Phadke, "Lost in translation: Overcoming divergent seasonal performance metrics to strengthen air conditioner energy-efficiency policies," *Energy for Sustainable Development*, no. 55, pp. 56-68, 2020.

DESIGN AND FABRICATION OF A 4-AXIS FDM 3D PRINTER

BINH-NGUYEN TRAN [1*] , NHAT-KHIEM TRAN [1*], BA-HUY NGUYEN [1*], NGOC CAM TIEN TRINH [1*], NGOC KIM NGA NGUYEN [1*], NGOC DANG KHOA TRAN [1], TRIEU KHOA NGUYEN [1**]

[1]*Faculty of Mechanical Engineering, Industrial University of Ho Chi Minh City;*
[*]*First author,* [**]*Corresponding author*
[*]*congtusoyeu@gmail.com, tranngocdangkhoa@iuh.edu.vn,* [**]*nguyenkhoatrieu@iuh.edu.vn*

Abstract: Although 3D printing technology was established early (around 1980), its application in the manufacturing industry (rapid prototyping, food, fashion, molten casting, ...) was only developed and become popular recently. And it can be classified as a special (non-traditional) processing technology. Currently, in Vietnam, 3D printing technology is developing rapidly and is applied in many different industries such as mechanics, interior decoration, medicine, biology, fashion, etc. However, the research and manufacturing of types of equipment that use 3D printing technology have not yet been invested in to meet actual needs. Therefore, a 4-axis 3D printer based on the structure of a CNC machine has been proposed to solve the above needs. This paper presents the results of developing, designing, and manufacturing a 4-axis 3D printer. With the 360-degree rotating A-axis, it is possible to print complex structural parts without the use of supporting structures. The device applies Slic3r software to control the 3D printing process of complex structural details that need to limit the amount of support to ensure the surface's aesthetics and minimize the product's post-processing after printing. In addition, the 4-axis 3D printer can be utilized for the teaching, research, and learning of lecturers and students.

Keywords: 3D printing, FDM, 4-axis, supporting structure, Slic3r, A-axis.

1 INTRODUCTION

3D printers using the fused deposition modeling (FDM) method are usually based on a three-linear axis mechanism [1]. However, due to the limited location of the workpiece, the shape of the model that can be created using this type of 3D printer is limited [2]. 3D printers create 3D models by stacking materials in one layer. Due to this principle, a base is required to support the laminate, and it is impossible to develop model shapes with overhangs without support components. While making a foundation out of base material can solve the problem, shaping and removing the material takes time. Therefore, this traditional method is very time-consuming [3]. Therefore, printers as well as 4D and 5D printing algorithms have been developed to overcome these disadvantages [4]. Some authors have researched 4D and 5D printers to take advantage of their advantage of not needing a support structure [4-6]. While many authors present the process of developing traditional 3D printers [7, 8], 4 and 5D printers have only been researched mainly on algorithms [9]. Therefore, there is a need for research on low-cost, easy-to-develop 4D printers.

Hence, a new three-axis 3D printer was developed using the FDM method and its control program was designed. In addition, the hardware consisting of the mechanical structure and servo control system was developed, and the lamination path that can exert the effect of the four-axis mechanism was calculated. The shape of the workpiece can be controlled by installing an A-axis tilt angle of 45 degrees, which allows the A-axis to rotate 180 degrees in the Z direction, adding to a three-axis configuration 3D printer. In addition, a 4-axis synchronous control program has been developed to control the 4-axis synchronous motion. The machining time of the 4-axis-controlled 3D printers was shorter than that of conventional 3-axis-controlled 3D printers.

2 MATERIALS AND METHODS

2.1 FDM 3D printing technique

FDM technology was developed in the late 1980s and commercialized in the early 1990s [10]. This technology has many advantages, including non-toxic materials, unlimited geometric complexity, and with

a wide range of materials, short operating cycle, easy material change, low printing temperature, small equipment size and low maintenance costs. In the conventional FDM process, the plastic filament is melted and extruded through the nozzle by following the cross-section of each layer of the product [11]. Therefore, the product consists of multiple layers of filaments combined. Hence, the final printed product is formed by a matrix of filaments except for the peripheral sheath. And the product can also be a porous model.

2.2 PLA materials

PLA plastic is the abbreviation for "Polylactic Acid". This is a biodegradable thermoplastic derived from renewable sources [12]. The composition of this plastic includes many additives such as cornstarch, sugarcane, cassava roots, or even potato starch. PLA printing resin is one of the popular FDM 3D printing resins on the market. This type of plastic is quite low-cost, easy to print, and comes in many vibrant colors. PLA has many outstanding advantages over other online petrochemical plastic products such as ABS (Acrylonitrile butadiene styrene) or PVA (Polyvinyl Alcohol). With the ability to self-decompose in the environment. PLA is widely used to produce everyday items. Products such as food packaging, trays or cups, food film, and so on.

3 RESULTS AND DISCUSSION

3.1 Calculation and Design of the A-axis

The print head assembly is optimized to a 360 rotation axis on the XOZ coordinate system, so we consider the print head to be a robot system with 1 Oz rotation and 2 Oz, Ox translation steps as shown in Figure 1 [3, 13].

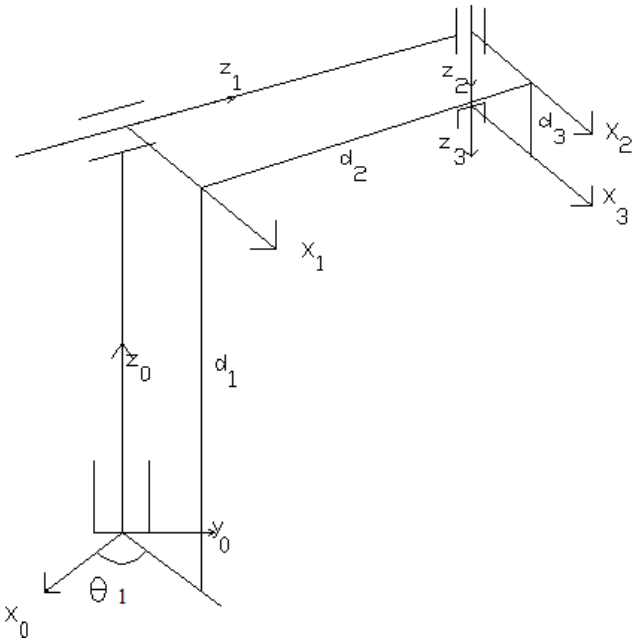

Figure 1: A-axis printhead principle diagram.

- **PROJECT KINEMATIC PROBLEM**

  Matrix representing the position and orientation of the links with respect to the fixed coordinate system O [14]:

$$ {}^{0}A_3 = {}^{0}A_1 . {}^{1}A_2 . {}^{2}A_3 = \begin{bmatrix} \cos(\theta_1) & \sin(\theta_1) & 0 & -d_2 \sin(\theta_1) \\ \sin(\theta_1) & -\cos(\theta_1) & 0 & d_2 \cos(\theta_1) \\ 0 & 0 & -1 & d_1 - d_3 \\ 0 & 0 & 0 & 1 \end{bmatrix} \quad (1) $$

  The matrix representing the direction of the operation:

$$ {}^{0}R_3 = \begin{bmatrix} \cos(\theta_1) & \sin(\theta_1) & 0 \\ \sin(\theta_1) & -\cos(\theta_1) & 0 \\ 0 & 0 & -1 \end{bmatrix} \tag{2} $$

Matrix representing the position of the end impact point:

$$ {}^{0}r_E = \begin{bmatrix} -d_2.\sin(\theta_1) \\ d_2.\cos(\theta_1) \\ d_1 - d_3 \end{bmatrix} = \begin{bmatrix} -216.\sin(\frac{\Pi}{5} + \frac{\Pi}{10}.t).t \\ 216.\sin(\frac{\Pi}{5} + \frac{\Pi}{10}.t).t \\ 1000 - 40.t \end{bmatrix} \tag{3} $$

Angle speed of manipulator:

$$ V_E = \begin{bmatrix} -\cos(\theta_1).d_2.\dot{\theta}_1 - \sin(\theta_1)\dot{d}_2 \\ -\sin(\theta_1).d_2.\dot{\theta}_1 + \cos(\theta_1)\dot{d}_2 \\ -\dot{d}_3 \end{bmatrix} = \begin{bmatrix} -\cos(\frac{\Pi}{5} + \frac{\Pi}{10}.t).216.7\,t.\frac{\Pi}{10} - \sin(\frac{\Pi}{5} + \frac{\Pi}{10}.t)216.7 \\ -\sin(\frac{\Pi}{5} + \frac{\Pi}{10}.t).216.7\,t.\frac{\Pi}{10} + \cos(\frac{\Pi}{5} + \frac{\Pi}{10}.t)216.7 \\ -40 \end{bmatrix} \tag{4} $$

Acceleration of the end point of impact [15]:

$$ a_E = \begin{bmatrix} \sin(\theta_1).d_2.\dot{\theta}_1^{\,2} - \cos(\theta_1).d_2.\ddot{\theta}_1 - 2\cos(\theta_1)\dot{\theta}_1\dot{d}_2 - \sin(\theta_1)\ddot{d}_2 \\ -\cos(\theta_1).d_2.\dot{\theta}_1^{\,2} - \sin(\theta_1).d_2.\ddot{\theta}_1 - 2\sin(\theta_1)\dot{\theta}_1\dot{d}_2 + \cos(\theta_1)\ddot{d}_2 \\ -\ddot{d}_3 \end{bmatrix} \tag{5} $$

Angular velocity of the links:

$$ {}^{0}\omega_1 = {}^{0}\omega_2 = {}^{0}\omega_3 = \begin{bmatrix} 0 \\ 0 \\ \frac{\Pi}{10} \end{bmatrix} \tag{6} $$

- **BUILDING ORIGINAL MOVEMENT**

Simulate the manipulation space on MAPLE 17, the results were shown in Figure 2.

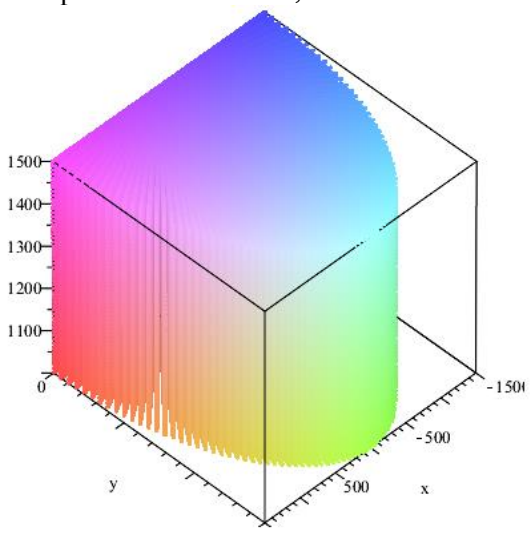

Figure 2: The manipulation space on MAPLE 17.

Simulate impact the end point, the results were shown in Figures 3 and 4.

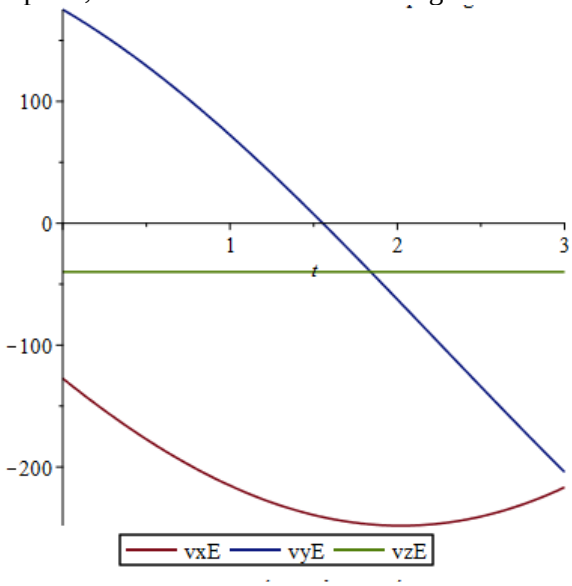

Figure 3: The velocity of the endpoint E.

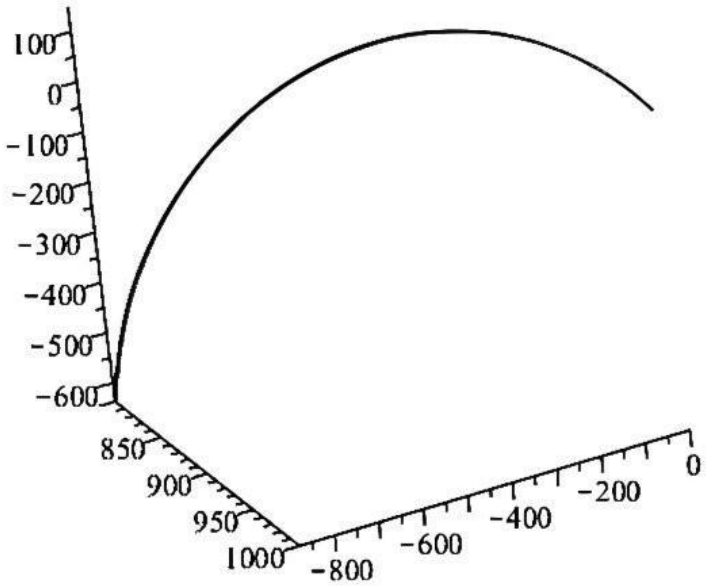

Figure 4: The trajectory of the endpoint E.

3.2 The Design of the Machine

- OBJECTIVE:

The main objective of our project is to design and fabricate a working model of a 4-axis FDM 3D Printer along with that we have perform some calculations on how to select the printhead tilt angle and analyze the amount of flow to optimize the surface of the workpiece when put into printing with a 4-axis 3D printer incorporating a Cartesian coordinate system with 2 translational degrees of freedom and 1 degree of freedom of rotation.

- NX MODELLING:

NX software was utilized to design a solid model as shown in Figures 5 and 6.

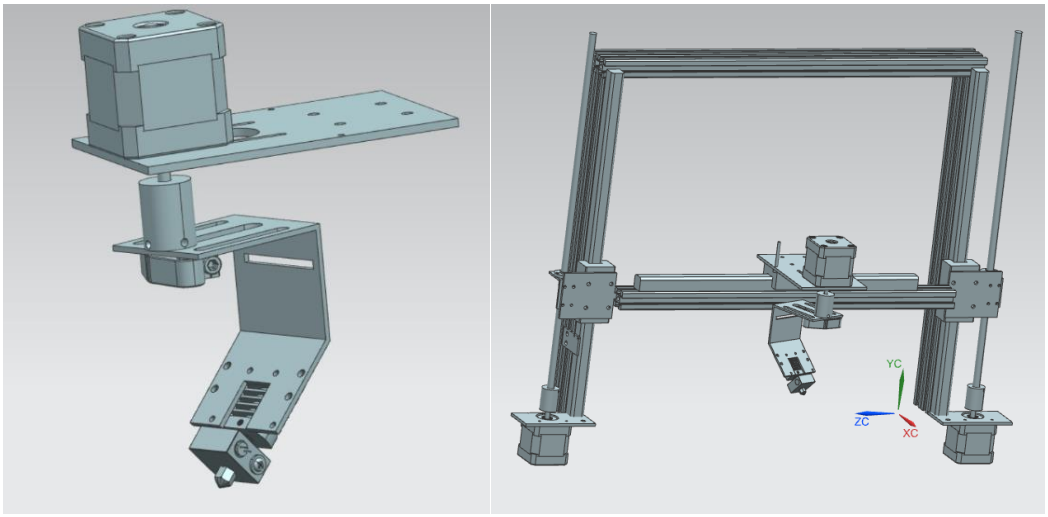

Figure 5: The model of the A-axis and the frame.

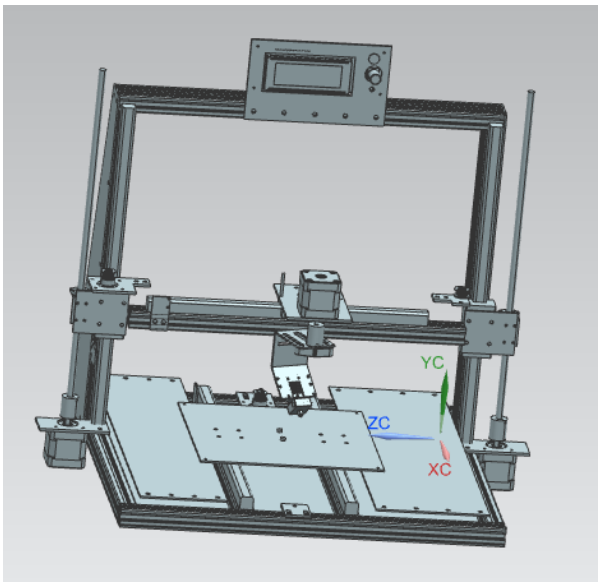

Figure 6: The model of the 4-axis printing machine.

3.3 Fabrication and Testing

The fabrication and testing process basically includes the following steps:

a/ Chassis installation: The chassis is made of 2020 EU Black aluminum. The four main axes include 3 moving axes X, Y, and Z of the nozzle and 1 rotating axis of the print head.

b/ Installing moving parts: Stepper motor, stepper motor mounting part, and belt for the X, Y, and Z axes to create translational motion, and the stepper motor of the print head creates a 360-degree rotation.

c/ Installing the electrical system: Wires, cables, switches, sensors, control circuits, power.

d/ Code loading: Arduino IDE and Visual Code are software for writing code and loading code into the control circuit.

e/ Hardware installation: Thermal nozzle, heat bed, fiber plastic extruder.

f/ Support software: Ultimate Cura and Slic3r are the control and slicing software for the machine. NX, Solid Works, and AutoCAD are 3D and 2D design software for details that form printers and printed products.

g/ Test print and evaluate printed samples.

The printer was fabricated and assembled as shown in Figure 7. The printer uses 5 stepper motors for the machine's 4D and 1 stepper motor for plastic extrusion. In particular, 2 stepper motors ensure that the print head moves up and down along the z-axis. The printing bed size is 210×210 without a heating device. Figure 8 shows the printer during test printing. The device can print special products without the need for a support structure.

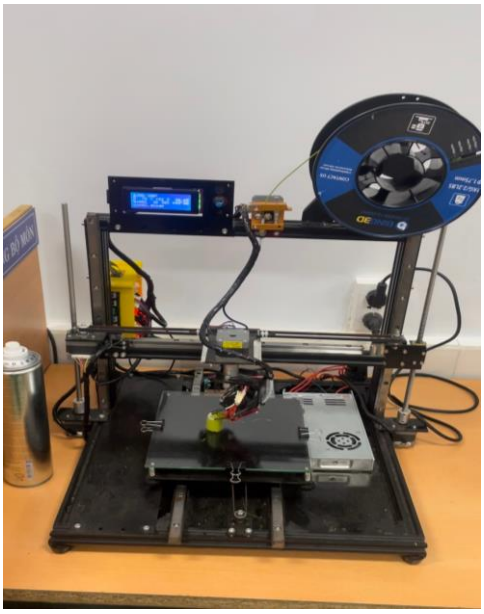

Figure 7: FDM 4 – Axis 3D printer.

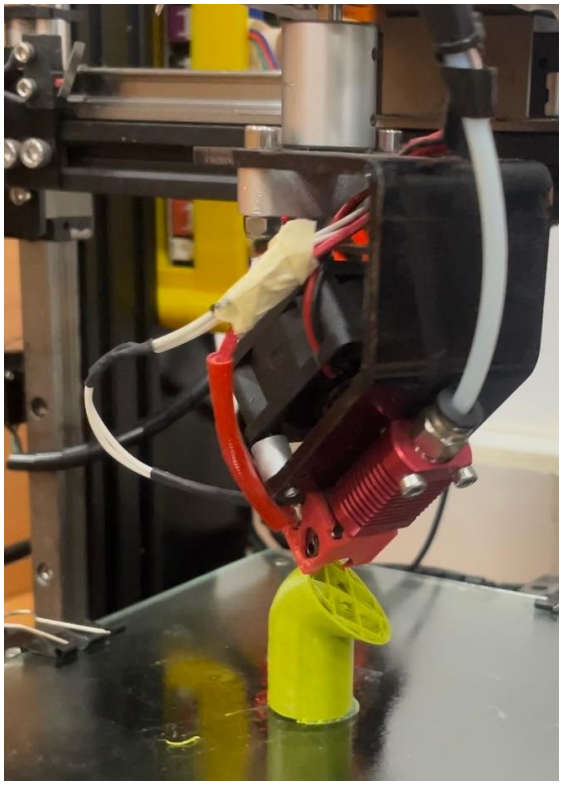

Figure 8: The FDM 4 – Axis 3D printer in testing.

4 CONCLUSION

In this study, a 4D printer was successfully designed, manufactured, and tested. First, research projects around the world on the process of building 3-4 D printers were compiled and analyzed. From the advantages and disadvantages of existing machines, a suitable 4D printer diagram was designed using NX. With the 360-degree rotating A-axis, the current device is capable of printing complex structural parts without the use of supporting structures. The kinematic equations of the A-axis were also calculated using Maple 17 to ensure that its rotation angle could be controlled using the Slic3r 3D printer control slicer software. With a low cost (about 5 million VND) and simple structure, this research project promises to provide the ability for users to build their own 4D printers and progress to 5D. Therefore, this work may contribute to the further development of the additive manufacturing industry in Vietnam.

ACKNOWLEDGMENT

This study was carried out with the support of the Faculty of Mechanical Engineering, Industrial University of Ho Chi Minh City.

REFERENCES

[1] E. Shi, L. Lou, L. Warburton, and B. Rubinsky, 3D Printing in Combined Cartesian and Curvilinear Coordinates, Journal of Medical Devices, vol. 16, 2022.

[2] J. Savaliya, K. Gosai, A. Sidapara, H. Parikh, B. Pithadiya, and H. Pandya, 3D Printer Movement Modelling Through Denavit–Hartenberg Theory and RoboAnalyzer, ed, 2022, pp. 355-371.

[3] T. Li, J. Li, X. Ding, X. Sun, and T. Wu, An error identification and compensation method for Cartesian 3D printer based on specially designed test artifact, The International Journal of Advanced Manufacturing Technology, vol. 125, pp. 1-15, 2023.

[4] M. Wüthrich, W. J. Elspass, P. Bos, and S. Holdener, Novel 4-Axis 3D Printing Process to Print Overhangs Without Support Material, in Industrializing Additive Manufacturing, pp. 130-145, 2021.

[5] F. Hong, S. Hodges, C. Myant, and D. Boyle, Open5x: Accessible 5-axis 3D printing and conformal slicing, 2022.

[6] B. Ramos, D. Pinho, D. Martins, I. Vaz, and L. Vicente, Optimal 3D printing of complex objects in a 5–axis printer, Optimization and Engineering, vol. 23, pp. 1-32, 2022.

[7] A. Gupta, G. Gupta, H. Srivastava, and E. Yadav, DESIGN AND FABRICATION OF 3D PRINTER, International Journal of Engineering Applied Sciences and Technology, vol. 6, 2021.

[8] K. Gomathi, K. R. Arangamuthalvan, S. Deepigkashri, C. B. Dharnieshwaran, S. Dhivya, and C. Praveen, Design and Fabrication of Low Cost 3D Printer, IOP Conference Series: Materials Science and Engineering, vol. 1055, p. 012036, 2021.

[9] K. Kawagishi, S. Umetani, K. Tanaka, E. Ametani, Y. Morimoto, and K. Takasugi, Development of Four-Axis 3D Printer with Fused Deposition Modeling Technology, International Journal of Automation Technology, vol. 11, pp. 278-286, 2017.

[10] T. T. Huynh, T. V. T. Nguyen, Q. M. Nguyen, and T. K. Nguyen, Minimizing Warpage for Macro-Size Fused Deposition Modeling Parts, Computers, Materials \& Continua, vol. 68, 2021.

[11] T. K. Nguyen, K. Chau Duc, and A.-D. Pham, Characterization of an FDM-3D Printed Moldcore in a Thermoforming Process Using Taguchi in Conjunction with Lumped-Capacitance Method, Arabian Journal for Science and Engineering, vol. 48, pp. 11989-12000, 2023.

[12] L. Auffray, P.-A. Gouge, and L. Hattali, Design of experiment analysis on tensile properties of PLA samples produced by fused filament fabrication, The International Journal of Advanced Manufacturing Technology, vol. 118, pp. 4123-4137, 2022.

[13] D. Plakhotnik, Y. Murtezaoglu, M. Lachmuth, M. Stautner, and T. Vaneker, Quality Implications of Applying 3+2 Axis Toolpaths in 3D Printing, 2021.

[14] S. Keaveney, P. Connolly, and E. D. O'Cearbhaill, Kinematic error modeling and error compensation of desktop 3D printer, Nanotechnology and Precision Engineering, vol. 1, pp. 180-186, 2018.

[15] A. R. Avdeev, A. A. Shvets, and I. S. Torubarov, Investigation of Kinematics of 3D Printer Print Head Moving Systems, in Proceedings of the 5th International Conference on Industrial Engineering (ICIE 2019), Cham, 2020, pp. 461-471.

RESEARCH AND DESIGN A ROSE HARVESTING ROBOT BASED ON IMAGE PROCESS

NGOC DANG KHOA TRAN [1]

[1] *Faculty of Mechanical Engineering, Industrial University of Ho Chi Minh City; tranngocdangkhoa@iuh.edu.vn*

Abstract. Rose is a flower with high economic value, especially in high-tech agriculture in Vietnam. However, the harvesting of roses in gardeners is still using human resources, leading to low yield and low quality. Therefore, applying technology in harvesting roses is an urgent need in florists. This paper presents the design and operation of an automatic rose harvesting robot. The robot employed image processing techniques to identify roses and control the manipulators to the respective flower locations to accurately perform the cutting and harvesting process and ensure flower quality. A prototype robot was built and operated. The robot can detect red roses and locate the position according to the xy coordinates, and the robot arm is responsible for picking and cutting the roses. Then transport the rose to the container and repeat the process. This robot is expected to save human labor. It can be integrated into different systems to create a 4.0 high-tech agricultural ecosystem.

Keywords. Rose, harvesting, image processing, control system.

1 INTRODUCTION

The Industrial Revolution 4.0 has profoundly affected the agriculture and floriculture industry. In order to satisfy the growing market demand, automation machines are applied to increase productivity and product quality while saving labor costs [1]. In particular, the rose is a high value flower that symbolizes luxury beauty. For that reason, roses are chosen by many people to decorate their homes or give to their loved ones on important days. Harvesting roses at large farms requires large human resources and expensive costs, so applying high technologies in rose harvesting is a practical necessity today.

Robots are applied in harvesting flowers and different agricultural products [2]. A simple flower-harvesting robot model was presented by VinothKumar et al. [3], a robotic arm responsible for harvesting flowers and a camera capable of detecting 80% of the experimental flowers. Rath and Kawollek [4] designed a robot for harvesting Gerbera Jamesonii. The robot includes a 6-DOF arm and a linear belt to transport the tree to the robot arm. An algorithm was developed for the robot to detect flowers based on the image, transmit the position to the robot arm, and perform flower cutting. A real-time flower harvesting robot was introduced by Bhaskar et al. [5]. Robots help increase flower harvest productivity and limit direct human involvement. Robots that move automatically in flower fields can detect pests, spray pesticides, and harvest flowers. The control process combines image processing, IOT to distinguish flowers, and a Raspberry Pi microprocessor to help manipulate and operate the robot. Zhang et al. [6] developed a robot that can pick safflower with ant colony algorithm. The actuator utilizes two rollers to collect flowers. The image processing technique is applied to harvest flower size parameters in space, and the optimal algorithm controls the robot arm to collect flowers.

Besides, Roses are flowers of different sizes that do not follow specific rules. Therefore, the types of robots that serve to harvest roses have specific characteristics. Gurel et al. [7] developed an algorithm to locate suitable roses for stem cutting. The algorithm investigates the size of the flower stem and the branch points to apply the optimal method and select suitable cutting positions for roses while still ensuring flower quality. A simple rose harvesting robot introduced by Abarna and Selvakumar [8], the robot is composed of a 2-DOF robotic arm and works on an automated guided vehicle body, color detection sensor, and the profile is used to define the flower. Manikanta et al. [9] simulated an autonomous robot that detect blossomed rose with a Gaussian Naïve Bayes algorithm with high accuracy to catch the rose. Raspberry Pi is also

implemented to detect roses during harvesting [10]. The system includes many boards and drivers that improve the capture of objects with high precision. A 4-DOF robot is employed to collect roses, as demonstrated by Kohan et al. [11]. The stereo vision techniques indicate the flower's position and send the signal to the control unit. The successful harvesting flower of the robot is higher than the other. However, most of the research on rose harvesting robots is only at the experimental level, not in practical applications, so many environmental factors have not been researched and verified.

In this study, a robot model for rose harvesting was developed with cutting and picking mechanisms that ensure high product quality. The control system uses image processing to help predict the position and distance of the flowers and, from there, to give the execution command of the actuator. Practical experiments help determine the exact position and operating time of the robot.

2 MECHANICAL DESIGN

The robot structure consists of a stationary frame; flowers are placed inside the frame, and the camera is placed on top of the robot. The camera is responsible for taking pictures and transmitting signals to the control unit, from which the control unit will analyze and determine the coordinates of each flower. After that, the flower harvesting mechanism works. The mechanism, including the manipulator, moves forward in two X and Y axes. When the appropriate position coordinates are reached, the Z-axis moving mechanism will operate, the flower tube covers the flower stem, and the cutting mechanism will separate the flower and the stem. The flower will be kept in the flower tube and moved to the original coordinate. To harvest flowers and keep moving to new locations to harvest flowers. Figure 1 shows the structure of the robot and its components. The coordinate system is also shown in the figure.

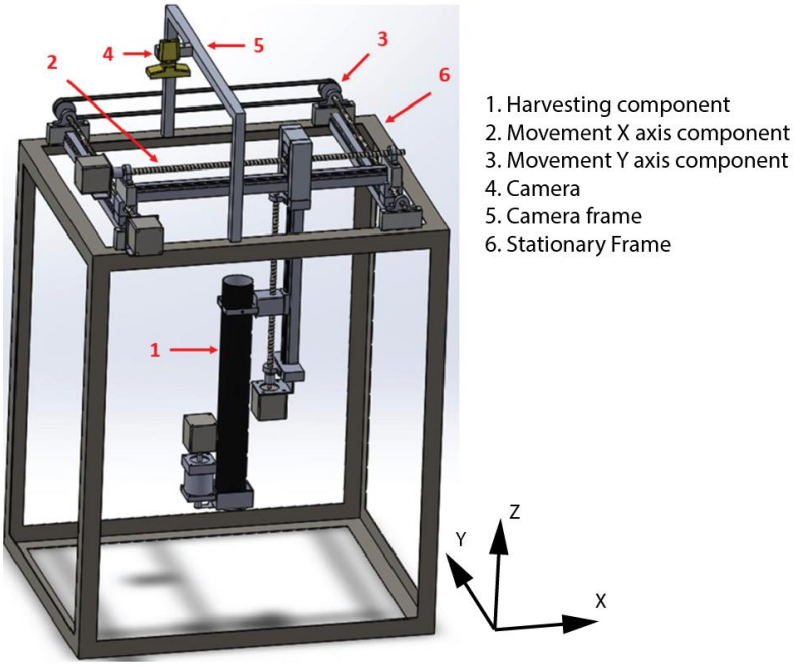

Figure 1: Components of rose harvesting robot.

Figure 2 depicts the details of the harvester. After determining the position of the flower and the robot arm moving in two x and y axes, the Z-axis motor works to move along the axis. The flower tube will insert the flower into the appropriate position, the cutting motor will work and cut the stem, the flower will be kept in the flower tube and moved up for flower transportation and storage. The cutting force of the knife is determined at the value of 117 N. This value is obtained after the actual flower stem cutting force evaluation tests. Using the loadcell, the cutting force is determined and used in the design of the robot cutter.

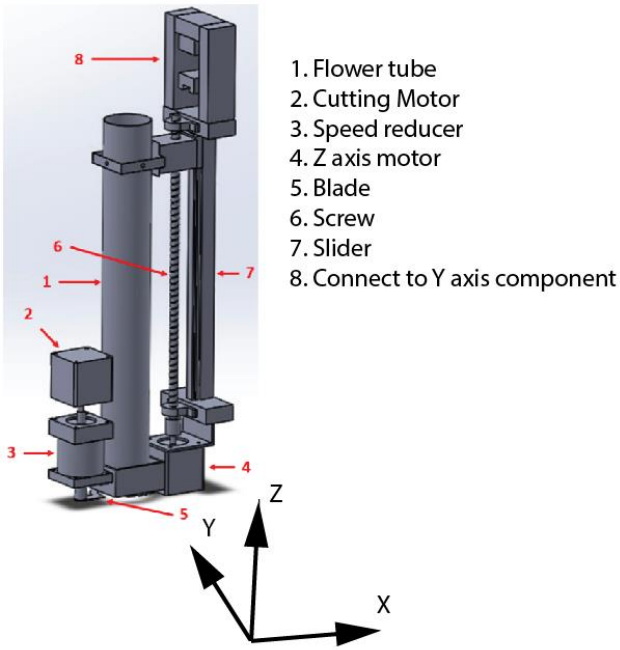

Figure 2: The details of harvesting component.

3 CONTROL SYSTEM

Based on the robot's mechanical model, the control system's components are presented in Figure 3. The central control block is responsible for receiving signals from push buttons, encoders, and processing data. The Arduino UNO R3 was applied to build the control unit. DC servo motors are used to control the X, Y and Z axis of the robot arm. Image processing and thereby provide implementations for axes motors. The motors perform the movement function monitored by encoders for precise feedback and position control. The cutting motor that drives the flower stem cutter is adopted as a stepper motor.

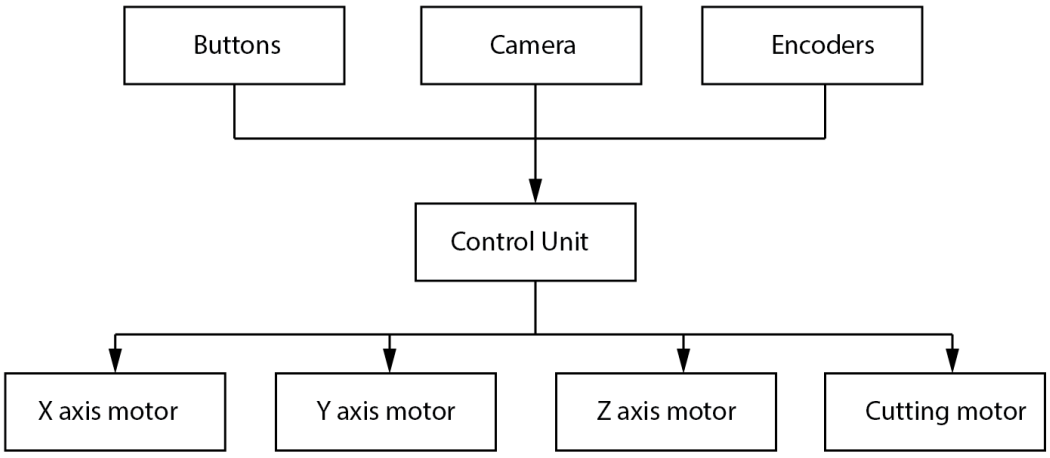

Figure 3: Basic components of the control system of rose harvesting robot.

The camera will capture the image from above, allowing to determine the position of the flower on the XY plane. Matlab software is used for image analysis and processing. Roses are mainly red, so the image is processed to filter white light so that the image only has the primary redRGB colors. Next, the image is red filtered, converted to grayscale, and brightness increases. In the final step, the image is converted to black and white, from which to export to pixels and determine the coordinates of the position of the flower. These coordinates will be included in the control unit for the calculation and execution of the manipulator. Figure 4a shows the original image acquired by the camera, and Figure 4b shows the detected flower coordinates in pixels. Through it, the computer catches the position of four red roses.

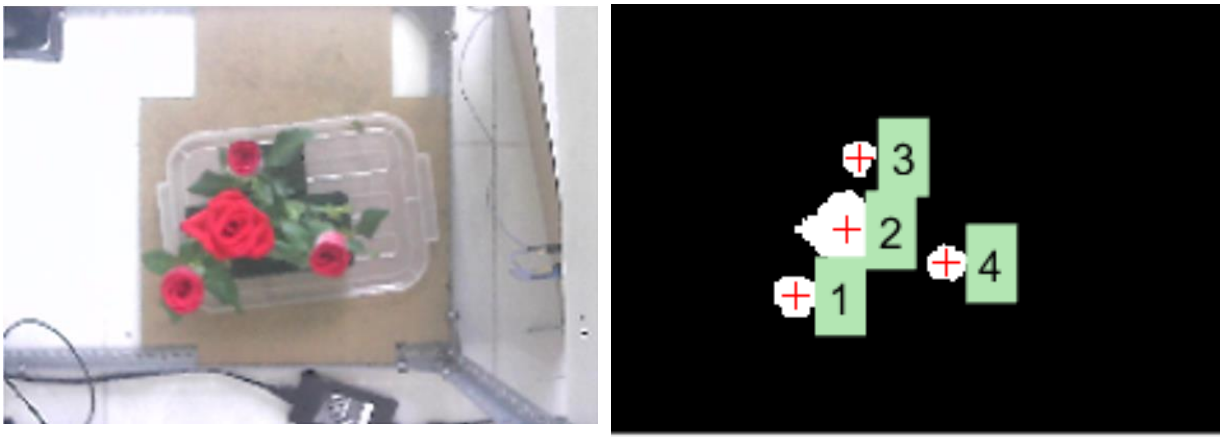

a) **b)**

Figure 4: Image processing of robot. a) Original image capture by camera, b) Image with coordinate of flower.

The camera is located at the center of the work area, and the flowers are distributed throughout the work area. As a result, the actual coordinates of the flower will be deviated. An experiment was carried out to correct this deviation and found the relationship between the parameters. D is the distance from the camera to the background, d is the height of the rose, L is the distance from the camera's center to the center of the rose in the image, and l is the distance of the rose. Figure 5 presents the distance and the parameters. D is a constant value.

After many experiments with the above parameters. The equation for the coordinate position on the computer follows:

$$l = L - (L * 0{,}44) \quad (1)$$

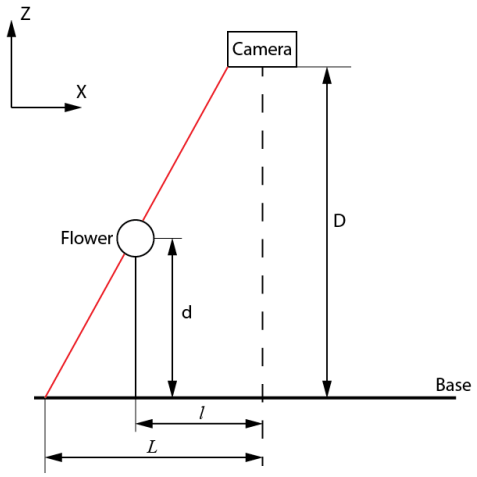

Figure 5: Parameter of image processing of rose harvesting robot.

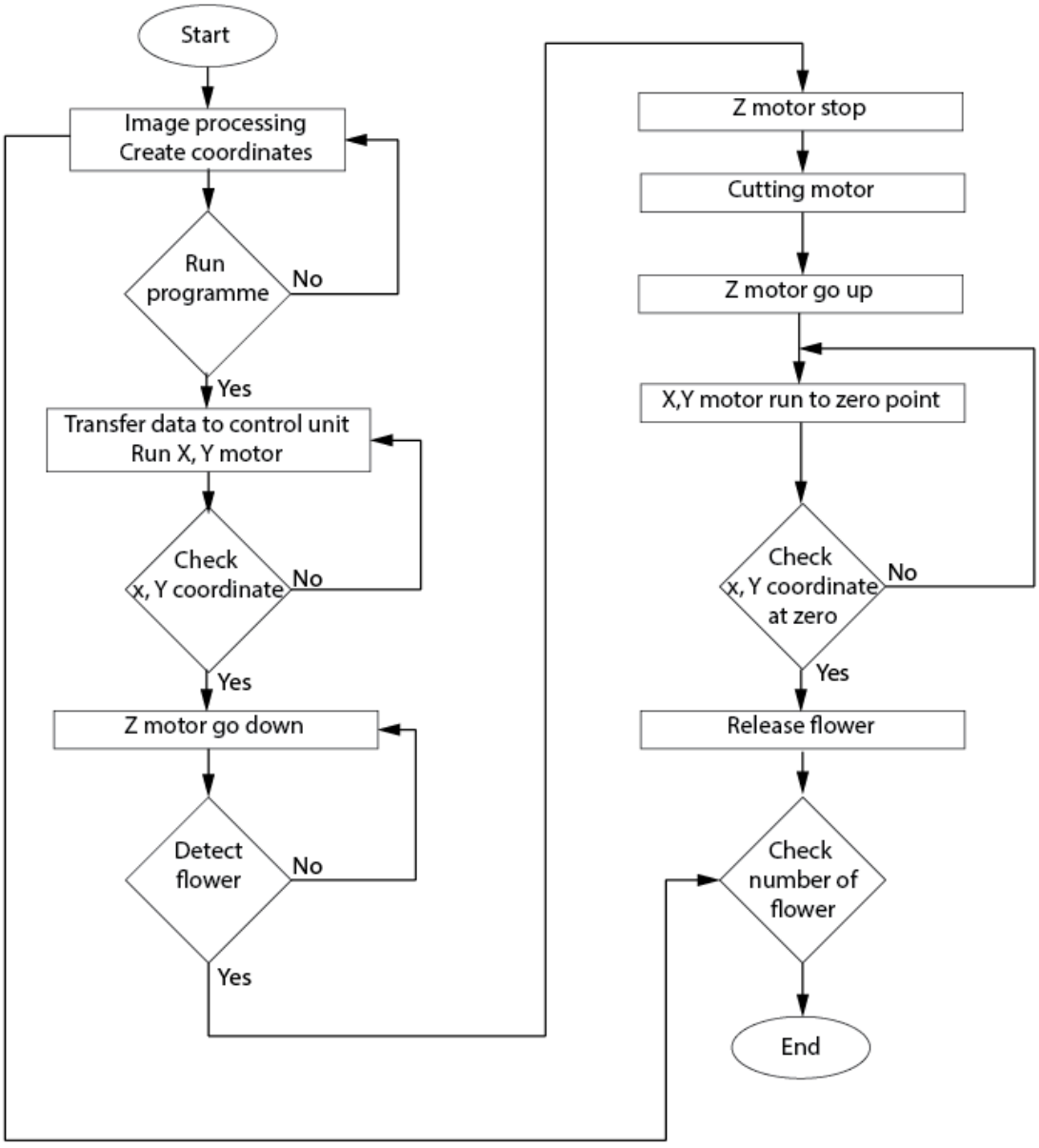

Figure 6: Algorithmic flow chart of the program.

Figure 6 displays the flow chart of the program for the autonomous detection and harvesting of flowers. Initially, the program checks the coordinates of X, Y, and Z motors at zero points. A picture of the flower was caught by camera and image processing analysis and indicated the coordinates of the flower. X, Y, and Z motors run to the flower's location, and the cutting motor executes. After that, X, Y, and Z motors move to the zero points and release the flower. The program matches the number of flowers in the picture and continues to harvest flowers.

4 RESULTS AND DISCUSSIONS

A prototype of a rose harvesting robot is fabricated with the dimensions of a stationary frame 577mm ,720mm and 1134 mm, respectively dimensions in the X, Y, and Z axes. Figure 7a shows the robot after assembly, and Figure 7b shows the flower stems after the cut and rose harvesting of the robot. The robot's successful rose harvest rate reaches 93%

a) b)

Figure 7: Prototype of rose harvesting robot. a) Real model, b) Rose after harvesting.

The interface of the control program is shown in Figure 8. On the interface that displays the original image of the red rose from above and the processed image in coordinate form, the coordinate values of each flower are also displayed on the image. The interface is designed to identify the number of 5 flowers. The harvest button helps the robot program to perform the actual flower harvesting. The manipulator prioritizes flowers that are located close to the origin.

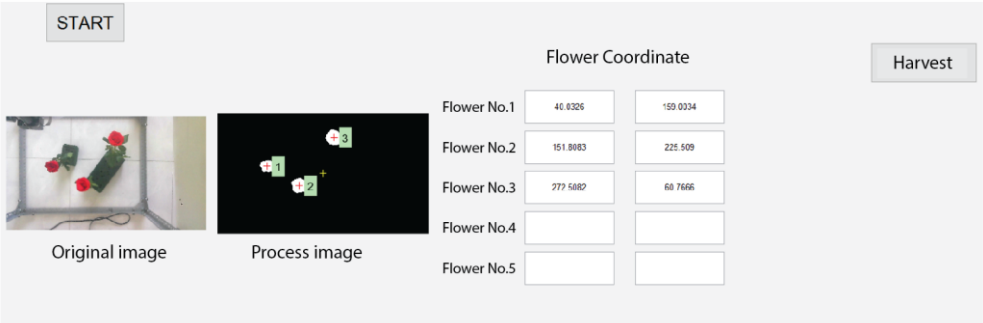

Figure 8: Interface of rose harvesting robot.

Table 1 shows the difference in the position of the flower on the x-axis after calculating according to formula (1), shown in the interface, and the real distance of the flower and the distance on the image are also presented. Thereby, the difference between the actual location and the location recorded on the software is less than 3%. Equation (1) is suitable for determining the position of the rose in the real image.

Table 1: Result of real distance and image distance in image processing.

No.	Real distance (mm)	*L* (mm)	*l* (mm)	Error (%)
1	10	18	10,26	2,1
2	30	53,65	30,28	1,1
3	50	88,27	50,31	1,1
4	70	122,88	70,04	1,0
5	90	157,5	89,78	1,0
6	110	192,12	109,51	1,0
7	130	226,73	129,24	0.9
8	170	295,96	168,7	1,1

5 CONCLUSIONS

A rose harvesting robot model has been researched and developed incorporating image processing technology. A robot with a manipulator moves on coordinate axes and performs the process of cutting and holding flowers. The image obtained from the camera is analyzed, and the coordinate positions are retrieved for the correct operation of the manipulator. An automatic control system has been built to keep the robot working continuously. A prototype was built and operated to harvest flowers with a 370-480 mm height and a 30-60 mm flower diameter. The robot can harvest flowers with a 93% success rate. The equation for calculating coordinates on the image is given and tested with a coordinate error of less than 1%. The robot applies optimization to control the manipulator and investigate the system's stability when harvesting flowers with different diameters and colors in future work.

6 ACKNOWLEDGMENT

The author is thankful for the support from the Industrial University of Ho Chi Minh City, Vietnam.

REFERENCES

[1] E. J. van Henten, Greenhouse Mechanization: State of The Art And Future Perspective, *Acta Hortic*, vol. 710, pp. 55-70, 2006.

[2] C. W. Bac, E. J. Henten, J. Hemming, Y. Edan, Harvesting Robots for High- Value Crops: State-of-the-art Review and Challenges Ahead, *Journal of Field Robotics*, 2014.

[3] A. VinothKumar, V. Kannarasu, S. Padmapriya, N. Partheeban and S. Arun,. Design and Implementation of Autonomous Flower Harvester using Image Processing. *International Journal of Recent Technology and Engineering* (IJRTE), vol. 8, no. 2, pp. 2638-2642, 2019.

[4] T. Rath and M. Kawollek, Robotic harvesting of Gerbera Jamesonii based on detection and three-dimensional modeling of cut flower pedicels, *Computers and Electronics in Agriculture*, vol. 66, issue 1, 2009.

[5] S. Bhaskar, M. P. Kumar, M. N. Avinash and S. B. Harshini, Real Time Farmer Assistive Flower Harvesting Agricultural Robot, *6th International Conference for Convergence in Technology (I2CT)*, pp. 1-8, 2021.

[6] H. Zhang, Y. Ge, C. Sun, H. Zhang and N. Liu, Picking Path Planning Method of Dual Rollers Type Safflower Picking Robot Based on Improved Ant Colony Algorithm, *Processes*, vol. 10, no. 6, 2022.

[7] C. Gurel, M. H. G. Zadeh and A. Erden, Rose Stem Branch Point Detection and Cutting Point Location for Rose Harvesting Robot, *The 17th International Conference on Machine Design and Production*, 2016.

[8] J. Abarna J. and A. Selvakumar, Rose Flower Harvesting Robot, *International Journal of Applied Engineering Research*, vol. 10, no. 55, pp. 4216-4220, 2015.

[9] Y. Manikanta, S. S. Rao and R. Venkatesh, The Design And Simulation Of Rose Harvesting Robot, International *Journal of Mechanical and Production Engineering Research and Development*, vol. 9, issue 1, pp. 191-200, 2019.

[10] C. Bhartiya and Ashish P, Image Processing Based Rose Harvesting System using Raspberry Pi, *International Journal of Engineering Research & Technology*, vol. 4, issue 4, 2015.

[11] A. Kohan, A. M. Borgahaee, M. Yazdi, S. Minaei and M. J. Sheykhdavudi, Robotic Harvesting of Rosa Damascena Using Stereoscopic Machine Visio, *World Applied Sciences Journal*, vol. 12, issue 2, pp. 231-237, 2011

HIGH CONTENT FLY ASH RCC AS AN EFFICIENT SOLUTION FOR HYDROELECTRIC DAM CONSTRUCTION

NGUYEN VIET DUC [1*], DANG HOANG MINH [2], DOAN HIEU LINH [2], LE TAN [2]

[1] *Thuyloi University, 175 Tay Son, Dong Da, Hanoi, Vietnam,*
[2] *Industrial University of Ho Chi Minh City, 12 Nguyen Van Bao, Ward 4, Go Vap District, Ho Chi Minh City, Vietnam;*
**ducnv@tlu.edu.vn*

Abstract. Hydroelectric power is electricity generated from hydropower. According to the latest statistics, it supplies a third of Vietnam's electricity, almost 95 TWh, which is more than all other renewable sources combined. Dam construction plays a key role in any project of hydroelectric power station. From the economic point of view, it involves a vast amount of concrete material, which normally accounts for a third of the overall project cost. While from the technical standpoint, heat from mass concrete placement during the construction that may result in a fault or defect for the dam urges an engineer to sort out the problem. To deal with this, one of the solutions is to lower cement content in a concrete mix proportion by using mineral addition such as granulated slag, pozzolan, ect. However, twenty-five coal-fired thermal power plants are currently in operation in Vietnam, producing an industrial waste with a total volume of ash and slag of around 13 million tons per year, of which fly ash accounts for 85%. If handled properly, fly ash could be an excellent option. The use of high fly ash content roller-compacted concrete, or RCC, for hydroelectric dam construction is proposed in this research. Several RCC mixes with two third fly ash of the total binder content have been produced successfully. This outcome promises not only to bring a cost-efficient material for the dam construction, but also to reduce the amount of fly ash in the disposing area of the thermal power plant.

Keywords. RCC, fly ash, dam construction, hydroelectric power station.

1 INTRODUCTION

Although the electricity system of Vietnam has changed a lot in terms of source structure and diversification of sources, hydroelectricity is still very important in electricity supply, serving the country's socio-economic development. In addition, medium and large hydropower plants also play an important role in flood regulation, ensuring water security and ecological environment. As the power system integrated with renewable energy sources increases, the role of hydroelectricity becomes even more important, helping the power system to operate stably, reliably and safely. At the same time, contributing to the implementation of green energy transition, clean energy, reducing CO_2 emission power sources and implementing Vietnam's international commitments at COP26, bringing net “zero” emissions to by 2050 [1, 11].

Vietnam has comparatively considerable hydropower resources due to its geographical location in the tropical climate, which is hot and humid with a lot of rain. Due to the topographical difference, the topographic distribution ranging from North to South with a coastline of more than 3400 km and a shift in altitude of more than 3,100 m to sea level has generated a vast potential energy source. Many studies have shown that Vietnam has a hydroelectric capacity of 25,000-26,000 MW, which equates to 90-100 billion kWh of energy. However, the potential for exploitable hydroelectric capacity is significantly greater. According to global hydroelectricity exploitation experience, the hydropower capacity in Vietnam that can be exploited in the future ranges from 30,000 MW to 38,000 MW, with an estimated capacity of 100 - 110 billion kWh. The greatest hydroelectric projects built and finished to date include Son La hydroelectric (2400 MW), Lai Chau Hydropower (1200 MW), and Huoi Quang Hydropower (560 MW) [2].

With respect to the report of the Electricity of Vietnam (EVN): By the end of 2022, the overall power capacity of the entire system will be around 77,800 MW, a 1,180 MW increase over 2021 (76,620 MW). In which, coal-fired thermal power plant with a total capacity of 25,312 MW (accounting for 32.5%), gas

thermal power plant with 7,160 MW (accounting for 9.2%) and renewable energy including hydropower. accounted for 55.4% of the whole system's capacity. In which, the total capacity of wind and solar power sources is 20,165 MW (accounting for 26.4%) and hydroelectricity (including small hydroelectricity) is 22,544 MW (accounting for 29.0%).

In terms of electricity production and supply for the whole system in 2022, it will reach 268,442 billion kWh, an increase of 5.26% compared to 2021, of which the power output from hydroelectricity will reach 95,054 billion kWh, an increase of 16,381 billion kWh compared to 2021; electricity from gas turbines increased by 3.252 billion kWh; electricity from renewable energy increased by 4,944 billion kWh; electricity from coal-fired thermal power decreased by 13.11 billion kWh. The maximum load capacity of the whole system in 2022 is 45,434 MW on June 21, 2022, an increase of 4.41% compared to 2021 (43,518 MW). The structure of power supply capacity of the whole system in 2022 is shown in Figure 1 [3].

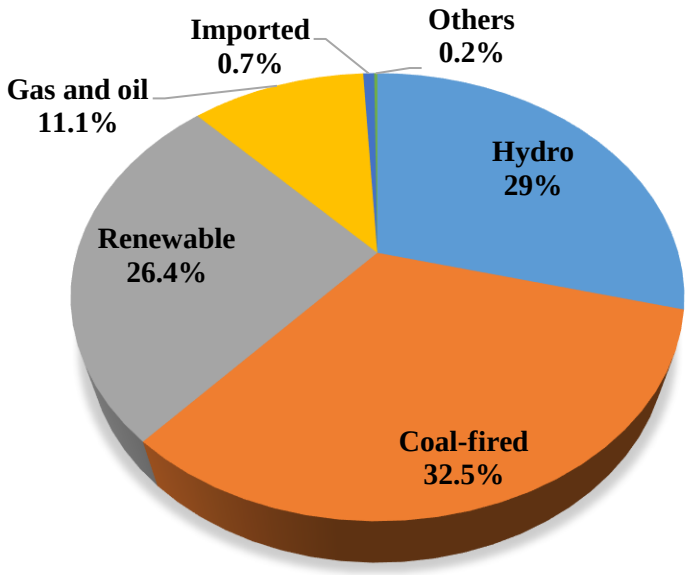

Figure 1: Electricity sources in Vietnam in 2022.

According to the Ministry of Industry and Trade's most recent data, the country has 25 coal-fired thermal power plants in operation, generating a total of around 13 million tons of ash and slag each year, of which fly ash accounts for 80% to 85%. Emissions are located mostly in the North, accounting for 65% of total emissions, with the Central region accounting for 23% and the South accounting for 12%. The quantity of ash and slag emitted by the EVN group's 13 coal-fired power stations is 8.57 million tons, accounting for 64% of the country's total emissions [4]. As an example, the Na Duong coal-fired power station in Lang Son province emits around 430,000 tons of ash and slag into the environment each year [5]. An increasing amount of trash without treatment poses a risk of dust pollution and requires a considerable amount of land to keep waste [6]. This necessitates the development of a method for recycling and reusing materials in order to make valuable items for human consumption.

On the other hand, dam construction is required for generating hydropower energy. To build it, it needs to cast a massive roller compacted concrete (RCC) [7]. However, the inherent drawback of massive RCC is the heat emission owing to the high cement content, which in turn results in crack propagation in the concrete matrix [8]. Under the pressure, water would penetrate through the crack and cause damage for the dam in the long term. Therefore, from the technical standpoint, it is necessary to lower the heat emission from the massive RCC. From the literature review, so far other authors have intended to use fly ash up to 60% of the powder content [4, 5, 12-14]. Therefore, this paper proposes the use of high-content fly ash, i.e. more the 60% of the powder content, for the RCC mix proportion, which not only minimizes heat emissions but also solves the issue of fly ash emissions from the country's coal-fired power plants.

2 MATERIALS AND METHOD

2.1 Cement and fly ash

The Portland cement PC40 with the But Son brand name was used, which meets the European cement standard EN 197-1. Furthermore, fly ash from the Na Duong coal-fired power station in Lang Son province is used as a supplemental cementitious material in the concrete mix, along with cement. Tables 1 and 2 show the chemical and physical properties of cement and fly ash, respectively.

It is noteworthy that the loss on ignition (LOI) of fly ash is almost fourfold that of cement, as it can be seen in Table 1, however, its value still complies with the one prescribed in the standard that are suitable for a concrete mix. Besides, Blaine fineness of fly ash is higher than that of cement, as it can be observed in Table 2. It depicts that fly ash particles are able to go inside the gap of cement particles, in order to have a dense matrix of cementitious paste [9].

Table 1: Chemical composition of cement and fly ash (in weight percentage).

Compound	Cement	Fly ash
SiO_2	23.32	35.54
Al_2O_3	4.95	20.19
Fe_2O_3	4.84	13.59
CaO	63.22	11.54
MgO	1.62	2.82
SO_3	-	6.71
K_2O	0.11	2.34
Na_2O	0.26	0.57
TiO_2	0.05	0.40
Loss on ignition	1.63	6.3

Table 2: Physical and mechanical characteristics of cement.

Parameters	Units	Cement	Fly ash
Specific density	g/cm^3	3.13	2.2
Bulk density	g/cm^3	1.31	0.8
Blaine fineness	cm^2/g	3230	4318
Consistency	%	28.5	-
Initial setting time	min.	150	-
Final setting time	min.	230	-
Soundness of cement	mm	1.0	-
3 days compressive strength	N/mm^2	26.1	-
28 days compressive strength	N/mm^2	47.6	-

2.2 Coarse and fine aggregates

This study advocates for the use of crushed stone sand in place of expensive natural river sand. RCC is proportioned using stone and sand from Kien Khe - Ha Nam Province. Furthermore, crushed stone with a maximum size of 40 mm is used for the RCC. Table 3 shows the compliant TCVN 7572:2006 characteristics. In addition, sieve analysis was performed to determine aggregate grading, and the results are shown in Table 4.

Table 3: Characteristic of sand and stone.

Parameters	Units	Sand	Stone
Specific density	g/cm^3	2.67	2.71
Bulk density	g/cm^3	1.65	1.48
Porosity	%	38.2	44.1

Moisture content	%	1.0	0.9
Clay, silt and dust content	%	0,5	1.5
Fineness modulus	-	2.57	-

Table 4: Gradation of sand and stone by sieve analysis.

Sieve size (mm)	Sand	Stone
70		0.0
40		2.9
20		49.5
10		80.3
5	0.0	98.0
2.5	9.0	
1.25	23.5	
0.63	46.3	
0.315	84.0	
0.14	94.5	
Pan	100	100

2.3 Chemical admixture and water

Chemical admixture used is a slow-setting admixture with commercial name VMAT. While water used in this study is tap water in the Hanoi area. Characteristics of water and admixture are shown in Table 5.

Table 5: Characteristic of water and admixture.

Parameter	Units	Admixture	Water
Specific density	g/cm^3	1,13 ÷1,17	1
pH value	-	9 ÷ 10	7

2.4 Experimental programme

In order to have the mixed proportion of RCC, the Bolomey-Skramtaev method is involved. Several trial mixes are prepared to adjust the constituent material content. Besides, for the evaluation of RCC fresh properties, the Vebe test is used, as it can be observed in Figure 2.

This test determines how quickly new concrete flattens when vibrated. A hollow conical frustum set in a bigger hollow upright cylinder, a clear plastic disk, a vibrating table, and a timer comprise the testing apparatus. The following is the testing procedure [10]:

- Concrete is poured into the frustum, which is then placed in the cylinder on the vibrating table, and the cone is removed.
- After that, the clear plastic disk is placed on top of the concrete and the vibrating table is activated.
- The vibration will cause the concrete to solidify.
- The time it takes for the entire transparent plastic disk to make contact with the concrete is measured. This is known as the Vebe time.

The Vebe test simulates how concrete would behave when compacted on site and is thus a great tool to see how concrete will behave during compaction. Furthermore, because it is a dynamic test, it is excellent for determining the workability of fresh concrete samples that are too stiff to be assessed by a standard slump test.

After the Vebe test, the fresh RCC is placed into the steel mould with the proper compaction, in order to prepare the specimens for mechanical test after that, as it can be seen in Figure 3. The cylindrical specimen is 150 mm in diameter and 300 mm in height.

Figure 2: Vebe test.

Figure 3: Specimen preparation.

Regarding the mechanical test, once the specimen hardens, the mould is removed, and all of the specimens are cured under the standard condition up to 28 days. After that, they are left in the outdoor condition up to the testing date.

In this study, compression and tensile tests are used to determine the hardened properties of RCC, as they are illustrated in Figure 4 and Figure 5 respectively. The specimens are tested at the age of 365 days.

Figure 4: Compression test on the specimens.

Figure 5: Tensile test on the specimens.

3 RESULTS AND DISCUSSION

3.1 RCC mix proportion

This study aims to prepare RCC mix proportion of strength class 15 MPa. Indeed, after several adjustments, two mixes M1 and M2 are the outcome of the concerned purpose. These mixes are presented in detail in Table 6 below.

Table 6: RCC mix proportion.

Mix	Cement PC40	Fly ash	Sand	Stone	Admixture	Water	Vebe time	Classification
	kg	kg	kg	kg	L	L	Second	-
M1	60	160	852	1385	1.45	110	16	Very stiff
M2	60	160	802	1445	1.45	115	16	Very stiff

Looking into Table 6, it can be seen that the binder content, which are cement and fly ash, is kept minimum, its volume is less than one tenth in a single cubic meter of the concrete. Besides, fly ash content is more than two third of the binder content. This means that a significant amount of cement can be replaced by fly ash, resulting in lowering the heat emission during the hydration [8, 9].
In the mix M2, the aggregate content is modified that stone content increases and sand content decreases. Doing that to have a content Vebe time, water dosage in the mix M2 is slightly higher than that in the mix M1. Both of mixes have the Vebe time being 16 seconds and classified as "very stiff", as it can be observed in Table 6. With the outcome of fresh properties, it is probably hard to compact the mixes at fresh state. However, this result is common for RCC mixes, because they are compacted by rollers of high capacity. Moreover, since the slow-setting admixture is used for the mixes, the rollers have enough time to do its work properly.

3.2 RCC hardened properties

The test results at hardened state of the mixes M1 and M2 are included in Table 7. It can be seen that they have almost a similar bulk density. Both compression and tensile strength of the M1 are higher than those of the M2. This is mainly due to the water content used in the M1 being less than that in the M2.
However, both of the mixes M1 and M2 behave well, as their compression and tensile exceed the minimum value prescribed by the strength class 15 MPa, as it can be observed evidently in Table 7. It points out that these RCC mixes have been successfully prepared for being used in the dam construction.

Table 7: RCC hardened properties.

Mix	Bulk density	Compression strength		Tensile strength	
		Experiment	Required minimum	Experiment	Required minimum
	g/cm^3	MPa	MPa	MPa	MPa
M1	2.55	23.6	16.5	1.51	1.3
M2	2.54	21.2	16.5	1.38	1.3

4 CONCLUSIONS

In this paper, fly ash from the Na Duong coal-fired power plant, which is stored abundantly in the dumping pond of the plant, was used for the mix proportion of roller compacted concrete (RCC). Two RCC mixes have been successfully prepared. Fly ash replaced more than two thirds of cement content in the conventional mix. Binder content by volume is less than one tenth of one cubic meter. Cement content was kept at 60 kg per one concrete cubic meter. This could minimize the heat emission during the hydration of RCC, besides less cement content would bring RCC mix with an economical cost expenditure.
Regarding the hardened state, compression and tensile strength of these RCC mixes have exceeded those values prescribed by the designed strength class. Besides, the bulk density of these mixes were quite similar and can be classified as heavy concrete. Since a huge amount of fly ash is effectively used for RCC to build the hydraulic dam, this would save land area for storage of ash and slag at the Na Duong coal-fired power plant and vitally diminish the impact on the surrounding environment.

ACKNOWLEDGMENT

Special thank is given to colleagues at Thuyloi University and Industrial University of Ho Chi Minh City for the interest and invaluable contributions to the paper.

REFERENCES

[1] Institute of Energy, EVN, Version of master plan No. VIII for power system in Vietnam, 2022.

[2] Quy hoạch phát triển điện lực Quốc gia thời kỳ 2021 – 2030 tầm nhìn đến năm 2045. Viện Năng lượng. Báo cáo Dự thảo tháng 11/2022.

[3] Nguyễn Huy Hoạch. Thủy điện trong bối cảnh điện gió, điện mặt trời chiếm ưu thế: Chính sách của Thái Lan. NangluongVietNam online. 29/12/2022.

[4] V.L. Tăng và Đ.T. Nguyễn, Nghiên cứu ảnh hưởng của hàm lượng tro bay và xỉ lò cao hoạt tính đến tính chất của bê tông cường độ cao hạt mịn không sử dụng chất kết dính xi măng, *Tạp chí Khoa học Thuỷ lợi và Môi trường*, Số 76, tr.11-20, 2021.

[5] C.H. Đặng, Nghiên cứu thực nghiệm gia cố đất thân đê hữu Đuống kết hợp làm đường giao thông bằng vật liệu xi măng và tro bay, *Tạp chí Khoa học Thuỷ lợi và Môi trường*, Số 58, tr.34-40, 2017.

[6] A. Mehra, M. E. Farago & D. K. Banerjee, Impact of fly ash from coal-fired power stations in Delhi, with particular reference to metal contamination, *Environmental Monitoring and Assessment*, 50, p. 15–35, 1998.

[7] B. Rouissat, N. Smail, S. Zenagui, Importance of using roller compacted concrete in techno-economic investigation and design of small dams. *Applied Water Science*, 7, p. 4777-4784, 2017.

[8] Neville A.M. (2002). Concrete Properties 4th edition. Person Education Limited, Edinburgh.

[9] Aitcin P.C. (1998) High performance concrete, CRC Press, Taylor & Francis, UK.

[10] ASTM C1170/C1170M (2020) Standard Test Method for Determining Consistency and Density of Roller-Compacted Concrete Using a Vibrating Table (https://www.astm.org/c1170_c1170m-20.html)

[11] X. Xue, Y. Wang, H. Chen & G. Xu, A coal-fired power plant integrated with biomass co-firing and CO_2 capture for zero carbon emission, *Frontiers in Energy*, 16, p. 307–320, 2022.

[12] Z. Li, C. Zhang, Effects of high-volume fly ash on the properties of roller compacted concrete: A review, *Academic Journal of Architecture and Geotechnical Engineering*, 4(1), p. 33-36, 2022.

[13] S. Krishna Rao, P. Sravana, T. Chandrasekhara Rao, Strength and compaction characteristics of fly ash roller compacted concrete, *International Journal of Scientific Research in Knowledge*, 3(10), p. 260-269, 2015.

[14] P. N. Ojhaa, B. Singh, S. Prakashc, P. Singhd, M. K. Mandree, S. Kumarf, Effect of high ratio fly ash on roller compacted concrete for dam construction, *Research on Engineering Structures and Materials*, 2, p. 1-18, 2022.

RESEARCH AND PROPOSAL TO APPLY OPTICAL PRESSURE SENSOR IN MEASURING EVAPORATIVE PRESSURE OF INDUSTRIAL REFRIGERATION SYSTEM

VAN-QUYET NGUYEN [1,2*], CHIA-CHIN CHIANG [1], HUU-NGHIA NGUYEN [2], DINH-KHUONG NGUYEN [2] AND LIREN TSAI [1*]

[1] *Department of Mechanical Engineering, National Kaohsiung University of Science and Technology, Kaohsiung 807, Taiwan,*
[2] *Faculty of Mechanical Engineering, Nha Trang University, Khanh Hoa 57000, Vietnam; liren@nkust.edu.tw, quyetnv@ntu.edu.vn*

Abstract. In today's engineering industries, measurement technology has developed very strongly according to trends and innovation needs, including pressure measurement. At present, most industrial refrigeration systems use pressure sensors such as solid-state pressure sensors, pressure transducers, and digital pressure sensors. Meanwhile, the optical pressure sensor has recently received intensive attention and research. It has shown great potential for application in general engineering and refrigeration engineering in particular. In this paper, the authors propose to apply a study on optical pressure sensors in measuring evaporative pressure in industrial refrigeration systems. The optical pressure sensor test shows very good sensitivity and linearity. Specifically, in the tested pressure range from 1 to 5 atm, a total wavelength shift of 3.498 nm was observed, corresponding to a sensitivity of 0.8745 nm/atm. The sensor demonstrates a linearity of more than 97%, indicating its high stability. The pressure range tested in this study corresponds to some low-pressure locations in the refrigeration system, such as the evaporator and liquid separator. Therefore, the application of this optical pressure sensor to the refrigeration system has great potential.

Keywords. Evaporative pressure, pressure sensor, refrigeration systems, fiber Bragg grating sensor, optical pressure sensor.

1 INTRODUCTION

Nowadays, optical sensors are strongly researched and applied in many technical fields with many outstanding features. Among them, optical pressure sensors are also of interest to scientists worldwide in the field of pressure measurement to improve sensitivity, stability, multiplexing capability, or measurability in harsh environments [1].

With the development of science and technology over the past decades, the importance of 3D printing technology cannot be overlooked. This innovation offers numerous advantages in the fabrication of devices and auxiliary frameworks for scientific, engineering, and manufacturing contexts. Its main advantages include automated processes, time and cost efficiencies, and, most importantly, a high degree of customization [2, 3].

Refrigeration systems are widely used on a daily basis, such as air conditioning systems, storage warehouses, frozen food and seafood storage [4]... Critical parameters such as pressure and temperature at key nodes are closely monitored during the system operation. Based on the parameters obtained from the system, the operator or the engineer can monitor and evaluate the working efficiency and predict the refrigeration system's possible failure of the refrigeration system. The current pressure measurement device mainly adopts solid-state pressure sensors, pressure transducers and digital pressure sensors. Of course, these types have their advantages, but their common disadvantages are signal delay, multiplexing capability and high cost.

In this report, the authors propose the application of an optical pressure sensor using a 3D printed structure, which has been tested in a pressure chamber from 1 atm to 5 atm to measure the evaporative pressure in

industrial refrigeration systems such as building air conditioning systems, cold storage systems, freezing warehouses.

2 BASIC PRINCIPLES OF INDUSTRIAL REFRIGERATION SYSTEM

The refrigeration system operates on the fundamental principle of transferring heat from a lower-temperature region to a higher-temperature one, using the phase change of a refrigerant [4]. This cycle involves four main components: a compressor, a condenser, an expansion valve (or throttle valve), and an evaporator (1). The refrigerant evaporates in the evaporator, absorbing heat and cooling the surrounding environment. The vapor is then compressed by the compressor, which increases its temperature and pressure. This high-pressure, high-temperature vapor flows into the condenser, where it releases heat to the environment and condenses into a liquid. The high-pressure liquid then passes through the expansion valve, reducing its pressure and temperature, and the cycle begins again. This process allows the system to maintain controlled cooling or refrigeration in various applications.

In industrial refrigeration systems, in addition to the main equipment mentioned above, there are several auxiliary equipment such as liquid separator, oil separator, cooling tower, high-pressure tank and low-pressure tank. The low-pressure tank is installed behind the solenoid valve, expansion valve and in front of the evaporator. This equipment is usually installed with a pressure gauge to monitor the evaporating pressure.

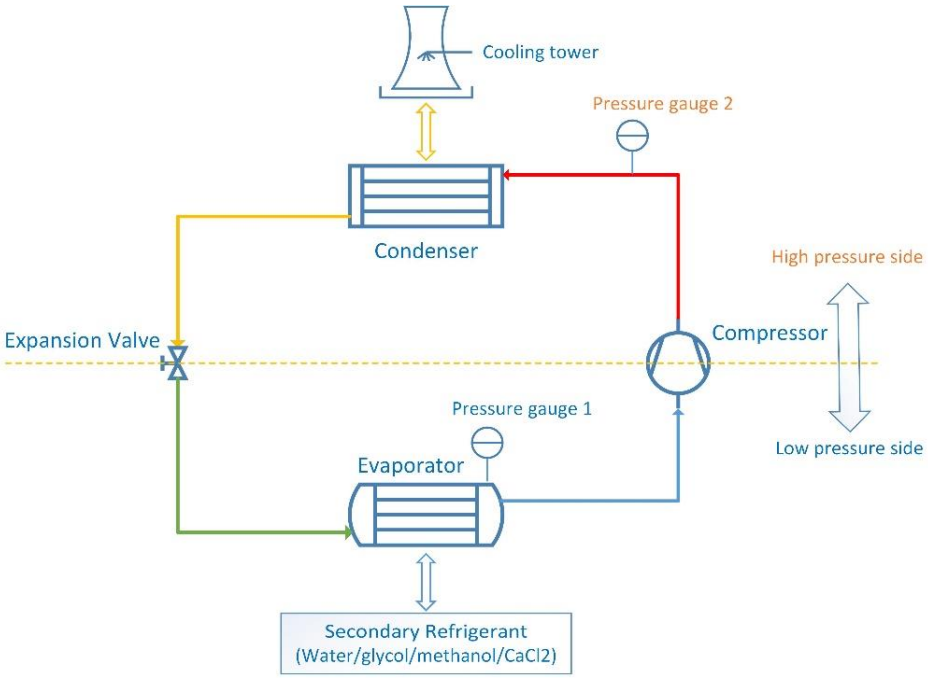

Figure 1: The basic working diagram of the refrigeration system.

3 THE OPTICAL PRESSURE SENSOR

3.1 Optical sensor manufacturing

The optical single optical fiber used in this study has an inner core diameter of 9.6 μm and an outer coating diameter of 124.9 μm, both produced by Fibercore Ltd. located in Southampton, UK. The Bragg gratings were inscribed onto the fiber using a pulsed KrF-laser system (Coherent Xantos, 248 nm wavelength, 12 mJ/cm2, Coherent, USA). The phase mask was used to create the fiber Bragg grating (FBG), and a peak wavelength of 1540.51 nm was selected for pressure-sensing purposes.

3.2 Sensor structure

The structure of the sensor is designed using Solidworks software and then sent to Cura software to set printing parameters. Finally, it is transferred to a 3D printer for printing. The printing material is polylactic

acid (PLA). Once the structure is completed, the FBG sensor is mounted inside the structure, as shown in Figure 2.

3.3 Working principle

The Fiber Bragg Grating refers to a cyclic refractive index modulation within the core of an optical fiber. When light is directed into the fiber core via an optical connector, the FBG reflects a specific narrowband wavelength while allowing the remaining broadband light to propagate. The center wavelength of the reflection spectrum is called the Bragg wavelength (λ_b). The relationship between the Bragg wavelength shift inside the FBG ($\Delta\lambda_b/\lambda_b$) and the axial strain ($\Delta\varepsilon$) and temperature in the operating environment (ΔT) for the fiber grating is expressed by the formula [1, 5]:

$$\frac{\Delta\lambda_b}{\lambda_b} = (1 - p_e)\Delta\varepsilon + (a_f + \xi)\Delta T \quad (1)$$

where, a_f is the thermal expansion coefficient, ξ is the thermal optic coefficient, p_e is the elastic-optical coefficient, and $p_e = 0.22$.

Based on the above formula, the optical Fiber Bragg Grating shows remarkable sensitivity to deformation and temperature changes. This property provides the basis for the FBG pressure sensor, which uses the change in wavelength as a direct indicator of pressure changes. Furthermore, the experiment was conducted in a well-controlled laboratory environment and at room temperature, so the effect of room temperature is considered negligible. This mechanism is conveniently illustrated in Figure .

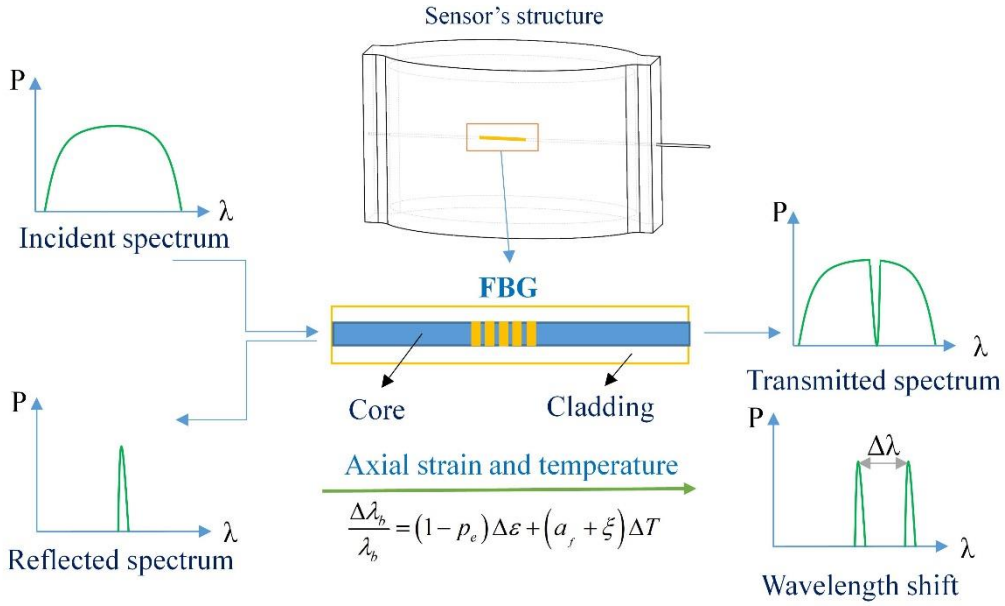

Figure 2: The working mechanism of an optical pressure sensor.

4 EXPERIMENT SETUP

The sensor is located in the pressure chamber, and it is well-controlled. The pressure inside the chamber is regulated by a manual piston pump that pushes water into the chamber. The light source is fed into the FBG through an optocoupler. The reflectance spectrum of the FBG is then transferred to the optocoupler and fed to the optical spectrum analyzer (OSA). The pressure in the chamber space will exert pressure on the wall of the sensing structure. This causes the structure to be pulled on both sides, creating axial stress in the FBG. The test pressure in this study ranged from 01 atm to 05 atm in 0.1 atm increments. The applied pressure change resulted in a corresponding change in the Bragg wavelength peak of the FBG and was recorded with OSA (Figure 3). This is one of the tests of the oval pressure sensor that the authors have performed repeatedly, with some slight variations related to the thickness of the structure and the structural material, with or without exterior paint. Different FBG sensors were used for each test. The sensor that gave

the best results both in terms of sensitivity as well as linearity and stability of the structure was selected [3]. The results presented in the next section also do not overlap with the published results.

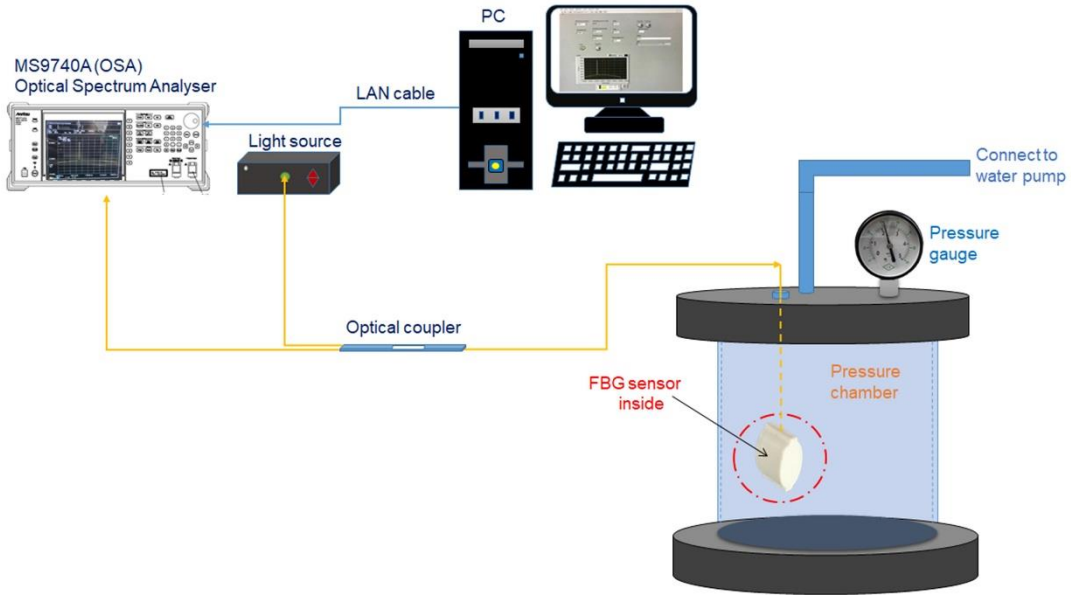

Figure 3: Devices layout diagram.

5 RESULTS AND DISCUSSIONS

5.1 Experiment results

Figure 4 shows that the spectrum of wavelengths recorded by the OSA shifts with respect to a pressure change from 1 to 5 atm with a step of 0.1 atm. The total Bragg wavelength shift over the applied pressure range is 3.498 nm, corresponding to a pressure sensitivity of 0.8745 nm/atm.

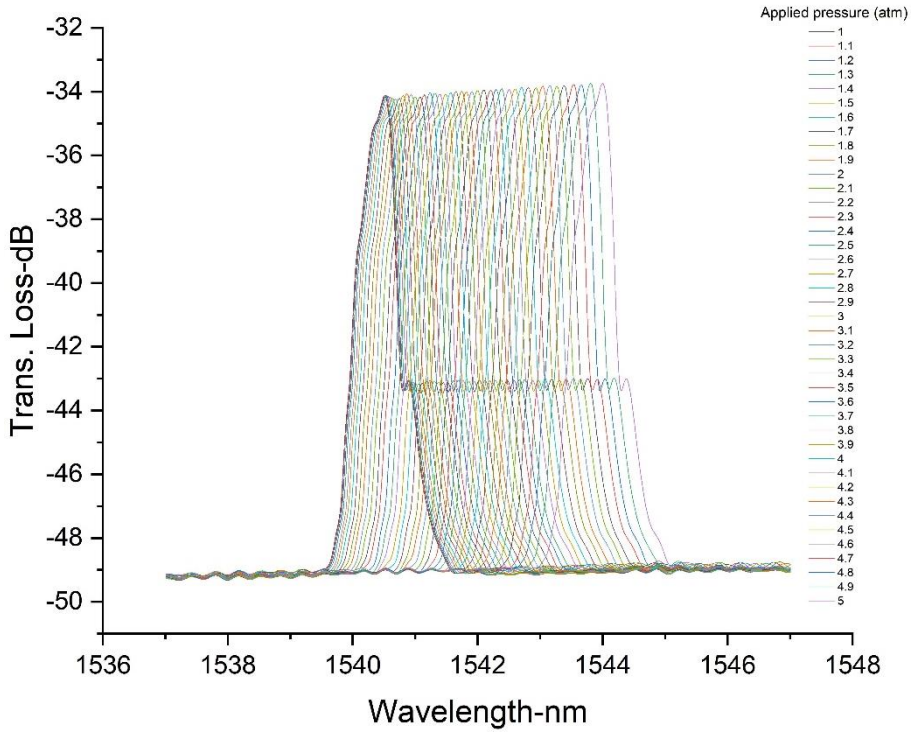

Figure 4: The reflectance spectrum of wavelength in FBG sensor.

Figure 5 shows the displacement of the Bragg wavelength peak with different pressures applied in the chamber space. It can be seen that the nodes tend to go up as the pressure gradually increases. This means

that there is a good linear relationship between the wavelength peak shift and the applied pressure. This linearity is greater than 97%, as shown in the figure below:

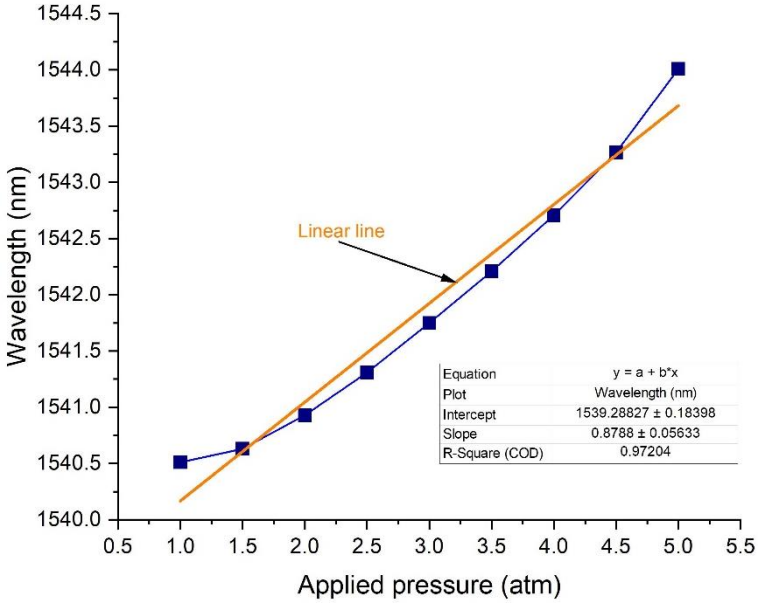

Figure 5: Bragg wavelength shift and linear line.

5.2 Discussing the application of optical pressure sensors in refrigeration systems

Many different types of refrigerants are used in industrial refrigeration systems today. Manufacturers also research and select the best refrigerant for their products. Some refrigerants commonly used in refrigeration systems currently and in the near future are listed below [6]:

Table 1: Evaporation temperature of some common refrigerants according to evaporator pressure (1-5 atm) [7].

Evaporating pressure (atm)	Evaporating temperature (°C)						
	R22	R404A	R407C	R410A	R32	R134a	R1234yf
1	-40.81	-45.47	-36.63	-51.36	-51.65	-26.07	-29.49
2	-24.85	-29.95	-21.38	-36.69	-37.02	-9.71	-12.42
3	-14.29	-19.67	-11.32	-27.02	-27.4	1.04	-1.12
4	-6.17	-11.75	-3.61	-19.6	-20.03	9.32	7.58
5	0.53	-5.21	2.75	-13.49	-13.96	16.15	14.76

1 also shows that the evaporating temperature of some refrigerants in the evaporating pressure range from 01 to 05 atm is relatively low, which is suitable for the needs of the evaporator temperature requirements in the corresponding range, such as storage systems, freezing (R22, R404A, R407C) or building air conditioning system (R22, R410A, R32) and even refrigerants for residential refrigeration systems such as R134a or R1234yf.

Based on the experimental results of the optical pressure sensor presented in the above sections, it can be seen that it has great potential and can be applied to measure the evaporative pressure in industrial refrigeration systems using the above refrigerants.

5.3 Schematic diagram of refrigeration system using proposed optical pressure sensor

From the diagram of the basic refrigeration system combined with the optical measurement system, the authors propose a diagram to connect the optical pressure measurement system to the refrigeration system. Some locations where optical pressure sensors can be placed to measure evaporator pressure are evaporator, low-pressure vessel (if any), and liquid separator (if any), as shown in Figure6 below.

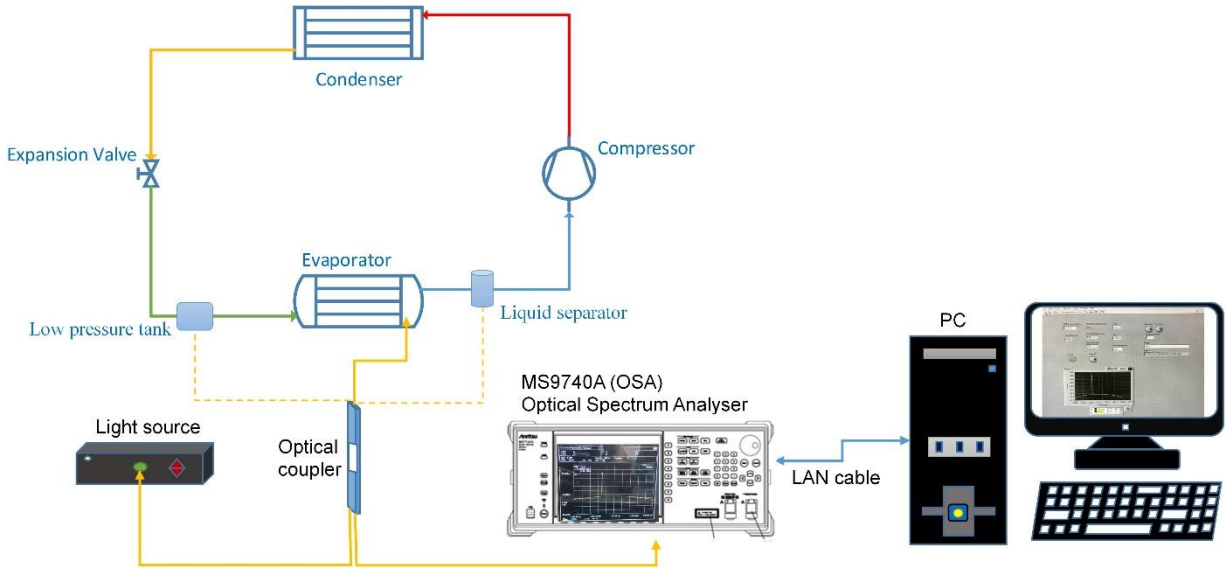

Figure 6: Schematic diagram of refrigeration system using proposed optical pressure sensor.

In addition, in the case of further development of high-pressure optical sensors to measure discharge pressure or condenser pressure, it is also easy to connect these optical sensors sequentially based on the advantages of the multichannel connection of optical measurement systems. However, it is clear that the measurement of the signal by the optical sensor will cost the measurement equipment of the attached plan, such as an optical spectrum analyzer (OSA), light source, fiber optic connector and computer. Overall, while there are potential benefits to using FBG pressure sensors in refrigeration systems, it is important to carefully consider the costs and technical requirements before making a decision to replace traditional pressure sensors with FBG sensors.

6 CONCLUSIONS

Based on the research results and analysis of the proposed application of the optical pressure sensor, the authors make the following conclusions and recommendations:

- The proposed optical pressure sensor has a working range from 01 to 05 atm, with a sensitivity of 0.8745 nm/atm and linearity up to over 97%.
- This sensor has potential application in evaporative pressure measurement in various industrial refrigeration systems with different refrigerants, corresponding to evaporator pressure and temperature.
- Optical sensors have many outstanding advantages, such as the ability to operate in harsh environments, high accuracy, and multi-channel connectivity... so it is predicted that there will soon be further development and application in the field of metrology.

REFERENCES

[1] H. Hisham, *Fiber bragg grating sensors: development and applications*. CRC Press, 2019.

[2] V. Q. Nguyen, C.-C. Chiang, and L. Tsai, Simple Pressure Sensor with Highly Customizable Sensitivity Based on Fiber Bragg Grating and Pill-Shaped 3D-Printed Structure, *Journal of Sensors*, vol. 2022, 2022.

[3] C.-C. Chiang and L. Tsai, Enhanced sensitivity of bare FBG pressure sensor based on oval-shaped 3D printed structure, *Optical Fiber Technology*, vol. 73, p. 103022, 2022.

[4] G. F. Hundy, A. R. Trott, and T. Welch, *Refrigeration and air-conditioning*. Butterworth-Heinemann, 2008.

[5] Y. Du, B. Sun, J. Li, and W. Zhang, *Optical fiber sensing and structural health monitoring technology*. Springer, 2019.

[6] V. Zanchi, L. Boban, and V. Soldo, Refrigerant options in the near future, *Journal of Sustainable Development of Energy, Water and Environment Systems*, vol. 7, no. 2, pp. 293-304, 2019.

[7] Danfoss. (2023) reftools. [Online]. Available: https://reftools.danfoss.com/spa/tools/ref-slider

DESIGNING, MODELING AND CONTROLLING A PHOTOVOLTAIC STRING IN DIFFERENT WEATHER CONDITIONS USING VIRTUAL TECHNOLOGY

NGOC-TRAN LE [1]

[1] *Industrial University of Ho Chi Minh City, Vietnam;*
lengoctran@iuh.edu.vn

Abstract. The demand for renewable energy for Ho Chi Minh City citizens is increasing due to the continuous intense heat throughout the year. However, most households here have installed fixed rooftop solar power systems leading to low efficiency. To improve the photovoltaic efficiency by maximizing the solar radiation, a photovoltaic string prototype with a two-axis tracking mechanism driven by the linear actuator electric cylinders is proposed, this solution aims to maximize the received solar radiation and to minimize the consumption for tracking regardless of the weather conditions changes. The proposed design of a PV tracker string has been developed based on the digital platform on integrated software such as SOLIDWORKS for the development of a solid solar tracker model, ADAMS for investigating the dynamic behaviour of the mechanical system, and MATLAB/Simulink for developing control systems. The simulation results on the virtual prototype model demonstrate the proposed solution can be applied to the real.

Keywords. Two-axis solar tracker, linear actuator electric cylinder, virtual prototype technology, tracking mechanism, photovoltaic string, control system, co-simulation system.

1 INTRODUCTION

Vietnam is located geographically in the sub-equatorial region, so it has a lot of the advantages of solar energy with a total number of high sunshine hours up to over 2,500 hours/year, the average total amount of radiation per year in about 5 KWh/m^2/day, increasing gradually to the south. Therefore, the area of Ho Chi Minh City (HCMC) and the southern province of Vietnam has the advantage of exploiting this solar energy source, to attend to the needs of life and manufacturing as well as reducing the cost of buying electricity from the national grid. Most of the solar power systems installed in Ho Chi Minh City are rooftop solar systems, which means the string of photovoltaics is fixed on the rooftop of the building so the efficiency is not high, it mainly just synchronises to the grid to reduce the electricity bill and heat protection for the building from the sun directly. Until now many people do not still understand the productivity of the PV solar tracker compared to the fixed rooftop PV solar system. For a fixed solar method, the PV solar panels are mounted on the rooftop of the building while the sun cannot stand still in a fixed position. It moves from the east to the west in a parabolic arc from sunrise to sunset and its trajectories across the sky change with the season and time of day. Baraa et al. [1] have provided a comparative analysis of the performance of both systems fixed and tracker systems, and they have concretely illustrated via simulation studies that the single-axis tracker system yields about 15% more energy than the conventional fixed-mounted system when being implemented across Peninsular Malaysia at a large-scale manner. Some authors [2,3] showed that the photovoltaic system with tracking is more efficient than the same module without tracking (fixed) and the efficiency increasing of the conversion system from 20% up to 50%. To improve the yields of the PV solar panel, currently, several research focusing on the solar trackers model which is to increase the photovoltaic efficiency by maximizing the degree of use of solar radiation have been studied and proposed [2-23].

For studying the solar tracker system, according to P. Gerro et al. [4], solar trackers can be categorized into two types such as single-axial and dual-axial systems based on the number of degrees of freedom. Single-axis system allows the sun to track a single axis corresponding to the diurnal movement or elevation movement. Meanwhile, a bi-axial tracking system allows both movements.

The solar tracker system is seen as a mechatronic system that is completely integrated with mechanics, electronics, and information technology. Therefore, to increase the efficiency of the photovoltaic system, it

is necessary to develop an optimized mechanical design and propose an appropriate control strategy simultaneously. Table 1 shows some types of PV tracking systems based on achieved energy gain from the literature [5].

Table 1: The achieved energy gain by some solutions of the PV tracking systems.

Ref.	Solar Tracker Mechanism	Control Strategy	Achieved Energy Gain
[6]	bi-axial	open-loop	41.45%
[7]	mono-axial	open-loop	24.2%
[8]	bi-axial	closed-loop	44.89%
[9]	mono-axial/bi-axial	closed-loop	20%/40%
[10]	mono-axial/bi-axial	open-loop	30.04%/39.96%
[11]	bi-axial	open-loop	26.9%

Based on the analyzed result in Table 1 shows the highest energy gain achieved when using the PV tracking system with a combination of a bi-axis mechanism and closed-loop control strategy. Therefore, in this research, this solution is proposed to apply for the PV tracking system on the roof of a building in Ho Chi Minh City – Vietnam.

For developing a solar tracker mechanical system: The PV tracking system includes many complex mechanisms such as linkages, joints, gear mechanisms, cam mechanisms, and chain or belt transmission which are driven by a controlled motor or linear actuator cylinder. Previous studies showed that it is difficult to develop a PV tracking mechanism in the actual stage due to there being no unitary modellings on structural, kinematical, and dynamical models in designing the mechanical structure of the PV tracking systems. Therefore, the development of a solar tracker design from conceptual to derive a new structural synthesis for a solar tracker mechanism is missing. In this research, to make a unitary modelling method of mechanism, the multi-body system (MBS) method [12-15] is proposed for execution. This method facilitates the self-formulating algorithms experiment, having goal the reducing of the processing time and cost in the design phase.

Regarding the control system of the PV tracking systems, Authors [16-18] applied a closed-loop control system in which the photoresistor sensors traditionally are used. These photo sensors are responsible for distinguishing the sun's position based on the change in resistance of sensors and sending electrical signals for rotation or stopping the actuators (motor or linear cylinder), serving for tracking the direction of the sun. However, the orientation based on the detecting sensors may introduce errors in the detection of the real position of the sun for variable weather conditions. To eliminate the influence of the weather factor, another algorithm is proposed based on predefined Sun's position trajectories, which can be precisely established based on the Earth-Sun astronomical system [20, 21]. Lastly, by combining closed-loop and open-loop strategies, so-called hybrid control systems are obtained [22,23].

This paper proposes a strategy for developing a photovoltaic string, which aims to increase the efficiency of solar energy conversion into electric energy by using a dual axis tracking mechanism with two degrees of freedom. In the meantime, the control strategy is a closed-loop method based on predefined Sun's position trajectories. A virtual prototyping platform, which includes CAD (Computer Aided Design)—SOLIDWORKS, MBS (Multi-Body Systems)—ADAMS, and DFC (Design for Control)—MATLAB/SIMULINK software solutions, was used to design and test the proposed tracking system. The proposed solar tracker model will test, evaluate and apply for the roof of the building in HCM-Vietnam.

2 MATERIAL AND METHODS

2.1 Determining the sun position and orientaion

The relative position of the sun with a point on the ground is determined by the elevation angle (altitude) and direction angle (azimuth) based on the time and location of observation. The algorithm for PV tracking based on the trajectories of the elevation and azimuth to compute the tilt angle for the PV tracking will be adjusted. For determination of the elevation and azimuth angles of the sun, is based on the literature [24].

The input parameters to determine the solar position include Local Solar Time (LST), declination angle (δ),

Hour angle (H) and latitude (φ). The equation of time (ET) is determined based on calculating the difference between solar Greenwich mean time (GMT) and local solar time (LST).

$$ET = 9,87\sin(2B) - 7,53\cos(B) - 1,5\sin(B) \text{ [min]} \quad (1)$$

Where:

$B = \frac{360(d-81)}{365}$ [deg], with d is the number of days in the month of a year.

Conversion between local solar time (LST) and local solar time (LT) is expressed through the corrected local solar time (LST) expression:

$$LST = LT + \frac{TC}{60} \text{ [hour]} \quad (2)$$

Time correction coefficient (TC):

$$TC = 4.(Longitude - LSTM) + ET \text{ [min]} \quad (3)$$

Where Longitude is the observation longitude, LSTM is the local standard longitude.

The hour angle (H) is calculated through the following expression:

$$H = 15^o(LST - 12) \text{ [Degree]} \quad (4)$$

Declination angle (δ) is calculated through the following expression:

$$\delta = \sin^{-1}[\sin(23,45^o).\sin(\frac{360}{365}(d-81))] \text{ [deg]} \quad (5)$$

The sun position from the observation point on the earth's surface is described in Figure 1.

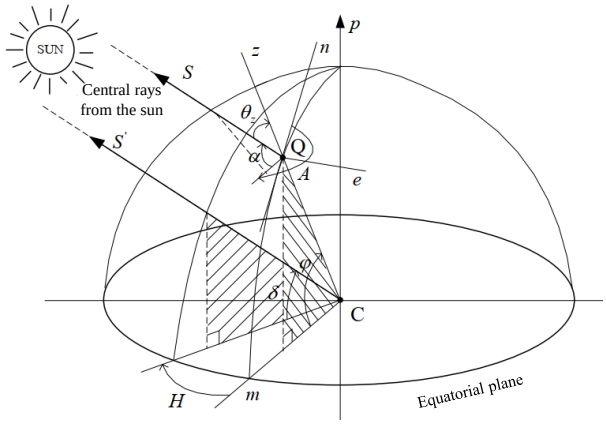

Figure 1: Combined coordinate system with vector parallel solar rays S, S'.

The elevation angle (α) at the observed latitude is determined by the formula:

$$\alpha = \sin^{-1}[\sin\delta.\sin\varphi + \cos\delta.\cos H.\cos\varphi] \text{ [deg]} \quad (6)$$

The azimuth angle (A) at the observed latitude is determined by the formula:

$$A = \cos^{-1}[\frac{\sin\delta.\cos\varphi - \cos\delta.\cos H.\sin\varphi}{\cos\alpha}] \text{ [deg]} \quad (7)$$

Based on Eq.6 and Eq.7 we can calculate the elevation angle and azimuth angle which help to define the Sun position.

Applying the above formula for determining position of the Sun, we have determined its position on certain days of the year. According to "Solar Window", the tracking time of the day will start from 9 am to 3 pm, the time to track positioning angle of the Sun is every 15 minutes.

2.2 Designing the PV tracking system

Based on the Sun position and orientation analyzed above, we propose to design a PV tracker system with a string of three solar panels and a PID controller is developed to control the PV tracker string to follow precisely the Sun's trajectories over one year.

The proposed PV tracker string uses a two-axis tracking mechanism, including two degrees of freedom, which correspond to the daily and seasonal movements. For daily (azimuth) movement, a linear actuator electric cylinder is used (Figure 2a), which is mounted on the frame of the PV model. This linear actuator electric cylinder directly drives three panels, it is to push or pull the connecting rods (3,4,5,6) which create a rotational driver of the PV solar panels based on the hinge mechanism. Meanwhile, in the seasonal (elevation) motion, another linear actuator electric cylinder is used to push/pull the auxiliary joint (3) (Figure 2b), which is linked to the rods supporting the PV solar panels based on the rotary joints (E), the linked mechanism will move accordingly, the mobile bar will slide on the sliding joint (4) helping this mechanism to raise and lower to create to the system's elevation angle. The mechanism for driving the PV solar panels follows daily motion and seasonal motion is described in Figure 2a, b.

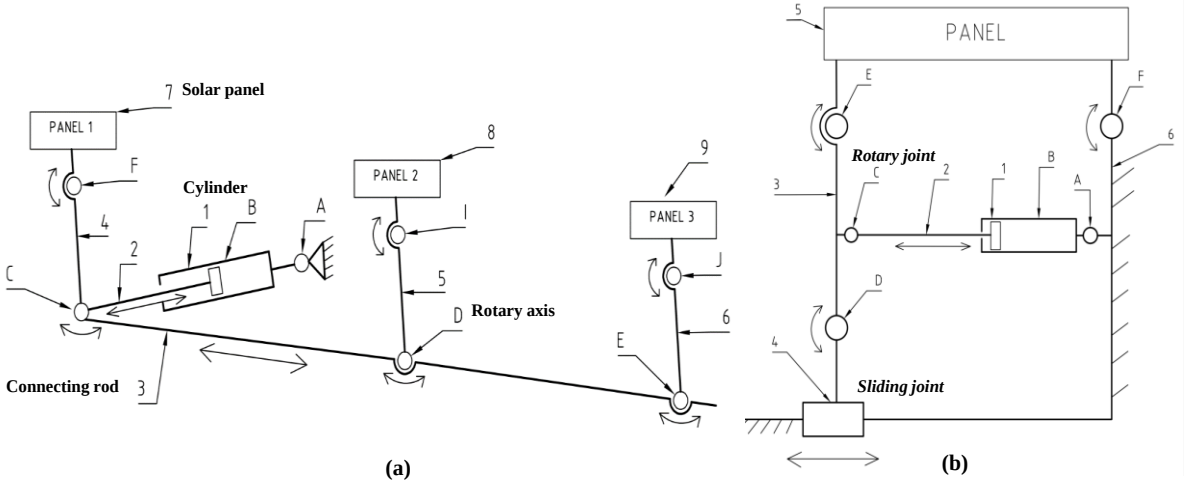

Figure 2: Linear cylinders drive the daily motion (a) and the seasonal motion (b).

For simulation of the proposed PV tracker dynamic behaviour, the PV string virtual prototype has been developed in mechatronic concept based on the integrated-software solution [25]: CAD—Computer Aided Design (SOLIDWORKS) - for creating the solid model, this model contains information about the mass & inertia properties of the rigid PV tracker parts. MBS—MultiBody Systems (ADAMS\View) - for modelling and simulating the PV tracker mechanical devices to analyze and optimize the mechanical device, and MATLAB/Simulink is used to develop a control system. The proposed PV tracker geometric model is transferred from SOLIDWORKS to ADAMS/View utilizing the STEP file format, the dynamic model is then assembled by utilizing the geometric constraints based on the object characteristics. The PV tracker virtual prototype model is presented in Figure 3.

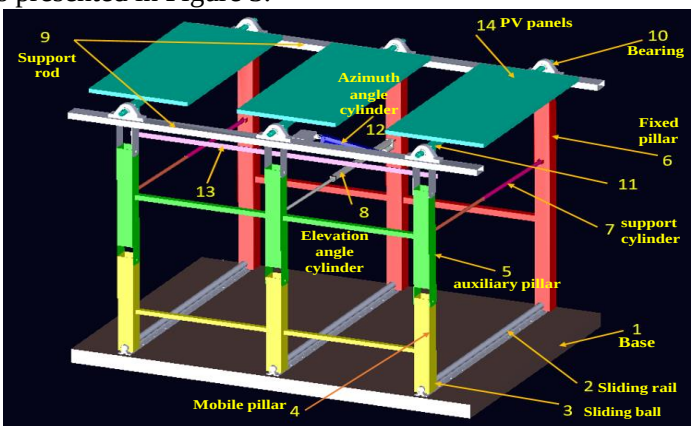

Figure 3: The PV tracker virtual prototype model with two-axis tracking system.

For dynamic behaviour simulation of the PV tracking system, the constraints for the components of this system must be done, it can be described as follows:

The constraints of components in the elevation motion: The cylinder shell and piston of the elevation cylinder are linked together by translational motion (translation joint-1), and the elevation cylinder is connected to the auxiliary pillars, which are rotated rotary joints (2,3) so that the cylinder extend or retract will work easier. In position (4), the horizontal bars supporting the PV module are attached to the auxiliary pillar and the fixed pillar with the rotary joint. The sliding ball and movable pillar (5) move forward along the rail using a sliding joint.

The constraints of components in the azimuth motion: The cylinder shell and azimuth piston are connected through a sliding joint (6). Strings of PV modules can operate synchronously by being attached to the connecting rod via a rotary joint (9). The azimuth piston (7) and the PV connecting rod are attached by a rotary joint, creating a transition between the cylinder's translational action to the PV chain's rotational action. The elevation cylinder is attached to the PV string support rod using a rotary joint (8). The solar panel support shaft is attached to the two supporting beams at both ends with a rotary joint (10). Additionally, this dynamic model is considered for configuring the mass forces, the reaction in joints, and the joint frictions.

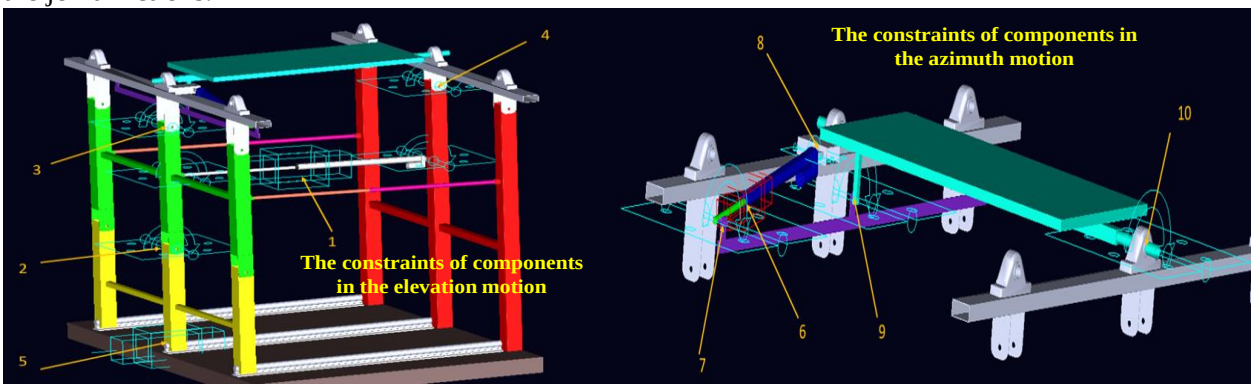

Figure 4: The constraints for the components of the PV tracking system.

2.3 Designing the control system for PV tracking string

The control algorithm for the PV tracking string was proposed in the concurrent engineering concept which integrated the electronic control system embedded in the mechanical device at the virtual prototype level [14]. The control system of the virtual prototype is designed as a control loop comprised of the MBS mechanical model connected with the dynamic model of the linear electric device. Thus, the physical testing and verifying processes are greatly simplified, and the risks of the control law being conflicted with the real model are eliminated. In this study, the control scheme of the mechatronic solar tracker string was developed using MATLAB/Simulink software, and the data transfer between two mechanical and control models is managed through the ADAMS/Controls interface. To connect the mechanical PV string model (developed in ADAMS/View) and the control scheme (developed in MATLAB/Simulink), the input & output parameters of the PV tracking model are configured first. The control forces are then generated by two linear actuator electric cylinders (for the daily and seasonal motions) representing the input parameters of the mechanical PV tracker model. The output signals transferred to the controller are the azimuth and elevation angles, which are measured on the PV tracker string module. The ADAMS model of the PV tracker string is then transferred to the MATLAB/Simulink environment where a *.m* file and an adams_sys is generated. The adams_sys denotes the non-linear MSC.ADAMS model as described in Figure 5. The ADAMS block of the PV tracker string model was created based on the information from the *.m* file and a control system is developed in MATLAB/Simulink based on the adams_sys has just been created. Two input signals of the adams_sys is generated from two controllers, and the output signals are the measured values of two azimuth and elevation angles, respectively.

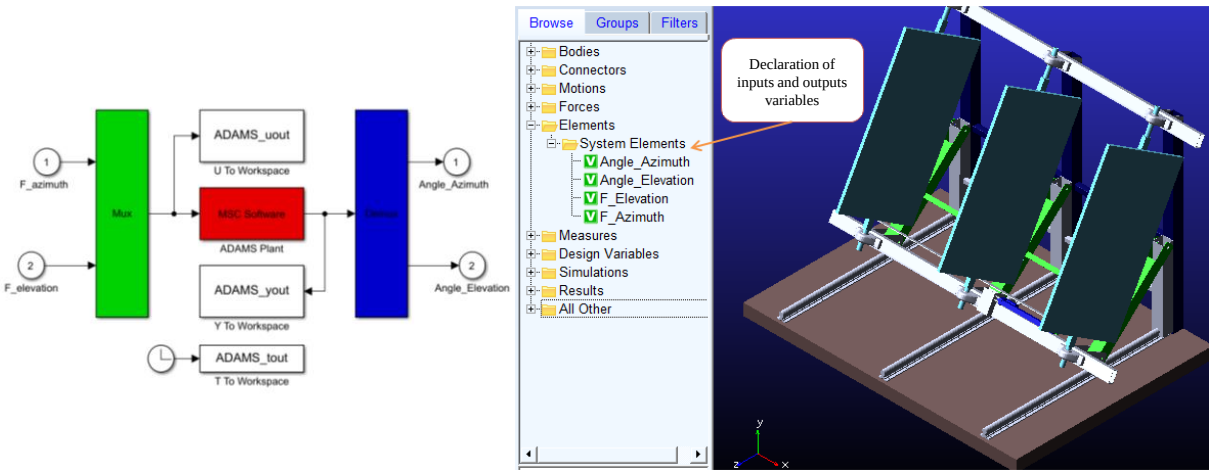

Figure 5: Configuration of the ADAMS block in adams_sys.

The PV tracking system works in different weather conditions, from the controller point of view, to reduce position errors, a PID controller with a control loop system was developed. The controller tuning includes the proportional (P), integral (I), and derivative (D) gains are performed based on the trajectories of azimuth and elevation angles. The block diagram of a PID control system for the PV tracking string is shown in Figure 6.

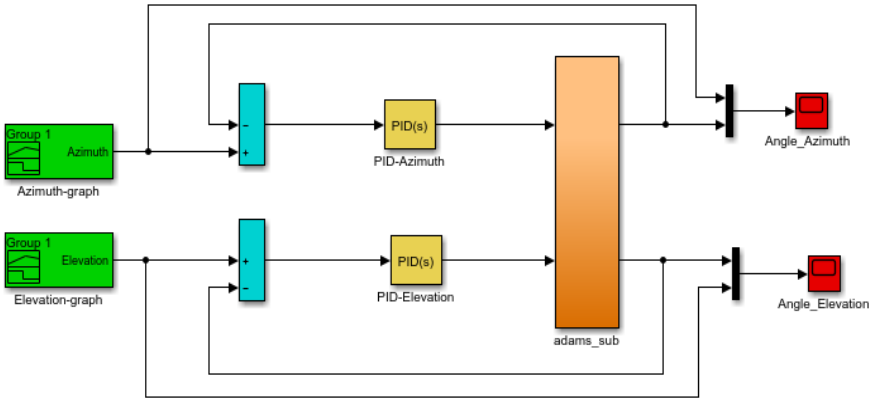

Figure 6: The block diagram of PID control system for PV tracking string.

2.4 Simulation results

The testing and validating the proposed control method is executed based on the sun trajectory on Decembe21st, 2021 at Industrial University of HCM (located at 106.6871 degrees East Longitude, 10.8221 degrees North latitude). The co-simulation process is implemented with input references as the table of Sun's points trajectory on December 21st, 2021, at IUH. The disturbances are considered with the wind parameters changes.

Table 2: The achieved values of PID controller parameters of the PV virtual prototype model.

The PID elevation controller		The PID azimuth controller	
Reference	elevation points trajectory	Reference	Azimuth points trajectory
Kp	16000	Kp	2000
Ki	24000	Ki	200
Kd	2030	Kd	90
RiseTime: t_r (s)	0.035	RiseTime: t_r (s)	0.051

Settling Time (s)	0.576	Settling Time (s)	0.135
Overshoot(%)	1.233	Overshoot(%)	3.672
Error (%)	2.822	Error (%)	0.424

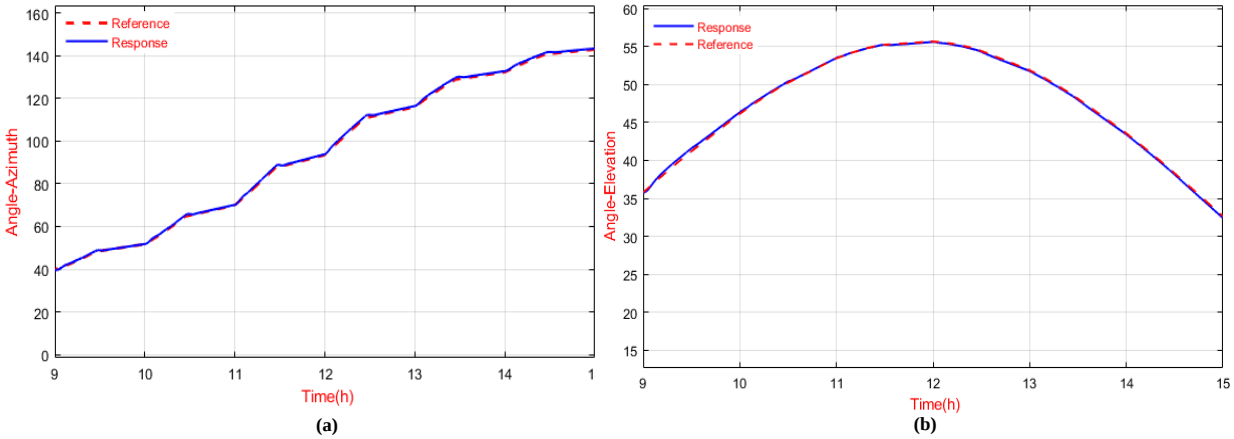

Figure 7: The controlled simulation results of the elevation and the azimuth angles.

3 CONCLUSIONS

In this study, the simulation results of the behaviour dynamic of the PV tracker string virtual prototype using ADAMS were implemented. The testing was then executed to verify the mechanical behaviour of this PV tracker string based on the virtual prototype model in accordance with the real PV string model. The co-simulation prototype of the PV tracker control model based on the PID control technology was formed in ADAMS and MATLAB/Simulink to study the performances of PID controller in the cases of the weather condition changes. Through this method the analysis and evaluation of the PV tracking mechanism can be executed without using the traditional develop-and-test approach. The proposed method to help the design engineers to modify the mechanism and control algorithms to remove the exis errors and reduces time and cost for developing the real system.

REFERENCES

[1] M. D. Baraa and C. L. Siow, Performance comparison of fixed and single axis tracker photovoltaic system in large scale solar power plants in Malaysia, *Indonesian Journal of Electrical Engineering and Computer Science*, vol. 21, no. 1, pp. 10-17, 2021.

[2] S. Abdallah and S. Nijmeh, Two-Axis Sun Tracking with PLC Control, *Energy Conversion and Management*, vol. 45, pp. 1931-1939, 2004.

[3] H.D. Mohring, F. Klotz, and H. Gabler, Energy Yield of PV Tracking Systems, *21st European Photovoltaic Solar Energy Conference* - EUPVSEC, WIP Renewable Energies, Dresden, pp. 2691-2694, 2006.

[4] Gerro PrinSloo, *Solar Tracking Ebook*, 2015.

[5] Cătălin Alexandru, Optimization of the Bi-Axial Tracking System for a Photovoltaic Platform, *MDPI Journal of Energy*, 2021.

[6] C. Alexandru, The Energy Balance of the Photovoltaic Tracking Systems Using Virtual Prototyping Platform, *Proceedings of the 5-th IEEE International Conference on the European Electricity Market—EEM*, Lisbon, Portugal, 8–30, pp. 253–258, May 2008.

[7] B. J. Huang, Y. C. Huang, G. Y. Chen, P. C. Hsu, K. Li, Improving solar PV system efficiency using one-axis 3 position sun tracking, *Energy Procedia 2013*, vol.33, pp. 280–287.

[8] C. Jamroen, P. Komkum, S. Kohsri, W. Himananto, S. Panupintu, S. Unkat, A low-cost dual-axis solar tracking system based on digital logic design: Design and implementation, *Energy Technol Assess*, vol.37, 100618, 2020.

[9] J. Parthipan, B. Nagalingeswara Raju, S. Senthilkumar, Design of one axis three position solar tracking system for paraboloidal dish solar collector, *Mater Today Proc*, vol. 3, pp.2493–2500, 2016.

[10] S. Seme, B. Stumberger, M. Hadziselimovic, A novel prediction algorithm for solar angles using second derivative of the energy for photovoltaic sun tracking purposes, *Energy* 2016, vol. 137, pp. 201–211, 2016.

[11] M. H. M. Sidek, N. Azis, W. Z. W. Hasan, M. Z. A. Ab Kadir, S. Shafie, M. A. M. Radzi, Automated positioning dual-axis solar tracking system with precision elevation and azimuth angle control, *Energy 2017*, vol. 124, pp. 160–170, 2017.

[12] M. Comsit and I. Visa, Design of the Linkages-type Tracking Mechanisms by using MBS Method, *12th IFToMM World Congress, IFToMM & CFPSMM, Besançon*, pp. 582-587, 2007.

[13] W.O. Schiehlen, Multibody Systems Dynamics: Roots & Perspectives, *Multibody Systems Dynamics*, vol. 1 (2), , pp. 149-188, 1997.

[14] Catalin ALEXANDRU, The energy balance of a pv string equipped with solar tracker, *Annals of the oradea university Fascicle of Management and Technological Engineering*, Issue.1, May 2014.

[15] I. T. Nicoleta and Cătălin Alexandru, Designing the tracking system for a string of photovoltaic modules, *Proceedings of 2011 International Conference on Optimization of the Robots and Manipulators*, February 2012.

[16] M. E. H. Chowdhury, A. Khandakar, B. M. Hossain, R. Abouhasera, A low-cost closed-loop solar tracking system based on the sun position algorithm. J. Sens 2019, pp.1–11, 2019.

[17] S. Palomino-Resendiz, D. Flores-Hernández, N. Lozada-Castillo, A. Luviano-Juárez, High-precision luminosity sensor for solar applications, *IEEE Sens. J. 2019*, pp. 12454–12464, 2019.

[18] J. M. Wang, C. L. Lu, Design and implementation of a sun tracker with a dual-axis single motor for an optical sensor-based photovoltaic system, *Sensors 2013*, vol.13, pp. 3157–3168, 2013.

[20] K. K. Chong, C. W. Wong, Application of on-axis general sun-tracking formula in open-loop sun-tracking system for achieving tracking accuracy of below 1 mrad, *Int. J. Energy Eng. 2011*, vol. 1, pp. 25–32, 2011.

[21] M. A. Ionită, C. Alexandru, Dynamic optimization of the tracking system for a pseudo-azimuthal photovoltaic platform. J. Renew Sustain, *Energy 2012*, 4, 053117, 2012.

[22] Y. M. Safan, S. Shaaban, M. I. Abu El-Sebah, Performance evaluation of a multi-degree of freedom hybrid controlled dual axis solar tracking system, *Sol. Energy 2018*, vol.170, pp.576–585, 2018.

[23] J. Zhang, Z. Yin, P. Jin, Error analysis and auto correction of hybrid solar tracking system using photosensors and orientation algorithm, *Energy 2019*, vol. 182, pp. 585–593, 2019.

[24] H. Mousazadeh, A. Keyhani, A. Javadi, H. Mobli, K. Abrinia, and A. Sharifi, A review of principle and sun-tracking methods for maximizing solar systems output, *Renewable and sustainable energy reviews*, vol. 13, pp. 1800-1818, 2009.

[25] H. S. Park, N. T. Le, Modeling and controlling the mobile harbour crane system with virtual prototyping technology, *International Journal of Control, Automation and Systems volume*, vol. 10, pp. 1204-1214,2012.

LINEAR-TO-ROTARY MOTION TRANSDUCTION BY AN ELECTROTHERMAL ACTUATOR

NGO TIEN HOANG
Faculty of Mechanical Engineering, Industrial University of Ho Chi Minh City;
ngotienhoang@iuh.edu.vn

Abstract. A mechanism to convert linear motion to rotary motion has been studied for application in microelectromechanical systems (MEMs). The means to achieve the linear-to-rotary motion transduction is attributed to a symmetric arrangement of two linear motion inputs. The linear motion is provided by a comdrive actuator suspended by a symmetrical springs system. The translational movement is formed by the electrostatic force that acts between the movable comb-drive acting as V_- and the fixed comb-drive working as the V_+. In order to achieve a transduction ratio of the rotation compared to the linear motion, the Genetic Algorithm is used to optimize the design for the Bézier parametric curve. In this investigation, composite materials consisting of a metal layer and a silicon dioxide SiO_2 layer above and below the metal layer were used to fabricate the structure. With the strong development of science and high technology, this mechanism can be used for enormous optical applications like attenuation, switching diffraction, etc. The behaviors of the transduction mechanism were carried out by using finite element analyses. To meet the fabrication requirements, the mechanism integrating the control circuit will be designed using Cadence Virtuoso software.

Keywords. Linear-to-rotary, motion transduction, comb-drive actuator.

1 INTRODUCTION

In application of hard disk drives [1], positioning stages [2], and micro-manipulators [3], rotary micro positioners emerge as an important and useful conclusion. A rotary micro-positioner actuated by thermal expansion of silicon/polymer composites to acquire the stroke requirements without consuming more power or decreasing the mechanical resonant frequency presented by Lau et al. [1]. In this study, the rotary micro-positioner reaches a 35 kHz sway resonant frequency and produces a six to seven time's larger stroke at the slipper apex than the lateral design. In addition, a pseudo-rigid-body model, a beam deflection theory and a thermal circuit model are presented in this analytical modeling to estimate the electro-thermo-mechanical response. However, the low cut-off frequency and the gain decay are the weaknesses of this rotary micro-positioner. Yi et al. [2] illustrated a 3DOFs micro positioning mechanism compound of flexural hinges. This mechanism has 12 piezoelectric actuators to acquire 2DOFs and 1DOF angular of their platform. In their work, the simulation results are more or less compliant as compared to the experimental results. There are several possibilities for this reason. A rotary stage mechanism includes linear motion inputs and flexural hinges reported by Chao et al [3]. In order to reach high precision, a piezoelectric ceramic element is selected as actuators. Arefin et al. [4] introduced a rotary stage actuated driven by thermal expansion of beam segments. They provided an analytical model to investigate steady state temperature profile along the length of actuator and predict the rotational behavior of the cold segment under driving voltage. In their result, rotational behavior obtained from both FEA and analytical model with that of acquired form testing illustrates close agreement. A produced model used to analyze the steady state behavior of the rotary type micro actuator [5]. It contemplates longitudinal conduction throughout polysilicon structure and heat conduction from the bottom of device goes through the surrounding air to the substrate. A FEA model was figured out by calculating an air volume from the level of top surface of the actuator followed by substrate. The results show good agreement from analytical and existing finite element analysis results of the rotation behavior of the cold segment. To deal with heat conduction from the actuator to the air surrounding, Lin

and Chiao et al. [6] established a parameter named conduction shape factor. Janak et al. [7] developed a thermal actuated free space single crystal silicon micromirror device by using one wafer low-cost fabrication process. The device with a set of four thermal bimorph actuators placed on the opposite sides of a central mirror plate through flexural springs. The micromirror was investigated to obtain up to 10o repeatable angular deflection, 8-13ms thermal response time. However, when the angular deflection was increased more than 10o the switching behavior could not be repeatable. All the structural components of the device are fabricated in single crystal silicon using bulking silicon micromachining technology. The device is useful for optical communication networks or scanning type of applications. Butler et al. [8] used CMOS compatible actuator arrays for positioning surface micro machined scanning and rotating micromirrors. A computer based digital pulse control system was developed for the precise positioning of the mirrors. A piezoelectric material is deformed under the application of electric field. This type of actuator can generate large deflection and force. The advantages of this are that piezoelectric material are high force, high switching speeds, low power dissipation, sensitive to temperature variation and it needs further development in fabrication process to prove its potential. On the other hand, the disadvantage of piezoelectric material is that small strains must be engineered into useful displacement, complex fabrication and nontrivial materials. Zhang et al [9] presented the cantilever actuators which are composed of a PZT thin film on a low stress silicon nitride. The long cantilever achieved a large downward tip displacement of 30 μm with increasing various driving voltages. The measurement results for this geometry agree well with the simulation. Motions of a micro thermal actuator mainly based on its structural topology. The amount of force and deflection will be obtained by relative arrangement of various sections of an asymmetrical thermal actuator. For designing a new actuator, the effects of existing structural topology on the behavior of actuators are vital study for researcher at the beginning. Enikov et al. [10] presented the analytical solution of the electro-thermal and thermo-mechanical problem of Chervon type beam actuators by using the theory of beam columns. The results of analytical predictions, FEA models and experimental observations indicated excellent agreement. However, at higher thermal loading nonlinear effects such as lateral buckling results in reduced tip displacement.

2 OPERATION PRINCIPLES

In this project, we design a compliant linear-rotary transduction mechanism. Figure 1(a) shows a schematic of the mechanism. It consists of a rotary stage, two Bézier curved beams, four serpentine springs and two comb drives. A Cartesian coordinate system is also shown in the figure. When DC voltages, and , are applied the fixed combs and the anchors, respectively, as shown in Figure 2(b), the movable combs are attracted to the fixed combs with a displacement , resulting in a rotary motion of the rotary stage with a rotation angle . Due to geometric symmetry, the center of the rotary stage has no translation in the plane. Figures 1(d) and (e) are enlarged views of the mechanism in the circled area A and B in Figure 1(a), respectively. Geometry parameters of the comb fingers and the serpentine are marked Figures 1(d) and (e), respectively. The original and deformed configuration of the linear-rotary transduction mechanism are represented by solid lines and dashed lines, respectively, in Figure 2. In this project, we use two sets of fixed combs and movable combs to drive the mechanism (see Figure 1(b)). The electrostatic force exerted to the mechanism can be estimated as

$$F_{elec} = \frac{N\varepsilon h}{g_c} V^2 \tag{1}$$

where *N* is the number of combs, h is the depth of the comb, is the gap between neighboring movable comb and fixed comb, ε is the dielectric constant of the medium between combs, and *V* is the voltage bias between the movable combs and the fixed combs. *V* can be expressed as

$$V = V_+ - V_- \tag{2}$$

3 DESIGN

An optimization approach is adopted for design of the mechanism. The objective functions are:

$$Max\ \frac{\theta}{d}$$
$$Min\ \sigma_{max} \tag{3}$$

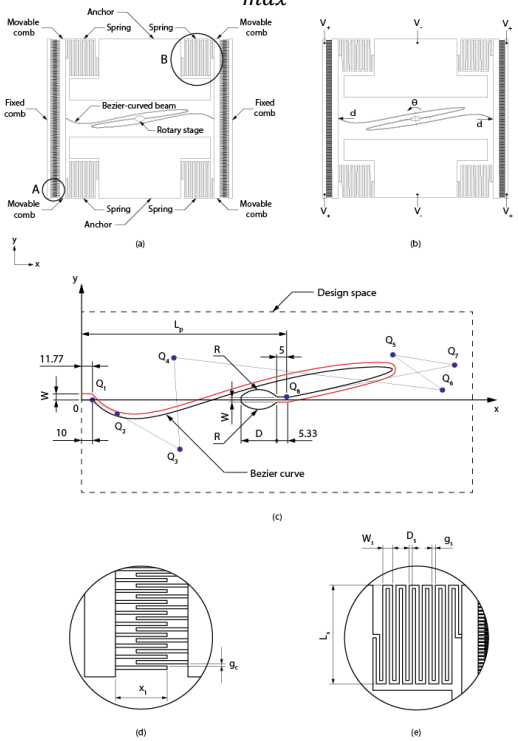

Figure 1: (a) A schematic of a linear-rotary transduction mechanism. (b) Electrostatic actuation of the mechanism. Geometry parameters of the Bézier curved beam and the rotary stage (c); the comb fingers (d); the serpentine spring (e).

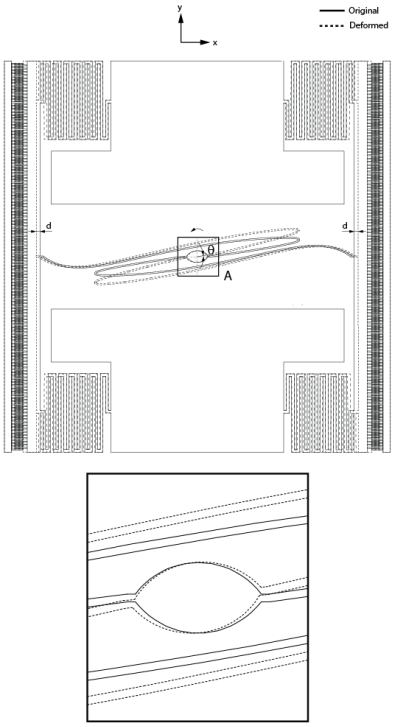

Figure 2: Original and deformed configuration of the mechanism.

where σ_{max} is the maximum von Mises stress of the mechanism. The maximum input displacement is taken as 10um during the optimization process. Based on the Mises yield criterion, the mechanism may yield when σ_{max} is greater than the yield stress of the material of the mechanism. The geometrical parameters *R, D* and *W* of the rotary stage have values of 45 um, 80 um and 5 um, respectively. The design of the mechanism for high transduction ratio $\frac{\theta}{d}$ is optimized via the parameters of the Bézier curved beam. The Bézier curve has eight-point Bézier polygon Q_1, Q_2, Q_3, Q_4, Q_5, Q_6, Q_7, Q_8 as shown in Figure 1(c). The points Q_1 and Q_8 on the curve coincide with the first and last points of the defining polygon as described. The tangent vectors at the ends of the curve have the same directions as the first and last polygon spans, respectively. The parametric Bézier curve is given by:

$$P(t) = \begin{bmatrix} (1-t)^7 \\ 7t(1-t)^6 \\ 21t^2(1-t)^5 \\ 35t^3(1-t)^4 \\ 35t^4(1-t)^3 \\ 21t^5(1-t)^2 \\ 7t^6(1-t) \\ t^7 \end{bmatrix}^T \begin{bmatrix} P_{Q_1} \\ P_{Q_2} \\ P_{Q_3} \\ P_{Q_4} \\ P_{Q_5} \\ P_{Q_6} \\ P_{Q_7} \\ P_{Q_8} \end{bmatrix} \qquad 0 \le t \le 1 \tag{4}$$

where t is the parameter, and P_{Q_i} is the position vector of the point Q_i. The transduction ratio $\frac{\theta}{d}$ is optimized by allowing points Q_2 through Q_7 to move in the design space enclosed by the dashed rectangle in Figure 1(c). The positions of the points Q_1 and Q_8, located at the center of the movable comb and at the right end of the rotary stage, respectively, are fixed. The width of the Bézier curved beam *W* is taken as 5 um. An optimization procedure is developed and outlined in Figure 3. The nondominated sorting genetic algorithm is applied to the optimization of the mechanism. Two-dimensional finite element analysis by a commercial software ABAQUS is utilized to obtain the curve and of the mechanism. 4-node element CPE4R of the finite element program ABAQUS is used for the finite element model. The finite element model has 43620 elements. It is assumed that the out-of-plane motion of the mechanism is small and does not affect its in-plane motion. To design and optimize the profile of the Bézier curved beam and the coordinates of all nodes, the commercial software MATLAB used to perform genetic algorithm optimization procedure.

4 MATERIALS

In this investigation, the mechanism consists of only the metal 6 (ME6) layer and the silicon dioxide above and below the ME6 layer. The metal and oxide are assumed to be linear elastic materials. Their material properties are listed in Table 1. A homogeneous material of the laminate is used in the finite element analyses. The equivalent Young's modulus E_c and Poisson's ratio v_c of the laminate are given by:

$$\begin{aligned} E_c &= f_1 E_{ox} + f_2 E_{al} + \frac{f_1 f_2 E_{al} E_{ox} (v_{ox} - v_{al})^2}{f_1 E_{ox}(1 - v_{al}^2) + f_2 E_{al}(1 - v_{ox}^2)} \\ v_c &= \frac{f_1 E_{ox} v_{ox}(1 - v_{al}^2) + f_2 E_{al} v_{al}(1 - v_{ox}^2)}{f_1 E_{ox}(1 - v_{al}^2) + f_2 E_{al}(1 - v_{ox}^2)} \end{aligned} \tag{5}$$

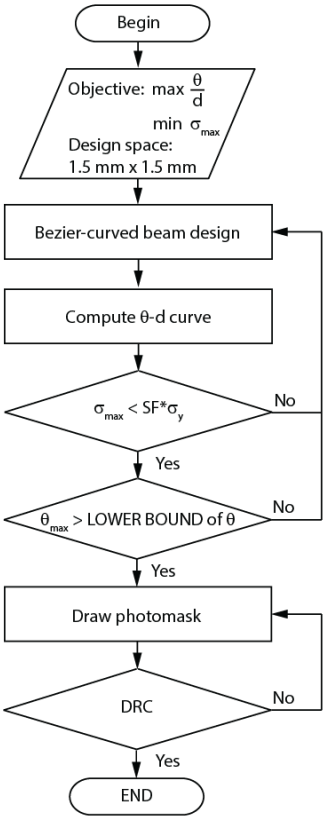

Figure 3: Design flowchart.

where $f_1 = h_1/(h_1 + h_2)$ and $f_2 = h_2/(h_1 + h_2)$ represent the volume fraction of the ME6 layer and the oxide layer, respectively.

Table 1: Properties of the metal, the oxide and the composite.

	Property	Value
Metal	Young's modulus E_{al}	70 GPa
(aluminum)	Poisson's ratio ν_{al}	0.3
	Thickness h_1	2.06 μm
	Density ()	2700 kg m^{-3}
Oxide	Young's modulus E_{ox}	75 GPa
(silicon dioxide)	Poisson's ratio ν_{ox}	0.17
	Thickness h_2	7.80 μm
	Density	2200 kg m^{-3}
Composite	Young's modulus E_c	71.26 GPa
	Poisson's ratio ν_c	0.27

The number of generations is chosen to be 45 and the population of each generation is set to be 30 for the optimization process. Figure 4 shows the dimensions of the optimal design. The dimensions of the comb drive and the serpentine spring are shown in Figures 5(a) and (b), respectively.

5 RESULTS

Figures 6 and 7 shows the $\theta - d$ and $\sigma_{max} - d$ curve of the optimal design of the mechanism based on the finite element analyses. θ and σ_{max} increase as d increases. When the input displacement reaches a value of 9.6 um, the rotation angle has a value of and the σ_{max} is 39.4 MPa, a value well below the typical yield stress of aluminum 124 MPa and oxide 320 MPa.

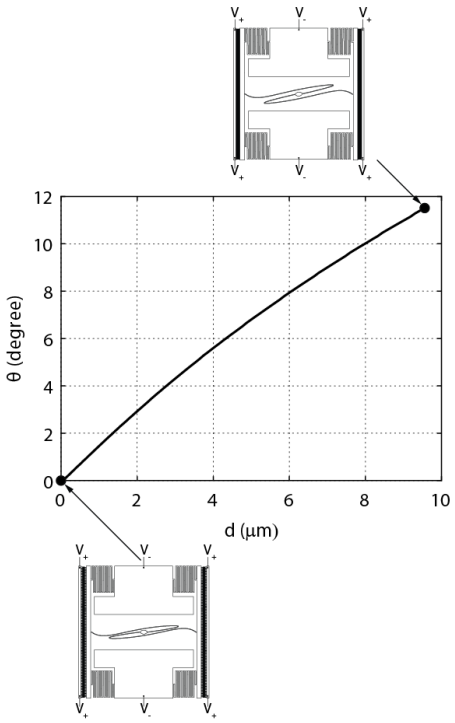

Figure 4: The input displacement versus output angular displacement.

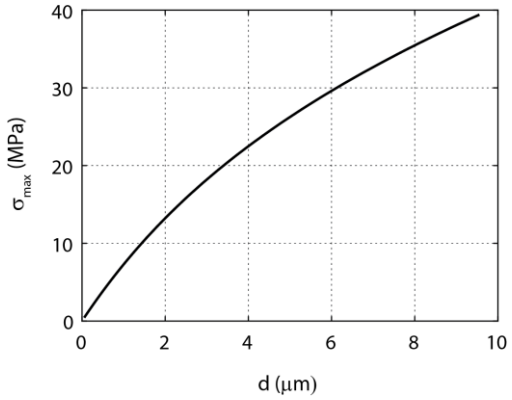

Figure 5: The maximum misses stress versus input displacement curve.

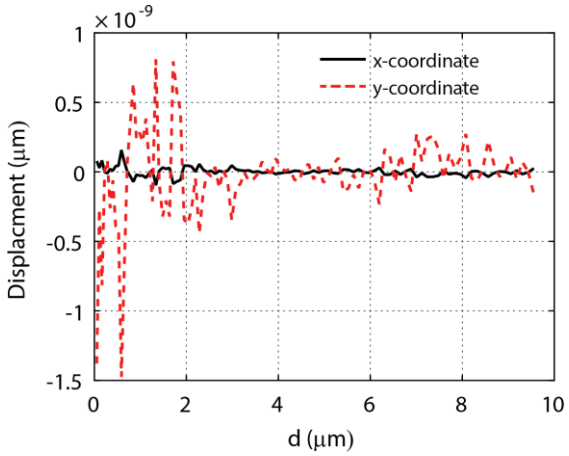

Figure 6: The displacement of the centroid of the rotary stage versus input displacement.

Figure 6 shows the displacement in the x direction and y direction of the centroid of the rotary stage for the input displacement ranging from 0 to 9.6 um based on the finite element analyses. It appears that the centroid has a very small displacement in the range of the input displacement considered.

6 CONCLUSION

Due to the considerable benefits, micro-actuators in MEMS continue to be researched, developed and used for new designs. This study presents a flexible mechanism that converts reciprocating motion into circular motion dynamically. Different design topologies for this actuator are also considered to achieve maximum transduction ratios. The report also presents the design and modeling of motion transmission with comparative results. It is clear that controlling the position of the points of the Bézier parametric curve is quite complicated to achieve the desired goal. The optimization goal will be implemented by the NSGA-II genetic algorithm. The results of the CAE technical analysis show that the reactions and stresses in the structure are within safe levels. In addition, the mechanism achieves a transduction ratio between translation and rotation of approximately 1.2 degrees/μm when the maximum displacement is 9.6 μm. An experimental setup was presented in preparation for testing after the device was built. The structure is machined, packaged in a chip with integrated circuits.

REFERENCES

[1] G. K. Lau, J. Yang, C. P. Tan and N. B. Chong, An electro-thermally activated rotary micro-positioner for slider-level dual-stage positioning in hard disk drives, *J. Micromech. Microeng*, vol. 26, 035016, 2016.

[2] B.-J. Yi, G. B. Chung, H. Y. Na, W. K. Kim and I. H. Suh, Design and experiment of a 3-DOF parallel micromechanism utilizing flexure hinges, *IEEE Transactions on Robotics and Automation*, vol. 19, pp. 604-611, 2003.

[3] D. Chao, G., Zong and R. Liu, Design of a 6-DOF compliant manipulator based on serial-parallel architecture, in *2005 IEEE/ASME International Conference on Advanced Intelligent Mechatronics*, vols. 1 and 2, IEEE (2005), pp. 765–770.

[4] M. Arefin, M. Packirisamy and A. K. W. Ahmed, Disc type thermal actuator with straight beams for angular motion, *Applied Thermal Engineering*, vol. 51, pp. 988-999, 2013.

[5] M. Arefin Anwar, Muthukumaran Packirisamy and A. K. Waiz Ahmed, Electro thermal analysis of rotary type micro thermal actuator, in *Proceedings Volume 5970, Photonic Applications in Devices and Communication Systems*, 597015, 2005.

[6] L. Lin and M. Chiao, Electrothermal responses of lineshape microstructures, *Sensor and Actuators A*, vol. 55, pp. 35-41, 1996.

[7] J. Singh, T. Gan, A. Agarwal, Mohanraj, S. Liw, 3D free space thermally actuated micromirror device, *Sensor and Actuators A*, vol. 123-124, pp. 468-475, 2005.

[8] J.T. Butler, V.M. Bright, J.R. Reid, Scanning and rotating micromirrors using thermal actuators, in *Proc. SPIE 3131, Optical Scanning Systems: Design and Applications*, vol. 134, 1997.

[9] Q.Q. Zhang, S.J Gross, S. Tadigadapa, T.N Jackson, F.T Djuth, S. Trolier-McKinstry, Lead zirconate titanate films for d33 mode cantilever actuators, *Sensor and Actuators A*, vol. 105, pp. 91-97, 2003.

[10] E.T. Enikov, S.S. Kedar, K.V. Lazarov, Analytical Model for Analysis and Design of V-Shaped Thermal Microactuators, *Journal of Microelectromechanical Systems*, vol. 14, no. 4, 2016.

LOWER BACK EXOSKELETON: A NEW DESIGN FOLLOWING THE AUGMENTED MECHANISM PRINCIPLE WITH LOW ENERGY CONSUMPTION

THI TRUC THAO PHAN [1], KHANG HOANG VINH NGUYEN [2], VAN CHI LE [2], XUAN PHU DO [2*]

[1] *Faculty of Mechanical Engineering, HCMC University of Technology and Education (HCMUTE), Ho Chi Minh City, Vietnam,*
[2] *Mechatronics and Sensor Systems Technology, Vietnamese-German University (VGU), Vietnam;*
*thaoptt.ncs@hcmute.edu.vn, khang.nhv@vgu.edu.vn, levanchi1991@gmail.com, *phu.dx@vgu.edu.vn*

Abstract. Back injuries pose a significant occupational health concern that can be mitigated through the use of wearable robots. However, current exoskeletons face limitations in terms of weight, energy consumption, and lifting force. In light of these challenges, this study introduces a new design approach centered around a lockable floating spring mechanism capable of modulating the stiffness and output force without affecting the stored energy. The proposed variable stiffness mechanism is aimed at providing higher stiffness and output forces to support workers when lifting heavy loads, all while minimizing the initial compression force. The dynamic model is formulated based on the proposed structure, and subsequent simulations are conducted to evaluate its dynamic performance. The results demonstrate the promising potential of the proposed mechanism, indicating its applicability in real working conditions. Furthermore, the lockable floating spring mechanism proves to be a viable solution for the development of wearable robots designed to provide lower back support.

Keywords. Back exoskeleton, back injuries, back kinematic, lower back exoskeleton, variable stiffness.

1 INTRODUCTION

In the 21st century, the development of the global economy has resulted in a higher demand for productivity across all economic sectors, especially in construction and industry. However, the repetitive heavy lifting involved in these sectors has detrimental effects on the human spine. According to a 2016 statistic from the American Bureau of Labor Statistics (BLS) [1], back injuries accounted for 16% of non-fatal injuries in construction, with over one million workers experiencing back injuries each year. These injuries rank among the top five workplace injury cases, leading to significant compensation expenses that amount to billions of dollars annually [1].

The load on the human spine is typically a combination of external forces, moments produced during physical activities, gravitational forces, and muscle tension [2]. These loads exert a compression force on the spine, particularly on the lumbar lordosis section (from the sacrum S5 to the thoracic vertebrae T12 [3]), which is primarily responsible for supporting the weight of the human body [4]. The compression force is the highest in the lumbar spine, ranging from 200 N to 300 N in a lying position and increasing up to 1400 N while standing without any external load at a 30-degree trunk angle. External loads can significantly amplify this force, especially during dynamic lifting. Additionally, lifting posture plays a crucial role in low back injuries, with the peak compression force being much higher during stoop lifting compared to squat lifting [5].

Over the past two decades, studies have demonstrated that industrial exoskeletons can reduce total work, fatigue, and load while increasing productivity and work quality [6, 7]. However, back-support exoskeletons face challenges in meeting the stringent requirements for enhancing human capabilities while reducing weight and initial energy consumption [8, 9]. State-of-the-art mechanisms utilizing variable stiffness springs have been developed to address these demands [10, 11, 12], but they come with increased costs due to the high energy required to store energy in the springs [8, 13, 14]. A new approach involves the application of zero-energy cost stiffness modulation theory, enabling independent modulation of stiffness and stored spring energy [15].

This paper introduces a novel mechanism designed to assist the lower back spine, specifically the five weakest lumbar vertebrae, during heavy lifting in a stooped posture. The mechanism utilizes flexible mechanical springs optimized for energy efficiency. It can adjust spring stiffness and stored potential energy independently, generate greater reflected forces during extension, and provide stiffness at any deflection to accommodate a broader range of applications.

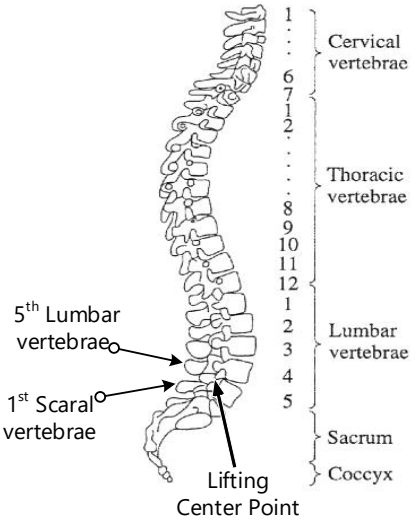

Figure 1: Weak points of the human spine [3].

2 PROPOSED MECHANISM

2.1 Design requirements

The human spine undergoes rotation around the hip during the lifting motion, which impacts the load on the lumbar vertebral disks [15]. Consequently, the mechanism needs to accommodate the ranges of motion (ROM) of the human spine and hips, as well as adhere to the dimensions dictated by human anatomy. The design of the mechanism is constrained by the need to facilitate motion in the sagittal plane. The ROM of the human spine is provided in Table 1 [5].

Table 1: Human spine and hip range of motion.

Parts	Range of motion		
	Flexion	Extension	Lateral bending
Trunk	~180°	~50°	~50°
Extension	~60°	~30°	~20°
Hip	~120°	~15°	Abduction~50°
			Adduction~30°

The purpose of the back exoskeleton is to alleviate compression and shear forces that contribute to low back pain in the lumbar vertebral disks. An analytical model can be employed to estimate the impact of the assistive force on reducing forces in the human spine and muscles [5]. Figure 2 illustrates the force analysis of a human bending over to lift a box. The force equilibrium between the human and the exoskeleton mechanism is described as follows:

$$F_e.D_e = -F_{exo}.D_{exo} + M_{load}.g.D_{load} + M_{hm}.g.D_{hm} \quad (1)$$

$$F_{com} = F_e + M_{hm}.g.cos\theta + M_{load}.g.cos\theta \quad (2)$$

$$F_{sh} = -F_{exo} + M_{hm}.g.sin\theta + M_{load}.g.sin\theta \quad (3)$$

where, F_{com} and F_{sh} are compressive and shear forces; M_{hm} and M_{load} represent the masses of the human and load; F_e is the lumbar muscle force; F_{exo} represents the force generated by the back exoskeleton; D_{load}, D_{exo}, D_{hm}, and D_e are the force arms of the load, exoskeleton mechanism, human, and muscle, respectively. Simultaneously increasing the exoskeleton force will result in the reduction of the erector muscle force, compressive force, and shear force. Furthermore, the detrimental effects on the lumbar region during load

lifting are also mitigated.

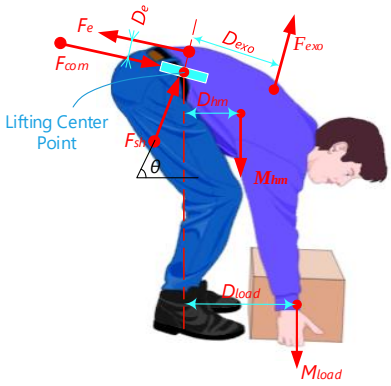

Figure 2: Human lifting force analysis.

2.2 Lockable floating spring mechanism design

The proposed mechanism is depicted in Figure 3(a) and consists of two rigid links connected by a cylindrical joint. It also includes a constant stiffness spring with an adjustable position. The endpoints of the spring are attached to two sliders that can move along the rigid links, altering the position values of x while keeping the spring length locked at $l = l^*$. In Figure 4, the upper endpoint of the spring is shifted from x_{11} to x_{12} resulting in a change in the force deflection relative to the mechanism. This adjustment enables in increase in output force at the same deflection q.

The design of the adjustable spring mechanism is illustrated in Figure 3(b). It consists of two linear bars connected by a cylindrical joint, and each endpoint of the spring is held by lockable sliders. To control the positions of the spring during working cycles, a motor and timing belt system, as depicted in Figure 3(c), are utilized.

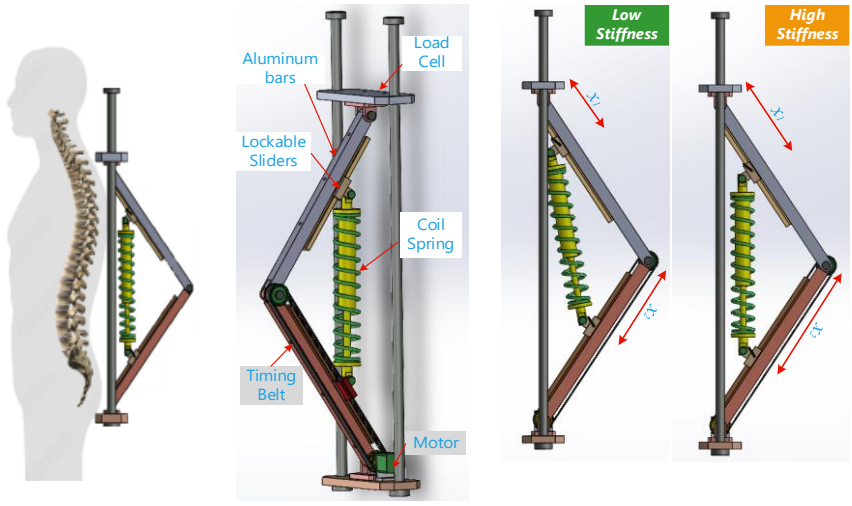

(a) (b) (c)

Figure 3: Proposed mechanism: (a) Configuration, (b) Detailed structure, (c) Stiffness variations.

The operating principle, as depicted in Figure 4, involves three steps: compressing the spring to the desired value and locking its length, moving it to a new position, and releasing the stored energy at maximum output force and stiffness. Initially, the two endpoints of the spring are locked to the inflexible links, and the spring is compressed to the desired value (indicated in black). Subsequently, the length of the spring is locked, and it is moved to its new position (indicated in red). Since the length of the spring is locked, no energy is released during the movement of the spring from its upper to lower positions. Once again, the endpoints of the spring are locked to the mechanism, and its length is released. As a result, the spring extends and releases the stored energy during compression, but at a higher output force and stiffness.

3 STIFFNESS MODULATION ANALYSIS

The mathematical model of the proposed structure is presented in Figure 4. In this figure, the initial positions are denoted as x_{11} and x_{21}, while the desired positions are represented by x_{12} and x_{22}. The deflection is indicated as q, and the output force is denoted as $F(q)$.

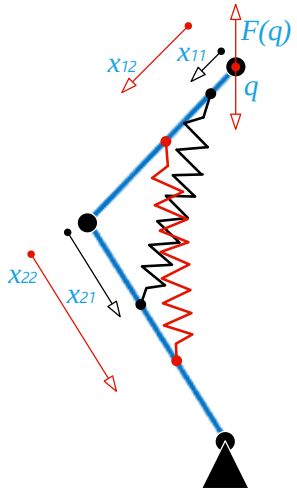

Figure 4: Mathematical model of the proposed mechanism.

The potential energy of the movable spring can be expressed as:

$$V = \frac{1}{2} k_s \Delta l(q, x1, x2)^2 \tag{4}$$

where, k_s represents the stiffness of the spring, and Δl is the change in the spring length determined by the resulting position and two variables, x_1 and x_2. The output force and output stiffness can be calculated using the following equations:

$$\mathrm{F} = -\frac{\partial \mathrm{V}}{\partial \mathrm{q}} = k_s \Delta l(q, x_1, x_2) \frac{\partial \Delta l(q, x_1, x_2)}{\partial q} = F_s \frac{\partial \Delta l(q, x_1, x_2)}{\partial q} \geq F_s \tag{5}$$

$$\mathrm{k} = \frac{\partial^2 V}{\partial^2 q} = k_s \left(\frac{\partial \Delta l(q, x_1, x_2)}{\partial q} \right)^2 + k_s \Delta l(q, x_1, x_2) \frac{\partial^2 \Delta l(q, x_1, x_2)}{\partial q^2} > k_s \tag{6}$$

The condition for the independence of energy stored by the spring with respect to the change of position, δx_1, and δx_2, can be determined as:

$$\forall q: \delta \mathrm{V} = \frac{\partial \mathrm{V}}{\partial x_1} \delta x_1 + \frac{\partial \mathrm{V}}{\partial x_2} \delta x_2 = 0 \tag{7}$$

The condition for stiffness at any output variation is determined as follows:

$$\forall q: \delta \mathrm{k} = \frac{\partial \mathrm{k}}{\partial x_1} \delta x_1 + \frac{\partial \mathrm{k}}{\partial x_2} x_2 \neq 0 \tag{8}$$

The design of the proposed variable stiffness mechanism focuses on meeting the requirement that the deflection δx_1, δx_2 can be modified simultaneously satisfy equations (7) and (8). Equation (7) can be satisfied if the endpoint positions of δx_1, δx_2 remain unchanged, meaning that no mechanical work needs to be done: $\delta V = -F_1 \delta x_1 - F_2 \delta x_2 = 0$. However, the condition in equation (8) cannot be satisfied. It is possible to use sub-motors to independently change the positions x_1, x_2. However, it is important to note that no mechanical work does not imply no energy cost, as electric motors require energy to generate static forces. Another method can be employed to satisfy equation (7) by ensuring that the input motors are not affected by the spring force:

$$\forall q : F_{1,2} = 0 \tag{9}$$

The design of the variable stiffness mechanism aims to satisfy the condition (9) without being influenced by the output positions q. This condition not only ensures that the input motors do not perform mechanical work but also allows for the use of small input motors to demonstrate the independence of stiffness modulation from the energy stored in the spring. By locking the movable spring, conditions (7) and (9) can be satisfied:

$$\forall q: \Delta l^* = \Delta l(q, x_1, x_2) \tag{10}$$

Locking the spring leads to the following condition:

$$\forall q: \Delta l^* = \frac{\partial \Delta l}{\partial x_1}\delta x_1 + \frac{\partial \Delta l}{\partial x_2}\delta x_2 = 0 \tag{11}$$

As a result of equation (11), the potential energy stored in the spring remains constant regardless of changes in q, x_1, x_2:

$$\forall q:\ V^*(q, x_1, x_2) = \frac{1}{2}k_s \Delta l^{*2} = constant \tag{12}$$

The outcome of equation (12) demonstrates that by using locking mechanisms, it is possible to modify the stiffness of the mechanism (5). Consequently, the released force during extension (6) in work cycles increases irrespective of the stored energy. This provides additional force to support workers when lifting heavy loads.

4 SIMULATION RESULT AND DISCUSSION

A simulation of the proposed mechanism was conducted to demonstrate the force-deflection and stored energy-deflection characteristics. Figure 5(a) depicts the force-deflection relationship, while Figure 5(b) illustrates the stored energy-deflection relationship. The results indicate that the spring releases higher forces and exhibits greater stiffness during extension, even at the same stored energy. By employing a lockable sliding mechanism, the spring can be locked while the stiffness changes with a small applied force at one endpoint, regardless of the stored energy. As a result, the energy required to adjust the stiffness is independent of the stored energy in the spring and the output deflection. This additional force capability can effectively support workers in lifting heavy loads.

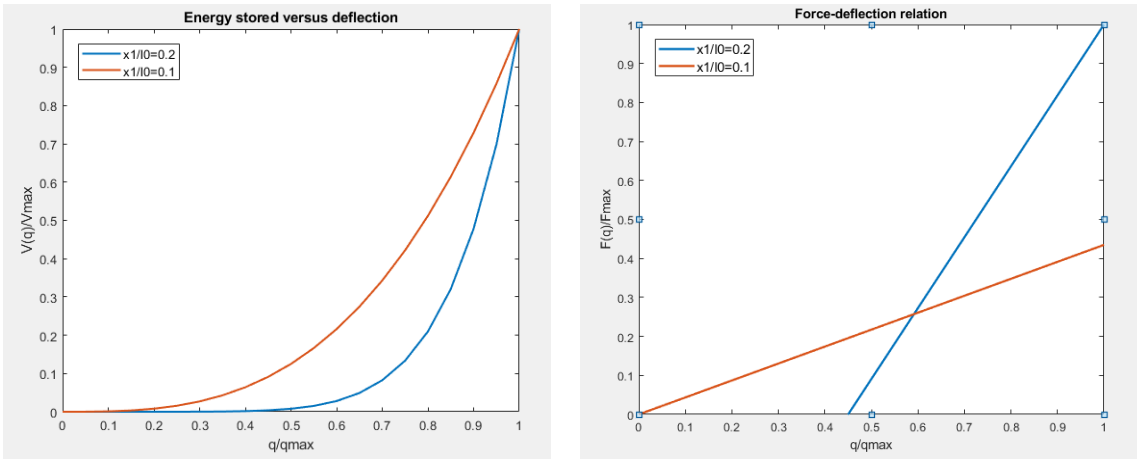

(a) (b)

Figure 5: Simulation results: (a) force versus deflection (b) stored energy versus deflection.

In general, the simulation illustrates that the proposed concept can be further developed to design a new mechanism that supports employees when lifting heavy loads in work conditions. The results clearly demonstrate that by utilizing locking mechanisms, it is feasible to adjust the stiffness of the mechanism and enhance the released force during extension in work cycles, all without impacting the stored energy. This capability provides an additional force to support workers who are lifting heavy loads.

5 CONCLUSION

This paper introduces a novel lockable spring mechanism that allows for independent modulation of spring stiffness without affecting the energy stored in the spring. The mathematical model of this innovative structure was derived, and its features were validated through simulation. The proposed design successfully demonstrates that stiffness modulation of the spring can be achieved at any deflection with minimal energy consumption. The simulation results also indicate that the spring is capable of generating higher forces and stiffness during extension in work cycles, thereby providing additional support for workers engaged in

lifting heavy loads. This concept can be applied to the design of a new mechanism aimed at assisting the lower back spine, particularly the five weakest lumbar vertebrae, during the lifting of heavy objects in a stooped posture. The mechanism utilizes flexible mechanical springs following optimized energy principles. Furthermore, the model can be extended to design upper exoskeletons, specifically targeting the upper-shoulder-arm and elbow regions. In future developments, the proposed structure will be enhanced with a magnetorheological damper, and its performance will be compared with existing models.

6 ACKNOWLEDGMENT

This research is funded by the Ministry of Education and Training (Vietnam) under grant number B2024-VGU-02.

REFERENCES

[1] The Bureau of Labor Statistics (BLS), Back injuries prominent in work-related musculoskeletal disorder cases in 2016, in *Injuries, Illness, and Fatalities*, 2018.

[2] N. Boos and M. Aebi, Spinal disorders : fundamentals of diagnosis and treatment, New York: Springer, 2008.

[3] Britannica, The Editors of Encyclopaedia, Vertebral column, in *Encyclopedia Britannica*, Encyclopædia Britannica, Inc., 2023.

[4] B. Bazrgari, A. Shirazi-Adl and N. Arjmand, Analysis of squat and stoop dynamic liftings: muscle forces and internal spinal loads, *European spine journal : official publication of the European Spine Society, the European Spinal Deformity Society, and the European Section of the Cervical Spine Research Society*, vol. 16, no. 5, pp. 687–699, 2007.

[5] X. Yang, T. H. Huang, H. Hu, S. Yu, S. Zhang, X. Zhou, A. Carriero, G. Yue and H. Su, Spine-Inspired Continuum Soft Exoskeleton for Stoop Lifting Assistance, *IEEE Robotics and Automation Letters*, vol. 4, no. 4, 2019.

[6] D. E. Fournier, M. Yung, K. G. Somasundram, B. B. Du, S. Rezvani and A. Yazdani, Quality, productivity, and economic implications of exoskeletons for occupational use: A systematic review, *PLOS ONE*, vol. 18, 2023.

[7] M. Looze, T. Bosch, F. Krause, K. Stadler and L. O'Sullivan, Exoskeletons for industrial application and their potential effects on physical work load, *Ergonomics*, vol. 59, pp. 1-11, 2015.

[8] H. F. Lau, A. Sutrisno, T. H. Chong and D. J. Braun, Stiffness Modulator: A Novel Actuator for Human Augmentation, in *IEEE International Conference on Robotics and Automation (ICRA)*, 2018.

[9] S. Toxiri, A. Calanca, T. Poliero, D. G. Caldwell and J. Ortiz, Actuation Requirements for Assistive Exoskeletons: Exploiting Knowledge of Task Dynamics, in *Wearable Robotics: Challenges and Trends*, Springer International Publishing, 2019, pp. 381-385.

[10] A. Sutrisno and D. Braun, How to run 50% faster without external energy, *Science Advances*, vol. 6, no. 13, 2020.

[11] A. Jafari, N. G. Tsagarakis and D. G. Caldwell, A Novel Intrinsically Energy Efficient Actuator With Adjustable Stiffness (AwAS), *IEEE/ASME Transactions on Mechatronics,* vol. 18, pp. 355 - 365, 2013.

[12] T. Sugar and K. Hollander, Adjustable stiffness leaf spring actuators. USA Patent US7527253B2, 09 06 2006.

[13] Y. Lu, Y. Yang, Y. Xue, J. Jiang, Q. Zhang and H. Yue, A Variable Stiffness Actuator Based on Leaf Springs: Design, Model and Analysis, *Actuators,* vol. 11, 2022.

[14] S. Y. Kim and D. J. Braun, Novel Variable Stiffness Spring Mechanism: Modulating Stiffness Independent of the Energy Stored by the Spring, in *2021 IEEE/RSJ International Conference on Intelligent Robots and Systems (IROS)*, 2021.

[15] J. Liu, Y. He, J. Yang, W. Cao and X. Wu, Design and analysis of a novel 12-DOF self-balancing lower extremity exoskeleton for walking assistance, *Mechanism and Machine Theory*, vol. 167, 2022.

APPLICATION OF RESIN 3D PRINTING IN MAKING PATTERN FOR INVESTMENT CASTING: A REVIEW

HUU NGHI HUYNH [1,3*], TAN PHAT CAO [1,3], DINH TAM NGO [1,3], TRONG HIEU BUI [2,3]

[1] *Division of Manufacturing Engineering, Faculty of Mechanical Engineering, Ho Chi Minh City University of Technology (HCMUT), 268 Ly Thuong Kiet Street, District 10, Ho Chi Minh City, Vietnam,*
[2] *Division of Machine Design, Faculty of Mechanical Engineering, Ho Chi Minh City University of Technology (HCMUT), 268 Ly Thuong Kiet Street, District 10, Ho Chi Minh City, Vietnam,*
[3] *Vietnam National University Ho Chi Minh City, Linh Trung Ward, Thu Duc City, Vietnam;*
hieubt@hcmut.edu.vn, phat.caoky1410@hcmut.edu.vn, tam.ngodinh124@hcmut.edu.vn,
**hhnghi@hcmut.edu.vn*

Abstract. Due to its capability to meet essential requirements such as high accuracy and superior surface quality, AM (Additive Manufacturing) resin has a lot of potential for use in the production of investment casting. Selecting and adjusting the proper process parameters as well as controlling variables that have an impact on the manufacturing process's quality are important to produce a high-quality investment casting. Because desktop resin may be produced at a lower cost and in a smaller size, scientists have been researching its usage in pattern casting in recent years. The goal of this research is to examine the AM resin's technological characteristics and how they affect the final product's quality. From there, further research directions are suggested which will result in better casting samples, higher productivity, and more cost-effective manufacturing pattern processes employing AM desktop or open-source equipment suitable for the circumstances of developing nations, such as Viet Nam. The findings indicate that technological factors such as slice thickness, exposure period, and build orientation have the biggest effects on the objective. Support parameters also require more research in order to speed up manufacturing and conservation materials.

Keywords. AM resin, desktop equipment, effect of technological parameters, investment casting, technological parameters.

1 INTRODUCTION

In many industries, additive manufacturing (AM) technology is employed to produce "samples" or "products" prior to mass production or commercialization. Using layer-by-layer addition and bonding of materials, additive manufacturing (AM) constructs products by creating a cross-section of the final object from the original CAD data. Material Extrusion, Vat Photopolymerization, Binder Jetting, Direct Energy Deposition, Sheet Lamination, Powder Bed Fusion, and Material Jetting are the seven categories of AM technology which are organized in accordance with ASTM International standards [1]. This technology is developing and expanding in popularity. The statistical data by Wohlers [2] demonstrated the versatility of AM technology. As a result, the cost of production utilizing AM technology rises annually. According to Wholer, the cost of production utilizing this technology would be close to $1.5 billion by 2019. Prototyping for the process of pattern casting accounts for 9% of all other uses. When compared to conventional methods, using AM technology speeds up prototyping while maintaining quality, which improves the pattern casting method of product manufacture.

Otto Munz first proposed the concept of AM resin in 1956 [3], and Hideo Kodama from the Nagoya Municipal Industrial Research Institute demonstrated the use of UV light in the creation of 3D objects in 1981 [4]. When Charles Hull invented, commercialized, and patented the first 3D printer in 1986, he also created the word "Stereolithography" [5]. The following technologies can be used to categorize AM resin: Stereo Lithography Appearance (SLA), Digital Light Processing (DLP), Liquid Crystal Display (LCD),

Multi-jet Printing (MJP), Continuous Liquid Interface Production (CLIP), and Two-photon 3D Printing (TPP) [6]. SLA, DLP, and LCD technologies are among them, and they are the three most widely used ones today. The first method, in particular, is SLA, which uses laser energy to harden liquid photosensitive plastic materials (regulated in accordance with a pre-programmed profile). The only technology that can produce large-scale items is SLA. However, this technology has a very low productivity. SLA technology will have a lower resolution than other resin technologies since the resolution of the SLA technology depends on the size of the laser [6]. DLP technology, on the other hand, solidifies plastic materials using projector energy [7]. A projector directs light from tens of thousands of small mirrors known as DMDs (Digital Micromirror Devices) to cover the whole area of a section and solidify the necessary plastic portions [8]. Small-scale product fabrication uses DLP. At the same time, DLP is relatively expensive [6]. Like DLP, LCD technology also employs the LCD screen's energy source to harden the plastic into the desired cut shape. This technology is inexpensive and offers a modest resolution.

Photosensitive resin is the substance that is utilized to make AM resin [6]. Photochemical resin procedure is the name of the process used to harden the resin. UV light is used to start this process, which is used to link the polymers together to make solid objects by shining it into the plastic tank. Three elements monomer, oligomer, and photoinitiator are contained within the resin. A catalyst for the bonding process between monomers and oligomers will be released by the photoinitiator under the influence of UV light, causing the resin to solidify [7]. Manufacturers have introduced specialized resins, such as Wax Castable Resin [9], which the producer claims is akin to wax, to suit the need for using AM resin technology in casting. It is utilized for jewelry, particularly surface samples and samples with stone settings, and it burns cleanly following the lost wax process. Dark Sharp Castable Resin [10], the second option, is a resin that works well, for example with fine features and stone settings.

The processes in the overall procedure used to create AM resin products are as follows: converting concepts into 3D models with CAD tools like Inventor, SolidWorks, etc. The 3D model will be made once everything is finished and converted into STL format. Specialized software is used to edit and perform "slicing" on STL files. The slicing program for AM resin technology generates a series of photos for each layer of the 3D model. The technical parameters, support production, and positioning are all under the control of the slicing program [11]. There are several popular slicing programs, including Chitubox, Lychee Slicer 3, Photon Workshop, etc. The process of creating things using 3D printing technology follows the completion of the slicing. The following categories apply to these gadgets: In terms of technological security, desktop and industrial equipment is included, as is equipment that is open and closed source. These devices differ mostly in terms of product size, quality, and price. After fabrication, the product is taken off the machine plate, cleaned, and subjected to post-processing, which may involve removing the support, washing with an appropriate solution, like alcohol, exposure in a UV chamber, and sanding the product's surface. Numerous variables affect the quality of AM resin products, but the selection and setup of technical parameters are the most crucial.

2 TECHNOLOGICAL PARAMETERS

Product parameters and Support structure parameters are two categories for the technical parameters.

2.1 Product parameters

Build orientation: The sample is in this position and tilted at this angle in the printer's three axes (X, Y, and Z). Build orientation is a parameter that impacts the sample's error probability, flexural strength, adhesion between layers [12], dimensional correctness, and force-resistance [13].

Layer thickness: This represents a single layer's thickness in the printing direction (often the Z axis). The typical layer height for resin 3D printing is 0.05 mm. This parameter is also a crucial one that influences the sample's flexural strength [14], surface roughness [15], and tensile strength [16].

Exposure time: This is a significant parameter, just like the previous two. This is how long a UV light source needs to cure (or harden) a layer. The exposure time will vary for various materials. In addition to layer thickness and build orientation, exposure duration is another parameter that affects the sample's numerous properties, including dimension accuracy [16], flexural strength [14], surface roughness [15], etc.

Bottom layer count: is the number of first layers to be printed, and first layers typically have exposure times that are longer than second layers. These layers aid the sample's grip on the printing platform, preventing falling and other printing mistakes. A light source's service life will be shortened by an excessive adjustment to the number of bottom layers, which will also lengthen the lead time and working time of the light source. Experience suggests that there should be five or more of these layers.
Bottom layer exposure time: Bottom layers have exposure time just like top layers do. In contrast to upper layers, bottom layers will be exposed for a longer period of time. This amount should be 8–12 times more than the exposure duration for typical layers, per Chitubox's recommendation. The printing process will take longer if the exposure period is too long. The grip of these initial layers will not be ensured, though, if the exposure duration is too brief.

2.2 Support structure parameters

Three components, including top, bottom, and center, will make up the supporting framework of objects made with resin during 3D printing. Since the top support structure has a direct relationship to the sample, the top support structure's specifications will have an impact on the sample's surface quality. The component that attaches the printing platform to the sample is made up of the bottom support structure and the middle support structure. The characteristics of these two structures will determine how well the sample adheres to its platform. The support structure has a raft in addition to the previously mentioned three components. Between the printing platform and the bottom support structure, there are layers in the raft. The raft has the effect of improving the bottom support structures' platform stickiness. Additionally, the raft aids in uniting the bottom support structures into one block, making it simpler to remove the sample off the printing platform. However, using a raft requires more material.
Muslim Muhktarkhanov et al.'s research from 2020 [2] indicated that a pattern for the investment casting process must satisfy specifications like high accuracy, low melting temperature, good surface quality, hardness, durability and leaving no ash after finishing wax process. Since then, the purpose of this paper is to find out how those process factors affect the sample's accuracy, mechanical characteristics (flexural strength, tensile strength), and surface quality. Following that, to enhance the sample's quality with the intention of using resin 3D printing technology to create investment casting patterns. To achieve that goal, this research bases its findings on analysis of each technological aspect to determine how it affects the sample's quality.

3 EFFECT OF TECHNICAL PARAMETERS ON SAMPLES QUALITY

3.1 Dimensional accuracy

Dimensional accuracy is an important factor for casting. J. S. Shim et al. [12] studied the effect of build orientation on the dimensional accuracy by testing with rods specimens designed according to ISO 178 with dimensions of 80 × 10 × 4 mm on an SLA machine. The results showed that build orientation 900 gives the lowest error rate in length and build orientation 450 gives the highest error rate in thickness. A. Unkovski et al [13] conducted the experiment with a bar specimen designed according to DIN EN ISO 4049 with dimensions of 30 × 5 × 5 mm. The results showed that the vertical dimensions of the SLA samples were more prone to deviation than the other two directions, and the sizes of the SLA samples at the edge of the print bed are more prone to deviation than when in the center position. A. Ibrahim et al [16] studied the influence of two parameters, layer thickness and exposure time, on the dimensional accuracy of samples generated by DLP technology. The results showed that when the layer thickness and exposure time parameters were 0.05 mm and 9 s, the size deviation would reach 3.8%. S. L. Sherman et al. [17] reported that layer thickness values of 0.05 mm and 0.1 mm and at the center of the table an open-source 3D printer would give an acceptable dimensional accuracy of the DLP sample. In addition, temperature was also a parameter that affects the dimensional accuracy of the product. A. Katheng et al. [18] studied the effect of temperature on sample dimensional accuracy and showed that low temperature corresponded to tolerances and geometric tolerance of samples fabricated by SLA technology. S. L. Campanelli et al. [19] studied to optimize the parameters including Hatch Overcure (HO), Border Overcure (BO) and layer thickness to

dimensional accuracy. The prototype was designed according to the following criteria: there were small and medium sizes to apply to small details such as jewelry, without consuming too many materials and manufacturing time. The research team has determined the optimal set of parameters as follows: for layer thickness of 0.05 mm, HO = 0.25 mm and BO = 0.225 mm; for layer thickness 0.1 mm, HO = 0.05 mm and BO = 0.3 mm. P. Zmarzly et al [20] studied the possibility of applying AM technology to the casting process with samples fabricated by AM. The results showed that the product after casting has a size deviation of about 5%. Meanwhile, A. Iftikhar et al [21] has studied and fabricated turbine blades using FDM technology and resin with the size of 30.2 × 44.2 × 88.5 mm. The authors say that SLA technology has dimensional accuracy less than 160 μm and FDM has dimensional accuracy greater than 240 μm. A. L. Giudice et al. [22] evaluated the dimensional accuracy of dental samples fabricated on three different devices, including two common types, Anycubic Photon S, Elegoo Mars Pro and EnvisionTEC Vector 3SP specialized equipment. The results showed that conventional 3D printing equipment for samples had lower dimensional accuracy. M. N. Islam et al. [23] did a comparative study on dimensional accuracy between two SLAs and PBP technologies with the same test sample. The results showed that the SLA product has better dimensional accuracy in the Z-axis while PBP gave the product with better dimensional accuracy in the X, Y directions. G. Budzik [24] compared the propeller prototyping capabilities of the two technologies SLA and 3DP and found that the propeller made by SLA technology gave higher dimensional accuracy than 3DP technology. Besides dimensional accuracy, the mechanical properties of the sample such as flexural strength, tensile strength, impact resistance were also factors that scientists are interested in studying.

3.2 Mechanical properties

The mechanical properties (flexural strength, tensile strength…) of AM resin products are also influenced by technological parameters. Romli el al. [14] also studied the effect of layer thickness and exposure time on the flexural strength of samples created by AM DLP technology. The test samples were designed according to ASTM 7790. The results showed that the layer thickness affects 10%, exposure time affects 2% on the flexural strength of the sample and the interaction between the two parameters to the target is 87%. R. Bangalore et al. [16] studied the effect of layer thickness, build orientation and line spacing parameters on flexural strength, tensile strength, and impact resistance of SLA test specimens. The tensile strength test specimens were designed according to ASTM D638-01, the flexural strength test specimens were designed according to ASTM D790-03 and the impact resistance test specimens were designed according to ASTM D256-04. The results showed that all parameters affected the target and the optimal set of parameters found includes: layer thickness 0.125 mm, build orientation 90^0 and hatch spacing 0.015 mm. J. S. Shim et al. [17] showed that the build orientation had a value of 90^0 for the sample with the lowest flexural strength and A. Ibrahim et al. [22] showed for a parameter set consisting of layer thickness 0.05 mm, an exposure time of 9s would give the sample high flexural strength and tensile strength valued with tensile strength and flexural strength valued of 8.98 N/mm^2 and 18.39 N/mm^2 respectively.

3.3 Surface quality

In addition to the two factors mentioned above, surface quality is also one of the quality criteria that should be paid special attention to the sample used for the casting process. The improvement of surface quality will reduce the time for post-processing making the casting process more optimal. Like dimensional accuracy and mechanical properties, surface quality is also influenced by technological parameters. D. P. Putra et al [15] studied optimizing the parameters for DLP 3D printers with the desire to achieve the lowest surface roughness. Parameters included layer thickness, exposure time and bottom layer exposure time. The bar specimen has dimensions of 30 × 15 × 4 mm. The results showed that with the obtained optimal set of parameters including layer thickness 0.035 mm, exposure time 19,542s and bottom layer exposure time 60,679s. Then the surface roughness of the sample had a value of 0.469 μm. At the same time, the authors also concluded that the DLP 3D printer could fabricate samples with high dimensional accuracy and detailed surface. A. Iftikhar et al [21] showed that AM resin gave the product a higher surface quality than FDM with the surface roughness of the resin sample being 0.866 μm and the FDM sample being 1,345 μm. A. Tulcan et al. [25] studied the influence of support on the quality of flat and curved surfaces of 55 × 35×5

mm test pieces with 3 bobbins and 3 cylinders with sequential diameter values are 5 mm, 10 mm and 15 mm and height 10 mm. The test results compared with the ISO 2768-2 standard, showed that a support density in the range of 50% - 52% will give a good flat surface quality. C. Arnold et al. [26] studied the effect of layer thickness, support, sample position and build orientation on the surface roughness of SLA samples. Experimental results showed that the SLA sample has a much smoother surface than the one made by the turning method.

4 DISCUSSION

Due to its advantages, resin 3D printing is used in many sectors with a lot of potential. Investment casting is one of these fields. High precision and an excellent surface polish are needed for molded samples. Another benefit of this technology is cost reduction compared to the conventional approach. In order to facilitate this process, plastic producers have introduced a variety of resins having wax-like characteristics. These resins are frequently known as castable resin such as: Dark Sharp Castable Resin, Wax Castable Resin. With this resin, there won't be any leftover ash from the casting process burning to enhance the final product. Additionally, this application is a study topic. Numerous studies have been conducted in this area with the goal of enhancing the investment casting process through technological considerations, such as comparing shell thickness or simply evaluating the pattern-making abilities of various 3D printing technologies. Accordingly, many studies are based on different experimental methods with the aim of evaluating the influence of technological parameters on the dimensional accuracy, mechanical properties and surface quality of casting pattern. Test specimens in many researches are often used according to ISO and ASTM standards to evaluate dimensional accuracy, mechanical properties, surface roughness. However, the majority of the apparatus used in many current researches are industrial apparatus. Therefore, researchers are also concentrating on managing and altering technological parameters on open source, desktop equipment with strong production process to help reduce costs and suitable for the condition of developing countries.

5 CONCLUSION

Technological characteristics have a significant impact on the sample quality, as may be demonstrated by surveys of technological parameters and research studies. The parameter that has generated the most interest in research is layer thickness. This suggests that this factor has the greatest impact on the quality of the final result. Additionally, the settings for build orientation and exposure time are crucial elements. Particularly, the layer thickness, orientation, exposure time, temperature, and sample location have an impact on dimensional accuracy. The parameters of layer thickness, exposure duration, orientation, hatch spacing (SLA technique), and material all have an impact on the specimen's mechanical characteristics, including flexural strength, tensile strength, and impact resistance. The characteristics of layer thickness, exposure time, initial layer exposure time, support structure, pattern orientation, and sample position all have an impact on the surface quality of the sample. Because the support structure is the component immediately related to the surface of the sample in further study, improving its parameters will assist increase the surface quality and accuracy of the sample. The casting process will be improved with the use of AM technology by optimizing these parameters, which will also assist in cutting down on the amount of time and resources needed for prototypes.

6 ACKNOWLEDGEMENT

We acknowledge Ho Chi Minh City University of Technology (HCMUT), VNU-HCM for supporting this study.

REFERENCES

[1] The International Organization for Standardization (ISO)/ American Society for Testing and Materials (ASTM) 52900:2015 standard.

[2] M. Mukhtarkhanov, A. Perveen, and D. Talamona, Application of Stereolithography based 3D printing technology in investment casting, *Micromachines,* vol. 11, pp. 1-27, 2020.

[3] M. O. John, "Photo-glyph recording", US2775758A, 1956.

[4] H. Kodama, Automatic method for fabricating a three-dimensional plastic model with photo-hardening polymer, *Review of Scientific Instruments*, vol. 52, pp. 1770-1773, 1981.

[5] C. W. Hull, Apparatus for production of three-dimensional objects by stereolithography, US4575330A, 1986.

[6] H. Quan et al, Photo-curing 3D printing technique and its challenges, *Bioactive Materials,* pp. 110-115, 2020.

[7] M. Pagac et al, A Review of Vat Photopolymerization Technology: Materials, Applications, Challenges, and Future Trends of 3D Printing, *Polymers*, vol. 13, pp. 2-10, 2021.

[8] (2022) SLA vs DLP vs LCD 3D Printing. "Which Is Best?". [Online]. Available: https://www.3dsourced.com/3d-printing-technologies/sla-vs-dlp-3d-printing.

[9] (2022) WAX Castable Resin."Powerresins". [Online]. Available: https://powerresins.com/products/powercast-wax-castable-resin.

[10] (2022) DARK Sharp Castable Resin. "Powerresins". [Online]. Available: https://powerresins.com/products/powercast-dark-castable-resin-for-jewelry-dlp-led.

[11] (2022) The Best Resin/SLA. "3D Printer Slicer Software of 2022. All3DP 2022". [Online]. Available: https://all3dp.com/2/sla-slicer-resin-printer.

[12] J. S. Shim et al, Printing accuracy, mechanical properties, surface characteristics, and microbial adhesion of 3D-printed resins with various printing orientations, *J Prosthet Dent*, pp. 1-8, 2020.

[13] A. Unkovskiy et al, Objects build orientation, positioning, and curing influence dimensional accuracy and flexural properties of SLA printed resin, *Dental Materials*, vol. 34, pp. e324-e333, 2018.

[14] D. Seprianto et al, The Effect of parameters on the process of making objects with rapid prototyping DLP technology on the bending stress, *Journal of Physics: Conference Series*, vol. 1500, 2020.

[15] D. P. Putra et al, Optimization of production process parameters of DLP type 3D printer design for product roughness value, Proceedings *of the 4th Forum in Research, Science*, vol.7, pp. 179-183, 2021.

[16] A. Ibrahim and M. Ibrahim, Optimization of process parameter for Digital Light Processing (DLP) 3D printing, *International Journal of Mechanical And Production Engineering*, ISSN: 2320-2092, 2017.

[17] S. L. Sherman, O. Kadioglu, G. F. Currier, J. P. Kierl, and J. Li, Accuracy of digital light processing printing of 3-dimensional dental models, *J Orthod Dentofacial Orthop,* vol. 157(3), pp.422-428, 2020.

[18] A. Katheng et al, Evaluation of dimensional accuracy and degree of polymerization of SLA photopolymer resin under different postpolymerization conditions: An in vitro study, *The Journal of Prosthetic Dentistry*, vol. 125, pp. 695-702, 2021.

[19] S. L. Campanelli et al, Statistical analysis of the stereolithographic process to improve the accuracy, *Computer*-Aided *Design*, vol. 39, pp. 80-86, 2007.

[20] P. Zmarzły and D. Gogolewski, Design guidelines for plastic casting using 3D printing, *Journal of Engineered* Fibers *and Fabrics,* vol. 15, pp. 1-10, 2020.

[21] A. Iftikhar et al, Turbine blade manufacturing through rapid Tooling (RT) process and its quality inspection, Materials *and Manufacturing Processes,* vol. 28, pp. 534–538, 2013.

[22] A. Giudice et al, Evaluation of the accuracy of orthodontic models prototyped with entry-level LCD-based 3D printers: a study using surface-based superimposition and deviation analysis, *Clinical Oral Investigations,* 2021.

[23] MN. Islam et al, Comparison of dimensional accuracies of stereolithography and powder binder printing, *The International Journal of Advanced Manufacturing Technology*, vol. 88, pp. 3077–3087, 2017.

[24] G. Budzik, Properties of made by different methods of RP impeller foundry patterns, *Archives of Foundry* Engineering, vol. 7, pp. 83-86, 2007.

[25] A. Tulcan et al, Study of the influence of technological parameters on generating flat part with cylindrical features in 3D printing with resin cured by optical processing, *Polymers,* pp. 2-24, 2020.

[26] C. Arnold, D. Monsees, J. Hey, and R. Schweyen, Surface quality of 3D printed models as a function of various printing parameters, *Materials,* 2019.

APPLICATION OF PPG'S PEAK IN DETECTING CARDIOVASCULAR DISEASES

TUNG THANH LUU [1*], TRIEU VAN NGUYEN [1]

[1] *Department of Construction Machinery and Handling Equipment, Faculty of Mechanical, Engineering Ho Chi Minh City University of Technology (HCMUT) 268 Ly Thuong Kiet Street, District 10, HCMC, Vietnam;*
**ttluu@hcmut.edu.vn, millionguyen2k@gmail.com*

Abstract. Photoplethysmography (PPG) is an optical technique used to measure the blood volume in the microvascular bed of tissue. The change of blood volume is cyclic. Thus, the PPG signal can be used to determine the heart rate by counting the peaks of PPG signal. In this paper, samples of PPG signal are extracted from the MIMIC III data set. Recorded samples consist of 763 records from 390 patients. In which, 61% of the samples are from patients affected with cardiovascular diseases (CVD) and the others are records of those with normal sinus rhythm (NSR). The algorithm in this paper shows the application of PPG in deciding the CVD health status of a person. The algorithm has an accuracy of 94% in deciding whether someone has a cardiovascular disease or not. The detection run on PPG is extremely useful for doctors to diagnose their patients.

Keywords. Photoplethysmography signal, cardiovascular disease, detect for peak PPG signal.

1 INTRODUCTION

Photoplethysmography (PPG) is a low-budget and non-invasive optical technique that can detect changes in blood volume. The PPG signal acquired from this technique provides valuable data regarding our cardiovascular system. In addition, PPG signal is applied to clinically track the patients' conditions such as heart rate (HR) or blood's oxygen level (SPO2) changes, … Moreover, the PPG has also been integrated into small devices, specifically smart watches. These smart watches use PPG sensors to collect, calculate and display the HR for the users.

PPG's signal the repetition of basic signals bearing the distinctive features shown in Figure 1. A PPG signal contains Systolic Peak, Diastolic Peak, Dicrotic Notch and on/off-set points.

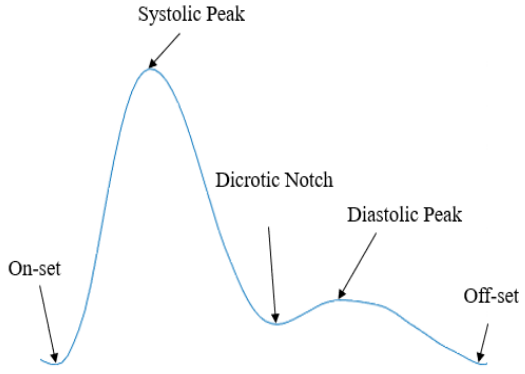

Figure 1: Distinctive features of a basic PPG signal.

In recent years, there have been many studies regarding the applications of PPG signals, especially in diagnosing the conditions of the cardiovascular system, and other heart diseases as well as atherosclerosis. Machine learning (ML) or Deep learning algorithms are also applied to increase the effectiveness of the diagnoses. The algorithms mentioned are: CNN, RNN, U-net, LSTM. Many achievements have been made: Early detection of cardiovascular disease with photoplethysmography (PPG) sensor [1]. Atrial fibrillation detection from wrist photoplethysmography signals using smart-watches [2]. Estimating blood pressure from the photoplethysmography signal and demographic features using machine learning techniques [3-4].

Continuous blood pressure estimation using exclusively PPG by LSTM-based signal-to-signal translation U-Net architecture-based approach [5] or LSTM [6].
Due to the wide range of applications, the need to determine the features of PPG signals is crucial. This would require the accuracy from the algorithms used in extracting or acquiring data from the PPG signals. Algorithms such as: motion artifact filtering, HR calculation, and especially the Systolic Peak, Diastolic Peak detection were very popular many years ago. Some other algorithms related are: Adaptive threshold method for the peak detection of PPG waveform [7], Systolic peak detection in acceleration PPG measured from emergency responders in tropical conditions [8]. The mountaineer's method for peak detection in PPG signal in 2019 [9].
To determine the peaks and on/off-sets of the signals, we can find the second derivative of the PPG signal combining with the extreme point detection algorithm since the peaks and set points are the extreme points of the signal from the mathematical point of view. The important feature of this method is that we determine the extreme points of the PPG signal not only from the original signal itself but also from its second derivative to reduce the error of calculations. From this algorithm, we can calculate instantaneous HR and compare it to the HR before and after that. There have been many researches using the instantaneous HR to detect HR-related diseases like: Atrial fibrillation detection using a novel cardiac ambulatory monitor based on photoplethysmography at the wrist [10], Detecting atrial fibrillation and atrial flutter in daily life using photoplethysmography data [11], Premature atrial and ventricular contraction detection using photoplethysmography data from a smart-watch [12].
PPG's parameters can be used to evaluate the heart rate variability (HRV), this index is usually applied in ECG, giving evaluation results of the patient's conditions. Most cardiovascular diseases can be detected by evaluating the fluctuation of instantaneous HR throughout a period of time. We can observe the variation of the HR using transformation methods like the Poincaré plot [12]. However, if we only focus on determining the variations of HR without considering the changes in blood flow then we will not be able to detect every potential patient affected by cardiovascular diseases. For instance, if the patient has a disease but the instantaneous HR does not change dramatically then the methods mentioned above will not be able to process and determine the diseases. The reason is that the mentioned algorithms only focus on the variation of only one heart rate. In some cases, despite a stable HR, the patient is diagnosed to have a cardiovascular disease based on the data set from MIMIC III. Therefore, we need to also take the blood flow changes into consideration besides the HRV index. The method will be presented in the sections below. Many cases also showed that a patient has a normal HR but also has an abnormal change in blood flow. This paper will give an algorithm that can detect potential patient even with a stable HR.

2 DATA AND METHOD

2.1 Data

The data resource for this paper is acquired from MIMIC III, an open and public clinical source. The MIMIC III contains 763 PPG's signals from 390 individuals, aged 22 – 87. The signal is sampled at 125Hz and contains 4001 data points/signal; sampling duration lasts 32 seconds. The short duration of time is the result of filtering, picking and removing motion artifacts. The entire research, including signal processing and algorithm building, is conducted on Matlab 2020b.

2.2 Proposed Method

Peak Determination Algorithm: As seen from Figure 1, the PPG signal shows the Systolic Peak, Diastolic Peak and the on/off set points as the extreme points of the signal's graph. Mathematically, the signal's peaks and feet will be the extreme points; the extreme points will show the peak positions of wave a and wave b in the second derivative of the PPG's signal. Figure 2 shows a PPG cycle and its second derivative, this shows the difference between mathematical theories and actual data. From the data recorded, the Peaks and the set points have a large variation from the positions of waves a and b. These errors can be caused by

noises (no motion artifact) which leads to the fact that these positions are near accurate if we can filter the bandwidth with a small enough domain of frequency [4].

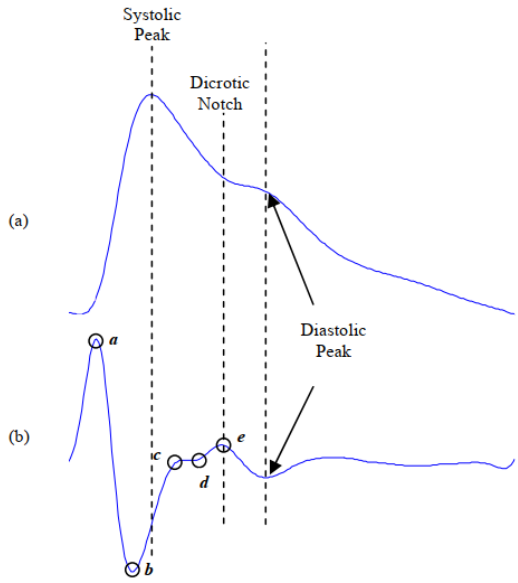

Figure 2: PPG signal taken from fingertips. (a). Photoplethysmogram signal. (b) second derivative of the photoplethysmogram signal [13].

For this reason, we should not directly determine the peaks and set points on the PPG but instead reach the solution based on its second derivative. To calculate the position of the 2 waves a and b, we use the 2 Elgendi's average lines [14]. The algorithm is shown in Figure 3.

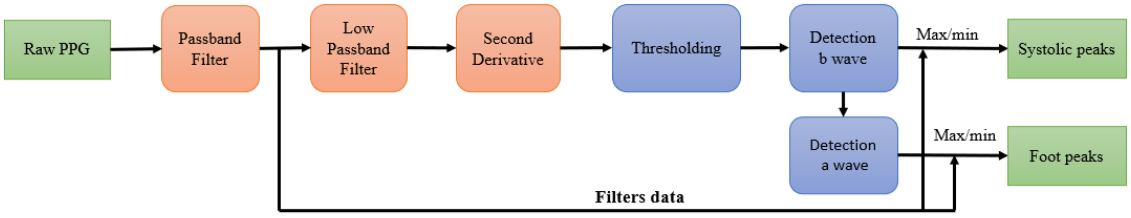

Figure 3: Algorithm to determine the peaks.

Band-pass Filter: Based on the algorithm, we will perform the filtering twice with the first one focusing on filtering the PPG input using the Chebyshev 2 algorithm. This applies for 4 degrees of freedom (DOF) (Phase 0) with the bandwidth from 0.5 – 10 Hz and below 20 dB to remove a part of the noises or the motion artifact. After the first filtering, we will receive the fPPG[n].

Meanwhile, the second filtering will be performed on the fPPG[n] with a bandwidth within 0.5 - 5Hz. The aim of the second filtering is to optimize the calculation of the peaks using waves a and b. Some of the researches mentioned the filtering of low frequency bandwidth to remove parts of the PPG's noises but did not state the exact frequency domain. As mentioned in previous sections, if the bandwidth filter domain is small enough, then the positions of the peaks and the set points will be approximate to the positions of waves a and b. Although the bandwidth domain of 0.5 – 5 Hz contains certain errors, they will be removed in the following steps. The result after filtering will be $S_2[n]$.

Second Derivative: To reach the second derivative of the PPG signal, we perform the derivation of $S_2[n]$ twice using the formulas (1) and (2). From the filtered $S_2[n]$ above, we can use the functions in Matlab to create the APG signal.

$$S_2'[n] = \frac{dS_2}{dt} = \frac{1}{2T}(S_2[n+1] - S_2[n-1]) \quad (1)$$

$$APG[n] = \frac{dS_2'}{dt} = \frac{1}{2T}(S_2'[n+1] - S_2'[n-1]) \quad (2)$$

With: T as the sampling cycle equals the inverse of the sampling frequency of F_s, n as the order of the sample data.

Cancellation of a wave: According to Elgendi [14], we must first determine the position of wave a on the APG signal. However, there are some cases where the Diastolic Peak is shown very clearly, but the Dicrotic notch is very deep. As seen from Figure 4, from the APG signal shows a very similar amplitude between waves a and c; this can lead to mistaking the c wave for the a wave. As a result, solving the b wave in the first place would be much easier since there is only one distinctive Systolic Peak separated from the Diastolic Peak, the result of the second derivative will give a clear position of wave *b*. Wave *b* can hardly be mistaken with wave *d* because *d* has a rather small amplitude (Figure 2). In this step, the APG signal will be reversed to remove wave a by using the formula (3).

$$F[n] = -1 * APG[n] \quad (3)$$

with $F[n]$ being the reversed signal from APG. Wave a's amplitude will be negative after the reversal of the signal. Therefore, we transform all negative signals to 0 with formula (4).

$$F[n] = 0 \ if \ F[n] < 0 \quad (4)$$

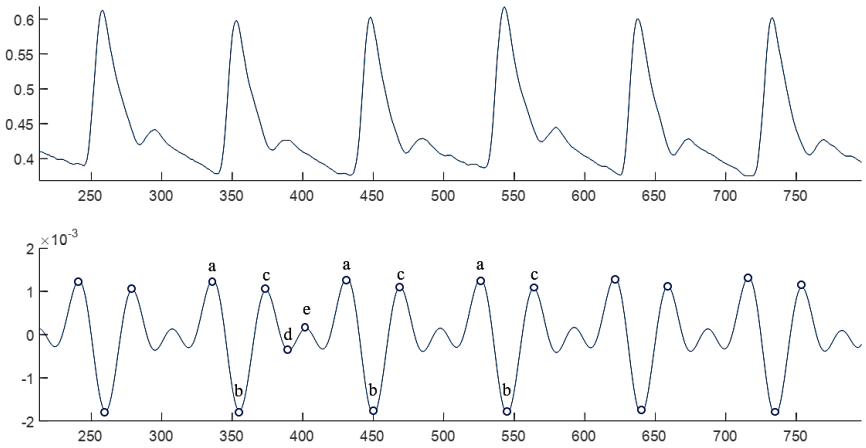

Figure 4: Example of similarity between the amplitude of c wave and a wave. PPG data (upper) and APG data (below).

Square: After the removal of the wave a, we receive $F[n]$. This step aims to clarify the amplitude of the wave b by squaring the signal after removing a wave. Formula (5) is displayed below:

$$g[n] = F[n]^2 \quad (5)$$

Generating blocks of interest: We will calculate the 2 *moving average values* to mark the positions where the wave b emerges. Elgendi specified that the optimal values $W_1 = 175ms$ and $W_2 = 1000ms$ [14]. W_1 is the amount of time for sampling the average values indicating the window size of the Systolic Peak and W_2 is the amount of time for sampling the average values indicating the window size of a heartbeat. The first moving average line is the MA_{peak} and the second moving average line is the MA_{beat} .

$$MA_{peak}[n] = \frac{1}{W_1}\left(g\left[n - \frac{W_1-1}{2}\right] + \cdots + g[n] + \cdots + g\left[n + \frac{W_1-1}{2}\right]\right) \quad (6)$$

$$MA_{beat}[n] = \frac{1}{W_2}\left(g\left[n - \frac{W_2-1}{2}\right] + \cdots + g[n] + \cdots + g\left[n + \frac{W_2-1}{2}\right]\right) \quad (7)$$

Threshold: Many blocks created will contain the functions of PPG. Amongst those, there were some blocks created by noises. The removal of noise blocks is based on the width of the Systolic Peak, the blocks with

a width wider than the $THR2$ threshold will contain the Systolic Peak. Equation (8) and (9) will be used to determine the thresholds called $THR1$ and $THR2$.

$$THR1 = MA_{beat}[n] + \alpha \quad (8)$$

$$THR2 = W1 \quad (9)$$

In which, α equals β*$\bar{z}$, the optimal value for β is 2% [14], where $\bar{z}$ is the average value of the filtered $F[n]$ signal. Here, the $THR2$ is given the value $W1$. The blocks are then created by comparing MA_{peak} and $THR1$.

Determining wave b and the Systolic Peak: In this step, wave b is calculated by the highest value of $F[n]$ according to each block and the width of the block must be higher than that of the $THR2$.

Each wave b determined will yield the position of a Systolic Peak. We look for the highest position in the filtered data (fPPG[n]), a range surrounding the position of the wave b we just determined in the previous steps. As mentioned, due to the inaccurate position of the bandwidth that needs filtering, there is a certain error to the position of the Systolic Peak and the wave b.

To simplify the calculations, we will take the highest value in the domain of 70 -100 ms to both sides of the positions of the wave b's peaks. Figure 5 shows the methods to determine the positions of wave b and the Systolic Peak. The waveform is the PPG input: The positions of the b wave and the position of the Systolic Peaks.

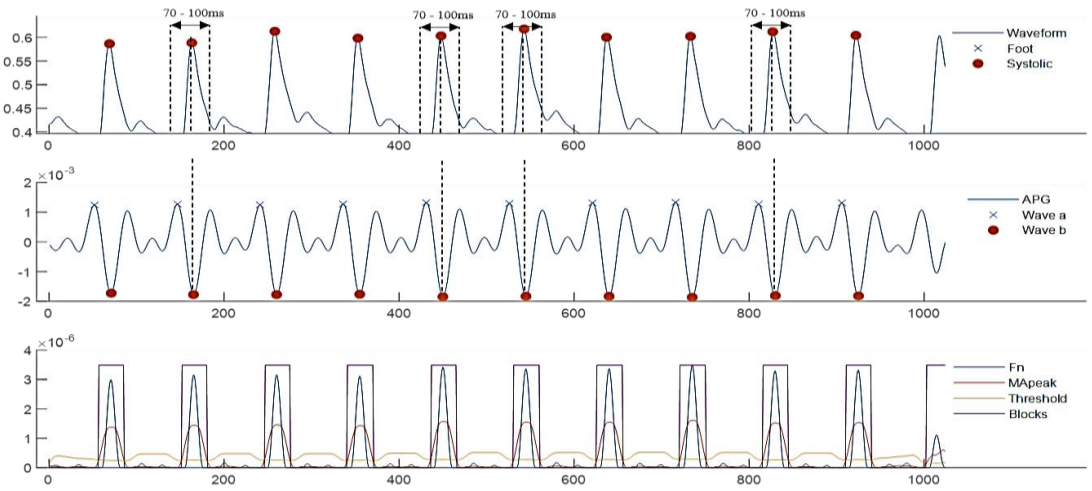

Figure 5: The positions of the Systolic Peaks compared to those of wave b's peaks. Top figure: Shows the PPG and the position of the Systolic Peak; Middle figure: Second derivative of the PPG and the calculated position of wave b; Bottom figure: Shows the 2 moving average lines and the block created from the threshold.

Determining the a wave and the foot of the signal: In the APG's signal shown in Figure 4, we can clearly see that the position of the a wave is also the position of the highest point before the b wave. Therefore, the acquisition of the a wave is performed by finding the position of the highest peak on the APG signal, tracing back from the position of the b wave to the beginning of the recorded signal, the range of time for this is k ms; with k ranging from 8 ms to 136 ms [14].

For each wave, we calculated a position of a foot of the signal. Similar to the Systolic Peak, the foot of the signal will be determined through the lowest position on the filtered signal (fPPG[n]) in proximity of the position of the a wave. To simplify the calculations, we will take the lowest point during the period of 80 -120ms to both sides of the position of the a wave as shown in Figure 6:

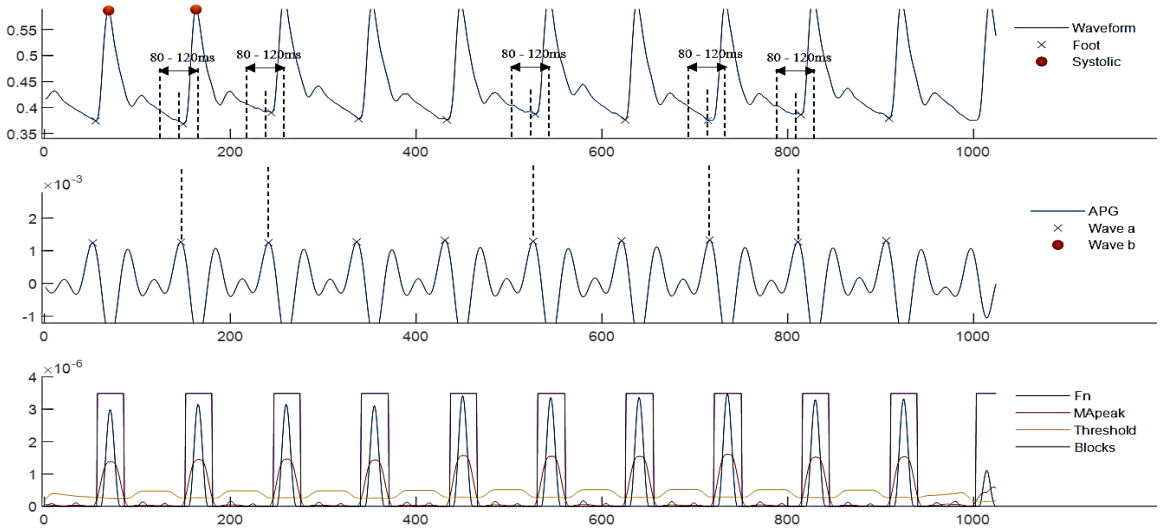

Figure 6: Position of the foot of the signal and wave a.

Heart diseases detection algorithm: Patients with cardiovascular diseases will usually have unstable or abnormal heart rates through time. Another case is when they have a stable heart rate but coupled with abnormal PPG. Therefore, detecting heart diseases requires the calculation of the changes and fluctuation of the heart rate through time. After the calculation of the instantaneous heart rate, we can draw out the changes in heart rate through time as in Figure 7 or through the Poincaré plot as in Dong Han [12]. Besides, we can evaluate the instability of the heart using the HRV index normally seen in ECG. Then, we can come to the assessment of the chance of having a heart disease or not? Common cardiovascular diseases can be atrial fibrillations, arrhythmias and premature ventricular contractions.

Calculating changes in the heart rate: From the peak finding algorithm, we can determine the instantaneous heart rate at a point in time using the formula (10):

$$BPM_{tucthoi} = \frac{60 * F_s}{N_s} \tag{10}$$

In which, F_s is the sampling frequency of the signal, N_s is the number of samples in 1 heart rate cycle (the signal range between 2 continuous peaks). Figure 7 is an example representing the peak-finding algorithm and the deviation of heart rates through time of a patient diagnosed with cardiovascular diseases.

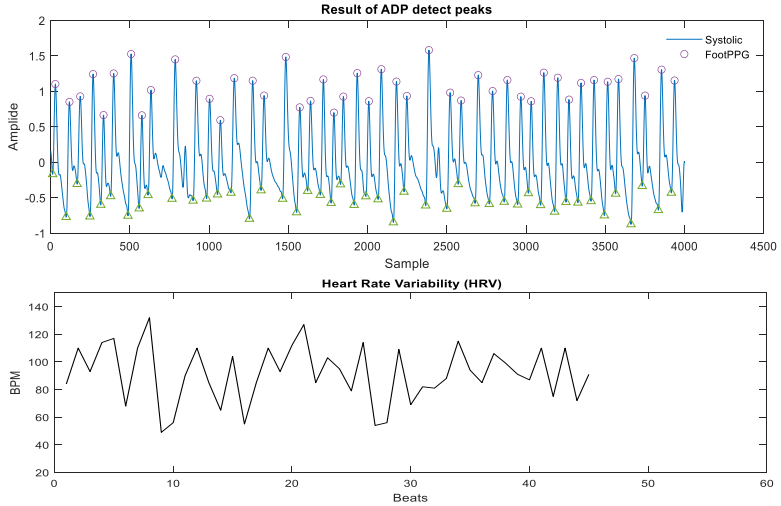

Figure 7: An example for a peak calculation algorithm(upper) and the changes of the heart rate through each cycle (below). This is the record of patient 85.

Display of changes in the heart rate using the Poincaré plot [12]: Poincaré shows the difference between 2 continuous heart rates. With x-axis represents ΔHR^{n-1} and y-axis represents ΔHR^{n}. Both of which are calculated using formula (11) below. The usage of Poincaré is to evaluate changes of the continuous heart rate from a wide point of view. Furthermore, cardiovascular diseases can also be detected by calculating specific positions in the plot. Figure 8 shows examples of the Poincaré plot being applied to the set of data.

$$\Delta HR^{n} = BPM^{n} - BPM^{n-1} \quad (11)$$

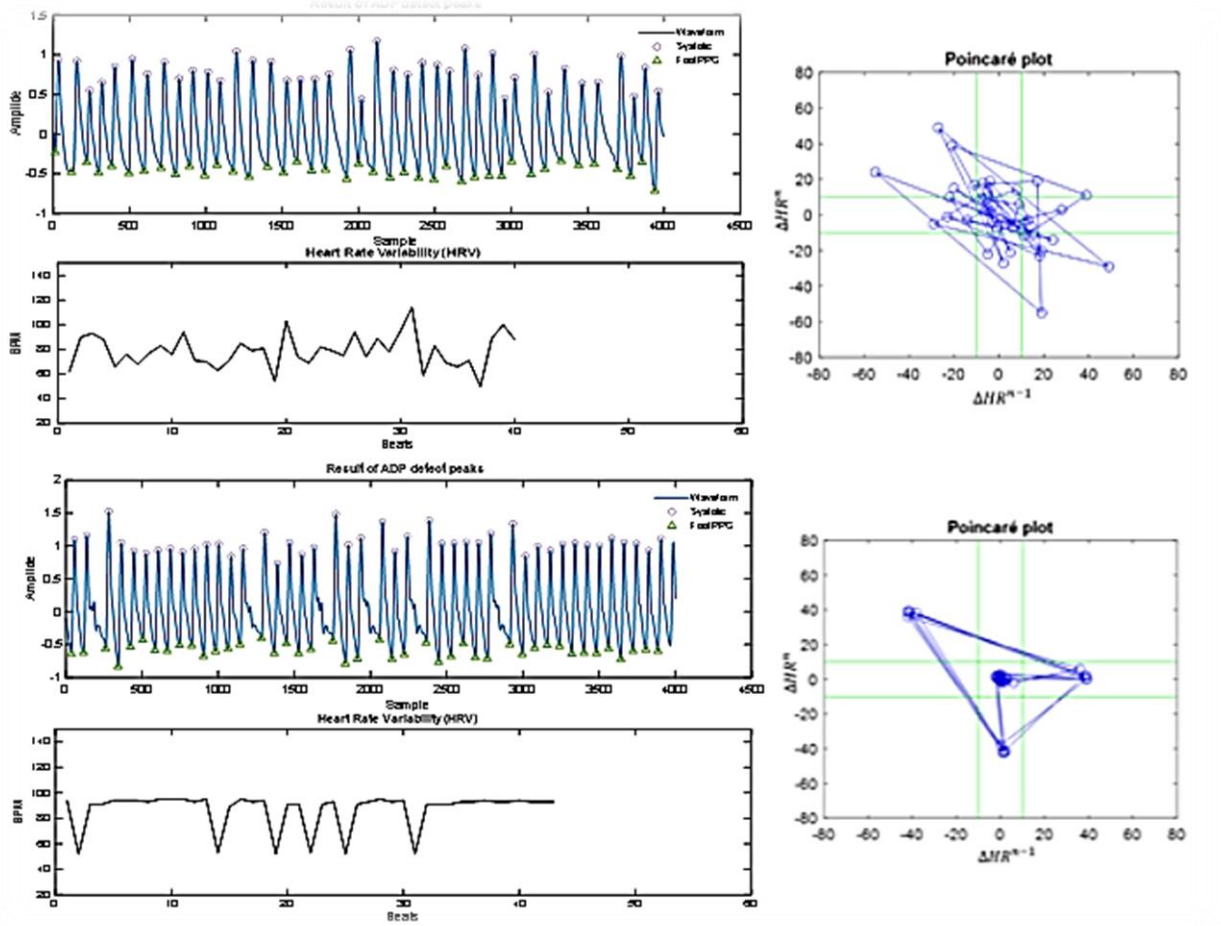

Figure 8: A Poincaré plot of a PPG heart rate for records No.45 (upper) and No.124 (below).

According to [12], algorithms developed for detection of atrial fibrillations and atrial flutters have been very effective. For example (Figure 9), despite the changes of heart rate through each stable cycle (the figure below the HRV), the Poincaré plot remains stable (The points showing the changes of sequential cycles are still positioned around the center). The heart rate does not change drastically if we only look at the Poincaré plot. However, this record of PPG possesses signs of atrial fibrillations or atrial flutters as the amplitude of the PPG's signal fluctuates abnormally. If this occurs regularly throughout the PPG, repeating several times in a minute, then the subject has a high chance of having cardiovascular diseases. Several abnormal heart beats in a day, in this case, will be a warning for a potential cardiovascular disease. The health conditions in this case relies on the frequency of these sudden heart rates.

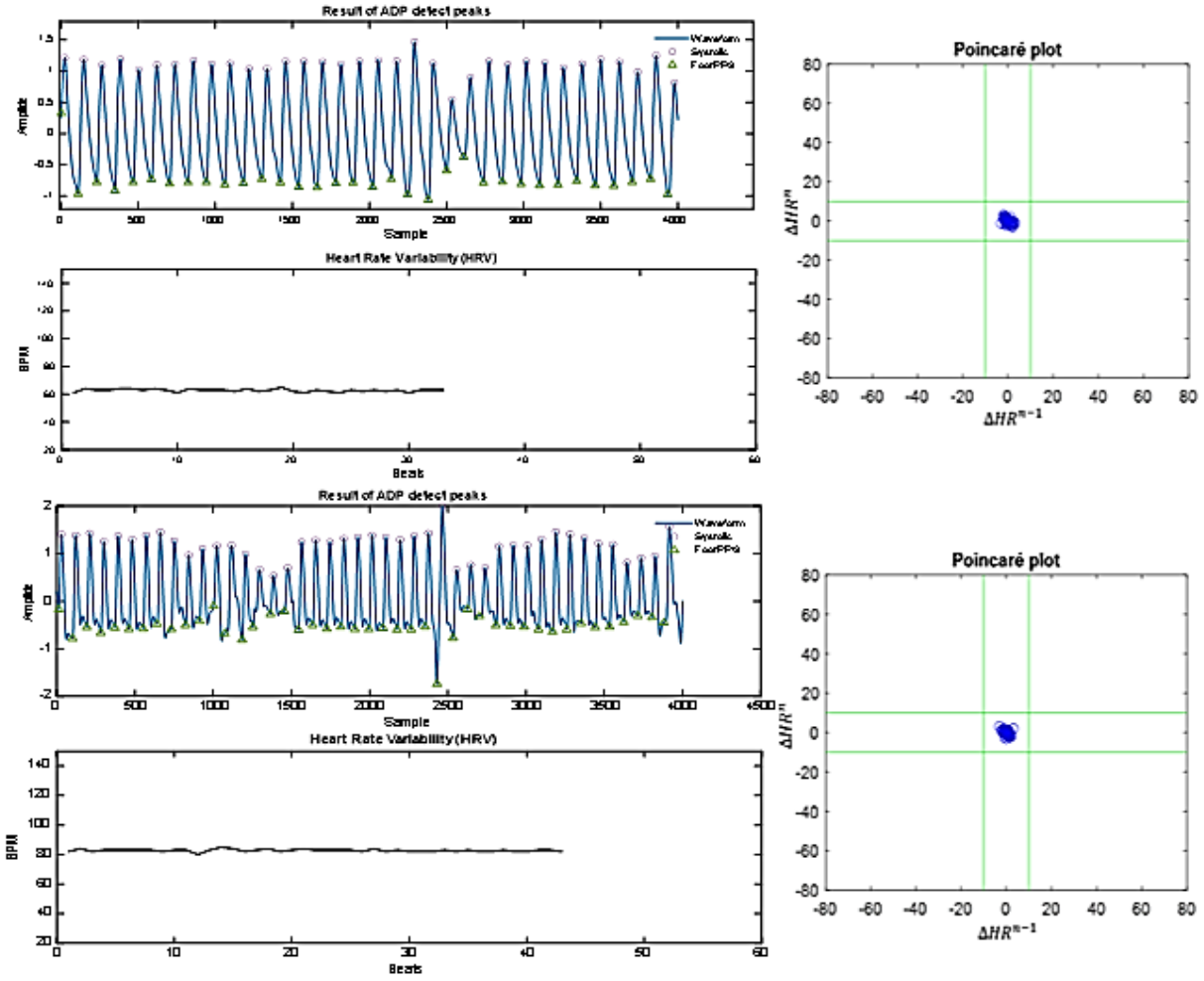

Figure 9: A Poincaré plot of records with sudden surges in amplitudes. Record no.7 and no.73.

As seen from Figure 9, there are positions where the heart rate's cycle does not change compared to its proximity while the amplitude contains considerable deviations. These deviations are clear symptoms of a cardiovascular disease which cannot be detected using the methods from [10-12]. Clearly, if we only use the changes in heart rate through time and the Poincaré plot, we would not be able to detect patients having cardiovascular diseases in cases where the amplitudes have anomalies despite a steady heart rate. Normally, the amplitude of the PPG will depend on the blood flow, this is what we can see from the signal when the blood flow suddenly surges or drops. Those are amongst the symptoms of cardiovascular disease. If we consider the instantaneous heart rate as the main criteria, we could never observe these fluctuations in the signal's amplitude. As can be seen from Figure 10, a cycle of heart rate consists of 2 parts: first is the crest time (from the foot to the systolic peak) called CT and the rest is from the Systolic Peak to the foot of the next cycle called GT. As a result, the amount of time for a heart rate cycle equals CT plus GT.

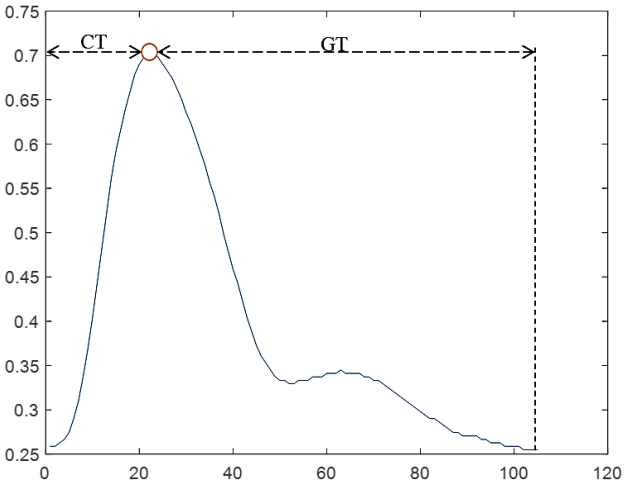

Figure 10: Components of a heart rate through time (CT + GT).

Looking back at Figure 9, we can observe that in cases where the heart rate does not change much then the use of a Poincaré plot cannot assess or decide whether someone is having cardiovascular diseases or not. This ultimately means that a patient can have cardiovascular disease even when their heart rate is steady. Taking a single cycle into consideration, the heart rate not changing may happen when the CT increases and the GT drops with a similar amount and vice versa. Consequentially, we can consider changes in proportion between CT and GT to assess if a heart rate is abnormal or not. The result can be seen in Figure 11, combining the Poincaré, CT and GT.

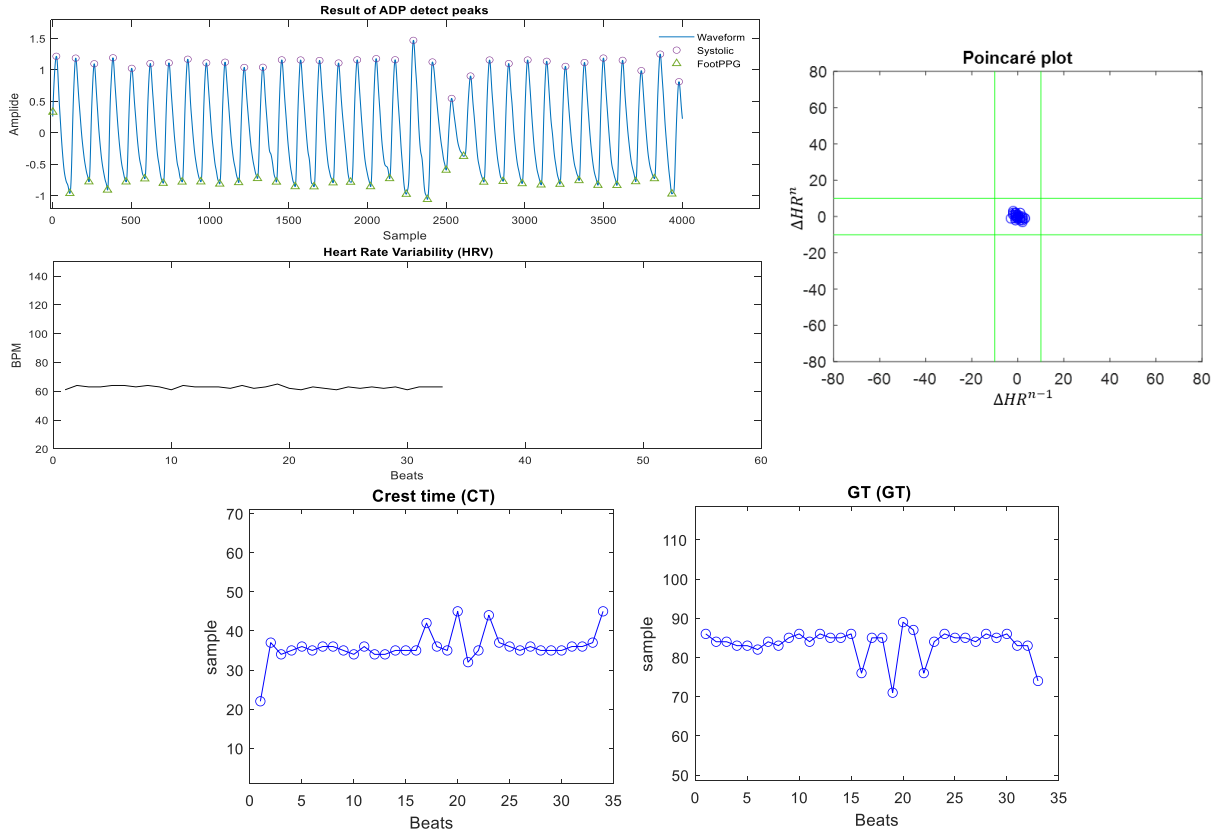

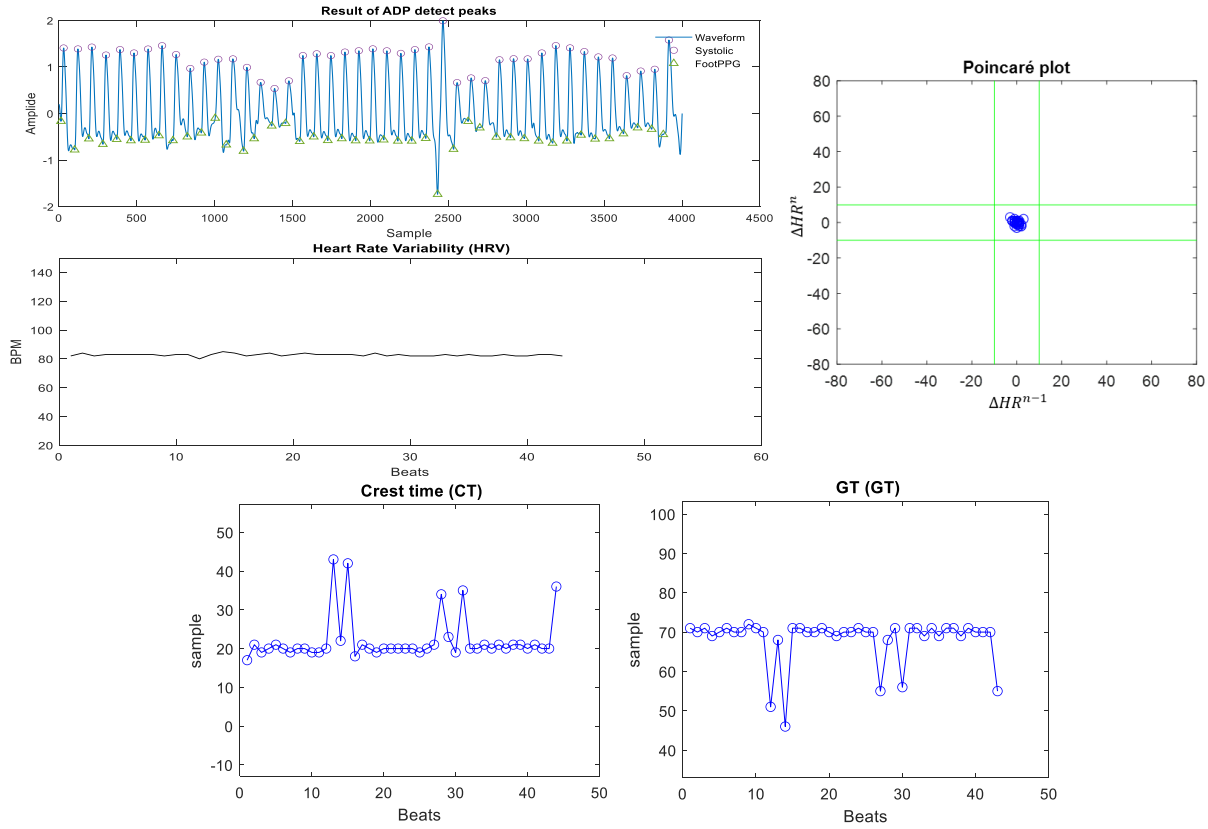

Figure 11: Poincaré + CT + GT from records 7, 73.

From the graph that shows the fluctuation of CT and GT in Figure 11, we can observe sudden changes of the CT and GT even when the heart rate remains stable. This is what the [12] did not mention.

Following that, instead of a diagnosis based solely on the Poincaré plot, we will perform the task based on the graph of CT and GT. There are 2 indexes that require optimization for the algorithm: CT and GT's thresholds. In this paper, we will consider the difference between the time (or sample) of CT and GT's continuous values. When the values reach a certain threshold for CT and GT, the sampled person has a chance of having cardiovascular diseases. Figure 12 below is the optimizing process of the 2 indexes mentioned. For the difference in CT, we will take 1 to 10 samples. As for GT, the amount will be from 1 to 30 samples. The change in the number of samples is a result from the data set where the fluctuation of CT is often insignificant compared to that of the GT.

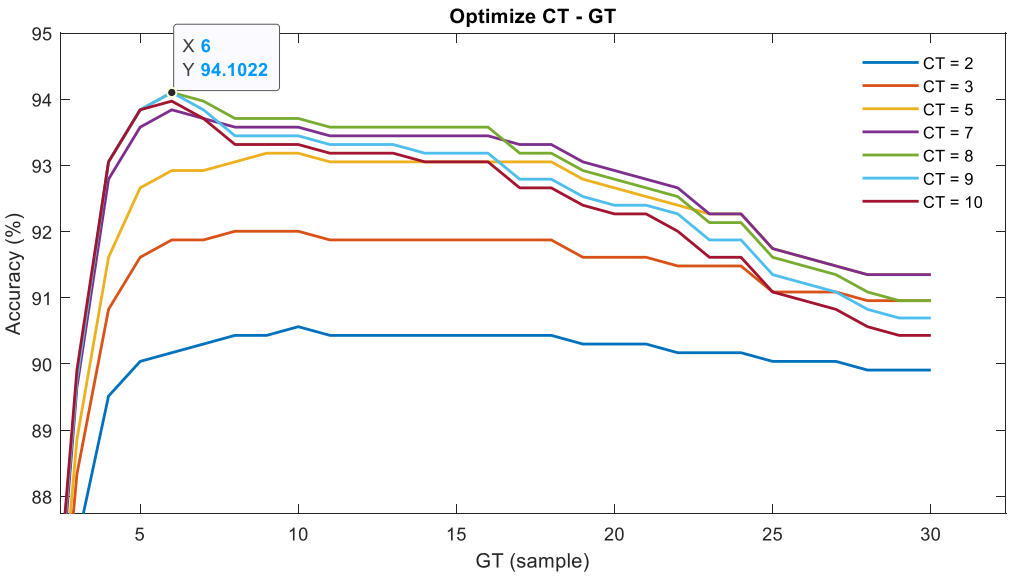

Figure 12: The results of the CT-GT optimization process.

From Figure 12, we can clearly see the impact of CT and GT's values on the effectiveness of the algorithm. The values are at their optimal when $CT = 8,\ GT = 6$ or when $CT = 9,\ GT = 6$, both of which possess an accuracy of up to 94.10% compared to the labels of the data set. Labels of the data set are listed in MIMIC III and have been categorized in 2 groups: one is diagnosed with cardiovascular diseases one is healthy in terms of their cardiovascular system. We set the data into 2 categories: PPG signal of those with disease will have the value of 1 and others will be set to 0. From our sampling, we can observe that as the sample size gets larger, the more accurate the algorithm gets. However, this only applies when the sample size is lower than a certain value. We also optimize the GT, as we increase the GT to a specific value, the efficiency of the algorithm is at its highest. The efficiency then gradually decreases as the GT's values keep increasing past the threshold value. In contrast, when CT values increases the efficiency of the algorithm decreases, therefore, the graphs only show 1 – 10 CT samples. This results in the optimal value for CT is 64 – 72ms and for GT is 48ms.

In brief, the method applied to detect potential patients are based around the calculation of changes in the values of CT and GT through time. If the difference between the values of CT passes 64 ms or 48ms for GT (equivalent to 6 samples at F_s = 125 Hz), the sampled person may carry a cardiovascular disease. Figure 13 is some typical results of the algorithm.

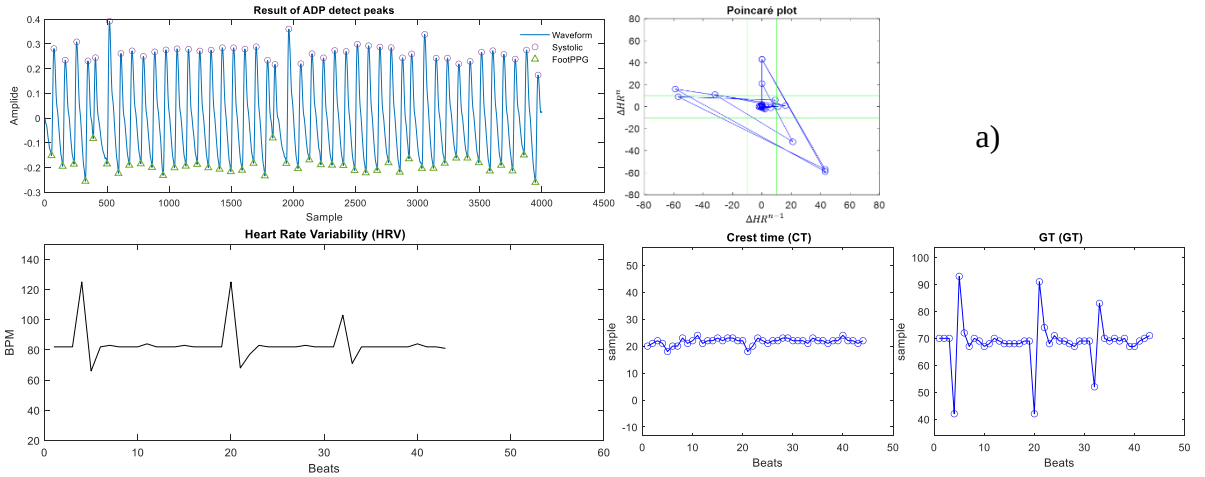

a)

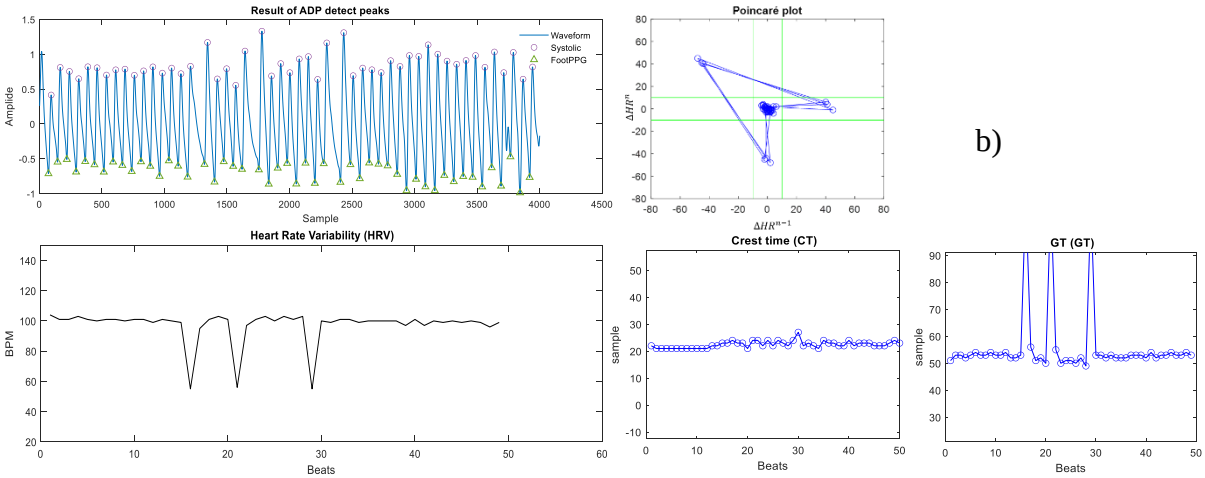

b)

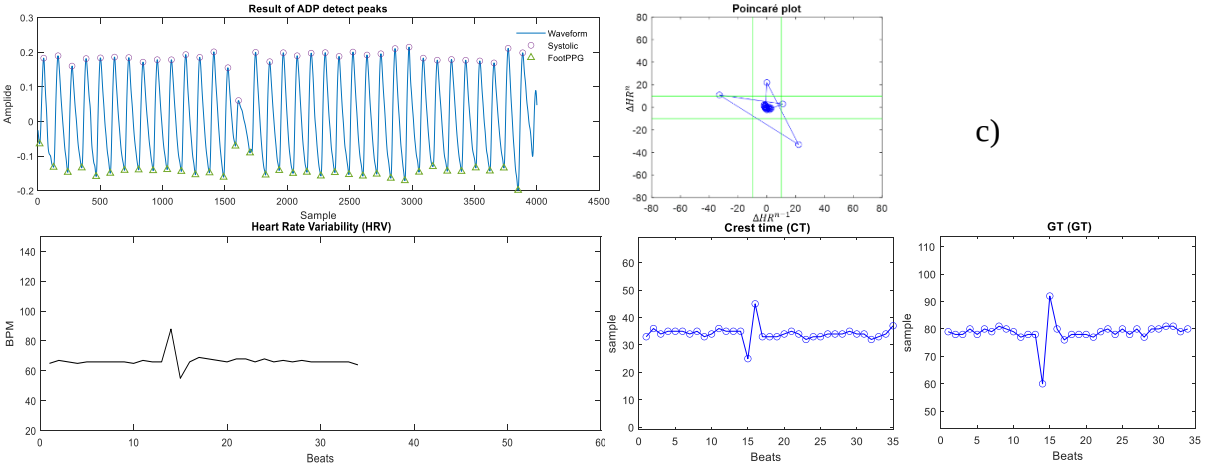

c)

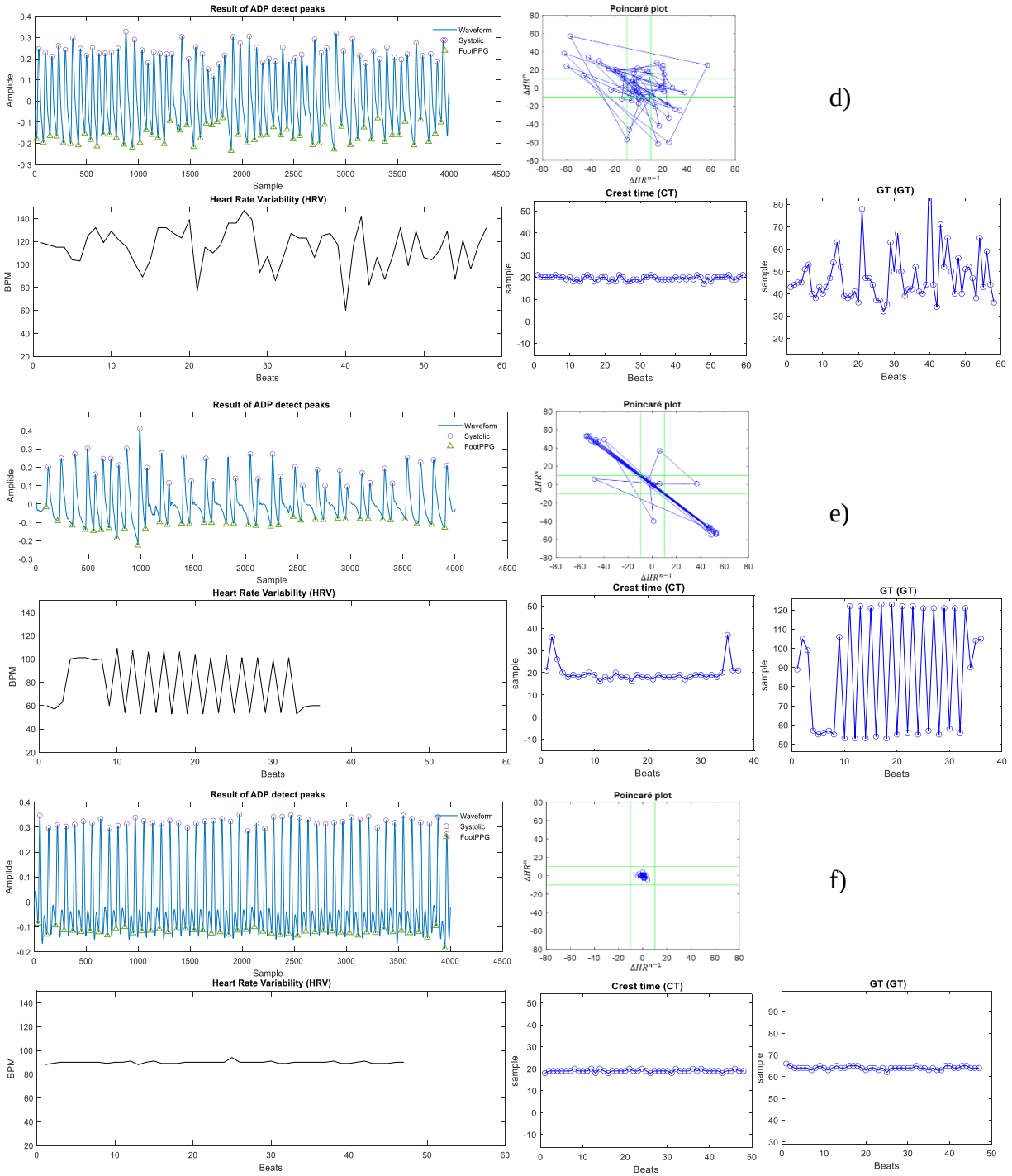

Figure 13: a), b), c), d), e) Some data samples of patients diagnosed with AF (Atrial fibrillation or atrial flutter) and f) is the data record of a normal person (NSR).

3 RESULTS AND DISCUSSIONS

3.1 Algorithm for detecting peaks:

The efficiency of each algorithm is evaluated by using the sensitivity (SE) and its correct predicted values (+P) by a percentage of the total amount of samples. In which, SE and +P are calculated using formula (12) and (13):

$$SE = \frac{TP}{TP + FN} \quad (12)$$

$$+P = \frac{TP}{TP + FP} \quad (13)$$

Where: TP, FN and FP are respectively true positive number (Systolic Peak is marked), false negative number (Systolic Peak present but not detected) and false positive number (Systolic Peak falsely marked).

Table 1: Results of the algorithm for peak finding.

Reference peaks	Algorithm	TP	FN	FP	SE (%)	+P (%)	Error (%)
32428	ADP	32236	191	84	99.41	99.73	0.85

Table 2: Results for the foot of the signal.

Reference peaks	Algorithm	TP	FN	FP	SE (%)	+P (%)	Error (%)
32432	ADP	32104	326	227	98.99	99.30	1.71

The application of the second derivative to calculate the signal's peak has an accuracy/efficiency of up to 99.41% and 98.99% for the foot of the signal. However, the effectiveness of the algorithm depends largely on filtering processes aimed at removing noises and motion artifacts. Causes for errors in the results of the algorithm: most of the miscalculations in the peak's positions come from the inconsistent noise filtering. It results in the appearance of multiple signal surges in the proximity of the Systolic Peak while the focus of this method is to detect the highest values in the signal. Similarly, the errors while detecting the foot of the signal also come from the drop points in the signal near the Systolic Peak. Figure 14 will demonstrate the cases with errors.

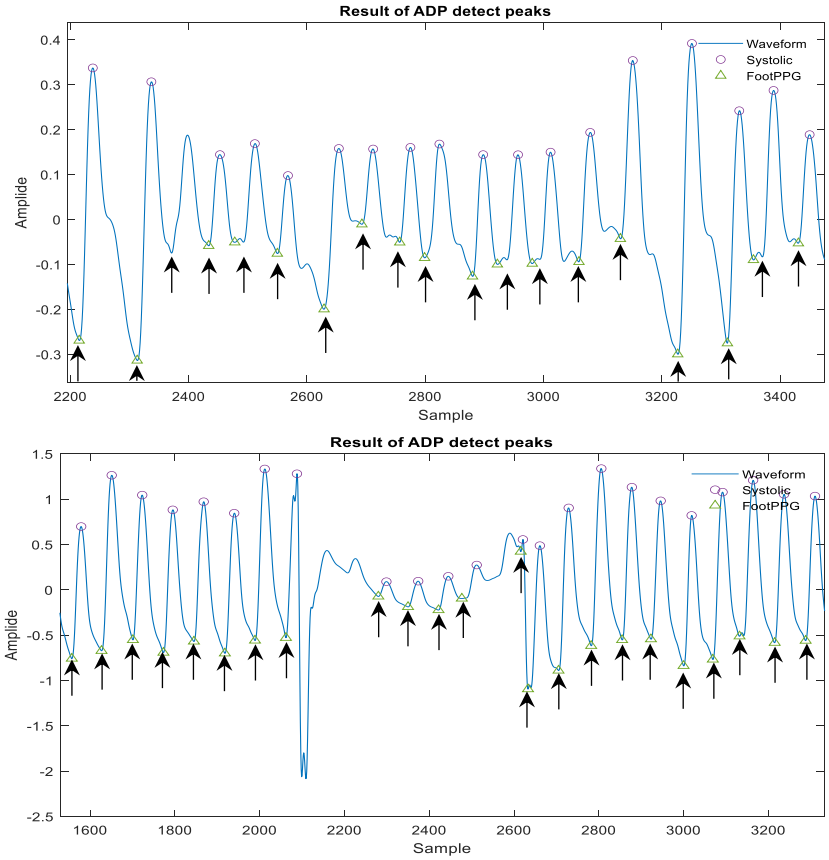

Figure 14: Faulty cases of the peak-finding algorithm.

Another cause for the miscalculation of the peaks stemmed from our use of second derivative on the b wave to detect the Systolic Peak, as the algorithm relied on detecting the peak of the b wave, if the signal of the b wave is unclear then the detection of the b wave cannot be completed. Consequently, the errors of the Systolic Peak and the foot of the signal were inevitable. The aim of these steps is to calculate the time cycle of the heart rates, therefore, we needed to accurately pin point the peaks of the PPG signal for the algorithm to detect cardiovascular diseases in the most efficient way.

3.2 Algorithm for detecting patients:

Evaluation indexes for a classification algorithm:

- Accuracy: The percentage of correct predictions of the labels compared to results in reality.
- +P (Precision): The percentage of correct predictions of True Positive(TP) divided by the sum of TP and FP.
- SE (Recall): The percentage of correct predictions of TP divided by the sum of TP and FN.
- F1 Score: The combined result of Precision and Recall.

In order to display all the parameters, we needed to calculate a confusion matrix (the matrix of TP, TN, FN, FP).

Table 3: An example of a confusion matrix

N = Amount of Samples		Predicted label		TP = True Positive
		Negative(0)	Positive(1)	TN = True Negative
TRUE	Negative(0)	TN	FP	FP = False Positive
	Positive(1)	FN	TP	FN = False Negative

Algorithm's calculation results:

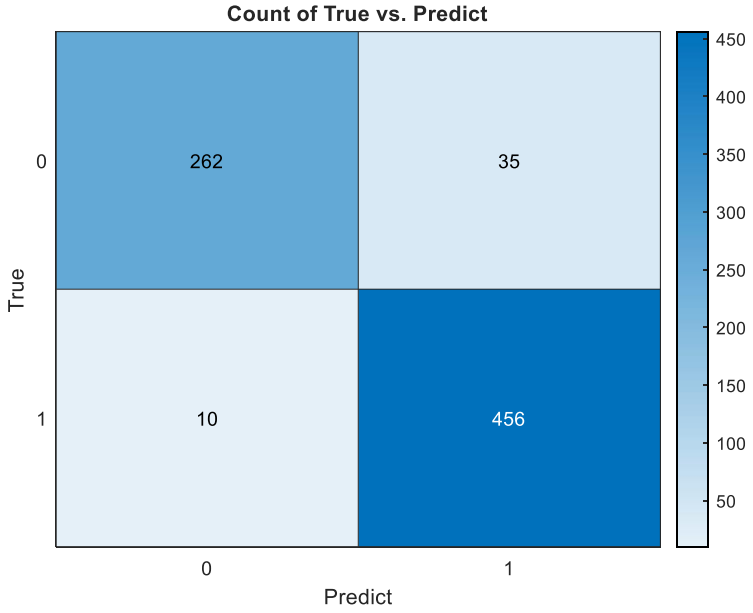

Figure 15: Confusion matrix of the algorithm.

Table 4: Results evaluation.

	precision	recall	F1- score	support
0	0.96	0.88	0.92	297
1	0.93	0.98	0.95	466
accuracy			0.94	763
macro avg	0.95	0.93	0.94	763
weighted avg	0.94	0.94	0.94	763

The labels of the data set were referenced from the MIMIC III. After editing, we chose 763 samples as shown above. After the calculations to give the predictions and comparison to the results of the data set, we received the data shown in Figure 15, the algorithm detected almost all the patients with cardiovascular disease (456/466 patients). The algorithm has an accuracy of 94% in deciding whether someone has a cardiovascular disease or not. This accuracy went up to 98% for the results that showed positive with cardiovascular diseases.

4 CONCLUSION

The paper has explained the peak finding algorithm to calculate the instantaneous heart rate and detect cardiovascular diseases; some conclusions can be made:

- The application of detecting the peak and foot of the PPG signal using the wave a and the wave b on the signal's second derivative has very high accuracy at 99.41% and 98.99%.
- Detection of cardiovascular diseases using the fluctuation of heart rates is possible. However, if we only focus on the changes of heart rate, we will not detect anomalies in changes of the blood flow. Therefore, consideration of CT and GT is also required to fully evaluate a heart rate.
- Besides the use of the Poincaré plot, we can also consider the CT and GT plot to fully detect patients with cardiovascular diseases, especially in cases where blood flow rapidly changes.

The algorithm is effective in spotting cardiovascular diseases. To precisely diagnose which disease is active, we can combine the use of Poincaré plot as in Dong Han [12] with CT and GT plots. The result of this combination can be applied to give warnings or diagnosis which can be used as reference points for doctors to use. Last but not least, an algorithm to detect the PPG's signal peaks in crucial to the diagnosis and prediction processes.

5 ACKNOWLEDGEMENTS

We acknowledge the support of time and facilities from Ho Chi Minh City University of Technology (HCMUT), VNU-HCM for this study.

REFERENCES

[1] Ave, Arrozaq, et al., Early detection of cardiovascular disease with photoplethysmogram (PPG) sensor, *2015 International Conference on Electrical Engineering and Informatics (ICEEI)*, IEEE, 2015.

[2] Bashar, Syed Khairul, et al., Atrial fibrillation detection from wrist photoplethysmography signals using smartwatches, *Scientific reports*, 9(1), pp. 1-10, 2019.

[3] Hasanzadeh, Navid, Mohammad Mahdi Ahmadi, and Hoda Mohammadzade, Blood pressure estimation using photoplethysmogram signal and its morphological features, *IEEE Sensors Journal*, 20(8), pp. 4300-4310, 2019.

[4] Chowdhury, Moajjem Hossain, et al., Estimating blood pressure from the photoplethysmogram signal and demographic features using machine learning techniques, *Sensors,* 20(11), p. 3127, 2020.

[5] Athaya, Tasbiraha, and Sunwoong Choi, An estimation method of continuous non-invasive arterial blood pressure waveform using photoplethysmography: A U-Net architecture-based approach, *Sensors,* 21(5), p. 1867, 2021.

[6] Harfiya, Latifa Nabila, Ching-Chun Chang, and Yung-Hui Li, Continuous blood pressure estimation using exclusively photopletysmography by LSTM-based signal-to-signal translation, *Sensors,* 21(9), p. 2952, 2021.

[7] Shin, Hang Sik, Chungkeun Lee, and Myoungho Lee, Adaptive threshold method for the peak detection of photoplethysmographic waveform, *Computers in biology and medicine,* 39(12), pp. 1145-1152, 2009.

[8] Elgendi, Mohamed, et al., Systolic peak detection in acceleration photoplethysmograms measured from emergency responders in tropical conditions, *PloS one,* 8(10), p. e76585, 2013.

[9] Argüello-Prada, Erick Javier, The mountaineer's method for peak detection in photoplethysmographic signals, *Revista Facultad de Ingeniería Universidad de Antioquia,* 90, pp. 42-50, 2019.

[10] Bonomi, Alberto G., et al., Atrial fibrillation detection using a novel cardiac ambulatory monitor based on photo-plethysmography at the wrist, *Journal of the American Heart Association,* 7(15), p. e009351, 2018.

[11] Eerikäinen, Linda M., et al., Detecting atrial fibrillation and atrial flutter in daily life using photoplethysmography data, *IEEE journal of biomedical and health informatics,* 24(6), pp. 1610-1618, 2019.

[12] Han, Dong, et al., Premature atrial and ventricular contraction detection using photoplethysmographic data from a smartwatch, *Sensors,* 20(19), p. 5683, 2020.

[13] Elgendi, Mohamed, On the analysis of fingertip photoplethysmogram signals, *Current cardiology reviews,* 8(1), pp. 14-25, 2012.

[14] Elgendi, Mohamed, et al., Detection of a and b waves in the acceleration photoplethysmogram, *Biomedical engineering online,* 13(1), pp. 1-18, 2014.

ADDRESSING SUSTAINABLE ENERGY CHALLENGES WITH DREDGED SOIL BACKFILL IN REMOTE AREAS

SANG YUM LEE [1], LAN PHUONG THAO TRAN [2], THI TO TRINH VO [3], TRI HO MINH LE [3*]

[1] *Induk University, 12 Choansan-ro, Nowon-gu, Seoul 01878, Republic of Korea,*
[2] *Faculty of Civil Engineering, Mien Tay Construction University, 20B Pho Co Dieu Street, Ward 3, Vinh Long, Viet Nam,*
[3] *Faculty of Civil Engineering, Nguyen Tat Thanh University, 300A Nguyen Tat Thanh Street, Ward 13, District 4, Ho Chi Minh City, Vietnam;*
yummy10041004@gmail.com, tranlanphuongthao@gmail.com, vtttrinh@ntt.edu.vn, lhmtri@ntt.edu.vn

Abstract. This study investigates the feasibility of utilizing dredged soil as a sustainable alternative for backfilling, with a primary focus on sub-base construction in remote and rural regions. Experimental testing involves substituting natural construction sand with varying proportions of dredged soil (50%, 75%, and 100%) while incorporating bottom ash. Additionally, the introduction of air-foam technology at a 15% volume ratio enhances self-leveling characteristics and reduces overall weight. Compressive strength tests indicate a reduction in strength (ranging from 10% to 30%) when compared to the original composition; nevertheless, these values remain suitable for sub-base construction in remote and rural environments. Beyond the technical aspects, this research aligns with principles of sustainable development and the circular economy by repurposing locally available dredged soil. These findings support the adoption of this environmentally friendly backfill solution for sub-base construction while addressing sustainable energy challenges. This research also introduces innovative solutions that promote energy efficiency within the construction industry by integrating air-foam technology, reducing reliance on energy-intensive compaction machinery and equipment, and aligning with broader sustainable energy objectives.
Keywords. Sustainable construction, dredged soil, subbase, mix design, silica fume, air-foam.

1 INTRODUCTION

The demand for sustainable infrastructure development has become imperative in today's world, with increasing emphasis on environmentally conscious solutions that can cater to the needs of both urban and remote regions [1]. One critical aspect of this pursuit is the efficient utilization of construction materials, particularly in sub-base construction for rural roads and isolated areas [2]. The significance of this lies not only in the structural integrity of the built environment but also in the broader context of resource conservation and sustainable practices [3].

Traditional construction materials often involve significant resource extraction, transportation, and energy consumption, contributing to environmental degradation and carbon emissions [4]. In contrast, the exploration of alternative materials derived from locally available resources has emerged as a pivotal strategy for achieving sustainable development goals. Dredged soil, a byproduct of waterway maintenance, presents a unique opportunity in this regard [5]. Historically considered a waste material with limited applications, dredged soil holds the potential to transform into a valuable resource when carefully examined and incorporated into construction practices. Stabilization techniques, such as cementitious additives and air-foam technology, have been explored to enhance their mechanical characteristics [4]. Challenges concerning variability and contaminants are acknowledged, emphasizing the importance of quality control [5].

Despite its potential benefits, the application of dredged soil as a construction material does come with limitations. One notable limitation is the variability in the composition and quality of dredged soil obtained from different sources [6]. This variability can affect the engineering properties and performance of the material, making it challenging to establish consistent design guidelines and specifications. Furthermore, the presence of potential contaminants, such as heavy metals or organic matter, in dredged soil could raise

concerns about its long-term environmental impact and suitability for certain construction applications [7]. Addressing these issues necessitates rigorous testing, quality control measures, and site-specific assessments to ensure that the use of dredged soil aligns with both safety standards and sustainable development objectives.

This study delves into the potential of dredged soil as a viable and sustainable alternative for sub-base backfilling applications in rural and remote areas. By redirecting dredged soil from disposal sites to construction sites, not only can the environmental impact of dredging operations be mitigated, but also an innovative and eco-friendly construction solution can be realized. Consequently, within the context of these challenges and opportunities, this study investigates the use of dredged soil as a sustainable alternative for backfilling applications, with a specific focus on sub-base construction for rural roads and remote areas. The experimental investigation encompasses a range of innovations, including the substitution of dredged soil with varying proportions of natural construction sand (50%, 75%, and 100%), the incorporation of bottom ash with fixed Portland cement of 120kg/m^3, and the implementation of air-foam technology at a volume ratio of 15% to concurrently reduce self-weight and enhance self-leveling properties. The evaluation of these formulations extends to comprehensive compressive strength tests, providing a thorough assessment of the resulting mixtures' mechanical properties and their potential in meeting the unique demands of sustainable construction in challenging environments.

2 MATERIALS AND METHODS

2.1 Materials

Dredged Soil: As shown in Figure 1a, the dredged soil used in this study was collected from District 12, Ho Chi Minh City, Viet Nam. The physical and geotechnical properties of the dredged soil were thoroughly characterized. Specific gravity was measured using the pycnometer method, and the plasticity index was determined according to ASTM D4318 [8]. Construction sand exhibits a larger grain size range of 0.2 to 2.0 mm, while dredged soil spans from 0.1 to 4.0 mm. The specific gravity of construction sand is slightly higher at 2.65, compared to 2.35 for dredged soil. Moisture content varies with construction sand at 1-3%, while dredged soil replacement tends to be higher, ranging from 10-15%. In terms of organic matter content, construction sand maintains minimal levels (<1%), whereas dredged soil replacement can have elevated levels of 2-5%. In this research, the material is termed as controlled low-strength material (CLSM) to meet the requirement for the actual application of this material.

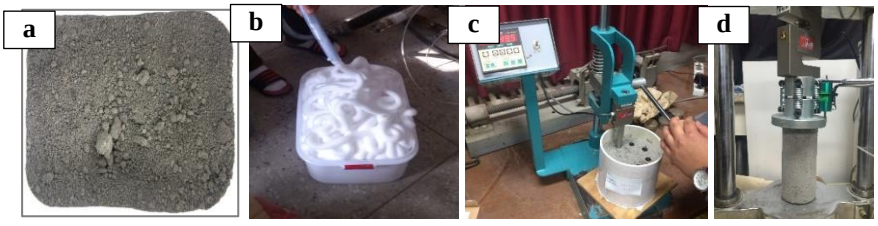

Figure 1: (a) Preparation of dredged soil, (b) air foam, (c) setting time, (d) unconfined compressive strength test.

Bottom Ash and Portland Cement: Bottom ash was characterized by its chemical composition and physical properties. Portland cement, used as a stabilizing agent in the mixtures, was analyzed for the specific surface area using the Blaine method and fineness according to ASTM C204 [9]. Table 1 summarizes the Cementous materials used in this research.

Air-Foam Technology: As presented in Figure 1b, the air-foam generator produced foam with a stable volume ratio of 15%. The foam's density, determined using the ASTM D6103[10], was monitored to ensure consistent foam quality across various mixtures.

Silica Fume: Silica fume, an essential component in this research, is incorporated into the mixture at a proportion of 2%. Renowned for its high reactivity and elevated silicon dioxide (SiO_2) content, silica fume profoundly enhances the compactness of the concrete matrix due to its minute particle size.

Table 1: Summary of Material Properties: Portland Cement, Bottom Ash, and Silica Fume.

Material	Property	Portland Cement	Bottom Ash	Silica Fume
Chemical compositions	SiO_2	22.5%	42.3%	92.8%
	Al_2O_3	5.3%	14.7%	1.2%
	Fe_2O_3	3.1%	6.5%	0.5%
	CaO	62.1%	20.9%	2.1%
	MgO	1.8%	1.8%	0.3%
Physical Properties	Specific Surface Area (m^2/kg)	380	280	20,000
	Fineness (Blaine Value, cm^2/g)	350	300	23,000
	Particle Size Distribution	<75μm (25%)	<75μm (30%)	<45μm (90%)
Chemical Properties	Loss on Ignition (%)	<1	7	<0.5
	Chemical Reactivity	Moderate	Low	High

Mixing Procedure: The mixing process involves dry-blending the constituents, which encompass dredged soil, natural construction sand, bottom ash with varying Portland cement percentages, and air-foam technology, at a steady mixing rate of 30 rounds per minute. This dry mixing is followed by the gradual addition of water to achieve the desired workability while accounting for the foam volume. Subsequently, air-foam technology is introduced at the final stage to ensure the durability of the foam structure. After this, the well-mixed material is promptly placed into cylindrical molds measuring 100 mm in diameter and 200 mm in height, ensuring proper compaction and eliminating voids. The specimens are then cured in a controlled environment at 20°C and 100% relative humidity for 24 hours before undergoing subsequent testing.

2.2 Testing methods

Flowability test of flowable materials: The flowability test for the material involves filling a flow cone apparatus with the CLSM mixture and allowing it to flow freely from the cone as followed by ASTM D6103[10]. The flow height achieved after the material stops flowing is measured, and the flowability is calculated as the ratio of the flow height to the cone diameter, multiplied by 100. The target range for flowability is typically set at 200 mm ± 20 mm, ensuring that the CLSM achieves a desirable flow height while maintaining consistency in placement characteristics. The flowability test outcomes presented are derived from averaging measurements collected across three replicates of every CLSM mixture.

Setting time test: Using a penetration resistance apparatus with a standardized needle, the initial setting time is determined by recording the moment the needle fails to penetrate to a specific depth, such as 5 mm, after applying gentle pressure on the CLSM's surface following ASTM C403 [11] as shown in Figure 1c. Subsequent penetrations are conducted at regular intervals to identify the final setting time, indicated by the point at which the needle no longer penetrates to the specified depth. The setting time test results provided are an average compilation of measurements taken from three repetitions of each CLSM sample.

Compressive Strength Testing: The unconfined compressive strength test involves evaluating the mechanical characteristics of the materials following ASTM D4832 [12] as presented in Figure 1d. Cylindrical specimens, each with dimensions of 100 mm in diameter and 200 mm in height, were prepared following the mix design. A dataset comprising 10 specimens, numbered sequentially, was subjected to axial loading using a universal testing machine at a constant loading rate of 1.0 mm/min. The reported test results represent the average unconfined compressive strength obtained from three replicates of each specimen.

3 RESULTS AND DISCUSSIONS

3.1 Flowability test results

The flowability test results, as depicted in Figure 2a, offer valuable insights into the behavior of various mixtures distinguished by different percentages of dredged soil replacing construction sand. The data showcases flowability values in mm for mixtures prepared with distinct air foam ratios (20% and two instances of 15%), with one of the latter ratios combined with bottom ash. Analysis of the dataset reveals a

consistent trend: as the dredged soil replacement percentage increases, a corresponding reduction in flowability is observed across all compositions. This trend is particularly evident in mixtures with the same air foam ratios, such as 15% air foam. For instance, at 0% dredged soil replacement, the flowability is 213.9 mm, which decreases to 145.6 mm at 100% replacement. Moreover, a comparison between mixtures utilizing 15% and 20% air foam ratios indicates a slight decrease in flowability with higher air foam content. These findings underscore the intricate interplay between dredged soil content and air foam ratio in influencing flowability, which holds significant implications for optimizing workability in sub-base construction.

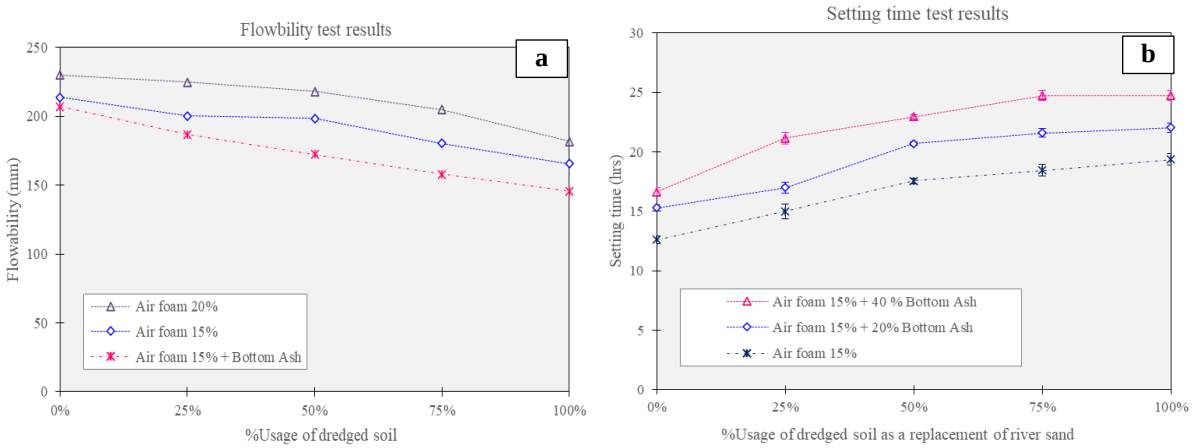

Figure 2: (a) Flowability test result, (b) Setting time test results.

3.2 Setting time test results

The setting time results, outlined in the provided Figure 2b, provide insight into the setting characteristics of different mixtures distinguished by varying percentages of dredged soil replacing construction sand. The data indicates setting time values in hours for mixtures formulated with different combinations of air foam and bottom ash, specifically utilizing a 15% air foam ratio. A clear trend emerges as the dredged soil replacement percentage increases: setting time progressively extends across all three types of mixtures, which involve 15% air foam and 40% bottom ash, 15% air foam and 20% bottom ash, and a pure 15% air foam mixture. For instance, at 0% dredged soil replacement, the setting times are 16.65 hours, 15.3 hours, and 12.6 hours, respectively. As the dredged soil replacement percentage rises to 100%, the setting times also increase, reaching values of 24.75 hours, 22.05 hours, and 19.35 hours. This dataset underscores the interplay between dredged soil replacement and setting time, underscoring the need to consider these characteristics when refining mix designs for sub-base construction, particularly concerning construction scheduling and workability adjustments.

3.3 14 days unconfined compressive strength

The dataset presented in Figure 3a reveals a conspicuous and consistent trend in the unconfined compressive strength of the developed mixtures, closely linked to the varying percentages of dredged soil replacing construction sand. A discernible reduction in compressive strength is evident as the replacement percentage increases, a pattern uniformly observed across all mixtures. This trend is manifest within both the category of normal cement mortar and the mixtures incorporating air foam and bottom ash. For instance, in the normal cement mortar category, the compressive strength diminishes from 0.41 MPa at 0% replacement to 0.30 MPa at 100% replacement after a 10-day curing period. This downward trajectory is consistently echoed in the mixture containing 15% air foam and 20% bottom ash, where the compressive strength decreases from 0.40 MPa to 0.22 MPa under identical replacement conditions. Intriguingly, the introduction of air foam has a marginal compounding effect on this trend, leading to a slight additional reduction in strength. This multifaceted trend is underpinned by the intrinsic mechanical distinctions between dredged soil and construction sand. The escalation in dredged soil content introduces an elevated fines component, potentially hampering particle interlocking and load transfer efficiency. Concurrently, the presence of air

foam and bottom ash exerts an additional influence on the mixture's matrix, impacting particle cohesion and frictional characteristics, thereby further shaping compressive strength.

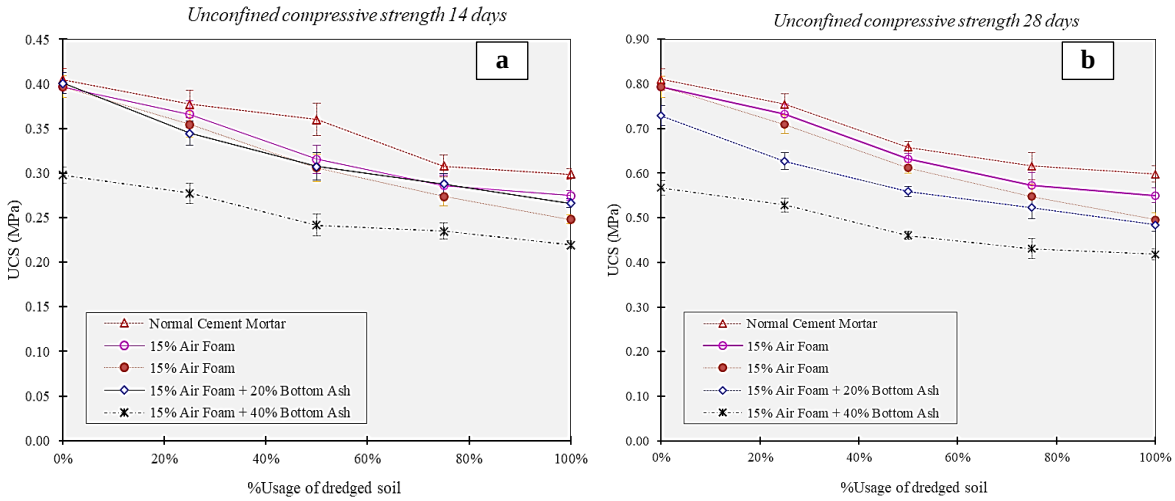

Figure 3: (a) 14 days unconfined compressive strength results; (b) 28 days unconfined compressive strength results

3.4 28 days unconfined compressive strength

Figure 3b serves as a comprehensive insight into the outcomes of the unconfined compressive strength assessments conducted after a 28-day curing period for various mixtures. The presented data intricately showcases the impact of different percentages of dredged soil utilized as replacements for construction sand, while concurrently considering the influence of distinct mix designs involving normal cement mortar and combinations of air foam and bottom ash. A discernible pattern in the development of compressive strength emerges over the extended curing duration. Within the domain of normal cement mortar, the compressive strength ranges from 0.60 MPa (at 100% dredged soil replacement) to 0.81 MPa (at 0% replacement). This pattern resonates across diverse compositions, such as the mixture with 15% air foam and 20% bottom ash, where the strength decreases from 0.48 MPa to 0.73 MPa, respectively, under identical replacement conditions. Percentage-based comparisons significantly underscore the sway of dredged soil replacement on compressive strength. Notably, in normal cement mortar, a 26% decrease in compressive strength is apparent when transitioning from 0% to 100% dredged soil replacement, while the mixture containing 15% air foam and 20% bottom ash experiences a 34% reduction under an equivalent replacement scenario. It is noteworthy that although a majority of dredged soil was used, these mixtures still meet the required strength criteria for backfill and the basement of a roadway, surpassing the threshold of 500 kPa (0.5 MPa). The dataset provides valuable insights into the persistent impact of dredged soil content on compressive strength and divulges the cumulative nature of strength evolution over time. It underscores the necessity for a judicious approach to mix design, catering to both immediate and long-term performance needs. Furthermore, the presence of air foam and bottom ash perpetuates the overarching trend, signifying the vital role of precise compositional modifications.

3.5 Effect of silica fume

The impact of Silica Fume on unconfined compressive strength at 28 days is elucidated through the provided Figure 4. The data highlights the performance of different mixtures with varying dredged soil replacement percentages and the inclusion of Silica Fume. Four distinct mixture types are considered: normal cement mortar, Silica Fume at 12% combined with normal cement, Silica Fume at 12% combined with 15% air foam and 20% bottom ash, and Silica Fume at 12% combined with 20% bottom ash. Analysis reveals that the incorporation of Silica Fume generally enhances compressive strength compared to standard cement mortar. This enhancement is evident across dredged soil replacement scenarios, showcasing the potential of Silica Fume as an effective additive to improve the structural performance of mixtures, even in

the context of using alternative materials like dredged soil. For instance, even at 100% dredged soil replacement, the compressive strength remains notably higher with Silica Fume than in the absence of this additive. These findings underscore the valuable role of Silica Fume in addressing the challenges posed by the use of alternative materials and in advancing the overall sustainability and durability of sub-base construction.

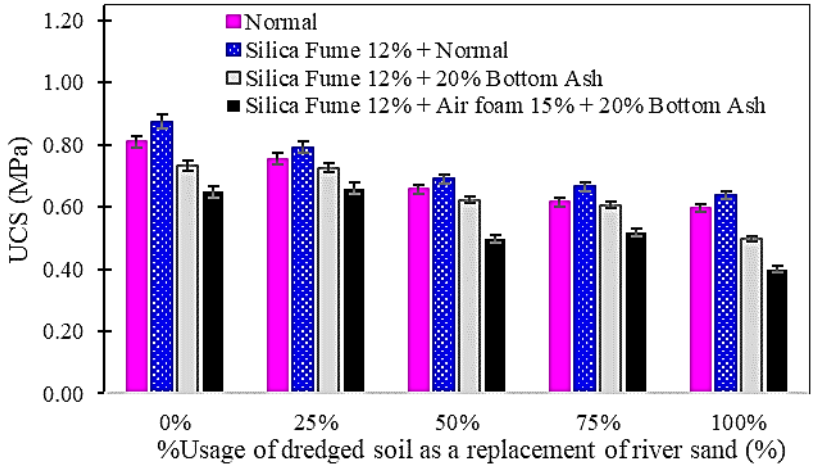

Figure 4: Impact of silica fume on unconfined compressive strength test results.

3.6 Energy Effectiveness

In the context of sustainable development, this research introduces innovative solutions that indirectly promote energy effectiveness within the construction industry. The incorporation of air-foam technology into the self-leveling material significantly reduces the reliance on energy-intensive compaction machinery and handling equipment during construction. This reduction streamlines construction processes, leading to diminished energy consumption and a decreased carbon footprint, which align with the broader sustainable energy objectives. Additionally, the lightweight air-foam structure within the material has the potential to enhance thermal insulation, resulting in reduced energy consumption for heating and cooling in buildings, thus contributing to energy efficiency and the wider goals of sustainable energy conservation and environmentally responsible building methods.

4 CONCLUSIONS

This manuscript delves into the sustainable utilization of dredged soil as a viable alternative in subbase construction for rural and remote areas. Through a meticulous experimental investigation, we explore the interplay of various mixed components, including dredged soil, construction sand, bottom ash, air foam, and Silica Fume. By systematically analyzing unconfined compressive strength, flowability, and setting time data, the test results reveal intricate trends that provide valuable insights for optimizing mix designs.

The dataset for unconfined compressive strength at 10 and 28 days consistently demonstrates a decline as the percentage of dredged soil used for replacing construction sand increases. This decline underscores the challenge of achieving comparable strength with higher dredged soil content. However, despite this reduction, the compressive strength values remained within acceptable limits for sub-base construction, with values exceeding 0.5 MPa even at 100% replacement.

The incorporation of air foam at varying ratios (15% and 20%) demonstrates a slight reduction in compressive strength across all mixtures. While this reduction is within the expected range, it emphasizes the role of air content in modulating the mechanical properties of the mixtures.

A noteworthy trend in setting time is observed as the proportion of dredged soil replacement increases. The setting time consistently prolongs for all mixture types, indicating a potential impact on construction scheduling and workability adjustments.

Flowability decreases uniformly with increasing dredged soil replacement. This emphasizes the potential challenge of achieving optimal workability with higher dredged soil content, which is crucial for efficient

construction practices.

The inclusion of Silica Fume at 12% demonstrates a positive impact on compressive strength, particularly evident in comparisons with normal cement mortar. This effect is significant across all dredged soil replacement percentages, suggesting Silica Fume's potential to bolster structural performance, even when alternative materials are incorporated.

The comprehensive dataset underscores the delicate balance between achieving sustainable practices and maintaining the requisite mechanical properties. While dredged soil can be a sustainable alternative, a judicious mix design is essential to ensure optimal strength without compromising workability and performance.

5 ACKNOWLEDGMENT

The author's team would like to thank Nguyen Tat Thanh University, Ho Chi Minh City, Vietnam for the support of time and facilities for this scientific research.

REFERENCES

[1] B.F. Schlue, S. Kreiter, T. Moerz, Time-Dependent Deformation of Dredged Harbor Mud Used as Backfilling Material, *J. Water. Port, Coastal, Ocean Eng*, 135, pp. 154–163, 2009. doi:10.1061/(ASCE)0733-950x(2009)135:4(154).

[2] T. Satoh, M. Kitazume, Sea Reclamation with Dredged Soft Soil for Central Japan International Airport, *Soft Gr. Eng. Coast. Areas*, pp. 311–318, 2003. doi:10.1201/9781439833919.ch35.

[3] I.L. Howard, F. Vahedifard, J.M. Williams, C. Timpson, Geotextile Tubes and Beneficial Reuse of Dredged Soil: Applications near Ports and Harbours, *Proc. Inst. Civ. Eng. Gr. Improv.*, 171, pp. 244–257, 2018. doi:10.1680/jgrim.17.00059.

[4] T.H.M. Le, T.W. Lee, J.W. Seo, D.W. Park, Feasibility Study of Locally Excavated Soil in Foamed Cement Mixture as Backfill Material for Abutments of Railway Bridges, *J. Test. Eval.*, 51, 2021. doi:10.1520/JTE20210169.

[5] T.H.M.Le, D.-W. Park, J.-W. Seo, Evaluation of Ponded Ash as a Sustainable Backfill Material. *J. Mater. Civ. Eng.*, 30, p. 04018158, 2018. doi:10.1061/(ASCE)mt.1943-5533.0002359.

[6] T.H.M. Le, D.W. Park, J.W. Seo, J.W. Lee, K.J. Kim, Applicability Evaluation of Ponded Ash as a Sustainable Backfill Material Using Air Foam. *Sustain. Constr. Mater. Technol.*, 2016-Augus, 2016.

[7] D.-W. Park, H.V. Vo, Y. Lim, Recycling of Dredged Soil Waste Using Air-Foam Stabilization Method as Highway Construction Material, *Innovative and Sustainable Use of Geomaterials and Geosystems*, pp. 41–48, 2014. doi:10.1061/9780784478455.006.

[8] ASTM D4318 Standard Test Methods for Liquid Limit, Plastic Limit, and Plasticity Index of Soils. *Report*, 04, pp. 1–14, 2005.

[9] ASTM C204 Standard Test Methods for Fineness of Hydraulic Cement by Air-Permeability. *ASTM Int. West Conshohocken, PA* 2011, pp. 1–10.

[10] ASTM D 6103-04 Standard Test Method for Flow Consistency of Controlled Low Strength Material. *ASTM Int. West Conshohocken*, pp. 1–4, 2004.

[11] ASTM C403/C403M-99 Standard Test Method for Time of Setting of Concrete Mixtures by Penetration Resistance. *Annu. B. ASTM Stand.*, 04, pp. 1–6, 1999.

[12] ASTM D4832 – 02 Standard Test Method for Preparation and Testing of Controlled Low Strength Material. *ASTM Int.*, 04, pp. 1–5, 2002.

DEVELOPMENT OF AUTONOMOUS SURFACE VEHICLES FOR REALTIME WATER QUALITY MONITORING IN SHRIMP PONDS

HAI - VU PHAN MINH [1*], TRAN – LE NGOC [1*], PHUC – NGUYEN AN [1]

[1] *Faculty of Mechanical Engineering, Industrial University of Ho Chi Minh City; haiminhvuphan30111@gmail.com, lengoctran@iuh.edu.vn*

Abstract. In shrimp farming, monitoring water quality is a very important factor to ensure the health and living environment of shrimp. However, traditional monitoring methods require manual data collection using boats and handheld sensors, which are costly, time-consuming, and inefficient. To address this issue, the method of using autonomous surface vehicles (ASVs) has been developed to automatically collect data and display real-time water quality parameters in shrimp farming. The ASV is optimized in mechanical design through computer simulation and 3D printing technology to ensure efficiency. ASV is equipped with a GPS module and ultrasound sensor to automatically set the path according to predetermined points and avoid obstacles in the shrimp farming pond, minimizing manual intervention. The GPS system improves accuracy and data collection speed, leading to improved performance and data management. The ASV is powered by a Lithium Polymer (Li-Po) battery to optimize usage time. ASV uses ESP32 and Raspberry Pi 4 with Wi-Fi and Internet connectivity to develop a web server displaying real-time water environmental data collected from sensors on the ASV. The expected results of this study are to continuously and accurately collect water quality data from the ASV, and for the ASV to navigate precisely to the predetermined points on the map with an error less than 3m. The evaluation criteria include position accuracy, continuous operating time, and sensor accuracy. In summary, the ASV is a breakthrough and effective approach to monitoring water quality in shrimp farming, helping to reduce costs, improve data accuracy, and enhance overall efficiency in shrimp farming activities.

Keywords. Shrimp farming, water quality monitoring, dissolved oxygen, autonomous surface vehicles (ASVs), real-time monitoring.

1 INTRODUCTION

Regular water quality monitoring is essential for healthy and productive shrimp aquaculture. However, the current manual sampling methods using boats or buoys have significant limitations in terms of cost, labor, and data continuity [1-3]. Autonomous surface vehicles (ASVs) present an opportunity to automate the water quality monitoring process with increased flexibility, lower cost, and reduced human time and risks compared to manual sampling [4-6]. While ASVs have been researched and utilized for applications such as ocean data gathering and maritime security [7,8], there has been limited focus on developing ASVs customized for the specific conditions and needs of small aquaculture ponds and farms.

Therefore, the overarching goal of this research study is to design, develop, and evaluate an autonomous surface vehicle tailored specifically for continuous, real-time monitoring of water quality parameters in small shrimp ponds. The primary research objectives are: 1) To design an ASV with compact physical dimensions optimized for stable navigation in tight 1 hectare ponds; 2) To develop effective navigation algorithms and obstacle avoidance capabilities suited for operation in confined pond environments; 3) To incorporate water quality sensors and wireless transmission mechanisms for acquiring and transmitting real-time data; and 4) To collect performance metrics on key parameters including position accuracy, data transmission reliability, sensor validation, and battery/operational lifetime.

The customized shallow water ASV developed through this research is expected to enable collection of substantially more frequent and reliable water quality data compared to existing manual sampling approaches. The results are anticipated to demonstrate the potential for ASVs to provide ubiquitous real-time water quality monitoring on shrimp farms, allowing early disease prevention and growth optimization through precision aquaculture management approaches.

2 HARDWARE DESIGN

2.1 Mechanical Design

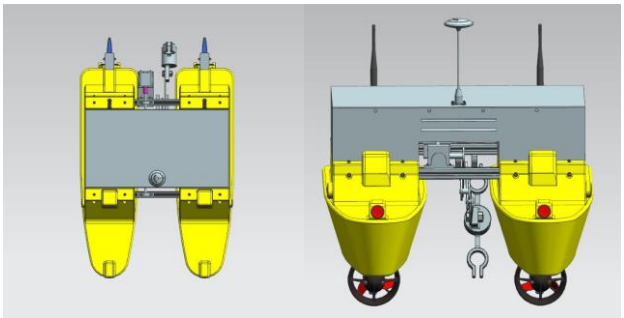

Figure 1: Autonomous Vessel Model.

The autonomous vessel incorporates a specialized bi-rudder propulsion system and brushless motors to enhance maneuverability, efficiency, and adaptation to aquaculture ponds (Figure 1). The twin hull structure improves stability while providing modular mounting points for monitoring sensors. Shaped aluminum bars interconnect the hulls to achieve both structural rigidity and lightweighting. A stepper motor adjusts sensor elevation. Key advantages of this optimized mechanical design include accurate motion control via dual rudders; increased propulsive efficiency with brushless motors; reduced noise pollution; eco-friendly, efficient power system; simplified maintenance; and adaptability to various pond conditions. The modular architecture facilitates sensor upgrades for multifaceted monitoring applications.
In summary, the vessel's mechanical design is optimized for stable navigation, efficient propulsion, and flexibility in shallow, confined ponds while supporting specialized environmental monitoring payloads. The focus on eco-friendly operation and modular upgradability provides a versatile platform tailored for sustainable, precision aquaculture applications.

Table 1: Summary of key mechanical specifications of the ASV.

Specification	**Dimension/Value**
Dimensions	680 × 520 × 230 mm^3
Maximum Speed	2 m/s
Weight	15 kg
Maximum Load	5 kg
Rudder Dimensions	8 × 4 × 20 cm^3
Lifting Mechanism Dimensions (Moving)	200 × 12 × 60 mm^3
Lifting Mechanism Dimensions (Measuring)	200 × 12 × 870 mm^3

2.2 Electronic Design

The electrical system comprises a control subsystem for autonomy and a communications subsystem for data transfer (Figure 2). The control layer employs three interconnected ESP32 modules to coordinate GPS navigation, obstacle avoidance, propulsion, and sensor positioning. The communication layer exchanges data between the on-board systems and a shore-based web server via a LoRa transceiver module. A Raspberry Pi hosts the web server with custom Python and JavaScript applications. This enables real-time monitoring and control of the vessel. The optimized multi-controller architecture provides versatile and efficient autonomous operation capabilities alongside flexible cloud-based data logging and analysis.
In summary, the system integrates specialized ESP32 microcontrollers for real-time vessel control with long-range wireless communications to a cloud-based web server. This allows continuous monitoring and

data collection during autonomous surveys, while enabling remote commanding when required. The dual-layer design provides adaptability for evolving aquaculture applications.

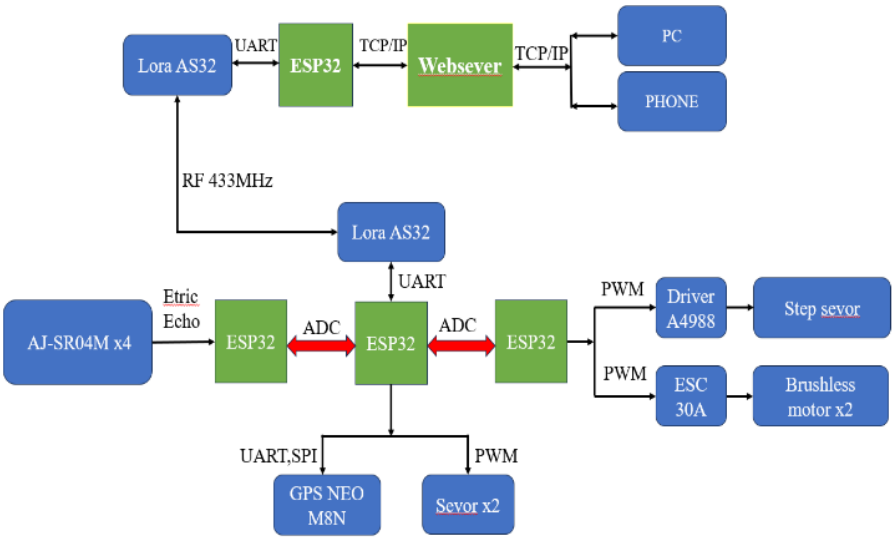

Figure 2: Overview diagram of the electrical system of the autonomous vessel.

The power system utilizes a multi-voltage design to meet the specific requirements of each component (Figure 3). A 24V supply drives the stepper motor for sensor positioning. The propulsion motors operate at 16.8V for efficient brushless control. Microcontrollers, GPS, ESCs, and other support electronics run on a 5V rail. This optimized power architecture provides stable, efficient operation by powering each subsystem at its ideal voltage level.

In summary, the stratified power supply with isolated rails for motors, digital logic, and analog circuits enhances system stability and efficiency. This allows optimal voltage allocation tailored to each subsystem's needs.

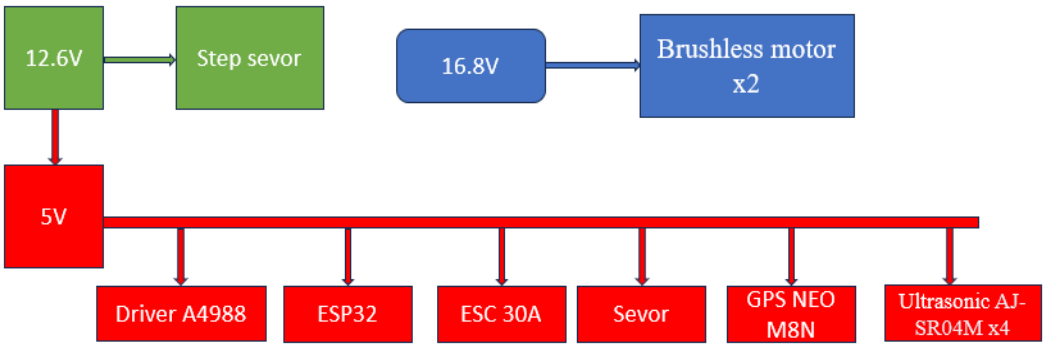

Figure 3: Power supply diagram of the autonomous vessel.

2.3 Complete Design

The final vessel configuration strategically locates the port and starboard motor controllers symmetrically to balance weight distribution and reduce electromagnetic interference while the main circuit board is centrally mounted to serve as an integration hub for electronic subsystems (Figure 4). The GPS receiver is deliberately positioned at the highest point of the vessel to optimize signal reception from satellites above by minimizing obstructions. In summary, the completed design utilizes intentional component placement to enhance system performance through symmetric weight balancing for stability, centralized circuits for simplified integration, and optimized topside GPS positioning to maximize navigation accuracy.

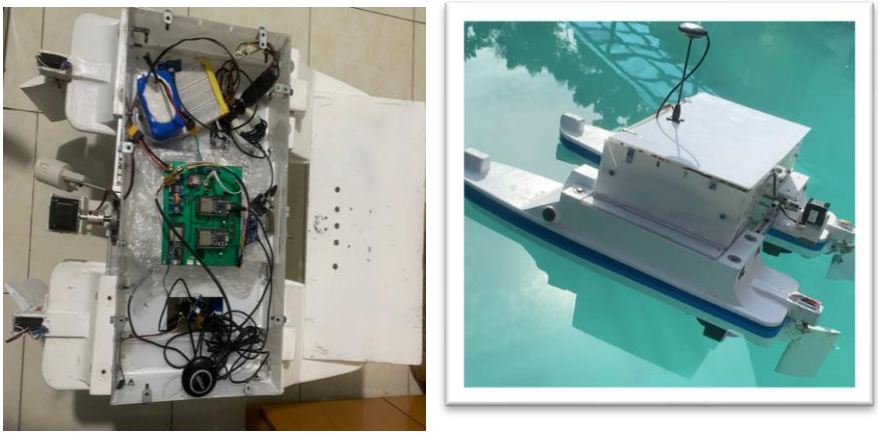

Figure 4: Final System Layout showcases the finalized configuration of the system after the design and installation phases have been completed.

3 SOFTWARE PROGRAMING

3.1 System Architecture

The system's architecture is compartmentalized into three fundamental modules: Sensors, Data Processing, and Actuation, each fulfilling a distinct role within the operational workflow of the vessel.

Sensors: The Sensing module employs GPS sensors for geospatial positioning and utilizes ultrasonic sensors for the real-time detection of obstacles in the vessel's path.

Data Processing: The Data Processing module is engineered around an ESP32 microcontroller platform. Sophisticated algorithms, incorporating machine learning and artificial intelligence paradigms, are deployed to process incoming sensor data. These computational techniques contribute to optimizing the vessel's navigational efficiency.

Actuation: In the Actuation module, processed data is employed to dynamically control the propulsion motors and steering mechanisms. This ensures that the vessel navigates accurately and efficiently toward its predetermined or dynamically computed destination points destination.

3.2 Algorithms and Diagrams

Algorithm for controlling the vessel: The Navigation Algorithm serves as the decision-making kernel within the autonomous navigation system. This algorithm uses input data from the Global Positioning

System (GPS) sensor and optimization techniques to determine the direction and speed of progress, minimizing time and energy consumption when reaching the destination.

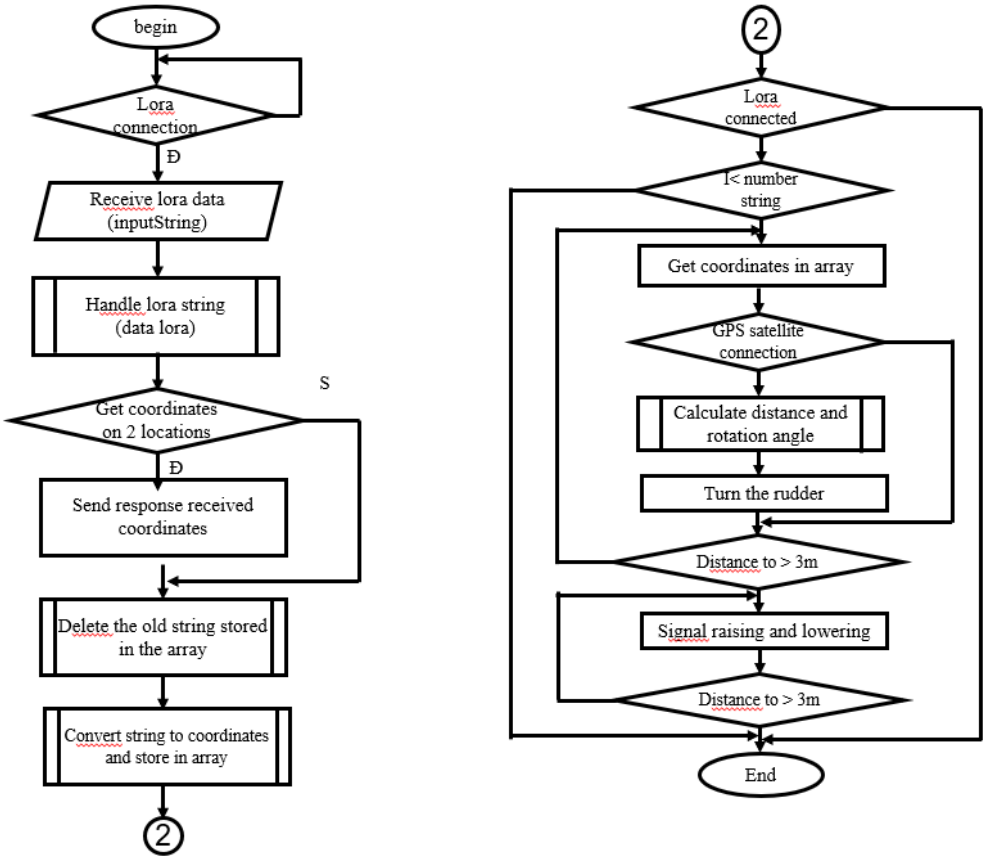

Figure 5: Flowchart of the boat control algorithm.

Explaining the flowchart:

1. Initialization: On power-up, the system syncs with the Lora Master Module for route and position data.
2. Coordinate Setup: Preset coordinates from the web are received, confirmed, and parsed into an array.
3. Navigation: The boat connects to GPS, calculates distance and angle to the next point, and moves while avoiding obstacles.
4. Motor Activation: Motors are turned on to hold the boat at a specific location.
5. Sensor Deployment: If closer than 3m to the destination, the boat stops and deploys sensors.
6. Loop or Return: The boat moves to the next point or returns to the start if all points are visited.

Obstacle avoidance algorithm: The Obstacle Avoidance Algorithm uses data from ultrasonic sensors to detect potential obstacles in the boat's path. Integrated with machine learning techniques, this algorithm is capable of making real-time collision avoidance decisions.

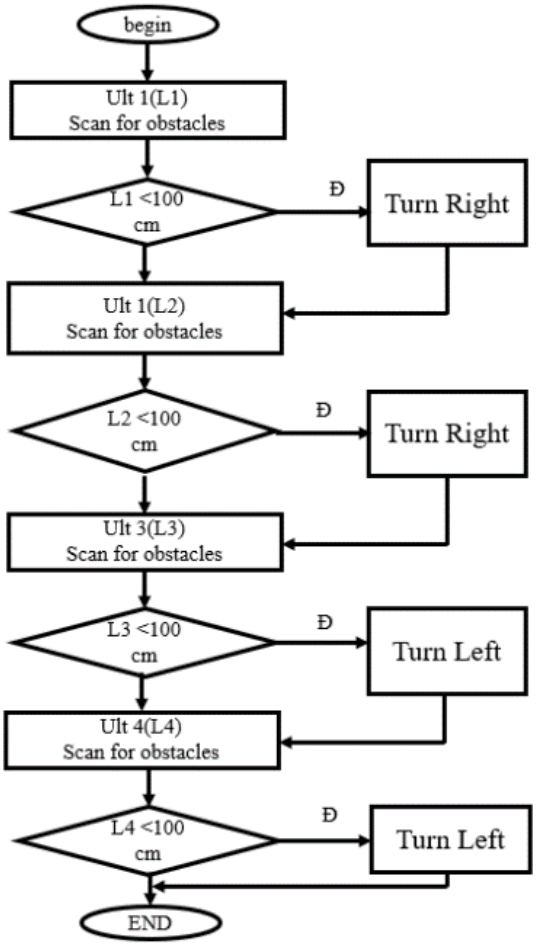

Figure 6: Flowchart of the Obstacle Avoidance Algorithm.

Explaining the flowchart:

1. Start calculations and measure the distance from the boat to the obstacle.
2. If the distance to the obstacle in front (L1) and to the left side (L2) is short, the boat will turn right to avoid the obstacle.
3. If the distance to the obstacle in front (L3) and to the right side (L4) is short, the boat will turn left to avoid the obstacle.
4. If there are no obstacles, the boat will proceed straight.
5. Without any obstacles, the boat will steer according to the set waypoint to reach the predetermined position.

Boat Navigation Algorithm: The Direction Control Algorithm is an essential part of ensuring navigational stability and performance. It utilizes optimization techniques to calculate the angle needed

for adjustment based on the current and target directions, and then controls the engine and steering system to implement this adjustment.

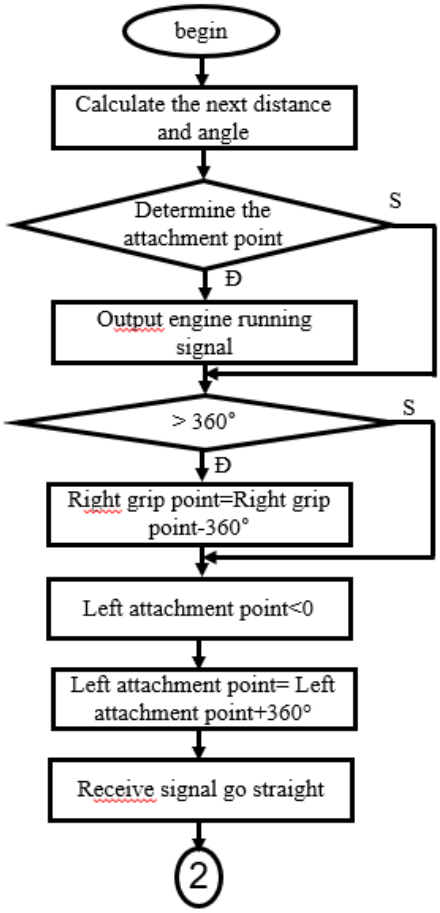

Figure 7: Flowchart for determining rotation angle.

Explaining the flowchart:

1. Once the anchoring point is determined, the engine is started.
2. Allow for an angular margin according to the left and right anchoring points. If the right anchoring point is greater than 360, it needs to be converted, for example, 380 would become a 20-degree angle. Similarly, if the left anchoring point is -5, it should be converted to 355 degrees.
3. With the left and right anchoring points determined, the steering is then adjusted to guide the boat to the next position.
4. If the boat encounters obstacles, it will prioritize avoiding them; otherwise, it will continue in the target direction.

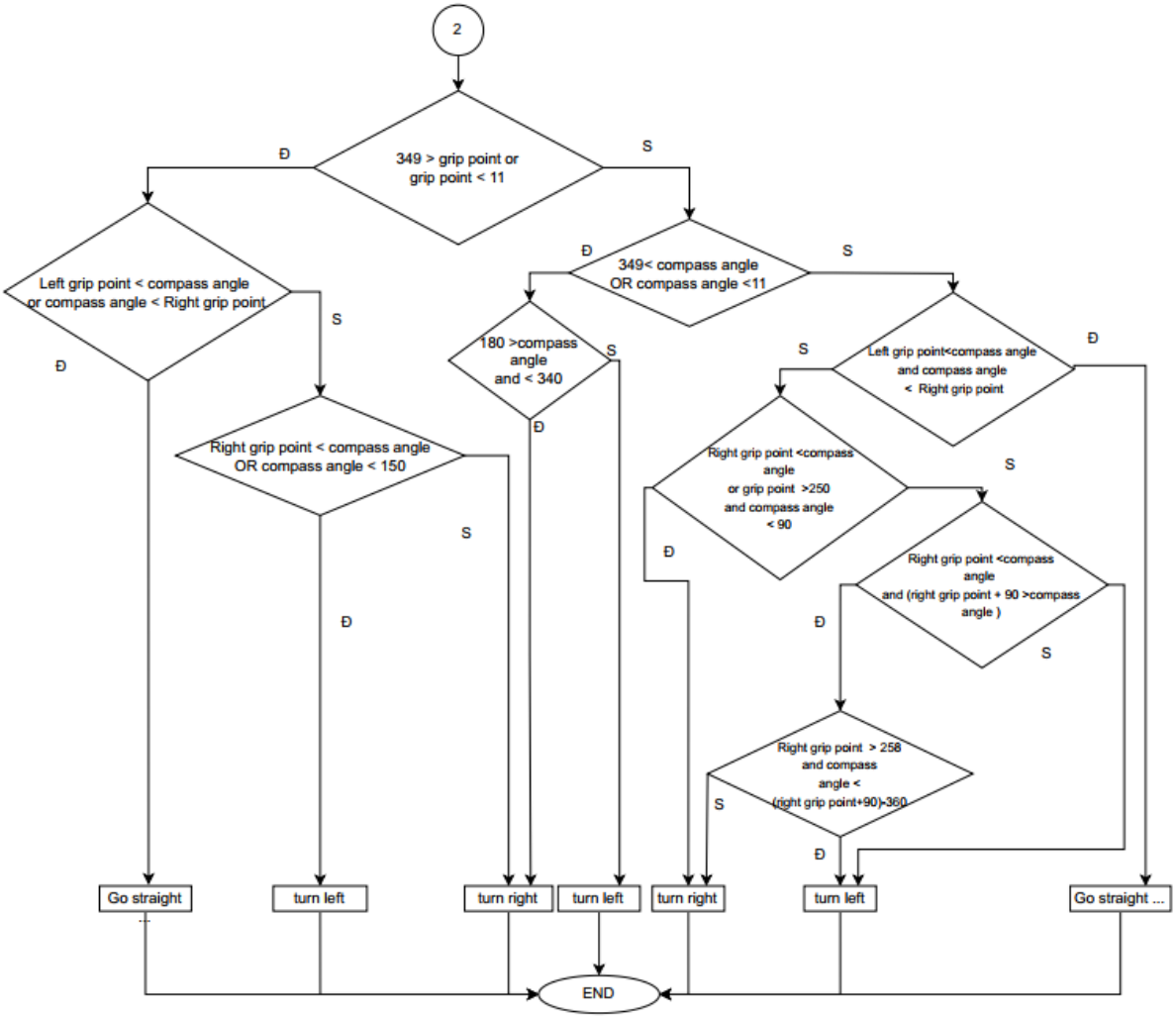

Figure 8: Flowchart for rotation direction algorithm.

Explaining the flowchart:

1. Normally, the right anchor point will be greater than the left anchor point. However, in special cases where the anchor angle ranges from 349 to 11 degrees and we allow for a 10-degree margin of error, this theory fails and requires different handling.
2. In other cases, the ship will move as usual. However, there is another special circumstance where, if the compass angle is between 349 and 11 degrees, the above theory about the right being greater than the left will not hold true. Therefore, in each case, we handle it differently to ensure the most accurate movement of the ship.
3. If the ship is at any rotation angle, it will calculate to find the shortest rotation angle to turn towards the required direction.

3.3 Control Algorithm

The primary logic for autonomous navigation and sensor data acquisition is written in Python and C++. The Python scripts are mainly running on the Raspberry Pi, focusing on high-level tasks like data management, GPS waypoint following, and web server communication. The C++ code runs on the ESP32 and handles real-time tasks, such as sensor data collection, motor control, and LoRa communication.

For navigation, we employ a waypoint-following algorithm that uses the GPS module's data to calculate the distance and angle to the next waypoint. Depending on this information, the microcontroller adjusts the speed and direction of the ASV.

3.4 Data Acquisition and Communication

The ASV's water quality sensors interface with an ESP32 controller module to package and wirelessly transmit data to a shore-based LoRa receiver module up to 2 km away using long-range LoRa communication (Figure 9). The shore LoRa gateway module passes the ASV sensor data via WiFi to a Raspberry Pi server for real-time processing, storage and hosting, allowing remote monitoring via WiFi. The system also enables complete remote command and control over LoRa by sending waypoints and actuation commands from the Raspberry Pi to the ASV's ESP32 controller via the shore LoRa module. This integrated data harvesting and wireless control architecture provides flexible real-time water quality monitoring and unmanned operation.

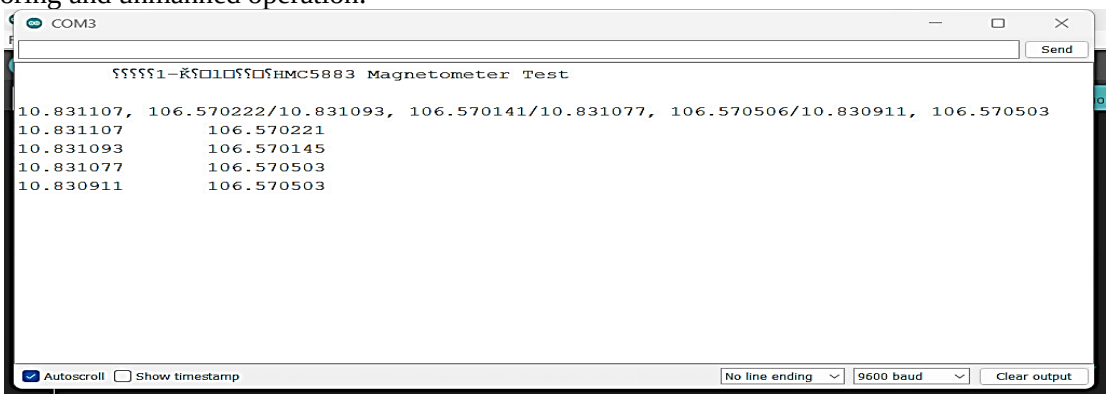

Figure 9: Send coordinate string from home Lora and parse into ship's movement coordinates.

3.5 Web Server Development

The web server is developed using Django, a high-level Python web framework. The server runs on the Raspberry Pi and provides a real-time dashboard that displays water quality parameters, such as temperature, pH, and dissolved oxygen levels, among others. The Django server also provides API endpoints that can be used for more advanced data analytics and integration with other systems.

4 SENSOR DATA ACQUISITION

Real-time water quality monitoring is critical for productive aquaculture, but traditional manual sampling has limitations, thus sensor-based systems are needed to enable continuous measurement and early detection of issues like low oxygen levels. The proposed system incorporates various sensors to monitor parameters including dissolved oxygen using optical fluorescence quenching, electrical conductivity via measuring diffusion currents, pH through electrodes detecting potential differences, and turbidity by measuring backscattered light. Regular calibration and temperature compensation of the sensors are required to ensure accurate readings. By integrating appropriate technologies, the system aims to provide automated, reliable, and continuous monitoring of key water quality parameters to support effective aquaculture management.

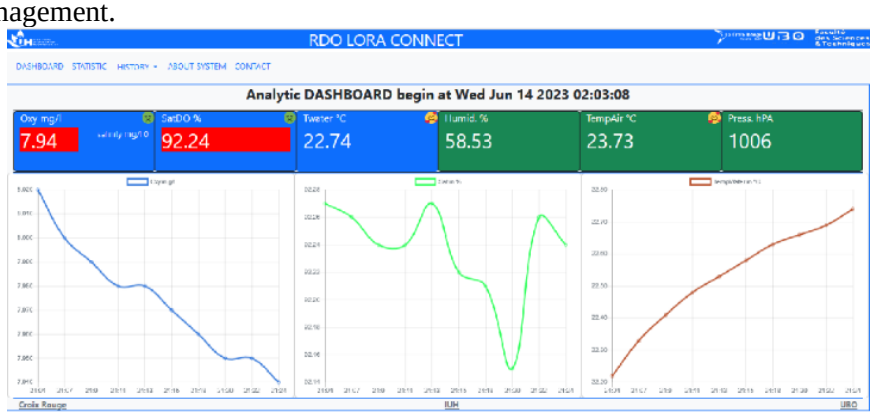

Figure 10: IHM real time inside the PI board.

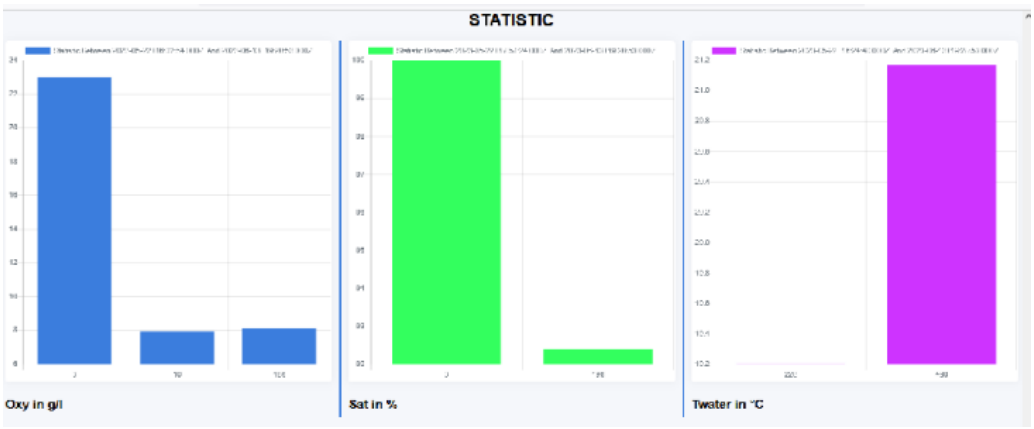

Figure 11: Statistic on all values (1000 max).

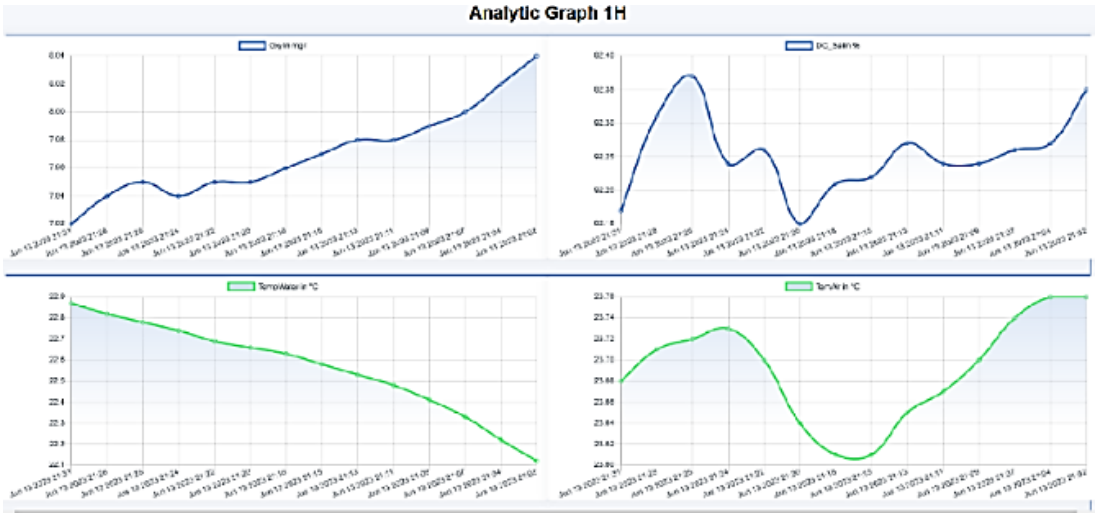

Figure 12: History on 1H, 8H or 24H.

5 EXPERIMENTS

Test Case: The autonomous boat navigates in a ZigZag pattern:

Step 1: Select the travel destination on the map.

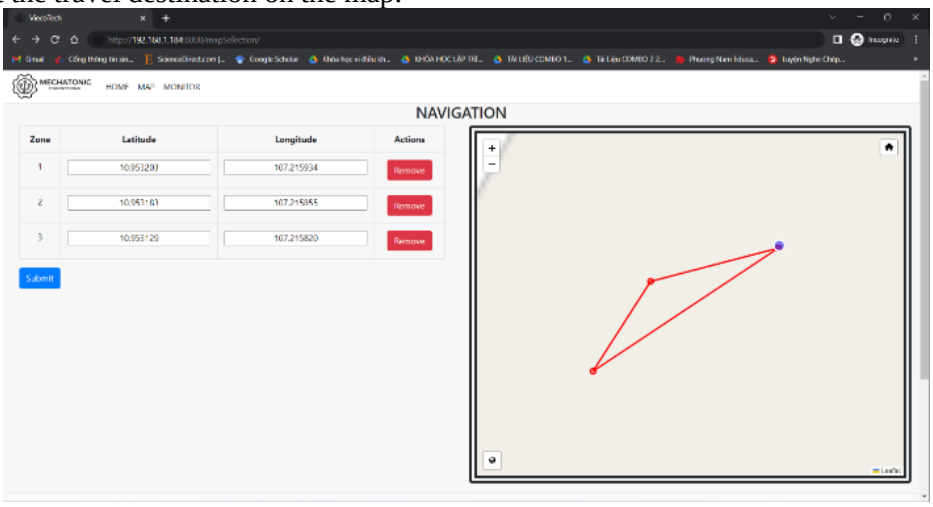

Figure 13: Select points for ZigZag path for the autonomous boat.

Step 2: The autonomous boat receives data from the website.
Step 3: The autonomous boat moves along the path.

a. The autonomous boat goes from point 1 to point 2.

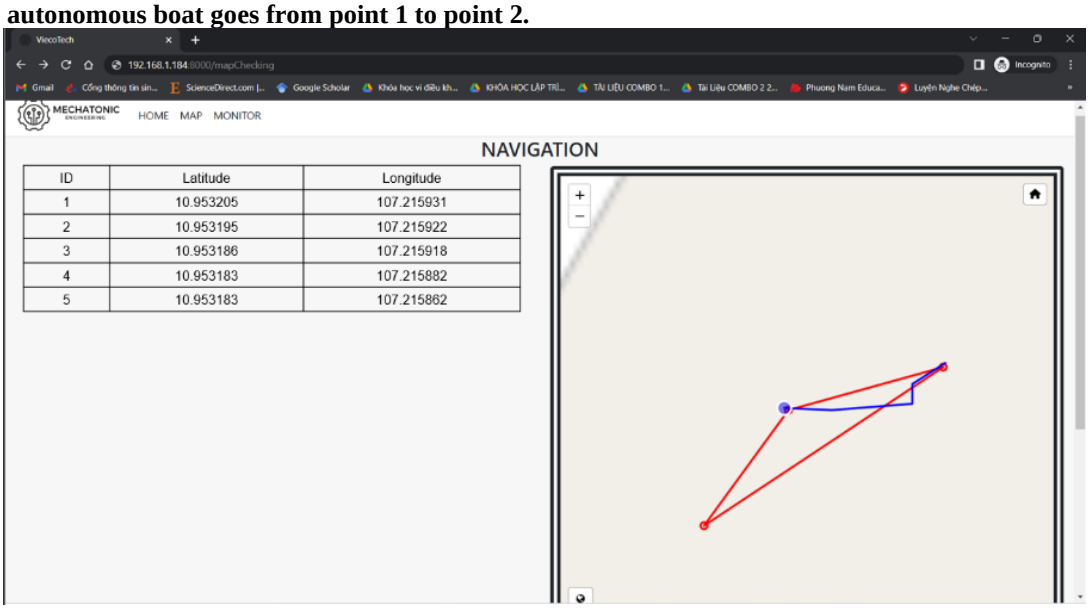

Figure 14: The autonomous boat moves to point 2 in a ZigZag pattern as marked on the website.

b. The autonomous boat moves from point 2 to point 3.

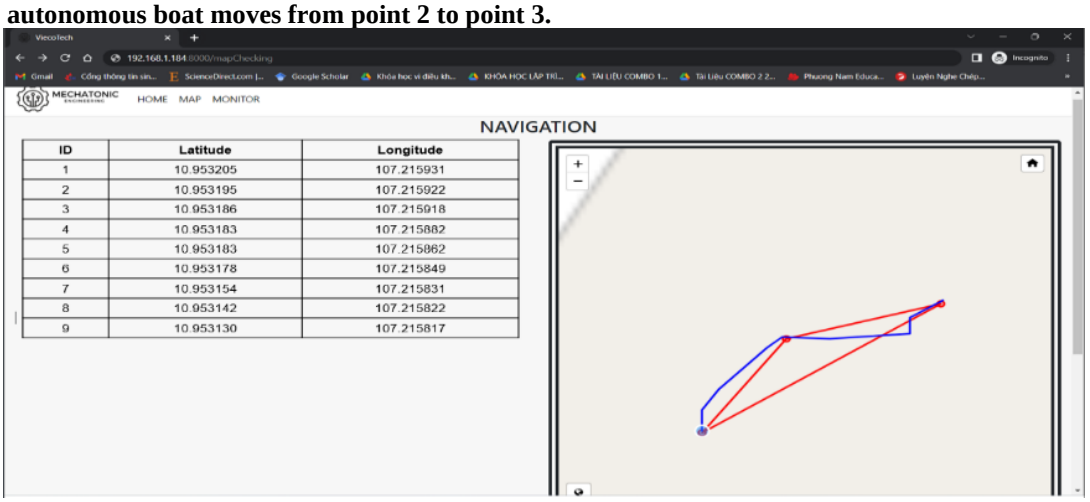

Figure 15: The autonomous boat moves to point 3 in a ZigZag pattern when marked on the web.

6 CONCLUSION AND SUMMARY

This paper has presented a comprehensive design and implementation of an Autonomous Surface Vessel (ASV) tailored for the continuous monitoring and management of water quality in shrimp ponds. By addressing the limitations of traditional monitoring methods, our ASV model introduces a cost-effective, reliable, and flexible solution that minimizes human risk and optimizes data acquisition.

6.1 Key Contributions

Modular Design: The mechanical, electronic, and software components were designed with modularity in mind, enabling straightforward upgrades and adaptability to various environmental conditions.
Advanced Algorithms: Utilizing machine learning and artificial intelligence techniques, our ASV adapts in real-time to environmental variables, thereby enhancing navigational efficiency and obstacle avoidance.

Multifaceted Application: Beyond water quality monitoring, the vessel's versatile design permits a range of other applications, including shrimp feed distribution, thus contributing to sustainable aquaculture practices.
Power Efficiency: A well-thought-out power supply scheme enhances operational efficiency and ensures system stability.

6.2 Technological Implications

The operational efficacy of the ASV in navigating through varying water conditions, combined with its real-time data collection capability, indicates its potential to be a game-changer in aquaculture management. Furthermore, the incorporation of the LoRa Gateway and a Raspberry Pi-based web server enables long-range communication, adding an additional layer of functionality for remote monitoring and control.

6.4 Future Work

Although the current implementation has exhibited robust performance, there are avenues for further improvement. Future research could delve into the integration of more sophisticated sensor technologies for a deeper understanding of environmental factors. Additionally, adaptive algorithms that learn from long-term operational data could be developed to further enhance the ASV's capabilities.

6.5 Final Remarks

The integration of advanced computational algorithms, modular design, and practical utility in our ASV model represents a significant leap forward in the field of automated environmental monitoring. As global aquaculture industries continue to grow, innovations like this offer a vision of a future marked by smarter, more sustainable operations.

REFERENCES

[1] A.B. Smith, Challenges of manual water quality monitoring in aquaculture facilities, *Journal of Aquaculture Studies*, 2020.

[2] C.K. Lee, Limitations of fixed/buoy monitoring systems in aquaculture, *Monitoring and Management Technologies for Aquaculture*, 2019.

[3] F. Johnson, Labor requirements for boat sampling in aquaculture facilities, *Journal of Aquaculture Studies*, 2018.

[4] W. Chen, Automated ASV-based monitoring for aquaculture applications, *Aquacultural Engineering*, 2019.

[5] A.B. Wilson, Cost savings from using autonomous surface vehicles for water quality monitoring, *Aquaculture Economics and Management*, 2021.

[6] G.N. Roberts, Improved safety from removing human samplers: A review of autonomous surface vehicles in aquaculture, *Reviews in Aquaculture*, 2020.

[7] A.R. Clark, Ocean data collection using autonomous surface vehicles, *Journal of Marine Research*, 2021.

[8] S.J. Davis, Maritime security applications of autonomous surface vehicles: A review, *Annual Review of Control, Remote Sensing, and Autonomous Systems*, 2017.

CONTROL OF PARALLEL ROTARY DOUBLE INVERTED PENDULUM USING POLE PLACEMENT TECHNIQUE

MINH-TAI VO [1*], CHI-HUNG NGUYEN [3], VAN-SI TRAN [3], THI-HONG-XUAN TRAN [3], MINH-DUC TRAN [2], THI-THANH-HOANG LE [3], THANH T. TRAN [1], HOAI-NGHIA DUONG [4]

[1] School of Science, Engineering & Technology, RMIT University Vietnam,
[2] Ho Chi Minh City University of Technology (HCMUT), VNU-HCM,
[3] Ho Chi Minh City University of Technology and Education (HCMUTE),
[4] School of Engineering, Eastern International University (EIU);
tai.vo3@rmit.edu.vn, {20151554, 20151487, 21151190 }@student.hcmute.edu.vn,
tmduc.sdh222@hcmut.edu.vn, hoangltt@hcmute.edu.vn, thanh.tran37@rmit.edu.vn,
nghia.duong@eiu.edu.vn
**tai.vo3@rmit.edu.vn*

Abstract. In this study, a new system which is named Parallel Rotary Double Inverted Pendulum (for short PRDIP) has been studied by using pole placement technique (for short PPT). PRDIP is an upgraded version of Single Rotary Inverted Pendulum (SRIP). Controlling PRDIP is a difficult problem in control engineering due to its nonlinearity and instability. The construction of PRDIP has two parallel pendulums which are placed at direct drive motor. In this article, two equilibrium points of PRDIP consist of two pendulums stabilize at vertical upright position, and one pendulum stabilizes at upward position – the other stabilizes at downward position, are validated using PPT. Besides, pole placement controller is designed in two forms include pole placement with integral action and without integral action. Simulation results in MATLAB/Simulink environment are shown and discussed to prove the effectiveness and robustness of two control schemes at two operation points.

Keywords. Parallel rotary double inverted pendulum (PRDIP), pole placement technique, pole placement with integral action, pole placement without integral action.

1 INTRODUCTION

Underactuated Single Rotary Inverted Pendulum system (SRIP) or Furuta Pendulum (FP) has been studied in many articles after being introduced 31 years ago by Professor Katsuhisa Furuta and his colleagues [1-3]. Until now, studies on underactuated systems still play a pivotal role and have attracted attention in control system theory. Therefore, researchers continuously study and develop new systems based on SRIP [4, 5]. Separated the rotary inverted pendulum into parallel mechanism or series mechanism. In the case of series mechanisms, construction of system uses only a motor to control two serially connected pendulums. This system is known as Serial Rotary Double Inverted Pendulum (SRDIP) [6, 7]. Stabilization control schemes [6], swing-up approaches [7] have been qualified and discussed on SRDIP. In the case of the parallel mechanism, PRDIP [8, 9] and Triple Furuta Pendulum (TFP) [10] are represented in this class. For the TFP system, there are three freedom links which are controlled by a motor. For the PRDIP system, two freedom links are mounted on an arm and opposite each other. The most important thing in controlling the parallel mechanism is when the natural frequency of the pendulum is match, system becomes uncontrollable. Therefore, the length of pendulums is designed to be different.

In this study, application of pole placement techniques including pole placement with integral action and without integral action is focused on controlling of PRDIP. PRDIP is controlled in two positions: two pendulums stand at vertical upright position and one pendulum stands at upward position – other stands at downward position.

The organization of this article consists of five sections. The first section introduces PRDIP and research purposes. In the second section, mathematical modeling of PRDIP is derived and expressed in state space equation. Section 3 presents pole placement architectures include pole placement with integral action and

without integral action. In the next section, simulation results are shown, and discussed. Finally, in Section 5, conclusion and final remarks are drawn.

2 PRDIP DESIGN DYNAMIC MODEL

2.1 Mathematical Modeling

The PRDIP system is shown in Figure 1. According to [9], the equations of motion in matrix form are presented in Equation (1)

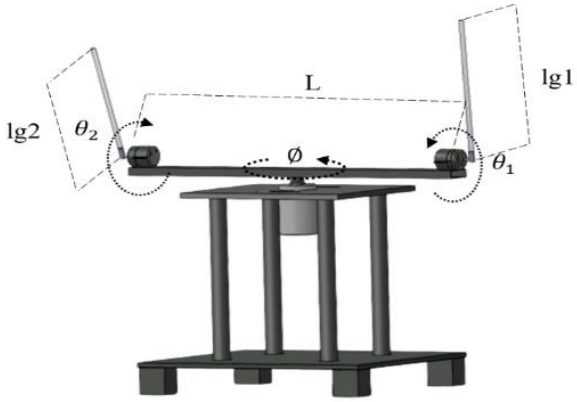

Figure 1: PRDIP system.

$$\begin{bmatrix} D_{11} & D_{12} & D_{13} \\ D_{21} & D_{22} & D_{23} \\ D_{31} & D_{32} & D_{33} \end{bmatrix} \begin{bmatrix} \ddot{\phi} \\ \ddot{\theta}_1 \\ \ddot{\theta}_2 \end{bmatrix} + \begin{bmatrix} G_1 \\ G_2 \\ G_3 \end{bmatrix} = \begin{bmatrix} V_c \\ 0 \\ 0 \end{bmatrix} \tag{1}$$

where

$D_{11} = J_0 + m_1 l_{g1}{}^2 \sin^2\theta_1 + m_1 L^2 + m_2 l_{g2}{}^2 \sin^2\theta_2 + m_2 L^2$

$D_{12} = -m_1 L l_{g1} \cos\theta_1$

$D_{13} = -m_2 L l_{g2} \cos\theta_2$

$D_{21} = -m_1 L l_{g1} \cos\theta_1$

$D_{22} = J_1 + m_1 l_{g1}{}^2$

$D_{23} = 0$

$D_{31} = -m_2 L l_{g2} \cos\theta_2$

$D_{32} = 0$

$D_{33} = J_2 + m_2 l_{g2}{}^2$

$G_1 = m_1 l_{g1}{}^2 \dot{\theta}_1 \dot{\phi} \sin(2\theta_1) + m_1 l_{g1} L \dot{\theta}_1^2 \sin\theta_1 + c_0 \dot{\phi} + m_2 l_{g2}{}^2 \dot{\theta}_2 \dot{\phi} \sin(2\theta_2) + (c_0 + \frac{K_t K_b}{R_m})\dot{\phi}$

$G_2 = -m_1 l_{g1}{}^2 \dot{\phi}^2 \sin\theta_1 \cos\theta_1 - m_1 g l_{g1} \sin\theta_1 + c_1 \dot{\theta}_1$

$G_3 = -m_2 l_{g2}{}^2 \dot{\phi}^2 \sin\theta_2 \cos\theta_2 - m_2 g l_{g2} \sin\theta_2 + c_2 \dot{\theta}_2$

$V_c = \frac{K_t}{R_m} e$

e (counts): Motor driving command

System parameters and their values are shown in Table 1. Those values are captured based on real-time experiment setup in our previous research [11].

Table 1: System parameters and values.

Parameters (unit)	Value		
	Arm (*i=0*)	Pendulum 1 (*i=1*)	Pendulum 2 (*i=2*)
m_i – Mass of the ith link (kg)	na	0.059	0.127
l_{gi} – Length of the ith link (m)	na	0.038	0.082
J_i - Inertia of the ith link (kgm^2)	0.75	0.00267	0.00137
C_i - Viscous coefficient (Nm.s)	1.5260e-04	4.6930e-04	1.443
L – Length of arm link (m)	na	na	0.51
g - Gravity constant (m/s^2)	9.81		
K_b - Back emf constant (V/(rad/sec))	0.064943		
K_t – Torque constant (V/(rad/sec))	0.064943		
R_m – Armature resistance (Ω)	6.835271		

2.2 Linear Model

As mentioned in the beginning of this paper, PRDIP is controlled at two operation points, including $\phi \approx 0; \theta_1 \approx 0; \theta_2 \approx \pi; \dot{\phi} \approx 0; \dot{\theta}_1 \approx 0; \dot{\theta}_2 \approx 0$ and $\phi \approx 0; \theta_1 \approx 0; \theta_2 \approx 0; \dot{\phi} \approx 0; \dot{\theta}_1 \approx 0; \dot{\theta}_2 \approx 0$. The system model can be linearized by using the small-angle approximation. Let

$$x = [\phi \quad \theta_1 \quad \theta_2 \quad \dot{\phi} \quad \dot{\theta}_1 \quad \dot{\theta}_2]^{\mathrm{T}} \tag{2}$$

The linear model at the equilibrium points can be obtained by

$$\begin{cases} \dot{x} = A_j x + B_j e \\ y = Cx \end{cases} \text{ with } j = 1,2 \tag{3}$$

In this paper, the output matrix C is defined as follows:

$$C = \begin{bmatrix} 1 & 0 & 0 & 0 & 0 & 0 \end{bmatrix} \tag{4}$$

To check the controllability of PRDIP, we create a matrix M_{ct}, known as controllability matrix. For the system to be completely state controllable, the controllability matrix:

$$M_{ctj} = \begin{bmatrix} B_j & A_j B_j & \cdots & A_j^5 B_j \end{bmatrix} \tag{5}$$

For equilibrium point: $\phi \approx 0; \theta_1 \approx 0; \theta_2 \approx \pi; \dot{\phi} \approx 0; \dot{\theta}_1 \approx 0; \dot{\theta}_2 \approx 0$ (Called Position 1 (*j=1*)). The purpose of this position is to combine two control strategies, including balancing control and anti-oscillation control.

$$A_1 = \begin{bmatrix} 0 & 0 & 0 & 1 & 0 & 0 \\ 0 & 0 & 0 & 0 & 1 & 0 \\ 0 & 0 & 0 & 0 & 0 & 1 \\ 0 & 0.1008 & 0.0388 & -3.7506 & -0.0002 & 0 \\ 0 & 20.4029 & 0.0410 & -3.9575 & -0.0424 & 0 \\ 0 & -0.0985 & -18.8431 & 3.6667 & 0.0002 & 0 \end{bmatrix}; \; B_1 = \begin{bmatrix} 0 & 0 & 0 & 0.0124 & 0.0130 & -0.0178 \end{bmatrix}^T \tag{6}$$

Besides, $rank(M_{ct1}) = 6; \; \det(M_{ct1}) = 8.3893\text{e-}04$. The rank of M_{ct1} is equal to the number of states (n=6), thus the matrix is full rank, and $\det(M_{ct1}) \neq 0$. The system is controllable at Position 1.

For equilibrium point: $\phi \approx 0; \theta_1 \approx 0; \theta_2 \approx 0; \dot{\phi} \approx 0; \dot{\theta}_1 \approx 0; \dot{\theta}_2 \approx 0$ (Called Position 2 (*j=2*)). The purpose of this position is to control two inverted pendulums stabilized in vertical orientation.

Accordingly, $rank(M_{ct2}) = 6; \; \det(M_{ct2}) = 1.2022\text{e-}06$. The rank of M_{ct2} is equal to the number of states (n=6), thus the matrix is full rank, and $\det(M_{ct2}) \neq 0$. PRDIP is controllable at Position 2.

$$A_2 = \begin{bmatrix} 0 & 0 & 0 & 1 & 0 & 0 \\ 0 & 0 & 0 & 0 & 1 & 0 \\ 0 & 0 & 0 & 0 & 0 & 1 \\ 0 & 0.1008 & 0.0388 & -3.7506 & -0.0002 & 0 \\ 0 & 20.4029 & 0.0410 & -3.9575 & -0.0424 & 0 \\ 0 & 0.0986 & 18.8631 & -3.6667 & -0.0002 & 0 \end{bmatrix}; \; B_2 = \begin{bmatrix} 0 & 0 & 0 & 0.0123 & 0.0130 & 0.0121 \end{bmatrix}^T \tag{7}$$

3 POLE PLACEMENT TECHNIQUE [12]

Consider the PRDIP in Figure 1. The control target is to keep the inverted pendulums at two proposed positions as given in subsection 2.2 and control the position of the arm link. In this section, two control strategies are built up to control of PRDIP system at Position 1 and Position 2. For the case of Pole Placement Control without Integral Action (known as Type 0). For the case of Pole Placement Control with Integral Action (known as Type 1).

3.1 Pole Placement Control without Integral Action (Type 0)

The block diagram of Figure 2 is a basic form of Pole Placement Control without Integral Action (Type 0).

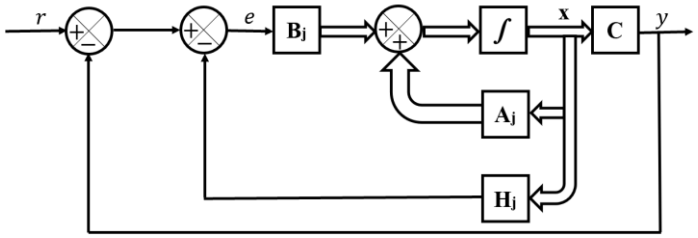

Figure 2: Pole placement control without integral action architecture.

Referring to Figure 2, we obtain the equations for the system as follows:

$$\begin{cases} \dot{x} = A_j x + B_j e \\ y = Cx \end{cases} \tag{8}$$

The control signal e is given by Equation (9)

$$e = -H_j x \tag{9}$$

The control design and time-response requirements are as follows: the settling time of approximately 2 ~ 4 seconds and the maximum overshot of 20% in the step response of the arm link. Let choose the desired closed-loop poles at $s = \kappa_p$ (p = 1, 2, 3, 4, 5, 6) for Position 1 and Position 2.

Table 2: The desired closed-loop poles for Position 1 and Position 2.

Position	Poles					
	κ_1	κ_2	κ_3	κ_4	κ_5	κ_6
1	$-2+2.091j$	$-2-2.091j$	-5	-5	-5	-5
2	$-1.9941+2.091j$	$-1.9941-2.091j$	-5	-10	-20	-30

The state-feedback gain matrices H_j are computed by using the MATLAB command $H_j = ac\ker\left(\hat{A}, \hat{B}, J\right)$. The value of H_j are obtained in Table 3:

Table 3: The state-feedback gain matrices H_j of Position 1 and Position 2.

Position	Value of H_j
1	$H_1 = 1.0e+06\left[-0.1111 \quad 1.8519 \quad -0.1131 \quad -0.1126 \quad 0.4090 \quad 0.0975\right]$
2	$H_2 = 1.0e+06\left[0.0531 \quad 4.0196 \quad -4.4954 \quad 0.0465 \quad 0.8638 \quad -0.9743\right]$

3.2 Pole Placement Control with Integral Action (Type 1)

The block diagram of Figure 3 is a basic form of Pole Placement Control with Integral Action (Type 1).

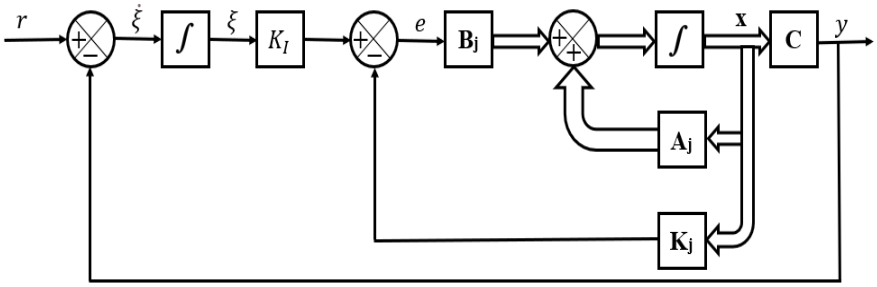

Figure 3: Pole placement control with integral action architecture.

Referring to Figure 3, we obtain the equations for the system as follows:

$$\begin{cases} \dot{x} = A_j x + B_j e \\ y = Cx \end{cases}$$
$$e = -K_j x + K_I \xi \tag{10}$$
$$\dot{\xi} = r - y = r - Cx$$

Where e is control signal; y is output signal; ξ is output of the integrator; r is reference input signal.

The state error equation as given by Equation (11):

$$\dot{e}_r = \hat{A}_j e_r + \hat{B}_j e_v \tag{11}$$

where

$$\hat{A} = \begin{bmatrix} A_j & 0 \\ -C & 0 \end{bmatrix};\ \hat{B} = \begin{bmatrix} B \\ 0 \end{bmatrix}$$

The control signal is given by Equation (12):

$$e_v = -\hat{K}_j e_r \tag{12}$$

where $\hat{K}_j = \begin{bmatrix} K_j & \vdots & -K_I \end{bmatrix}$

The control design and time-response requirements are as follows: the settling time of approximately 2 ~ 4 seconds and the maximum overshot of 20% in the step response of the arm link. Let choose the desired closed-loop poles at $s = \kappa_p$ (p = 1, 2, 3, 4, 5, 6 ,7) for Position 1 and Position 2.

Table 4: The desired closed-loop poles for Position 1 and Position 2.

Position	Poles						
	κ_1	κ_2	κ_3	κ_4	κ_5	κ_6	κ_7
1	$-2+2.091j$	$-2-2.091j$	-5	-5	-5	-5	-5
2	$-1.9941+2.091j$	$-1.9941-2.091j$	-5	-10	-20	-30	-40

The state-feedback gain matrices $\hat{K}_j$ are computed by using the MATLAB command $\hat{K}_j = ac\ker\left(\hat{A}, \hat{B}, J\right)$.

The value of $\hat{K}_j$ for Position 1 and Position 2 are obtained in Table 5:

Table 5: The state-feedback gain matrices $\hat{K}_j$ of Position 1 and Position 2.

Position	Value	
	K_j	K_I
1	$K_1 = 1.0e+04\begin{bmatrix} -0.8219 & 3.916 & 0.3742 & -0.5837 & 0.865 & 0.1276 \end{bmatrix}$	$1.0e+04[0.5555]$
2	$K_2 = 1.0e+07\begin{bmatrix} -0.1378 & 1.1523 & -0.0004 & -0.1537 & 0.2544 & 0.0103 \end{bmatrix}$	$1.0e+07[-0.2125]$

4 VALIDATION

4.1 Simulation Results of PRDIP With Type 0 Controller

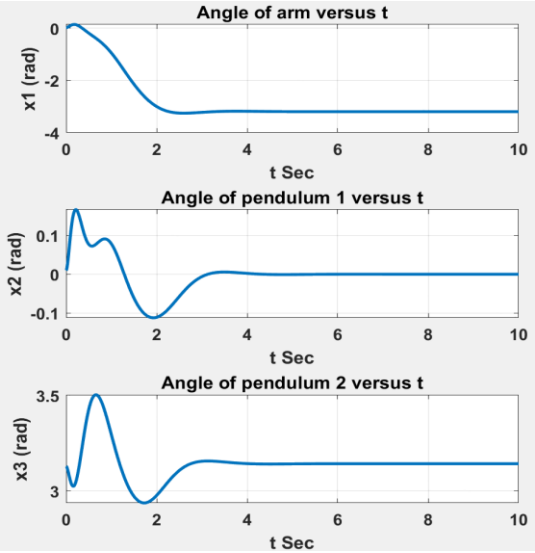

Figure 4: Responses of output system with Type 0 at Position 1.

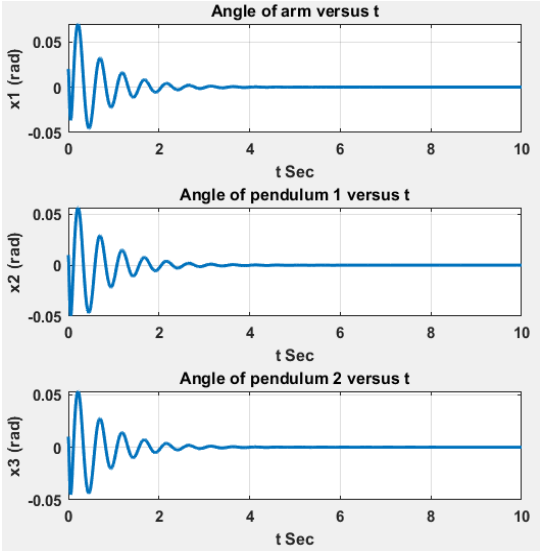

Figure 5: Responses of output system with Type 0 at Position 2.

Simulation results of responses of PRDIP with Type 0 architecture are shown in Figures 4 and 5. Firstly, we concentrate on Figure 4. We expect the angular position of the arm to operate at 0 rad but Type 0 controller cannot control at zero radian. The angle of the arm with Type 0 controller is stable at -3.23 rad after 4 seconds. While the pendulum 1 and pendulum 2 are stable at setting points after 4 seconds. Next look on Figure 5, PRDIP is set up to control the system at Position 2. The angle of arm, pendulum 1 and pendulum 2 stabilize at vertical upright position after 4 seconds. The maximum overshot ranges of arm, pendulum 1, pendulum 2 are [-0.05; 0.05] rad, [-0.05; 0.05] rad, and [-0.048; 0.05] rad, respectively. In conclusion, target control of PRDIP at Position 2 meet expectation. However, the performance of the system with Type 0 at Position 1 failed.

4.2 Simulation Results of PRDIP With Type 1 Controller

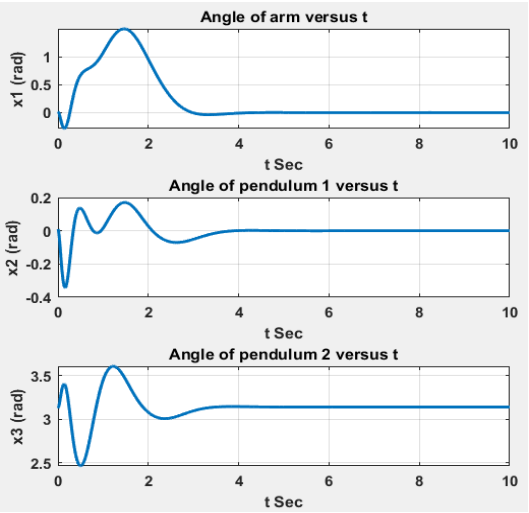

Figure 6: Responses of output system with Type 1 at Position 1.

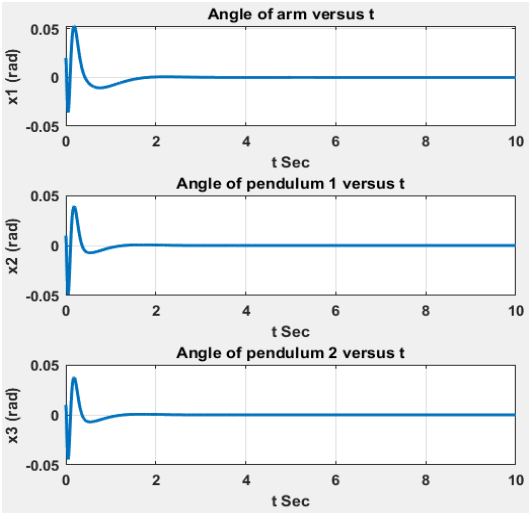

Figure 7: Responses of output system with Type 1 at Position 2.

Simulation results of responses of PRDIP with Type 1 architecture are presented in Figures 6 and 7. In Figure 6, we observe that Type 1 controller can fix the issue which is caused by Type 0 control scheme.

The curved angle of arm versus t (x_1), angle of pendulum 1 versus t (x_2), angle of pendulum 2 versus t (x_3) are stable at setting points after 4 seconds. We analyze the settling time of PRDIP in Figure 6, the responses of output system with Type 1 stand at "0" radian after 2 seconds. It is faster than the system that is controlled by Type 0. Next concentrating on maximum overshoot range of each curve, maximum overshoot ranges of arm, pendulum 1, pendulum 2 are [-0.033; 0.05] rad, [-0.05; 0.039] rad, and [-0.041; 0.037] rad, respectively. The maximum overshot range of each curve is reduced when compared to the system with Type 0. Long story short, targets control of PRDIP at Position 1 and Position 2 meet expectation.

5 CONCLUSION

In this paper, PPT is designed in pole placement with integral action and pole placement without integral action for controlling the PRDIP at two equilibrium points. As simulation results are given in validation section, PRDIP with pole placement with integral action architecture has better performance than pole placement without integral action. The performance of output system with pole placement control with integral action (Type 1) proves the effectiveness and meets expectation at two equilibrium points. In the future research, we focus on deploying pole placement control with integral action control scheme on the real-time experimental setup.

REFERENCES

[1] K. Furuta, M. Yamakita, S. Kobayashi, Swing-up control of inverted pendulum using pseudo-state feedback, *Journal of Systems and Control Engineering*, vol. 206, no. 6, pp. 263-293, 1992, doi: https://doi.org/10.1243/PIME_PROC_1992_206_341_02.

[2] Y. Xu, M. Iwase, K. Furuta, Time optimal swing-up control of single pendulum, *Journal of Dynamic Systems, Measurement, and Control*, vol. 123, no. 3, pp. 518-527, 2001, doi: https://doi.org/10.1115/1.1383027.

[3] M. Iwase, KJ. Astom, K. Furuta, J. Akesson, Analysis of safe manual control by using Furuta pendulum, in *2006 IEEE Conference on Computer Aided Control System Design*, Munich, Germany, 2006, doi: 10.1109/CACSD-CCA-ISIC.2006.4776708.

[4] O. Qasem, H. Gutierrez and W. Gao, Experimental Validation of Data-Driven Adaptive Optimal Control for Continuous-Time Systems Via Hybrid Iteration: An Application to Rotary Inverted Pendulum, *IEEE Transactions on Industrial Electronics*, 2023, doi: 10.1109/TIE.2023.3292873.

[5] A. Nagarajan and A. A. Victoire, Optimization Reinforced PID-Sliding Mode Controller for Rotary Inverted Pendulum, *IEEE Access*, vol. 11, pp. 24420-24430, 2023, doi: 10.1109/ACCESS.2023.3254591.

[6] Sondarangallage D.A. Sanjeewa, M. Parnichkun, Control of rotary double inverted pendulum system using LQR sliding surface based sliding mode controller, *Journal of Control and Decision*, vol. 9, no. 1, pp. 89-101, 2022, doi: https://doi.org/10.1080/23307706.2021.1914758.

[7] F. Liang, X. Xin, Y. Li, Swing-up and Balance Control of Rotary Double Inverted Pendulum, in *2023 3rd International Conference on Robotics and Control Engineering*, Nanjing China, 2023, doi: https://doi.org/10.1145/3598151.3598163.

[8] Z. Yu, L. Liu, J. Yu, X. Zhang, Y. Guo and S. Wang, EFC/H∞ Based Dual-mode Switching Global Control of the First-order Parallel Rotating Double Inverted Pendulum System, in *ECON 2022 – 48th Annual Conference of the IEEE Industrial Electronics Society*, Brussels, Belgium, 2022, doi: 10.1109/IECON49645.2022.9969113.

[9] H. D. Khoi, Using LQR Algorithm to Control Circular Two Stage Parallel Inverted Pendulum System, *Bulletin of College of Engineering National Ilan University*, vol. 9, pp. 101-114, 2013, doi: 10.6176/BCE.2013.09.17.

[10] K. Sugawara, M. Izutsu, S. Hatakeyama and M. Iwase, Stabilization of Triple Furuta pendulum by sliding mode control, in *IECON 2014 - 40th Annual Conference of the IEEE Industrial Electronics Society*, Dallas, TX, USA, 2014, doi: 10.1109/IECON.2014.7048916.

[11] M. T. Vo, M. D. Vo, V. D. Nguyen, V.D.H. Nguyen, M. D. Tran, H. N. Duong, T. T. Tran, Development and Control of Underactuated Parallel Rotary Double Inverted Pendulum System, in *The 12th International Conference on Robotics, Vision, Signal Processing and Power Applications (RoViSP 2023)* , Penang, Malaysia, 2023. (Accepted)

[12] K. Ogata, Control Systems Design in State Space, in *Modern Control Engineering*, New Jersey, Pearson, 2009, pp. 732-827.

THE EFFECTS OF DIFFERENT DRYING METHODS ON SLICED PURPLE YAM DRYING

LE ANH DUC [1], PHAN VAN PHUC [2], PHAM VAN KIEN [2*]

[1] *Faculty of Engineering and Technology, Nong Lam University, Ho Chi Minh City, Vietnam,*
[2] *Faculty of Automotive Engineering, School of Technology, Van Lang University*
Ho Chi Minh City, Vietnam;
kien.pv@vlu.edu.vn

Abstract. The study focused on the effect of different drying methods such as hot air (HA) drying method, heat pump (HP) drying method and infrared (IR) assisted heat pump (HP) drying method (IR+HP) on drying rate and color change of dried sliced purple yam. The experimental drying process was conducted with the drying air temperature of 45ºC and the drying air velocity of 2.5 m/s. The experimental drying results showed that the IR assisted HP drying method got the highest drying rate with the shortest drying time of 105 minutes, that reduced about 56% and 65% as compared to HP drying (240 minutes) and HA drying (300 minutes). However, dried yam after heat pump drying achieved the best color retention with the lowest color change index of 2.40 as compared to IR assisted HP drying (4.66) and HA drying (7.58). The dried products of all drying methods got the requirement of drying process, the dried product surface was not cracked, and the dried product still retained the characteristic flavor of purple yam.

Keywords. Purple yam, color change index, drying time, hot air drying, heat pump drying, infrared assisted heat pump.

1 INTRODUCTION

Yam has been statistically one of the most important food crops for many tropical countries such as Burkina Faso, Ghana, Togo, Nigeria, and Vietnam with over 600 classifications, in which, a few of them as purple yam, yellow yam and water yam were used commonly for food purpose [1]. Yams contain many nutrients that are very good for people's health such as proteins, starch, minerals, lipids, and vitamin C [2]. Yam was also considered as a good source of carbohydrate [3]. However, like many agricultural products, yam has a high moisture content of about 50 – 80 % (w.b). High moisture content in food products stimulates bacterial activities, and biochemical reactions [4]. So, it is easily spoiled during storage, and difficult to store fresh yams for a long period [5]. Drying has become an effective food preservation method. The drying process was a complex thermal process of simultaneous heat and mass transfer [6]. After drying process, the moisture content of dried agricultural products reduced, and its shelf life was extended for long time preservation [7]. Dried yam could be stored for a longer period, and used for cooking, and extraction of resistant starch [8]. Drying process includes three major methods of heat transfer such as conduction, convection and radiation [9]. There were some common drying technologies which have been applied for drying agricultural products including sun drying, hot air convective drying, heat pump drying, vacuum drying, radio frequency drying, microwave drying, infrared drying and hybrid drying [10]. Hot air drying has been widely used because of its main advantages as high drying rate, easy operation and low operating costs [11]. But the temperature of drying air can affect the quality of dried products reasonably. In heat pump drying, the drying air has low humidity and low temperature, that supports the moisture diffusion process from the inside of the material to the surface and shortens the drying time [12]. The drying techniques using infrared radiation have several advantages such as higher heating rate, shorter drying time and higher drying product quality [13]. In which, IR heating mechanism is the effect of the electromagnetic radiation on drying material, that causes the internal heating within material and supports the heating rate [14, 15]. The hybrid drying using IR combining with other drying methods as hot air drying and heat pump drying can obtain an effective drying process [16 – 19].

There were some previous studies of yam drying to identify the efficiency of yam drying method and quality

of dried yam. Ononogbo et al, conducted the experimental drying of yam by hot air drying at temperature in range of 55ºC – 75ºC, drying air velocity in range of 1.0 – 2.0 m/s and the sample slice thickness of 1.0 – 2.0 mm. The results of drying time varied from 195 – 705 minutes [20], and the drying rate became higher at higher temperature and velocity of drying air. Adebimpe et al., studied the thin layer drying characteristics of blanch-assisted and un-blanch-assisted water yam slices by hot air drying with the drying air temperature of 50, 60 and 70ºC, the drying air velocity of 0.8 m/s and yam slice thickness of 0.8cm. The results showed that the drying rate of blanch-assisted slices was significantly higher than un-blanch-assisted slices [21]. Chineze et al., investigated the effect of different drying technics in drying of some kinds of yam such as oven drying, solar drying and sun drying. The results indicated the drying time of oven drying was the shortest (180 – 300 minutes), followed by solar drying (390 – 480 minutes) and sun drying (780 – 960 minutes). In which, in oven drying method, purple yam dried faster (180 mins) followed by yellow yam (240 mins) and white yam (300 mins) [22]. Nurdi et al., investigated the effect of drying method on quality of dried yam with Oven drying, blanching Oven drying and blanching freeze-drying. In which, the color change index of dried yam in Oven drying got the highest value, followed by blanching Oven drying and blanching freeze-drying. This confirmed that the dried yam of blanching freeze-drying process retained the original color best [23].

The objectives of the study were to conduct the experimental drying of yam by HA drying, HP drying, and IR assisted HP drying in order to evaluate the effectiveness of drying methods. In which, the output parameters of drying process were drying time and color change index of dried yam.

2 MATERIAL AND METHODS

2.1 Material

Raw material was fresh purple yam purchased at Thu Duc Agricultural Market, Ho Chi Minh City, Vietnam. After purchasing, purple yams were washed, peeled, and sliced to 2.5 mm thickness. The initial moisture content of fresh yam samples was 73.8 ± 0.1 (%, w.b). The weight of yams was 2 kg per drying batch. The fresh yam samples were given in Figure 1.

Figure 1: Fresh sliced purple yam samples.

2.2 Experimental methods

The drying methods were used to dry purple yam including HA drying, HP drying, and IR assisted HP drying. The input experimental drying parameters were controlled in drying process such as drying air temperature of 45ºC, and drying air velocity of 2.5 m/s.

A hot air convective dryer was used for experimental drying of yam has a maximum operation capacity of 2 kW. The drying air was sucked into the drying chamber by a centrifugal fan (1) and heated by thermistors (2) to reach the desired drying temperature. The drying air temperature and drying air velocity could be controlled in the drying process. The HA drier was given in Figure 2.

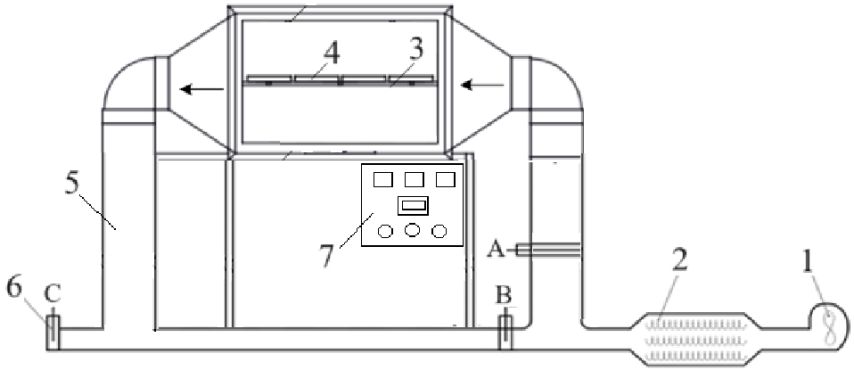

Figure 2: The HA dryer.

In which, 1. Fan, 2. Thermistors, 3. Drying tray, 4. Yam samples, 5. Pipe, 6. Air controlling valves, 7. Controller unit,

The heat pump drier used for experimental drying of yam had the maximum operating capacity of 0.75 kW. The HP dryer is also the IR assisted HP dryer as shown in Figure 3, in which the HP only drying method was conducted as the infrared light was off. The drying air was pumped through the heat pump unit concluding compressor, condenser, expansion valve and evaporator in order to achieve the specific temperature, humidity and velocity. Then, the drying air continued to enter the drying chamber to perform the yam drying process.

The IR assisted HP drier was composed of an infrared light installed inside the drying chamber of the heat pump dryer. The IR assisted HP drier was given in Figure 3. The infrared light had electromagnetic wavelengths ranging from 0.76 - 1,000μm, frequency of 50Hz and operating capacity of 220W. After passing through the heat pump unit, the drying air would combine with infrared energy for the drying process.

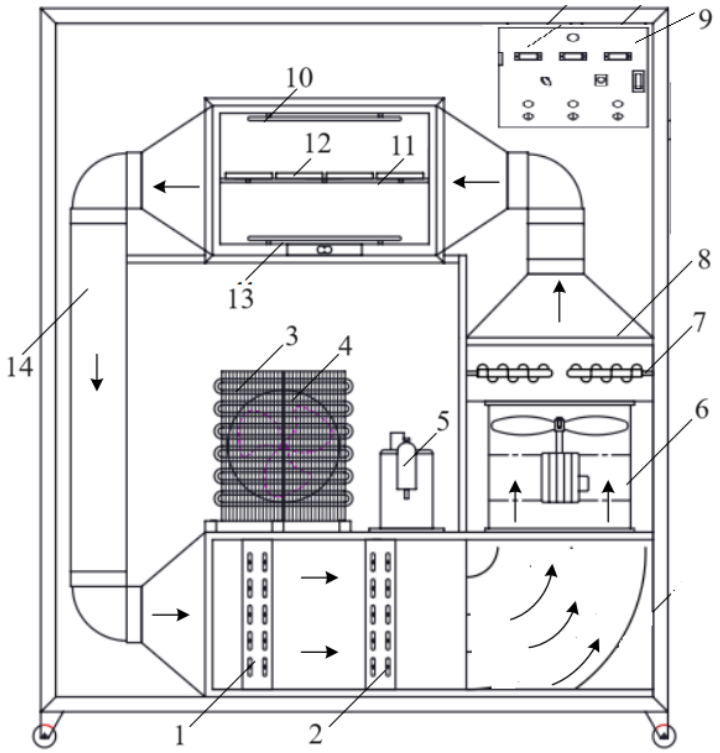

Figure 3: The IR assisted HP dryer.

In which, 1. Evaporator, 2. Condenser, 3. Sub-condenser, 4. Sub-condenser fan, 5. Compresser, 6. Fan, 7. Thermistors, 8. Pipe reducer, 9. Controller unit, 10. Infrared light, 11. Drying tray, 12. Yam samples, 13.

infrared light, 14. Pipe.

The initial moisture content of the yam was determined by a moisture analyzer (YOKE DSH-100A-10, maximum analyzed sample weight: 100 ± 0.01 g, analyzed moisture range: 0 –100 ± 0.01%).

The moisture content of sliced yam was determined by using an infrared moisture-drying balance of A&D-MX 50 brand of Japan, the sensitivity of the scale was 0.001 gram; the analytical temperature range was 50 - 200°C. An electronic balance measures the mass of the dried material and the moisture content at the drying time *t* is determined by the equation (1) [24].

$$M_t = 100 - \frac{W_0}{W_t}(100 - M_0) \quad (1)$$

Where: M_t: moisture content of sliced yam at drying time t (% wb.); M_0: initial moisture content of sliced yam (%wb.); W_t: weight of sliced yam at drying time t (h); W_0: initial weight of sliced yam (g).

An electronic scale (Lutron GM-5000, maximum measurement value of 5000 ± 0.01 g) was used to weigh yam samples during the drying process, regularly every 15 minutes. Each experiment was conducted until the drying material achieved the moisture content of 12 ± 0.2 (%, w.b) and completed in triplicates.

An X-rite colorimeter (Ci64) was used to evaluate the color of fresh yam samples and dried yam samples based on the CIELab color scale. About 10 yam slices per drying batch were chosen for color measurement and the average measurement value was obtained. The following indicators assess the color change of the dried product was determined by equation (2).

$$\Delta L^* = L_0 - L^*; \Delta a^* = a_0 - a^*; \Delta b^* = b_0 - b^* \quad (2)$$

The overall color change of yam was determined by the overall color change index ΔE* which was determined by equation (3) [24].

$$\Delta E^* = \sqrt{\Delta L^{*2} + \Delta a^{*2} + \Delta b^{*2}} \quad (3)$$

In which, the L-value (lightness color) varied in range of 0 (black) to 100 (white); the a-value (red and blue color) varied in range of 0 to 60 (red) or 0 to -60 (blue); b-value (yellow and green color) varied in range of 0 to 60 (yellow) or 0 to -60 (green).

3 RESULTS AND DISCUSSION

3.1 The effect of different drying methods on drying time

The moisture content versus drying time during HA drying, HP drying, and IR assisted HP drying of sliced purple yam process was presented graphically in Figure 4.

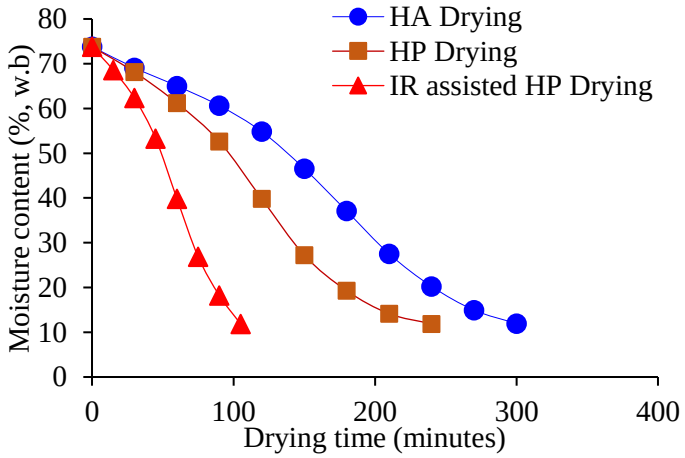

Figure 4: The moisture content of the drying material versus drying time.

As shown in Figure 4, the yam's moisture content reduction during drying process with different drying methods had a similar trend that was consistent with the agricultural drying curve theory. In IR-assisted HP drying method, the support of IR could improve the drying rate significantly and shorten the drying time appreciably as compared to HP drying and HA drying. In IR-assisted HP drying method, the drying time

required was 105 minutes, whiles, drying time of HP drying was 240 minutes and drying time of HA drying was 300 minutes. The drying time of IR-assisted HP drying reduced about 56% and 65% as compared to HP drying and HA drying. This was explained by the IR heating mechanism, in which, the effect of the electromagnetic radiation on drying material surface causes changes in the electronic, rotational, and vibrational states of atoms and molecules [25]. When the materials absorb IR radiation energy, the constituent molecules would vibrate at high frequency and intermolecular friction occurs which results in the internal heating within material and the surface temperature increases quickly, which is much faster than that in conduction and convection heat transfer [14, 15]. The result was that the drying rate in IR-assisted HP drying process was improved. During the heat pump drying process, the drying air that passed through the heat pump system would have relatively low humidity, that made the process of diffusion of moisture from the inside of the drying material to the surface become faster than that of hot air-drying process. The result was to improve moisture reduction rate and shorten drying time by 20% as compared to hot air drying.

3.2 The effect of different drying methods on color change of the drying material

The color change index of drying material corresponding to the different drying methods was given in Table 1. The dried products of different drying methods were shown in Figure 5.

Table 1: The color change index value of sliced purple yam corresponding to different drying methods.

Drying method	Color change index			
	L*	a*	b*	ΔE
HA drying	74.8	0.74	11.45	7.58
IF assisted HP drying	77.61	-0.25	13.25	2.40
HP drying	79.58	-0.27	12.15	4.66
Raw sliced purple yam	81.71	-0.35	14.36	–

(a) (b) (c)

Figure 5: The products of HA drying (a), HP drying (b) and IR assisted HP drying (c).

Table 1 showed that in HA drying process the color change (ΔE) of dried yam got the highest value (7.58), followed by the IR assisted HP drying process (4.66) and HP drying (2.40). This indicated that the color of dried yam in HP drying process got the smallest change after drying. The change in color was attributed to enzymatic browning because of differences in phenolic compounds, which were associated with oxidative browning of yam [26]. Lightness (L*) values of HA drying process (74.8), IR assisted HP drying process (77.61) and HP drying process (79.58) indicated that in HP drying process, the dried yam became brighter than the other drying methods. This was explained by the fact that in HA drying process, the drying material exposed longer with hot air and the color of dried yam would become darker. In HP drying and IR assisted HP drying process, the shorter drying time would support the color of dried material being brighter. Blueness (a*) value of yam in HP drying got the lowest value of -0.27 and followed by IR assisted HP drying (-0.25), while in HA drying, the a* index got the redness value of 0.74. This showed that the dried

yam retained the color of greenness well in HP drying and IR assisted HP drying. In HA drying, the color of dried yam would change into light redness because of thermal effect. Yellowness (b*) value of dried yam was 12.95, 10.75 and 9.78 corresponding to HA drying, IR assisted HP drying and HP drying. This confirmed that in HA drying, the prolonged exposure of yams to hot air has resulted in changing into more yellow color of dried yams. The shorter drying time of IR assisted HP drying and HP drying made the color of dried yam change into less yellow than HA drying. The values of L*, a* and b* showed the improvement in the appearance of yam after drying, in which, the dried yam in HP drying obtained the best color retention and followed by IR assisted HP drying and HA drying.

Besides, Figure 5 showed that the dried yam after HA drying had the best color retention, the products has maintained the original bright green color of fresh yam samples. Although the products of IR assisted HP drying still retained the unique color of fresh yam, the bright green color of the yam was reduced and darker than that of HP drying because of the thermal effect of infrared power in drying process. Meanwhile, the color change of the products of HA drying got the highest due to thermal effect with prolonged drying time and the dried yam lost the original bright green and changed into light redness and yellow.

In general, the dried products of three drying methods have got the requirement of drying process, the product surface was not cracked, and the dried product still retained the characteristic flavor of purple yam. The surface quality and flavor of dried products were evaluated through human senses.

4 CONCLUSIONS

The experimental drying of sliced purple yam by different drying methods as HA drying, HP drying and IR assisted HP drying method was carried out with drying air temperature of 45^{o}C, drying air velocity of 2.5 m/s. The drying results showed that HP drying, and IR assisted HP drying method obtained high drying efficiency such as reducing the drying time and maintaining the color of the dried product better than HA drying. In which, the drying time of IR-assisted HP drying reduced about 56% and 65% as compared to HP drying and HA drying. Although the drying time of HP drying was shorter than HA drying and longer than IR-assisted HP drying, the products of HP drying obtained the best quality when the dried products has maintained the original bright green color of fresh purple yam samples. In general, the dried products of three drying methods have got the requirement of drying process, the product surface was not cracked, and the dried product still retained the characteristic flavor of purple yam.

REFERENCES

[1] Olatoye K.K., Arueya G.L., Nutrient and phytochemical composition of flour made from selected cultivars of aerial yam (Dioscorea bulbifera) in Nigeria, *Journal of Food Composition and Analysis*, vol. 79, pp. 23–27, 2019.

[2]. Lasztity R., Hidvegi M., Bata A., Saponins in food, *Food Reviews International*, vol. 41, pp. 371–390, 1998.

Thermal efficiency and drying Behaviour of Yam slices in a dryer driven by the waste heat of exhaust gases

[3] Amandikwa C., Iwe M.O., Uzomah, A., Olawuni A.I., Physico-chemical properties of wheat-yam flour composite bread, *Nigerian Food Journal*, vol. 33, pp. 12–17, 2015.

[4] Kaveh M., Sharabiani V.R., Chayjan R.A., Taghinezhad E., Abbaspour-Gilandeh Y., Golpour I., ANFIS and ANNs model for prediction of moisture diffusivity and specific energy consumption potato, garlic and cantaloupe drying under a convective hot air dryer, *Information Processing in Agriculture*, vol. 5, pp. 372–387, 2018.

[5] Chen X., Li X., Mao X., Huang H., Wang T., Qu Z., Miao J., Gao W., Effects of drying processes on starch-related physicochemical properties, bioactive components and antioxidant properties of yam flours. *Food Chemistry*, vol. 224, pp. 224–232, 2017.

[6] Doymaz I., Thin-layer drying characteristics of sweet potato slices and mathematical modeling. *Heat and Mass Transfer*, vol. 47, pp. 277–285, 2011.

[7] Abbaspour Gilandeh Y., Jahanbakhshi A., Kaveh M., Prediction kinetic, energy, and exergy of quince under hot air dryer using ANNs and ANFIS, *Food Science and Nutrition,* vol.5, pp. 594–611, 2019.

[8] Srikanth K.S., Sharanagat V.S., Kumar Y., Bhadra R., Singh L., Nema P.K., Kumar V., Convective drying and quality attributes of elephant foot yam (Amorphophallus paeoniifolius), *LWT - Food Science and Technology*, vol. 99, pp. 8–16, 2019.

[9] Liu Z., Bia J., Wang S., Meng J., Wang H., Yu X., Gao Z., Xiao H., Prediction of energy and exergy of mushroom slices drying in hot air impingement dryer by an artificial neural network, *Drying Technology,* vol. 38, pp. 1959-1970, 2019.

[10] Kaveh M., Jahanbakhshi A., Abbaspour Gilandeh Y., Taghinezhad E., Moghimi M.B.F., The effect of ultrasound pre-treatment on quality, drying, and thermodynamic attributes of almond kernel under convective dryer using ANNs and ANFIS network. *Journal of Food processing engineering*, vol. 41, pp. 123–134, 2018.

[11] Omari, A., Behroozi-Khazaei, N., Sharifian, F., Drying kinetics and artificial neural network modeling of the mushroom drying process in a microwave-hot air dryer, *Journal of Food Processing Engineering*, vol. 41, 1–10, 2018.

[12] Fakhreddin Salehi, Recent applications of heat pump dryer for drying of fruit crops: A Review, *International Journal of Fruit Science,* vol. 21, pp. 546-555, 2021.

[13] Rastogi N.K., Recent trends and developments in infrared heating in food processing, *Critical Reviews in Food Science and Nutrition,* vol. *5*2, pp. 737–760, 2012.

[14] Fasina O., Tyler B., Pickard M., Zheng G.H., Wang N., Effect of infrared heating on the properties of legume seeds, *International Journal of Food Science and Technology,* vol. 36, pp. 79–90, 2001.

[15] Dan Huang, Pei Yang, Xiaohong Tang, Lei Luo, Bengt Sunden, Application of infrared radiation in the drying of food products, *Trends in Food Science & Technology*, Vol. 110, pp. 765-777, 2021

[16] Onwude D.I., Hashim N., Abdan K., Janius R., Chen G., The effectiveness of combined infrared and hot-air drying strategies for sweet potato, *Journal of Food Engineering*, vol. 241, pp. 75–87, 2019.

[17] Qu F., Zhu X., Ai Z, Ai Y., Qiu F., Ni D., Effect of different drying methods on the sensory quality and chemical components of black tea, *LWT - Food Science and Technology*, vol. 99, pp. 112–118, 2019.

[18] Wu X.F., Zhang M., Bhandari B., A novel infrared freeze drying (IRFD) technology to lower the energy consumption and keep the quality of Cordyceps militaris, *Innovative Food Science and Emerging Technologies,* vol. 54, pp. 34–42, 2019.

[19] Xie L., Mujumdar A.S., Fang X.M., Wang J., Dai J.W., Du Z.L., Xiao H.W., Liu Y., Gao Z.J., Far-infrared radiation heating assisted pulsed vacuum drying (FIR-PVD) of wolfberry (Lycium barbarum L.): effects on drying kinetics and quality attributes, *Food and Bioproducts Processing,* vol. 102, pp. 320–331, 2017.

[20] Ononogbo C., Nwakuba N.R., Nwaji G.N., Nwufo O.C., Nwosu E.C., Okoronkwo C.A., Igbokwe J.O., Anyanwu E.E., Thermal efficiency and drying Behaviour of Yam slices in a dryer driven by the waste heat of exhaust gases, *Scientific African,* vol. 17, pp. (e01310) 1–11, 2022.

[21] Adebimpe Fatimat Okeleye, Charles Taiwo Akanbi, Tunde Afolabi Morakinyo, Modeling Of Thin Layer Drying Characteristics Of Blanch-Assisted Water Yam (Dioscorea Alata) Slices, *Croatian Journal Of Food Science And Technology*, vol. 13 (1), pp. 43–50, 2021

[22] Chineze G., Okeke1 B.E., Eje1 P.C., Eze, Drying Characteristics of Yam Varieties: A Comparative Analysis, *Agricultural Engineering*, vol. 1, pp. 20–37, 2020.

[23] Nurdi Setyawan, John Solomon Maninang, Sakae Suzuki and Yoshiharu Fujii, Variation in the Physical and Functional Properties of Yam (Dioscorea spp.) Flour Produced by Different Processing Techniques, *Foods*, vol. 10, pp. 1341, 2021.

[24] Le Anh Duc, Nguyen Lan Phuong, The effects of infrared radiation drying conditions on drying properties of shell shrimp, *Lecture Notes in Mechanical Engineering book series (AMAS2021),* pp. 727–733, 2021.

[25] Sakai N., Hanzawa T., Applications and advances in far-infrared heating in Japan, *Trends in Food Science and Technology*, vol. 5, pp. 357–362, 1994.

[26] Santos P.H.S., Silva M.A., Retention of vitamin C in drying process of fruits and Vegetables – A review. *Drying Technology*, vol. 26, pp. 1421–1437, 2008.

RESEARCH, CALCULATION AND DESIGN ON A VIBRATING PRESS PART OF THE VIBRATING CONCRETE PRESSER WITH ITS CAPACITY OF 100,000 QTC IN VIETNAMESE CONDITIONS

SAM NHAN NGUYEN [1], CUONG MINH NGUYEN [2], THANH TRUNG BUI [2*]

[1]*Department of Science Management &International affair of Industrial University of Ho Chi Minh City,*
[2]*Faculty of Heat and Refrigeration Engineering of Industrial University of Ho Chi Minh City;*
**buitrungthanh@iuh.edu.vn*

Abstract. The article's content discusses the analysis and selection of the vibration table pressing principle for calculating and designing the assembly of a vibration table press used in concrete brick production. The design calculations yield the following results: The produced brick is a 4-hole brick, measuring 80 × 80 × 180 mm^3, with a mass of 1.5 kg per brick; The mold accommodates 72 bricks; The press's capacity is 100,000 bricks per shift. The vibrating table's mass is 1100 kg; The mass of the lower mold is 934 kg; The vibration amplitude is 0.6mm; The vibration angular velocity is 314 rad/s; The required vibration force is 126.716kN; The optimal pressing force is 5,202 kN, suitable vibrating concrete column height is under 200cm; The maximum pressure to ensure collision safety is 4,270 kN; Each working cycle lasts 15 seconds; The cylinder's working stroke (*L*) is 470mm; The maximum force applied to the cylinder is 103.06 kN; The impact load on each vibrating rod amounts to 23.287 kN.

Keywords. Unburnt bricks, vibrating press, concrete block press machine, vibrating platform, vibration frequency.

1 INTRODUCTION

Based on the survey and an analysis of the trends for concrete brick applications of [1], compared to other static pressing techniques (SPT), vibration pressing technology (VPT) has a 50% lower investment, faster feeding time from 12 - 25s, machine productivity is 3-5 times higher than the SPT in the same segment, machine structure is simple and easy to maintain and repair. It is evident that the VPT surpasses SPT in terms of productivity. The VPT proves versatile in handling input materials and is exceptionally well-suited for various production environments. In the contemporary landscape, it stands as the most advanced technology worldwide.

For designing of the VP mechanism of the concrete brick presser, we undertake an examination of three distinctive options for configuring the VP assembly, as detailed below:

Option 1: The operational sequence is outlined in Figure 1: Raw materials are introduced onto the conveyor and subsequently fed by the feeder (5) towards the mold (4). During the feeding process, the vibrator (8) activates to facilitate material settling. Once the material filling is accomplished, the vibrator (8) ceases operation. Subsequently, the feeder (5) retracts to its initial position for the next material acquisition. Cylinder (1) extends and lowers the male mold, aligning it with the surface of the material residing on the female mold (4). Following this, the vibrator (8) reactivates, initiating the next phase. The pressing mold (3) progressively descends until it reaches the predetermined height for the brick, at which point it halts. Concurrently, the vibrator (8) also ceases operation. Cylinder (9) elevates the female mold (4) to a level exceeding the brick's height before coming to a stop. During this interval, Cylinder (1) retracts, returning the male mold (3) to its original position. The Conveyor (6) triggers, transporting a fresh pallet to the position on the vibrating table. Simultaneously, the newly formed brick-laden pallet is pushed onto Conveyor (11), prepping for the subsequent brick pressing cycle. Conveyor (11) undertakes the task of transporting the brick-laden tray to the designated stacking location for eventual placement in the curing area. With the new pallet in position courtesy of the rear conveyor, Cylinder (9) lowers the female mold back to its initial placement, primed for the ensuing forming cycle.

Option 2: The operational principle closely resembles Option 1, with a notable alteration in the arrangement of the female mold driving cylinder (9). This modified configuration is depicted in Figure 2.

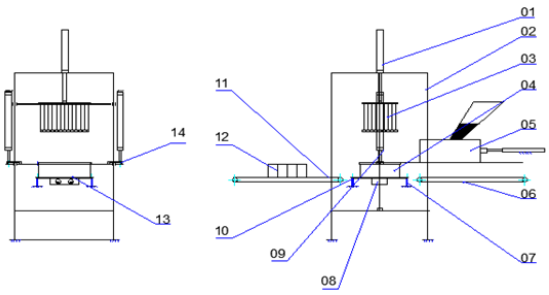

1- Male mould drive cylinder; 2- Chassis; 3- Male mold; 4- Female mold; 5- Feeder; 6- Pallet feed conveyor; 7- Spring; 8- Vibrator; 9- Cylinder drive the mold; 10- Vibrating table; 11- Product pickup conveyor; 12- Brick products; 13- mould pedestal; 14- Female mold clamping kit.

Figure 1: Operation principle concrete brick press vibrating table principal Option 1.

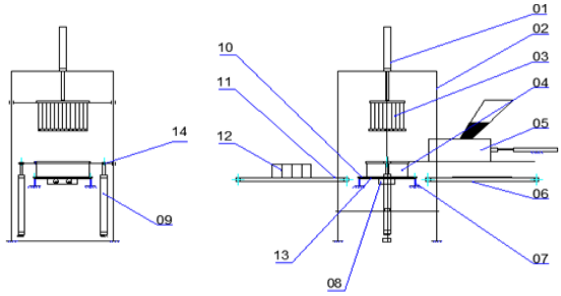

1-Male mould drive cylinder; 2- Chassis; 3- Male mold; 4- Female mold; 5- Feeder; 6- Pallet feed conveyor; 7- Spring; 8- Vibrator; 9- Cylinder drive the mold; 10- Vibrating table; 11- Product pickup conveyor; 12- Brick products; 13- mould pedestal; 14- Female mold clamping kit.

Figure 2: Operation principle concrete brick press vibrating table principal Option 2.

Option 3**:** For this option, we will bring the vibrator (14) above the male mold as shown in Figure 3.

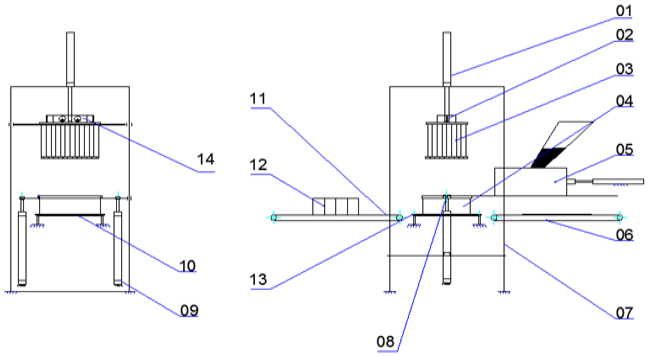

1- Male mould drive cylinder; 2- Spring; 3- Male mold; 4- Female mold; 5- Feeder; 6- Pallet feed conveyor; 7- Chassis; 8- Female mold clamping kit; 9- Cylinder drive the mold; 10- Frame supporting the mold; 11- Product pickup conveyor; 12- Brick products; 13- mould pedestal; 14- Vibrating table;

Figure 3: Operation principle concrete brick press vibrating table principal Option 3.

Reviews on the options**:** In the Option 2, adopting the cylinder placement as illustrated in Figure 2 leads to heightened pressure on the cylinder head during the manipulation of lifting and lowering the female mold (4). Consequently, to uphold structural integrity and manage the load effectively, the implementation of a larger capacity cylinder system becomes essential. This accommodation, while ensuring proper load handling, inadvertently contributes to an escalation in overall costs.

Regarding Option 3, the arrangement involving positioning the vibrator (14) at the uppermost point, as depicted in Figure 3, carries implications for material compaction efficiency. This setup is anticipated to yield a lower efficiency in material compaction in comparison to Option 1. Moreover, due to the substantial dimensions of the vibrating table, there arises a challenge of unwieldiness concerning the mold mounting structure. This unwieldiness, in turn, adversely impacts both the pressing process and the seamless feeding of materials into the mold.

Conclusion: Upon analyzing the operational principles of the three outlined options, it becomes evident that Option 1 stands out as the most rational choice. This choice guarantees the integrity of the machine's structure while maintaining its aesthetic appeal. In practice, the survey results corroborate that Option 1 has been adopted by numerous manufacturers of unbaked brick presses within advanced production lines globally.

2 MATERIALS AND METHODS

2.1 Stages of Concrete Forming Using Vertical Vibrating Tables

The process of forming concrete structures through the utilization of vibrating tables encompasses three

distinctive phases: two primary phases and one secondary phase, namely the forming and pressing stages. As delineated in references [2] and [3]: **(i)** In the initial stage, the arrangement of aggregates necessitates a methodical layer-by-layer pouring of the concrete. Based on practical experience, the most optimal concrete mixture loading speed is ≤ 0.5 ÷ 1 m/min in accordance with the height of the structure. This approach involves pouring one layer, followed by vibration, and subsequently pouring the subsequent layer, ensuring the expulsion of air from the concrete. This stratified pouring process enhances air elimination. Consequently, the primary impact is attributed to vibration, making static loading largely unnecessary during this phase. It is recommended to conclude stage 1 before introducing additional loads, thereby optimizing the vibration's effect. For concrete mixtures with limited fluidity, the culmination of this phase signifies the completion of the compacting process. This concluding step can augment structural strength by up to 15% [2]. **(ii)** The second stage, referred to as the pressing stage, is of particular significance for robust concrete mixtures. This phase necessitates the application of loads, whether dynamic or static, to realize the most effective operational mode of the press, characterized by controlled collision. Moreover, these loads induce pressure that contributes to the consolidation of the concrete mixture. In instances of less rigid concrete, loading primarily serves the purpose of generating pressure for compacting the mixture. The determination of the optimal non-inertial load value is achievable through the utilization of Equation 1[4].

$$Q_{t\ddot{o}} = Q_{bt}(0.39\frac{P_0}{Q_{bt}^* + Q_R}\frac{Q_{bt}^*}{Q_{bt}} - 1) \quad (1)$$

Where: Q_{tu}- optimal load value.

The inertial force, N: $P_0 = (K.\omega^2)/g$

Where:K- The coefficient of static moment of the rotating object creates vibration; ω- angular velocity rad/s; G- Gravitational acceleration, m/s^2; Q_{bt}- concrete mass, kg; Q_{bt}^*- The volume of concrete participating fluctuates, kg;

$$Q_{bt}^* = (0.2 \div 0.4)Q_{bt} \quad (2)$$

For components with height H ≤ 0,5m then:

$$Q_{bt}^* = (0.2 \div 0.4)Q_{bt} + \frac{1}{5}(0.2 \div 0.4)Q_{bt} \quad (2')$$

For components with height H ≥ 1m then:

$$Q_{bt}^* = (0.3 \div 0.6)Q_{bt} \quad (2'')$$

The duration of vibration during stage 2, under the presence of a load, is contingent upon several factors, including the concrete mixture's hardness, the operational mode of the press, as well as the configuration and weight of the components involved. As the second stage culminates, the fundamental cutting and shaping procedures are concluded.

(iii) Stage 3: occurs to redistribute moisture in the structure. At this stage, large static pressure is required:

$$Q_{ep} = 2.5Q_{tu} \quad (3)$$

Q_{ep} usually, 2.5 times greater than the optimum load pressure value at stage 2. The end of phase 3 will make the concrete tighter and more beautiful [4].

2.2 Hypotheses about the process of tightening concrete mixture

As stated in reference [5], the effectiveness of vibration is influenced by factors, encompassing the composition of the mixture, its mechanical and physical properties, and the attributes of external forces. The theories regarding the process of concrete compaction can be categorized into two distinct directions:

(i) One theoretical perspective involves perceiving the mixture as possessing a lattice structure, where the nodes represent sizeable aggregate particles, interconnected by a cementitious mortar. Within this framework, concrete mixtures are visualized as compositions of substantial aggregate particles, bound together by a cohesive cement mortar. This hypothesis provides a lens through which the rheological

processes occurring during vibration in the concrete mixture can be comprehended. Within the context of this first hypothesis, it becomes conceivable to formulate the concept of resonant vibration within the confines of fixed-profile aggregate particles. This entails the judicious selection of a vibration frequency, contingent upon the size of the aggregates;

(ii) The second perspective revolves around material mixtures characterized by properties like continuity, viscoelasticity, and elasticity attributed to the presence of air bubbles. According to this premise, the process of compacting concrete with considerable height is explicable through the application of the wave equation. However, it is important to note that this hypothesis falls short in elucidating the vibration mechanism involved in compacting rigid, coarse-aggregate concrete compositions.

Both of the aforementioned hypotheses fall short in fully elucidating the mechanism of compaction and fail to provide the most plausible operational modes for vibrator mechanisms. Instead, the hypothesis of "reasonable vibration intensity" emerges as a solution, rooted in experimental evidence.

In the context of harmonic oscillations, the quantification of vibration intensity is established through the equation 4 [4]: $I = A^2.\omega^3$ (4)

Where: A – amplitude, m; ω - angular velocity (also known as angular frequency, rad/s)

This means that if the working mode has the same, *I* value, then the same vibration effect.

Therefore, it is necessary to choose the amplitude and angular frequency reasonably. If we hypothesize the harmonic oscillation system:

$$X = A.sin\omega t; \quad \dot{X} = A.\omega.\cos\omega t; \quad \ddot{X} = -A.\omega.2\sin\omega t \tag{5}$$

Thus, the amplitude of acceleration $a = |-A\omega^2|$ largest $\leq [a]$

In there: $[a]$ - The limit amplitude determined experimentally for each type of mixture (also called concrete aggregate): $a = |A\omega^2|$ (6)

$$I = |A^2\omega^3| \tag{7}$$

Inferred: $I.\omega \leq [a]$

Value $[a]$ = 70 m/s^2 for most types of concrete mixtures, [10]

$$I \leq \frac{[a]}{\omega} = \frac{70}{\omega} \tag{8}$$

Thus, the tightening efficiency increases as the value of vibration intensity (I) must be larger.

Consequently, guided by the "Reasonable Vibration Intensity" hypothesis, the process of concrete compaction is delineated into two distinct steps: (i) Step 1: The initial step involves crafting an extensive network of large aggregate structures within the mixture. To achieve this, a substantial amplitude coupled with a low frequency (falling within a specific value range) is necessary. This phenomenon is characterized by vertical oscillations lasting 2-3 minutes; (ii) Step 2: The second step entails the catalytic action on the cement mortar, accompanied by the liberation of entrapped air bubbles within the mixture.

2.3 Theoretical basis for tightening concrete by vibration

According to references [4] and [5], the categorization of vibrators based on frequency reveals three distinct types: type 1, characterized by a low frequency range of 20 – 33 Hz; type 2, featuring a medium frequency range of 33 – 66 Hz; and type 3, encompassing high frequencies within the 66 – 100 Hz range.

Regarding the concrete tightening mechanism: The concrete mixture comprises aggregates, cement mortar, and air bubbles. As the vibrating table operates, the aggregate particles within the concrete undergo a sliding motion over one another. For instance, let's consider a scenario where a single aggregate particle is sliding upon another aggregate particle with a velocity denoted as V.

The force that propels the movement of these aggregate particles holds significant importance [5].

$$F \geq f.N \tag{9}$$

Where: f – Friction coefficient; N – compression force, N;

Because the concrete mixture consists of several phases, the pressure should be given.

$$F = f.N + N_0 \quad (10)$$

Where: – adhesive force (the special case is that dry friction acts on the aggregate particle with a small force Q, of any direction relative to the motion).

To induce movement of the particle in the direction of force Q, requiring only a slight velocity adjustment, the force can be expressed as follows:

$$Q \geq N.f_d \quad (11)$$

Where: f_d – coefficient of dynamic friction

For vertical vibrators, where the dry friction force is the main one, the average value of the aggregate particle submersible velocity (V_{tb}) is calculated according to equation 12 [4].

$$V_{tb} = 2.\mathrm{k}_a.Q.F / \pi\left(F^2 - Q^2\right) \quad (12)$$

For horizontal vibrators, according to [4]

$$V_{tb} = 2\,\mathrm{k}_a\, Q / \pi \sqrt{F^2 - Q^2} \quad (13)$$

Where: k_a– amplitude value of sliding velocity of aggregate particles, m; Q - Gravity of the particle, N; F - The force that moves the particle, N;

When considering vertical vibration, it's important to acknowledge that the force of gravity, denoted as Q, aligns with the particle's direction of movement. Consequently, the rate at which the particle descends is consistently higher compared to scenarios involving horizontal vibration.

Focusing solely on "equation 12" and "equation 13," it becomes evident that when "equation 12" surpasses "equation 13" by an amount defined by Equation (14), a specific outcome follows.

$$\frac{F}{\sqrt{F^2 - Q^2}} > 1 \quad (14)$$

As the velocity magnitude grows, the rate at which the grain sinks accelerate, leading to an enhanced tightening process. When maintaining a consistent amplitude magnitude and elevating the frequency, the sliding velocity will also experience an increase.

To prevent the concrete mixture from detaching from the mold and introducing air into the concrete structure, it's imperative to choose the amplitude of oscillation in accordance with the formula presented as equation 15

$$A \leq \frac{7g}{\omega^2} \quad (15)$$

This means that (ka) the amplitude of the particle's sliding velocity is controlled by Equation (15) when the upward acceleration does not exceed 7g (in there: g– gravitational acceleration) [4].

2.4 Determining method of the excitation force for vibration.

To ensure that the amplitude of both the mold and concrete aligns with the permissible lifting capacity and operational frequency of the vibrating table, it is essential for the vibration excitation force (F_k) applied to the vibrator to operate outside the resonance zone.

The vibration excitation force is calculated [4].

$$F_k = m_r.A.w^2 \quad (16)$$

Where: ω - oscillation frequency, *rad/s*; A – oscillation amplitude, *m*; m_r- Oscillating volume, kg;

$$m_r = m_k + m_m + km_{bt} \quad (17)$$

Where: m_k - mold mass, kg; m_m - The volume of machines participating in oscillations, kg; km_{bt} - The volume of concrete involved fluctuates, kg;

The required moment of static inertia of the eccentric wheel causes vibration according to [5][4]

$$k = m_0 r = \frac{F_k g}{\omega^2} \quad (18)$$

3 DESIGN CALCULATIONS

3.1 Vibrator design

According to the principle of pedestal vibration, the vibration system plays an important role in shaping and creating mechanical properties for bricks. Based on the stated theoretical bases and research process from Patent No. US4830597A, 16/5/1989, by Klaus F. et al on-pedestal vibration system in concrete brick forming machine [7].

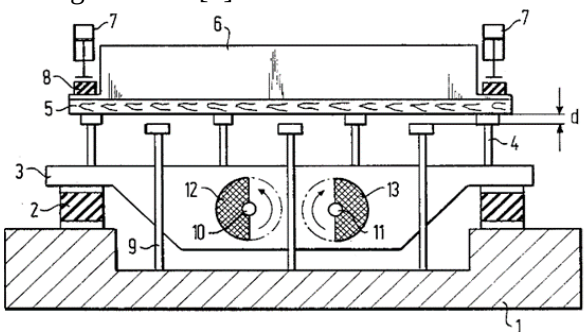

1- frame; 2- spring; 3- vibrating table; 4- support bar; 5- pallet; 6- Mold; 7- hydraulic cylinder; 8- spring; 9- table support bar trembles; 10, 11- axis of rotation; 12, 13- eccentric wheel

Figure 4: Vibration model according to Patent No. US4830597A [7].

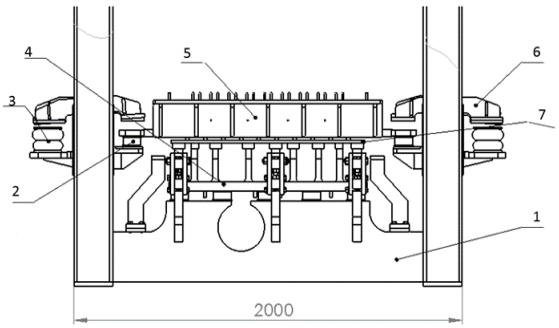

1-Pedestal; 2- Rubber dampers; 3- Air cushion; 4- Vibrator; 5- Mold; 6- Mold gripper kit; 7- Pallet

Figure 5: Vibration system design for brick molding machine [7].

Our vibration system is meticulously crafted around the concept of generating vibrational force through the synchronized rotation of eccentric wheels in opposing directions. This force acts directly upon the brick pallets and molds within predefined timeframes. Our design is heavily influenced by Patent No. US4830597A, although specific modifications are being introduced to accommodate a range of factors, including overall dimensions, the machine's operational principles, and, most notably, the need to meet productivity targets such as: The dimensions of the vibrating table are meticulously calculated by factoring in the pallet size and a host of technical prerequisites. This approach is aimed at ensuring that the transmission of vibrational force to both the pallets and molds is fully optimized, thereby enhancing the efficiency of the entire process.

The components of the system are organized as follows: The pedestal (1) provides support for the vibrating tables and pallets; Rubber dampers (2) play a vital role in attenuating undesirable impacts stemming from the vibrating table, safeguarding other components from potential damage; The air cushion (3) facilitates convenient mold adjustments during mold replacement and disassembly. It also prevents damage caused by the vibration force exceeding permissible limits; The vibrator (4) exerts vibrations onto the pallet. Positioned beneath the vibrating table is a vibrating gearbox housing eccentric wheels, which generates the necessary vibrational force; The mold (5) houses the compacted material; The mold gripper (6) securely holds and positions the mold, contributing to noise reduction. The use of soft joints facilitates easy disassembly for mold replacement or cleaning; Pallets (7) shoulder the load during compaction and transportation of bricks. Pallets are integral in the brick shaping process, as well as conveying bricks to subsequent stages such as feeding and surface grinding. Given their high operating frequency, it's crucial to thoughtfully select optimal manufacturing materials and design features for pallets. Simplicity is key, ensuring mechanical robustness, durability, ease of replacement, and seamless transport on chain conveyors to subsequent stages.

Within this design context, the pallets are expertly tailored to measure 1000 x 900mm. This sizing is derived through careful interpolation from the mold dimensions and chassis width. These pallets boast a thickness of 12mm, and their construction employs C55 steel material, chosen for its remarkable load-bearing capacity and resistance to wear.

The vibrating table has been meticulously designed to incorporate several key components, ensuring

optimal functionality. These components include the Vibrating Base (1), Vibrating Bars (2), and Vibrating Gearbox (3). The lower vibrating gearbox (3) is composed of 4 drive shafts and 8 vibrating eccentric wheels. The selected material for the vibrating table is SS400, which not only fulfills all operational requirements but also proves to be an economically viable choice. The yield stress limit of this material ranges from 240 to 280 N/mm². Because of the vibrating table which encounters highest load when the pressure surpasses the vibration excitation force, In addition, during work, the vibrating table is constantly bumped onto the surface, so it wear out very quickly, so we design vibrating bars (2) to be mounted on the surface to easily replace. Besides we also use rubber shock absorbers to reduce unnecessary impact forces on other parts

3.2 Vibrating table design

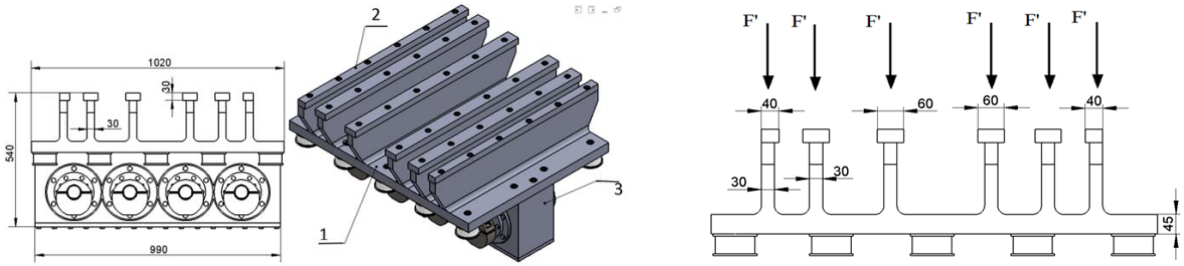

Figure 7: Vibrator in the vibrating system.

3.3 Calculation of the kinematic parameters of the vibration system

The product of 4-hole brick with dimensions of 80 x 80 x180 mm, in which the mass of each brick has a mass of m = 1.5 kg, the number of bricks pressed on the mold is 72.

We call: m_{br} -The vibrating table mass is $m_{br} = 1100\,kg$; m_{kd} - The lower mold mass is m_{kd} = 934 kg A - The vibration amplitude is A = 0.6; ω - The angular velocity of vibration is ω = 314 rad/s ; m_{bt} - The mass of concrete on the mold (including 72 bricks)

Thus: m_{bt} =72 bricks. m = 72.1.5 = 108 kg

m_r - The vibration part mass $m_r = m_{kd} + m_{br} = 934 + 1100 = 2034\,kg$

m_R - The vibration mass $m_R = m_r + m_{bt} = 2034 + 108 = 2142kg$

According to [4] vibration excitation force

$$F_k = \frac{K.\omega^2}{g} = m_R.A.\omega^2 = 2142.6.10 - 4.3142 = 126715.51N = 126.716\ kN \quad (19)$$

Also, according to [4], Optimum force (Q_{tu})

$$Q_{tu} = Q_{bt}(0.98\frac{P_0}{Q_{bt}^* + Q_r}.\frac{Q_{bt}^*}{Q_{bt}} - 1) = 1059.48\left(0.98\frac{126715.5}{1059.48 + 19953.54}.\frac{1059.48}{1059.48} - 1\right) = 5.202\text{kN}$$

In there: P_0 : the vibration excitation force, N ;

$$P_0 = F_k = 126.716\ KN$$

According to [4] concrete column height cases $H < 0.2\ m$

Thus $Q^*_{bt} = Q_{bt} = 108.9.81 = 1059.48\ N$ (20)

$$Q_r = m_r.g = 2034.9.81 = 19953.54\ N \quad (21)$$

Optimum pressure at stage 3 $Q_{tu3} = 2.5\ Q_{tu} = 13004.39N$ =13kN (22)

The maximum pressure ensures a collision [4]:

$$Q_e^{\max} = \frac{P_0 Q_{bt}}{(Q_{bt} + Q_R)} - 2.Q_{bt} = \frac{126715.5 \times 1059.48}{(Q_{bt} + Q_R)} - 2.1059.48 = 4270.05N = 4.27kN \quad (23)$$

According to [4] specific capacity for tightening concrete blocks [m^2/s^3]

$$\overline{N} = \frac{(2\pi)^2}{4\pi} \cdot \frac{\mathrm{k}^2\omega^3}{m_R\left(m_{\mathrm{bt}} + m_{\mathrm{R}}\right)} = \frac{\mathrm{k}^2\omega^3}{m_R\left(m_{bt} + m_R\right)} \tag{24}$$

When $m_{bt} = m_R$, we have the formula 25 [4]:

$$\overline{N} = \pi \frac{\mathrm{k}^2.\omega^3}{2m_R{}^2} = 1.57 \frac{\mathrm{k}^2\omega^3}{m_R\left(m_{bt} + m_R\right)} \tag{25}$$

Where: k is the static moment of inertia calculated according to equation 18 has the value:

$$K = \frac{F_k g}{\omega^2} = \left(\frac{126715.51 \times 9.81}{314^2}\right) = \frac{1243079.2}{98596} = 12,6$$

Substituting the values into equation 24 we calculate

$$\bar{N} = 3.14 \frac{K^2\omega^3}{(m_r + m_{bt})m_r} = 3.14 \frac{1.28^2 \times 3.14^3}{(2034+108)2034} = 36.5 \frac{m^2}{s^3}$$

According to the results of Kavinop O.A was presented in [4]

The required vibration time in equations (26)

$$\tau_r = \overline{W} / \overline{N} \tag{26}$$

Where: τ_r- required vibration time, s; $\overline{W}$ - specific capacity tightening, m^2/s^2; $\overline{N}$ - smallest specific capacity. Also, according to Kavinop, O.A was presented by [4], he got the empirical table for less hard concrete. The specific power tightens $\overline{W}$ variability is 100 ÷ 200 m^2/s^2; We choose $\overline{W}$ =150 m^2/s^2

We calculate the required load and vibration time $\tau_r = \frac{150\ \mathrm{m}^2/\mathrm{s}^2}{36.5 m^2/s^3} = 4.1s$

We set the working time of one pressing cycle.

$$\tau = \tau_1 + \tau_2 + \tau_3 + \tau_4 = 6 + 2 + 4 + 3 = 15\mathrm{s}$$

Where: τ_1 is the feed time. ($\tau_1 = 6s$); τ_2 is the time the cylinder lowers the pressing head to the contact position. ($\tau_2 = 2s$); τ_3 is loading and vibration timing ($\tau_3 = 4s$); τ_4 is cylinder time back to its original position. ($\tau_4 = 3s$)

We preliminarily select the working stroke of the cylinder $L = 470\ mm$

The greatest force applied to the cylinder:

$$F = F_{\mathrm{k}} + Q'_{\mathrm{e}} - Q_{\mathrm{kt}} - Q_{\mathrm{R}} \tag{27}$$

Where: The impact force of the vibrating part: $F_k = 126715.5N$

Force reaction (Q'_{e}): $Q'_{\mathrm{e}} = Q_{\mathrm{e}}^{\max} = 4270.05N$

Upper mold weight (Q_{kt}): $Q_{kt} = m_{kt}.g = 704 \times 9.81 = 6906.24\mathrm{N}$ (28)

Weight of vibration (Q_R): $Q_R = 2142. \times 9.81 = 21013.02N$

F=126715.5+4270.05-704.9.81-21013.02=103066.3N=103.1kN

The load acting on each vibrating rod (we designed 6 vibrating rod).

$$F' = \frac{F_k + Q_{tu}}{6} = \frac{126715.5 + 13004.39}{6} = 23287N \tag{29}$$

Where: F_k - vibration excitation force, N; Q_{tu} -Optimum force, N.

After calculating and designing the vibrating table structure, we calculate and design the vibrating gearbox with the task of creating vibration force acting on the vibrating table and the mold to create mechanical properties for the brick.

4 CONCLUSIONS

The research team presented the analysis and selection of the vibration table pressing principle for calculating and designing a concrete brick press's vibration table assembly.

Design calculation results are as follows: The pressed brick product is a 4-hole brick with dimensions of $80 \times 80 \times 180$ mm^3, weighing 1.5 kg per brick. The injection mold accommodates 72 bricks, with a pressing capacity of 100,000 bricks per shift. The vibrating table mass of 1100 kg, while the mass below the mold is 934 kg. The vibration amplitude is 0.6 mm, and vibration angular velocity is 314 rad/s. The required vibration force is 126.716 kN, and the optimal pressing force is 5.202 kN, with a vibrating concrete column height of under 200cm. The maximum pressure ensuring collision safety is 4.270 kN.

The working cycle consists of 1 cycle lasting 15 seconds, wherein feeding time (τ_1) is 6 seconds, time taken by the cylinder to lower the press head to the contact position (τ_2) is 2 seconds, loading time (τ_3) is 4 seconds, and the cylinder time to return to the original position (τ_4) is 3 seconds. The cylinder's working stroke (L) spans 470 mm, and the maximum force exerted on the cylinder is 103.06 kN. The impact load on each vibrating rod is 23.287 kN.

5 ACKNOWLEDGMENTS

The research team extends sincere gratitude to the Ho Chi Minh City Science and Technology Development Fund for their generous funding in support of our project titled "Development of an Automated Concrete Brick Molding Machine with Combined Vibration Mold and Vibration Table, Capable of Producing 100,000 Bricks QTC per Shift." This endeavor is carried out under contract No. 67/2020/HD-QPTKHCN.

REFERENCES

[1] B. T. Thanh, N. Q. Hung, N. M. Cuong, T. T. Ngoc, T. N. D. Khoa, C. M. Quang, & N. N. Sam, Research on technology selection and processing for creating a concrete brick production line suitable for Vietnamese conditions, *Journal of Rural Industry*, volume 46, pp 21-31, 2022.

[2] V. H. Nam & L. D. Long, Technology of concrete brick production. In Project for increasing production and use of adobe bricks in Vietnam: Training material on adobe bricks, Module *4*, *the Construction Publishing House*., 2019.

[3] B. D. Thien et al., Technology for manufacturing building materials and building components: Fired bricks. Project for increasing production and use of unburnt bricks in Vietnam. Ministry of Science and Technology, for Universities and Technical Colleges, *Construction Publishing House*, 2019.

[4] T. V. Tuan, Technical basis of vibration in construction and building materials production, *Construction Publishing House*, 2005.

[5] N. D. Chieu, N. Trong & N. A. Tuan, Technical basis of vibration in construction, *Science and Engineering Publishing House*, 2004.

[6] T. T. Hong & N. T. H. Ngan, Vibration techniques in construction machines, *National University Publishing House* of Ho Chi Minh City, 2008.

[7] Klaus F. Steier, Munich; Erich W. Holthaus, Remscheid; Hermann Kargl, Vibrator for a block molding machine, Germany United States, Patent Number: Patent Number: 4,830,597 Date of May 16, 1989.

CRASHING BEHAVIOR OF THE BIO-INSPIRED FOAM-FILLED MULTI-CELL TUBES UNDER VARIOUS LOADING CONDITION

TU PHAM HOANG [1], VAN NGUYEN THAI [2], MINH LE HOANG [3], DAT TRAN QUOC [4], DUC HIEU LE[5], KET TRAN MINH [1], TRONG NHAN TRAN [6]

[1] *Faculty of Automotive Engineering, School of Technology, Van Lang University, Ho Chi Minh City, Vietnam*

[2] *Department of Scientific Management and International Cooperation; Vinh Long University of Technology Education, Vietnam*

[3] *Department of Engineering, Waterway Transport College No 2, Ho Chi Minh City, Vietnam*

[4] *Department of Mechanical, Nam Sai Gon Polytechnic College, Ho Chi Minh City, Vietnam*

[5]*Faculty of Automobile Technology, Hanoi University of Industry, Bac Tu Liem District, Hanoi, Vietnam*

[6]*Faculty of Mechanical Engineering, Industrial University of Ho Chi Minh City, Ho Chi Minh City, Vietnam;*

Corresponding author: *tu.ph@vlu.edu.vn, ket.tm@vlu.edu.vn, vannt@vlute.edu.vn, trantrongnhan@iuh.edu.vn,*

Abstract. This study aims to numerically investigate the crashworthiness performance of a bio-inspired foam-filled multi-cell tube (BFMT) that mimics the microstructure of bamboo culm. The BFMT combines the advantages of bionic structures, foam, and thin-walled tubes, resulting in remarkable properties such as superior energy absorption, shock absorption, and a high energy absorption-to-mass ratio. The focus of this research is to explore the impact resistance of the BFMT under various loading conditions and to analyze its behavior during impact processes and failure modes. The results demonstrate that the crushing behavior of the BFMT is significantly influenced by loading conditions and impact velocity. Specifically, increasing the impact velocity leads to a decrease in initial peak load (IPL) and an increase in specific energy absorption (SEA) and crushing deformation energy (CDE). However, this ability to protect passengers decreases as larger impact velocities lead to extensive deformation, reducing the passenger's survival space. Additionally, it was observed that a larger load angle leads to a decrease in peak impact loading and specific energy absorption.

Keywords. Bio-inspired multicell tube, crashworthiness, energy absorption, foam, impact.

1 INTRODUCTION

In the design of crashworthy structures for automobiles, the primary objective is to manage and minimize damage effectively during accidents by utilizing controlled and progressive plastic deformation to absorb impact energy. The focus of crashworthiness design is achieving high performance levels while considering weight constraints and enhancing safety within mass and volume limitations. Consequently, multi-cell tubes with foam cores have emerged as superior energy absorbers compared to other alternatives.

Over the past two decades, investigations have been conducted to explore potential enhancements of crushed tube performance through the use of filler materials. One promising material that has been extensively studied is aluminum foam, which has demonstrated favorable energy-absorption characteristics under dynamic loading conditions [1]. In a study by Kılıçaslan et al. [2], the mechanical properties of aluminum foam-filled tubes were examined under axial impact loading. The results indicated that corrugated double-circular tubes filled with aluminum foam exhibited the highest values of specific energy absorption (SEA), with SEA values increasing as the radius of the inner circular tube increased. Another study by Abdulqadir et al. [3] focused on the energy absorption properties of thin-walled aluminum alloy tubes filled with aluminum foam under both direct and oblique loads. The findings revealed that the

incorporation of aluminum foam led to an enhancement in the deformation mode of the filled tubes and an increase in their energy absorption capacity.

In nature, multi-cell structures, such as bamboo [4] and beetle forewing [5], serve as inspiring examples of low-density, high-strength, and high-energy absorption capacities. These natural structures provide motivation for the design of novel multi-cell structures with exceptional energy absorption properties. For instance, Zhang et al. [6], proposed a novel bionic fractal hierarchical tube, drawing inspiration from the intricate structure of a spider web. The incorporation of bionic fractal hierarchical configurations into traditional thin-walled structures was found to significantly enhance their energy absorption capabilities.

Previous studies have investigated the crash behavior of different tubes under various conditions, including impact velocities of 7.67 m/s [7], 10 m/s [8] and 15.6 m/s [9]. Some researchers have also focused on studying the deformation of tubes under axial or oblique loading [10]. In this study, we aim to examine the crash behavior of a bio-inspired foam-filled multi-cell tube (BFMT) that mimics the microstructure of bamboo culm under different loading conditions. Specifically, we select impact velocities of 7.67 m/s, 10 m/s, and 15.6 m/s, while varying the loading angle from 0 degrees to 15 degrees in 5-degree increments.

2 METHODOLOGY

With increasing velocity, traffic accidents pose a significant threat to passenger safety and result in substantial economic losses in road traffic. Extensive research into the history of traffic accidents has revealed that these accidents cannot be completely avoided, even with the implementation of many active protection technologies in vehicles. To enhance passenger safety and reduce losses from accidents, it is crucial to investigate the crash response of tubes used as crash boxes under various loading conditions. The steps involved in this investigation are outlined in Figure 1.

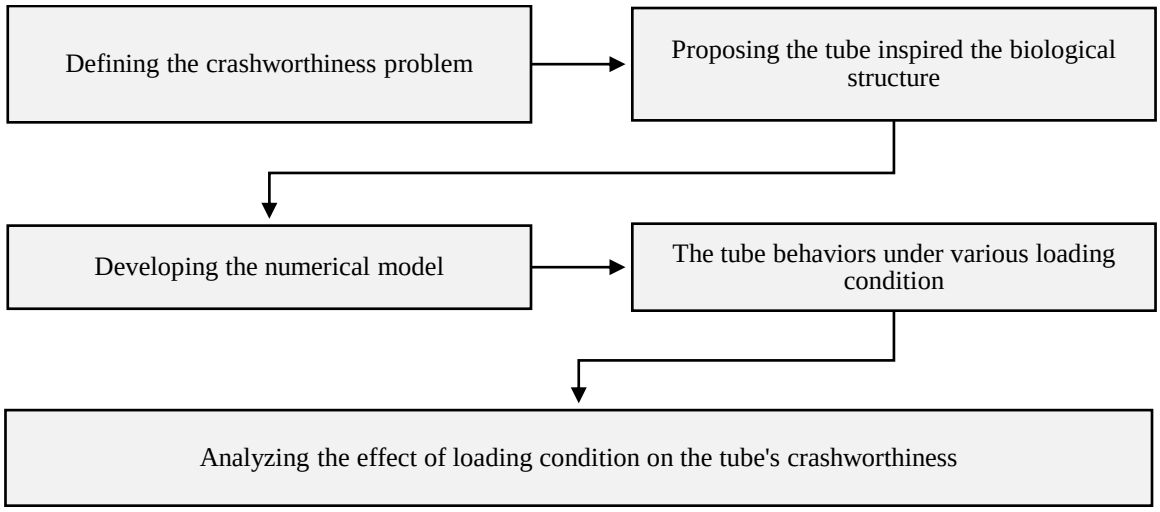

Figure 1: Flowchart of the crashworthiness problem.

2.1 Crashworthiness indexes

By analyzing and comparing the crashworthiness indicators, the crashworthiness performance of the BFMT, as a bio-inspired foam-filled multi-cell tube, can be effectively evaluated. The following indicators are then defined as follows:

Energy Absorption (EA): EA is calculated as the area under the load-crushing distance curve up to the compaction zone. The formula for EA is given by

$$EA = \int_0^x F(f)dx, \quad (1)$$

where F(x) represents the crushing force and x is the crushing distance.

Specific Energy Absorption (SEA): SEA quantifies the absorbed crash energy per unit mass of the crushed specimen. It is defined as

$$SEA = \frac{EA}{m}, \quad (2)$$

where m denotes the mass of the BFMT.

Initial Peak Load (IPL): IPL is a critical parameter during the impact of samples and represents the first peak observed in the load-crushing distance curve.

Crushing distance efficiency (CDE) is used to evaluate the deformation of the tube, which is defined as the ratio of the crushing distance (d) to the initial length (l) of the tube. Mathematically, it is expressed as

$$CDE = \frac{d}{l} \quad (3)$$

2.2 Bio-inspired tube

Through the process of natural evolution, living organisms that have survived have displayed remarkable survival traits. Researchers have been captivated by the exquisite features found in animals and plants. By studying and drawing inspiration from nature, researchers have gained valuable insights into various biologically-inspired structural designs, leading to the development of bio-inspired approaches in engineering. These approaches hold great potential for significantly enhancing mechanical performance by leveraging the lessons learned from nature's optimized solutions.

As shown in Figure 1(a), the microstructure of a bamboo culm exhibits the arrangement of vascular bundles and parenchyma cells. Taking cues from this microstructure, the present study introduces a bionic foam-filled multi-tube structure with cylindrical shapes, as depicted in Figure 1(b). The structure includes one large square tube of 60x60x2 mm and four small square tubes of 30x30x2 mm. To improve its performance, four cores of aluminum foam were inserted into the four small tubes. The figure also provides an overview of the tube parameters. It is important to note that the length of the tube in this investigation is 120 mm.

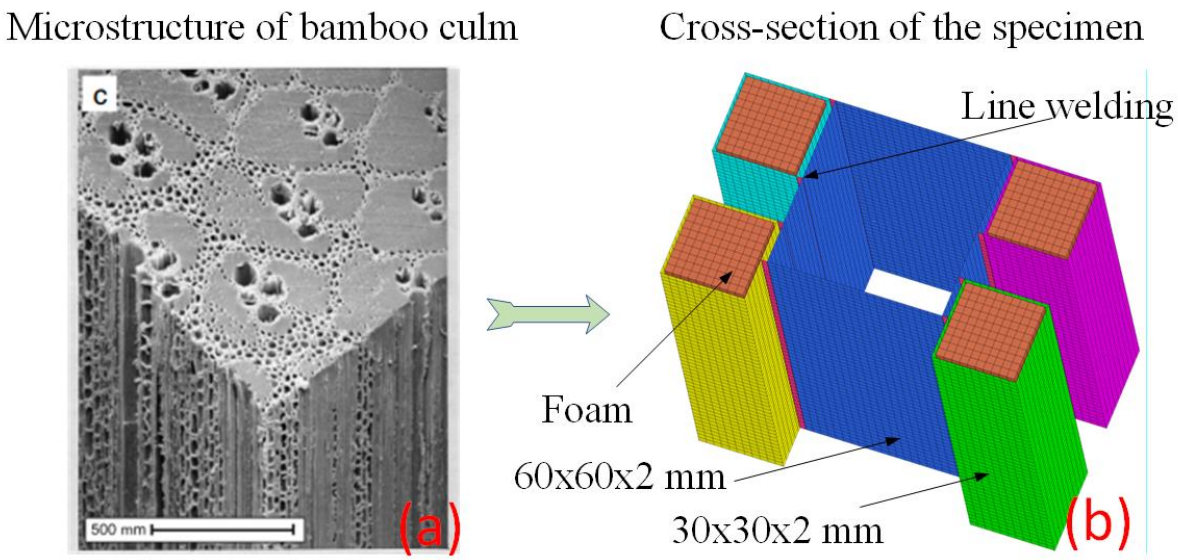

Figure 2: a) microstructure of the bamboo culm [4] and b) cross-section of bio-inspired foam-filled multi-cell tube (BFMT).

2.3 Numerical simulation

The collapse performance and energy absorption features of the BFMT were investigated using the Hypermesh/Ls-Dyna software. The finite element (FE) model is depicted in Figure 3. For the foam materials, the MAT_CRUSHABLE_FOAM material model was found to be suitable. The SEAM in connectors was used to simulate line welding. Finally, the MAT_PIECEWISE_LINEAR_PLASTICITY material model was used for the aluminum tubes.

The boundary conditions applied to the tubes involved the introduction of two walls. The bottom end of the tube is supported by a rigid platform, while the top end of the tube is crashed by a moving rigid plate.

The "CONTACT_AUTOMATIC_NODES_TO_SURFACE" was applied to simulate the contact relationship between the moving rigid plate and the tube. The "CONTACT_AUTOMATIC_SINGLE_SURFACE" was applied to the tube to prevent interpenetration during the crashing process. A general contact formulation with a friction coefficient of 0.25 was employed in the FE model. To ensure numerical accuracy, an average element size of 2.5 mm was utilized for both the tube and foam components.

The tube and foam materials used in the simulation consisted of aluminum alloy 6063-T5 and closed-cell aluminum foam, respectively [7]. The mechanical properties of these materials are provided in Table 1.

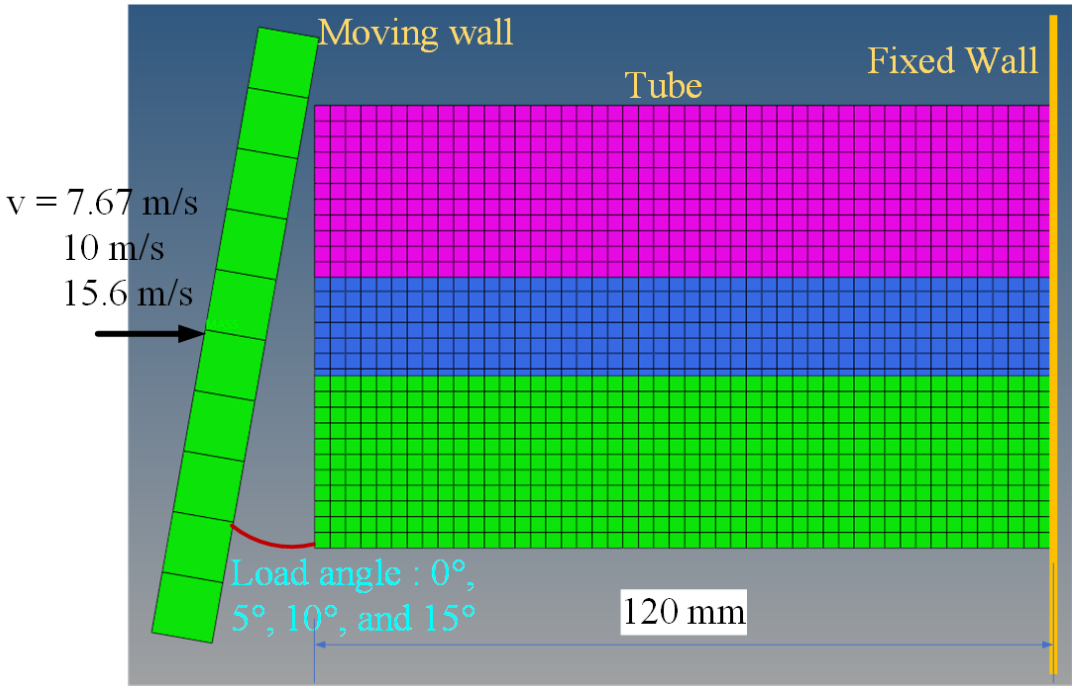

Figure 3: Schema of model.

3 SIMULATION RESULT

In terms of deformation mode, a stable progressive collapse behavior is observed, indicating a high energy absorption capacity. Figure 4 illustrates the plastic collapse deformations for the investigated cases. A comparison between the impact velocities of 7.67 m/s, 10 m/s, and 15.6 m/s reveals that the number of folds increases with higher velocities. Under axial impact and with the same impact duration, the number of folds for the respective velocities are as follows: one complete fold and one non-complete fold for 7.67 m/s, two complete folds for 10 m/s, and three complete folds and one non-complete fold for 15.6 m/s. Similar trends are observed for oblique impact cases at angles of 5°, 10°, and 15°. Therefore, regardless of the loading cases, the number of folds increases with the increase in impact velocity.

Table 1: Mechanical properties of aluminum alloy 6063-T5 and closed-cell aluminum foam.

AA 6063T5	ρ (kg/m3)	σy (Mpa)	σu (Mpa)	E (Gpa)	μ
	2631.00	123.3	147.4	51.3	0.33
Foam	ρ (kg/m3)	Plateau stress	Densification strain	E (Gpa)	μ
	252.00	1.98	0.6	75.58	0.3

It is evident that an increase in impact velocity leads to a larger crushing distance in the tube, resulting in greater material involvement in plastic deformation and higher energy dissipation. Therefore, the energy absorbed increases with increase of impact velocity. Although a slight bending to the left is observed in the

case of oblique impact at 15° with an impact velocity of 15.6 m/s, it is noteworthy that no significant bending collapse occurs in most oblique impact cases. Bending deformation in the tube is undesirable as it significantly reduces the energy absorption capacity.

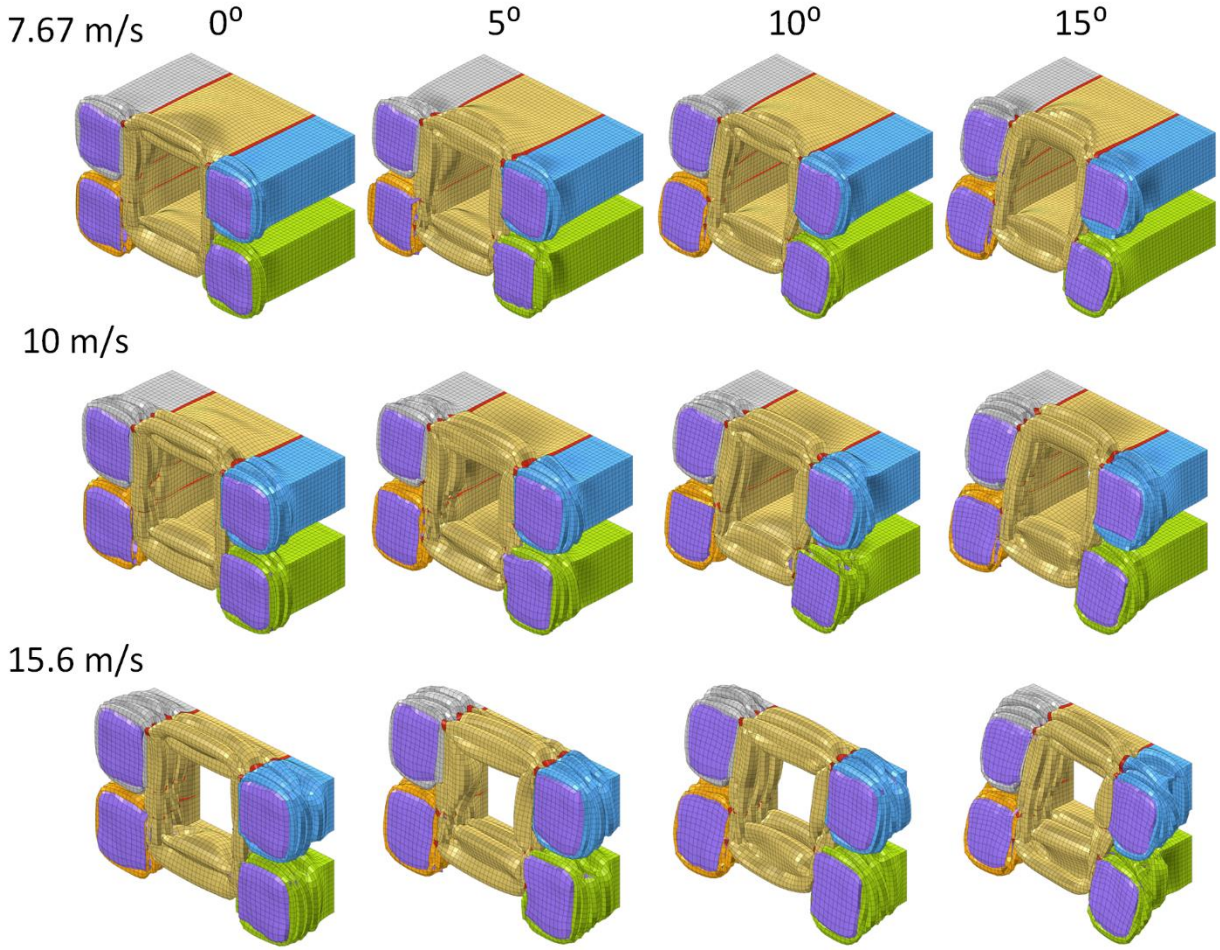

Figure 4: Deformations of a bio-inspired foam-filled multi-cell tube under various loading conditions.

The load and energy absorption responses of the BFMT under the investigated loading conditions are presented in Figures 5-7. These figures reveal that the load and energy absorption behaviors are similar among the different impact velocities, with differences in their load and energy absorption levels. In the case of an impact velocity of 7.67 m/s, the mean load of the tube at different loading cases is 163 kN. Regarding the case of an impact velocity of 10 m/s, the mean load at different loading cases is 172 kN, while the mean load at different loading cases at an impact velocity of 15.6 m/s is 183 kN. Accordingly, the BFMT exhibits the largest mean loads and energy absorptions at an impact velocity of 15.6 m/s, while the smallest values are observed at an impact velocity of 7.67 m/s.

In the case of axial impact, the load initially rises to its peak value, then slightly decreases before rising to a second peak. Subsequently, the load drops suddenly and fluctuates around a mean load value. For a small oblique impact with a load angle of 5°, the load gradually rises to its peak and then fluctuates around the mean load. In the cases of oblique impacts with load angles of 10° and 15°, a similar load response trend is observed, as in the case of oblique impact with a load angle of 5°. However, the peak loads for these angles are smaller and significantly lower compared to the oblique impact with a load angle of 5° (Figures 5(a)-7(a)). A common observation for all loading cases at different impact velocities is that, during the steady deformation stage, their average forces remain approximately the same.

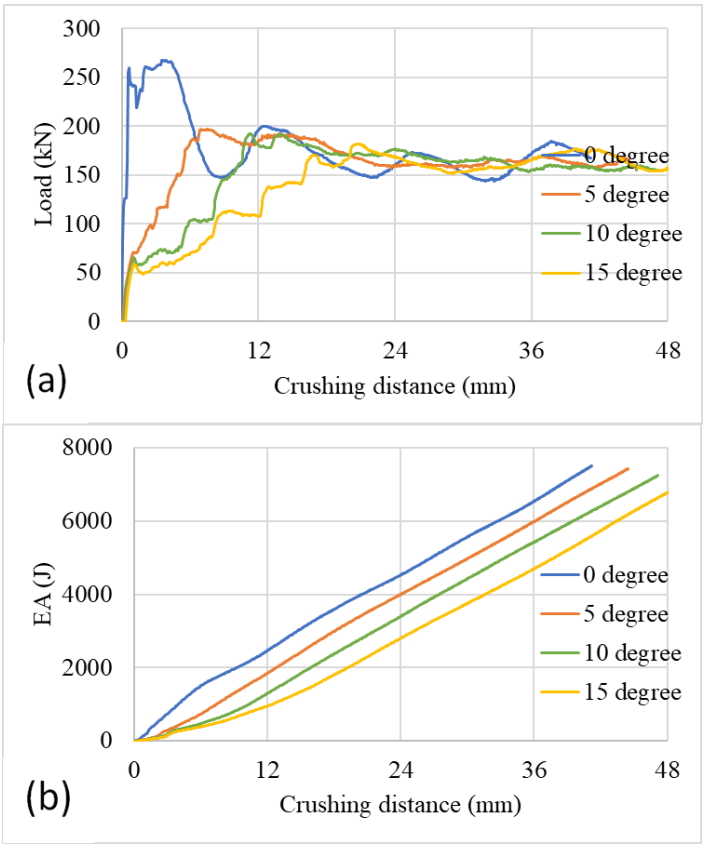

Figure 5: a) Load and b) energy absorption responses at 7.67 m/s.

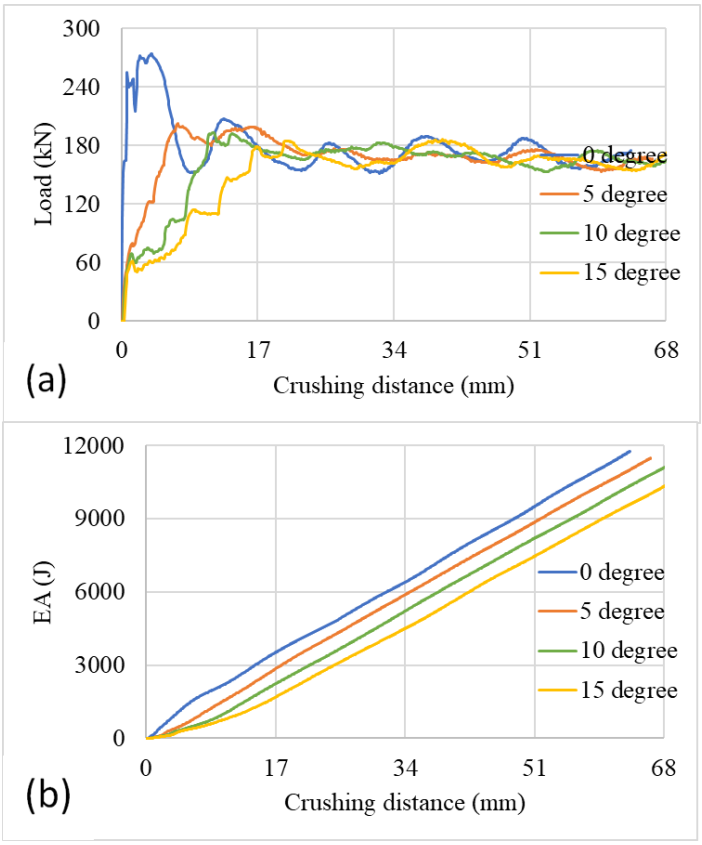

Figure 6: a) Load and b) energy absorption responses at 10 m/s.

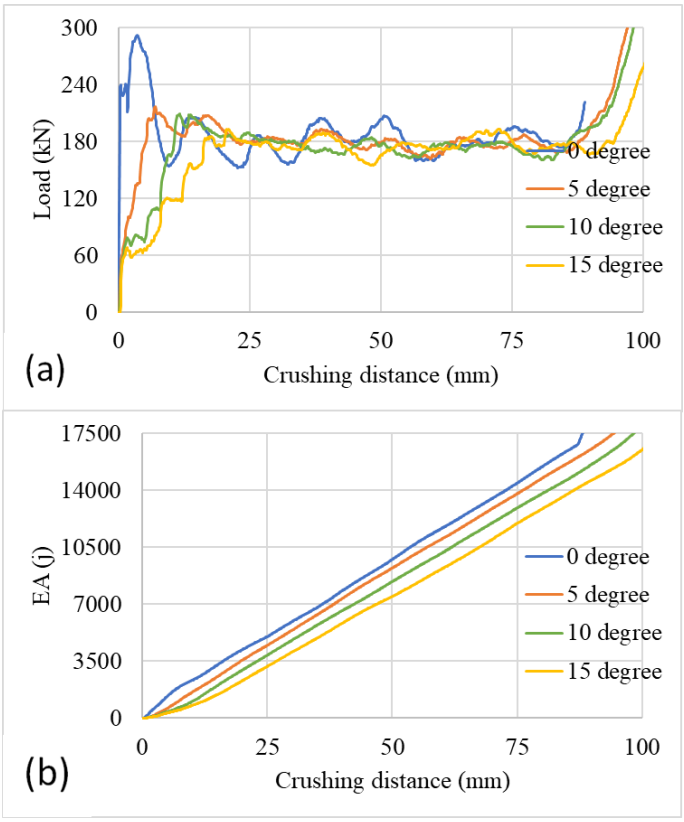

Figure 7: a) Load and b) energy absorption responses at 15.6 m/s.

Regarding the energy absorption response shown in Figures 5(b) to 7(b), it can be observed that the BFMT exhibits the highest energy absorption capacity under axial impact, while the energy absorption capacity is significantly reduced for oblique impact with a load angle of 15°. Thus, an increase in the load angle results in a substantial decrease in energy absorption.

4 INFLUENCE OF LOADING CONDITIONS ON CRASHWORTHINESS

To evaluate the impact of loading conditions on crashworthiness indicators, the values of initial peak load (IPL), specific energy absorption (SEA), and crushing distance efficiency (CDE) were plotted in Figure 8. The results show that IPL, SEA, and CDE decrease with increasing load angle. Figure 8(a) shows that the IPLs of the BFMT under an impact velocity of 7.67 m/s are larger than those of the BFMT subjected to impact velocities of 10 m/s and 15.6 m/s at all loading angles. This can be explained by the longer contact time between the moving mass and the BFMT at an impact velocity of 7.67 m/s, as opposed to the impact velocities of 10 m/s and 15.6 m/s. The decrease ratios in IPL under all three impact velocities in cases of oblique impacts with load angles of 5°, 10°, and 15° are quite similar.

Under impact velocities of 7.67 m/s, 10 m/s, and 15.6 m/s, the decrease ratios in IPL of load angles of 5°, 10°, and 15° when compared to the axial impact (load angle of 0°) range from 73.1% to 78.7%, from 73.1% to 83.6%, and from 74.5% to 84.3%, respectively. This suggests that the decrease in IPL increases with an increase in the impact velocity, as expected, since a higher impact velocity results in greater energy dissipation. It is also noticeable that the decrease in IPL is greater for higher loading angles.

In contrast to the IPL, the SEA and CDE of the BFMT under impact velocities of 10 m/s and 15.6 m/s are greater than those under an impact velocity of 7.67 m/s at all loading angles. The average SEA and CDE of the BFMT under an impact velocity of 10 m/s are 46.38% and 38.84% larger, respectively, than those under an impact velocity of 7.67 m/s. Similarly, the average SEA and CDE of the BFMT under an impact velocity of 15.6 m/s are 164.39% and 134.15% larger, respectively, than those under an impact velocity of 7.67 m/s. Therefore, the loading conditions including impact velocity and load angle have a significant effect on the crashworthiness performance of the tube.

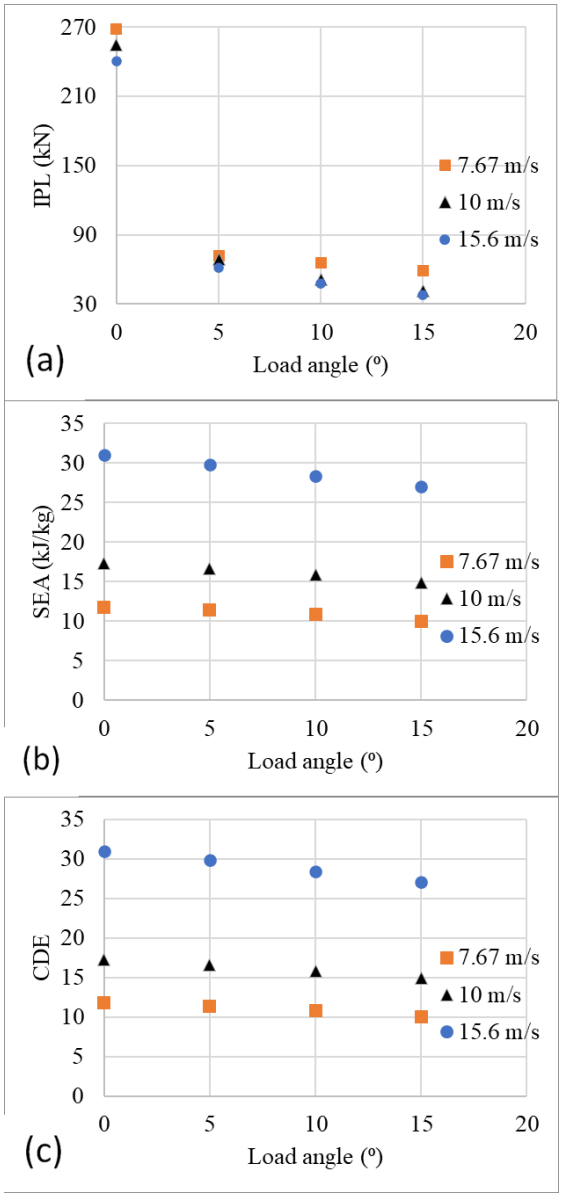

Figure 8: Influence of tube parameter on: a) IPL, b) SEA, and c) CDE.

5 CONCLUSIONS

In this study, the crashworthiness performance of a bio-inspired foam-filled multi-cell tube, which mimics the microstructure of the bamboo culm, was numerically investigated. The loading conditions, including the impact velocity and load angle, have a significant influence on the tube's crashworthiness performance. An increase in impact velocity results in a decrease in initial peak load (IPL) and an increase in specific energy absorption (SEA) and crushing deformation energy (CDE). As a result, the ability to protect passengers decreases with larger impact velocities due to extensive deformation, which reduces the passenger's survival space.

Furthermore, an increase in the load angle reduces the IPL, SEA, and CDE. However, with a load angle of 5°, the IPL plummets by about 73%, while SEA only experiences a slight decrease of about 3.4%. These results provide valuable insight for designers in the development of impact energy absorbers.

ACKNOWLEDGEMENT: We acknowledge Van Lang University, Industrial University of Ho Chi Minh city and Vinh Long University of Technology Education (Vietnam) for supporting this study.

REFERENCES

[1] H. Kanahashi, T. Mukai, Y. Yamada, K. Shimojima, M. Mabuchi, T.G. Nieh, K.J.M.S. Higashi, E.A.-s.M.P. Microstructure, Processing, Dynamic compression of an ultra-low density aluminium foam, 280 (2000) 349-353.

[2] C. Kılıçaslan, Numerical crushing analysis of aluminum foam-filled corrugated single- and double-circular tubes subjected to axial impact loading, Thin-Walled Structures, 96 (2015) 82-94.

[3] S. Abdulqadir, B. Alaseel, M.N.M. Ansari, Simulation of thin-walled double hexagonal aluminium 5754 alloy foam-filled section subjected to direct and oblique loading, Materials Today: Proceedings, 42 (2021) 2822-2828.

[4] U.G.K. Wegst, Bending efficiency through property gradients in bamboo, palm, and wood-based composites, Journal of the Mechanical Behavior of Biomedical Materials, 4 (2011) 744-755.

[5] N.S. Ha, V.T. Le, N.S. Goo, Investigation of punch resistance of the Allomyrira dichtoloma beetle forewing, Journal of Bionic Engineering, 15 (2018) 57-68.

[6] Y. Zhang, J. Wang, C. Wang, Y. Zeng, T. Chen, Crashworthiness of bionic fractal hierarchical structures, Materials & Design, 158 (2018) 147-159.

[7] X. Li, X. Zhu, R. Wang, T. Li, Y. Gu, Q. Zhang, Experimental study on the impact resistance of hollow thin-walled aluminum alloy tubes and foam-filled aluminum tubes (6063-T5), International Journal of Crashworthiness, (2023) 1-20.

[8] S. Hou, X. Han, G. Sun, S. Long, W. Li, X. Yang, Q. Li, Multiobjective optimization for tapered circular tubes, Thin-Walled Structures, 49 (2011) 855-863.

[9] F. Tarlochan, S. AlKhatib, Energy absorption capabilities of complex thin walled structures, IOP Conference Series: Materials Science and Engineering, 257 (2017) 012027.

[10] A. Baroutaji, M. Sajjia, A.-G. Olabi, On the crashworthiness performance of thin-walled energy absorbers: Recent advances and future developments, Thin-Walled Structures, 118 (2017) 137-163.

CRASHWORTHINESS PERFORMANCE OF THE THIN- WALLED SQUARE SINGLE AND NESTED TUBES UNDER AXIAL AND OBLIQUE IMPACT LOADINGS

SON DOAN THANH [1], VAN LUONG VAN [2], KET TRAN MINH [1], SON LE HUU [1], TRONG NHAN TRAN[3], HOANG DO KIM [1], TRANG DAM VAN [4]

[1] *Faculty of Automotive Engineering, School of Technology, Van Lang University, Ho Chi Minh City, Vietnam*

[2] *Faculty of Automobile Engineering Technology, Vinh Long University of Technology Education, Vietnam*

[3] *Faculty of Mechanical Engineering, Industrial University of Ho Chi Minh City, Ho Chi Minh City, Vietnam*

[4] *Faculty of Mechanical Engineering, District twelve Technical Economic College,*

Corresponding author: son.dt@vlu.edu.vn, son.lh@vlu.edu.vn, vanlv@vlute.edu.vn, trantrongnhan@iuh.edu.vn,

Abstract. Thin-walled square tubes are widely utilized in energy-absorbing components due to their superior energy absorption capabilities and strength. This study aims to examine the crashworthiness characteristics of these tubes under axial and oblique loading conditions. Quasi-static tests are performed to analyze the influence of the crushing angle on the behavior of a single tube, while dynamic impacts are executed to investigate the crash behaviors of nested tubes under small loading angles. This paper offers a comprehensive overview of the entire crushing process, encompassing force-displacement curves and deformation patterns. The results eveal that the crushing angle significantly impacts the tube's behavior during crushing. An increase in the load angle results in a decrease in both First Peak Load (FPL) and Specific Energy Absorption (SEA), with the decrease in FPL being more pronounced than that in SEA. The study identifies oblique crushing with smaller angles as the most efficient condition, as it demonstrates superior energy absorption characteristics, promotes plastic collapse deformation, and enhances passenger safety. The results underscore the benefits of oblique impact with small load angles and the potential of bio-inspired nested tubes to enhance crashworthiness performance.

Keywords. Axial loading, bio-inspired nested tube, crashworthiness, oblique loading, square tube.

1 INTRODUCTION

Energy-absorbing devices play a pivotal role in dissipating kinetic energy during impacts and are extensively employed in various sectors such as automobiles, ships, and aircraft. In the event of an accident, these devices serve to protect the vehicle by reducing severe damage and ensuring the safety of occupants. Thin-walled tubes, recognized for their cost-effectiveness and high energy absorption capabilities, have been widely adopted in collision kinetic energy absorption systems across different types of vehicles [1].

Studies conducted by Yamashita et al. [2], Nia and Hamedani [3], Lu and Yu [4] have primarily concentrated on examining the influence of cross-sectional shape on energy absorbers within a vehicle's crushing system. Their findings consistently indicate that metallic polygonal axially loaded tubes with a greater number of corners display increased crushing strength and enhanced energy absorption capacity. These studies underscore the significance of geometric factors in optimizing the performance of energy-absorbing devices.

In relation to oblique loading, a study conducted by Kim and Wierzbicki [5] investigated two possible impact modes: angled and off-axis loading. They used nonlinear finite element analysis to determine the most efficient oblique loading condition based on the impact angle, using square and rectangular tubes as their subjects of analysis. Reyes et al. [6] investigated oblique impact up to a 30° angle under off-axis loading using aluminum square tubes. They found that tube performance was primarily influenced by

factors such as tube wall thickness and initial length. Cornered oblique impact was therefore identified as a more effective loading condition across all investigated crushing angles.

The trend of mimicking biological structures in crashworthiness design has opened up new possibilities for developing more efficient and effective energy absorbing systems. Researchers continue to explore and draw inspiration from various biological systems to enhance crashworthy structures. For instance, Yin et al. [7] conducted a study on bio-inspired energy-absorbing structures that replicated the cross-sectional characteristics of five horsetail plants. Their findings highlighted the significant influence of tube parameters on the crashworthiness performance of the structure.

This study serves as an example of the ongoing endeavors to harness biological inspirations in order to enhance energy absorption in engineered systems. Initially, the research investigates the behavior of a single square tube under quasi-static axial and oblique loading, specifically considering load angles of 5° and 10°. Subsequently, drawing inspiration from the microstructure of wood [8], a bio-inspired nested configuration is proposed, and its performance is studied under axial and oblique impacts, focusing on small load angles of 2°, 4°, and 6°, with the aim of improving the crashworthiness characteristics.

2 METHODOLOGY

An analysis of crushing behavior was conducted to enhance the crashworthiness performance of the front structure. This analysis involved the use of both quasi-static and impact testing methods. The objective was to investigate impact loading conditions with small load angles, with the aim of reducing the first peak load (FPL) while maintaining the specific energy absorption (SEA) during crash scenarios. The flowchart for the crashworthiness problem is presented in Figure 1.

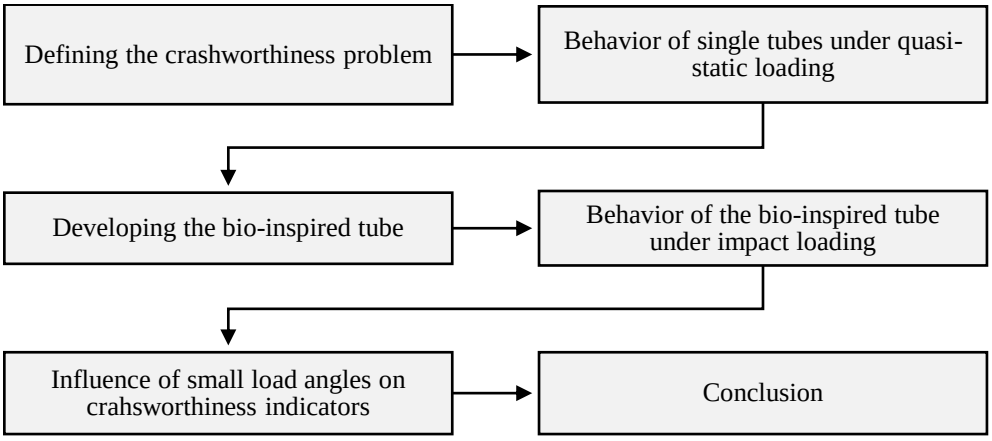

Figure 1: Flowchart of the crashworthiness problem.

2.1 Crashworthiness indexes

Assessing the energy dissipation capabilities of different designs and materials through plastic deformation is crucial to crashworthiness. To quantitatively measure the amount of energy dissipated through deformation, both the crushing force and the material's deformation during the crushing process must be evaluated. In this context, several indicators are defined, including energy absorption (EA), specific energy absorption (SEA), and first peak load (FPL).

Energy absorption (EA) represents the energy absorbed during plastic deformation and can be calculated using the integral:

$$EA = \int_0^x P(x)dx, \quad (1)$$

where P(x) denotes the crushing force and x represents the collapsing displacement.

Specific energy absorption (SEA) measures the energy absorbed by a mass during plastic deformation and is determined by the equation:

$$SEA = \frac{EA}{m}, \quad (2)$$

where m corresponds to the mass of the tube.

First Peak Load (FPL), also known as the initial crush force in the load displacement response, signifies the deceleration transmitted to the vehicle occupant during a crash. It corresponds to the highest point on the load displacement curve at the beginning of the crushing process. Minimizing the FPL is of utmost importance, as it reflects the minimum load required to initiate collapse, and reducing this value significantly contributes to improved crashworthiness.

2.2 Bio-inspired structural configuration

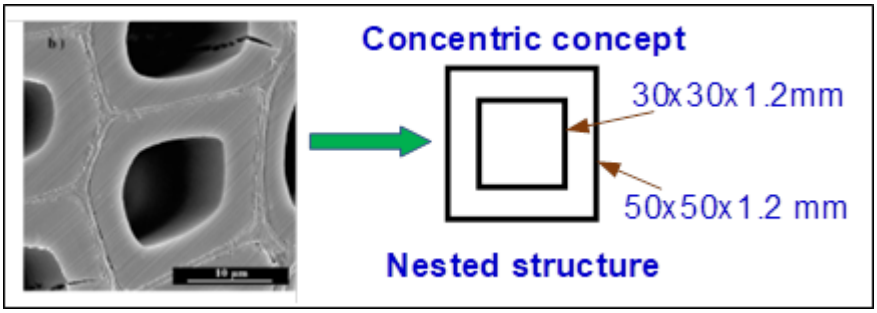

Figure 2: Bio-inspired tube [8].

As organisms have evolved, they have developed physical adaptations to better cope with the demands of their environments. By mimicking biological structures, we can create stronger structures that can withstand extreme conditions. Wood is a prime example of such a structure, known for its strength, lightness, and stiffness due to its structural design, which allows for efficient energy absorption. Inspired by this concentric microstructure, we have employed these lightweight and crash-resistant principles to create thin tubes. This design has progressed even further, as we have developed bio-inspired nested tubes (Figure 2).

2.3 Material and testing

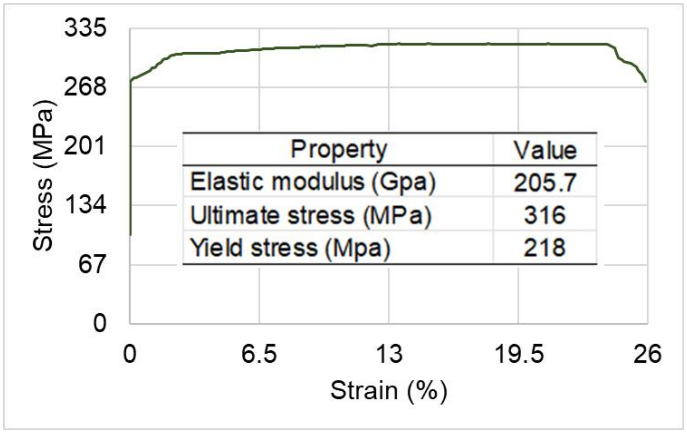

Figure 3: Stress-strain curve of mild steel.

This investigation employed square tubes with dimensions of 30x30x1.2 mm and 50x50x1.2 mm as samples. These specimens were fabricated from mild steel, and their mechanical properties are presented in Fig. 3. Quasi-static testing was performed on a universal testing machine with a maximum load of 500 kN at a loading rate of 7 mm/min (Figure 4(a)). For the quasi-static test, load angles of 0º, 5º, and 10º were selected. The schema for the impact test using finite element analysis is depicted in Figure 4(b). The impact velocity was set to 15.6 m/s at small load angles of 0º, 2º, 4º, and 6º to enhance the crashworthiness performance of the tube used in the design of crashworthy structures.

A three-dimensional finite element model (FEM) was established using the explicit nonlinear solver in ABAQUS for numerical simulation. Figure 4(b) illustrates the FEM model of a sample, which includes a fixed rigid wall at the bottom and an impactor of 500 kg at the top. The impactor and rigid wall were modeled as Rigid elements with a mesh size of 10 mm. The tube was modeled using an S4R element with five integration points along the thickness direction. The model utilized a friction coefficient of 0.25 for

contact behavior at all surface pair locations. The bottom surface of the tube was tie-constrained with the bottom plate using master and slave surfaces to maintain the tube's stability during the crash.

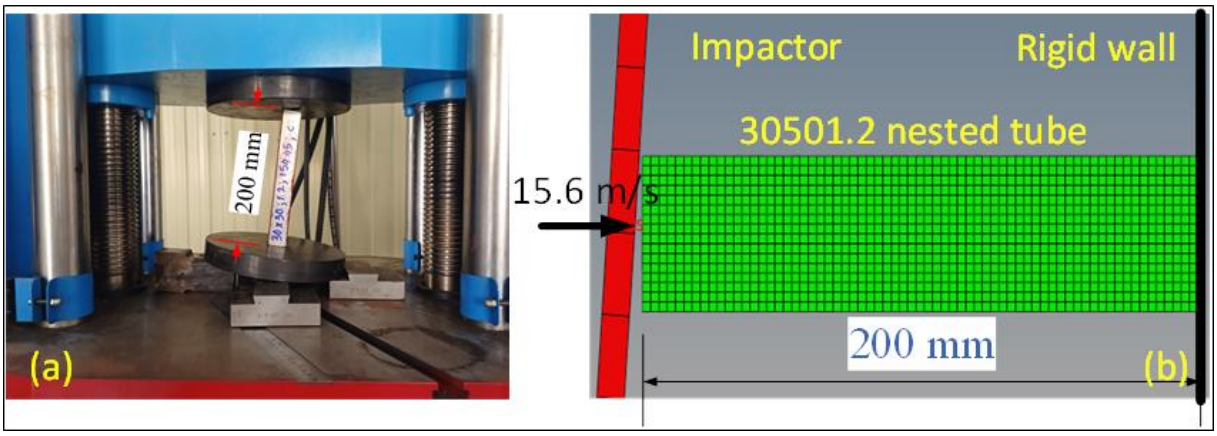

Figure 4: Schema of testing: a) Quasi-static compression with load angles of 0º, 5º, and 10º and b) impact with small load angles of 0º, 2º, 4º, and 6º.

3 C RUSHING RESPONSE

3.1 Quasi-static loading case

Following the testing of single square tubes with dimensions 30x30x1.2 and 50x50x1.2, the resulting deformations are depicted in Figures 5 and 6, respectively. The observations reveal that for the single square tube of dimensions 30x30x1.2, the initial wrinkle emerges at the top end of the tube, and subsequent wrinkles propagate towards the bottom end (Figure 5). The deformation process of the single square tube of dimensions 50x50x1.2 (Figure 6) exhibits similarities to that of the single square tube of dimensions 30x30x1.2. In both types of tubes, wrinkles gradually develop without experiencing bending deformation in all three loading scenarios. This progressive wrinkle mode is the preferred deformation pattern for tubes subjected to axial or oblique loading due to its stable deformation characteristics and higher energy dissipation capacity during collapse.

Table 1: Crashworthiness indicators in case of quasi-static load.

Tube	Load angle (º)	FPL (kN)	SEA (kJ/kg)
30301.2-0	0	38.01	21.32
30301.2-5	5	29.80	21.03
30301.2-10	10	28.13	20.84
50501.2-0	0	57.20	13.89
50501.2-5	5	41.10	13.71
50501.2-10	10	28.22	13.49

While the number of wrinkles remains approximately consistent across all three loading cases, the compacting level of the tube under axial compression (load angle of 0º) surpasses that of the tube under oblique compression with load angles of 5º and 10º. This discrepancy indicates that the tube requires greater energy dissipation under axial compression. Moreover, the deformations of both tube types indicate that the smaller tube exhibits a higher number of folds compared to the larger tube. Furthermore, the larger tube (50x50x1.2) possesses a greater wavelength compared to the smaller tube (30x30x1.2). Consequently, the larger tube exhibits enhanced energy dissipation capabilities in comparison to the smaller tube.

Figure 7 illustrates the load and energy responses of the 30x30x1.2 and 50x50x1.2 single square tubes. The graph demonstrates a gradual decrease in FPL as the load angle increases, and it can be observed that the load and energy absorption responses of the 50x50x1.2 tube are greater than those of the 30x30x1.2 tube across all loading cases.

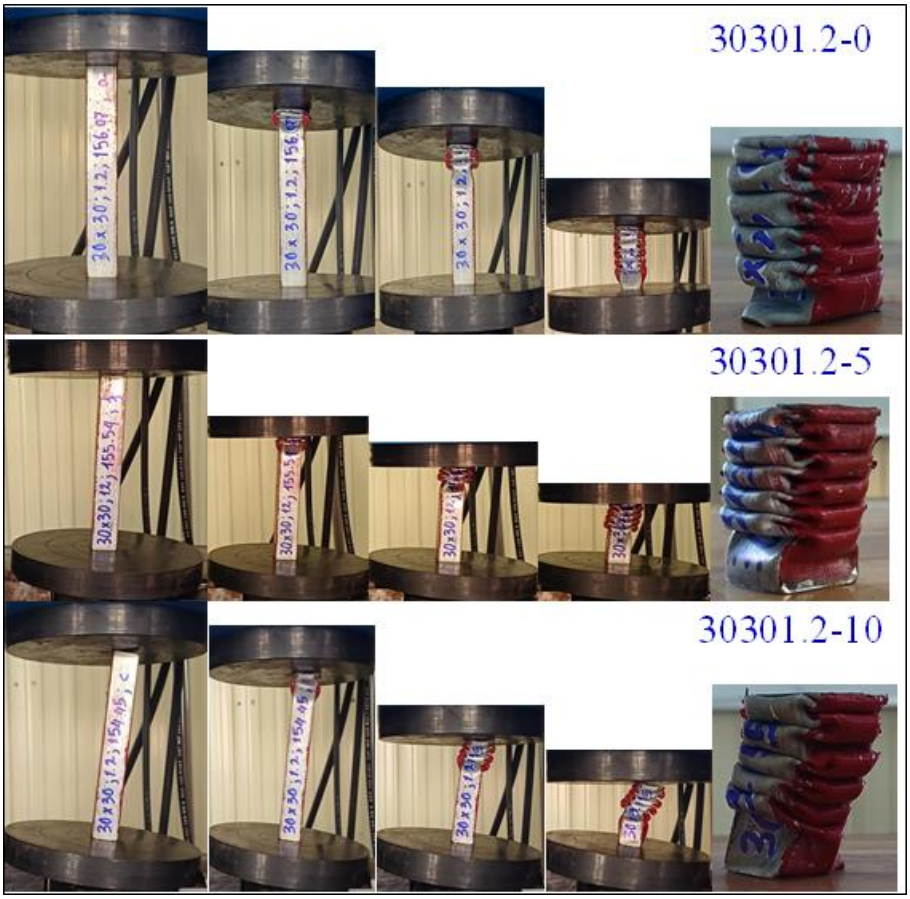

Figure 5: Deformation process of single square tube 30301.2 under quasi-static compression.

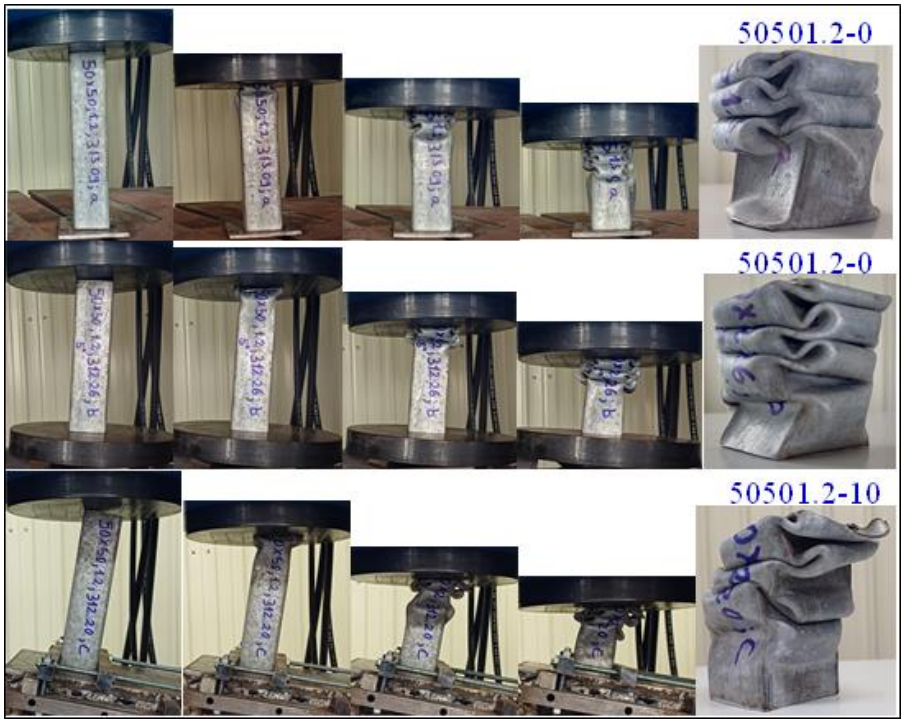

Figure 6: Deformation process of single square tube 50501.2 under quasi-static compression.

When comparing both tube types, the load responses under oblique loading with load angles of 5° and 10° exhibit similar behavior, while they slightly differ from the load response observed under axial loading with a load angle of 0°. This variation in the load response can be attributed to the complete contact between the

upper platen of the compression machine and the upper end of the tube in the case of axial loading with a load angle of 0°. Conversely, under oblique loading, there is only partial contact between the upper platen and the upper end of the tube.

In terms of the energy absorption response, both tube types exhibit similar behavior during the compression process. The difference in energy absorption between the two types is relatively small, as there is not a significant variation in the amount of material involved in deformation.

The variations in crashworthiness indicators under axial and oblique loading are presented in Table 1. For the 30x30x1.2 tube, when comparing the indicators of tubes under oblique loading with load angles of 5° and 10° to those of the tube under axial loading, there is a decrease of 21.6% and 26% in FPL, and a decrease of 1.3% and 2.3% in SEA, respectively. In the case of the 50x50x1.2 tube, the decreases in these indicators under oblique loading with load angles of 5° and 10°, compared to axial loading, are 28.1% and 50.6% in FPL, and 1.3% and 2.8% in SEA, respectively.

Under the same loading conditions, while the decrease in SEA is the same for both tube types, the decrease in FPL of the 50x50x1.2 tube is larger than that of the 30x30x1.2 tube due to the higher initial value of FPL in the 50x50x1.2 tube. Table 2 highlights the advantage of using oblique loading in crashworthy design, as it leads to a greater decrease in FPL compared to SEA. This reduction in FPL helps to minimize the negative impact on passengers in the event of an accident.

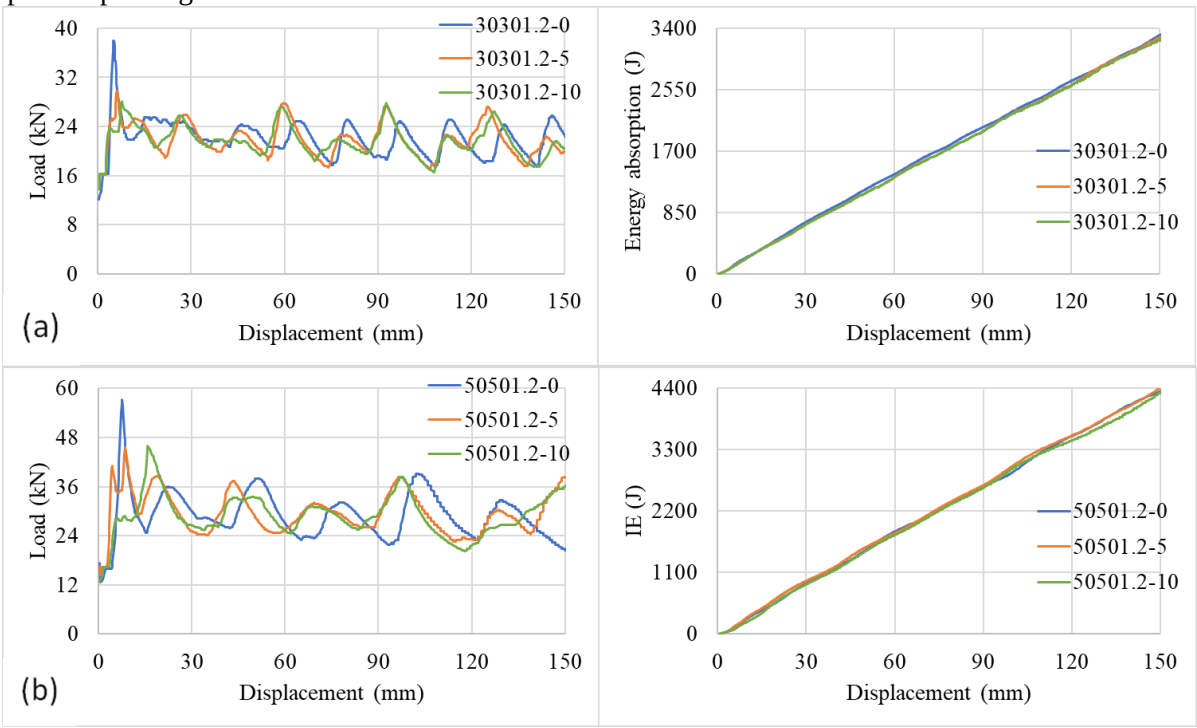

Figure 7: Load and energy absorption responses: a) single tube 30301.2 and b) single tube 50501.2.

3.2 Impact loading case

Leveraging the favorable features observed in single tubes under oblique loading, this section focuses on investigating the crashworthiness performance of a 30x50x1.2 bio-inspired nested configuration. The bio-nested tube consists of two component tubes, namely the 30x30x1.2 and 50x50x1.2 tubes. The dynamic loading is applied at axial and oblique impact with load angles of 0°, 2°, 4°, and 6°, with an impact velocity of 15.6 m/s.

Figure 8 presents the collapsing processes of the 30x50x1.2 bio-inspired nested tubes under different loading conditions, demonstrating similar progressive deformation modes. Notably, no bending phenomenon is observed in the deformation when subjected to small load angles of 2°, 4°, and 6°. Although these tubes exhibit the same number of wrinkles, the wavelengths vary due to differences in the compacting level.

It is evident that the tube under axial impact demonstrates the highest compacting level, while the tube

under oblique impact with a load angle of 6° exhibits the lowest compacting level. Consequently, the tube with a lower compacting level requires less energy dissipation to undergo collapse.

Figure 9 illustrates the load and energy absorption responses of the 30x50x1.2 bio-inspired nested tube under both axial and oblique impacts. The graph highlights the influence of the loading condition on the tube's load and energy absorption characteristics.

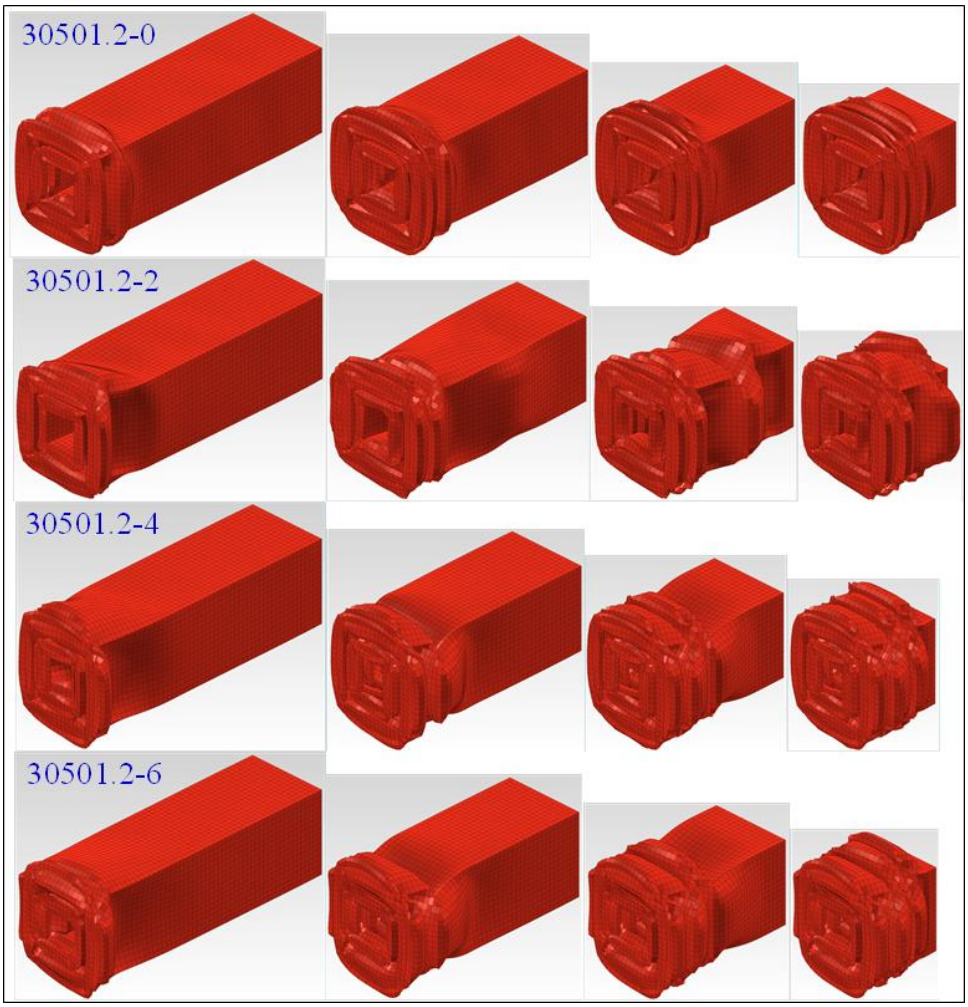

Figure 8: Deformation process of the bio-inspired nested tube 30501.2 under impact load with load angles of 0º, 2º, 4º, and 6º.

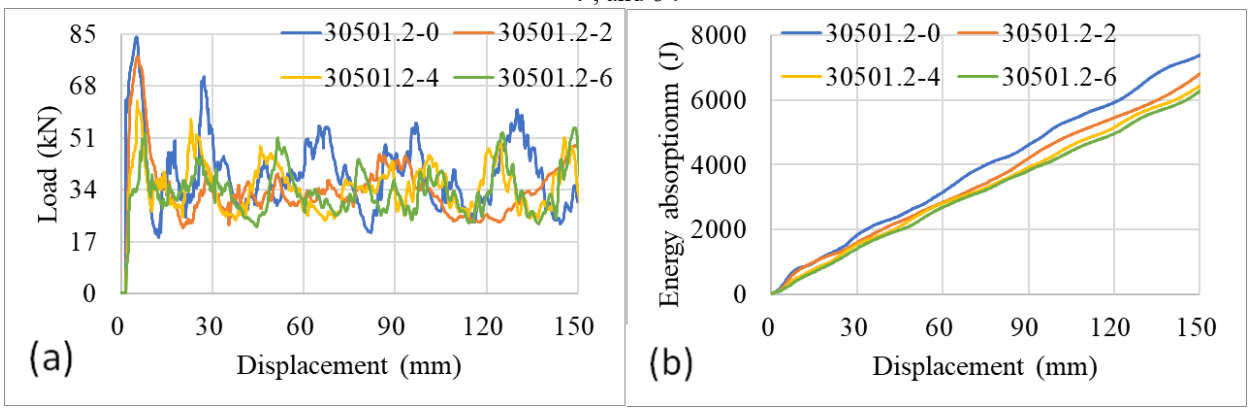

Figure 9: a) load and b) energy absorption responses.

Regarding the load response, larger fluctuations are observed in the 30x30x1.2-0 tube under axial impact compared to the other cases. This results in a higher energy absorption capacity, as depicted in Figure 9(b).

In contrast, the load and energy responses of the 30x30x1.2-2, 30x30x1.2-4, and 30x30x1.2-6 tubes under oblique impact with small load angles of 2°, 4°, and 6° exhibit similarities with minor deviations. This similarity in load conditions contributes to their comparable energy absorption behaviors.

4 DISCUSION

This section focuses on analyzing the impact of load angles on the crashworthiness performance of the bio-inspired nested tube under dynamic loading. Table 2 presents the First Peak Load (FPL) and Specific Energy Absorption (SEA) indicators, demonstrating the influence of load angles on these performance measures. A decrease in load angle leads to a decrease in both FPL and SEA, but the magnitude of the decrease differs significantly between FPL and SEA.

Compared to the 30501.2-0 tube under axial impact with a load angle of 0°, the 30501.2-2, 30501.2-4, and 30501.2-6 tubes under oblique impact with load angles of 2°, 4°, and 6°, respectively, exhibit significant decreases in FPL of 18.5%, 25.1%, and 39.8%, respectively. On the other hand, the decreases in SEA for the 30501.2-2, 30501.2-4, and 30501.2-6 tubes under oblique impact with load angles of 2°, 4°, and 6°, respectively, compared to the 30501.2-0 tube under axial impact with a load angle of 0°, are 7.7%, 13.1%, and 15.1%, respectively. These results indicate that oblique impact with small load angles has a significant effect on the crashworthiness performance of the tube, with a much larger impact on FPL compared to SEA. Additionally, the bio-inspired nested tube demonstrates an increased crushing resistance without occupying additional space.

Table 2: Crashworthiness indicators in case of impact load.

Tube	Load angle (º)	FPL (kN)	SEA (kJ/kg)
30501.2-0	0	84.20	12.69
30501.2-2	2	68.55	11.70
30501.2-4	4	63.03	11.02
30501.2-6	6	50.64	10.76

5 CONCLUSIONS

This paper investigated the influence of load angle on the crashworthiness performance of single square tubes and bio-inspired nested tubes under both quasi-static and dynamic loading conditions. The findings of this study highlight the significant impact of load angle on the crashworthiness performance of the tubes. It was observed that an increase in load angle resulted in a decrease in both FPL and SEA. However, the decrease in FPL was found to be larger than the decrease in SEA.

The FPL in cases of 2°, 4°, and 6° decreases by 18.5%, 25.1%, and 39.8%, respectively, compared to that in the case of axial impact, while the SEA in cases of 2°, 4°, and 6° decreases by 7.7%, 13.1%, and 15.1%, respectively, compared to that in the case of axial impact. Additionally, under these loading cases, its deformation mode is a progressive folding mode, which is a desirable deformation type in case of crushing loading. This suggests the advantage of utilizing small loading angles in the design of crashworthy structures, as it can lead to a greater reduction in FPL, which is a crucial indicator of crash energy absorption.

Furthermore, the bio-inspired nested tube configuration demonstrated its effectiveness in enhancing the crushing resistance of the tube without requiring additional space. This highlights the potential benefits of adopting bio-inspired designs in crashworthy structures.

ACKNOWLEDGEMENT: We acknowledge Van Lang University, Industrial University of Ho Chi Minh city and Vinh Long University of Technology Education (Vietnam) for supporting this study.

REFERENCES

[1] V. Patel, G. Tiwari, R. Dumpala, Review of the crushing response of collapsible tubular structures, Frontiers of Mechanical Engineering, 15 (2020) 438-474.

[2] M. Yamashita, M. Gotoh, Y. Sawairi, Axial crush of hollow cylindrical structures with various polygonal cross-sections: Numerical simulation and experiment, Journal of Materials Processing Technology, 140 (2003) 59-64.

[3] A. Alavi Nia, J. Haddad Hamedani, Comparative analysis of energy absorption and deformations of thin walled tubes with various section geometries, Thin-Walled Structures, 48 (2010) 946-954.

[4] G. Lu, T. Yu, Energy Absorption of Structures and Materials, Woodhead Publishing, (2003).

[5] H.-S. Kim, T. Wierzbicki, Numerical and analytical study on deep biaxial bending collapse of thin-walled beams, International Journal of Mechanical Sciences, 42 (2000) 1947-1970.

[6] A. Reyes, M. Langseth, O.S. Hopperstad, Crashworthiness of aluminum extrusions subjected to oblique loading: experiments and numerical analyses, International Journal of Mechanical Sciences, 44 (2002) 1965-1984.

[7] H. Yin, Y. Xiao, G. Wen, Q. Qing, X. Wu, Crushing analysis and multi-objective optimization design for bionic thin-walled structure, Materials & Design, 87 (2015) 825-834.

[8] D. Xing, J. Li, S. Wang, Comparison of the chemical and micromechanical properties of Larix spp. after eco-friendly heat treatments measured by in situ nanoindentation, Scientific Reports, 10 (2020) 4358.

RESEARCHING, ANALYSING THE PERFORMANCE OF ELECTRIC RENAULT ZOE IN SIMULATION AND EXPERIMENT

QUOC-VIET HUYNH, THIEN-DINH NGUYEN

Ho Chi Minh City University of Technology and Education,
viethq@hcmute.edu.vn, dinhnt@hcmute.edu.vn

Abstract

Nowadays, the global electric vehicle (EV) has continued their strong growth and is being studied with many research works. This paper accomplishes the electric Renault ZOE 2020 simulation by the Advanced Vehicle Simulator (ADVISOR) software and compares reality test cases in the road test. One of the most widely used computer simulation tools for HEVs and EVs is ADVISOR developed by the National Renewable Energy Laboratory. This program is flexible enough to operate on most platforms in the popular MATLAB/SIMULINK programming environment. This research applied ADVISOR to simulate the operation of Renault ZOE 2020 and estimate the vehicle performances such as acceleration time, the distance of EV on one charge, charge or discharge current of the battery, State of Charge (SOC), torque of wheel, ... Besides, the paper presents experimental results, performed in Renault ZOE 2020 with road test following EUDC driving cycle. The paper compares simulation and experimental results to help the researcher design and estimate EV components.

Keywords. ADVISOR; Electric Vehicle (EV); Renault ZOE; Performances of EV; Energy Consumption

1 INTRODUCTION

The emissions of the greenhouse effect are the unwanted product, which usually related to burning of fossil fuel for energy needs. The severity of climate change due to greenhouse effect emissions has reached a threatening level and can be easily seen with the present global warming and melting of large icebergs. The research group in China realized that increasing emissions from road transportation endanger China's objective to reduce national greenhouse gas emissions. Through analysis of the emissions, they proposed to promote electric vehicles and biofuels [1]. Countries such as United Kingdom, France, Germany, Netherlands and other countries have adopted the Paris agreement goals and pursued developing strategies predicated on electrification of the transportation sector by revealing a schedule to stop producing internal combustion engine vehicles by 2040 [2]. Electric vehicles show remarkable ability with comparable lower life cost per kilometer to that of internal combustion engine vehicles and can be researched more improvements by the development of more durable electric vehicles [3]. In recent years, Electric vehicles, as a promising way to reduce the greenhouse effect, have been researched extensively. Big automakers now offer 40-plus EV models such as Tesla Cybertruck, Audi E-tron, Hyundai Ioniq 5, Toyota bZ4X, ..., boasting at least 200 kilometers of range, unique high-tech features and increasing performance.

Gaizka et al [4] compared and contrasted the different electrical equivalent circuit models, impedance models, and runtime models for battery-based EV applications, addressing their characteristics, advantages, disadvantages, and usual applications in the field of electromobility.

Advanced Vehicle Simulator (ADVISOR) was researched and developed in November 1994 at the National Renewable Energy Laboratory in USA. It is designed to quickly analyze the performance and fuel economy of conventional, electric and hybrid vehicles. ADVISOR is a MATLAB/Simulink based simulation program. MATLAB provides an easy-to-use matrix-based programming environment for performing calculations while Simulink can be used to represent complex systems graphically using block diagrams [5, 6].

ADVISOR is a simulation software for electric and hybrid vehicles. A significant advantage of using a model that is in the MATLAB/Simulink environment is the flexibility, ease of analysis and ease of changing the model, such as replacing one control strategy or regenerative braking algorithm with another [7], [8].

This paper presents simulation results from ADVISOR software based on the technical specifications of Renault ZOE 2020. Besides that, this paper also shows experimental results when testing on Renault ZOE

2020 such as acceleration time, state of charge, charge or discharge current of battery, torque of the motor. The aim of this study is to research and compare the features of the electric vehicle, thereby contributing to the improvement of electric vehicles in the future.

2 OVERVIEW OF THE ELECTRIC VEHICLE MODEL

The features of electric vehicles are represented by specifications such as: the distance of an electric vehicle can travel on a full charge, the ratio between the vehicle's traveling power and energy consumption (energy efficiency), the time it takes to fully charge the vehicle's battery, the ratio of the capacity of the battery to its nominal capacity after a period of use and indicates the maximum amount of electricity that can be stored in the battery (state of charge (SOC)).

The construction of the electric vehicle is represented by Figure 1, the main components of model consist of energy storage system, motor/controller and vehicle.

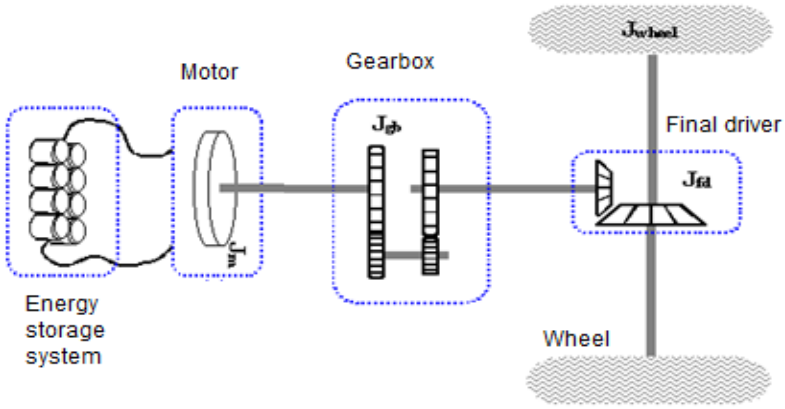

Figure 1: Electric vehicle configuration of Renault ZOE in Advisor.

2.1 Energy Storage System (ESS)

The ESS was implemented with internal resistance battery model (R_{int}). The voltage source (open-circuit voltage, or OCV) is the function which depended SOC and temperature (t). The resistor (internal resistance, or R) is the parameters vary with OCV and the direction of current flow (e.g. if the battery is charging or discharging). The thermal model is a lumped capacity model. The SOC for the R_{int} model was estimated by performing amp counting, including Coulombic efficiency losses when charging, as shown in Eq. (1) [9,10]:

$$SOC = \frac{Ah_{max} - Ah_{use}(\eta_{coul})}{Ah_{max}} \quad (1)$$

In which:

- SOC is State of charge.
- Ah is battery capacity.
- $Ah_{use} = \int_0^t A\eta_{coul}\, dt$ for A < 0 (charge)

2.2 Motor/controller

The motor/controller model include loss data, rotation inertia, and performance limits. Available torque (T) is computed from available power (P) by assuming that the ratio of rotor torque to input (electric) power is the same for the actual/achievable situation as was computed for the request. This is mathematically equivalent to assuming that the motor/controller efficiency (η). Rotor speed for the actual/achievable calculations is as computed in the 'request' branch such as Eq. (3).

$$P = T.\omega.\eta^k \text{where k = -1 (for propulsion mode), k = 1 (for generating mode)} \quad (2)$$

2.3 Vehicle model

The longitudinal vehicle dynamics can be represented by Eq. (3)

$$Ma = F_t - F_r \quad (3)$$

Where M, a, F_t, and F_r are mass of vehicle, acceleration of vehicle, traction force from motor, and resistance force (include in aerodynamic drag resistance, rolling resistance, inertia resitance and road gradient resistance), respectively.

This block uses the required vehicle speed with vehicle parameters and the previous speed and classic, straightforward equations to determine the tractive force required at the tire/road interface.

Renault is a famous automaker in the world, under Renault Group in France. Renault Group is at the forefront of a mobility that is reinventing itself and researching many works related to electric vehicles. One of the best electric vehicles of Renault is Renault ZOE with modern technologies.

Renault ZOE is a full-electric vehicle with outstanding advantages and superior technical specifications such as more battery capacity, more range and more technology [12].

Table 1: 2020 Renault ZOE Z.E50 - Specifications.

ELECTRIC MOTOR		**BATTERY**	
Manufacturer	Renault	Manufacturer	Renault and LG Chem
Model	R110	Model	Z.E 50
Location of the motor	Front	Type of rechargeable battery	Lithium-Ion
Power	80 kW (kilowatts) 107.3 hp (mechanical horsepower)	Battery capacity	54.66 kWh
Maximum power RPM	3395 - 10886 rpm	Number of cells	192
Torque	225 Nm (Newton meters) 22.9 kgm (kilogram meters) 166.0 ft-lb (foot-pounds)	Number of modules	12
Maximum torque RPM	500 – 3395 rpm	Voltage	400 V
Driving modes	Eco, Normal, B-mode, D-mode	**BATTERY CELL**	
Regenerative braking	Yes	Battery cell model	LGX E78
		Battery cell voltage	3.65 V
		Battery cell capacity	78 Ah

3 SIMUALATION AND RESULT

ADVISOR is a simulate software to analyze and research about features of vehicles. With the versatility, convenience and efficiency of ADVISOR, authors simulated some features of Renault ZOE such as acceleration time, the distance of EV on one charge, charge or discharge current of the battery, State of Charge (SOC), moment of the motor.

3.1 Set-up vehicle parameters in Advisor

For setting up, the authors manipulate the parameters of Renault ZOE (energy storage, motor, wheel, powertrain control, ...) and add to ADVISOR as figure 2.

Figure 2: ADVISOR vehicle input screen with Renault ZOE parameters.

Simulation on a standard cycle is tested. A driving cycle is a set of speed points over time. It is used to estimate fuel consumption and pollutant emissions of a vehicle in a standardized way, so that we can compare the different between vehicles. The European cycle (CYC_ECE_EUDC – Figure 3) is chose as a reference. It can mimic the conditions encountered on European roads. This cycle consists of acceleration, deceleration and constant speed bearings [13]. This cycle is mainly used for measuring fuel consumption and vehicle emissions and the analysis of these performances.

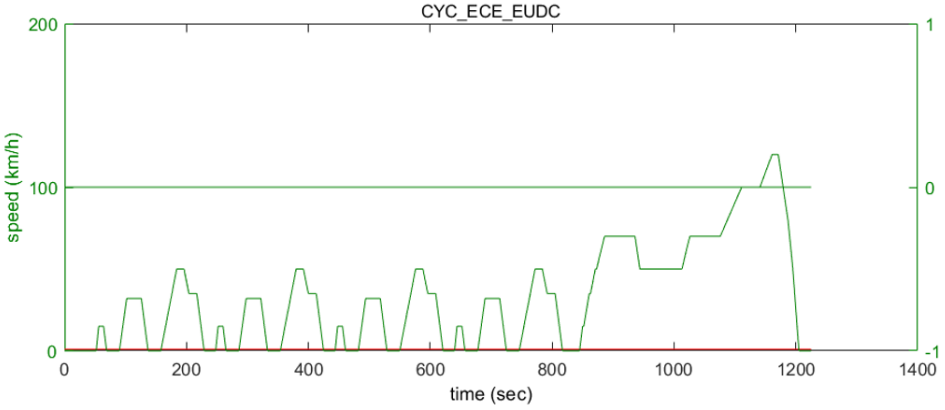

Figure 3: Using CYC_ECE_EUDC driving cycle.

3.2 Simulation Results

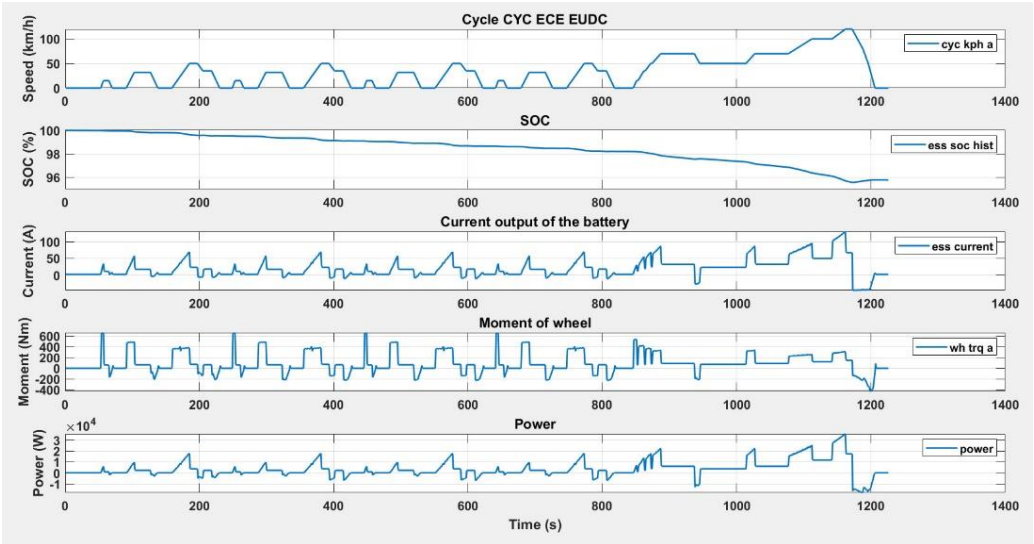

Figure 4: Simulation results: Speed, SOC, Current, Torque, Power.

After the simulation with Renault ZOE parameters, tests were made for European road EUDC cycle on the distance of approximately 10.93 km for 1200 s, maximum speed 120km/h. The simulation results are suitable with theories.

- State of charge (SOC): The initial SOC is 100% for batteries, after performing EUDC driving cycle, SOC is reduced by about 4%. With regenerate brake, the graph line is not a straight line but curves and increases SOC values at the points where the car slows down.

- Current: When the vehicle accelerates at a higher speed, the high-voltage battery will give a larger current to meet the requirements and the larger current from the regenerative operates to recharge the high-voltage battery.

- Torque: When the vehicle accelerates, the torque increases and decreases gradually when the desired speed value is reached. At points less than zero, the regenerative brake operates to recharge the high-voltage battery.

4 TESTING EXPERIMENT

After simulating in ADVISOR, authors set up test devices to Renault ZOE and performed some modes of the EUDC driving cycle, from which the author makes comparisons of vehicle performance in simulation and reality.

4.1 Set-up for vehicle test

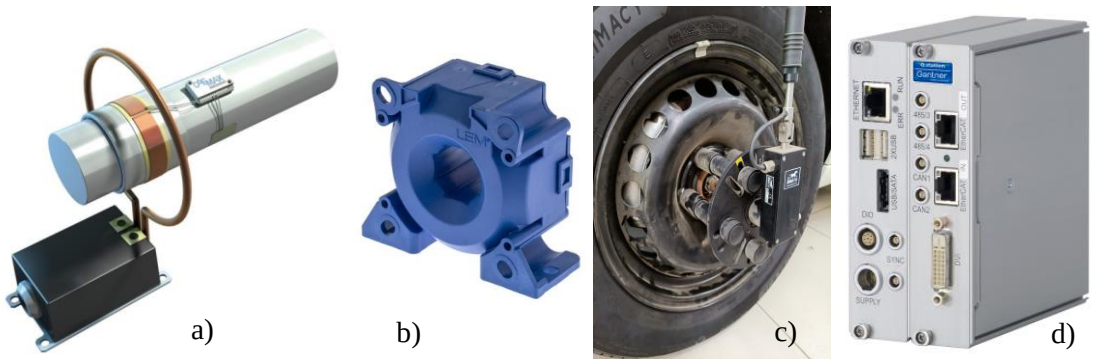

Figure 4: Sensors for testing experiment: a) Torque sensor; b) Current sensor; c) Wheel speed sensor; d) Q.brixx STATION.

Torque sensor (Dx transmitter unit with strain gauge; supply via ring stator) is a robust and compact wireless telemetry systems for the non-contact transmission of measurement data for torsion on vehicles. When the metal wire on the surface of the sensor is pulled, the cross-sectional area will be smaller and the wire length will increase, so the resistance will also increase and vice versa. Changing the sensor's resistance will change the voltage signal and send it to the DX transmitter SCT [14].

Current sensor (LEM sensor) is applied closed loop Hall effect to create voltage Hall when current passes through the sensor [15].

Wheel speed sensor (PEGASEM) is set up at the wheel and operates based on encoder method. Thereby helping to calculate vehicle speed with tire parameters.

Q.brixx A127 model of Q.brixx STATION is able to measure the high voltage of battery directly; after that, equation (1) is applied to show SOC value [16].

4.2 Experiment Results

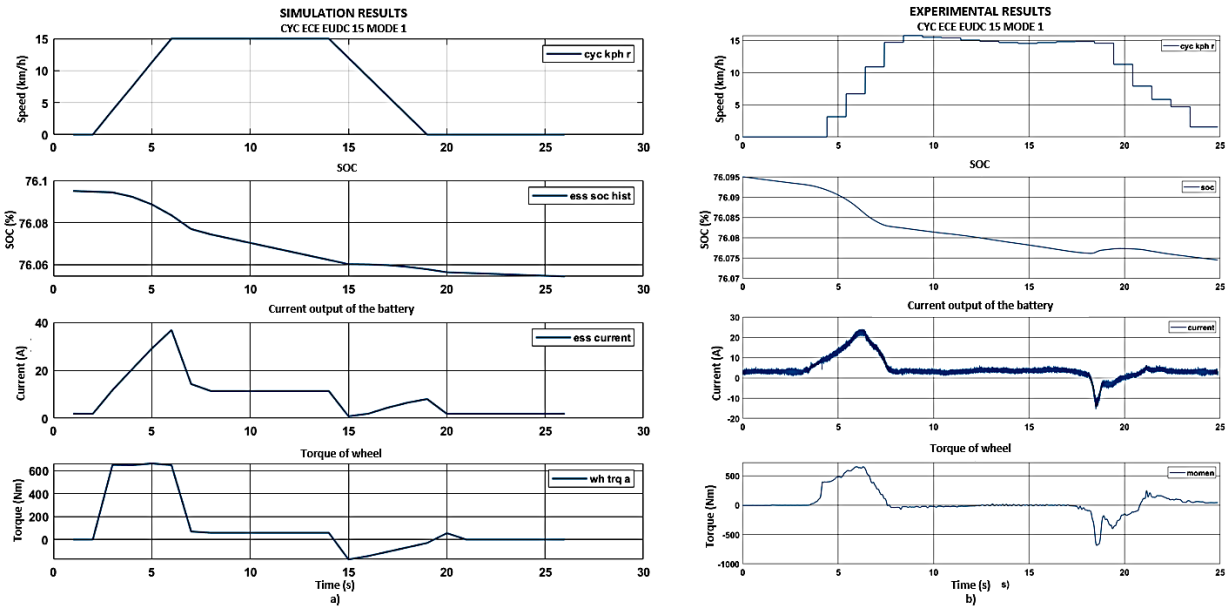

Figure 5: The result chart of EUDC driving cycle at mode 1 (15 km/h):
a) Simulation results; b) Experimental results.

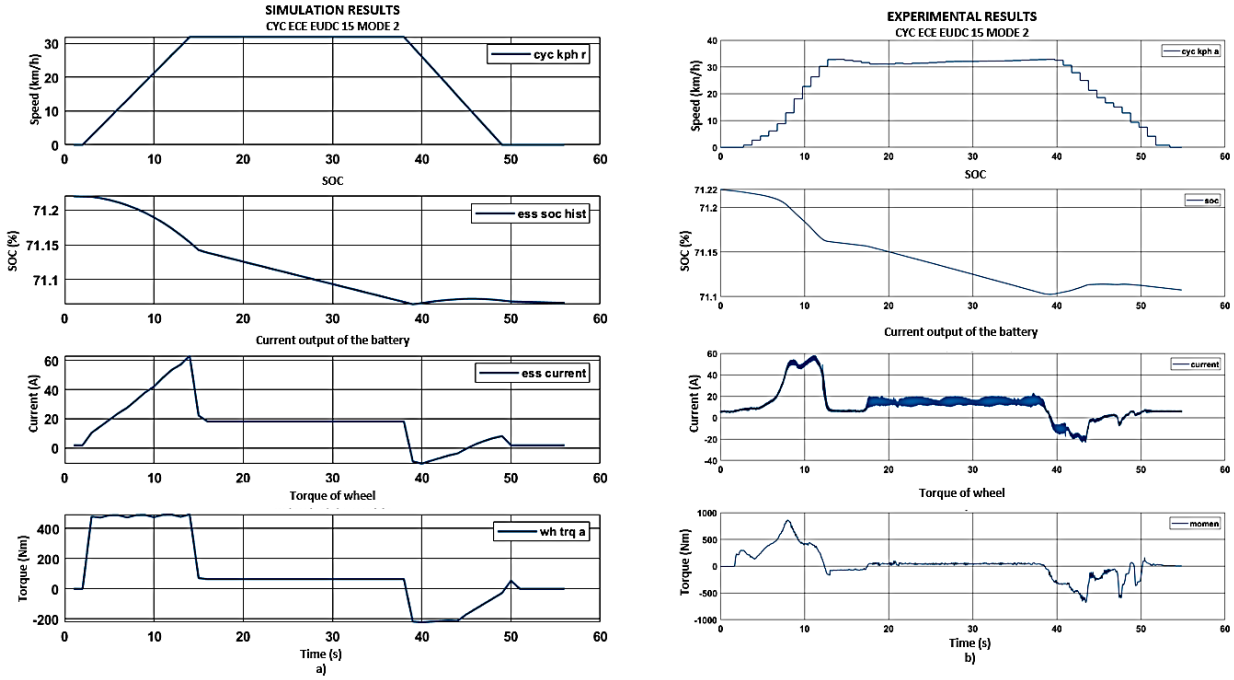

Figure 6: The result chart of EUDC driving cycle at mode 2 (32 km/h):
a) Simulation results; b) Experimental results.

Figure 5 and Figure 6 show result graphs in simulation and experimental as vehicle speed, state of charge (SOC), current output of battery and torque. The outlines of result graphs in simulation and experimental are the same and suitable with expectation.

However, the loss SOC of experimental is smaller than simulation. Differences in torque between simulation and experimental are affected by realistic driving behavior, to achieve the desired speed threshold, the driver push acceleration pedal and when the vehicle speed is approximated expected value, the driver will reduce acceleration pedal; that's why the torque can not maintain a specific value. The currents value at the deceleration shows the charging of the regenerative brake for battery and the SOC value is increased a little.

5 CONCLUSIONS

In this study, a simulation model of an electric vehicle system (Renault ZOE) is developed and applied to simulate the performance of Renault ZOE with EUDC driving cycle, Matlab-Simulink simulation environment and plus package ADVISOR is used. Next, the testing devices is set up to measure vehicle speed, state of charge (SOC), current of battery and torque of wheel. The comparation between simulation and experimental results is done with 2 modes (0 - 15 - 0 km/h; 0 - 32 - 0 km/h) in EUDC driving cycle. Its effectiveness were evaluated via simulation results, the outlines of the simulated and experimental graphs are the same. Besides, we realize the regenerative braking process on Renault Zoe during the operation of the vehicle. Accordingly, the measurement of the experimental progress with testing devices helps to reliably assess the performance of Renault ZOE and experimental progress in other vehicles will be conducted for further evaluation.

REFERENCES

[1] Zheng, Bo; Zhang, Qiang; Borken-Kleefeld, Jens; Huo, Hong; Guan, Dabo; Klimont, Zbigniew; Peters, Glen P.; He, Kebin, How will greenhouse gas emissions from motor vehicles be constrained in China around 2030?, *Applied Energy*, vol. 156, pp. 230-240, 2015.

[2] Frank W. Geels, Disruption and low-carbon system transformation: Progress and new challenges in socio-technical transitions research and the Multi-Level Perspective, *Energy Research & Social Science*, vol. 37, pp. 224-231, 2018.

[3] F. Sioshansi and J. Webb, Transitioning from conventional to electric vehicles: The effect of cost and environmental drivers on peak oil demand, *Economic Analysis and Policy*, vol. 61, pp. 7-15, 2019.

[4] Saldaña, Gaizka; San Martín, José Ignacio; Zamora, Inmaculada; Asensio, Francisco Javier; Oñederra, Oier. Analysis of the Current Electric Battery Models for Electric Vehicle Simulation. *Energies 2019*, 12, 2750, 2019.

[5] T Markel, A Brooker, T Hendricks, V Johnson, K Kelly, B Kramer, M O'Keefe, S Sprik, K Wipke, ADVISOR: a systems analysis tool for advanced vehicle modeling, *Journal of Power Sources*, vol. 110, pp. 255-266, 2002.

[6] B. Adrian, M. Florea, Modeling and testing of electric vehicle propulsion systems, *U.P.B. Sci. Bull*, vol. 77, pp. 201-212, 2015.

[7] S. Bradai, M. Ghariani and A. Guermazi, Study of the traction chains of different models of electric vehicles with the ADVISOR tool, 2016 *7th International Renewable Energy Congress (IREC)*, pp. 1-6, 2016.

[8] A. Saleki, S. Rezazade and M. Changizian, Analysis and simulation of hybrid electric vehicles for sedan vehicle, *2017 Iranian Conference on Electrical Engineering (ICEE)*, pp. 1412-1416, 2017.

[9] V. H. Johnson, Battery Performance Models In Advisor, *Journal of Power Sources*, Volume 110, Issue 2, 22 August 2002, Pages 321-329

[10] Mohammad Kamrul Hasan, Md Mahmud, A.K.M. Ahasan Habib, S.M.A. Motakabber, Shayla Islam, Review of electric vehicle energy storage and management system: Standards, issues, and challenges, *Journal of Energy Storage*, vol. 41, 2021.

[11] Quoc-Viet Huynh, Ngoc Tham Ngo Thi, Development of Torque-Speed Control Algorithms for Power-Split Hybrid Electric Vehicle, *International Conference on Green Technology and Sustainable Development (GTSD)*, 2022.

[12] EVSpecifications. (2020) 2020 Renault Zoe R110 - Specifications. [online]. Available: https://www.evspecifications.com/en/model/dc3eac.

[13] Bekheira Tabbache, Sofiane Djebarri, Abdelaziz Khelouiand, Mohamed Benbouzid, A Power Presizing Methodology for Electric Vehicle Traction Motors, *International Review on Modelling and Simulations*, 6 (1), pp. 29-32, 2013.

[14] *CAEMAX Dx telemetry - Modular, multi-channel telemetry system for a variety of applications*, IMC, 2017.

[15] *Current Transducer LF 205-S*, LEM, 2022.

[16] *Q.brixx station Controller*, Gantner Instruments, 2022.

DESIGNING A LQR CONTROLLER FOR ACTIVE SUSPENSION SYSTEM OF QUARTER HEAVY VEHICLE MODEL WITH AN ELECTRONIC SERVO-VALVE HYDRAULIC ACTUATOR

TRONG TU DO[1], VAN TAN VU[2], OLIVIER SENAME[3], KIEU DUC THINH[4]

[1] *Mechanical and Power Engineering Faculty, Electric Power University, Hanoi, Vietnam,*

[2] *Department of Automotive Mechanical Engineering, Faculty of Mechanical Engineering, University of Transport and Communications, Hanoi, Vietnam,*

[3] *Univ. Grenoble Alpes, CNRS, Grenoble INP, GIPSA-Lab, 38000, Grenoble, France,*

[4] *Faculty of Mechanical Engineering, Thuyloi University, Hanoi, Vietnam;*

tudt@epu.edu.vn, vvtan@utc.edu.vn, olivier.sename@grenoble-inp.fr, kieuducthinh@tlu.edu.vn

Abstract. Heavy vehicles are gaining increasing importance in transportation and goods transshipment, constituting over 70% of total freight transport in developing countries. However, the operation of these vehicles requests improvement due to the impact of changing dynamic loads, which contributes to degradation of infrastructure systems such roads surface and bridges. Although air suspension systems have been considered for addressing these issues, their complex structure, high installation and maintenance costs, and inability to meet strict criteria for heavy vehicles have hindered their widespread implementation. Owing to its large force generation, fast-acting time, quick response to transient requirements, controlled suspension system with an integrated electro-hydraulic actuator promises significant benefits in ones. This paper investigates full representation of quarter suspension system on truck utilizing hydraulic electric servo valve actuator. The Linear Quadratic Regulator controller is elaborated to satisfy the system's principal prerequisites: vehicle comfort and road safety, reducing dynamic load acting on road sur-face and causing damage to road facilities. The time and frequency domains simulation results for road excitation in the ideal sine-wave shape with different frequency range endorsed the superiority of proposed system in-creased vehicle comfort criteria up to 90.12%, compared to the passive sus-pension system.

Keywords. Heavy Vehicle, Hydraulic Electric Servo Valve Actuator, Linear Quadratic Regulator Controller, Vehicle Comfort, Road Holding.

1 INTRODUCTION

In recent years, active suspensions have gained significant attention and popularity in automobile applications due to their numerous advantages over semi-active and passive suspensions. The utilization of sensors within the control structure has emerged as a primary challenge in enhancing passenger comfort and safety, particularly in terms of road holding. Consequently, extensive research efforts have been dedicated to developing various control approaches for active suspensions, focusing on different types of shock absorbers such as MR, ER, and air actuators in suspension systems of commercial vehicles. However, these advancements have primarily been limited to cars, passenger vehicles, and trucks, while heavy vehicles face a distinct challenge related to the force requirements of the controller.

Studies exploring electro-hydraulic actuator systems have revealed the substantial force generation capabilities of current or voltage-controlled actuators, reaching levels as high as 30-120kN [1, 2]. These actuator systems have proven effective in applications demanding significant forces and moments. Consequently, integrating electro-hydraulic actuators into heavy-duty trucks has been extensively investigated, particularly in the context of active anti-roll bar systems [3]. Many researchers have employed servo-valve-controlled electro-hydraulic actuators in quarter car models to generate controlled forces for the suspension system. While some studies have examined PID, SMC, and Fuzzy-PID controllers for the Active Suspension Systems (ASS) using electro-hydraulic actuators [3–5], the linearized actuator models

employed in these studies impose limitations [6, 7].
Furthermore, the application of servo-valve control and Artificial Neural Network (ANN) prediction has been explored for ASS utilizing electro-hydraulic actuators [8–10]. In adaptive dynamic surface control strategies have also been proposed to address uncertainties related to electro-hydraulic actuators and unknown external disturbances in vehicle ASS [11]. Additionally, the development of controllers for nonlinear half-car ASS with hydraulic actuator dynamics has been investigated using frequency domain analysis and time domain simulations [12]. Furthermore, the supervision of a half-car active suspension model using an MPC-LQR-LPV controller has been demonstrated to satisfy comfort and road-holding criteria [13]. However, these studies have primarily focused on system response in the time domain and have not adequately addressed the stability of the system under varying parameter instabilities.
To address these research gaps, this study aims to develop a controlled sus-pension system for a quarter heavy vehicle model, focusing on the following objectives: constructing a model of a heavy-duty vehicle integrated with an Electronic Servo-Valve Hydraulic (ESVH) actuator and designing an LQR controller to regulate the current of the servo-valve in the ESVH actuator. This research intends to enhance the smoothness and traction of heavy-duty vehicles, thereby contributing to the advancement of ASS tailored specifically for heavy vehicles.

2 QUARTER HEAVY VEHICLE MODELLING

A quarter heavy vehicle model represents a single corner of a heavy vehicle with two degrees of freedom, as shown in Fig. 1. This model, which contains the vertical chassis and wheel bounce displacement, allows studying only the vertical dynamic behaviour of the heavy vehicle. This simple model consists of the sprung mass m_s represents a quarter of the vehicle body (chassis). The unsprung mass m_u represents the wheel and the tire of the vehicle. Z_s, Z_u stand for the vertical displacement of sprung mass and unsprung mass, respectively. The suspension is composed of a spring with the stiffness coefficient k_s and a damper with the passive damper coefficient c_s. The tire is modeled by a spring with the stiffness coefficient k_t. Finally, q represents the road profile vertical disturbance.

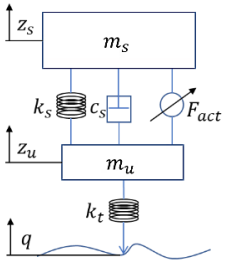

Figure 1: Quarter heavy vehicle model.

The dynamic equations of the system around the equilibrium can be derived using Newton's second law of motion.

$$\begin{cases} m_s \ddot{z}_s = -k_s(z_s - z_u) - c_s(\dot{z}_s - \dot{z}_u) - F_{act} \\ m_u \ddot{z}_u = k_s(z_s - z_u) + c_s(\dot{z}_s - \dot{z}_u) - k_t(z_u - q) + F_{act} \end{cases} \quad (1)$$

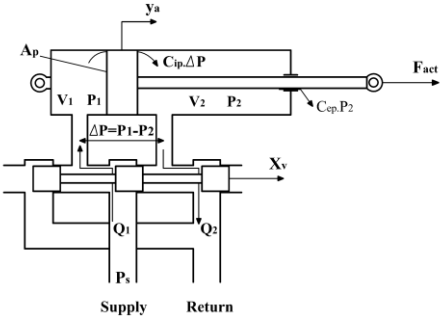

Figure 2: Diagram of the ESVH actuator.

Fig. 2 illustrates the diagram of a hydraulic cylinder in combination with an electronic servo-valve. The spool valve of the electronic servo-valve is controlled by a current that generates a displacement X_v. The high-pressure oil supply P_s is always stored outside the electronic servo valve, and the moving spool valve distributes the high-pressure oil into two chambers of the hydraulic cylinder. The difference in pressure $\Delta P = P_1 - P_2$ between the two chambers within the area of the piston A_p produces the output force F_{act} given by:

$$F_{act} = A_p \Delta P \tag{2}$$

Therefore, the equations in each chamber become:

$$\begin{cases} A_p \dfrac{dy_a}{dt} + \dfrac{V_0 + A_p y_a}{\beta_e} \dfrac{dP_1}{dt} = Q_1 - C_{ip}(P_1 - P_2) - C_{ep} P_1 \\ -A_p \dfrac{dy_a}{dt} + \dfrac{V_0 - A_p y_a}{\beta_e} \dfrac{dP_2}{dt} = C_{ip}(P_1 - P_2) - C_{ep} P_2 - Q_2 \end{cases} \tag{3}$$

With $C_{tp} = 2C_{ip} + C_{ep}$ is the total leakage coefficient of the hydraulic cylinder, now it becomes.

$$2Q_L = Q_1 + Q_2 = 2C_{tp}\Delta P + 2A_p \frac{dy_a}{dt} + \frac{V_0}{\beta_e}\frac{d\Delta P}{dt} \tag{4}$$

From equations (3) and (4), the dynamic equation of the servo-valve hydraulic cylinder is obtained as follows:

$$\frac{V_t}{4\beta_e}\frac{d\Delta P}{dt} + (K_P + C_{tp})\Delta P - K_x X_v + A_p \frac{dy_a}{dt} = 0 \tag{5}$$

Where y_a is the displacement of the piston inside the hydraulic cylinder.

The three-land-four-way spool valve is used in the ESVH actuator has the electrical current u controls displacement of the spool valve X_v. The effects of hysteresis and flow forces on the servo-valve are neglected here, then the dynamical behaviour of the electronic servo-valve can be approximated by a first-order model as:

$$\frac{dX_v}{dt} + \frac{1}{\tau} X_v - \frac{K_v}{\tau} u = 0 \tag{6}$$

where τ is the time constant and K_v the gain of the servo-valve model.

From (1), (2) and (6), the formulation that describes the characteristic of the quarter heavy vehicle integrated ESVH can be determined as:

$$\begin{cases} m_s \ddot{Z}_s = -k_s(z_s - z_u) - c_s(\dot{z}_s - \dot{z}_u) - A_p \Delta P \\ m_u \ddot{Z}_u = k_s(z_s - z_u) + c_s(\dot{z}_s - \dot{z}_u) - k_t(z_u - q) + A_p \Delta P \\ \dfrac{d\Delta P}{dt} = \dfrac{4\beta_e . A_p}{V_t}(\dot{z}_s - \dot{z}_u) + \dfrac{4\beta_e .(K_P + C_{tp})}{V_t}\Delta P - \dfrac{4\beta_e . K_x}{V_t} X_v \\ \dfrac{dX_v}{dt} - - = \dfrac{K_v}{\tau} u_{(v)} - \dfrac{1}{\tau} X_v \end{cases} \tag{7}$$

Table 1: Parameter for the quarter heavy vehicle model [14].

Symbols	Description	Value	Symbols	Description	Value
A_p	Area of the piston	$0.0123\, m^2$	K_v	Servo-valve gain	$0.0243\, m/A$
K_x	Valve flow gain coefficient	$2.5\, m^2/s$	m_s	Sprung mass	4638 kg
K_P	Total flow pressure coefficient	4.2×10^{-11} m^5/Ns	m_u	Unsprung mass	584 kg
C_{tp}	Total leakage coefficient of the actuator	0	c_s	Damper coefficient	$25000\, N/m$

V_t	Total volume of trapped oil	$0.0014\,m^3$	k_s	Suspension stiffness	$226209\,N/m$
β_e	Effective bulk modulus of the oil	6.89×10^6 N/m^2	k_t	Tyre stiffness	1793290 N/m
τ	Time constant of the servo-valve	0.01s			

3 DESIGN LINEAR QUADRATIC CONTROLLER FOR HEAVY VEHICLE

3.1 LQR Control Theory

The linear approach basically commences with the conversion of nonlinear into linear systems. Thus, the Linear Time Invariant (LTI) dynamical modelling is commonly adopted for control and observation purposes for both Single-Input-Single-Output and Multi-Input-Multi-Output systems. LTI dynamic system equations are given by:

$$\begin{cases} \dot{x}_{(t)} = Ax_{(t)} + B_{01}u_{(t)} + B_{02}w_{(t)} \\ z_{(t)} = Cx_{(t)} + D_{01}u_{(t)} + D_{02}w_{(t)} \end{cases} \tag{8}$$

Where $x_{(t)}$ denotes state, $w_{(t)}$ is disturbance, $u_{(t)}$ represents control input and $z_{(t)}$ is the output.

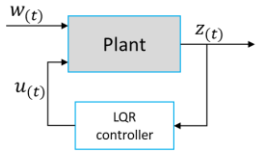

Figure 5: Schematic of LQR controller.

A general LQR controller in Fig. 3 uses feedback signal from output $z_{(t)}$ to generate appropriate control input $u_{(t)}$. For LQR controller design, it assumes that all states can be measured or estimated. The main objective of LQR controller is to determine the control input U in order to minimize performance index J. This index consists of not only performance characteristic requirement but also the controller input limitations, which is usually presented by:

$$J = \int_0^\infty \left(X^T QX + U^T RU + 2X^T NU \right) dt \tag{9}$$

Where Q, R and N are positive definite weighting matrices.

Consider the state feedback control law as follows:

$$u = -KX \tag{10}$$

Where K denotes the state feedback gain matrix and has the following form:

$$K = R^{-1}\left(B^T P + N^T\right) \tag{11}$$

And where the matrix P is the solution of Riccati equation as follows:

$$A.P + A^T.P - P.B.R^{-1}B^T.P + Q = 0 \tag{12}$$

The optimal closed-loop system is achieved from equations (9) and (12) as:

$$\begin{cases} \dot{x}_{(t)} = (A - B_{01}.K)x_{(t)} + B_{02}w_{(t)} \\ z_{(t)} = (C - D_{01}.K)x_{(t)} + D_{02}w_{(t)} \end{cases} \tag{13}$$

3.2 Design Controller for Quarter Heavy Vehicle

By selecting the input vector $x_{(t)}$ in equation (13) as $x_{(t)} = [x_1, x_2, x_3, x_4, x_5, x_6]^T = [Z_s, \dot{Z}_s, Z_u, \dot{Z}_u, \Delta P, X_v]^T \in R^6$ the output vector $z_{(t)} = x_{(t)} \in R^6$, the control input vector $u_{(t)}$ is the current of the ESVH.

The main objective of designing an LQR controller for an active suspension system in quarter heavy vehicles is to minimize vehicle displacement, velocity, and acceleration. Because of their direct impacts on

vehicle comfort and road holding, these characteristics should decrease to meet control objectives mentioned. Furthermore, the F_{act} generated by ESVH is required to be within the bearable saturation of actuators. Therefore, the performance index J in equation (9) is chosen as follows:

$$J = \int_0^\infty \left(\rho_1 Z_s^2 + \rho_2 \dot{Z}_s^2 + \rho_3 Z_u^2 + \rho_2 \dot{Z}_u^2 + \rho_2 \Delta P^2 + \rho_2 X_v^2 \right) dt \tag{14}$$

Where $\rho_1, \rho_2, \rho_3, \rho_4, \rho_5, \rho_6$ are weighting parameters of performance index J

From equations (9) and (14), the matrices Q, R and N are selected as:

$Q = diag\left[\rho_1 \quad \rho_2 \quad \rho_3 \quad \rho_4 \quad \rho_5 \quad \rho_6\right]$; $R = eye(1)$; $N = zeros(6,1)$.

4 SIMULATION RESULTS ANALYSIS

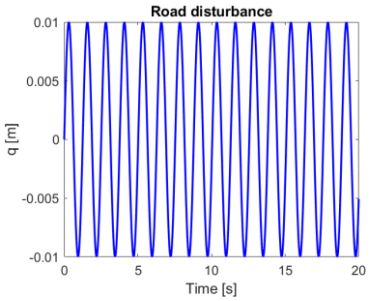

Figure 6: Road disturbance.

In the time domain, the quarter-heavy vehicle integrated with ESVH is simulated as sine-wave excitation with an oscillation amplitude of 0.01m in the frequency of 5 rad/s, as in Fig. 4.

Fig. 5 displays the time response $z_s, \ddot{z}_s, z_u$ due to the time. The blue line represents the truck's passive suspension model, and the dashed red line represents the resulting model with ESVH integration with LQR controller. The effectiveness of the proposed model is evaluated explicitly through the Root Mean Squared (RMS) of the displacement, velocity, and acceleration signals of both suspended and unsuspended masses, illustrated in Table 2. We find that, when compared to the system with an integrated controller, the suspended mass displacement is markedly reduced by 90.12% while its acceleration is reduced at 89.7%. In addition, the RMS of the unsuspended mass was also significantly reduced. Namely, its acceleration, displacement, and velocity were reduced at 11.09%, 10.87%, and 4.95%, respectively. Under different ranges of vibration excitation frequency 5÷10rad/s, the characteristics of sprung mass acceleration in passive and active model are shown in Fig. 6.

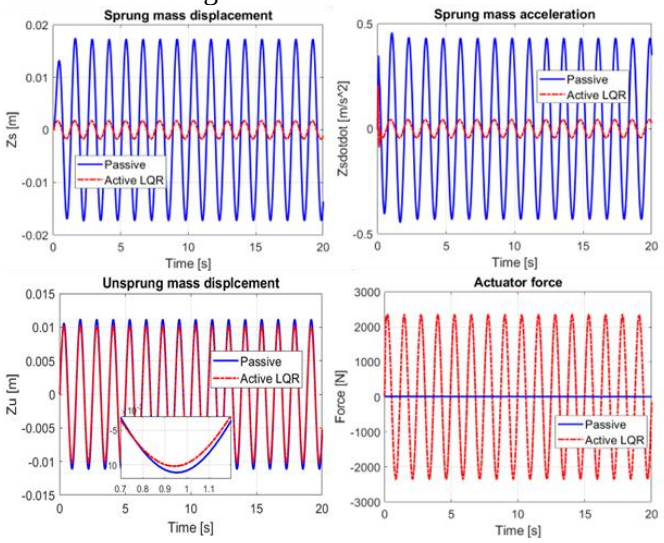

Figure 7: Time response of sprung mass displacement, sprung mass acceleration, unsprung mass displacement, unsprung mass velocity, controlled force by hydraulic actuator.

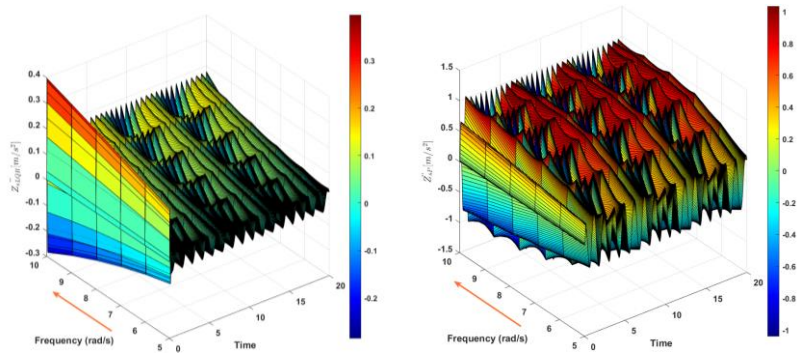

Figure 8: Sprung mass acceleration responds due to frequency of disturbance: LQR controller (left), Passive (right).

Table 2: Root Mean Square of the referred signals.

Signal	Passive	LQR	Reduction	Signal	Passive	LQR	Reduction
Z_s	0.0125	0.0012	90.12%	Z_u	0.0081	0.0072	10.87%
$\dot{Z}_s$	0.0583	0.0061	89.50%	$\dot{Z}_u$	0.0379	0.0360	4.95%
$\ddot{Z}_s$	0.3135	0.0323	89.70%	$\ddot{Z}_u$	0.2244	0.1995	11.09%

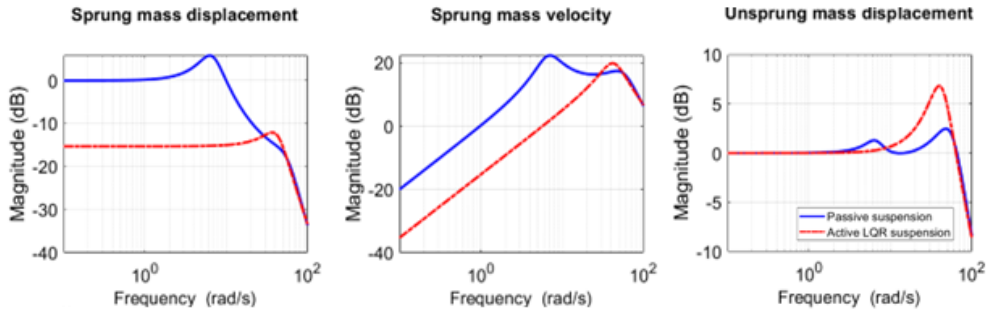

Figure 9: Frequency response of sprung mass displacement, sprung mass velocity, unsprung mass displacement due to the disturbance of 5 rad/s.

In Fig. 7, a comparison is presented regarding the reductions in sprung mass displacement, sprung mass velocity, and unsprung mass displacement in the frequency domain. It is observed that when subjected to road surface excitation at a frequency of 5rad/s, the controller outperforms the system. Specifically, the suspension shift is reduced from 5dB to -15dB, while the mass displacement experiences a reduction of approximately 2dB.

5 CONCLUSION

This paper presented the design and implementation of an integrated electro-hydraulic actuator and LQR controller for an active suspension system in a quarter of a heavy vehicle model. The simulation results have showcased substantial improvements in vehicle smoothness, comfort, and performance when compared to a passive suspension system. Notably, the proposed model achieved a remarkable 90.12% reduction in the root mean square (RMS) of sprung mass displacement, accompanied by an 89.7% reduction in acceleration. Moreover, significant reductions were observed in the RMS of unsprung mass, with acceleration, displacement, and velocity decreasing by 11.09%, 10.87%, and 4.95%, respectively. These findings serve as evidence of the effectiveness of the integrated system in fulfilling the critical criteria for mitigating vibrations transmitted from the road surface and improving the overall performance of the vehicle suspension system. This research contributes to the body of knowledge in the field of vehicle dynamics and serves as a foundation for further advancements in ASS for heavy vehicles.

REFERENCES

[1] S. Qu, D. Fassbender, A. Vacca, and E. Busquets, A high-efficient solution for electro-hydraulic actuators with energy regeneration capability, *Energy*, vol. 216, pp. 1–25, 2021.

[2] G. Yang and J. Yao, High-precision motion servo control of double-rod electro-hydraulic actuators with exact tracking performance, *ISA Trans.*, vol. 103, pp. 266–279, 2020.

[3] D. N. Nguyen and T. A. Nguyen, Proposing an original control algorithm for the active suspension system to improve vehicle vibration: Adaptive fuzzy sliding mode proportional-integral-derivative tuned by the fuzzy (AFSPIDF), *Heliyon*, vol. 9, no. 3, e14210, 2023.

[4] D. N. Nguyen and T. A. Nguyen, A Novel Hybrid Control Algorithm Sliding Mode-PID for the Active Suspension System with State Multivariable, *Complexity*, vol. 2022, 2022.

[5] D. N. Nguyen and T. A. Nguyen, A Hybrid Control Algorithm Fuzzy-PI with the Second Derivative of the Error Signal for an Active Suspension System, *Math. Probl. Eng.*, vol. 2022, 2022.

[6] K. M. Elbayomy, Z. Jiao, and H. Zhang, PID controller optimization by GA and its performances on the electro-hydraulic servo control system, *Chinese J. Aeronaut.*, vol. 21, no. 4, pp. 378–384, 2008.

[7] Y. Song, Z. Hu, and C. Ai, Fuzzy Compensation and Load Disturbance Adaptive Control Strategy for Electro-Hydraulic Servo Pump Control System, *Electron.*, vol. 11, no. 7, pp. 1–13, 2022.

[8] R. Jiao, V. Nguyen, and V. Le, Ride comfort performance of hydro pneumatic isolation for soil compactors cab in low frequency region, *J. Vibroengineering*, vol. 22, no. 5, pp. 1174–1186, 2020.

[9] M. Ghoniem, T. Awad, and O. Mokhiamar, Control of a new low-cost semi-active vehicle suspension system using artificial neural networks, *Alexandria Eng. J.*, vol. 59, no. 5, pp. 4013–4025, 2020.

[10] O. A. Dahunsi, J. O. Pedro, and O. T. Nyandoro, Neural network-based model predictive control of a servo-hydraulic vehicle suspension system, in *IEEE AFRICON Conf.*, no. July 2014, 2009.

[11] S. Liu, R. Hao, D. Zhao, and Z. Tian, Adaptive dynamic surface control for active suspension with electro-hydraulic actuator parameter uncertainty and external disturbance, *IEEE Access*, vol. 8, pp. 156645–156653, 2020.

[12] J. E. D. Ekoru and J. O. Pedro, Proportional-integral-derivative control of nonlinear half-car electro-hydraulic suspension systems, *J. Zhejiang Univ. Sci. A*, vol. 14, no. 6, pp. 401–416, 2013.

[13] D. Rodriguez-Guevara, A. Favela-Contreras, F. Beltran-Carbajal, C. Sotelo, and D. Sotelo, An MPC-LQR-LPV Controller with Quadratic Stability Conditions for a Nonlinear Half-Car Active Suspension System with Electro-Hydraulic Actuators, *Machines*, vol. 10, no. 2, 2022.

[14] V. T. Vu, Enhancing the roll stability of heavy vehicles by using an active anti-roll bar system, PhD Thesis, Université Grenoble Alpes, 2017.

OPTIMAL NEURAL SLIDING MODE CONTROLLER FOR COUPLED TANK SYSTEM USING CENTRAL FORCE OPTIMIZATION

NGUYEN ANH TUAN [1,2,3+], HO PHAM HUY ANH [1,2*]

[1]*Ho Chi Minh City University of Technology (HCMUT), 268 Ly Thuong Kiet Street, District 10, Ho Chi Minh City, Viet Nam*
[2]*Vietnam National University Ho Chi Minh City (VNU-HCM), Linh Trung Ward, Thu Duc District, Ho Chi Minh City, Viet Nam*
[3]*Sai Gon University (SGU), 273 An Duong Vuong Street, District 5, Ho Chi Minh City, Viet Nam*
Email: + natuan@sgu.edu.vn, +nguyenanhtuan.sdh21@hcmut.edu.vn
**Corresponding author: hphanh@hcmut.edu.vn*

Abstract. This paper proposes a Central Force Optimization (CFO) algorithm to optimize the coefficients of an Adaptive Neural Sliding Mode Controller (ANSMC) for water level control in a coupled tank system (CTS). The controlled plant is a nonlinear system with high time delay and various uncertain factors. The controller consists of a Sliding Mode Controller (SMC) combined with an indirectly adaptive neural controller to online update the controller parameters and compensate for uncertain factors, even without explicit knowledge of the controlled object. The CFO algorithm optimizes the coefficients of the ANSMC, reducing the learning time of the neural network and improving the overall performance of the controller. To demonstrate the effectiveness of the proposed control algorithm, simulations are conducted, and compared with the SMC controller, ANSMC, and PID controller. The simulation results show that the proposed controller achieves better performance compared to the other algorithms.

Keywords. Central Force Optimization (CFO) algorithm, Adaptive Neural Sliding Mode Controller (ANSMC), Adaptive Neural Sliding Mode Controller optimized by CFO algorithm (ANSMC-CFO), sliding mode controller (SMC), sliding mode controller optimized by CFO algorithms (SMC-CFO), Proportional-Integral-Derivative controller (PID), coupled tank system (CTS).

1 INTRODUCTION

The CTS is a nonlinear and time-delay system in industrial applications. Therefore, controlling the fluid level and flow of this system effectively is a challenge for control experts. First, sliding mode control algorithms were proposed to control the liquid levels in tanks for improved control quality in papers [1-3]. The next, research [4] proposed an Adaptive Sliding Mode Controller for the Quadruple tank system, yielding better robustness against input changes and external disturbances than other control methods. Additionally, papers [5-8] leveraged the convergent and rapid learning capabilities of sliding mode controllers, combined with the strong generalization ability of neural networks, resulting in enhanced control quality.

Calculating and selecting optimal parameters for controllers is a complex issue. Therefore, in recent years, intelligent algorithms combined with heuristic optimization algorithms have been employed to control and identify various system models, resulting in significantly improved control quality. Notable algorithms include Differential Evolution (DE) [9], Genetic Algorithm (GA) [10], Jaya algorithm [11], Particle Swarm Optimization (PSO) [12], central force optimization (CFO) [13-16], etc. Among these, the central force optimization (CFO) algorithm has emerged as a search meta-heuristic method developed by Formato in 2007 [13], functioning based on the interaction of gravitational fields. Subsequently, this algorithm has been effectively applied in diverse domains, such as neural network training [14], and optimal stable gait solutions for nonlinear uncertain humanoid robots [16].

However, according to the scope of the research team's investigation, the optimal CFO algorithm has not yet been applied to the optimization of coefficients for the Adaptive Neural Sliding Mode Controller (ANSMC) for the CTS system control. The ANSMC controller in [8] has certain coefficients chosen through trial and error, making it challenging to achieve optimal values. Thus, this paper proposes the ANSMC-CFO controller, which incorporates the ANSMC controller from [8] with coefficients optimized

using the CFO algorithm.
This paper is divided into 5 sections: Section 1 presents the introduction, and Section 2 presents the modeling and system description of the control plant. Subsequently, Section 3 outlines the proposed algorithm. Section 4 presents the simulation results. Finally, Section 5 provides the conclusion.

2 MODELING AND DESCRIPTION OF THE CONTROL PLANT

Figure 1 depicts the interconnected nonlinear uncertain CTS system based on the Quanser tank model with two degrees of freedom. The parameters are specified in Table 1.

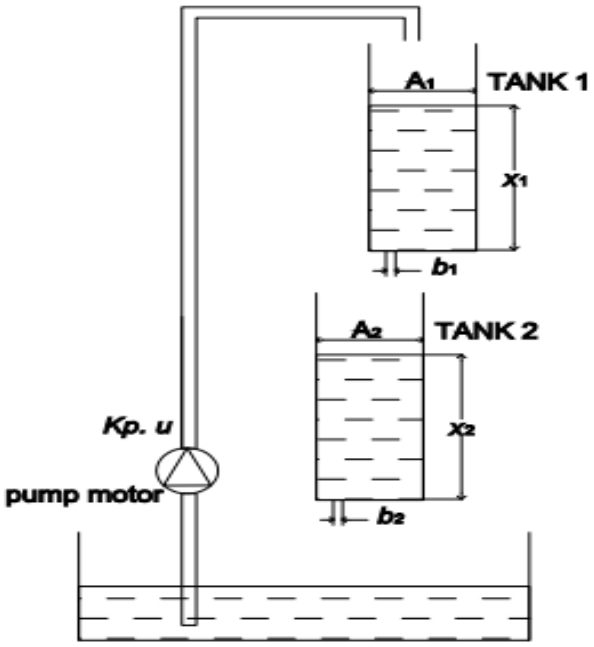

Figure 1: Liquid CTS system.

The mathematical model of the CTS system [9] is as follows:

$$\begin{cases} \dot{x}_1 = \left(\frac{1}{A_1}\right)\left(K_p u - b_1 C_1 \sqrt{2g x_1}\right) \\ \dot{x}_2 = \left(\frac{1}{A_2}\right)\left(b_1 C_1 \sqrt{2g x_1} - b_2 C_2 \sqrt{2g x_2}\right) \end{cases} \quad (1)$$

Where u is the control voltage applied to the pump motor, and x_1, x_2 represent the water levels of tank 1 and tank 2, respectively. The significance of the parameters is presented in Table 1. These values will be used in the simulation.

Table 1. The CTS system parameters used in the simulation.

Symbol	Physical meaning	Value	Unit
A_1	The surface area of the inner tank 1	16.619	cm^2
A_2	The surface area of the inner tank 2	16.619	cm^2
b_1	The cross-sectional area of the drain pipe in Tank 1	1	cm^2
b_2	The cross-sectional area of the drain pipe in Tank 2	1	cm^2
C_1	Tank 1 – discharging ratio of the outlet	0.8	
C_2	Tank 2 – discharging ratio of the outlet	0.8	
g	Gravitation	981	cm/s^2
K_p	Pump flow value	50	$cm^3/(s.V)$

The main objective of this paper is to design an adaptive sliding mode neural network controller with optimized coefficients to achieve an output that closely follows the desired trajectory.

3 THE PROPOSED ALGORITHM

3.1 ANSMC controller and problem formulation

The ANSMC control algorithm [8] is summarized as follows:
From equation (2.1), the state equation of the CTS system is as follows:

$$\begin{cases} \dot{x} = f(x) + g(u) \\ y = h(x) \end{cases} \tag{2}$$

Where $h(x) = x_2$, the equation (3.1) can be rewritten:

$$\begin{cases} \dot{x}_1 = \dfrac{1}{A_1}(K_p u - b_1 c_1 \sqrt{2gx_1}) \\ \dot{x}_2 = \dfrac{1}{A_2}(b_1 c_1 \sqrt{2gx_1} - b_2 c_2 \sqrt{2gx_2}) \\ y = x_2 \end{cases} \tag{3}$$

The ANSMC controller:

$$u = u_{ce} + u_{si} \tag{4}$$

The controlled system $\ddot{y} = a(x) + b(x)u$ has two degrees of freedom.

The adaptive neural SMC controller estimates the functions of $\hat{a}(x); \hat{b}(x)$

$$\begin{cases} u_{ce} = \hat{b}^{-1}(x)\left(-\hat{a}(x) + v(t)\right) \\ v(t) = \ddot{y}_d + k\dot{e} + Ksign(s) \end{cases} \tag{5}$$

Where the chosen sliding surface being $s = \dot{e} + ke$, and y_d being the reference signal.

The neural RBF has 3 basic functions in the hidden layer to estimate the functions of $\hat{a}(x); \hat{b}(x)$

$$\begin{cases} \hat{a}(x) = \theta_a^T \xi_a(x) \\ \hat{b}(x) = \theta_b^T \xi_b(x) \end{cases} \tag{6}$$

Where the parameter vectors θ_a and θ_b are the neural network's weights which are updated online to approach optimal values: $\theta_a \to \theta_a^*$, $\theta_b \to \theta_b^*$, and the basic functions are defined as follows

$$\xi(x) = e^{-\frac{\left[(x-\mu)^2\right]}{\sigma^2}} \tag{7}$$

Choose the Lyapunov function as follows.

$$V = \frac{1}{2}s^2 + \frac{1}{2}\tilde{\theta}_a^T Q_a \tilde{\theta}_a + \frac{1}{2}\tilde{\theta}_b^T Q_b \tilde{\theta}_b \tag{8}$$

Take the derivative of the Lyapunov function

$$\begin{aligned} \dot{V} &= \dot{s}s + \tilde{\theta}_a^T Q_a \dot{\tilde{\theta}}_a + \tilde{\theta}_b^T Q_b \dot{\tilde{\theta}}_b \\ &= -sKsign(s) + s\left(-\delta_a(x) - \delta_b(x)u_{ce}\right) + \\ &\tilde{\theta}_a^T\left(\xi_a s + Q_a\dot{\theta}_a\right) + \tilde{\theta}_b^T\left(\xi_b u_{ce} s + Q_b\dot{\theta}_b\right) - b(x)u_{si}s \end{aligned} \tag{9}$$

Where $\delta_a(x)$ and $\delta_b(x)$ are the structure variations compared to the ideal model, $\tilde{\theta}_a = \theta_a^T - \theta_a^*$, $\tilde{\theta}_b = \theta_b^T - \theta_b^*$

Choose a sliding control law so that the $\dot{V}$ is definite negative.

$$u_{si} = \frac{1}{\underline{b(x)}}\left(\overline{\delta_a(x)} + \overline{\delta_b(x)}|u_{ce}|\right)sign(s) \tag{10}$$

Then choose the adaptive law as

$$\begin{cases} \dot{\theta}_a = -Q_a^{-1}\xi_a s \\ \dot{\theta}_b = -Q_b^{-1}\xi_a u_{ce} s \end{cases} \tag{11}$$

Then

$$\dot{V} \le -sKsign(s) + |s|\left(\overline{\delta_a(x)} + \overline{\delta_b(x)}|u_{ce}|\right) - b(x)u_{si}s \tag{12}$$

$$u_{si} = \frac{1}{\underline{b(x)}}\left(\overline{\delta_a(x)} + \overline{\delta_b(x)}|u_{ce}|\right)sign(s) \tag{13}$$

where $\overline{\delta_a(x)}, \overline{\delta_b(x)}$ are the upper limits of parameters variation; $\underline{b(x)}$ represents the lower limit of $b(x)$.

$$\dot{V} \le -sKsign(s) - \left(\frac{b(x)}{\underline{b(x)}} - 1\right)\left(\overline{\delta_a(x)} + \overline{\delta_b(x)}|u_{ce}|\right)|s| \le 0 \tag{14}$$

Since the Lyapunov function $\dot{V} \le 0$. Thus the system is asymptotically stable.

The issue with the algorithm presented above is that the coefficients include *k*, *K*, σ , Q_a and Q_b in the equations (3.4), (3.6), and (3.7) are chosen through trial and error which is highly complex. Therefore, this paper proposes the addition of the CFO algorithm to find optimal values for these coefficients.

3.2 The proposed CFO optimization algorithm

The proposed CFO optimal algorithm is a search meta-heuristic method developed by Formato in 2007 [13]. The algorithm's process is depicted in the flowchart shown in Figure 2. Under the influence of gravitational forces, the acceleration of probe *p* is generated by probe *n* as follows:

$$\begin{cases} \vec{a}_{j-1}^{\,p} = \dfrac{G.U(F_{j-1}^n - F_{j-1}^p).(F_{j-1}^n - F_{j-1}^p)^\alpha.(\vec{x}_{j-1}^{\,n} - \vec{x}_{j-1}^{\,p})}{\left|\vec{x}_{j-1}^{\,n} - \vec{x}_{j-1}^{\,p}\right|^\beta} \\ U(z) = \begin{cases} 1 & \text{if } z \ge 0 \\ 0 & \text{otherwise} \end{cases} \end{cases} \tag{15}$$

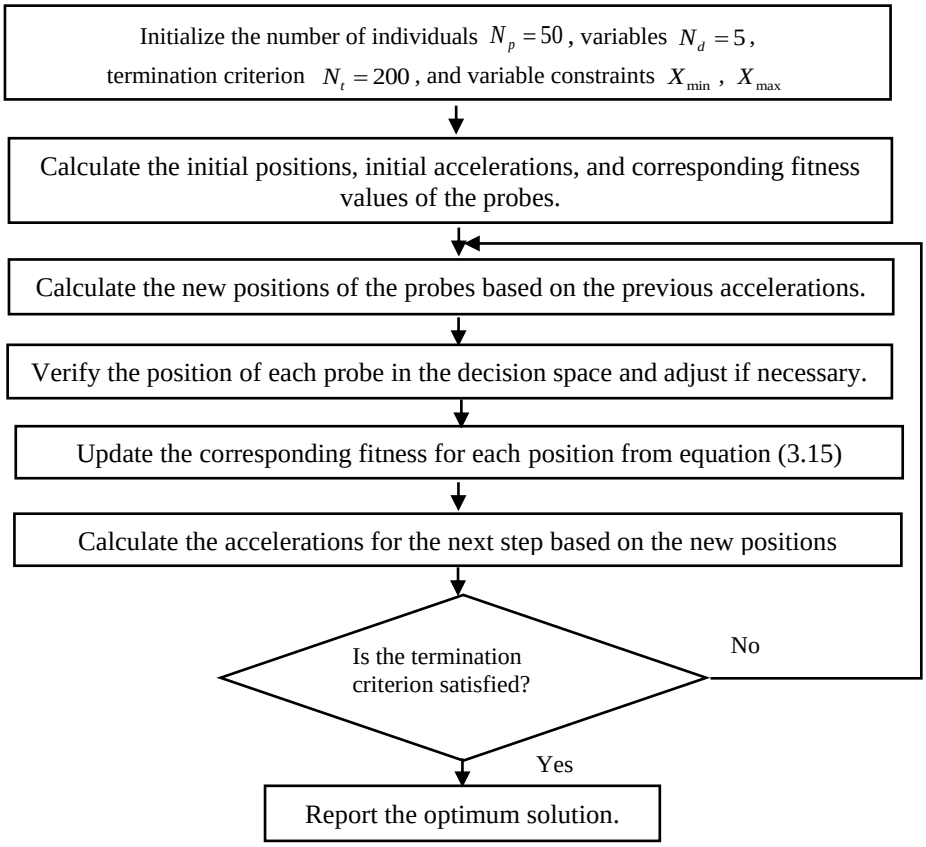

Figure 2: Flowchart of optimal CFO algorithm.

3.3 Optimizing the coefficients of the proposed ANSMC controller using the CFO optimization algorithm

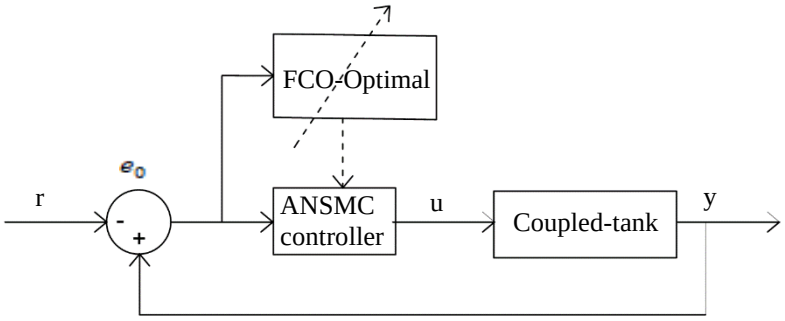

Figure 3: Diagram of the proposed ANSMC controller with coefficients optimized by the CFO algorithm.

Figure 3 illustrates the ANSMC algorithm with the coefficients of the ANSMC optimized by CFO. Select the fitness function based on the integral of squared error (ISE) criterion over the time interval t=1000 seconds, as follows:

$$\text{fitness} = \frac{1}{\int_0^t e^2(t)dt} \tag{16}$$

Table 2: The values of the decision variables after optimization by the CFO algorithm

	Decision variables				
Solution X	k	K	σ	Q_a	Q_b
Value	2.9559	1.9757	2.4666	64.0511	0.1

Where the coefficients k, K, σ , Q_a , Q_b from equations (3.4), (3.6), and (3.7), and optimized offline.

4 SIMULATION RESULT

Perform the simulation of the ANSMC controller with the coefficients tuned using the CFO algorithm in Section 3.3 to control the CTS system. The results are compared against the other algorithms.

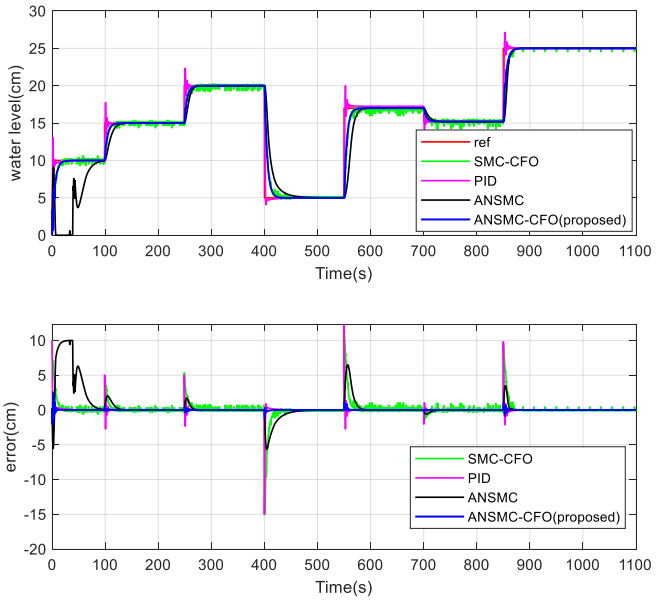

Figure 4: Compare the output responses of the CTS system among the algorithms with trained ref signals.

Table 3: Compare the control system quality indices among the algorithms.

	ANSMC-CFO	ANSMC	SMC-CFO	PID
IAE	**18.17**	744.5	422.9	93.42
ISE	**14.08**	4521	1859	387.7
ITAE	**6004**	1.449 x 10^5	1.899 x 10^5	3.857 x 10^4
ITSE	**1.426 x** 10^4	1.956 x 10^4	7.631 x 10^4	1.438 x 10^4

Figure 4 presents the results of comparing output responses among the algorithms with the trained signal. With the reference signal change, the proposed algorithm for higher quality outperforms the remaining algorithms, including fast response, no overshoot, low error, and zero steady-state error. The control quality indices in Table 3 demonstrate that the ANSMC-CFO controller outperforms the other three algorithms in terms of control quality.

Comparison of step information between the ANSMC and SMC-CFO controllers

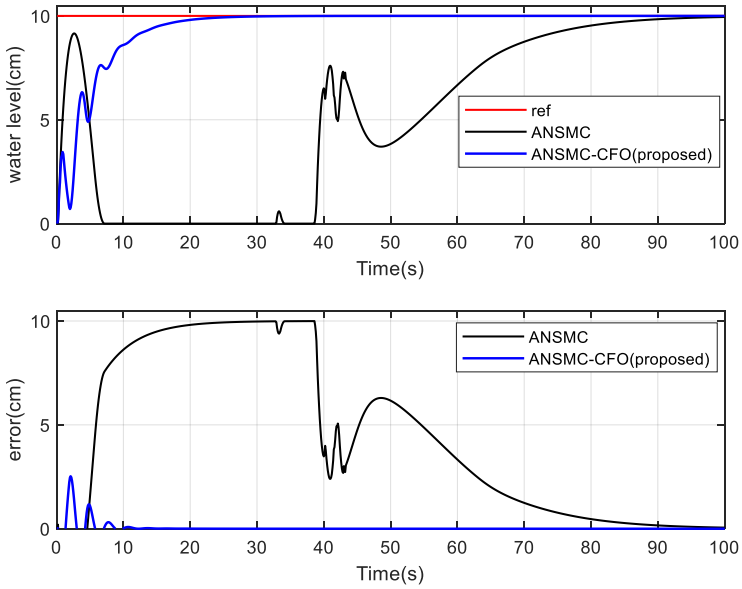

Figure 5: Compare the step response of the output signal x_2 of the CTS system among the algorithms with the trained reference signal ref.

Figure 5 depicts that the ANSMC-CFO controller gives the output response with significantly faster initial learning time and much lower error compared to the ANMSC controller.

Table 4: Compare the step response information of the output signal for the system among the algorithms.

	Rise Time	Settling Time	Settling Min	Settling Max	Over shoot	Under shoot	Peak	Peak Time
ANSMC-CFO	11.384	**19.690**	**9.023**	**10**	0	0	**10**	100
ANSMC	1.923	87.829	0	9.947	0	0	9.94	100

The step response indices in Table 4 indicate that both algorithms yield zero Overshoot and zero Undershoot results. The remaining indices of the ANSMC-CFO algorithm are superior to those of the ANSMC algorithm. These results emphasize the superiority of the ANSMC algorithm combined with the CFO optimization algorithm compared to the conventional ANSMC algorithm.

5 CONCLUSIONS

This paper proposes the novel ANSMC-CFO controller, which integrates the CFO optimization algorithm in optimally tuning the coefficients of the ANSMC controller [8] for controlling the liquid level of the complex CTS system, representing a highly nonlinear and time-delay system. To demonstrate the effectiveness of the proposed algorithm, simulation comparisons are conducted among the proposed algorithm, the ANSMC controller [8], the PID controller, and the SMC-CFO controller which includes the traditional SMC algorithm with its coefficients optimized by the CFO algorithm. Simulation results show that the proposed controller achieves rapid response, zero overshoot, and zero steady-state error in the output response. Specifically, the initial learning time of the proposed controller is significantly faster, and the overall response quality is superior to the conventional ANSMC controller [8]. Moreover, the control quality metrics are all improved compared to other advanced control algorithms. Hence, the proposed ANSMC-CFO algorithm has the potential to be effectively applied in controlling various other nonlinear SISO as well as multivariable nonlinear MIMO systems.

6 ACKNOWLEDGMENT

This study is funded by Saigon University (SGU) under grant number CSB2022-53. We acknowledge Ho Chi Minh City University of Technology (HCMUT), and VNU-HCM for supporting this study.

REFERENCES

[1] Geylani, O. and B. Ata. Adaptive Sliding Mode Control of a Coupled Tank System. in 2022 International Congress on Human-Computer Interaction, Optimization and Robotic Applications (HORA). 2022. IEEE.

[2] Choueikh, S., M. Kermani, and F.J.C. M'sahli, A Comparative Study of Nonsingular Terminal Sliding Mode and Backstepping Schemes for the Coupled Two-Tank System. 2021. 2021: p. 1-18.

[3] Mehri, E., M.J.J.o.C. Tabatabaei, Automation, and E. Systems, Control of quadruple tank process using an adaptive fractional-order sliding mode controller. 2021. 32: p. 605-614.

[4] Osman, A., T. Kara, and M.J.I.J.o.R. Arıcı, Robust adaptive control of a quadruple tank process with sliding mode and pole placement control strategies. 2023. 69(5): p. 2412-2425.

[5] Sun, J. and K.J.I.J.o. A.R.S. Zhao, Adaptive neural network sliding mode control for active suspension systems with electrohydraulic actuator dynamics. 2020. 17(4): p. 1729881420941986.

[6] Chu, Y., et al., Adaptive global sliding-mode control for dynamic systems using double hidden layer recurrent neural network structure. 2019. 31(4): p. 1297-1309.

[7] Dat, N.T., C. Van Kien, and H.P.H. Anh. Advanced Adaptive Neural Sliding Mode Approach Applied in PMSM Speed Control. in Computational Intelligence Methods for Green Technology and Sustainable Development: Proceedings of the International Conference GTSD2022. 2022. Springer.

[8] Tuan, N.A., et al. Robust Adaptive Neural Sliding Mode Method for Coupled-Tank System Intelligent Control. in 2022 6th International Conference on Green Technology and Sustainable Development (GTSD). 2022. IEEE.

[9] Van Kien, C., H.P.H. Anh, and N.N.J.A.I. Son, Adaptive inverse multilayer fuzzy control for uncertain nonlinear system optimizing with differential evolution algorithm. 2021. 51: p. 527-548.

[10] YILMAZ, M., et al., PI+ Feed Forward Controller Tuning Based on Genetic Algorithm for Liquid Level Control of Coupled-Tank System. 2021. 11(2): p. 1014-1026.

[11] Van Kien, C., N.N. Son, and H.P.H. Anh. Adaptive MIMO Fuzzy Controller for Double Coupled Tank System Optimization by Jaya Algorithm. in 2020 5th International Conference on Green Technology and Sustainable Development (GTSD). 2020. IEEE.

[12] Vavilala, S.K., et al., Design and Implementation of the FOIMC Using the PSO Algorithm for the Coupled Tank System, in Design and Control Advances in Robotics. 2023, IGI Global. p. 127-151.

[13] Formato, R., Central force optimization: a new metaheuristic with applications in applied electromagnetics. Prog Electromagn Res 77: 425–491. 2007.

[14] Green II, R.C., L. Wang, and M.J.E.S.w.A. Alam, Training neural networks using central force optimization and particle swarm optimization: insights and comparisons. 2012. 39(1): p. 555-563.

[15] Chen, Y., et al., Modified central force optimization (MCFO) algorithm for 3D UAV path planning. 2016. 171: p. 878-888.

[16] Huan, T.T. and H.P.H.J.E.C. Anh, Optimal stable gait for a nonlinear uncertain humanoid robot using central force optimization algorithm. 2019. 36(2): p. 599-621.

DESIGN TRAFFIC LIGHTS CONTROL BASED ON FUZZY LOGIC CONTROLLER AND FPGA

VU THI HONG NGA[1], LAM HOANG PHUC [1], NGUYEN ANH KHOI [1]

[1] *Industrial University of Ho Chi Minh City;*

[1]*vuthihongnga@iuh.edu.vn,* [2]*lamhoangphuc78@gmail.com,* [3]*anhkhoi7610@gmail.com*

Abstract: The paper designs traffic lights controller applying fuzzy control algorithm on Field Programmable Gate Array (FPGA). The fuzzy controller is programmed in C language, using the Mamdani algorithm and implemented on the ALOGIC_V4 board, using the Cyclone IV EP4CE6F17C8N chip [1]. The two inputs of the fuzzy controller are *Maximum Queue Length* and *Average Fill Rate* from each approach of the intersection. The data is obtained through image processing on the Raspberry Pi 4 and communicates with the FPGA via UART. The output of the controller is *weights* with values from 0 to 100. From the output value, we calculate the optimal time to control the traffic lights. Users can observe the system's operation and control traffic lights directly on the Website. Besides, the image captured from the camera will be saved on SQL server [2]. By using a fuzzy controller on the FPGA to control traffic lights, it contributes to hardware optimization and reduces traffic congestion.

Keywords: FPGA, fuzzy logic, Mamdani algorithm, traffic light control, Cyclone IV EP4CE6F17C8N, Raspberry Pi 4, SQL Server.

1 INTRODUCTION

In general, with the rapidly growing urbanization process all over the world and in Vietnam particular, the traffic infrastructure planning using smart traffic is an issue that is being oriented in the future. All types of transport vehicles are increasing at a rapid rate. That requires us to always find appropriate solutions to meet traffic needs and reduce traffic jams in big cities. Along with that is the great development of FPGA technology, a semiconductor chip with high processing speed, typically it can change the hardware structure in accordance with the improvement and development of the algorithm of the programmer. In this paper, we performed image processing to identify traffic density and design a traffic light controller using the fuzzy control algorithm in the Field Programmable Gate Array (FPGA), which saves maximum hardware production cost, high working speed with frequency f = 50 MHz and can change hardware flexibly according to user requirements [3].

2 FUZZY CONTROLLER DESIGN ON FPGA

2.1 Fuzzy controller structure

Fuzzy controller uses Mamdani algorithm, fuzzy rules are written according to the programmer's thinking and practical experience, from that we execute on FPGA and control traffic lights according to users' wishes. [1].

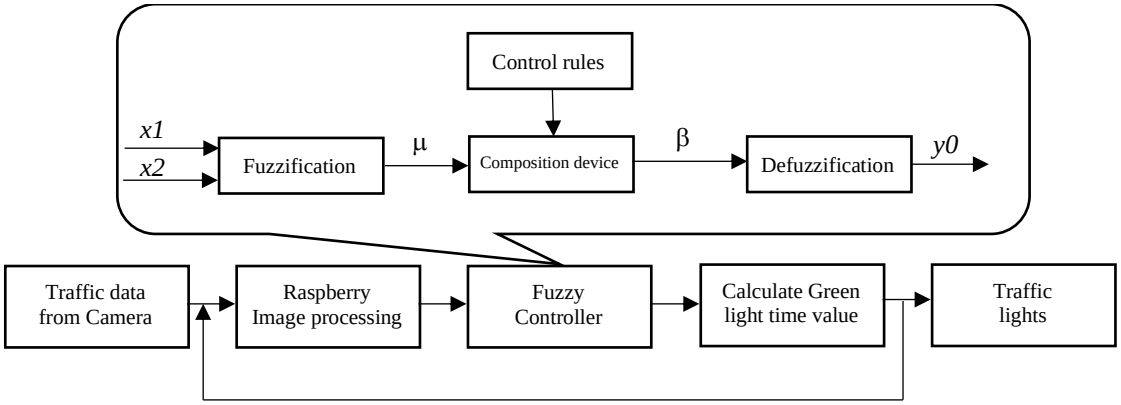

Figure 1: Functional diagram of fuzzy controller.

In there:

- x_1, x_2: inputs to fuzzy controller.
- μ: the value after being fuzzification
- β: the result after implementing the composition rule
- y_0: is the clear value after defuzzification.
- Fuzzification block: transform the traffic density value into a vector μ whose value element corresponds to the number of input fuzzy sets.
- Composition device: implement Max-Min composition rule based on fuzzy control rules.
- Defuzzification block: convert the output fuzzy set to the corresponding y_0 clear value.

2.2 Traffic flow modeling

To calculate the number of vehicles on the road, we use image data collected from cameras through two directions, East-West and South-North, and obtain two values: ***Maximum queue length*** and ***Average fill rate*** of traffic density [4].

- ***Maximum queue length (m)***: the queue length is the distance from the stop line of the traffic light to the queuing traffic (Figure 3). During the Red light period, the camera records the longest part of the queue (maximum queue length) of that lane every second. Then take the last value at the start of the Green light period as input to the fuzzy controller.
- ***Average fill rate (%)***: The detection area is set from the stop line of the traffic light back to a space to record the fill rate. Understand as the ratio of vehicles detected in the detection area to the area of the area (figure 3). During the green light period, the camera records the fill rate per second. At the start of the red light period, the average fill rate during the green light period is taken as the input of the fuzzy controller.

From the above two values, after defuzzification, we get the weights with values from 0 to 100. These weights decide the light time of the Green, Red, and Yellow lights in the two directions South-North and East-West.

2.3 Fuzzy control process

The Green light time in the next cycle is calculated from the data in the previous cycle. Here, the system uses information about the *maximum queue length* and the *average fill rate* of the traffic density to estimate the appropriate Green light time of each phase [5]. From this, the time of the Red and Yellow lights is inferred. In which, the fixed Yellow light is 3 seconds or can be adjusted depending on the programmer.

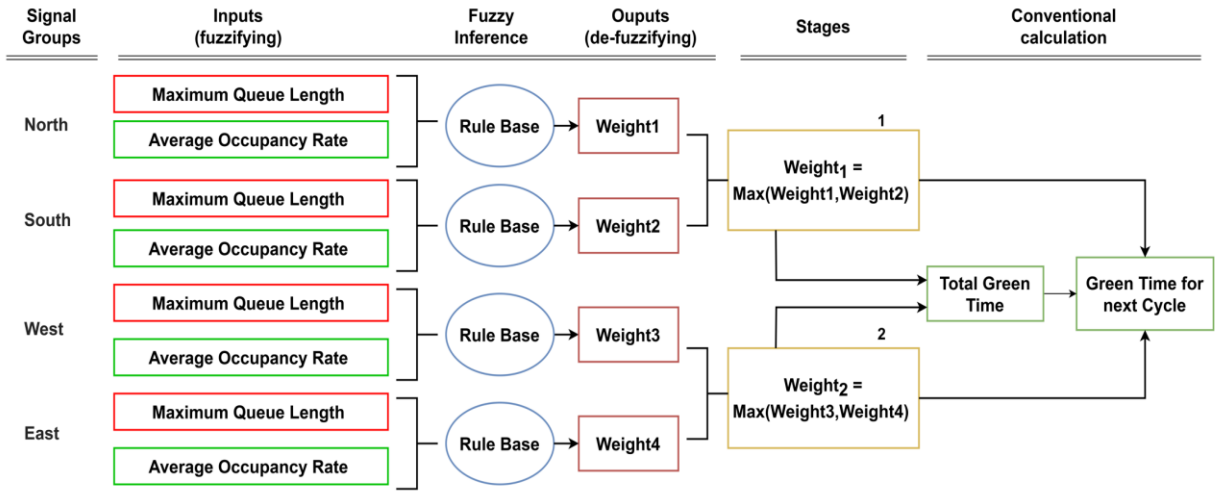

Figure 2: Calculation of Green light time value for next cycle.

Fuzzy controller uses the maximum queue length and average fill rate collected in the previous cycle to calculate the weights (Weight) of each signal direction. The maximum weighted value between two opposite directions North-South is chosen as the W1-weighted value of period 1. Similarly, this is also applied to period 2. Finally, the values W1 and W2 is used to calculate the total green time of a cycle. Combined with the phase weights and the total Green light time to estimate the reasonable Green light time of each direction for the next cycle. The calculation is applied according to the following formula:

$$Total\_GT = (\sum W_n - Min1) * \left[\frac{Max2 - Min2}{Max1 - Min1} \right] + Min2 \quad (1)$$

$$GT\_Stage_n = \frac{W_n * Total\_GT}{\sum W_n} \quad (2)$$

In there:
- *Total_GT*: Total green time of a cycle.
- $\sum W_n$: Sum of the weights of the stages.
- Min1 and Max1: Minimum and Maximum value of the total weight.
- Min2 and Max2: Minimum and Maximum value of total Green time in a cycle.
- n: number of stages, experimental results are applied with n = 2.
- GT_Stagen (Green Time Stage n) is the Green time of n stages

2.4 Fuzzification and membership function

We use trapezoidal and triangular membership functions to fuzzification the input and output values of the system, because these functions are diverse and efficient for calculating values. The partition numbers on the output fuzzy use trial and error method to select the numbers. Fuzzy variables are conventionally and described as follows [6]:
Queue length: {Low, Medium, High, Very High}
Average fill rate: {Low, Medium, High, Very High}
Weight output value: {Very very low, Very low, Low, Medium, High, Very high, Very very high}.

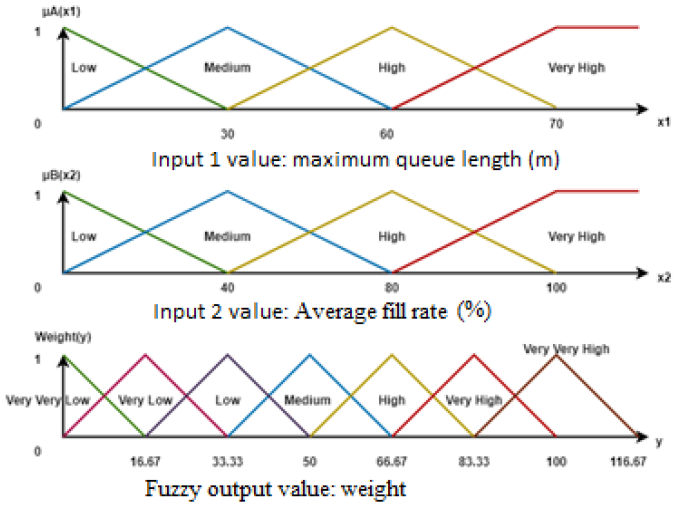

Figure 3: Diagram of input and output membership functions.

2.5 Fuzzy control law

The fuzzy control rule has the function of representing the rule in the form of an if-then structure. It consists of a combination of inputs and outputs that have been represented as fuzzy. The number of fuzzy rules will correspond to the combination of the inputs. For a problem with two inputs, each input has four levels, so the fuzzy rule will consist of sixteen rules. In fuzzy rule, because queue length has higher priority, fuzzy rule will be chosen so that it is optimal according to maximum queue length [6].

Weight		Maximum queue length			
		L	M	H	VH
Occupancy medium	L	VVL	L	M	H
	M	VL	L	H	VH
	H	L	M	H	VVH
	VH	M	H	VH	VVH

Figure 4: Fuzzy control rules.

Note: VVL: Very Very Low, VL: Very Low, L: Low, M: Medium, H: High, VH: Very High, VVH: Very Very High

There are two common types of fuzzy controllers, Mamdani and Sugeno. However, here we use Mamdani method and weighted average defuzzification method for fuzzy controller on FPGA so that the system runs optimally and can easily change the output values.

3. EXPERIMENT AND EVALUATION

3.1 Creating embedded chips and programming NIOS II on FPGA

Create 32-bit embedded chip using Qsys tool in Quartus II software with necessary modules to build a traffic light control system: PIO, Timer, UART [1]. With the flexible customization of the FPGA on the ALOGIC_V4 circuit, it allows creating or changing the hardware configuration according to the programmer's wishes [2]. After creating the microprocessor, we used it. Use the Nios II Software Build Tools for Eclipse to install a fuzzy controller on it using the embedded programming language C [7].

3.2 Model Deployment

Here we develop a miniature model with corresponding model cars, the deployment model consists of 4 lanes defined as North - South - West - East, each lane will correspond to a fuzzy value.The model consists of four lanes with four traffic lights and four double seven-segment LEDs, which show the time when the lights are on. The model has a camera that collects data from above that will transmit the signal through the Raspberry. In Raspberry will process the data to give the input of the fuzzy rule. The model will capture the image from the camera, the image will be processed in the Raspberry to pass the FPGA ALOGIC_V4 input values for fuzzy processing in the fuzzy controller. Output the values to calculate the two Green light parameters corresponding to the two directions of North-South and West-East [8].

Figure 5: Model of crossroad traffic lights.

3.3 Data collection and labeling

In order for vehicle image data, including images of motorcycles, cars, etc. to be used for training, it is necessary to label the data with the *LabelImg* labeling tool. This step will label fixed objects in the image, to help identify the classification between cars and motorbikes on the road by drawing a rectangle around the vehicles. The obtained data includes *.txt* files with the names corresponding to the labeled images as follows [9]:

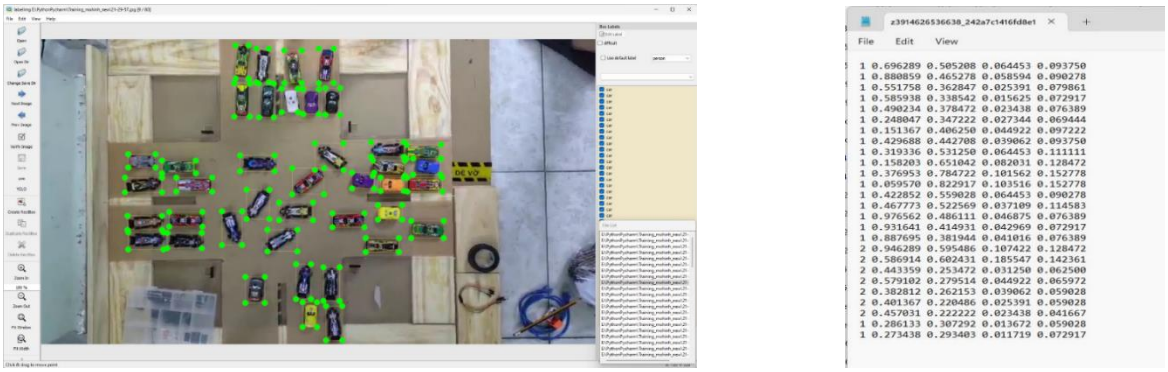

Figure 6: Data Labeling.

3.4 Identification of data

The labeled data will be trained with the *Yolov4* model with the darknet library. Yolov4 is a deep neural network model that allows processing and recognition of video and image objects. Fast and accurate processing speed. To train the data with Yolov4, we use Colab which provides a third-party GPU, which will help the training speed be faster and not be interrupted by external agents. The results will produce "*.weight"* files, these files have the effect of identifying vehicles participating in traffic on the road with high accuracy, the chart checks the accuracy of the recognition is good about 94%. To make it possible to process this data to identify vehicles on the road with the camera, we use the *cv2* library, which is an image processing library on Python [2].

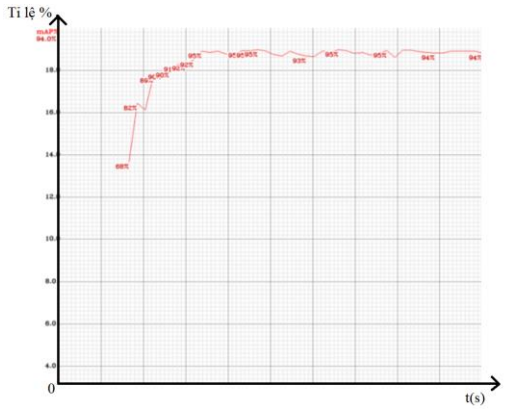

Figure 7: Level of recognition.

3.5 Data processing

Fuzzy controller controls traffic lights, whose inputs are data processing values that have been image processed by Python on raspberry. One fuzzy output corresponding to two data inputs. This will collect two data parameters, "Maximum Queue Length" and "Average Fill Rate". The use of these two data is based on evaluation, observation, "Maximum Queue Length" will be collected while the Red light time of that lane, i.e. the longest length value, and "Average Fill Rate" will be collected while the Green light period of that lane, i.e. will take the average ratio of the total area occupied (filled) by vehicles during the Green light period, The average area of the total vehicles will be considered with the area of the specified lane.

The result will produce four pairs of values corresponding to four directions: North - South - West - East. These values will be transmitted through the FPGA as input to the fuzzy controller via the UART transmission protocol [10].

3.6 Website, database and winform

We build a local website and simultaneously connect and store data on Microsoft SQL Server using Raspberry Pi 4. To connect to SQL Server, we use smartphones to broadcast wifi network connected to Server computer and Raspberry Pi. At that time, the smartphone acts as a router device providing internet service. Then we use the open source FreeTDS driver used in the Linux environment. It allows connecting, manipulating and accessing databases to SQL Server using python code [2]. To connect successfully, it is necessary to perform the steps to public Microsoft SQL Server over the Internet including the default port 1433 and the IP address of the Server machine[8].

We use Microsoft SQL Server Management Studio software. Proceed to initialize the table with columns including ID, Image, Time, Date with basic query statements. The image data needs to be converted to binary and then stored in the data table.

In addition, we also create a simple Winform in C# programming language. Images stored on the Server will be accessed on the screen according to the date and time that the user chooses.

4. TRAFFIC LIGHT CONTROL USING FUZZY CONTROL RESULTS

4.1 Results of running on the model

Figure 8: Results of running on the Yellow, Red, and Green lights model.

4.2 Results run on the website

Running the model, we will get the data displayed on the website of 4 lanes as follows:

Figure 9: Parameter display interface.

4.3 Modelsim simulation results

The simulation results of modelsim control normal traffic lights and control traffic lights based on fuzzy logic as follows:

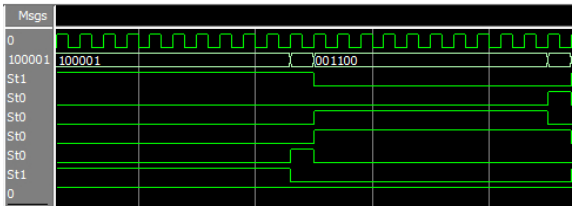

Figure 10: Simulation of normal traffic lights

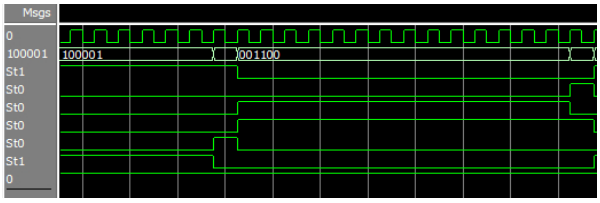

Figure 11: Simulation of traffic lights based on *fuzzy logic*.

Based on the above two simulation results with the same traffic conditions, we can see the efficiency of traffic light control based on fuzzy logic controller. Because the simulation results of the open controller show that the Green light time is extended on the side of the road with higher traffic density. It will free up more queues than normal traffic light control in the same operating cycle [3].

5. Conclusions and directions for development

The article presented how to design a fuzzy controller on FPGA to control traffic lights, including the hardware used ALOGIC_V4 kit, Raspberry Pi 4 Model B kit combining software such as Quartus, Python, C languages , SQL Server. The result of the paper is a traffic light model running in real time, showing high efficiency in traffic control of the fuzzy controller with different test cases. The system works well, the website accesses real-time monitoring and traffic light control runs stable. Research and development directions for the topic to become more and more complete, such as: traffic accident identification, giving way to priority vehicles, red light detection, cloud storage for system data.

REFERENCES

[1] Nguyễn Đức Điển, Hoàng Đình Cơ, tài liệu học tập điều khiển mờ và mạng nơron, Trường Đại học Kinh tế Kỹ thuật Công nghiệp, 2019.
[2] Hans-Petter Halvorsen, Python and SQL Server, University of South-Eastern Norway, 2020.
[3] ThS. Vũ Thị Hồng Nga, bài giảng thiết kế mạch tích hợp với HDL, Trường Đại học Công Nghiệp TP.HCM, 2022.
[4] PGS. TS. Lê Hùng Lân, Đặng Quang Thạch, điều khiển tín hiệu nút giao thông trên cơ sở logic mờ, Trường Đại học GTVT Hà Nội, 2021.
[5] Budi Yulianto, Traffic Signal Controller for Mixed Traffic Conditions, Universitas Sebelas Maret, 2012.
[6] Mani Shankar Anand, Barjeev Tyagi, Design and Implementation of Fuzzy Controller on FPGA, Department of Electrical Engineering, Indian Institute of Technology, Roorkee, India, 2012.
[7] Walter Banks, Gordon Hayward, Fuzzy Logic in Embedded Microcomputers and Control Systems, Associate professor in the School of Engineering at the University of Guelph, 2002.
[8] Querying MSSQL serverfrom a Raspberry Pi 3 using Python, FressTDS and pyodbc in website stackoverflow.com, 2012.Raspberry Pi 4 Model B Datasheet Copyright Raspberry Pi (Trading) Ltd. 2019.
[9] Engineer from Xiaoyue Electronics, ALOGIC_V4 document, 2022.
[10] TS. Nguyễn Anh Vinh, bài giảng Thực hành thiết kế SOC, Trường Đại học Công Nghiệp TP.HCM, 2022.

RESEARCH AND DEVELOPMENT OF MONITORING AND PRESERVATION SYSTEMS FOR SEEDS IN WAREHOUSES USING ZIGBEE AND SCADA

MAI VAN HAU [1] , VO VAN AN(S) [2*] , NGO THI THU HUONG [3]

[13] *Faculty of Electrical-Electronic Engineering, University of Transport and Communications – Campus in Ho Chi Minh City, Ho Chi Minh City, Vietnam,*

[2] *School of Engineering, Eastern International University, Binh Duong Province, Vietnam; haumv_ph@utc.edu.vn, an.vovan@eiu.edu.vn, huongntt1_ph@utc.edu.vn*

Abstract. The paper presents a control and monitoring system for seed storage in storage using ZigBee wireless network, the UART communication standard, incorporating the SCADA interface designed on Visual. The system is designed with 2 Slaves and 1 Master. Each slave is designed based on an Arduino UNO microcontroller connected to ZigBee, DHT11 temperature and humidity sensors, and modules to shut off electrical devices, lights, fans, heaters, etc. The Master is connected to ZigBee to receive and send data to the Slaves according to the UART communication standards. The Master is connected to the WinForm interface via the Serial Port to receive and send data to SCADA, monitor, and control through the interface on WinForm. The SCADA interface allows users to collect and monitor actuators' temperature, humidity, and operating status parameters in different seed warehouses in 1 central control room via a wireless ZigBee network.

Keywords. ZigBee, Agriculture, Seed Preserving, Visual Studio, SCADA

1 INTRODUCTION

Vietnam is an agricultural country. But currently, the arable land area is shrinking, especially the seedling areas are decreasing. Therefore, it is necessary to manage and preserve the quality of seeds. Some seed warehouses and farms manually monitor the quality of sources, checking the temperature and humidity of each warehouse or placing LCD screens outside the warehouse for monitoring. However, warehouse managers have no centralized control room for easy tracking and control. The primary method of seed preservation in warehouses relies on weather conditions. Each warehouse stores different seeds in a seed warehouse or station, so it is tough to connect all warehouses to a central control room, not to mention the high electricity.

Studies on seed preservation in storage are relatively common in agricultural countries such as Bangladesh, China, Thailand, India, etc. Research on wireless networks applied in various human-related fields, with a particular focus on agriculture, has also attracted the attention of scientists [1-8]. A smart home that controls the status of electronic devices, lighting, TV, and household appliances using the LoRa network [1]. In the study [2], a software system for monitoring, collecting sensor data, detecting and alerting water leakage through WSNs and Java Web technology was developed. The advantages and challenges of agricultural applications and IoT-based agricultural software are presented in the research [3]. In [4], the author built an intelligent agricultural service system using the LoRa network to collect light intensity, temperature, soil moisture, and carbon dioxide concentration in greenhouses and warehouses. Research [5], an IoT-based system for automating maintenance, pesticide control, crop management, and monitoring is in question. The monitoring system for cereal grains through PLC and HMI using the ZigBee network is mentioned in the study [6]. In the research [7], WSNs collect temperature and humidity data using RF waves. In [8], a low-power IoT network for intelligent agriculture is built to monitor soil moisture through a 4G Modem. However, these studies may experience transmission interruptions when network nodes lose connection, affecting the entire system. In this study, the author proposes to use a ZigBee wireless network and SCADA interface to solve limited wiring problems, reduce power consumption, increase control and monitoring information in the system, monitor seed preservation in storage, and maintain wireless network connectivity in case one of the connections in a warehouse fails without disrupting communication with other warehouses.

The main content of the research paper is to build hardware systems on Arduino and software on

computers using WinForm C# to create SCADA interfaces to control and monitor temperature, humidity, devices, and actuators at seed storage warehouses. Enhance efficiency in monitoring and preserving seeds, reducing incidents while ensuring quality and cost savings. The article structure consists of Part 1 – Introduction. Part 2 – Wireless Sensor Networks and Zigbee Technology. Part 3 – Design and construction of the system. Part 4 – Complete the model and evaluate the system operation. Finally, there is a conclusion section and reference materials.

2 DESIGN AND CONSTRUCTION OF THE SYSTEM

2.1 System Block Diagram

Figure 1 presents the block diagram of the system with three main functional blocks. The first block, Central Controller (MASTER), receives, processes, and sends data to Warehouse 1, Warehouse 2, and SCADA. The second block consists of sensor network nodes Slave 1 and Slave 2, representing Warehouse 1 and Warehouse 2. This block is a Slave node with the function of collecting data from the DHT 11 temperature and humidity sensor, waiting to receive data from the Master, then executing to the actuators and the ZigBee CC2530 module has the function of wireless communication between the Slave and Master blocks. Finally, the SCADA block serves as a user interface and communication management software with the Central Controller through a Serial Port. This allows operators and managers to control and monitor the system easily on a computer at a low cost.

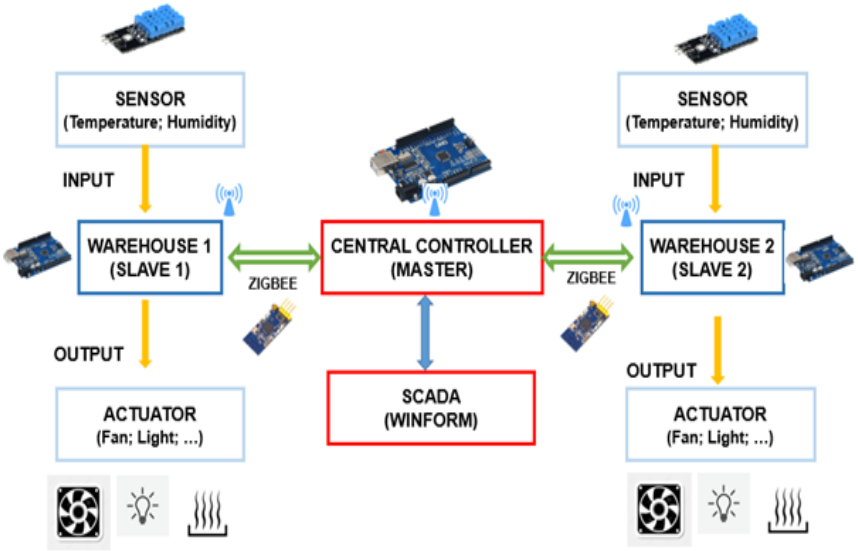

Figure 1: System Block Diagram.

a) Central Controller (Master)

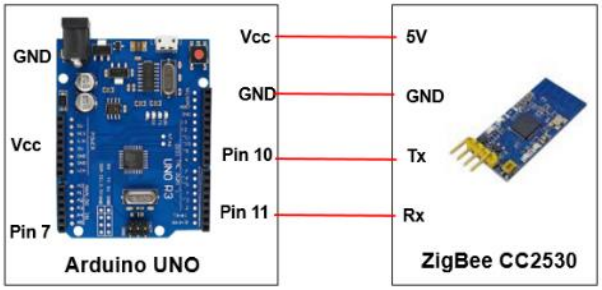

Figure 2: Schematic of Master block.

The Central Controller is considered a Master responsible for handling important tasks of the system. This block is designed to include an Arduino UNO microcontroller combined with a Zigbee CC2530 module. The UART communication standard connects the two devices, as illustrated in Figure 2.

The ZigBee CC2530 module was chosen as the wireless communication network of the system.

Combines the excellent performance of the RF transceiver with the industry-standard MCU 8051, resulting in a compact-sized product of the ZigBee CC2530. It allows the construction of network nodes with a maximum Baudrate of up to 115200, an ideal transmission distance of up to 250m, commonly used voltage: 3-5.5 VDC, ZigBee 2.4Ghz frequency band, and especially low power consumption <30mA [9].

b) WareHouse (Slave)

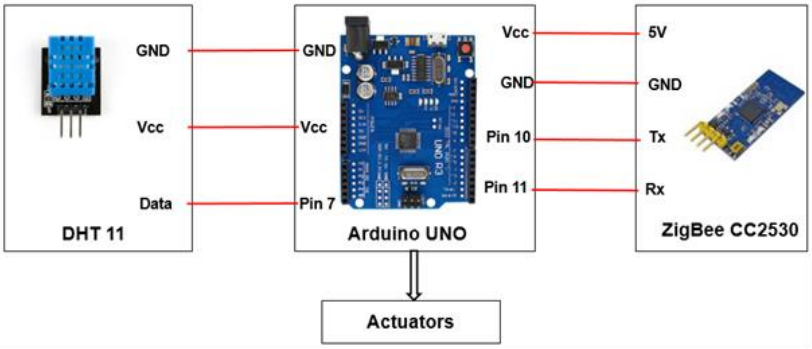

Figure 3: Schematic of Slave block.

Each Slave acts as the network node of the system (figure 3). Each node is based on Figure 3 and includes an Arduino UNO microcontroller that connects to the ZigBee module via UART standard. Input is a DHT11 sensor device, push buttons and switches. Output is actuators such as Fans, Heat, Light, etc.

DHT11 temperature and humidity sensor has an operating voltage range: 3.5V – 5.5V easy to connect to microcontrollers, Operating current: 0.3mA (measuring) 60uA (standby), Output: Serial data, Temperature Range: 0°C to 50°C, Humidity Range: 20% to 90%, Accuracy: ±1°C and ±1% [10]. Since the specifications are suitable for the Vietnamese environment and the cost is low, the author chose to use the DHT11 sensor for data measurement in the system. Follow two steps to communicate DHT 11 with Arduino Uno [10].

Step 1: Send the Start signal you want to measure to DHT 11, then DHT 11 confirms

Step 2: Once communicating with DHT 11, the sensor will send back 5 bytes of data and the measured temperature. If Byte 5 = (8 bits) (Byte1 + Byte2 + Byte3 + Byte4), then the humidity and temperature values are correct. If incorrect, the measurement results are meaningless.

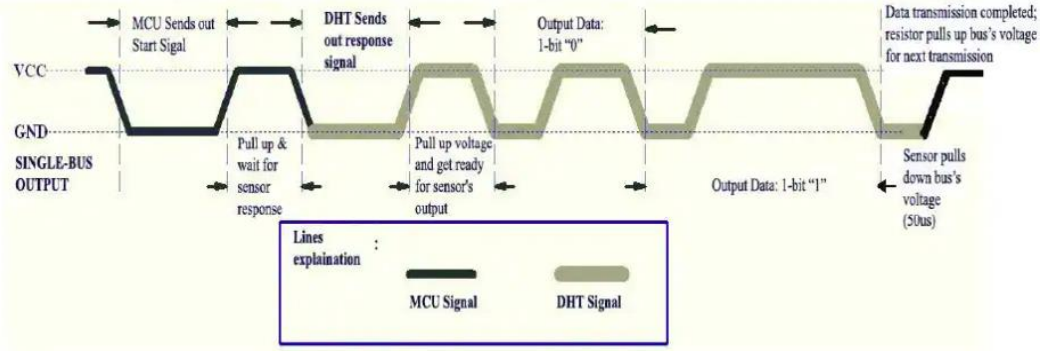

Figure 4: Sensor communication DHT 11 with MCU [10].

c) SCADA

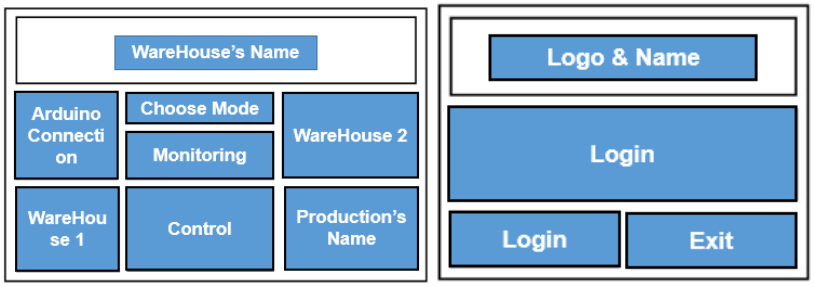

Figure 5: System interface layout.

In this paper, the author builds a SCADA interface system with features for transmitting, receiving, controlling, and monitoring data using Visual Studio C# software.

A WinForm software designed to run on the Windows platform, allowing connection to Arduino UNO microcontroller by Serial Port saves license costs and does not require high computer configuration compared to other SCADA systems.

Figure 5 describes the system interface consisting of the Login Screen, WareHouse's Name, Arduino Connection, Warehouse 1, Warehouse 2, Control, Monitoring, etc. The author plans to design according to the operator's and manager's wishes. Therefore, Unifying the design to build and develop software is easy.

2.2 Algorithm flowchart.

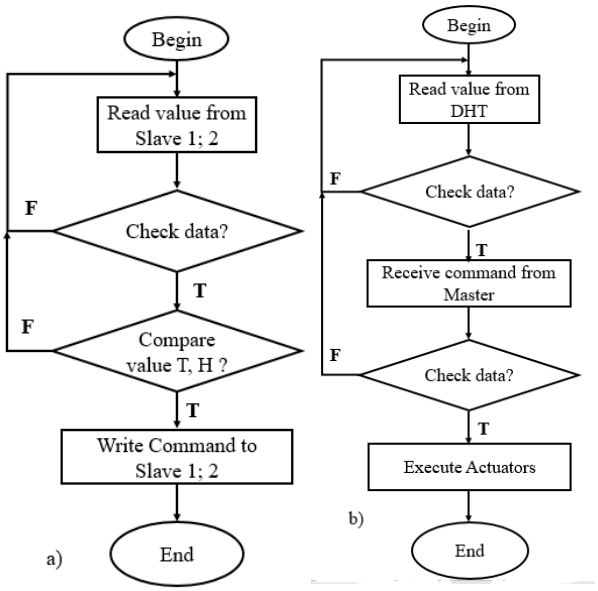

Figure 6: a) Flowchart of Master Algorithm, b) Flowchart of Slave Algorithm.

Figure 6a describes the operation algorithm of the Master block. Figure 6b describes the program algorithm of the Slave block. The communication standard between the Master and Slave blocks is UART, so data transmission and reception must be checked before executing commands.

3 COMPLETE THE MODEL AND EVALUATE THE SYSTEM OPERATION

3.1 Hardware model of the system

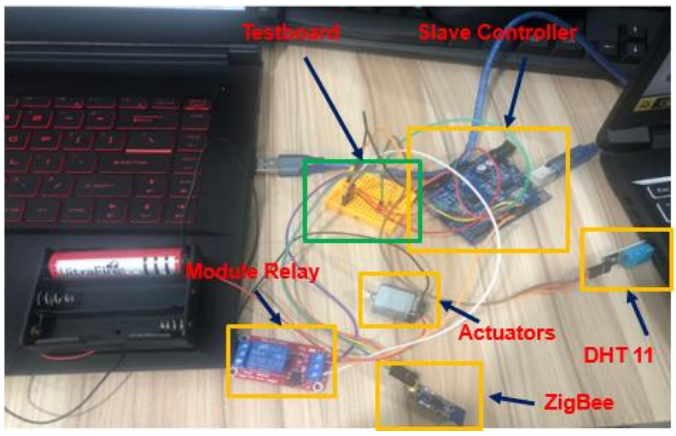

Figure 7: Hardware Model of Slave block.

Figure 7 depicts the hardware model of the WareHouse (Slave) designed based on the schematic diagram of the Slave block (Figure 2). The slave block consists of the Arduino UNO connected to ZigBee which is responsible for communicating data with the Master block. The Arduino UNO in the Slave block has input signals that are DHT 11 temperature sensors, push buttons, and output signals that are actuators.

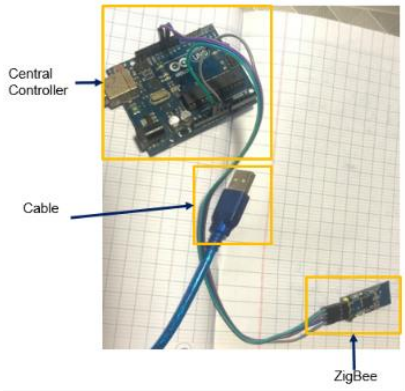

Figure 8: Hardware Model of Master Block.

Figure 8 is the Central Controller (Master) block consisting of an Arduino UNO microcontroller connected to the ZigBee module according to UART standards. The cable connects to the USB Serial Port of the laptop to both power the controller and connect to SCADA software.

This system uses the Zigbee network to monitor and preserve seeds in the Warehouse on SCADA with components such as sensors, computers, controllers, software, and wireless communication systems. The system allows humans to easily connect desired information and data at different locations within an area through the Zigbee wireless network. Slave sensor nodes in Warehouse 1 and 2 test and collect data from sensors. The central control unit (Master) retrieves data from Slave nodes through Zigbee and UART communication standards. If the temperature and humidity exceed the specified threshold, the Master sends a signal to the slave. Finally, the Slave network node that receives the signal from the Master will execute the requested task. Operators and relevant management staff can observe the Warehouse's temperature, humidity, and necessary information through the SCADA interface built on WinForm. In addition, operators can remotely turn on/off emergency devices such as fans, ventilation devices, and heating devices manually or automatically.

3.2 System operation results

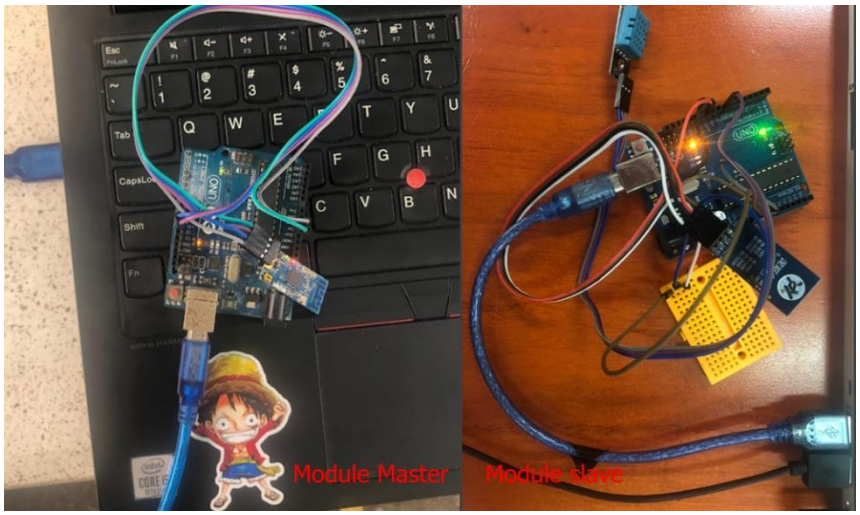

Figure 9: Model experimental activities.

Figure 9 depicts the actual operation of the model with the master module and the slave module positioned 80m apart. The model works well at different distances; the transfer speed of the master module

and the slave module will change at different rates to ensure that the transmitted data will not be interrupted (table 1).

A user interface logs into the system like Figure 10a. Design user permissions for different accounts to ensure the features as well as tasks of management departments in the system.

Figure 10b is the central monitoring interface of the system, including the following functions:

Connect Arduino:

- Set serial port parameters to connect to the control circuit (COM port name, baud rate).
- Button to connect and disconnect to the control circuit
- Display connection status and no connection with the control board.

The monitoring screen includes Man and Auto modes and cells showing the temperature and humidity of the two warehouses.

The control screen includes the following functions:

- Turn on the light, turn off the light.
- Turn on the fan, turn off the fan.
- Set temperature and humidity values for two warehouses.

Warehouse 1 and Warehouse 2 have the following functions:

- Displays temperature and humidity values sent by the control screen.
- Display temperature and humidity values sent by the control circuit.
- Display the current status of lights (on/off) and fans (on/off).

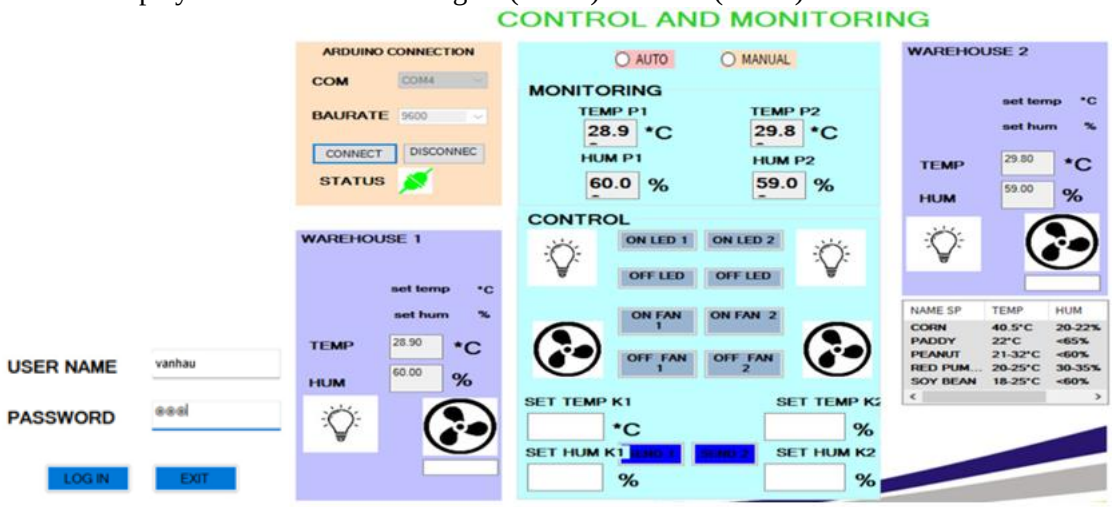

a) b)

Figure 10:a) System login interface, b) System SCADA Interface.

After successfully connecting the SCADA interface with Arduino, the temperature and humidity data from WareHouse 1 and WareHouse 2 are sent to the SCADA interface. The Monitoring area displays the temperature and humidity at the monitored positions. The Control area is used to remotely control objects in the warehouse when Manual mode is selected. By selecting auto mode, enter the Setpoint parameters (Set Temp K1, Set Temp K2, Set Hum K1, Set Hum K2) shown in Figure 10b for the system to operate fully automatically.

Table 1: ZigBee data transmission results table in different conditions.

Enviroment	Distance	Baud Rate Zigbee (bauds)
Open environment, no obstacles	100 m	38400
Classroom environment, with a retaining wall	80 m	19200
Classroom environment, with two retaining walls	50 m	14400
Classroom environment, with two retaining walls	30 m	9600
Classroom environment, there is a retaining wall made of glass	100 m	9600

Classroom environment, there are two retaining walls made of glass	70 m	4800
Classroom environment, there are three retaining walls made of glass	50 m	2400

Table 1 shows the results of transmission distance and speed in different environmental conditions. In conditions without any obstacles like walls or glass, the distance and speed of data transmission are highest. When passing through environments with many obstacles like between 2 classrooms or 3 classrooms, the distance and speed of data transmission are reduced. For the warehouses in this study, the ZigBee wave antennas are placed outside the room. Therefore, the distance and transmission speed in the wireless network can be ensured.

4 CONCLUSION

The paper presents a solution for building a monitoring and preservation system for seeds in a warehouse using the ZigBee wireless network on Visual Studio C# software. With the model and experimental results on communication distance and system stability, the system meets the conditions for application and deployment in small agricultural seed warehouses in villages with an area of about 4,000 m2 under suitable environmental conditions and surrounding obstacles. The system can be upgraded on a larger scale by using repeater devices to extend the coverage of the Zigbee wireless network. The system can also be applied to other goods, such as food, pharmaceuticals, or environmentally sensitive products. Additionally, to enhance the automation of the system, Smart control can be implemented, along with deploying the system on IoT to remotely collect data for analysis and evaluation, providing optimal conclusions to ensure seed quality.

REFERENCES

[1] F.A.R. Mu'amar Wildan and Eki Ahmad Zaki Hamidi, The Design of Application for Smart Home Base on LoRa, *2020 6th International Conference on Wireless and Telematics,2020.*

[2] Wang Xi-Kun, Yang Jing, Wang Yi-Xin and Zhang Xiao-Han, Integrated monitoring system of intelligent warehouse based on Wireless Sensor Network, *2020 5th International Conference on Electromechanical Control Technology and Transportation (ICECTT)*, pp. 256-258, 2020.

[3] Mohamed Rawidean Mohd Kassim, IoT Applications in Smart Agriculture: Issues and Challenges, *2020 IEEE Conference on Open Systems (ICOS)*, pp. 19-24, 2020.

[4] Yang Yang, Design and Application of Intelligent Agriculture Service System With LoRa-based on Wireless Sensor Network, *2020 International Conference on Computer Engineering and Application (ICCEA)*, pp. 712-716, 2020.

[5] Vaishali Puranik, Sharmila, Ankit Ranjan and Anamika Kumari, Automation in Agriculture and IoT, *2019 4th International Conference on Internet of Things: Smart Innovation and Usages (IoT-SIU)*, 2019.

[6] Jianjun Zhu, Min Yan and Zhijun Hu, Design of Food Situation Monitoring System Based on ZigBee and WinCC, *2019 18th International Symposium on Distributed Computing and Applications for Business Engineering and Science (DCABES)*, pp. 222-225, 2019.

[7] George Eldho John, Renjith G., Neil K Thomas and Rohit Joseph Mammutil, Application-specific WSN for precision agriculture, *2018 8th International Symposium on Embedded Computing and System Design (ISED)*, pp. 241-245, 2018.

[8] Soumil Heble, Ajay Kumar, K. V. V Durga Prasad, Soumya Samirana, P. Rajalakshm and U. B. Desai, A low power IoT network for smart agriculture, *2018 IEEE 4th World Forum on Internet of Things (WF-IoT)*, pp. 609-614, 2018.

[9] Texas Instruments, A True System On Chip Solution For 2.4GHz IEEE802.15.4 and ZigBee Applications, Texas Instruments Incorporated, 2011.

[10] DFRobot, DHT11 Humidity, Temp Sensor Datasheet. Available at https://www.digikey.at/htmldatasheets/production/2071184/0/0/1/dht11-humidity-temp-sensor.html.

AN EFFICIENT LONG SHORT-TERM MEMORY APPROACH FOR LOAD POWER PREDICTION IN SMART SOLAR MICROGRID

PHUONG NGUYEN THANH [1 2], MING-YUAN CHO [1], THUC MINH BUI [2], TIEN NGUYEN QUOC [3], VAN PHAM THI [4], THAO NGUYEN DA [4 5*]

[1] *Department of Electrical Engineering, National Kaohsiung University of Science and Technology, Kaohsiung City, Taiwan, R.O.C,*

[2] *Department of Electronic and Electrical Engineering, Nha Trang University, Khanh Hoa, Vietnam,*

[3] *Faculty of Tourism, Thai Binh Duong University, Khanh Hoa, Vietnam,*

[4] *Faculty of Economics and Management, Thai Binh Duong University, Khanh Hoa, Vietnam,*

[5] *Department of Tourism Management, Business Intelligence School, National Kaohsiung University of Science and Technology, Kaohsiung City, Taiwan, R.O.C*

thanhphuong@ntu.edu.vn, mycho@mail.ee.nkust.edu.tw, minhbt@ntu.edu.vn, nguyenquoctienkh@gmail.com, van.pt@tbd.edu.vn, thao.nd@tbd.edu.vn

Abstract. Predicting the load power of a base solar power plant is critical to improving the profit from available solar energy. This research develops a deep learning method to predict the load power utilizing the long short-term memory model. The proposed method could increase the accuracy in hourly predicting the full load power of commercial buildings integrated with a solar power plant. The load operation is generally influenced by the weather parameters such as temperature, dew point, humidity, pressure, wind direction, and wind speed. These parameters affect the load power, which is considered the target factor. Moreover, the advanced meter infrastructure also collects the internal parameters of the solar power microgrids over one year, including the battery-discharged power. These additional parameters were also examined as input parameters in the proposed method. The Long short-term memory (LSTM) algorithm is sought for predicting the full load power of the building. The performance and accuracy of the proposed LSTM are compared and evaluated with other deep learning methodologies with MSE and MAE benchmarks. The experiment results proved that the LSTM scores a higher performance with the maximum improvements of 39.64% MSE, 27.05% MAE in the training data, and 12.58% MSE, 19.94% MAE in the validating operation, respectively.

Keywords. Load power prediction; Load power prediction; Long short-term memory; Smart solar microgrid.

1 INTRODUCTION

Many assumptions are required for load-predicting analysis in smart solar microgrids to account for the unpredictability factor. These assumptions required thousands of nonlinear equations, which takes lots of computational analysis and the experience of experts. To eliminate these difficulties, the deep learning methodology is developed as an alternative to traditional neural network approaches to predict the load power based on input and output parameters. Predicting load power in smart solar microgrids based on a regression approach is the most common solution researched in the literature review. Deep learning methodologies control a system's response and unpredictability parameters for forecasting load power. Many real-life problems can be effectively solved and evaluated using machine learning approaches to improve accuracy of predictive models.

Accurate prediction of the load power in the smart solar microgrid improves electricity producers to be more successful in the market. Similarly, smart solar operators require accurate load information for reliable and secure smart solar operation. Also, short-term load power prediction is important in the energy resources management and operation of the smart solar microgrid. Load power is time series data, which

normally has complex behavior. The complexities of load power include nonlinear, time series complexity, and variable behavior. Many researches have been done in recent years due to the importance of short-term load power prediction [1][2][3][4][5][6][7][8][9]. Wi et al. employed fuzzy polynomial regression to forecast load power considering economic and weather parameters [10]. The effectiveness of the developed method was demonstrated by evaluating mutual data between weather and season to season. However, the predicting performance was influenced by the accuracy of weather forecasting algorithms. Lopez et al. developed self-organizing maps NN in load forecasting, which provide a deep analysis in real-world applications [11]. The study on the significance of meteorological parameters and frequency components was analyzed to build decision-support applications of the Spanish electricity market. Ahmad et al. evaluate the medium-term and long-term energy prediction based on the nonlinear autoregressive approaches and actual environmental information [3]. The optimal model could guarantee the predicting accuracy of the designed energy systems with the coefficient of variation of the LSBoost approach. The developed methodology was compared and analyzed with the previous Gaussian regression model, which demonstrated its effectiveness in real-world applications. Petra et al. deployed support vector regression to short-term load forecast to save cost and significant contribution to the grid innovations of the electricity market [12]. The proposed approach was compared with ten state-of-the-art forecasting models to demonstrate its accuracy with Irish CER data. The application of SVR in an online forecasting framework showed its advantages in smart city systems. Nazar et al. deployed wavelet Kalman machines for simultaneous load prediction, which combined the Kohonen Self-Organizing Map to find similar days of load components [13]. In the next stage, the MLP-ANN and ANFIS were employed to forecast the load and price variables, respectively. The developed method was compared with recent forecasting algorithms, which achieved better performance for day-ahead electricity prediction. Ekonomoou et al. developed a precise electric load prediction based on artificial neural networks and wavelet denoising methodology [14]. The combined algorithm provided better historical load signals during the training operation and achieved better forecasting accuracy. The short-term load predicting approach did not consider the holiday and economic developing factors, which greatly affected the predicting accuracy. Chen et al. provide a short-term forecasting model based on deep residual networks, which could integrate domain knowledge to improve the forecast performance [15]. Moreover, a two-stage ensemble strategy was deployed to predict probabilistic load with Monte Carlo dropout. The effectiveness of the developed method was simulated in three public datasets, which demonstrate its higher generalization ability in load forecasting. Rana et al. applied feature selections in the electricity demand forecast combined neural network, which utilized half-hourly electricity demand data [16]. The correlative feature selection could improve the coverage probability up to 97.44% and 91.89% for the Australian and British data, respectively. Gowri et al. utilized deep learning methodology to predict thermal load based on advanced feature selection, achieving computationally efficiently with higher accuracy [17]. The deep learning method could achieve better MAPE benchmarks, which provide lesser computation periods. Kouhi et al. developed short-term load prediction based on NN and chaotic intelligent feature selection [18]. The relevant input data are selected to improve the predicting accuracy of MLP NN with hybrid Levenverg-Marquardt and DE methodologies. The hybrid method was simulated in PJM and England datasets, which achieved higher performance in recent STLF technologies. Raza et al. proposed an intelligent hybrid ANN and GPSO in training technology, which improved forecasting demand due to exogenous meteorological variables [19]. The dataset of the New England grid demonstrated its significant improvement in forecasting accuracy and convergence velocity compared with contemporary methodologies in the literature. Therefore, the applications of deep learning algorithms have demonstrated their outstanding performance compared with traditional neural networks in short-term load prediction.

Although many methodologies have been developed to forecast the short-term load, no research concentrates on power prediction in the smart solar microgrid. Therefore, this research proposed the long short-term memory (LSTM) to predict the load power regarding weather factors, including temperature, precipitation, relative humidity, and battery discharge data. The predicting performance of the proposed LSTM algorithm is compared with the recurrent neural network (RNN) model to analyze and evaluate. The methodologies are illustrated in the next section. The experiment results are presented in the third part, and

the final section is the conclusion of this study.

2 METHODOLOGY

2.1 Data preparation

The general structure to integrate deep learning methodology is illustrated in Figure 1. The smart solar microgrid can collect different parameters based on IoT modules, including weather parameters and battery-discharged power. The hourly sequential data are accumulated for more than one year. The battery-discharged power data is selected as an additional input feature to improve the predicting efficiency. The collected data are normalized with the min-max method, which are calculated by Eq. (1). The x_{min} and x_{max} are the minimum and maximum data for each collected variable. The min-max normalization approach transfers all collected features in the same range (0,1), which could be comfortably proceeded by the deep learning machine.

$$\dot{x}_t = \frac{x_{min} - x_t}{x_{min} - x_{max}} \tag{1}$$

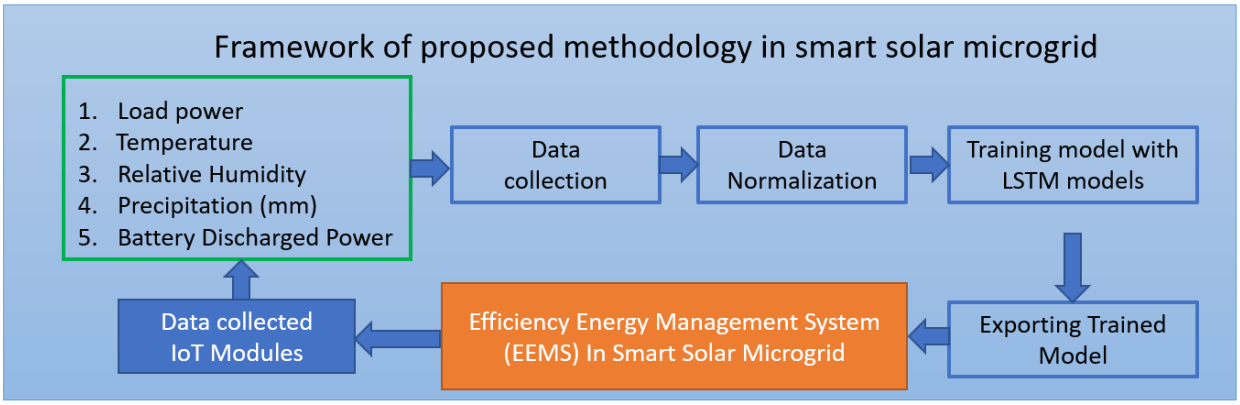

Figure 1: The general structure of developed deep learning methodology in the smart solar microgrid.

2.2 Introduction of deep learning methodologies

In this study, some deep learning, which can process sequential information data, is deployed to predict the load power in the smart solar microgrid. The recurrent neural network (RNN) could process the temporal dynamics in historical variables constructed from a feedforward NN [20]. The RNN could achieve knowledge from previous historical information in the short term, which deployed the input, hidden, and output gates. The RNN architecture could map previous historical variables by recursively transferring

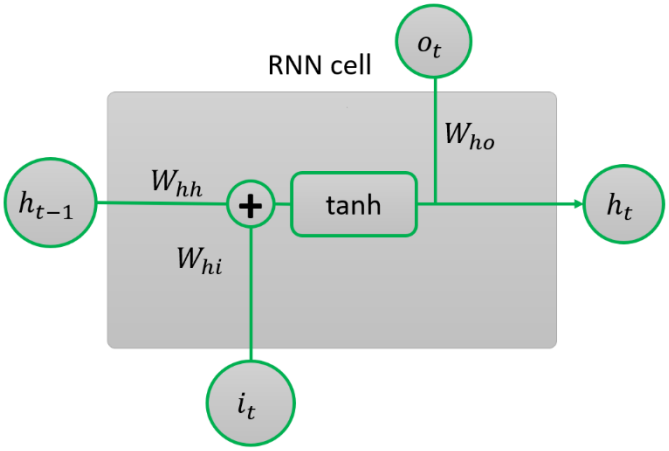

Figure 2: The general structure of recurrent neural network.

current input to the output data, as in Figure 2. The output information is calculated in Eqs. (2) and (3), which updated weight and bias vectors in training operations. However, the simple RNN architecture is generally affected by the gradient vanishing problem [21], [22].

$$h_t = tanh(W_{hh}h_{t-1} + W_{hi}i_t + b_{hh}) \quad (2)$$

$$o_t = tanh(W_{yo}h_t + b_{ho}) \quad (3)$$

Although the RNN model could maintain the previous memory, the standard architecture still experiences the vanishing gradient problem [23]. Therefore, the LSTM was introduced to solve this issue [22][24]. The LSTM could identify the optimal long-term variables for time-sequential historical data. The LSTM selects the primary correlation between historical input data and target output [25][26]. This structure involves different controllable gates, input, output, and forget gates, as illustrated in Figure 3. These gates continuously function resetting, writing, and reading operations that provide the storing and accessing data in the long-term memory, as described in Eq. (3a)-(3f). The sequential input vector, x^t, is calculated through the hidden state, h^t, to output the flow sequence, o_t, by iterating the following functions, where W and b are the weight matrix and bias vector in different gates. The x^t, f_t, c_t, and o_t are the input vector, the forget gate, the cell activation vectors, and the output vector of the LSTM cell.

$$f_t = sigmoid\ (W_{fh}h^{t-1} + W_{fx}x^t + b_f) \quad (3a)$$

$$i_t = sigmoid\ (W_{ix}x^t + W_{ih}h^{t-1} + b_i) \quad (3b)$$

$$z_t = tanh\ (W_{zx}x^t + W_{zh}h^{t-1} + b_z) \quad (3c)$$

$$o_t = sigmoid\ (W_{ox}x^t + W_{oh}h^{t-1} + b_o) \quad (3d)$$

$$c_t = f_t \odot c_{t-1} + i_t \odot z_t \quad (3e)$$

$$h_t = o_t \odot tanh\ (c_t) \quad (3f)$$

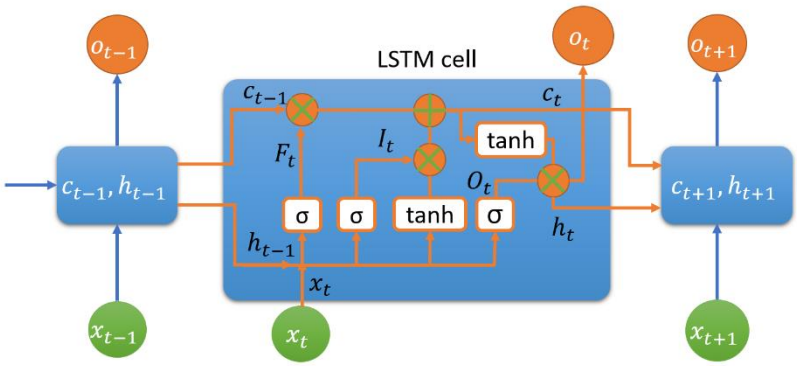

Figure 10: The general structure of long short-term memory cell

To evaluate the performance of predicting methodology, the mean square errors (MSE) and mean absolute error (MAE) are utilized as benchmark metrics, as computed as follows, where y_i and $\hat{y}_i$ are the predicted value and target variable respectively, as computed in Eqs. (4)-(5).

$$MSE = \frac{1}{n}\sum_{i=1}^{n}(y_i - \hat{y}_i)^2 \quad (4)$$

$$MAE = \frac{1}{n}\sum_{i=1}^{n}\left|y_i - \hat{y}_i\right| \quad (5)$$

3 EXPERIMENT RESULTS

To prove the effectiveness of the proposed LSTM methodology, the experiment results of LSTM and RNN are analyzed with different MSE and MAE benchmarks. The simulated results are presented in Table 1 with different window sizes in the sequential historical information. The window sizes are the number of sequential historical data which are deployed as two-dimensional features. All the data are collected in installed smart solar microgrid for more than one year in Kaohsiung, Taiwan. All the anomaly data are filtered before deploying in predicting methodology.

In the 6 sequential window sizes, the LSTM model achieves 0.0027, 0.0259, 0.0049, 0.0366, while the

RNN algorithm obtains 0.0033, 0.0355, 0.0056, and 0.0457 for MSE and MAE during the training and validating process, respectively. Compared with the RNN method, the LSTM outperforms the traditional RNN model, which attains 18.40% MSE, 27.05% MAE, 12.58% MSE, and 19.94% MAE improvements in training and validating operations. Therefore, the LSTM algorithms demonstrate their effectiveness and stability in processing load power historical information in smart solar microgrids.

In the 12 sequential windows, the RNN achieves 0.0038 MSE and 0.0349 MAE in the training process and 0.0060 MSE and 0.0424 MAE in the validating operation. In addition, the developed algorithm acquires 0.0023 MSE and 0.0260 MAE in the training process and 0.0053 MSE and 0.0402 MAE in the validating procedure. Compared with the traditional RNN model, the LSTM method obtained significant enhancements of 39.64% MSE, 25.53% MAE, 11.98% MSE, and 5.24% MAE, respectively. Therefore, the LSTM proves its capability in processing long-term sequential information with higher accuracy and better performance in both MSE and MAE benchmarks.

Table 1: The experiment results between RNN and LSTM models.

Model	Training Data		Validating Data		Improvement (%)			
					Training Data		Validating Data	
	MSE	MAE	MSE	MAE	MSE	MAE	MSE	MAE
6 sequential window size					**6 sequential window size**			
RNN	0.0033	0.0355	0.0056	0.0457	**18.40**	**27.05**	**12.58**	**19.94**
LSTM	0.0027	0.0259	0.0049	0.0366				
12 sequential window size					**12 sequential window size**			
RNN	0.0038	0.0349	0.0060	0.0424	**39.64**	**25.53**	**11.98**	**5.24**
LSTM	0.0023	0.0260	0.0053	0.0402				

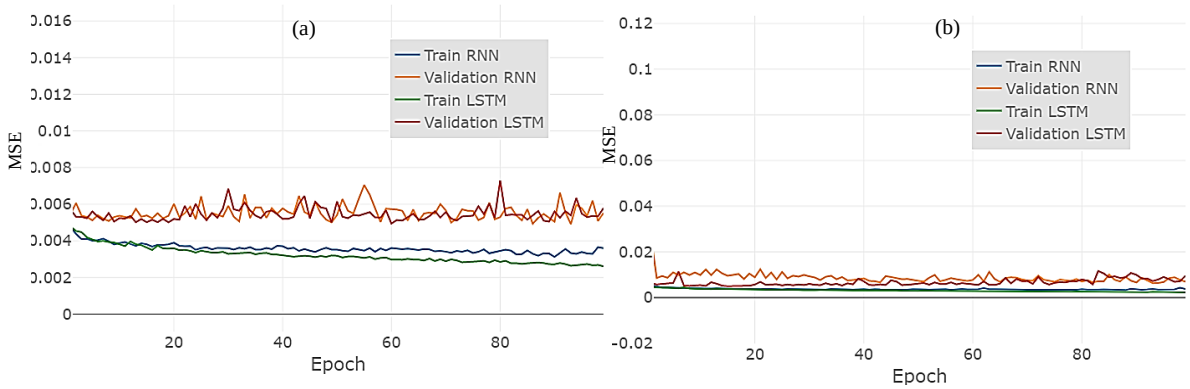

Figure 4: The MSE values during the training and validating process: (a) 6-window size, (b) 12-

In general, comparing across window size, the LSTM model scores a higher performance with the

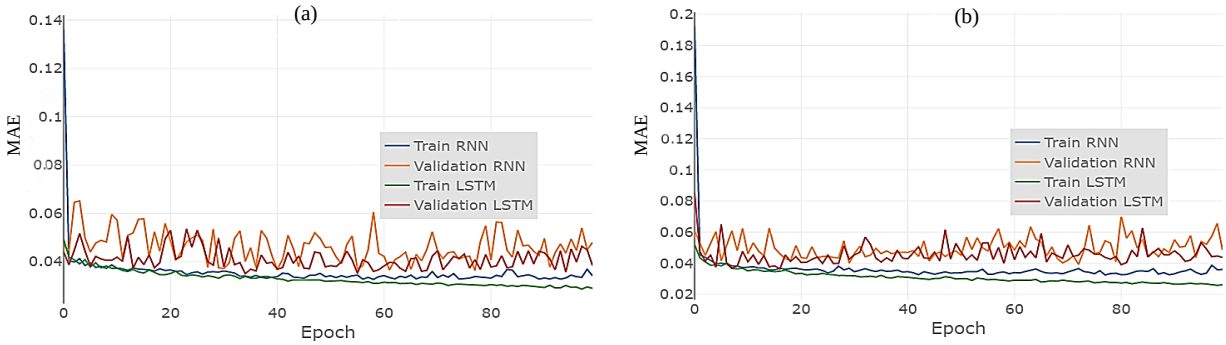

Figure 5: The MAE values during the training and validating process: (a) 6-window size, (b) 12-

maximum improvements of 39.64% MSE, 27.05% MAE in the training data, and 12.58% MSE, 19.94%

MAE in the validating operation, respectively. Therefore, the proposed LSTM algorithm demonstrates its effectiveness in predicting load power in smart solar microgrids, which achieves outstanding performance compared with the traditional RNN model. In addition, during the training and validating operations, the proposed LSTM converges better velocity compared with the RNN approach and obtains lower MSE and MAE benchmarks. Therefore, the LSTM achieves the highest performance in predicting the load power in the smart solar microgrid.

4 CONCLUSION

In this study, the load power in the smart solar microgrid is predicted based on the proposed LSTM algorithms. Many internal and external historical parameters are collected by deploying IoT modules in the solar system every hour. The proposed LSTM model is compared and analyzed with the RNN model in different window sizes. The experiment results proved that the LSTM scores a higher performance with the maximum improvements of 39.64% MSE, 27.05% MAE in the training data, and 12.58% MSE, 19.94% MAE in the validating operation, respectively. Therefore, the LSTM methodology could provide optimal accuracy in predicting load power, which is integrated into the energy management system of the smart solar microgrid.

REFERENCES

[1] R. Weron, *Modeling and forecasting electricity loads and prices: A statistical approach*. John Wiley & Sons, 2007.

[2] J. W. Taylor, "Short-term load forecasting with exponentially weighted methods," *IEEE Trans. Power Syst.*, vol. 27, no. 1, pp. 458–464, 2011.

[3] T. Ahmad and H. Chen, "Nonlinear autoregressive and random forest approaches to forecasting electricity load for utility energy management systems," *Sustain. Cities Soc.*, vol. 45, pp. 460–473, 2019.

[4] L. Wei and Z. Zhen-gang, "Based on time sequence of ARIMA model in the application of short-term electricity load forecasting," in *2009 International Conference on Research Challenges in Computer Science*, 2009, pp. 11–14.

[5] C. García-Martos, J. Rodriguez, and M. J. Sanchez, "Mixed models for short-run forecasting of electricity prices: Application for the Spanish market," *IEEE Trans. Power Syst.*, vol. 22, no. 2, pp. 544–552, 2007.

[6] N. Amjady and F. Keynia, "Short-term load forecasting of power systems by combination of wavelet transform and neuro-evolutionary algorithm," *Energy*, vol. 34, no. 1, pp. 46–57, 2009.

[7] L. Yin and J. Xie, "Multi-temporal-spatial-scale temporal convolution network for short-term load forecasting of power systems," *Appl. Energy*, vol. 283, p. 116328, 2021.

[8] B.-S. Kwon, R.-J. Park, and K.-B. Song, "Short-term load forecasting based on deep neural networks using LSTM layer," *J. Electr. Eng. Technol.*, vol. 15, pp. 1501–1509, 2020.

[9] H. H. H. Aly, "A proposed intelligent short-term load forecasting hybrid models of ANN, WNN and KF based on clustering techniques for smart grid," *Electr. Power Syst. Res.*, vol. 182, p. 106191, 2020.

[10] Y.-M. Wi, S.-K. Joo, and K.-B. Song, "Holiday load forecasting using fuzzy polynomial regression with weather feature selection and adjustment," *IEEE Trans. Power Syst.*, vol. 27, no. 2, pp. 596–603, 2011.

[11] M. López, S. Valero, C. Senabre, J. Aparicio, and A. Gabaldon, "Application of SOM neural networks to short-term load forecasting: The Spanish electricity market case study," *Electr. Power Syst. Res.*, vol. 91, pp. 18–27, 2012.

[12] P. Vrablecová, A. B. Ezzeddine, V. Rozinajová, S. Šárik, and A. K. Sangaiah, "Smart grid load forecasting using online support vector regression," *Comput. Electr. Eng.*, vol. 65, pp. 102–117, 2018.

[13] M. S. Nazar, A. E. Fard, A. Heidari, M. Shafie-khah, and J. P. S. Catalão, "Hybrid model using three-stage algorithm for simultaneous load and price forecasting," *Electr. Power Syst. Res.*, vol. 165, pp. 214–228, 2018.

[14] L. Ekonomou, C. A. Christodoulou, and V. Mladenov, "A short-term load forecasting method using artificial neural networks and wavelet analysis," *Int. J. Power Syst*, vol. 1, pp. 64–68, 2016.

[15] K. Chen, K. Chen, Q. Wang, Z. He, J. Hu, and J. He, "Short-term load forecasting with deep residual networks," *IEEE Trans. Smart Grid*, vol. 10, no. 4, pp. 3943–3952, 2018.

[16] M. Rana, I. Koprinska, and A. Khosravi, "Feature selection for interval forecasting of electricity demand time series data," in *Artificial Neural Networks: Methods and Applications in Bio-/Neuroinformatics*, 2015, pp. 445–462.

[17] G. Suryanarayana, J. Lago, D. Geysen, P. Aleksiejuk, and C. Johansson, "Thermal load forecasting in district heating networks using deep learning and advanced feature selection methods," *Energy*, vol. 157, pp. 141–149, 2018.

[18] S. Kouhi, F. Keynia, and S. N. Ravadanegh, "A new short-term load forecast method based on neuro-evolutionary algorithm and chaotic feature selection," *Int. J. Electr. Power Energy Syst.*, vol. 62, pp. 862–867, 2014.

[19] M. Q. Raza, M. Nadarajah, D. Q. Hung, and Z. Baharudin, "An intelligent hybrid short-term load forecasting model for smart power grids," *Sustain. Cities Soc.*, vol. 31, pp. 264–275, 2017.

[20] Y. LeCun, Y. Bengio, and G. Hinton, "Deep learning," *Nature*, vol. 521, no. 7553, pp. 436–444, 2015.

[21] Y. Bengio, P. Simard, and P. Frasconi, "Learning long-term dependencies with gradient descent is difficult," *IEEE Trans. neural networks*, vol. 5, no. 2, pp. 157–166, 1994.

[22] S. Hochreiter and J. Schmidhuber, "Long Short-term Memory," *Neural Comput.*, vol. 9, pp. 1735–1780, Dec. 1997, doi: 10.1162/neco.1997.9.8.1735.

[23] A. Graves, "Hierarchical subsampling networks," in *Supervised Sequence Labelling with Recurrent Neural Networks*, Springer, 2012, pp. 109–131.

[24] A. Graves, "Long short-term memory," in *Supervised sequence labelling with recurrent neural networks*, Springer, 2012, pp. 37–45.

[25] H. Sak, A. W. Senior, and F. Beaufays, "Long short-term memory recurrent neural network architectures for large scale acoustic modeling," 2014.

[26] P. Malhotra, L. Vig, G. Shroff, and P. Agarwal, "Long short term memory networks for anomaly detection in time series," in *Proceedings*, 2015, vol. 89, pp. 89–94.

ADVANCING LED LIGHTING SYSTEMS: INTEGRATED LUMINAIRES WITH WHITE FLAME BARRIER AND OPTICS FILM FOR ENHANCING EFFICIENCY

MINH-ANH TRAN[1], LANH-THANH LE[2], HIEN-THANH LE[3*]

[1]Faculty of Engineering, Dong Nai Technology University, Bien Hoa City, Vietnam,
[2]Faculty of Information Technology, Dong Nai Technology University, Bien Hoa City, Vietnam,
[3]Faculty of Electrical and Electronics Engineering, HCMC University of Industry and Trade, 140 Le Trong Tan, Ho Chi Minh City 760310, Vietnam*
trananhminh@dntu.edu.vn, lethanhlanh@dntu.edu.vn, lethanhhien2012@gmail.com

Abstract. This study explores the utilization of an optic film as an innovative optical enhancement in LED luminaires for rear lights. The optic film, functioning akin to an array of cylindrical convex lenses, is employed to replicate each LED as a series of virtual image lines. This optical arrangement mitigates the glare associated with high-intensity LED point sources and concentrates the emitted light within a specific angle, ultimately enhancing the efficiency of LED lighting. The paper delves into the principles behind the optic film's operation, including the critical angle α and the refractive index. Furthermore, it investigates the behavior of light within the optic film, classifying it into three distinct modes: emission, recursion, and high angle. Key parameters defining triangular units within the optic film are also discussed. Experimental results demonstrate a significant improvement in light output efficiency, with the LED luminaire incorporating the optic film achieving a 45.95% increase in intensity compared to its counterpart without the film. These findings underscore the effectiveness of the optic film in improving LED luminaire performance, making it a compelling choice for applications requiring enhanced lighting efficiency.

Keyword. LED luminaire, Flame barrier, 8750 safety regulation, LED design.

1INTRODUCTION

In the realm of lighting technology, the quest for energy efficiency, enhanced luminosity, and reduced glare has been a perennial challenge. In this pursuit, the integration of innovative optical elements has emerged as a pivotal avenue for achieving superior lighting performance. Among these advancements, the utilization of optic films has garnered substantial attention as a transformative solution, particularly in the context of Light Emitting Diode (LED) luminaires [1-2].

Past studies have laid the foundation for our exploration, revealing the transformative potential of optic films in enhancing LED luminaire efficiency. These studies have consistently demonstrated that optic films, by functioning as an array of cylindrical convex lenses, have the remarkable capability to replicate each individual LED within a luminaire as a series of virtual image lines. This seemingly subtle yet profound optical arrangement has the potential to revolutionize the efficiency and performance of LED lighting systems, particularly in applications where precise control of light distribution and intensity is paramount [3].

Building upon this rich legacy of research, our paper embarks on a comprehensive exploration of the application of optic films in LED luminaires, with a specific focus on their role in rear lighting systems. Through a systematic analysis of the underlying optical principles, the behavior of light within the optic film, and critical parameters that define its functionality, we aim to unveil the intrinsic advantages and practical implications of this innovative technology [4].

We present new experimental results that substantiate the efficacy of the optic film in enhancing the output of LED luminaires. These findings not only corroborate the earlier studies but also provide additional insights into the adaptability and versatility of optic films in various lighting scenarios.

As we delve into the intricacies of optic films and their impact on LED luminaire performance, we anticipate that this research will contribute to the evolving landscape of energy-efficient, visually appealing, and technologically advanced lighting solutions. It is within this context that we embark on our exploration, driven by the promise of illuminating a brighter and more efficient future in the world of lighting technology.

2 THE LIGHTING DESIGN

The LED luminaire design incorporates a meticulously engineered housing and heat sink, an efficient thermal pad, a high-performance LED PC board light engine, a protective White Flame Barrier (WFB), and an innovative Optic Film. This holistic design ensures not only the reliability and longevity of the luminaire but also delivers superior lighting performance with optimized light distribution, reduced glare, and enhanced energy efficiency, shown in Figure 1.

Housing and Heat Sink: The LED luminaire's design begins with a well-engineered housing and an efficient heat sink system. The housing not only provides protection for the internal components but also contributes to the luminaire's aesthetics and durability. It is typically crafted from a high-quality material that is both lightweight and thermally conductive, ensuring effective heat dissipation. Integrated into the housing is a robust heat sink mechanism. Heat sinks are essential to manage the heat generated by the LEDs during operation. These heat sinks are strategically designed with fins and channels to maximize surface area and facilitate the efficient transfer of heat away from the LEDs. This helps maintain optimal operating temperatures, which is critical for the longevity and performance of the LED modules.

Thermal Pad: To further enhance the heat dissipation capabilities of the luminaire, a thermal pad is employed. This thermal pad serves as a bridge between the LED PC board and the heat sink. It is composed of thermally conductive material that ensures effective thermal coupling. The thermal pad facilitates the transfer of heat from the LED PC board to the heat sink, enabling rapid dissipation and preventing thermal buildup that could otherwise degrade LED performance.

LED PC Board Light Engine: At the heart of the luminaire lies the LED PC board light engine. This component is designed to accommodate high-efficiency LEDs, which are carefully selected based on the specific lighting requirements and intended applications. The LED PC board incorporates multiple LED modules arranged in an optimal configuration to achieve the desired lumen output and light distribution. Sophisticated drivers and control circuitry are integrated into the LED PC board to regulate power supply, dimming capabilities, and ensure the LEDs operate within their specified parameters. The LED PC board is engineered for longevity and reliability, with features such as surge protection and thermal management.

Layer 1White Flame Barrier (WFB): The first layer within the luminaire is the White Flame Barrier (WFB). This component serves a dual purpose: it acts as a protective barrier for the LED modules and also enhances the overall optical performance of the luminaire. The WFB is designed to withstand high temperatures and provide thermal insulation, ensuring the safety and longevity of the LEDs. Additionally, it reflects and diffuses light, contributing to improved light distribution and reduced glare.

Layer 2 Optic Film: The final layer in the luminaire design is the Optic Film. This innovative component functions as an array of cylindrical convex lenses, each capable of replicating the LED light source as a series of virtual image lines. This optical arrangement serves to reduce glare and precisely control the direction and distribution of light. By concentrating and shaping the emitted light within specified angles, the Optic Film significantly enhances the efficiency and performance of the LED luminaire.

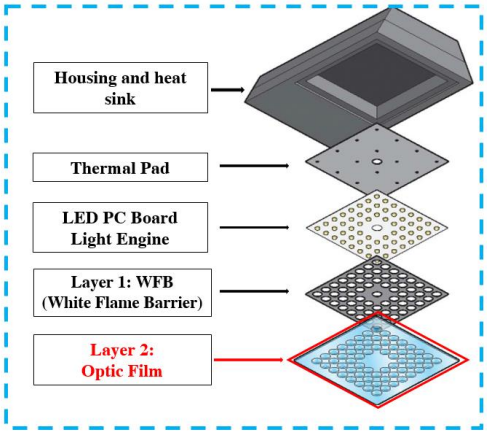

Figure 1: The principle of LED luminaries with optics film

3 THE PRINCIPLE OF OPTICS FILM

The optic film works like an array of cylindrical convex lenses, so it can replicate each LED of a rear light as a line of its virtual images. In consequence, if a LED light is used, multiple line source images will be formed and overlapped to each other. The glare incurred by the high brightness of LED point source will be thus decreased. Besides, the optic film can condense the divergent light from each LED to increase the optical intensity within a certain angle. The efficiency of LED light is enhanced consequently. The behavior of LED light interacted with the optic film is illustrated in Figure 2. Of the light rays emitted from the LED module, the angle α was defined by the value which are refracted by the ray parallel with the end surface of the prims sheet, and that was shown by the formula 1 [5-7]

The optical film functions akin to an array of cylindrical convex lenses, allowing it to reproduce each LED of a rear light as a series of virtual image lines. Consequently, when an LED light source is utilized, multiple line-shaped image sources are generated and superimposed upon each other. This diminishes the glare produced by the high luminosity of the LED's focal point. Additionally, the optical film can converge the divergent light emanating from each LED, thereby amplifying the optical intensity within a specific angle. This, in turn, enhances the efficiency of the LED light source. The interaction between the LED light and the optical film is depicted in Figure 4. Among the light rays emitted from the LED module, angle α is defined as the value resulting from refraction by the ray parallel to the end surface of the optical film, as expressed by Formula 1 [8].

Angle α is determined by the rays refracted when they are parallel to the end surface of the optic film, and this relationship is represented by Formula 1.

$$n_w \sin(\alpha) = 1 \quad (1)$$

The condition for a optic film to have a refractive index within the range $n_w > 1.4$ is important. In this context, the angle β is defined as $\beta = \pi/2 - \alpha$, and it's determined by the rays' incidence on the upper surface of the prism. The condition $n_w \sin(\beta) > 1$ signifies that the sine of angle β multiplied by the refractive index nw should be greater than 1. This condition is relevant for ensuring the desired optical behavior of the optic film [9-11].

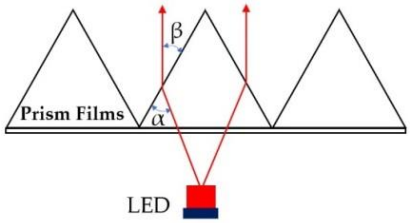

Figure 2: The interaction of light rays with the optic film.

The optic film are designed with the primary objective of concentrating the emitted light rays from the source. As illustrated in Figure 3(a), the behavior of light within the optic film can be categorized into three modes: *Emission mode:* In this mode, light is emitted from the upper surface of the optic film; *Recursion mode:* Light follows a path where it is reflected back through the optic film; *w*: Light is emitted at angles that fall outside the effective field of view [5-8].

Each triangular unit within the optic film is defined by specific parameters outlined in Figure 3(b). These parameters include: ϕ and θ: These values represent the inside corner angles of each triangular unit, both falling within the range of 0 to 90 degrees ($0° < \phi = \theta < 90°$); h: The thickness parameter, which varies within the range of 0.05 mm to 0.25 mm; x: The pitch parameter, which ranges from 0.024 mm to 0.05 mm.

These parameters play a crucial role in determining how light interacts with the optic film, and they are essential for achieving the desired optical effects and performance characteristics.

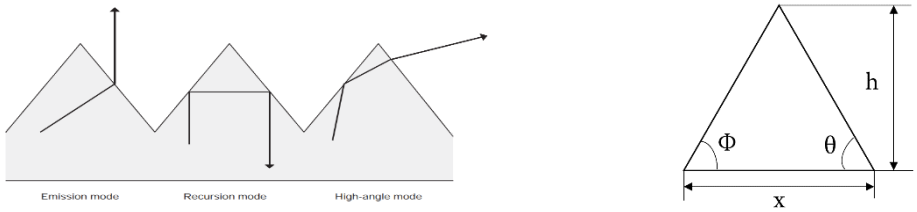

(a) (b)

Figure 3: (a) Behavior of light rays in the optic film layer; (b) the parameter of a unit of prism.

In order to evaluate the performance of the commercial rear position lamp shown in Figure 6(a), its optical model is built by Solid Work software and simulated by optical software Light Tools to get the illumination distribution. The inside corner angle of the prism element and pitch is set as $\phi = 60°$, $\theta = 60°$ and the optic film thin x = 0.05 mm at initial stage, respectively.

4 EXPERIMENTAL RESULTS

The experimental results, as depicted in Figure 4, provide valuable insights into the performance of the lighting designs. Specifically, the polar intensity of the commercial design was found to be weaker compared to that of the new design. This disparity is illustrated in Figure 4, where the polar intensity shape of the new design appears longer, indicating a higher light output efficiency in comparison to the commercial design. In more specific terms, at an angle of 60 degrees, the commercial design exhibited a polar intensity value of approximately 1016 cd/klm. Conversely, the new design achieved a significantly higher polar intensity value of 1880 cd/klm. This substantial increase in polar intensity highlights the improved performance and enhanced light output efficiency of the new design when compared to the commercial design.

These findings underscore the efficacy of the new design, showcasing its ability to generate higher levels of light output while maintaining optimal lighting efficiency. The significant difference in polar intensity values further emphasizes the superior performance of the new design, making it a compelling choice for applications where maximizing light output is essential.

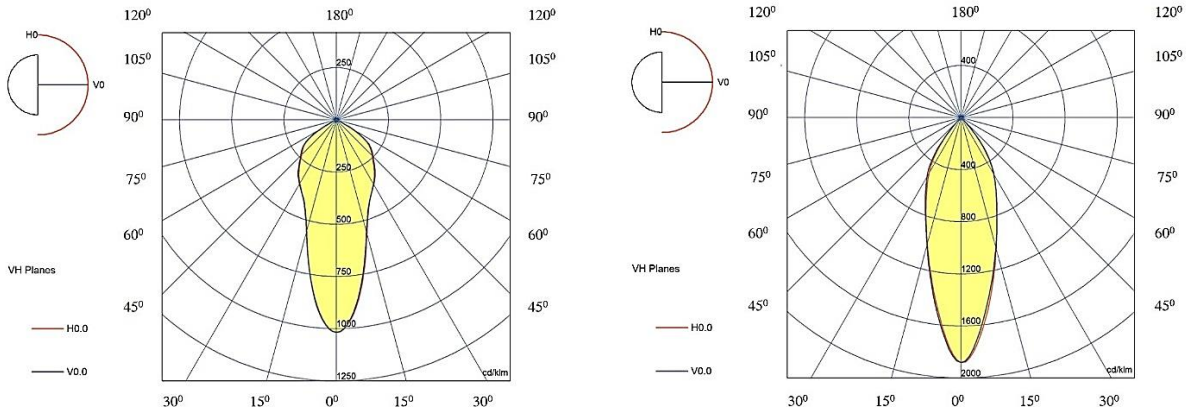

(a) (b)

Figure 4: Polar intensity diagram of integrated LED luminaire; (a) Commercial design without optic films; (b) New design with optic films

As depicted in Figure 4, the intensity data indicates that the LED luminaire with the optic film has an intensity of 1016 cd/klm whereas the LED luminaire without the optic film has an intensity of 1880 cd/klm. This result demonstrates that the LED luminaire with the optic film produces an intensity output that is 864 cd/klm higher than the luminaire without the optic film. To express this difference as a percentage, we can calculate the LED luminaire with the optic film provides an intensity output approximately 45.95% higher than the luminaire without the optic film.

5 CONCLUSIONS

The incorporation of an optic film in LED luminaires for rear lights has shown promising results in terms of improving light output efficiency. By replicating LEDs as virtual image lines and concentrating emitted light within specific angles, the optic film effectively reduces glare and enhances the overall efficiency of LED lighting systems.

The experimental results presented in this study clearly demonstrate the advantages of using the optic film. The LED luminaire equipped with the film exhibited a substantial 45.95% increase in intensity compared to the luminaire without the film, highlighting its potential to significantly improve lighting performance.

These findings have practical implications for various applications where maximizing light output and minimizing glare are essential considerations, such as automotive lighting and architectural lighting design. The optic film represents a valuable innovation in the field of LED lighting technology, offering a promising avenue for achieving enhanced lighting efficiency and improved visual comfort. Further research and development in this area hold the potential to drive advancements in energy-efficient and visually appealing lighting solutions.

REFERENCES

[1] Kim, Gayoung, Jung Wook Lim, Jieun Kim, Sun Jin Yun, and Min A. Park. "Transparent thin-film silicon solar cells for indoor light harvesting with conversion efficiencies of 36% without photodegradation." *ACS applied materials & interfaces* 12, no. 24 (2020): 27122-27130. https://doi.org/10.1021/acsami.0c04517

[2] Chang, Hong-Wei, Kun-Cheng Tien, Min-Hung Hsu, Yi-Hsiang Huang, Ming-Shiang Lin, Chih-Hung Tsai, Yu-Tang Tsai, and Chung-Chih Wu. "Organic light-emitting devices integrated with internal scattering layers for enhancing optical out-coupling." *Journal of the Society for Information Display* 19, no. 2 (2011): 196-204. https://doi.org/10.1889/JSID19.2.196

[3] Le, Hien-Thanh, Lanh-Thanh Le, Ming-Jui Chen, Thanh-Hong Lam, Hsing-Yuan Liao, Guo-Feng Luo, Yung-Cheng Li, and Hsiao-Yi Lee. "ECE/SAE dual functional superpin plus curved reflex reflector by use of new structured

corner cubes." Applied Sciences 10, no. 2 (2020): 454. https://doi.org/10.3390/app10020454

[4] Le, Hien-Thanh, Lanh-Thanh Le, Hsing-Yuan Liao, Ming-Jui Chen, Hsin-Yi Ma, and Hsiao-Yi Lee. "Design of low-glared LED rear light of automotive for EU ECE regulation by use of optimized micro-prisms array." Crystals 10, no. 2 (2020): 63. https://doi.org/10.3390/cryst10020063

[5] E.Brinksmeier; R.Glabe; C. Flucke; "Manufacturing of molds for replication of micro cube corner retroreflectors", Production Engineering, Vol 2, **(2008),** 33-38, DOI: https://doi.org/10.1007/s11740-008-0082-8

[6] H.D.Eckhardt; "Simple model of corner reflector phenomena",Appl Opt, Vol 10, **(1971)**, 1559–1566, DOI: https://doi.org/10.1364/AO.10.001559

[7] Lee, Jetter, Lanh-Thanh Le, Hien-Thanh Le, Hsing-Yuan Liao, Guan-Zhi Huang, Hsin-Yi Ma, Chan-Chuan Wen et al. "Low-glare freeform-surfaced street light luminaire optimization to meet enhanced road lighting standards." International Journal of Optics 2020 (2020): 1-12. https://doi.org/10.1155/2020/5683264

[8] Chen, Ming-Jui, Hien-Thanh Le, Lanh-Thanh Le, Wei-Hsiung Tseng, Wei-Yang Lee, Si-Yuan Chen, Sheng-Yen Chen, Hsing-Yuan Liao, Yung-Cheng Li, and Hsiao-Yi Lee. "Design of counter beam tunnel lights for CIE 88: 2004 regulation in threshold zone." International Journal of Optics 2020 (2020): 1-9. https://doi.org/10.1155/2020/6145638

[9] Joo, Chul Woong, Keunsoo Lee, Jonghee Lee, Hyunsu Cho, Jin-Wook Shin, Nam Sung Cho, and Jaehyun Moon. "Optical and structural approaches for improved luminance distribution and enhanced efficiency of organic light emitting diodes." *Journal of Luminescence* 187 (2017): 433-440. https://doi.org/10.1016/j.jlumin.2017.03.057

[10] Spinelli, Pierpaolo, V. E. Ferry, J. Van de Groep, M. Van Lare, M. A. Verschuuren, R. E. I. Schropp, H. A. Atwater, and A. Polman. "Plasmonic light trapping in thin-film Si solar cells." *Journal of Optics* 14, no. 2 (2012): 024002. https://10.1088/2040-8978/14/2/024002

[11] Le, H. T., Le, L. T., Nguyen, X. H., Le, T. N., & Lee, H. Y. (2022). Study of EU ECE Light Shaping Diffuser with high efficiency and uniformity for automotives. Optik, 265, 169487. https://doi.org/10.1016/j.ijleo.2022.169487

THREE-PHASE 3-LEVEL ACTIVE IMPEDANCE SOURCE T-TYPE INVERTER WITH DISCONTINUOUS PWM SCHEME

TAN-TAI-TRAN[1], DUC-TRI DO[2], HOANG-LINH THAI[2], TAN-HUNG NGUYEN[3], QUOC-THINH HO[4], TAN-LUONG VAN[4*]

[1]*Faculty of Electrical Engineering Technology, Industrial University of Ho Chi Minh City,*
[2]*Faculty of Electrical and Electronics Engineering, HCMC University of Technology and Education,*
[3]*Electrical and Mechanical Department, FPT Polytechnic,*
[4]*Faculty of Electrical and Electronics Engineering, HCM City University of Industry and Trade*
trantantai@iuh.edu.vn, tridd@hcmute.edu.vn, linhth@hcmute.edu.vn, hungnt169@fe.edu.vn, 1002221004@hufi.edu.vn, luongvt@hufi.edu.vn

Abstract. This paper presents a novel active quasi Z-source multilevel inverter, which incorporates an additional active switch and diode into the impedance-source network. The proposed topology consists of two main components: an active quasi-Z source to improve the inverter voltage gain and a front-side Three-phase 3-level T-type inverter. The shoot-through state is effectively incorporated into the operational state of the T-type inverter. This allows for appropriate input voltage handling by enabling the charging and discharging of components on the impedance network side, resulting in increased benefits. This paper proposes a discontinuous pulse width modulation (DPWM) scheme for controlling the inverter, which effectively reduces the number of commutations in comparison to traditional strategies. By adopting this approach, the inclusion of a shoot-through state does not result in any additional commutations when compared to conventional voltage-source inverters. This study will present analysis and simulation results as verification of the proposed approach's efficacy in order to ensure its reliability.

Keywords. DPWM, Multilevel Inverter, Impedance Source Network, Active quasi-Z Source inverter, T-type Inverter

1INTRODUCTION

The voltage source inverters (VSIs) have grown in popularity in modern industrial applications such as electric vehicles, renewable energy systems, energy storage systems, and motor control [1–3]. It is critical to choose an appropriate topology for these applications, taking into account factors such as high performance, compact size, cost-effectiveness, and availability. In this study, the use of a multilevel inverter appears to be a viable solution for meeting the aforementioned requirements. Figure 1 shows the conventional voltage source inverter.

The T-type inverter is a promising topology among various inverter topologies, offering significant advantages over other inverter family members. Because of its ability to achieve high energy conversion efficiency and improved power quality, this converter has gained popularity in automotive and photovoltaic (PV) systems [4]. In contrast to the traditional three-level neutral point clamped (NPC) inverter, the T-type inverter uses two active bidirectional switches connected to the DC-link voltage neutral point [5], reducing the need for two clamping diodes per phase leg [6]. Because of this design choice, conduction losses are reduced and the implementation is more compact. Furthermore, each bidirectional switch connected to the DC-link neutral point requires only half of the DC-link voltage to be withstandable, allowing for the use of lower voltage power devices [7].

The VSI and the current source inverter (CSI) are two common types of traditional two-level inverters. The VSI functions as a voltage buck converter, where the peak-to-peak value of the AC output phase voltage is lower than the DC link voltage. On the other hand, the CSI acts as a boost converter and requires additional

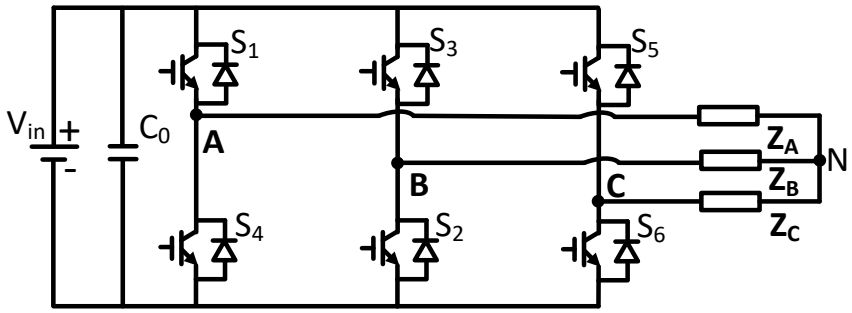

Figure 1: Conventional Voltage Source Inverter.

components such as diodes. There has been growing interest among researchers in inverters capable of accommodating a wide range of input voltages. However, conventional VSI and CSI inverters are not designed to handle such wide input voltage ranges [8]. As a solution, the conventional approach involves incorporating a DC-DC boost converter before the VSI, enabling buck-boost characteristics in a two-stage power conversion process. This configuration enhances the input voltage prior to feeding it into the inverter circuit. The operation of all switches in one or more phase legs, resulting in the formation of a short-circuit current, offers a considerable danger of system damage. This state, known as the shoot-through (ST) state, is absolutely forbidden in VSI.

To solve these issues, F.Z. Peng presented the Z-Source Inverter (ZSI) in 2003 as a novel approach based on impedance networks. The ZSI used an X-shaped arrangement with two inductors (L1, L2) and two capacitors (C1, C2) [9]. Figure 2 illustrates the topology of the Z-Source impedance network. The charge-discharge characteristics of these elements permitted an increase in the DC-Link voltage by selectively adding shoot-through operations. The ZSI, on the other hand, had some problems, such as discontinuous input current, higher beginning current, high voltage stress on capacitors, and bulky components. To address these shortcomings, the quasi-Z Source Inverter (q-ZSI) was developed. The q-ZSI preserved the benefits of the ZSI while adopting an alternative connecting approach based on passive power elements such as inductors (L) and capacitors (C). Notable features of the q-ZSI included continuous DC current, lower voltage stress on capacitors, and smaller component sizes. Because of these developments, the q-ZSI is a viable solution for dealing with the problems that traditional voltage source inverters [10].

A reduction in the required ST duty ratio corresponds to an increase in the boost factor or voltage gain. This decrease in duty ratio has the beneficial effect of lowering conduction loss and increasing system efficiency. Furthermore, the ST duty ratio has a significant impact on the current through the inductor. A lower duty ratio causes less inductor current ripple, reducing inductor size and increasing inverter power density [11]. The addition of the shoot-through state significantly increases the number of switching commutations. During the ST insertion process, conventional methods for impedance-source inverters generate at least two more commutations. These extra commutations contribute to increased switching losses in semiconductor devices. As an outcome, numerous studies on techniques for reducing switching commutations and minimizing the ST duty ratio have been conducted [12].

In this paper, a new active impedance source was presented by adding a switch and a diode to the traditional q-ZSI to eliminate the above disadvantages, which can be called an active quasi - z source inverter (Aq-ZSI). In addition, the discontinuous PWM algorithm (DPWM) is used to reduce switching commutations and increase efficiency for the T-type three-level inverter system. By changing the number of voltage levels, we only need to add the proposed impedance in quantity (n-1) where n is the number of level and n is an odd number. Theoretical analysis and simulation results will be performed in this study.

2 THREE-PHASE 3-LEVEL ACTIVE QUASI-Z SOURCE T-TYPE INVERTER

Fig.3 illustrates the topology of three-phase 3-level AqZS T-type Inverter (3L-AqZS-T^{2}I). This scheme includes a single-state boost DC-link and a three-level T-type inverter.

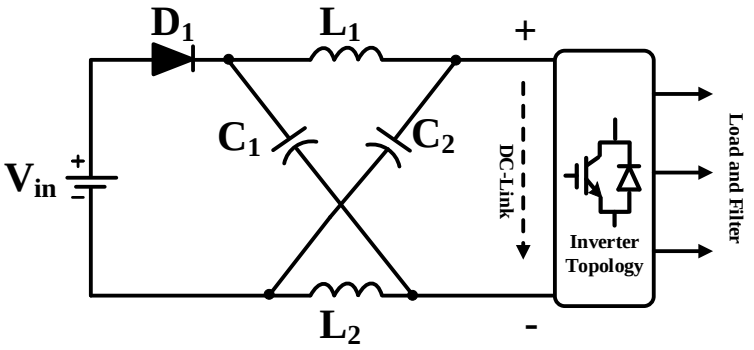

Figure 2: The topology of the Z-Source impedance network.

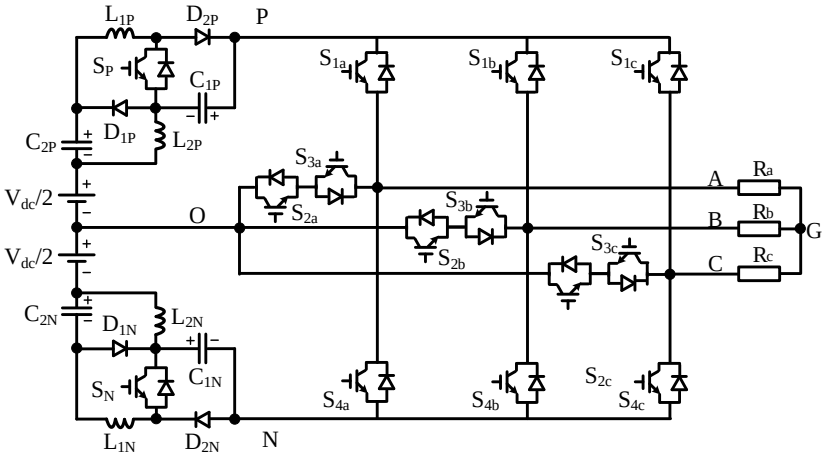

Figure 3: The topology of Three-phase 3-level AqZS T-type Inverter.

2.1Circuit Analysis

By focusing on the common-emitter node of the bidirectional switch, the 3L-AqZS-T^{2}I topology represents a significant advancement over conventional multilevel inverter design. The aim of this research is to effectively reduce the voltage stress experienced by the system's power switches. The 3L-AqZS-T^{2}I achieves enhanced voltage distribution and reliability by carefully analyzing and optimizing the common-emitter node. In terms of operation, the 3L-AqZS-T^{2}I topology is similar to a diode-free configuration. This eliminates the need for extra

diodes, which are commonly used in traditional designs. Like other three-level configurations, has three distinct voltage levels: positive (P), zero (O), and negative (N).

The 3L-AqZS-T^{2}I is operational in both ST and two non-shoot through (NST 1, NST 2) modes. Table 1 presents the output voltages that correspond to switching operating modes. Three states of the 3L-AqZS-T^{2}I are shown in Fig. 4. (in NST1, NST2 and ST). In the ST mode, all switches on at least one phase leg turn on, , and two switches (S_P and S_N) in impedance network turn off. Therefore charging the impedance network. Figure 4(a) shows the operation of the ST state

In the state of NST 1, S_P and S_N are turned on, diodes D_{2P} and D_{2N} are reverse biased while D_{1P} and D_{1N} are forward biased. This results in inductors L_{2P}, L_{2N} being shorted while L_{1P} and L_{1N} discharge. Capacitors C_{2P},C_{2N} discharge and C_{1P},C_{1N} charge due to the influence of energy from the inductors. The state of NST1 is shown in Figure 4(b). In NST 2, S_P and S_N are turn off, the topology works like a conventional T-type inverter. All diodes in impedance network are forward biased. Figure 4(c) illustrates the state of NST2.

The output voltages that correspond to the switch operating modes are shown in Table 1.

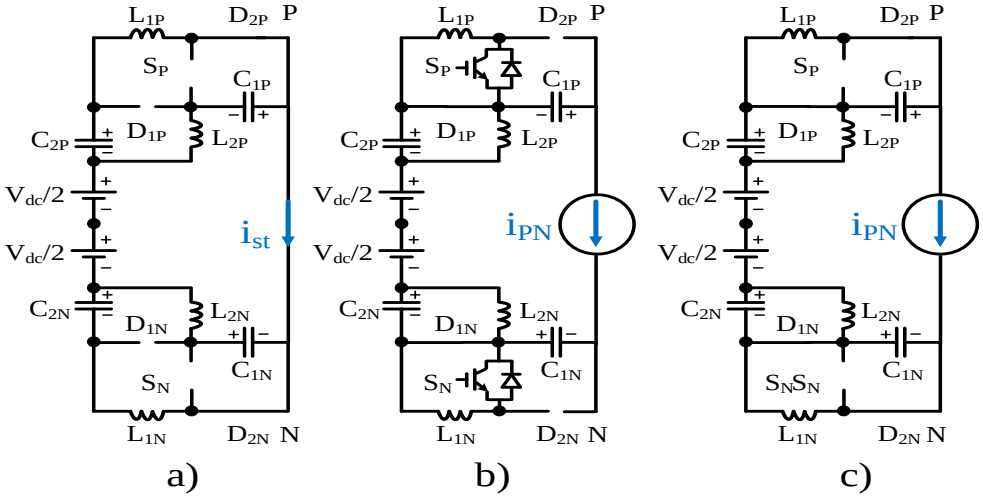

Figure 4: Operating modes of 3L-AqZS-T^{2}I. a) ST mode, b) NST1 mode, c) NST2 mode

2.2DPWM Scheme

To decrease switching commutation, the suggested approach adopts a DPWM mechanism for producing control signals to the inverter switches. To provide a complete description of this modulation approach, three signals $V_{ref\_x}\,(x=a,b,c)$ as follows:

$$\begin{cases} V_{ref\_a}=\dfrac{1}{\sqrt{3}}M\,\mathrm{Sin}\left(2\pi ft\right) \\ V_{ref\_b}=\dfrac{1}{\sqrt{3}}M\,\mathrm{Sin}\left(2\pi ft-120^0\right) \\ V_{ref\_c}=\dfrac{1}{\sqrt{3}}M\,\mathrm{Sin}\left(2\pi ft+120^0\right) \end{cases} \tag{1}$$

Where M is modulation index limited to $0<M<1$.

The above signals are re-modulated by subtracting the minimum from all 3 reference signals as follows:

$$\begin{cases} V^{*P}_{ref\_a}=V_{ref\_a}-\min(V_{ref\_a},V_{ref\_b},V_{ref\_c}) \\ V^{*P}_{ref\_b}=V_{ref\_b}-\min(V_{ref\_a},V_{ref\_b},V_{ref\_c}) \\ V^{*P}_{ref\_c}=V_{ref\_c}-\min(V_{ref\_a},V_{ref\_b},V_{ref\_c}) \\ V^{*N}_{ref\_a}=V^{*P}_{ref\_a}-180^0 \\ V^{*N}_{ref\_b}=V^{*P}_{ref\_b}-180^0 \\ V^{*N}_{ref\_c}=V^{*P}_{ref\_c}-180^0 \end{cases} \tag{2}$$

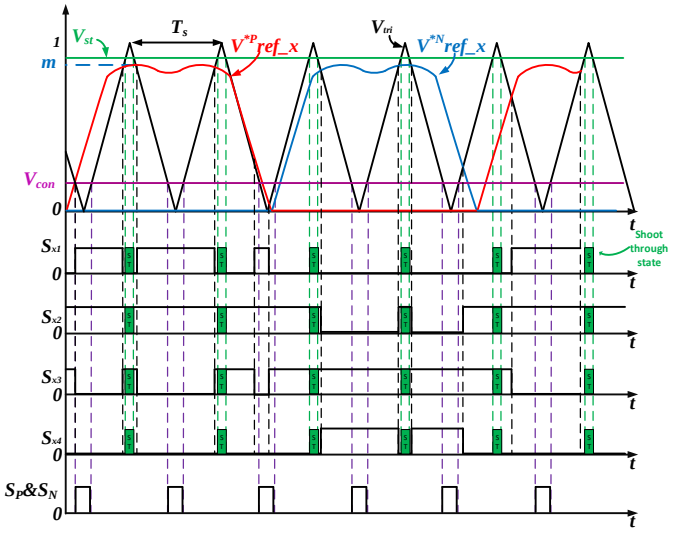

Figure 5: Waveforms of gating signals of control technique for the 3L-AqZS-T^{2}I inverter using DPWM algothirim

Table 1: The switching states and the output voltage of 3L-AQZS-T^{2}I

Mode	State of switches			Output voltage
	S_P	S_N	Other Switch (x=a, b, c)	
NST1	ON	ON	S_{1x},S_{2x}/S_{2x},S_{3x}/S_{3x},S_{4x}	+$V_{dc/2}$, 0, or -$V_{dc/2}$
NST2	OFF	OFF	S_{1x},S_{2x}/S_{2x},S_{3x}/S_{3x},S_{4x}	+$V_{dc/2}$, 0, or -$V_{dc/2}$
ST	OFF	OFF	S_{1x},S_{2x},S_{3x},S_{4x}	0

V_{ST} are constant reference voltages used to generate the shoot-through state. We have $V_{ST} = 1 - d$. With d is shoot-through ratio $(0 < d < 1)$.When the shoot-through condition occurs in this DPWM algorithm, all switches are switched on. The v_{con} signal provides the control signal for the two switches S_P and S_N. The V_{con} is defined as:

$$v_{con} = d_0 \tag{3}$$

Where d_0 is duty ratio of S_P and S_N. To ensure stable operation of the system, the value of vcon must satisfy the following requirements:

$$v_{con} \le \frac{\sqrt{3}M}{2} \tag{4}$$

All the above reference signals will be compared with a high frequency triangle pulse V_{tri} to generate control signals for the switches. Figure 5 illustrates the control scheme using DPWM.

From the operating principles and algorithms just presented, we determine $C_{1P}, C_{2P}, C_{1N}, C_{2N}$ as follows:

$$V_{C_{1P}} = V_{C_{1N}} = \frac{V_{dc/2}(1-d_0).d}{1-d_0-2d+d.d_0} \quad (5)$$

$$V_{C_{2P}} = V_{C_{2N}} = \frac{(V_{dc/2})d}{1-d_0-2d+d.d_0} \quad (6)$$

From equation (5) and (6), the DC-link voltage (V_{PN}) can be defined as:

$$V_{PN} = \underbrace{(V_{C_{1P}} + V_{C2P} + V_{dc/2})}_{\text{Upper impedace source network}} + \underbrace{(V_{C_{1N}} + V_{C2N} + V_{dc/2})}_{\text{Lower impedace source network}} = \frac{V_{dc}(1-d_0)}{1-d_0-2d+d.d_0} \quad (7)$$

The inverter's boost factor, B, can be described as:

$$B = \frac{V_{PN}}{V_{dc}} = \frac{1-d_0}{1-d_0-d(2+d_0)} \quad (8)$$

The determination of the peak value of the fundamental component of the output phase voltage is carried out according to the following procedure:

$$\hat{V}_x = M.B.\frac{V_{dc}}{2} \quad (9)$$

Where $\hat{V}_x$ is the input voltage of the inverter after impedance network. The voltage gain (G) is defined as:

$$G = \hat{V}_x / V_{dc} \quad (10)$$

3 SIMULATION RESULTS

To validate the performance of the DPWM approach for the 3L-AqZS-T^{2}I topology, extensive simulations were performed utilizing the PSIM simulation software. The simulations occurred with the settings listed in Table II, allowing a thorough examination of the technique's operation and effectiveness.

Table 2: Parameters used in simulation.

Parameters	**Value**
Input voltage	$180V_{DC}$
DC-link	$328V_{DC}$
Output voltage	$220V_{peak}$
Output current	$2.6A_{rms}$
Shoot-through ratio (D_{st})	0.2
Duty ratio of S_P and S_N	0.2
Modulation index	0.8
Carrier frequency	10kHz
Inductance(L_1,L_2,L_3,L_4)	500uH
Capacitance (C_1,C_2,C_3,C_4)	1mF
Load	40Ω
Lowpass Filter	3mH/10uF

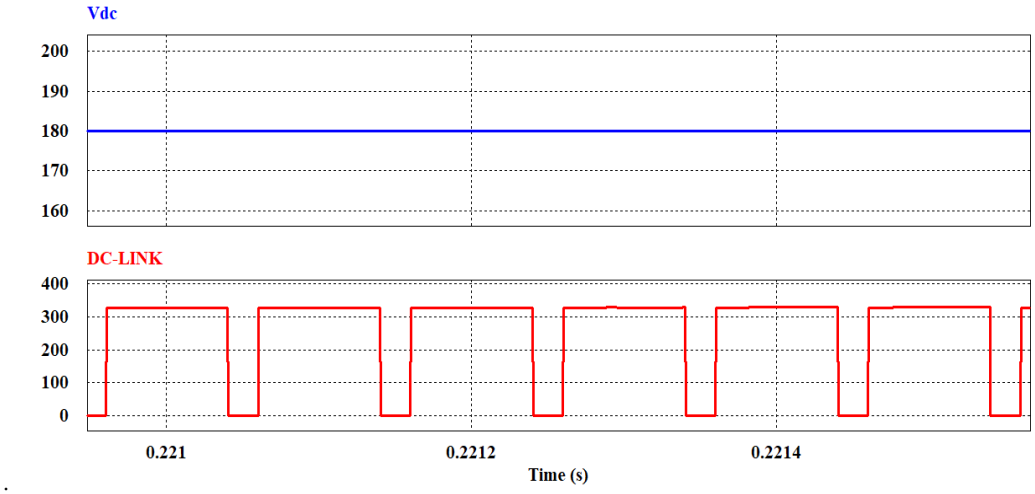

Figure 6: Simulation results of 3L-aqZS-T^{2}I are presented in order from top to bottom input voltage Vin, DC-link voltage.

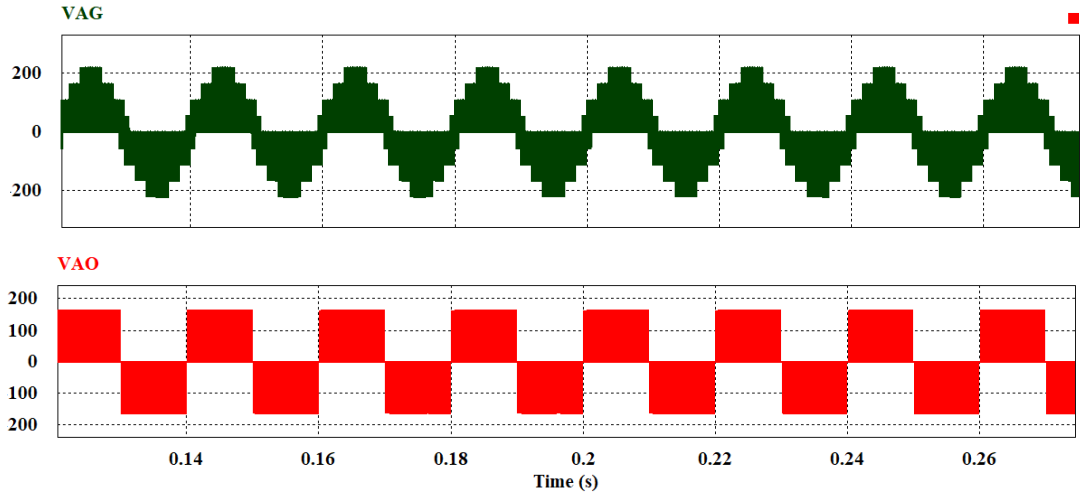

Figure 7: Simulation results of 3L-aqZS-T¬2I. From top to bottom waveform of the output phase voltage V_{AG}, the pole voltage V_{AO}

Figure 6 depicts the simulation results for the 3L-AqZS-T^{2}I configuration. The input voltage is specified as V_{in}=180Vdc, and the DC-Link voltage is 328 Vdc with a duty cycle of 0.2. Because of the reconfiguration of the shoot-through signal, the DC-Link voltage in the proposed topology exceeds that of a traditional impedance network. A single occurrence of the shoot-through signal causes an increase in the DC-Link voltage within each cycle, accounting for the observed increase

Figure 7 displays the waveform of the output phase voltage for the 3L-AqZS-T^{2}I configuration prior to being filtered by a low-pass filter. Notably, the output phase voltage exhibits 9 voltage levels, reflecting the multilevel nature of the inverter. On the other hand, the pole voltage V_{AO} illustrates the terminal voltage, which features 3 voltage levels: DC-link/2,0, -DC-link/2.

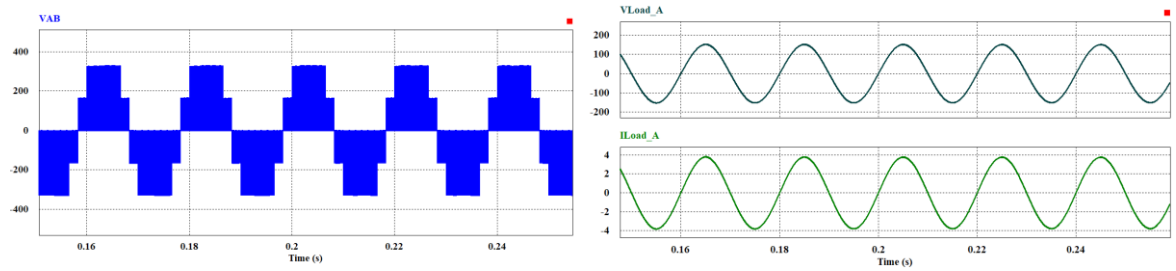

(a) (b)

Figure 8: Simulation results of 3L-aqZS-T^{2}I. (a)the output line voltage; (b) Phase voltage and current through the load after passing the LC filter.

Fig.8 (a) shows the line voltage of the 3L-AqZS-T^{2}I. This result is obtained between phase A and phase B with the value V_{AB}=218V_{RMS}; (b) shows the voltage and current through the load after being filtered by a low-pass filter. With a base frequency of 50Hz.

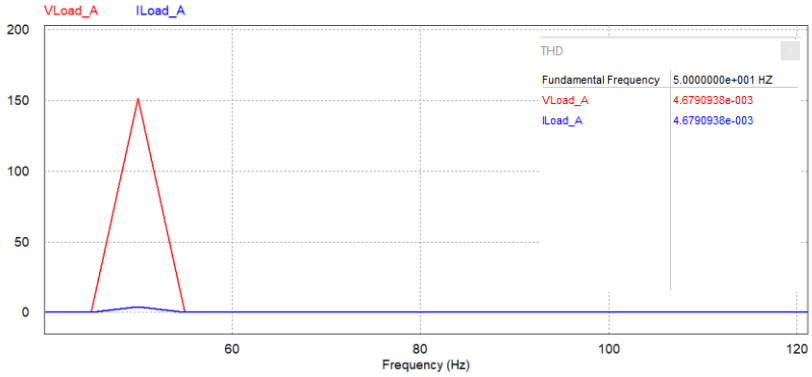

Figure 9: Harmonic analysis findings utilizing the FFT method on a linear load to obtain THD_u and THD_i

The author employed linear load in this work to simplify testing the proposed algorithm and topology. As a result of passing via the LC filter, we get THDu=THDi=4.67%. Fig.9 depicts the Psim software calculation findings.

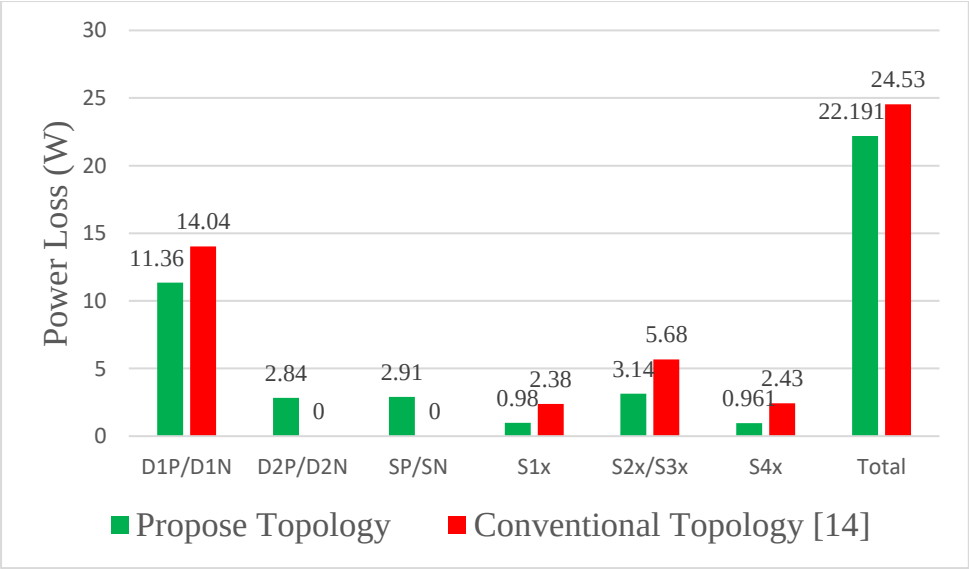

Figure 10: Calculation results comparing power loss between the proposed topology and conventional topology.

By evaluating the power loss components on the device, as shown in [13], we can see that the proposed topology has about 10% lower power loss than the conventional topology [14]. Fig.10 depicts the calculation results when configured to operate at 0.5kW output power.

4CONCLUSION

This study recommends the 3L-AqZS-T^2I topology for low to medium-power industrial applications that use a DPWM control scheme. The output voltage results obtained are in accordance with the specifications. The use of a shoot-through insertion algorithm and a Discontinuous PWM scheme effectively increases the output voltage while minimizing switching commutations in the system. To support the proposed approach, the study includes extensive circuit analysis and operating theory. The PSIM software simulation confirms the accuracy of the proposed method, as the simulation and calculation results agree. Overall, the 3L-AqZS-T^2I topology performs well and has the potential for practical implementation in relevant industrial applications.

REFERENCES

[1] A. Poorfakhraei, M. Narimani and A. Emadi, "A Review of Multilevel Inverter Topologies in Electric Vehicles: Current Status and Future Trends," in IEEE Open Journal of Power Electronics, vol. 2, pp. 155-170, 2021.

[2] C. Liao, W. Lin, Y. Chen and C. Chou, "A PV Micro-inverter With PV Current Decoupling Strategy," in IEEE Transactions on Power Electronics, vol. 32, no. 8, pp. 6544-6557, Aug. 2017.

[3] M. A. Hannan, J. A. Ali, P. J. Ker, A. Mohamed, M. S. H. Lipu and A. Hussain, "Switching Techniques and Intelligent Controllers for Induction Motor Drive: Issues and Recommendations," in IEEE Access, vol. 6, pp. 47489-47510, 2018.

[4] Do, D.T.; Tran, V.T.; Nguyen, M.K. Enhanced Boost Factor for Three-Level Quasi- Switched Boost T-Type Inverter. Energies 2021, Vol. 14, 13, 1-17.

[5] Do, D.T. A Single-Stage Neutral Point Clamp Inverter with Reduced Voltage Stresses on Power Elements. Measurement, Control, and Automation, Vol. 2, 2, 24-31, 2021.

[6] Y. Wang, W. W. Shi, N. Xie and C. M. Wang, "Diode-Free T-Type Three-Level Neutral-Point-Clamped Inverter for Low-Voltage Renewable Energy System," in IEEE Transactions on Industrial Electronics, vol. 61, no. 11, pp. 6168-6174, Nov. 2014.

[7] Mokhtar, A., Gamal, M. and Masahito, S. (2015) 'Design and validation of SVPWM algorithm for thermal protection of T-type threelevel inverters', IEEE International Telecommunications Energy Conference (INTELEC), Osaka, Japan.

[8] X. Guo, Y. Bai and B. Wang, "A Programmable Single-Phase Multilevel Current Source Inverter," in IEEE Access, vol. 7, pp. 102417-102426, 2019.

[9] Fang Zheng Peng, "Z-source inverter," in IEEE Transactions on Industry Applications, vol. 39, no. 2, pp. 504-510, March-April 2003.

[10] J. Anderson and F. Z. Peng, "Four quasi-Z-Source inverters," 2008 IEEE Power Electronics Specialists Conference, Rhodes, Greece, 2008, pp. 2743-2749.

[11] Y. Gu, Y. Chen and B. Zhang, "Enhanced-Boost Quasi-Z-Source Inverter With an Active Switched Z-Network," in IEEE Transactions on Industrial Electronics, vol. 65, no. 10, pp. 8372-8381, Oct. 2018.

[12] Y. Liu, B. Ge, H. Abu-Rub and H. Sun, "Hybrid Pulsewidth Modulated Single-Phase Quasi-Z-Source Grid-Tie Photovoltaic Power System," in IEEE Transactions on Industrial Informatics, vol. 12, no. 2, pp. 621-632, April 2016.

[13] Ahmed, M. H., Wang, M., Hassan, M. A. S., & Ullah, I. (2019). Power Loss Model and Efficiency Analysis of Three-phase Inverter Based on SiC MOSFETs for PV Applications. IEEE Access, 1–1.

[14] J. Anderson and F. Z. Peng, "Four quasi-Z-Source inverters," 2008 IEEE Power Electronics Specialists Conference, Rhodes, Greece, 2008, pp. 2743-2749.

PROCEEDING - ICSET2023 INTERNATIONAL CONFERENCE ON SUSTAINABLE ENERGY TECHNOLOGIES (ICSET2023)

TRƯỜNG ĐẠI HỌC CÔNG NGHIỆP THÀNH PHỐ HỒ CHÍ MINH

NHÀ XUẤT BẢN
ĐẠI HỌC CÔNG NGHIỆP TP HỒ CHÍ MINH
12 Nguyễn Văn Bảo – P. 4 – Q. Gò Vấp – TPHCM
ĐT: (028) 3894 0390 – 816
Email: nhaxuatban@iuh.edu.vn

Chịu trách nhiệm xuất bản: PHẠM TRUNG KIÊN

Biên tập: LÊ THỊ TIỂU NHI
Sửa bản in: ĐOÀN THANH ĐIỀN
Trình bày bìa: VĂN SANG

Đối tác liên kết: Trường Đại học Công nghiệp Thành phố Hồ Chí Minh

ISBN: 978-604-920-208-7

In 300 cuốn khổ 20 × 28 cm theo Quyết định xuất bản số: 33/QĐ-NXBĐHCN ngày 05/12/2023 với xác nhận đăng kí xuất bản số 3873-2023/CXBIPH/1–19/ĐHCNTPHCM ngày 01/11/2023. In tại Xưởng in NXB Đại học Công nghiệp TPHCM, nộp lưu chiểu tháng 12/2023.